

# MECHANISM-BASED DESIGN OF COMPOSITE STRUCTURES

## FINAL REPORT

### Volume I:

- Executive Summary
- Overview Papers
- Research Papers on Micromechanics and Computer-Aided Design Tools

### Volume II:

- Research Papers on Micromechanics and Computer-Aided Design Tools

DISTRIBUTION STATEMENT A

Approved for public release  
Distribution Unlimited

### Volume III:

- Research Papers on Processing and Performance

Program Director:  
George J. Dvorak  
Rensselaer Polytechnic Institute  
Troy, NY 12180-3590

University Research Initiative  
Contract No.: N00014-92J-1779  
May 1, 1992 - August 30, 1997

19980209 074

Sponsored by the Defense Advanced Research Projects Agency  
Dr. William Coblenz

Monitored by the Office of Naval Research  
Dr. Steven Fishman

DTIC QUALITY INSPECTED 4

# **MECHANISM-BASED DESIGN OF COMPOSITE STRUCTURES**

## **FINAL REPORT**

### **Volume I:**

- **Executive Summary**
- **Overview Papers**
- **Research Papers on Micromechanics and  
Computer-Aided Design Tools**

### **Volume II:**

- **Research Papers on Micromechanics and  
Computer-Aided Design Tools**

### **Volume III:**

- **Research Papers on Processing and Performance**

Program Director:  
George J. Dvorak  
Rensselaer Polytechnic Institute  
Troy, NY 12180-3590

University Research Initiative  
Contract No.: N00014-92J-1779  
May 1, 1992 - August 30, 1997

Sponsored by the Defense Advanced Research Projects Agency  
Dr. William Coblentz

Monitored by the Office of Naval Research  
Dr. Steven Fishman

## MECHANISM-BASED DESIGN OF COMPOSITE STRUCTURES

### Volume I:

- **Executive Summary**
- **Overview Papers** presented at The American Ceramic Society 21st Annual Cocoa Beach Conference and Exposition on Composites, Advanced Ceramics, Materials and Structures January 1997

Dvorak, G.J., Mechanism-Based Design of Composite Structures Program Overview and Accomplishments.

Wentorf, R., Shephard, M.S., Dvorak, G.J., Fish, J., Beall, M.W., Collar, R., and Shek, K.-L., Software Framework for Mechanism-Based Design of Composite Structures.

Adjerid, S., Aiffa, M., Flaherty, J.E., Hudson, J.B., and Shephard, M.S., Modeling and Adaptive Numerical Techniques for Oxidation of Ceramic Composites.

Fish, J., Shek, K.-L., Gomaa, S., Shephard, M.S., Dvorak, G.J., Bachrach, W.E., and Wafa, A.M., Modeling and Simulation of Failure Processes in Composites.

Sternstein, S.S., and Warren, R., Dynamic and Transient Characterization of Ceramic Fibers at Elevated Temperatures.

Augustin, S., Broglio, M., Lipetzky, P., and Stoloff, N.S., Improved Properties of Silicide Matrix Composites.

Lipetzky, P., Dvorak, G.J., and Stoloff, N.S., Multi-Axial Response of a Woven Continuous-Fiber Composite.

Lipetzky, P., Stoloff, N.S. and Dvorak, G.J., Atmospheric Effects on High-Temperature Lifetime of Ceramic Composites.

Lipetzky, P., Lieblich, M., Hillig, W., and Duquette, D., Effect of Salt Corrosion on Mechanical Properties of a SiC-SiC Composite in Dry and Moist High-Temperature Environment.

Lipetzky, P., Lieblich, M., Hillig, W. and Duquette, D., Behavior of SiC-Fiber/AL<sub>2</sub>O<sub>3</sub> Composite with NA-Based Salts in Dry and Moist Oxidizing Environments.

## MECHANISM-BASED DESIGN OF COMPOSITE STRUCTURES

- Research Papers on Micromechanics and Computer-Aided Design Tools

Adjerid, S., Flaherty, J.E., Hillig, W., Hudson, J. and Shephard, M.S., Adaptive Method of Lines Techniques for Vapor Infiltration Problems.

Adjerid, S., Flaherty, J.E., Shephard, M.S., Wang, Y.J., Adaptive Numerical Techniques for Reactive Vapor Infiltration.

Adjerid, S., Beall, M.W., Dvorak, G.J., Fish, J., Flaherty, J.E., Hudson, J., Shek, K.-L., Shephard, M.S., and Wentorf, R. Mechanism-Based Design of Composite Structures.

Adjerid, S. Babuska, Ivo, and Flaherty, J.E., A Posteriori Error Estimation for the Finite Element Method-of-Lines Solution of Parabolic Problems.

Bahei-El-Din, Dvorak, G.J., and Wu, J.F., Mechanics of Hot Isostatic Pressing in Intermetallic Matrix Composites.

Beall, M.W., Fish, J., Shephard, M.S., Dvorak, G.J., Shek, K.-L., and Wentorf, R., Computer-Aided Modeling Tools for Composite Materials.

Beall, M.W., Belsky, V., Fish, J., and Shephard, M.S., Automated Multiple Scale Fracture Analysis.

Beall, M.W., and Shephard, M.S., A Geometry-Based Analysis Framework.

Beall, M.W., and Shephard, M.S., A Geometry-Based Framework for Reliable Numerical Simulations.

Belsky, V., Beall, M.W., Fish, J., Shephard, M.S., and Gomaa, S., Computer-Aided Multiscale Modeling Tools for Composite Materials and Structures.

Belsky, V., and Fish, J., Towards an Ultimate Finite Element Oriented Solver on Unstructured Meshes.

Collar, R., Wentorf, R., Shephard, M.S., Fish, J., Qu, Y., and Shek, K.-L., Automated Analyses of Three-Dimensional Composite Unit Cells.



## EXECUTIVE SUMMARY

This research program was funded in 1992–1997 by the Defense Advanced Research Project Agency of the Department of Defense, under the University Research Initiative at Rensselaer Polytechnic Institute, and administered by the Office of Naval Research. The main focus of the program was to provide research support and computational tools for processing and design of high-temperature composite materials and structures.

Professor George Dvorak served as Program Director. The co-principal investigators included Professors David Duquette, Jacob Fish, Joseph Flaherty, William Hillig, John Hudson, Mark Shephard, Sanford Sternstein and Norman Stoloff, all of Rensselaer Polytechnic Institute. About 25 graduate students have participated at different stages of their degree programs.

The overall goal of the research program was the development of material behavior models, their implementation in a software framework, and completion of related material processing and characterization studies to support mechanism-based design of composite materials and structures. This included micromechanical modeling of elastic and inelastic behavior and damage, and implementation in multiscale computational analysis at the micro, meso and macrolevels; modeling of hot pressing of metal matrix composites, and of vapor deposition processes for fabrication of ceramic matrix composites and fibers; characterization of certain commercially available fibers and composite systems; and processing and characterization of  $\text{MoSi}_2$  and  $\text{Cr}_3\text{Si}$  – based composites.

### MICROMECHANICAL MODELING

Mechanism-based design of composite structures involves modeling of material responses and interactions on different physical scales, ranging from the reinforcement – matrix microscale, through the dimensions of plies or woven layers in a laminate, to the macroscale of actual composite parts. Evaluation of the overall thermomechanical response of the composite material systems and laminates in terms of the geometry and properties of the constituent phases was

accomplished by several methods. Among the available techniques were the averaging methods, such as the Mori-Tanaka and self-consistent estimates, and the Hashin-Shtrikman bounds. These provide the effective elastic moduli, thermal expansion coefficients, and thermal diffusivities, together with estimates of the average mechanical and thermal fields in the constituents and at their interfaces.

The techniques developed under the present program include the transformation field analysis (TFA) for evaluation of the inelastic response and the associated local fields in the phases and plies for systems with viscoelastic or thermo-viscoplastic matrices and/or fibers, both in the perfectly bonded state and after fiber decohesion. The transformation analysis regards any inelastic deformation, as well as thermal deformations or phase transformations, as a stress-free strain or eigenstrain that is applied to an otherwise elastic composite material or laminate together with the prescribed mechanical loads. Using certain transformation concentration factors and constitutive relations for the inelastic phases, this method provides a set of differential equations for evaluation of the instantaneous local fields in the phases, or at integration points in finite elements of subdivided unit cells. The instantaneous overall response of the composite or laminate is then obtained in terms of the local fields. Certain damage processes, such as progressive particle or fiber debonding and sliding, have also been modeled in terms of transformation strains. A unified procedure for determination of overall loading conditions that cause onset and initial evolution of local damage in laminates has been developed and the results displayed as initial and subsequent failure maps. These maps are plotted in laminate stress coordinates and consist of a number of branches that represent critical magnitudes of local stresses within individual plies which may initiate local cracking in the fibers, matrices or at interfaces. Such maps are now available for symmetric metal and ceramic matrix laminates. They include the effect of residual stresses, generated by thermal changes and inelastic deformation during processing and in service, on the onset of damage in laminates. Models of progressive interfacial debonding in particulate and fibrous composites were developed, together with studies the effect of fiber size on debonding energy. The results indicate that for given interface properties, small diameter fibers and particles are more resistant to debonding than larger ones.

Functionally graded composite materials with variable moduli and thermal expansion coefficients are useful in fabrication of coatings, parts subjected to thermal gradients, and also in joining ceramic and metal parts. Much work in recent years has been devoted to development of modeling methods for these material systems. Our work has been concerned with comparisons of average local fields and overall response of discrete and homogenized models for functionally graded materials under several typical thermomechanical loading conditions. Steady state heat conduction problem were also solved and the resulting temperature distributions compared. The results of these comparisons indicate that standard averaging methods can be used in replacing graded systems by homogenized layered systems, providing that the Mori-Tanaka method is used in those parts of the microstructure which have a well-defined matrix, and the self-consistent method in parts with skeletal microstructures. Nonlocal methods were also developed, but should be needed only in situations where field gradients are large and field averages small.

Experimental characterization of fabric reinforced SiC/SiC and SiC/Al<sub>2</sub>O<sub>3</sub> coupon and tube specimens, obtained from DuPont Lanxide, Inc., was a part of the modeling program. Apart from specific strength and endurance data at both ambient and elevated temperatures, the experiments provide information on overall response of these fabric-reinforced composites during damage development and in saturation damage state. A substantial part of the overall strength is preserved even after extensive matrix damage. Work is under way to determine and experimentally verify under combined plane-stress loading the constitutive equations that govern mechanical response of these systems.

## DESIGN AND ANALYSIS SOFTWARE

In the area of software development, we have completed development of mechanism-based multi-scale analysis tools for fabricating and designing high-temperature composite materials and structures. The new capability links deformation, damage and crack propagation behaviors at three physical scales, the fiber/particle microscale, ply/weave mesoscale and the part or structure macroscale. Detailed geometrical models with automatically generated meshes and modification tools, various homogenization methods and advanced visualization

modes and attributes are available at all three scales. For example, design changes in reinforcement shape and orientation can be translated into overall composite properties and hence to deformation of a part or structure under load. Any chosen structure can be evaluated under prescribed thermal and mechanical service loads at all three scales for local stresses, temperatures, and deformation and damage states. These capabilities are applicable to CMCs, MMCs and PMCs with complex architectures and possibly hybrid reinforcement, and allow for linear or nonlinear behaviors with temperature-dependent material properties. Both in-house and commercially available software codes and data bases were assembled to provide a range capabilities with different computational costs and complexities, and integration of computed results with material testing. Also, extensive work was completed on simulations of manufacturing processes, such a hot isostatic pressing, diffusion bonding, reactive vapor infiltration and chemical vapor deposition.

The CAD framework offers the designer numerous tools for modeling, analysis and design of both composite material systems and large composite structures, while controlling idealization errors through multiscale, adaptive or heuristic means. The high-temperature property database contains over 320 material systems or constituents, 18,000 values and 180 material characteristics. Geometric modeling tools built on commercial geometric modelers create microstructures, weaves, plies, laminates and part scale models, and source their data from a user-selected properties and design parameters in a spreadsheet format. An analysis attribute code links physical material properties and boundary conditions with the micro- and/or macro-structural geometry. Automatic meshing tools, generic mesh operations and data structures, and the interfaces to multiple finite element analysis codes complete the integration of automated modeling tools for finite element analysis.

The system invites the user to construct an "analysis goal" in terms of design description and analysis characteristics. These include functionality definitions, such as thermomechanical boundary conditions within prescribed deflections and heat flow direction; and specification of the type of analysis result, time and reliability needed to confirm the governing behavior. The goal description is converted into a data flow model and a sequence of code executions, or a "strategy" that provides the desired results to the user. The execution of

the analysis goal is similar to using a spreadsheet function, requiring no expertise in the underlying theories or software development. The user is informed of any specific problem with the selected design parameters. The results are automatically computed and returned to the spreadsheet, used as input in subsequent design steps, or displayed by a visualization code.

Material modeling capabilities of the system include codes for evaluation of elastic properties of various composite material systems, initial failure maps of the constituents and their interfaces, and mathematical homogenization of unit cells that represent behavior of periodic microstructures with complex internal geometries, such as aligned or random fiber and particle distributions and weaves. The composite material properties, such as elastic moduli, CTEs, and heat conductivities are evaluated with several micromechanical averaging methods, or in terms of Hashin-Shtrikman bounds, in terms of constituent properties, their geometry and volume fractions. Associated codes evaluate mechanical, thermal, and transformation concentration factors which provide averages of local stress and strain fields in the phases under prescribed overall stresses, temperature changes, or phase transformations. Inverse routines are available for evaluation of *in situ* reinforcement properties from overall composite and neat matrix experimental data. The results are displayed in comprehensive graphs which show, for example, overall property variations in terms of phase geometry, volume fractions and temperature.

Efficient procedures for accurate solutions of structural problems with inelastic materials, where the deformation history needs to be evaluated at all integration points and modeling scales involved have also been developed with novel modeling schemes based on mathematical homogenization theory with eigenstrains and the transformation field analysis. Solution of the very large systems involved is now possible at a cost comparable to problems in homogeneous media, without significantly compromising solution accuracy.

## PROCESS MODELING

Adaptive software has been developed for solving fabrication and longevity problems in ceramic matrix composites. Also, mathematical models were formulated for three processes, (i) manufacture of CMCs by reactive vapor

infiltration, (ii) coating of ceramic fibers by CVD, and (iii) oxidation of ceramic composites.

The adaptive software solves steady state or transient reaction, convection and diffusion problems in in two dimensions, and to a limited extent also in three dimensions. Estimates of discretization errors are used to monitor accuracy and control the adaptive solution procedure. Accurate and efficient simulations of complex phenomena, such as sharp moving interfaces and reaction zones, have been implemented through automatic mesh refinement and coarsening (h-refinement), method-order variation (p-refinement), and mesh motion (r-refinement). Severe material distortions that occur during deposition, heating and cooling can thus be followed. A user-friendly interface has been implemented that allows for changes in the mathematical model and system parameters. The software executes on both serial and parallel systems.

The reactive vapor infiltration work focused on fabrication of  $\text{MoSi}_2$  composites. The key reactions and dilatation driven mechanical deformation were reflected in the model that predicted reaction rates within 10%, and final porosities within 1-2% of observed values. Process improvements were suggested for reduction of severe swelling an possible cracking and confirmed by experiment. The improved process was started with a powdered mixture of Mo and  $\text{MoSi}_2$ , instead Mo alone. Predicted siliciding proceeded at twice the rate of the homogenous powder, and after compression to 45% porosity, the pores filled without appreciable swelling.

Coating by CVD of sapphire fibers with beta-alumina was modeled in hot and cold-water reactors. Critical process parameters for production of even coatings include the flow rate, the speed of the fiber, the injection rate of the (reactive) precursor species in the flow, and the reactor temperature. Strategies have been identified to minimize wall coating and process time while producing a uniform fiber coating. The model is capable of analyzing transient and steady flows of multiple species, heating by conduction, convection and radiation, chemical surface reactions, and geometry changes due to fiber motion and deposition. Cold-walled reactors appear to be much more efficient than hot-walled ones, and injecting the precursor into the flow near the fiber minimizes losses.

Oxidation of CMC matrices by gaseous species was modeled as a coupled reaction diffusion system for chemical species, with gaseous oxidants that permeate protective coatings and react with the viscous matrix material that deforms according to the Navier-Stokes equations. The reaction of oxygen and water vapor with a ceramic matrix in the vicinity of a small crack have been described as a two-phase diffusion of gases in the crack and their diffusion and convection in the solid matrix. Gaseous flows involve both bulk and Knudsen diffusion. Improvements under consideration include modeling of self contact to describe visco-elastic or visco-plastic material deformation after the crack has closed, and analyses of systems of interacting cracks and fibers of various distributions.

## MATERIALS PROCESSING AND CHARACTERIZATION

The processing effort focused on intermetallic compounds with attractive high temperature properties, such as high melting point, low densities and excellent oxidation resistance compared to nickel-based superalloys. Two Mo-modified  $\text{Cr}_3\text{Si}$  compounds were consolidated from prealloyed powders. To improve toughness, 15% volume fraction reinforcement by Saphicon short fibers, and ductile continuous Pt alloy fibers was introduced. Results have shown no significant changes in stiffness due to the reinforcement, but a significantly higher toughness was measured at elevated temperatures. Also, the unnotched strength at 1000–1100°C increased from that at the room temperature due to the inclusion of fibers. Oxidation tests at 500°C showed absence of the "pest" phenomenon, and good resistance at 1250°C. Another system studied was  $\text{MoSi}_2$  reinforced with SiC whiskers and/or particles. Consolidation by reactive sintering of elemental powders was used in an attempt to reduce cost and improve purity. The high temperature strength of reinforced  $\text{MoSi}_2$  increased until 1200°C, presumably indicating some effect from the smaller grains and cleaner product, and a major contribution from the reinforcement. The results suggest that both systems show promising high-temperature properties with a potential for further improvement.

Experimental investigation of fiber coatings by CVD was carried out in a low pressure reactor, with deposition of aluminum nitride from an organoaluminum precursor on sapphire fibers. Coherent, pinhole-free were prepared by this technique and incorporated into a  $\text{MoSi}_2$  matrix. the AlN coatings protected the

fibers from attack by HCl generated by forming the  $\text{MoSi}_2$  by the reaction of  $\text{SiCl}_4$  with bulk Mo in H atmosphere. Unprotected fibers were completely consumed by the reaction.

Coupon and tubular samples of two commercially available composite systems were obtained from DuPont Lanxide, Inc. One set was enhanced SiC/SiC combined with proprietary inhibitors, reinforced with a 8-10 layer (0/90) plain weave fabric, at 35% fiber volume fraction. The 15% void volume was unevenly distributed as macroscopic surface-connected pores within and between the plies. The second system was a SiC fabric (12-harness satin weave) reinforced  $\text{Al}_2\text{O}_3$  manufactured using the Lanxide DiMOx process. The matrix was formed by directional oxidation of a molten alloy, with about 2% trapped residual metal. Porosity is microscopic and well-dispersed, but extensive matrix microcracking was observed on as-received samples. Baseline data show Young's modulus and proportional limit approximately constant between 20°C and 1200°C, equal to 120 GPa and 75 MPa for SiC/SiC, and 130 GPa and 60 MPa for SiC/ $\text{Al}_2\text{O}_3$ , respectively. In the SiC/SiC, ultimate strength increases with temperature above 1000°C, but decreases in the SiC/ $\text{Al}_2\text{O}_3$  between 20°C and 1000°C. The cyclic endurance limit is strongly affected by temperature in both materials, it generally decreases from the maximum 170MPa at 20°C (10 Hz, R=0.1) to below 65 MPa above 850°C. Static fatigue life measurements at 1000°C over a range of stresses and rupture times up to 240 hrs show linear relationships between applied stress and logarithm of rupture time. No run-out was observed in the SiC/SiC system, while run-out under 80 MPa was found for the SiC/ $\text{Al}_2\text{O}_3$  composite.

Oxidation studies at 500-1200°C in dry air, oxygen, water vapor and argon up to 200 hrs. For both SiC/ $\text{Al}_2\text{O}_3$  and SiC/SiC, oxidation in dry environments causes outgassing of volatile species, followed by a stable weight gain independent of the environment. Inclusion of water vapor and addition of salts in the vapor both elevate oxidation rates.

Short-term tensile test data and long-term static and cyclic fatigue limits are not strongly affected by the presence of pure oxygen, air or water vapor up to 1000°C. No modulus decrease is observed at stresses below proportional limit. Conversely, stress-free exposure to 1200°C air, oxygen or argon for as little as 100 hrs. results in dramatic loss of strength and stiffness, due to deterioration of the fibers and internal reaction of surroundings with the fibers. As in other ceramic



systems, aggressive environments, such as water vapor and  $\text{Na}_2\text{SO}_4$  or  $\text{NaCl}$  reduce creep rupture life. Formation of internal and surface silica under stress-free oxidizing conditions may result in healing of internal cracks. For example, SiC/SiC samples with internal cracking due to loading above the proportional limit recovered 85% of the original modulus after 5hrs. in  $1000^\circ\text{C}$  air, oxygen or water vapor. Similar effects were observed in the SiC/ $\text{Al}_2\text{O}_3$  system. Finally, surface coating of specimens appears to play a vital role in lifetime. Removing as little as 25% of the SiC coating on the SiC/SiC system reduces static rupture time by 80% in  $1000^\circ\text{C}$  air or water vapor.

At high temperatures, many fibers exhibit deviations from linear elastic behavior, which influences component lifetime, and also dynamic properties, such as resonance frequencies and damping factors, of interest in design of turbine parts and other rotating components. An apparatus has been constructed for the forced vibration dynamic mechanical testing of single ceramic fiber samples at temperatures up to  $1600^\circ\text{C}$  and frequencies from 0.1 to 25 Hz. Experimentally based dynamic constitutive relations were developed for commercial sapphire, YAG, and several SiC fibers.

## CLOSURE

The described program was instrumental in bringing together the efforts of many investigators from mechanics, materials modeling, computer science and materials science, with an objective to model, fabricate, process and characterize composite materials for ambient and high-temperature applications. In addition to the numerous research papers, book chapters and reports, a significant product of the program is a comprehensive software package that incorporates a material data base, advanced micromechanical models for evaluation of overall properties of elastic and inelastic composite materials, novel process modeling procedures, and techniques for multiscale analysis and design of composite structures, together with user-friendly interfaces and visualization tools. Moreover, experiments with in-house fabricated and commercially available fibers and composite systems have produced a wealth of data and many useful insights into the behavior of high-temperature composite systems.

## MECHANISM – BASED DESIGN OF COMPOSITE STRUCTURES PROGRAM OVERVIEW AND ACCOMPLISHMENTS

George J. Dvorak  
Center for Composite Materials and Structures  
Rensselaer Polytechnic Institute  
Troy, NY 12180-3590

### ABSTRACT

This paper surveys the accomplishments of the title research program which was funded in 1992–1997 by the Defense Advanced Research Project Agency of the Department of Defense, under the University Research Initiative at Rensselaer Polytechnic Institute. The main focus of the program was to provide research support and computational tools for processing and design of high-temperature composite materials and structures. Micromechanical modeling, design and analysis software, process modeling, and materials processing and characterization are discussed.

### INTRODUCTION

Designing with composite materials for high-temperature applications presents numerous challenges that require an extensive background in material design and processing, structural analysis, and material behavior in adverse environments. The overall goal of the research program has been the development of a software framework and associated modules, and completion of related material processing and characterization studies to support mechanism-based design of composite materials and structures. This includes micromechanical modeling of elastic and inelastic behavior and damage, and implementation in multiscale computational analysis at the micro, meso and macrolevels; modeling of vapor deposition processes for fabrication of ceramic matrix composites and fibers; characterization of certain commercially available systems; and processing and characterization of  $\text{MoSi}_2$  and  $\text{Cr}_3\text{Si}$  – based composites.

The team of co-principal investigators include Professors Duquette, Fish, Flaherty, Hillig, Hudson, Shephard, Sternstein and Stoloff, as well as the writer who serves as program director. Research faculty include Drs. Adjerid, Belsky, Lipetzky and Wentorf. About 25 graduate students have participated at different stages of their degree programs.

## MICROMECHANICAL MODELING

Mechanism-based design of composite structures involves modeling of material responses and interactions on different physical scales, ranging from the reinforcement — matrix microscale, through the dimensions of plies or woven layers in a laminate, to the macroscale of actual composite parts. Evaluation of the overall thermomechanical response of the composite material systems and laminates in terms of the geometry and properties of the constituent phases can be accomplished by several methods. Among the available techniques are the averaging methods, such as the Mori-Tanaka and self-consistent estimates, and the Hashin-Shtrikman bounds. These provide the effective elastic moduli, thermal expansion coefficients, and thermal diffusivities, together with estimates of the average mechanical and thermal fields in the constituents and at their interfaces. The techniques developed under the present program include the transformation field analysis (TFA) for evaluation of the inelastic response and the associated local fields in the phases and plies for systems with viscoelastic or thermo-viscoplastic matrices and/or fibers, both in the perfectly bonded state and after fiber decohesion.

The transformation analysis regards any inelastic deformation, as well as thermal deformations or phase transformations, as a stress-free strain or eigenstrain that is applied to an otherwise elastic composite material or laminate together with the prescribed mechanical loads [1, 2]. Using certain transformation concentration factors and constitutive relations for the inelastic phases, this method provides a set of differential equations for evaluation of the instantaneous local fields in the phases, or at integration points in finite elements of subdivided unit cells. The instantaneous overall response of the composite or laminate is then obtained in terms of the local fields. Certain damage processes, such as fiber debonding and sliding, have also been modeled in terms of appropriate transformation strains, and their effect on the local fields and overall response determined in a similar way [3].

A unified procedure for determination of overall loading conditions that cause onset and initial evolution of local damage in laminates has been developed and the results displayed as initial and subsequent failure maps. These maps are plotted in laminate stress coordinates and consist of a number of branches that represent critical magnitudes of local stresses within individual plies which may initiate local cracking in the fibers, matrices or at interfaces. Such maps are now available for symmetric metal and ceramic matrix laminates [4].

Functionally graded composite materials with variable moduli and thermal expansion coefficients are useful in high-temperature applications involving thermal gradients. Other applications can be found, for example, in joining ceramic and metal parts. Our work has established that specific averaging methods can be selectively used to find overall properties and response of typical graded microstructures under both mechanical and thermal loading gradients [5].

## DESIGN AND ANALYSIS SOFTWARE

The different analysis procedures that describe constituent, composite, laminate and structural responses at the appropriate scales have been implemented in a comprehensive framework that offers the designer with numerous tools for modeling, analysis and design of both composite material systems and large composite structures, while controlling idealization errors through multiscale, adaptive or heuristic means. The framework provides application expertise and visualization tools at different design stages [6, 7].

Commercial programs are applied where possible. The Mvision<sup>TM</sup> format from MSC/PDA Engineering accommodates the material database constructed from available and our own data, which conforms to or can be translated into ASTM and applicable PDES/STEP standards [8]. The high-temperature property database contains over 320 material systems or constituents, 18,000 values and 180 material characteristics. Geometric modeling tools built on commercial geometric modelers create micro-structures, weaves, plies, laminates and part scale models, and source their data from a user-selected properties and design parameters in a spreadsheet format [9]. An analysis attribute code links physical material properties and boundary conditions with the micro- and/or macro-structural geometry. Automatic meshing tools, generic mesh operations and data structures, and the interfaces to multiple finite element analysis codes complete the integration of automated modeling tools for finite element analysis.

The system invites the user to construct an "analysis goal" in terms of design description and analysis characteristics. These include functionality definitions, such as thermomechanical boundary conditions within prescribed deflections and heat flow direction; and specification of the type of analysis result, time and reliability needed to confirm the governing behavior. The goal description is converted into a data flow model and a sequence of code executions, or a "strategy" that provides the desired results to the user. The execution of the analysis goal is similar to using a spreadsheet function, requiring no expertise in the underlying theories or software development. The user is informed of any specific problem with the selected design parameters. The results are automatically computed and returned to the spreadsheet, used as input in subsequent design steps, or displayed by a visualization code.

Material modeling capabilities of the system include codes for evaluation of elastic properties of various composite material systems, initial failure maps of the constituents and their interfaces, and mathematical homogenization of unit cells that represent behavior of periodic microstructures with complex internal geometries, such as aligned or random fiber and particle distributions and weaves. The composite material properties, such as elastic moduli, CTEs, and heat conductivities are evaluated with several micromechanical averaging methods, or in terms of Hashin-Shtrikman bounds, in terms of constituent properties, their geometry and volume fractions. Associated codes evaluate mechanical, thermal, and

transformation concentration factors which provide averages of local stress and strain fields in the phases under prescribed overall stresses, temperature changes, or phase transformations. Inverse routines are available for evaluation of *in situ* reinforcement properties from overall composite and neat matrix experimental data. The results are displayed in comprehensive graphs which show, for example, overall property variations in terms of phase geometry, volume fractions and temperature.

In addition to the averaging methods, mathematical homogenization theory is used together with unit cell designs in evaluations of elastic and inelastic responses of both simple and very complex microstructural geometries, such as weaves [10]. Although computationally more expensive, such techniques allow for a very fine resolution of the local fields, which is needed, for example, for accurate satisfaction of the local constitutive relations of viscoelastic or thermo-viscoplastic phases. The software framework provides facilities to automatically create the unit cell geometric models from size parameters of the constituent features. Composite thermoelastic moduli, instantaneous inelastic stiffnesses, thermal conductivities and chemical diffusivities can be predicted in this manner, and the results readily incorporated into a multiscale computation of both linear and nonlinear structural response.

In general, accurate solutions of structural problems for nonlinear heterogeneous materials present an enormous challenge, because the nonlinear deformation history needs to be evaluated at all integration points and modeling scales involved. Typically, about 99% of the CPU time is spent on constitutive equation solutions in the unit cells. Solution of such large systems in heterogeneous media is now possible at a cost comparable to problems in homogeneous media, without significantly compromising solution accuracy. This is accomplished by a novel modeling scheme based on mathematical homogenization theory with eigenstrains [11] and transformation field analysis [1, 2]. The overall response is computed for an elastic structure loaded by external loads and local eigenstrains equal to the inelastic strains. The latter are evaluated from the inelastic constitutive relations and eigenstrain concentration factors computed in the average sense for each phase, so that history data is updated only at two or three points (fiber, matrix, interphase) in the microstructure. Macroscopic history data is stored in the data base and then applied in the post-processing stage to unit cells in critical locations identified by microscale reduction error indicators. In an actual analysis of an engine flap, discretized with 788 tetrahedral elements (993 unknowns), and with the unit cell microstructure discretized with 98 elements for the fiber and 253 for the matrix, the CPU time on a SPARC 10/51 for the classical homogenization solution of this problem was 8 hours. The new technique with microhistory recovery required only 30 sec., with 3% maximum error in the micro-stress located in a critical region. Another application involves micromechanical analysis of ceramic composite seals for Allison Engine Co. This is a part with complex woven fiber microstructure, where fabrication-induced residual stresses and onset and evolution of damage have a significant influence on total lifetime.

## PROCESS MODELING

Mathematical models and software for analysis of multiscale processes, such as evolving reaction fronts, boundary layers and molecular interactions, have been developed with the aid of adaptive methods for solving systems of partial differential equations [12, 13]. Such methods automatically refine, coarsen and relocate meshes and vary method orders in both time and space; hence, they are capable of resolving local nonuniform behavior. Adaptive algorithms use estimates of discretization errors and/or other information obtained during the computation to improve solution accuracy. The adaptive software uses this information to create strategies to decrease the error to a desired level as quickly as possible. Error estimation techniques, optimal adaptive enrichment strategies, and time integration techniques are employed to improve efficiency, accuracy and robustness [14]. These tools are being incorporated into an object-oriented framework that will simplify development of new applications in materials science and mechanics.

Specific applications have been made in analysis of a cylindrical CVD reactor used in surface coatings of sapphire fibers with  $\text{Al}_2\text{O}_3$  and  $\text{La}_2\text{O}_3$ . The flow of carrier gas mixture of argon and oxygen is modeled as that of a compressible ideal fluid including convection, conduction and radiation. Precursor species are modeled by convection-diffusion systems. Surface reaction rates are assumed proportional to an impingement rate and dependent on temperature in an Arrhenius manner. Parameter studies of varying geometries and operating conditions revealed advantages and deficiencies of reactor design and function.

Protecting ceramic matrix composites from oxidation in hostile environments may require several layers of coating. Under stress, cracks may form and penetrate these coatings, thus opening the system to oxidizing vapors. The resulting damage may reduce useful life of composite components; lifetime predictions consider the size, number and distribution of cracks, as well as the properties of the constituents and their oxides. In some instances, volume expansion accompanying the oxidation seals the cracks and retards or eliminates further oxidation.

The reaction of oxygen and water vapor with a ceramic matrix in the vicinity of a small crack have been described as a two-phase diffusion of gases in the crack and their diffusion and convection in the solid matrix. Gaseous flows involve both bulk and Knudsen diffusion. The solid model describes a reaction-diffusion system combined with viscous deformation according to the Navier-Stokes equations. A volumetric flow law accounts for density changes. Computationally, the problem involves several complex reactions, moving boundaries, sharp transient reaction fronts and complex geometries. Specific results have been found for a crack in a SiC matrix exposed to oxygen. Improvements under consideration include modeling of self contact to describe visco-elastic or visco-plastic material deformation after the crack has closed, as well as analyses of systems of multiple interacting cracks and fibers of various distributions.

## MATERIALS PROCESSING AND CHARACTERIZATION

The processing effort focused on intermetallic compounds with attractive high temperature properties, such as high melting point, low densities and excellent oxidation resistance compared to nickel-based superalloys. Two Mo-modified  $\text{Cr}_3\text{Si}$  compounds were consolidated from prealloyed powders [15]. To improve toughness, 15% volume fraction reinforcement by Saphicon short fibers, and ductile continuous Pt alloy fibers was introduced. Results have shown no significant changes in stiffness due to the reinforcement, but a significantly higher toughness was measured at elevated temperatures. Also, the unnotched strength at 1000–1100°C increased from that at the room temperature due to the inclusion of fibers. Oxidation tests at 500°C showed absence of the "pest" phenomenon, and good resistance at 1250°C. Another system studied was  $\text{MoSi}_2$  reinforced with SiC whiskers and/or particles. Consolidation by reactive sintering of elemental powders was used in an attempt to reduce cost and improve purity. The high temperature strength of reinforced  $\text{MoSi}_2$  increased until 1200°C, presumably indicating some effect from the smaller grains and cleaner product, and a major contribution from the reinforcement. The results suggest that both systems show promising high-temperature properties with a potential for further improvement [16].

Coupon and tubular samples of two commercially available composite systems were obtained from DuPont Lanxide, Inc. One set was enhanced SiC/SiC combined with proprietary inhibitors, reinforced with a 8–10 layer (0/90) plain weave fabric, at 35% fiber volume fraction. The 15% void volume was unevenly distributed as macroscopic surface-connected pores within and between the plies. The second system was a SiC fabric (12-harness satin weave) reinforced  $\text{Al}_2\text{O}_3$  manufactured using the Lanxide DiMOx process. The matrix was formed by directional oxidation of a molten alloy, with about 2% trapped residual metal. Porosity is microscopic and well-dispersed, but extensive matrix microcracking was observed on as-received samples. Baseline data show Young's modulus and proportional limit approximately constant between 20°C and 1200°C, equal to 120 GPa and 75 MPa for SiC/SiC, and 130 GPa and 60 MPa for SiC/ $\text{Al}_2\text{O}_3$ , respectively. In the SiC/SiC, ultimate strength increases with temperature above 1000°C, but decreases in the SiC/ $\text{Al}_2\text{O}_3$  between 20°C and 1000°C. The cyclic endurance limit is strongly affected by temperature in both materials, it generally decreases from the maximum 170 MPa at 20°C (10 Hz,  $R=0.1$ ) to below 65 MPa above 850°C. Static fatigue life measurements at 1000°C over a range of stresses and rupture times up to 240 hrs show linear relationships between applied stress and logarithm of rupture time. No run-out was observed in the SiC/SiC system, while run-out under 80 MPa was found for the SiC/ $\text{Al}_2\text{O}_3$  composite [17, 18].

Oxidation studies at 500–1200°C in dry air, oxygen, water vapor and argon up to 200 hrs. For both SiC/ $\text{Al}_2\text{O}_3$  and SiC/SiC, oxidation in dry environments causes outgassing of volatile species, followed by a stable weight gain independent of the environment. Inclusion of water vapor and addition of salts in the vapor both elevate oxidation rates.

Short-term tensile test data and long-term static and cyclic fatigue limits are not strongly affected by the presence of pure oxygen, air or water vapor up to 1000°C. No modulus decrease is observed at stresses below proportional limit. Conversely, stress-free exposure to 1200°C air, oxygen or argon for as little as 100 hrs. results in dramatic loss of strength and stiffness, due to deterioration of the fibers and internal reaction of surroundings with the fibers. As in other ceramic systems, aggressive environments, such as water vapor and  $\text{Na}_2\text{SO}_4$  or  $\text{NaCl}$  reduce creep rupture life. Formation of internal and surface silica under stress-free oxidizing conditions may result in healing of internal cracks. For example, SiC/SiC samples with internal cracking due to loading above the proportional limit recovered 85% of the original modulus after 5hrs. in 1000°C air, oxygen or water vapor. Similar effects were observed in the SiC/ $\text{Al}_2\text{O}_3$  system. Finally, surface coating of specimens appears to play a vital role in lifetime. Removing as little as 25% of the SiC coating on the SiC/SiC system reduces static rupture time by 80% in 1000°C air or water vapor [19].

At high temperatures, many fibers exhibit deviations from linear elastic behavior, which influences component lifetime, and also dynamic properties, such as resonance frequencies and damping factors, of interest in design of turbine parts and other rotating components. An apparatus has been constructed for the forced vibration dynamic mechanical testing of single ceramic fiber samples at temperatures up to 1600°C and frequencies from 0.1 to 25 Hz [20, 21]. Experimentally based dynamic constitutive relations were developed for commercial sapphire, YAG, and several SiC fibers.

## CONCLUSION

The described program was instrumental in bringing together the efforts of many investigators from mechanics, materials modeling, computer science and materials science, with an objective to model, fabricate, process and characterize composite materials for ambient and high-temperature applications. A significant product of the program is a comprehensive software package that incorporates a material data base, advanced micromechanical models for evaluation of overall properties of elastic and inelastic composite materials, novel process modeling procedures, and techniques for multiscale analysis and design of composite structures, together with user-friendly interfaces and visualization tools. Moreover, experiments with in-house fabricated and commercially available fibers and composite systems have produced a wealth of data and many useful insights into the behavior of high-temperature composite systems.

## ACKNOWLEDGEMENT

This work was supported by ONR Contract No. N00014-92-J-1779. Dr. William Coblenz of DARPA and Dr. Steven Fishman of ONR served as program monitors.



## REFERENCES

1. G. J. Dvorak, Transformation field analysis of inelastic composite materials, *Proc. R. Soc. London*, **A437**, 311–326, 1992.
2. G. J. Dvorak, et al., The modeling of inelastic composites with transformation field analysis, *Modeling Simul. Mater. Sci. Eng.*, **2**, 571–586, 1994.
3. G. Dvorak, et al., Pseudoplasticity of fibrous composite materials: inelastic response of laminates with interfacial decohesion, *Micromechanics of plasticity and damage of multiphase materials*, edited by A. Pineau and A. Zaoui, Kluwer Academic Publishers, Dordrecht, pp. 43–50, 1996.
4. G. J. Dvorak and M. Sejnoha, Initial failure maps for fibrous CMC laminates, *J. Am. Ceram. Soc.*, **78**, 205–210, 1995.
5. T. Reiter and G. J. Dvorak, Micromechanical models for graded composite materials, *Journal of Mechanics and Physics of Solids*, 1997.
6. S. Adjerid, et al., Mechanism-based design of composite structures, AD Vol. 51/MD–Vol. 73, *Proc. ASME Aero and Materials Divs.*, 271–281, 1966.
7. M. S. Shephard and R. Wentorf, Toward the implementation of automated analysis idealization control, *Appl. Numer. Math.*, **14**, 105–124, 1994.
8. PDA Engng., M/VISION Material system builder user's guide and reference 1.2, publ. No. 2190011, 2975 Redhill Av. Costa Mesa, CA 92626.
9. M. S. Shephard, et al., Automatic construction of 3–D models in multiple scale analysis, *Computational Mechanics*, **17**, 196–207, 1995.
10. J. Fish and V. Belsky, Multigrid method for a periodic heterogeneous medium, Parts I and II, *Comp. Meth. Appl. Mech. Engng.*, **126**, 1–38, 1995.
11. J. Fish, et al., Computational plasticity for composite materials based on mathematical homogenization, *Comp. Meth. Appl. Mech. Engng.*, 1997.
12. S. Adjerid, et al., Adaptive numerical techniques for reactive vapor infiltration, *Ceram. Engng. Sci. Proc.*, **15**, 924–931, 1994.
13. S. Adjerid, et al., Modeling and adaptive solution of reactive vapor infiltration problems, *Model. Simul. Mater. Sci. Engng.*, **3**, 737–752, 1995.
14. S. Adjerid, et al., High-order F. E. methods for singularly-perturbed elliptic and parabolic problems, *SIAM J. Appl. Math.*, **55**, 520–543, 1995.
15. N. Stoloff and D. Alman, Processing and properties of MoSi<sub>2</sub>-Nb composites, *Ceramic International*, **21**, 289–292, 1995.
16. W. Hillig, et al., An exploratory study of producing non-silicate oxide composites by melt infiltration, *Mater. Sci. Engr.*, **A196**, 183–190, 1995.
17. P. Lipetzky, et al., Tensile properties of SiC/SiC composites, *Mat. Sci. Engng.*, **A216**, 11–19, 1996.
18. P. Lipetzky, et al., High-temperature cylindrical specimen grip for biaxial loading, *Rev. Sci. Instrum.*, **67** (5), pp. 1989–1992, 1996.
19. Duquette, D., Environmental resistance of intermetallic compounds and composite materials, in *Critical issues in the development of high-temperature structural materials*, ed. N. Stoloff, et al., TMS Warrendale, PA, 431–444, 1994.
20. S. Sternstein, et al., High-temperature dynamic mechanical testing of ceramic fibers, *Mater. Sci. Engng.*, **A215**, 9–17, 1996.
21. C. Weaver, et al., High temperature dynamic mechanical properties of various ceramic fibers, to be published.

## **SOFTWARE FRAMEWORK FOR MECHANISM-BASED DESIGN OF COMPOSITE STRUCTURES**

**R. Wentorf, M. S. Shephard, G. J. Dvorak, J. Fish, M. W. Beall, R. Collar, K.-L. Shek**  
Rensselaer Polytechnic Institute  
Troy, N. Y. 12180-3590

### **ABSTRACT**

A software framework supporting mechanism-based design of high temperature composite structures is described. The framework extends material property databases by allowing the investigation and simulation of small scale behaviors which cause full scale effects. The framework integrates a full range of modeling processes, including automated model generation tools, numerically efficient analysis codes, post-processing and visualization, so as to minimize the effort required to develop mechanism-based models for new behaviors and materials.

### **INTRODUCTION**

The need for advanced software capabilities are motivated by current fabrication technology, which allows the material's structure to be configured for an application, and by the complexity of phenomena governing the material's behavior during fabrication and during subsequent loading. Current research has developed mechanism-based models of thermomechanical behaviors for high temperature composites and the associated fabrication and degradation processes. From the standpoint of design, the new capability provides insight of the relationships between a material system's meso/micro structural design parameters and its overall behaviors.

The mechanism-based approach links behaviors at three physical scales: e.g. the fibrous (micro), the ply/weave (meso) and the part (macro) scales. For example, design changes in the reinforcement's shape and orientation can be translated into overall composite properties and hence to a part's deflection under load. Alternatively, a macro-scale cooling hole configuration under thermal-mechanical loading can be linked to the type and proximity of fiber-coating-matrix debonding. Mechanism-based models allow both current and alternative material and component designs to be evaluated more quickly without the expense of testing all macro scale configuration/environment permutations, and can also aid the design and sizing of test fixtures for those tests which are required.

The balance of the paper outlines some unique features of the software system, and is organized by the functional role of the framework tools in the overall modeling process [1]. The aim is to present a range of software tools which can be assembled to support specific design problems. Specific application examples are referenced where needed. Covered are the engineering modeling tools for geometry, material test data management, applications for modeling material behavior on multiple scales, tools for creating and manipulating numerical models, fast and efficient analysis codes required for large linear or non-linear problems, post-processing and visualization, and techniques by which the framework integrates the composite analysis tools.

## GEOMETRY AND ATTRIBUTE DEFINITION

The framework provides tools for the definition of engineering design geometry and the engineering attributes to be associated with engineering features on the model. Tools are provided which can construct standard geometric features from given design parameters, and assemble these into non-manifold geometric models. Example features on a small scale are cross sections of bundles, bundle paths, repetitive woven patterns, such as satin or plain weaves, standard reinforcement shapes such as fibers, cracked matrix layers and voids left as a result of vapor deposition type operations. Figure 1 illustrates the process where a) the cross-sectional shape and path parameters are defined to create a bundle, b) the bundle interlacing is defined by a schematic to form a weave, and c) the bundles and matrix are assembled into a unit cell for subsequent meshing and analysis. Not all geometry must come from parameters: micro-graphs can be scanned to define bundle paths. The geometric modeling is performed in stages, where the features to be combined are selected, defined in terms of their size and position parameters, translated into a sequence of basic

construction operations, and the operations are executed in terms of their equivalent commercial geometric modeling function calls. Features can be tagged for later identification of their topological entities after construction operations have been executed. Features can also be linked across multiple models, allowing a 1D idealization of a weave (its path) to be associated with the appropriate region in a solid model of a unit cell. Visualization tools are available to display 3D models in real time as both shaded and semi-transparent images. The same facilities have been used to create and modify macro scale models. Special tools are also available for matching topological entities for complex unit cells.

Attributes such as the constituent materials, periodic boundary conditions or prescribed displacements are defined with respect to the features and properties translated into analysis attributes. The SCOREC analysis attribute manager (SAM) manages the attribute information by defining distribution of its tensorial components, links to topological model entities, and how it fits into an organizational hierarchy. Example of a tensorial distribution is a parabolic loading produced by a pin or bolt normal to the surface of the hole, the state of residual stress in a fiber, or the temperature distribution on the surface of a part. Examples of links with topological entities are the association of an elastic modulus with a solid model region representing a fiber, or the association of an interface strength with the common surface (topological face) between a 3D fiber and matrix.

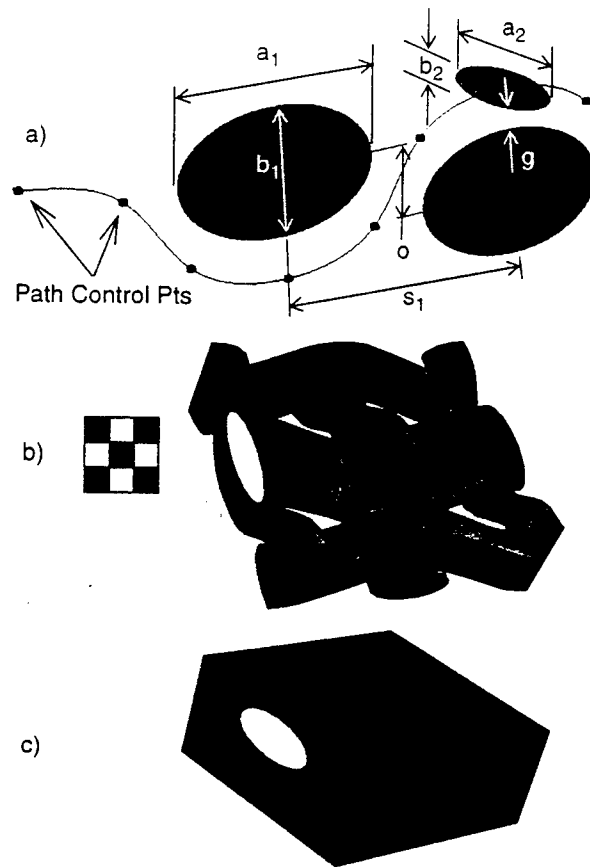


Figure 1: Parametric geometry definition

The task of collecting together all undamaged material properties which are related to the bundles of a weave would be accomplished by the organizational hierarchy.

#### **TEST DATA STORAGE AND PROCESSING**

The framework makes use of a material database which uses the commercial MSC M/ VISION™ format and which conforms to, or can be translated into ASTM and applicable PDES/ STEP standards [2]. The high temperature database developed for the project contains more than 320 material systems or constituents, 18,000 values, and 180 material characteristics. Database sources include published papers, industry data sheets, handbooks, and test data generated at Rensselaer. Constituent properties (matrix and reinforcements), data for dog-bone and tubular test specimens, and durability of tested parts in oxidizing and corrosive environments are stored. Manufacturing size, porosity or volume fraction limitation data are available where supplied by vendors, and background documentation and SEM images of material systems are also managed.

Several database related features are available which either directly support the conceptual design process in material selection, or support analysis strategies. The database application can be configured for automated merit indicy plotting [3], or for retrieval of material systems which have performed in similar environments. Supporting reliable analysis requires data structuring so as to define not only the analysis properties, but also the scale, specimen characteristics, source of data and the environmental parameters of the test - the "pedigree". Reliable analysis requires a pedigree consistent with the underlying analysis models. Translation between the standard procedures and nomenclature of the testing community and the material parameter needs of analysis and design is required in order to obtain meaningful data, e.g. a standard full scale "creep" test may quantify a behavior caused by mechanisms in a CMC which are effected by different conditions from those in metals. The material database is also a source of known behaviors caused by the environment. For example, the modulus of a CMC may vary with both temperature and time, depending on the degree of micro mechanical damage before the measurement, and the presence of water, oxygen and corrosive compounds [4, 5].

The commercial database package also provides a spreadsheet, by which design parameters are edited, organized and annotated, automatically flagged when in need of update, and connected with "back of the envelop" computations. The framework augments the spreadsheet with the means to execute analysis strategies with these design parameters. Additionally, image processing tools were developed to analyze images for composite modeling parameters, such as volume fractions, aspect ratios, spacing and relative positions of constituents.

#### **COMPUTED THERMOMECHANICAL PROPERTIES**

Design analyses require material properties not available directly from test data. The framework provides tools to compute missing properties from what is known. The tools are categorized as either for standard geometries and constitutive behaviors, which have fast execution times, or for complex geometries and behaviors, which employ more complex analysis procedures.

For standard geometries, which include plies of parallel fibers, random or aligned whiskers, or particulate reinforcement, tools are available to predict overall elastic and thermal expansion properties in terms of constituent thermo-elastic properties and volume fractions. The codes related to ply properties implement the Hashin-Strikman Bounds [6], the Mori-Tanaka [7] or the self-consistent methods [8]. The resulting properties computed from the methods can be compared graphically or plotted as a function of application temperature or reinforcement volume fraction. If tested properties for a constituent are not available, they can be computed "in-situ" by the Mori-

Tanaka or self-consistent methods if overall properties, phase volume fraction, and the properties of the other constituent are known.

Software tools also compute mechanical, thermal, and transformation concentration factors. These are useful for estimating phase stress and/or strain averages in two-phase and multi-phase composites subjected to uniform overall stress or strain, a uniform change in temperature, and uniform eigenstrains in the phases [9]. Such capabilities are used as part of post-processing for thermal-mechanical analysis at larger scales. Additional tools provide the plane stress stiffness, the compliance of asymmetric laminated plates under uniform in-plane loads, and the transversely isotropic coefficients of thermal expansion for symmetric laminated plate structures under a uniform temperature. The mechanical, thermal, and transformation distribution factors are estimated, leading to average stresses in plies of a symmetric laminated plate under uniform in-plane loads, temperature change, and ply eigenstrains. Other routines for standard geometries evaluate the Eshelby tensor for transformed homogeneous inclusions of an ellipsoidal shape in an anisotropic solid, compute the P-tensor for an ellipsoidal inclusion in an anisotropic solid, perform numerical operations with tensors or mathematical expressions, and convert between elastic constants, stiffness and compliance matrix forms. For non-linear behavior of fibrous MMCs, the periodic hexagonal array and bimodal plasticity models [10] are available as ABAQUS™ routines.

#### **UNIT CELL**

With the unit cell approach, the material designer can create custom material configurations with complex features or behaviors at micro or meso scales. This need arises when manufacturing processes or component loading/environments produce material defects or exercise internal mechanisms not represented by the theory underlying the standard configuration codes. The effects of including an additional geometric feature of a constituent or altering the size parameters of a constituent can be studied [11]. The main disadvantages have been the complex modeling process and the computational expenses of a general numerical approach. To overcome these, the software framework provides both automated modeling tools and efficient solvers.

The method requires that a representative geometry of the composite configuration be defined. In the framework this begins by user defined combinations of constituent features such as fibrous shapes, weaving patterns, crack or void patterns. The features are sized with dimensional parameters defined from processed images or as specified by the designer. Constituent material properties are either retrieved test data or computed from analysis on a smaller scale. Properties are assigned to the material regions of the geometric model, and orientation geometry, such as bundle center lines, are automatically created and linked with the solid constituents. Other geometric modeling tools automatically match corresponding geometric entities to ensure model periodicity. Automatic meshing works directly from the geometric model, and the analysis interface tools automatically assign the material properties and periodic boundary conditions. This method of constructing geometric and attribute models before meshing gives the framework considerable representative flexibility. Highly efficient solvers compute both homogenized properties (the equivalent properties of the material at a larger scale) and stress concentration factors for later post-processing. The classical mathematical homogenization theory for heterogeneous medium has been generalized [12] for this application to account for eigenstrains.

Unit cell modeling has been used in the multi-scale computational technique and for non-linear analysis with a plasticity model. Given a representative geometry, it can also predict linear elastic properties for woven composites for use directly with conventional macro-scale analysis tools, and can be readily adapted for thermal conductivity and chemical diffusion problems, e.g. for process

modeling. Parameterized unit cells for oriented fibers, periodic "random" fibers, "random" particles, and 2D woven fabrics with cracks and voids have already been developed.

### **NUMERICAL MODEL DEVELOPMENT**

Conversion of the engineering geometry to a finite element mesh is supported by automatic mesh generation, mesh modification and facilities for structuring and storing mesh data. SCOREC developed tools for automatic meshing of either 3D surfaces or volumes can be used [13]. The automatic meshing tools have features which automatically control the numerical solution around critical features or through the thickness of parts where the manufacturing or degradation processes will cause layered variations in behaviors or micro structures. The automatic meshing works for models on all scales, and are used for building periodic meshes of unit cells. Mesh modification tools can be used to remove the effects of undesired small features created unintentionally by geometric modelers, and were used for the crack propagation analysis [14]. Special mesh modification capability was developed which adjusts the volume of a material region. This capability is useful with unit cell models of meso scale weaves or micro scale reinforcements, allowing the volume fraction to be adjusted directly through the mesh. In addition, this provided an efficient means to study the sensitivity of overall properties to changes in volume fractions.

### **ANALYSIS**

The framework automatically constructs the input for analysis packages such as ABAQUS<sup>TM</sup> or specialized solvers by extracting the mesh data from the generic mesh database and the associated material properties, loads and boundary conditions from the attribute structures. The specialized solvers include an iterative solver with multiple right-hand-sides, which is both time and disk space efficient. The analysis efficiency is very useful for mechanism-based simulations, where complex micro-structures such as weaves and/or non-linear behaviors require large numerical models and/or many solution increments [15]. Efficient solutions for materials with nonlinear history dependent behaviors have been addressed in [12] and [16].

The design and performance of a HTC component is often governed by the mechanical behavior near highly stressed features, such as attachments. The seemingly straight forward approach of explicitly modeling the composite microstructure throughout the component would require computational resources far greater than available or needed. Unit cell or representative volume approaches make the computations feasible but are based upon assumptions of periodicity and uniformity of macroscopic fields, which are often not valid near critical features. To solve these problems, special analysis tools and techniques were developed which automatically locate critical areas and then coordinate and adapt the numerical models on multiple scales, so as to capture failure processes down to the micro scale [17, 18].

The multi-scale technology has also been used to simulate the growth of a crack in a fibrous composite [14], and the dominant factors affecting crack growth on the micromechanical level have been investigated. Automatic tools were developed that explicitly represent the microstructure of the composite at the crack front while using homogenized material properties elsewhere. A significant difference in the crack growth pattern was found when the microstructure model was incorporated into the analysis. Crack propagation criteria in the microstructure was based on the energy release rates, fracture toughnesses of the microconstituents and their interface.

The process modeling codes included in the framework simulate the time varying production, or degradation, of composite materials. The analysis codes find the solution for models involving the reaction and transport of chemical species and material flows. In the most basic applications, designers can alter process parameters to improve production rates and/or minimize manufacturing

defects. Since the analysis code is interfaced with the framework tools, the opportunity exists for designers to couple thermomechanical and chemical process simulations to estimate processing residual stresses or to simulate oxidation/hot corrosion for life prediction. Codes have been applied to the reactive vapor infiltration process for forming  $\text{MoSi}_2$  from Mo powder, CVD fiber coating with  $\beta\text{Al}_2\text{O}_3$ , and for oxidation simulations of SiC composites [19-21]. Inputs for the general analysis code are the initial geometry and mesh, process attributes per phase, and boundary condition distributions as a function of time. Models input to the code are categorized as chemical reaction models, expansion, mechanical models for solid phases, diffusion models of gaseous phases, and surface models for phase interfaces. Error control parameters are given for the adaptive refinement techniques. Outputs are the time varying volume change, shape, velocity, temperature, concentration and pressure fields

## POST PROCESSING

Post processing and visualization tools provided by the framework map analysis results into behaviors and graphics to aid interpretation and understanding for design of mechanism-based models. For linear elastic analysis, initial brittle and plastic material failure of fibrous composites due to thermal-mechanical loading can be graphically depicted by the software. Debonding at the interfaces between the fiber, coating and matrix, and fracture of the fiber, coating or matrix materials are predicted for symmetric laminated plate configurations. The framework tools provide the designer with an animated "through the thickness" sequencing of these micro scale failures at each lamination, allowing interior-exterior trends to be visualized. The software implements the theory found in [16, 9, 22], by mapping macro scale FEA temperatures and stress distributions onto the micro-mechanical failure map model. The model accounts for residual stress effects due to a difference between a stress

free state, e.g. the processing temperature, and the operating temperature. The codes have been applied to SiC/Ti MMCs and to a SiC/ $\text{Al}_2\text{O}_3$  woven CMC combustor housing with cooling holes and other hardware features, and loaded by large thermal gradients. Overall thermal stresses mapped to the fibrous scale result in the macro scale distribution shown in Figure 2 (top), where shading indicates proximity to fiber/matrix debonding failure on the inner ply.

Post processing tools are also used to recover the critical micro scale behaviors in unit cell models. The computational plasticity analysis tools described earlier rely on post-processing of the strain histories stored for each critical macro scale element (Gauss point). In an example problem

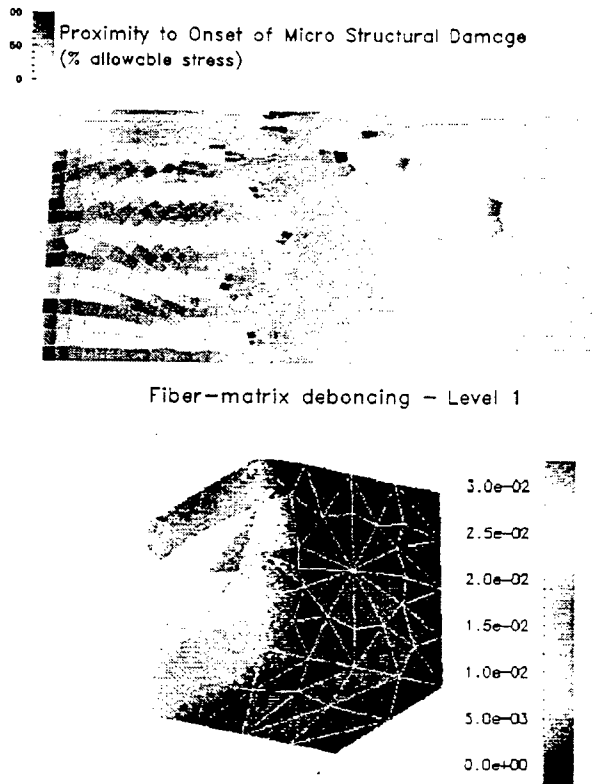


Figure 2: Post processing of macro scale stress

using a SiC/Ti fibrous composite, the recovered strain history was mapped to the micro scale, showing fiber and matrix stresses and areas of permanent deformation around the linkage connections [12]. The distribution of micro scale stresses are shown at the bottom of Figure 2.

### **INTEGRATION OF SOFTWARE TOOLS**

Several features of the framework allow it to utilize the software tools described earlier [1]. In order to communicate with commercial packages, such as geometric modelers, framework tools make queries and edit operations through a layer of generic operators. Each commercial code is then interfaced to the rest of the system by a set of functions which translate the generic instruction into the specific functions supported by the package. This avoids the need to customize a version of each framework tool for each commercial package, or version of a package. Relational database queries are specified in terms the SQL language, which performs a similar function. In order to write generic operators and support multiple, possibly specialized tool capabilities, the essential computational functions are abstracted, and the abstractions organized into type hierarchies.

Expertise in several areas, including material and process modeling, analysis techniques and detailed software operation are needed for reliable HTC mechanism-based analysis and design. For a given analysis goal desired by the user, the framework facilitates the sequencing of tools into analysis strategies, the execution of which provides the desired results. From the user's perspective, the execution of the analysis goal is no more involved than using any other spreadsheet function, requiring no expertise or involvement in software development. The current design parameters are recovered from the spreadsheet, and transferred to the goal processor. If data is missing or out of the applicability range of available strategies, the user is informed of the specific problem, otherwise the results are automatically computed and returned to the spreadsheet, used as input for other analysis, or displayed.

### **CONCLUSION**

High temperature composites have required progressively more complex micro-structures and behavioral understanding. Supporting design requires analytical tools which can yield insight into the underlying behaviors at multiple scales, are efficient to use, and which can be adapted to new material configurations. Application of these tools has shown their usefulness in design.

### **ACKNOWLEDGMENT**

The support of ARPA/ONR under grant number N00014-92J-1779 is gratefully acknowledged.

### **REFERENCES**

- [1] Beall, M. W., Fish, J., Shephard, M. S., Dvorak, G. J., Shek, K.-L., Wentorf, R., "Computer-Aided Modeling Tools for Composite Materials", Ceramic Engineering and Science Proceedings of the American Ceramic Society's 18th Annual Meeting and Exposition, Cocoa Beach, FL, January 9-12, 1994.
- [2] PDA Engineering, "M/VISION Material System Builder User's Guide and Reference", Release 1.2, Publication No. 2190011, 2975 Redhill Avenue, Costa Mesa, California, 92626, 1993.
- [3] Ashby, M. F., "Materials Selection in Mechanical Design", Pergamon Press, Oxford, New York, 1992.
- [4] Lipetzky, P., Stoloff, N. S., Dvorak, G. J., "Atmospheric Effects on High Temperature Lifetime of Ceramic Composites", to be published in the Proceedings of the 1997 ECD Meeting, The American Ceramic Society, Jan. 12-16, Cocoa Beach, FL, 1997.



- [5] Lipetzky, P., Lieblich, M., Hillig, W., Duquette, D., "Effect of Salt Corrosion on Mechanical Properties of a SiC-SiC Composite in Dry and Moist High Temperature Environment", to be published in the Proceedings of the 1997 ECD Meeting, The American Ceramic Society, Jan. 12-16, Cocoa Beach, FL, 1997.
- [6] Hashin, E., and Walter Rosen, B., "The Elastic Moduli of Fiber-Reinforced Materials", *Journal of Applied Mechanics*, Transactions of the ASME, pp. 223-232, June, 1964.
- [7] Mori, T. and Tanaka, K., "Average Stress in Matrix and Average Elastic Energy of Materials with Misfitting Inclusions", *Acta Metallurgica*, Vol. 21, pp. 571-574, May, 1973.
- [8] Teply, L., and Dvorak, G. J., "Bounds on Overall Instantaneous Properties of Elastic-Plastic Composites", *J. Mech. Phys. Solids*, Vol. 36, No. 1, pp. 29-58, 1988.
- [9] Dvorak, G. J., and Benveniste, Y., "On Transformation Strains and Uniform Fields in Multiphase Elastic Media", G. J. Dvorak and Y. Benveniste, *Proc. R. Soc. Lond.*, A 437, pp. 291, 1992.
- [10] Dvorak, G. J., and Bahei-El-Din, Y. A., "A Bimodal Plasticity Theory of Fibrous Composite Materials", *ACTA Mechanica*, 69, pp. 219-241, 1987.
- [11] Dasgupta, A., Agarwal, R. K., Bhandarkar, S. M., "Three-dimensional Modeling of Woven-fabric Composites for Effective Thermo-mechanical and Thermal Properties", *Composites Science and Technology*, 56, pp. 209-223, 1996.
- [12] Fish, J., Pandheeradi, M., Shek, K., Shephard, M. S., "Computational Plasticity for Composite Materials and Structures Based on Mathematical Homogenization: Theory and Practice", to appear in *Comp. Meth. Appl. Mech. Engng.*, 1996.
- [13] Shephard, M. S., Beall, M. W., Garimella, R., and Wentorf, R., "Automatic Construction of 3-D Models in Multiple Scale Analysis", *Computational Mechanics*, 17, pp. 196-207, 1995.
- [14] Beall, M. W., Belsky, V., Fish, J. and Shephard, M. S., 1996, "Automated Multiple Scale Fracture Analysis", SCOREC Report, 4-1996. Rensselaer Polytechnic Institute, Troy, NY., 1996.
- [15] Fish, J., Pandheeradi, M., Shek, K., Goma, S., Shephard, M. S., "Modeling and Simulation of Failure Processes in Composites", to be published in the Proceedings of the 1997 ECD Meeting, The American Ceramic Society, Jan. 12-16, Cocoa Beach, FL, 1997.
- [16] Dvorak, G. J., "Transformation Field Analysis of Inelastic Composite Materials", *Proc. R. Soc. Lond. A*, 437, pp 311-327, 1992.
- [17] Fish, J., Markolefas, S., Guttal, R. and Nayak, P., "On Adaptive Multilevel Superposition of Finite Element Meshes," *Applied Numerical Mathematics*, Vol 14., 1994.
- [18] Fish, J., Nayak, P., and Holmes, M. H., "Microscale Reduction Error Indicators and Estimators for a Periodic Heterogeneous Medium," *Computational Mechanics: The International Journal*, Vol. 14, pp. 323-338, 1994.
- [19] Adjerid, S., Flaherty, J. E., Hillig, W., Hudson, J., and Shephard, M. S., "Modeling and the Adaptive Solution of Reactive Vapor Infiltration Problems", *Modeling and Simulation in Materials Science Engineering*, Vol. 3, pp. 737-752, 1996.
- [20] Adjerid, S., Flaherty, J. E., Hudson, J. B., and Shephard, M. S., "Adaptive Solution For Fiber Coating Process", to be published in *Modeling and Simulation in Materials Science Engineering*.
- [21] Adjerid, S., Aiffa, M., Flaherty, J. E., Hudson, J. B., Shephard, M. S., "Modeling and Adaptive Techniques for Oxidation of Ceramic Composites", to be published in the Proceedings of the 1997 ECD Meeting, The American Ceramic Society, Jan. 12-16, Cocoa Beach, FL, 1997.
- [22] Dvorak, G. J., Chen, T. and Teply, J., "Thermomechanical Stress Fields in High-temperature Fibrous Composites. I: Unidirectional Laminates", *Composites Science and Technology*, Vol. 43, pp. 347-358, 1992.

## MODELING AND ADAPTIVE NUMERICAL TECHNIQUES FOR OXIDATION OF CERAMIC COMPOSITES

S. Adjerid, M. Aiffa, J. E. Flaherty, J. B. Hudson, M. S. Shephard

Scientific Computation Research Center  
Rensselaer Polytechnic Institute  
Troy, NY 12180-3590

### ABSTRACT

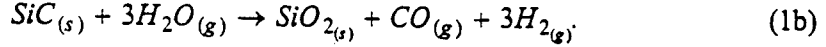
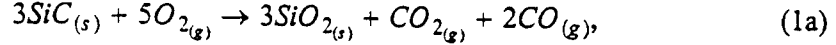
We develop a mathematical model for the oxidation of silicon carbide in a crack or pore. The model consists of a nonlinear partial differential system that is solved by adaptive finite element software that automates many of the computational decisions.

### 1. INTRODUCTION

Oxidation shortens the life of ceramic matrix composites by, e.g., changing the elastic properties of the medium, reducing bonding strength due to a loss of fiber coatings, and weakening fibers through reaction [1-3]. Composite materials are protected by coatings; however, cracks that form as a result of thermal or other loading may expose the matrix and fibers to hostile environments. We present a model for the oxidation of a cracked silicon carbide ( $\text{SiC}$ ) matrix that is exposed to a hot gaseous mixture of oxygen and water. The gases diffuse into the matrix and react with the  $\text{SiC}$  to form a layer of silicon dioxide ( $\text{SiO}_2$ ) between the gaseous mixture and the  $\text{SiC}$ . The oxidation proceeds into the composite at a rate that is controlled by the solid-state diffusion of oxygen and/or water vapor in  $\text{SiO}_2$ . Phase transformations due to the oxidizing reactions are accompanied by a volume expansion that causes the viscous  $\text{SiO}_2$  to flow and fill the crack [1-3]. This may reduce damage to the composite. The model, consisting of a nonlinear partial differential system, is solved by adaptive finite element software [4] with capabilities for unstructured mesh generation and combinations of automatic mesh refinement/coarsening (h-refinement), method-order variation (p-refinement), and mesh motion (r-refinement). Adaptivity helps control numerical accuracy and track moving material boundaries; hence, it provides an effective tool for solving oxidation and related [5] composite fabrication problems. The model and its solution by the adaptive software produce an efficient way to predict and understand changes in the chemical, physical, and mechanical properties of composites that will eventually lead to improved design and longer material life.

## 2. OXIDATION MODEL

Following [2,3], we expose a  $\text{SiC}$  matrix to  $\text{O}_2$  and  $\text{H}_2\text{O}$  that are absorbed into the matrix and react with  $\text{SiC}$  according to the overall reaction



These reactions occur at the interface between  $\text{SiC}$  and  $\text{SiO}_2$  with  $\text{O}_2$  and  $\text{H}_2\text{O}$  diffusing through  $\text{SiO}_2$  to reach the fronts.

The solid matrix consists of a mixture of reactants and products. Let the mass  $m_i$  (g) of chemical species  $i$  at time  $t$  in a control volume  $V$  be

$$m_i(t) = \int_V \rho Y_i d\omega, \quad i = 1, 2, \dots, 7, \quad (2)$$

where  $\rho$  is the density of the mixture,  $Y_i$  is the mass fraction of species  $i$  and  $d\omega$  is a volume element. Indices of the seven species involved in the reactions are listed in Table I. Considerations of mass conservation of species  $i$  yield

$$\frac{dm_i}{dt} = - \int_S \mathbf{J}_i \cdot \mathbf{n} d\sigma - \int_S \rho Y_i \mathbf{v} \cdot \mathbf{n} d\sigma + \int_V \dot{q}_i d\omega, \quad i = 1, 2, \dots, 7, \quad (3a)$$

where  $S$  is the boundary of  $V$ ,  $\mathbf{n}$  is a unit outer normal to  $S$ ,  $d\sigma$  is a surface element,  $\mathbf{v}$  is the mixture velocity, and  $\dot{q}_i$  and  $\mathbf{J}_i$  are, respectively, the mass production rate and diffusive flux of species  $i$ . Assuming Fickian diffusion and regarding the position of a material point  $\mathbf{x}$  as a function of  $t$  and its initial spatial location  $\mathbf{X}$ , we have

$$\mathbf{v}(\mathbf{X}, t) = \frac{\partial \mathbf{x}(\mathbf{X}, t)}{\partial t}, \quad \mathbf{J}_i = -D_i \nabla(\rho Y_i) \quad (3b, c)$$

with  $D_i$  being the diffusivity of species  $i$  in the mixture and  $\nabla$  being the gradient operator.

Applying the divergence theorem to (3a) while using (2) and (3c) yields

$$\frac{d(\rho Y_i)}{dt} = \nabla \cdot D_i \nabla(\rho Y_i) - \rho Y_i \nabla \cdot \mathbf{v} + \dot{q}_i, \quad \mathbf{x} \in \Omega(t), \quad t > 0, \quad (4a)$$

where

$$\frac{d(\rho Y_i)}{dt} = \frac{\partial(\rho Y_i)}{\partial t} + \mathbf{v} \cdot \nabla(\rho Y_i), \quad i = 1, 2, \dots, 7, \quad (4b)$$

is the material derivative and  $\Omega(t)$  is the spatial region occupied by the medium at time  $t$ .

Since mass production rates during high-temperature oxidation are much faster than diffusive rates, we assume all reactions are irreversible, isothermal, and have rates that are linear in each concentration to obtain

$$\dot{q}_1 = -5w_1M_1, \quad \dot{q}_2 = (2w_1 + w_2)M_2, \quad \dot{q}_3 = w_1M_3, \quad \dot{q}_4 = -(3w_1 + w_2)M_4,$$

$$\dot{q}_5 = (3w_1 + w_2)M_5, \quad \dot{q}_6 = -3w_2M_6, \quad \dot{q}_7 = 3w_2M_7. \quad (5a-g)$$

where

$$w_1 = k_1 \left[ \frac{\rho Y_1}{M_1} \right] \left[ \frac{\rho Y_4}{M_4} \right], \quad w_2 = k_2 \left[ \frac{\rho Y_4}{M_4} \right] \left[ \frac{\rho Y_6}{M_6} \right]. \quad (5h,i)$$

The parameters  $k_1$  and  $k_2$  are the rate constants for rate-controlling steps in reactions (1a,b) and  $M_i$  denotes the molecular weight of species  $i = 1, 2, \dots, 7$  (cf. Table I). Thus,  $\rho Y_i/M_i$ , is the concentration of species  $i$  in  $\text{mol}/\text{cm}^3$ .

Table I. Index and molecular weight  $M_i$  (g) of species  $i$ .

Species	$O_2$	$CO$	$CO_2$	$SiC$	$SiO_2$	$H_2O$	$H_2$
$i$	1	2	3	4	5	6	7
$M_i$	32	28	44	40	60	18	2

Assuming that a control volume  $V$  contains only chemical constituents without voids between the compounds, Adjerd et al. [5] show that

$$\nabla \cdot \mathbf{v} = \sum_{i=1}^7 \frac{1}{\hat{\rho}_i} [\dot{q}_i + \nabla \cdot D_i \nabla \rho Y_i], \quad \mathbf{x} \in \Omega, \quad t > 0. \quad (6)$$

where  $\hat{\rho}_i$  is the theoretical density of species  $i$ . In typical situations, there is very little free  $O_2$ ,  $H_2$ ,  $H_2O$ ,  $CO$ , and  $CO_2$  in the matrix; therefore, it is reasonable to neglect the  $\rho Y_i$  terms on the right of (6) for  $i = 1, 2, 3, 6, 7$ . Additionally,  $D_4$  and  $D_5$  are negligible so (6) becomes

$$\nabla \cdot \mathbf{v} = \sum_{i=4}^5 \frac{\dot{q}_i}{\hat{\rho}_i}. \quad (7)$$

The oxidizing reactions (1) are accompanied by nearly a 120% volume expansion that induces forces on the matrix causing it to flow. We assume that the material is capable of viscous deformation and describe its motion by the Navier-Stokes equations

$$\rho \frac{d\mathbf{v}}{dt} + \mathbf{v} \left[ \frac{\partial \rho}{\partial t} + \nabla \cdot (\rho \mathbf{v}) \right] = \nabla \cdot \mathbf{T} \quad (8a)$$

where the traction matrix  $\mathbf{T}$  has components

$$T_{kl} = (-p + \lambda \nabla \cdot \mathbf{v}) \delta_{kl} + \mu \left( \frac{\partial v_k}{\partial x_l} + \frac{\partial v_l}{\partial x_k} \right), \quad k, l = 1, 2, 3, \quad (8b)$$

with  $\lambda$  and  $\mu$  being Lamé parameters,  $p$  being the pressure, and  $\delta_{kl}$  being the Kronecker delta.

Initially, the matrix only contains  $SiC$ ; thus, the initial conditions are

$$Y_i(\mathbf{X}, 0) = \begin{cases} 0, & i \neq 4 \\ 1, & i = 4 \end{cases}, \quad i = 1, 2, \dots, 7, \quad \mathbf{v}(\mathbf{X}, 0) = 0, \quad p(\mathbf{X}, 0) = 0. \quad (9)$$

Boundary conditions prescribe the crack surface as traction free

$$\mathbf{T} \cdot \mathbf{n} = 0, \quad \mathbf{x} \in \Gamma, \quad t > 0. \quad (10a)$$

On planes of symmetry and in the far field, we prescribe

$$\mathbf{v} \cdot \mathbf{n} = 0, \quad \mathbf{n} \cdot \nabla[\mathbf{v} - (\mathbf{v} \cdot \mathbf{n})\mathbf{n}] = 0, \quad D_i \nabla(\rho Y_i) \cdot \mathbf{n} = 0, \quad i = 1, 2, \dots, 7. \quad (10b-d)$$

The rate of absorption and desorption of gaseous species  $i$  is assumed proportional to the deviation of  $Y_i$  from its maximum solubility  $s_i$  in  $\text{SiO}_2$ ,  $i = 1, 2, 3, 6, 7$ ; thus,

$$D_i \nabla(\rho Y_i) \cdot \mathbf{n} = -\phi_i(\mathbf{x}, Y_i - s_i), \quad i = 1, 2, 3, 6, 7, \quad \mathbf{x} \in \Gamma, \quad t > 0, \quad (10e)$$

where  $\Gamma$  is the surface of the crack and  $\phi_i(\mathbf{x}, z)$  is a saturation function as described in Section 3.

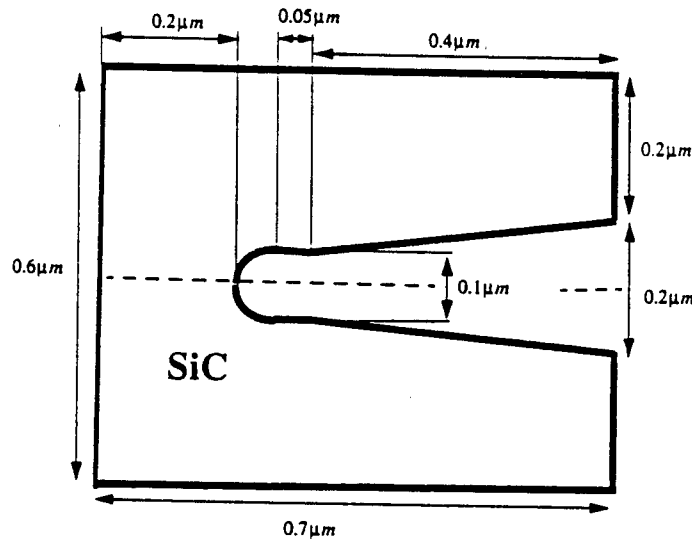


Figure 1. A two-dimensional SiC matrix containing a crack.

### 3. APPLICATION

We consider an idealized crack in a two-dimensional SiC matrix (cf. Figure 1) that is exposed to oxygen; thus, reaction (1b) is not present and  $\text{H}_2\text{O}$  and  $\text{H}_2$  are not involved. With the geometry of Figure 1 and the specified reactants, we prescribe

$$\phi_i(\mathbf{x}, z) = \begin{cases} -0.075zh(x_1)[1 + \tanh(10(x_1 - 2.5))], & i = 1, \\ 0, & i = 6, \\ 0.5 \times 10^{-4}z[1 + \tanh(z \times 10^5)], & i = 2, 3, 7 \end{cases} \quad (10f)$$

where  $z = Y_i - s_i$  and  $h(x_1)$  is half of the thickness of the crack at horizontal coordinate  $x_1$ . The topmost equation simulates a decrease in flux as the crack width narrows; the middle equation signifies that water vapor is not present in this example; and the bottom equation is a sharp but continuous transition from no flux to a saturation value.

A dimensionless version of the partial differential system (4, 5, 7-10) is solved using adaptive finite element software that has capabilities for automatic h-, p-, and/or r-refinement [4,5]. Although p-refinement is very efficient [4], we use hr-refinement with piecewise linear polynomials ( $p = 1$ ). The r-refinement is used to follow evolving reaction zones and track the solid-gas interface as the matrix expands. The h-refinement is used to increase solution resolution near sharp transitions. Adaptive h-refinement is guided by two elemental error indicators:  $\eta_\Delta$  is a mean-square average of jumps in  $\partial p Y_4 / \partial \mathbf{n}$  across the edges of element  $\Delta$  and  $\zeta_\Delta$  is a similar average of jumps in the components of  $\partial \mathbf{v} / \partial \mathbf{n}$  [6]. Letting  $\bar{\eta}$  and  $\bar{\zeta}$ , respectively, denote averages of  $\eta_\Delta$  and  $\zeta_\Delta$  over all elements, we refine those elements where  $\eta_\Delta > 1.8\bar{\eta}$  or  $\zeta_\Delta > 2.2\bar{\zeta}$ . A vertex is scheduled for coarsening when the error indicators on all elements containing it are less than  $0.3\bar{\eta}$  and  $0.7\bar{\zeta}$ . When this occurs, the low-error vertex is moved ("collapsed") to its neighboring vertex having the largest interior angle. This eliminates elements and coarsens the mesh. Badly shaped elements that may result from r-refinement are eliminated by a combination of edge swapping (exchanging the diagonal of the quadrilateral formed by two triangular elements) and vertex collapsing [6]. The variable-step, variable-order time integration [4-6] was performed with a temporal error tolerance of  $10^{-4}$  and was halted every five time steps to examine the error indicators and refine, coarsen, or move the mesh as necessary.

In order to overcome spurious pressure oscillations that arise in an (essentially) incompressible medium, we introduce an "artificial compression" and solve

$$\varepsilon \frac{dp}{dt} + \nabla \cdot \mathbf{v} = \sum_{i=4}^5 \frac{\dot{q}_i}{\hat{\rho}_i} \quad (11a)$$

instead of (7b). This stabilizes the viscous flow while not greatly affecting accuracy when  $\varepsilon$  is small. We choose

$$\varepsilon = \frac{\bar{\varepsilon} L^2}{\mu_5 D_1 s_1} \quad (11b)$$

where  $L$  ( $= 0.7 \mu\text{m}$ ) is the length of  $\Omega$  (cf. Figure 1),  $\mu_5$  is the viscosity of  $\text{SiO}_2$ , and  $\bar{\varepsilon}$  was selected as  $10^{-6}$ .

Dimensionless variables are obtained by scaling  $\mathbf{x}$  by  $L$ ,  $\rho$  by  $\hat{\rho}_5$ ,  $t$  by  $D_1 s_1 / L^2$ , and  $p$  by  $\mu_5 L^2 / (\bar{\varepsilon} D_1 s_1)$ . Using symmetry, we solve a problem on the upper half of the matrix shown in Figure 1. Those parameter values available in the literature [7] at an operating temperature of  $1100^\circ\text{C}$  are  $D_1 = 6.6 \times 10^{-13}$ ,  $D_6 = 3.6 \times 10^{-11}$  ( $\text{m}^2/\text{s}$ ),  $\hat{\rho}_4 = 3.2$ ,  $\hat{\rho}_5 = 2.2$  ( $\text{g}/\text{cm}^3$ ), and  $\lambda_5 = \mu_5 = 10^{12}$  ( $\text{Ns}/\text{m}^2$ ). The remaining parameters were estimated relative to these. For example, we selected  $\lambda_4 = \mu_4 = 10^{15}$   $\text{Ns}/\text{m}^2$  and assumed that the Lamé parameters for the mixture varied linearly between their  $\text{SiC}$  and  $\text{SiO}_2$  values in the reaction zone; thus,

$$\lambda = \mu = \mu_5 + (\mu_4 - \mu_5) Y_4. \quad (12)$$

The higher values of the Lamé parameters for  $\text{SiC}$  simulate its greater stiffness (at  $1100^\circ\text{C}$ ) relative to  $\text{SiO}_2$ . The value of the reaction rate  $k_1$  was selected as  $2 \times 10^{-4} \text{m}^3/\text{s}$  to ensure diffusion dominance. Increasing or decreasing this value yielded similar results with sharper or more diffuse reaction zones, respectively. We assumed that the diffusivity of  $\text{CO}$  and  $\text{CO}_2$  in  $\text{SiO}_2$  is faster than that of  $\text{O}_2$  and selected  $D_2 = D_3 = 10^{-10} \text{m}^2/\text{s}$ . Finally, maximum solubility limits were chosen as  $s_i = 10^{-3}$ ,  $i = 1, 2, 3$ . Those parameters that remain unspecified are irrelevant to this

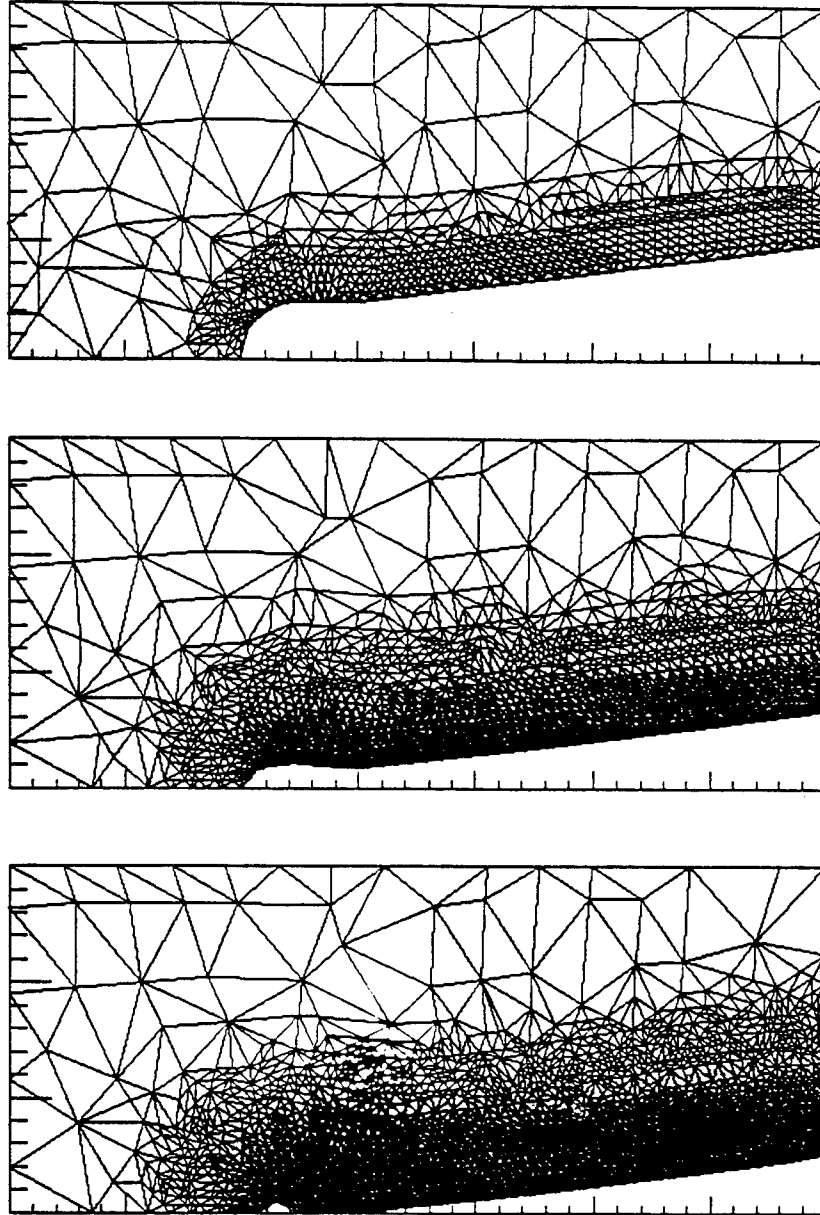


Figure 2. Mass fraction of  $SiC$  at  $t = 0.2, 1.77, \text{ and } 3.6$  min. Lighter shades indicate a high concentration of  $SiC$  and darker ones indicate a low concentration.

application.

The concentration of  $SiC$  and the corresponding adaptive meshes at  $t = 0.2, 1.77, 3.6$  min are shown in Figure 2. In Figure 3, we show the pressure with velocity vectors superimposed at  $t = 3.6$  min. The relative mass and volume changes  $m(t)/m(0) - 1$  and  $\Omega(t)/\Omega(0) - 1$  appear as functions of  $t$  in Figure 4. The oxidation

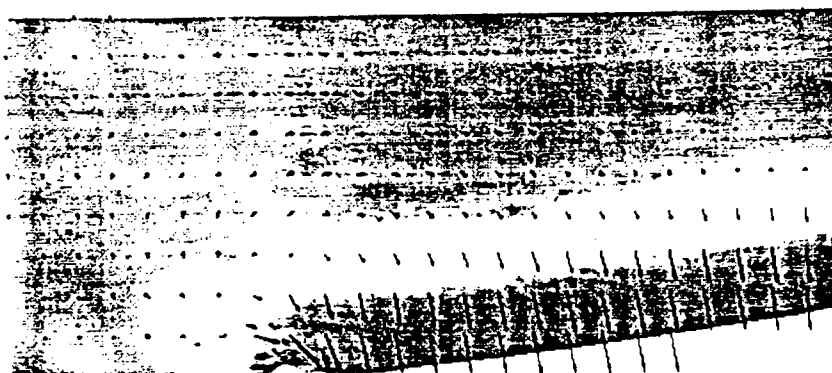


Figure 3. Pressure and velocity vectors at  $t = 3.6$  min with lighter shading indicating higher pressures.

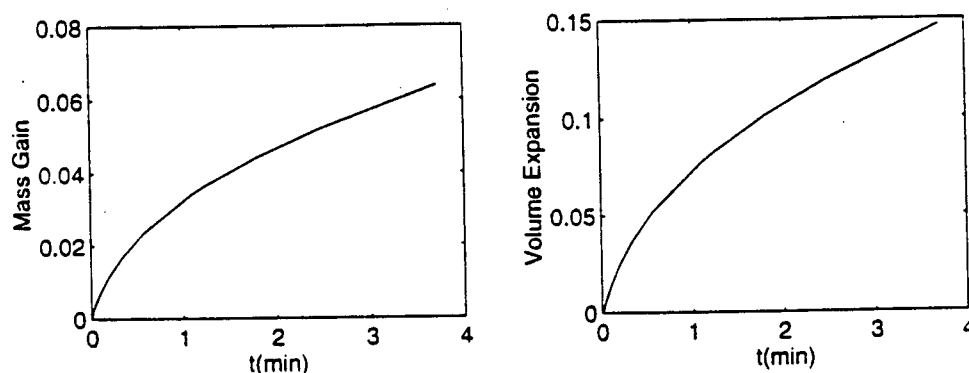


Figure 4. Total relative mass (left) and volume (right) changes vs. time.

front advances into the  $\text{SiC}$  matrix and  $\text{SiO}_2$  flows into the crack to ultimately close it; thereby, reducing the gaseous diffusion into the matrix (cf. Figure 2). Figure 3 displays a qualitatively correct high pressure in the reaction zone and a flow of  $\text{SiO}_2$  into the crack. The meshes of Figure 2 indicate that the adaptive software is placing fine meshes in the reaction zone where variables are changing rapidly while using coarse meshes elsewhere. The results of Figure 4 agree with experimental results [1,2] which predict that the system is diffusion-controlled; thus, indicating parabolic mass and volume change rates. Densities approach their correct theoretical values once reactions have passed.

#### 4. DISCUSSION

We have developed a reaction-diffusion model to analyze the oxidation of ceramic composites. When used with adaptive finite element software, the model predicted qualitatively correct chemical and mechanical behavior and quantitatively correct mass gain. Our model displays a closing crack, which should inhibit



oxidation. We will integrate this software into an overall mechanism-based design system [8] that will simplify future analyses. Computational results will be compared with existing [1,2] and planned experiments.

Several improvements are possible. We are testing a model for the gaseous flow in the crack that contains a combination of Fickian and Knudsen diffusion. We will also include oxidation by  $H_2O$  as described herein. Coated and uncoated fibers will be added to the matrix with their associated reaction and surface diffusion models. Parameter studies will endeavor to determine how damage varies with crack geometry and operating conditions. Solving contact problems as the crack closes is an essential capability that must be developed. With this, elastic, visco-elastic, and/or visco-plastic deformations should be investigated and possibly included in the mechanical model. With these, it should be possible to predict the formation of cracks in the  $SiO_2$  as oxidation progresses and stress patterns change. Coupling these micro-scale models with macro-mechanical models that anticipate the behavior of the composite structure are also envisioned [8].

#### ACKNOWLEDGEMENT

The authors gratefully acknowledge support of this project from ARPA/ONR under Grant N00014-92J-1779, "Mechanism-Based Design of Composite Structures," Steven Fishman and William Coblenz, Project Monitors.

#### References

1. L. Filipuzzi, G. Camus, R. Naslain, and J. Thebault, Oxidation Mechanisms and Kinetics of 1D-SiC/C/SiC Composite Materials: I, An Experimental Approach, *J. Am. Ceram. Soc.*, **77** (2), 459-466, 1994.
2. F. Lamouroux and G. Camus, Kinetics and Mechanisms of Oxidation of 2D Woven C/SiC Composites: I, Experimental Approach, *J. Am. Ceram. Soc.*, **77** (8), 2049-2057, 1994.
3. Y.G. Gogotsi and M. Yoshimura, Low-Temperature Oxidation, Hydrothermal Corrosion, and Their Effects on Properties of SiC (Tyranno) Fibers, *J. Am. Ceram. Soc.*, **78** (6), 1439-1450, 1995.
4. S. Adjerid, J.E. Flaherty, P.K. Moore, and Y.J. Wang, High-Order Methods for Parabolic Systems, *Physica D*, **60**, 94-111, 1992.
5. S. Adjerid, J.E. Flaherty, W. Hillig, J.B. Hudson, and M.S. Shephard, Modeling and the Adaptive Solution of Reactive Vapor Infiltration Problems, *Model. Simul. Mater. Sci. Engng.*, **3**, 737-752, 1995.
6. M. Aiffa, *Adaptive hp-Refinement Methods for Singularly Perturbed Elliptic and Parabolic Systems*, Ph.D. Dissertation, Dept. Math. Sci., Rensselaer Polytechnic Institute, Troy, 1997, in preparation.
7. R.H. Doremus, *Glass Science*, 2nd Ed., John Wiley & Sons, New York, 1994.
8. R. Wentorf, M.S. Shephard, G.J. Dvorak, J. Fish, M.W. Beall, R. Collar, and K.L. Shek, Software Frame for Mechanism-Based Design of Composite Structures, these proceedings, 1997.

## MODELING AND SIMULATION OF FAILURE PROCESSES IN COMPOSITES

Jacob Fish, Kamrun Shek, Said Gomma, Mark S. Shephard, George J. Dvorak  
Rensselaer Polytechnic Institute, Troy, NY 12180

and

William E. Bachrach, Amr M. Wafa  
General Electric Corporate Research and Development, Schenectady, NY 12345

**ABSTRACT** — The paper describes recent research conducted at Rensselaer aimed at modeling and simulation of failure processes in composite materials and structures using micromechanical and macromechanical approaches. The micromechanical approach is based on the mathematical homogenization theory with eigenstrains and a rapid post-processing procedure, which enables you to solve large scale structural systems in heterogeneous media at a cost comparable to problems in homogeneous media without significantly compromising on solution accuracy. The building blocks of the macromechanical approach are as follows: (i) enriching through-the-thickness kinematics of the shell to compute 3D effects, (ii) simulation of the delamination growth by incorporating discontinuous through-the-thickness interpolants, (iii) development delamination indicators to predict the critical regions so that enriched shell elements would be used only when and where it is necessary to do so, (iv) use of continuum damage mechanics approach to simulate evolution of delamination growth, and (v) calibration of critical damage parameters at the interface against the fracture toughnesses.

### MICROMECHANICAL APPROACH

The computational challenge of solving nonlinear heterogeneous systems is enormous. A solution of large scale history-dependent nonlinear systems that provides an accurate resolution of local fields is not feasible by means of the classical unit cell approach. For linear problems a unit cell or a representative volume problem has to be solved only once, whereas for nonlinear history dependent systems the unit cell problem has to be solved at every increment and for each integration point. Moreover, history data has to be updated at a number of integration points equal to the product of number of integration points at all modeling scales considered. To illustrate the computational complexity involved, we consider elasto-plastic analysis of the two-scale composite flap problem shown in Figure 1. The macrostructure is discretized with 788 tetrahedral elements (993 unknowns), whereas microstructure is discretized with 98 elements in the fiber domain and 253 elements in the matrix domain. The CPU time on a SPARC 10/51 for this problem was 7 hours, as opposed to 10 seconds if metal plasticity was used instead. This means that 99.7% of CPU time is spent on constitutive equations. This raises the question whether the observation made by Hill 30 years earlier stating that "... for nonlinear systems the computations needed to establish any constitutive law are formidable indeed ..." is still valid today. In the following we describe a novel modeling scheme based on mathematical homogenization theory with eigenstrains [5] and a rapid post-processing procedure, which enables the solution of large scale structural systems in heterogeneous media at a cost comparable to problems in homogeneous media without significantly compromising on solution accuracy.

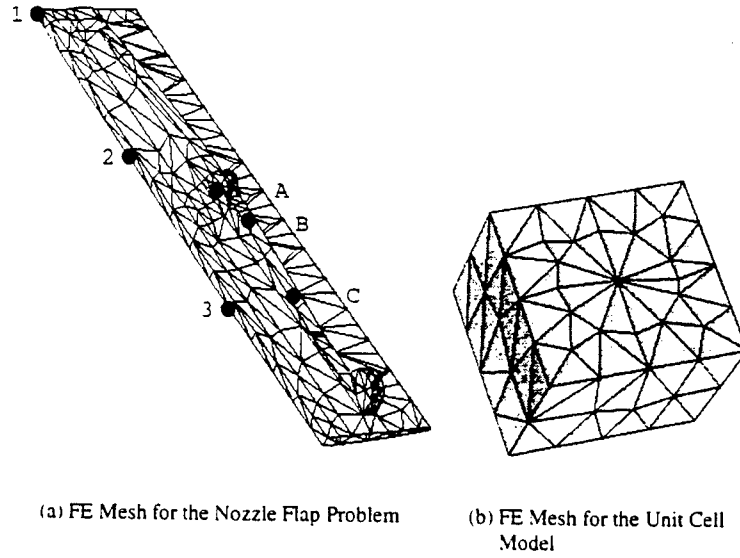


Figure 1: FE meshes for the Nozzle Flap Problem and the Unit Cell Model

We assume that the microstructure of a composite is periodic ( $Y$ -periodic) so that the homogenization process can be performed in a unit cell domain, denoted by  $\Theta$ . Thus, the response functions, such as displacements and stresses, are also periodic. Let  $x$  be a macroscopic coordinate vector and  $y \equiv x/s$  be a microscopic position vector.  $s$  is a small parameter representing the ratio between the scales. For any  $Y$ -periodic function  $f^s(x) \equiv f(x, y(x))$ , the indirect macroscopic spatial derivatives of  $f^s$  can be calculated by the chain rule as

$$f^s_{,x_i}(x) = f_{,x_i}(x, y) + \frac{1}{s} f_{,y_i}(x, y) \quad (1)$$

where subscripts followed by a comma denote partial derivatives with respect to the subscript variables (i.e.,  $f^s_{,x_i} = \partial f^s / \partial x_i$ ).

In modeling a heterogeneous medium, micro-constituents are assumed to possess homogeneous properties and satisfy the set of continuum mechanics equations

$$\sigma^s_{ij,x_j} + b_i = 0, \quad \sigma^s_{ij} = L_{ijkl}(\epsilon^s_{kl} - \mu^s_{kl}), \quad \epsilon^s_{ij} = u^s_{(i,x_j)} \quad (2)$$

and the appropriate boundary and interface conditions. In (2),  $\sigma^s_{ij}$  and  $\epsilon^s_{ij}$  are stress and strain tensors;  $L_{ijkl}$  and  $\mu^s_{ij}$  are elastic stiffness and eigenstrain tensors, respectively;  $b_i$  is a body force;  $u_i$  denotes a displacement vector; the subscript pair with parenthesis denotes the symmetric gradient defined as  $u^s_{(i,x_j)} = (u^s_{i,x_j} + u^s_{j,x_i})/2$ .

The displacement  $u_i^3(x)$  and eigenstrain  $\mu_{ij}^3(x)$ , subsequently denoted by  $u_i(x, y)$  and  $\mu_{ij}(x, y)$ , are approximated by the double scale asymptotic expansions:

$$u_i(x, y) \approx u_i^0(x, y) + s u_i^1(x, y) + \dots \quad \mu_{ij}(x, y) \approx \mu_{ij}^0(x, y) + s \mu_{ij}^1(x, y) + \dots$$

Expansion for strain and stress tensors can be obtained by manipulating the above expansions and (2) with consideration of the indirect differentiation rule (1):

$$\epsilon_{ij}(x, y) \approx \frac{1}{s} \epsilon_{ij}^{-1}(x, y) + \epsilon_{ij}^0(x, y) + s \epsilon_{ij}^1(x, y) + \dots \quad (3)$$

$$\sigma_{ij}(x, y) \approx \frac{1}{s} \sigma_{ij}^{-1}(x, y) + \sigma_{ij}^0(x, y) + s \sigma_{ij}^1(x, y) + \dots \quad (4)$$

The stress and strain tensors are related by the following constitutive rules:

$$\sigma_{ij}^{-1} = L_{ijkl} \epsilon_{kl}^{-1}, \quad \sigma_{ij}^r = L_{ijkl} (\epsilon_{kl}^r - \mu_{kl}^r) \quad \text{where } r = 0, 1, \dots \quad (5)$$

Substituting equation (5) into the equilibrium equation in (2), a set of equilibrium equations for various orders of  $s$  can be obtained. From the lowest order  $O(s^{-2})$  of equilibrium equation, we get  $u_i^0 = u_i^0(x)$ . Considering the  $O(s^{-1})$  equilibrium equation with arbitrary macroscopic strain and eigenstrain fields, and using the separation of variables for macroscopic and microscopic quantities yields the following two governing equations in  $\Theta$ :

$$\{L_{ijkl}(\delta_{km}\delta_{ln} + \Psi_{klmn})\}_{,y_j} = 0 \quad (6)$$

$$(L_{ijkl}\Psi_{klmn})_{,y_j} d_{mn}^\mu - (L_{ijkl}\mu_{kl}^0)_{,y_j} = 0 \quad (7)$$

where  $\delta_{km}$  is the Kronecker delta,  $d_{mn}^\mu$  is a macroscopic portion of the solution resulting from eigenstrains and  $\Psi_{klmn}$  is related to the elastic strain concentration factor  $A_{klmn}$  such that for the case of zero eigenstrain, the microscopic strain can be written in terms of the overall strain  $\bar{\epsilon}_{mn}$  as follows:

$$\epsilon_{kl} = A_{klmn} \bar{\epsilon}_{mn} \quad \text{and} \quad A_{klmn} = \frac{1}{2}(\delta_{km}\delta_{ln} + \delta_{kn}\delta_{lm}) + \Psi_{klmn} \quad (8)$$

In the following, we will adopt a matrix notation such that  $\mathbf{A}$  is the matrix notation of  $A_{klmn}$ . Equation (6) is the standard linear unit cell equation [2] subjected to periodic boundary conditions that can be solved in  $\Theta$ . Finite element methods can be used for calculating  $\Psi$  [6]. The elastic homogenized stiffness tensor  $\bar{\mathbf{L}}$  follows from the  $O(s^0)$  equilibrium equation and is given as:

$$\bar{\mathbf{L}} \equiv \frac{1}{|\Theta|} \int_{\Theta} \mathbf{L} \mathbf{A} d\Theta = \frac{1}{|\Theta|} \int_{\Theta} \mathbf{A}^T \mathbf{L} \mathbf{A} d\Theta \quad (9)$$

in which  $|\Theta|$  is the volume of a unit cell.

After solving equation (7), we obtain a closed form expression for  $d^\mu$ , and thus the  $O(s^0)$  approximation to asymptotic strain field (3) reduces to  $\epsilon = \mathbf{A} \bar{\epsilon} + \Psi d^\mu$ . Again, using the separation of variables for eigenstrains, the asymptotic expansion of the strain field (3) can be expressed as follows:

$$\epsilon(x, y) = \mathbf{A}(y) \bar{\epsilon}(x) + \sum_{\eta=1}^{N_e} \mathbf{D}_\eta(y) \mu_\eta^0(x) \quad (10)$$

in which  $\mathbf{D}_\eta(y)$  are the eigenstrain influence functions given in terms of strain concentration function  $\Psi(y)$  as follows:

$$\mathbf{D}_\eta(y) = \frac{1}{|\Theta|} \Psi(\tilde{\mathbf{L}} - \tilde{\mathbf{L}})^{-1} \int_{\Theta} \Psi^T \mathbf{L} \Psi_\eta d\Theta \quad (11)$$

Finally, the macroscopic equilibrium can be obtained as

$$\bar{\sigma}_{ij,x_j} + b_i = 0, \quad \bar{\sigma}_{ij} = \frac{1}{|\Theta|} \int_{\Theta} \sigma_{ij}^0 d\Theta \quad (12)$$

Consider a composite medium consisting of two phases, matrix and reinforcement, with respective volume fractions  $c_m$  and  $c_f$  where subscripts  $m$  and  $f$  represent matrix and reinforcement phases, respectively. Assuming that the eigenstrain is uniformly distributed within each phase, equation (10) can be reduced to

$$\epsilon_r = \mathbf{A}_r \bar{\epsilon} + \mathbf{D}_{rm} \mu_m + \mathbf{D}_{rf} \mu_f, \quad r = m, f \quad (13)$$

in which  $\mathbf{A}_r$  is the phase concentration factors and  $\mathbf{D}_{rs}$  can be expressed in terms of the phase stiffnesses and concentration factors [3, 5].

We consider an anisotropic reinforcement material which remains elastic throughout the loading history and an elasto-plastic matrix phase with isotropic elastic properties. Thus, the phase eigenstrains can be expressed as  $\mu_f = \epsilon_f^0$  and  $\mu_m = \epsilon_m^p + \epsilon_m^0$  where  $\epsilon_m^p$  is the matrix plastic strain and  $\epsilon_r^0$  (where  $r = m, f$ ) is the phase thermal strain. For a known temperature distribution,  $\epsilon_r^0$  is a prescribed quantity depending on the phase thermal expansion tensor  $\mathbf{m}_r$ . Also, we assume that all the elastic moduli are not functions of temperature; thus, the concentration factors and eigenstrain influence functions are constant matrices.

In order to maintain a quadratic rate of convergence for the Newton's method, the formation of a tangent stiffness matrix that is consistent with the integration procedure employed is required. The rate form of the constitutive equation can be written in terms of the consistent tangent operators  $\mathfrak{D}$  [5] and  $\mathfrak{d}$  as

$$\dot{\sigma} = \mathfrak{D} \dot{\epsilon} + \mathfrak{d} \dot{\theta} \quad (14)$$

in which

$$\mathfrak{D} = c_f \mathfrak{D}_f + c_m \mathfrak{D}_m, \quad \mathfrak{d} = - \sum_{r=m}^f (c_m \mathbf{Q}_{mr} + c_f \mathbf{Q}_{fr}) \mathbf{m}_r$$

where

$$\begin{aligned} \mathfrak{D}_m &= \left( \mathbf{I} + \Delta\lambda_m \mathbf{Q}_{mm} \mathbf{P} + \frac{9-6(1-\beta)H\Delta\lambda_m}{4H\hat{\sigma}_m^2} \mathbf{Q}_{mm} \mathcal{N}_m \mathcal{N}_m^T \right)^{-1} \mathbf{R}_m \\ \mathfrak{D}_f &= \mathbf{R}_f - \left( \Delta\lambda_m \mathbf{Q}_{fm} \mathbf{P} + \frac{9-6(1-\beta)H\Delta\lambda_m}{4H\hat{\sigma}_m^2} \mathbf{Q}_{fm} \mathcal{N}_m \mathcal{N}_m^T \right) \mathfrak{D}_m \end{aligned}$$

and  $\dot{\theta}$  is the temperature rate;  $\mathbf{I}$  and  $\mathbf{P}$  are the identity and projection matrices;  $\mathcal{N}_m$  is the normal to the yield surface;  $H$ ,  $\beta$  and  $\hat{\sigma}_m$  are material constants.

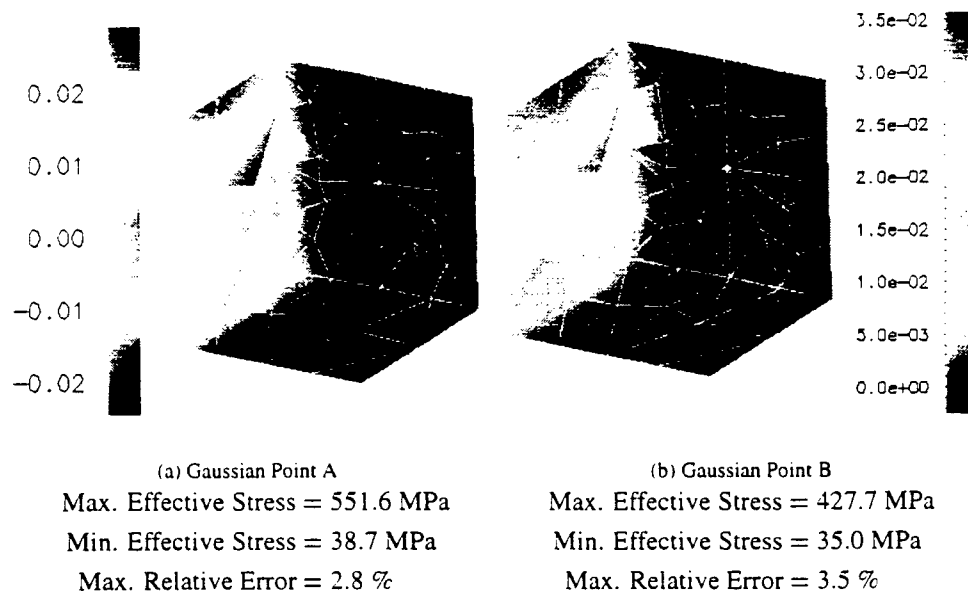


Figure 2: Unit Cell Relative Error for Effective Stress

The overall analysis procedure is divided into two stages. In the first stage, a nonlinear composite structural problem is solved using a finite element method based on the two-point averaging approach developed in previous sections. The macroscopic analysis of the composite structure is then carried out and the macroscopic strain histories are stored in a history database at Gaussian points in the critical regions. In the second stage, the microstress distribution in  $\Theta$  is sought. The strain history at macroscopic Gaussian points for critical regions is extracted from the database. Subsequently, the macroscopic strain history is applied to the unit cell through the incremental homogenization procedure discussed in [5]. Since the micro-history recovery is performed only at a select number of Gaussian points of interest without affecting macroscopic analysis, the computational cost is low.

For the flap problem considered in Figure 1 the CPU time for the averaging scheme with variational micro-history recovery is only 30 seconds on a SPARC 10/51 as opposed to 7 hours using classical mathematical homogenization theory. The memory requirement ratio for these two approaches is roughly 1:250. Figure 2 shows that the maximum error in the micro-stress in the unit cell located in two critical locations is only 3% in comparison to the maximum error in the classical mathematical homogenization theory.

## MACROMECHANICAL APPROACH

Composite laminates are prone to wide range of damage, such as matrix cracking, fracture of fibers, fiber-matrix debonding and delamination. In the previous section we attempted to describe the microstructure of a composite in detail and to develop fast homogenization techniques. In this section we adopt a macromechanical description that views composite as homogeneous anisotropic medium. Our primary objective here is to develop computationally efficient macromechanical progressive dam-

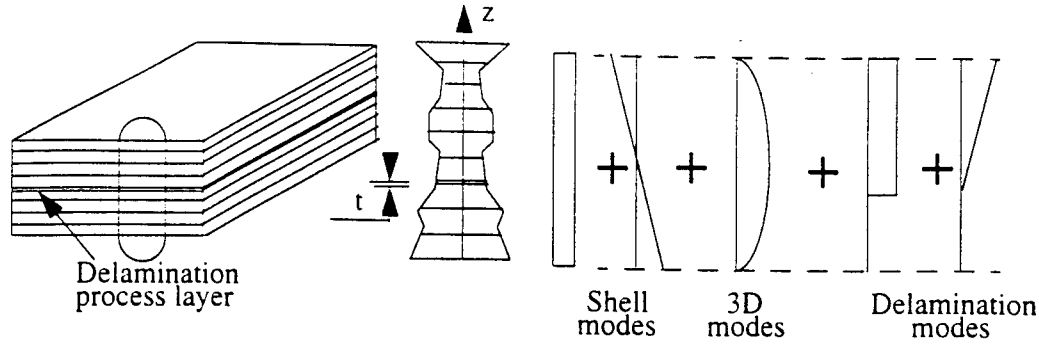


Figure 3: Enriched Kinematics of Shell Element

age modeling capabilities and to embed those within the framework of commercial finite element code. The following subtasks and limitations have been identified:

- Evolution of delamination should be modeled using rigorous fracture mechanics philosophy. At the same time, for the large scale problems considered, such as the composite fan blade subjected to impact loading, it is not feasible to continuously remesh the component under consideration at every time/load step.
- 3D effects should be captured in the vicinity of the boundary layers, although the use of 3D elements should be avoided due to the computational cost involved.
- Micromechanical failure modes should be accurately predicted, but the use of unit cells or representative volume elements is not desired due to the computational cost involved.

To meet these objectives the following strategy has been devised:

- Compute the 3D effects by enriching through-the-thickness kinematics of the shell with quadratic modes as shown in Figure 3.
- Simulate the delamination by incorporating discontinuous through-the-thickness interpolants to enrich the set of the element shape functions. The kinematics of the enriched shell element is summarized in Figure 3. The strain field within the process layer is obtained as ratio between the displacement jump and the thickness of the process layer.
- Use the continuum damage mechanics approach pioneered by Kachanov [7] to simulate evolution of delamination growth in the process layer [1, 9], but calibrate the critical damage parameters at the interface against the fracture toughnesses as follows:

$$G_i^c = t Y_i^c \quad i = \text{I, II, III}$$

where  $G_i^c$  is mode  $i$  fracture toughness,  $Y_i^c$  the critical continuum energy release rate, and  $t$  the thickness of the process layer.

- Develop delamination indicators to predict the critical regions so that enriched shell elements would be used only when and where it is necessary to do so. The formulation of delamination

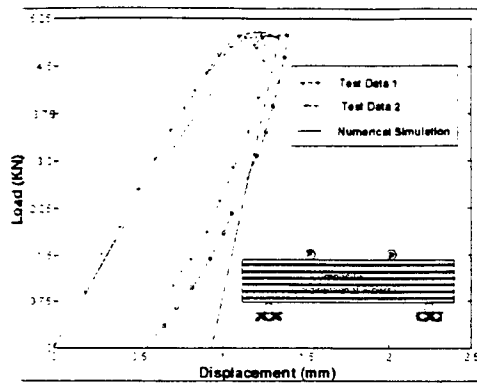


Figure 4: Macroscopic Model Validation

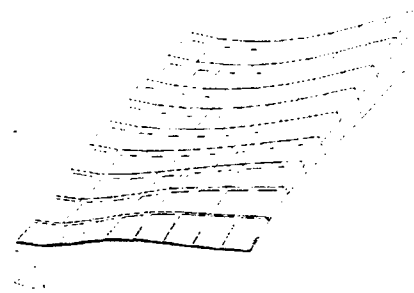


Figure 5: Deformed Mesh of FOD panel

indicator is based on estimating whether it is necessary to locally enrich the formulation of the shell element with a discontinuous displacement mode ( $ddm$ ), i.e.,

$$u^{enriched} = u^{shell} + \Psi^{ddm} \beta$$

where  $\Psi^{ddm}$  is a shape function for discontinuous displacement mode and  $\beta$  its amplitude. The value of  $\beta$  is determined by solving a local discrete problem with  $\beta$  as a single unknown keeping the nodal solution fixed. The value of  $\beta$  is estimated at each node and for each interface. The delamination will most likely occur in those layers and nodes where incorporation of the jump mode results in the maximum change in energy. This philosophy resembles the concept of energy release rate. A similar strategy has been employed for hierarchical error estimation in laminated shells [4].

The final product that has been developed and implemented in ABAQUS is a 15 degrees-of-freedom per node hierarchical shell element which includes: 6 degrees-of-freedom to simulate classical shell modes, 3 quadratic modes for 3D effects, 6 jump modes to simulate mode I, II, III fracture. In absence of delamination, the element has an identical formulation to that of the Assumed Natural Strain shell element [8].

Figure 4 shows the comparison between the numerical simulation and the experimental data in four-point bend test. The plate has been modeled with 10 by 10 shell elements. It can be seen that the critical load is 4.7 kN when delamination in the mid-layer has been observed. Numerical results have been found to be in good agreement with experimental measurements.

The next example shows the simulation of a Foreign Object Damage (FOD) test. During the test, a cylindrical gelatin projectile is fired at a composite panel using a large gas gun. Figure 5 shows the deformed finite element mesh of half of the panel after impact. Numerical results agreed well with experimental measurements.

## SUMMARY

Two approaches for modeling inelastic behavior of heterogeneous materials have been describes. The micromechanical approach, which models composite material on the scale of heterogeneity, and



the macromechanical approach, which views the composite as anisotropic homogeneous media. Our micromechanical approach is based on the mathematical homogenization theory with eigenstrains and a rapid post-processing scheme. It provides a comparable accuracy to the classical theory but at a fraction of computational cost. For the numerical example considered, the speedup factor was over three orders of magnitude as compared to the classical theory, whereas the maximum error in stresses was less than 3%. The macromechanical approach presented here is based on higher order shell theory with built in discontinuous through-the-thickness interpolants, delamination indicators, and damage mechanics approach calibrated to fracture mechanics. Numerical examples in four point bending test and FOD panel problems agreed well with experimental data.

## References

- [1] O. Allix and P. Ladeveze. Interlaminar interface modeling for the prediction of delamination. *Composite Structures*, 22, 1992.
- [2] A. Benssousan, J. L. Lions, and G. Papanicoulau. *Asymptotic Analysis for Periodic Structure*. North-Holland, 1978.
- [3] G. J. Dvorak. Transformation field analysis of inelastic composite materials. *Proceedings of Royal Society of London*, A437, 1992.
- [4] J. Fish and R. Guttal. The s-version of finite element method for laminated composites. *International Journal of Numerical Methods in Engineering*, 39, 1996.
- [5] J. Fish, K. Shek, M. Pandheeradi, and M. S. Shephard. Computational plasticity for composite structures based on mathematical homogenization: Theory and practice. *Computer Methods in Applied Mechanics and Engineering*, to appear, 1997.
- [6] J. M. Guedes and N. Kikuchi. Preprocessing and postprocessing for materials based on the homogenization method with adaptive finite element methods. *Computer Methods in Applied Mechanics and Engineering*, 83, 1990.
- [7] L. M. Kachanov. Time of the rupture process under creep conditions. *Izvestiya Akademia Nauk, USSR otd. Tekh*, 8, 1958.
- [8] K. C. Parks and G. M. Stanley. A curved C<sup>1</sup> shell element based on assumed natural coordinate strains. *Journal of Applied Mechanics*, 108, 1986.
- [9] S. Rinderknecht and B. Kroplin. A finite element model for delamination in composite plates. *Mechanics of Composite Materials and Structures*, 2, 1995.

# **DYNAMIC AND TRANSIENT CHARACTERIZATION OF CERAMIC FIBERS AT ELEVATED TEMPERATURES**

S. S. Sternstein and R. Warren  
Center for Composite Materials and Structures  
Rensselaer Polytechnic Institute  
Troy, N. Y. 12180

## **ABSTRACT**

Ceramic fibers at elevated temperatures exhibit time or frequency dependent mechanical behavior, the most studied of which is creep. Several techniques for characterizing time dependent mechanical properties have been developed in this laboratory. Fibers studied to date include single crystal alumina, YAG, and seven compositions of SiC. Dynamic mechanical spectroscopy methods are used to examine short relaxation time processes associated with periodic deformation phenomena, and provide both dynamic modulus and loss factor versus temperature (to 1600°C) and frequency (from 0.1 to 25 Hz). Pulsed periodic creep and recovery tests are used to examine the longer relaxation time phenomena, and provide an accelerated means to identify and separate anelastic and inelastic creep rates. Taken together these methods provide a comprehensive understanding of the multiplicity of mechanisms and time scales that are relevant to the proper application and design of ceramic fiber reinforced composites.

## **INTRODUCTION**

The analysis of the potential performance of high temperature composite materials and the design of components made from such materials requires detailed information about the constituents of the composite. It is well known that ceramic fibers exhibit high temperature behavior which is time-dependent, i.e., not entirely elastic. In order to gain a more complete understanding of the behavior of ceramic fibers at elevated temperatures and to provide a database for the engineering analysis of composites using these fibers as a reinforcement phase, this laboratory has investigated single fiber behavior using a variety of techniques. In this paper, a periodic creep and recovery technique [1] is utilized for the investigation of the viscoelastic properties of ceramic fibers.

## BACKGROUND

Materials scientists and engineers commonly use creep testing as a primary means to characterize long term high temperature behavior under applied loads. Generally, creep strain can include elastic, anelastic (viscoelastic) and inelastic (plastic) strain components. Refer to Figure 1 for a schematic of a creep and recovery test. The elastic contribution to a given creep strain is readily measured by simply removing the sample load and observing the incremental strain change. Decomposition of the remaining strain into anelastic and inelastic strains can be a challenging task, however. In general, given only a creep curve (strain vs. time) it is not possible to determine what fraction of the strain is anelastic and what fraction inelastic. This determination can be done only by performing a recovery test in which the (recovering) strain vs. time is observed following the removal of the load. The difficulty lies in the fact that as a rule, creep recovery is much slower than creep itself. Presumably, this is because creep recovery occurs with no externally applied load, and given any sort of activated rate theory for the processes involved, the reverse (recovery) process would be expected to involve a higher activation barrier than for the (forward) creep process itself. As a general rule, full recovery of anelastic strains can take as much as ten times longer than the creep itself. Thus a one month creep test might take ten months to fully recover if the strains were entirely anelastic. Clearly, the decomposition of a creep curve into anelastic and inelastic components would involve a series of creep tests for various times, each of which is followed by a longer recovery process. In this way, a long term creep curve could be decomposed into its component anelastic and inelastic strains. From both a mechanistic and design viewpoint, this decomposition is essential. As a corollary, it follows that the measurement of plastic strain rates from a single creep curve is potentially misleading since there would be no basis by which to judge the anelastic (time dependent but recoverable) strains. It is emphasized that the shape of the creep curve (e.g., constant rate) is a very misleading and poor delineator of whether the strain is inelastic or anelastic (or both), as discussed below.

There is evidence in the literature that ceramic fibers do exhibit surprising amounts of anelastic strain. An important observation is given by DiCarlo [2] who performed a creep test on a silicon carbide fiber (SCS-6), followed prudently by an accelerated recovery test at a higher temperature. The creep test was done at 1275°C and 612 MPa, and followed by recovery at 1450°C. Nearly complete recovery was obtained which suggests that the creep curve was primarily anelastic.

Additional creep and recovery tests for short time periods have been reported by Lara-Curzio [3].

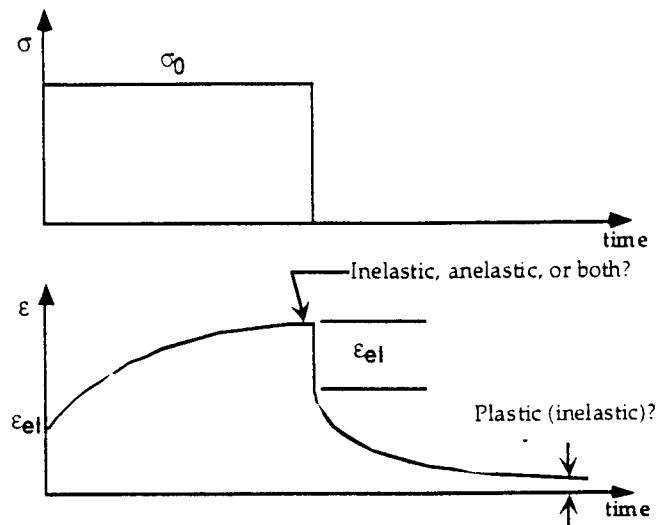


**Figure 1:** Loading history and strain response for a typical creep and recovery test.

Guidance regarding the shape of a creep curve which is anelastic can be obtained directly from the theory of linear viscoelasticity (which is not to say that all anelastic processes are linear processes). Anelasticity can be represented by a series of recoverable strains each with a characteristic retardation time, or differently stated, an anelastic process can be represented by its corresponding distribution (or spectrum) of retardation times. For each retardation time, 63% of the anelastic strain component is obtained after a load application for a time equal to one retardation time. It becomes obvious then, that the shape of an anelastic creep curve is dependent on the distribution of retardation times characterizing the creep process. Without additional information, it becomes clear why the shape of the creep curve is a very poor determination of whether the creep is anelastic or inelastic. It follows that a recovery curve of 100 seconds, for example, may fully recover anelastic strains with 10 second or less retardation times, but would not recover any appreciable amount of anelastic strains having retardation times of longer than 1000 seconds. It is for this reason that we noted earlier that the decomposition of a creep curve into its anelastic and inelastic components requires a series of recovery tests, conducted for several creep times, and not a single recovery test.

Mathematically related to the distribution of retardation times is another distribution referred to as the distribution of relaxation times, which is useful in describing anelastic processes such as stress relaxation or dynamic modulus. Initially, this laboratory engaged in

dynamic mechanical modulus studies on single ceramic fibers at elevated temperatures, as described elsewhere [4]. In that method a fiber is subjected to a sinusoidally varying displacement and the resulting load measured (without averaging or filtering). The load and displacement signals are then fast Fourier transformed (FFT) to obtain the component of force in-phase and out-of-phase with the displacement, providing ultimately the real (in-phase or storage or elastic) modulus and the imaginary (out-of-phase or loss or viscous) modulus.

While the real and imaginary components of modulus provide equivalent information on the anelastic processes as does a creep/creep recovery test, they do so at a far different time scale. Dynamic measurements typically emphasize short time scale processes (e.g., relaxation times of milliseconds or less) while creep/recovery tests provide information on long time scale processes (typically retardation times of seconds to years). Thus, the two methods of measurement are complementary and provide a broad picture of material anelastic behavior over many decades of time scale. However, the dynamic modulus measurement method, being intrinsically periodic with a short time scale, quickly reaches steady state, whereas the creep/recovery method being transient, and specifically not periodic, never indicates steady state behavior. A perspective now emerges on the difficulties involved in anelastic/inelastic decomposition of creep and recovery data. The problem of reconstruction of a creep curve into its underlying component anelastic vs. time and inelastic vs. time creep curves is the basis of the test method described here.

## **PULSED PERIODIC CREEP AND RECOVERY TESTING**

One of the useful features of the dynamic test method is its periodic nature, which enables one to quickly establish steady state behavior. The test method utilized here combines the attributes of a periodic test while still offering the benefits of transient (creep) testing which emphasizes long time processes. Referring to Figure 2, consider a test protocol in which a load is periodically applied to a sample for a period of time  $t_1$  and then removed for some period of time  $(t_p - t_1)$  and then the entire cycle repeated every  $t_p$  seconds, where  $t_p$  is the "period." Further, let the strain at the end of each loading cycle be measured, as well as the strain at the end of each recovery cycle, as shown by the arrows in Figure 2.

This test is implemented using the apparatus described elsewhere [4] for dynamic modulus testing, but modified with a stiff closed-loop control

system and computer which generates the periodic program shown in Figure 2 and provides for automatic data acquisition. In practice, the load application or removal is done in less than 2 milliseconds without overshoot or ringing, and is made possible by a very stiff and well tuned servo. Data acquisition is done using 18 bit D/A conversion which is required for the high accuracy needed to implement the periodic pulse test. Precision timing for the pulse test history and data acquisition is done in hardware using a 6 MHz crystal, 64 bit pulse counter and interrupt generator. This provides for very precise and reproducible pulse cycles and data acquisition. Cycle periods from 0.5 seconds to days are readily obtained and the number of cycles is limitless, since the data is routinely written to hard disk. The parabolic temperature profile of the fiber testing device requires deconvolution of isothermal strain data from the measured displacements by simple calculations described by Feldman and Bahder [5]. A creep activation energy of 580 kJ/mol was found by true isothermal creep testing of CVD SiC fibers by Lara-Curzio [3], and is supported by DiCarlo [2] for testing under similar conditions as used in the present study.

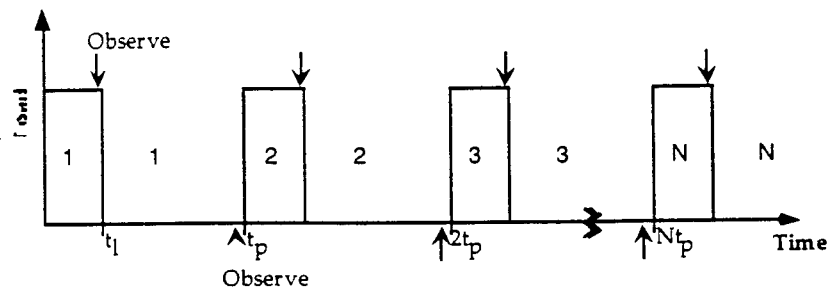


**Figure 2:** Loading history and strain measurement for pulsed periodic creep and recovery testing. Strain measured at  $(kt_p)^+$ ,  $k=1...N$  and  $(kt_p + t_l)^+$ ,  $k=0...(N-1)$ .

From the theory of linear viscoelasticity, it can be shown that the history described in Figure 2 produces a slowly accumulating peak strain (the strain measured at the end of each loading cycle) and slowly accumulating recovery strain, with the rate of accumulation being strongly dependent on the ratio of the test time parameters ( $t_l$ ,  $t_p$ ) relative to the retardation times of the material. The mathematics will not be presented here. Suffice it to say that anelastic creep processes having retardation times substantially longer than  $t_p$  are effectively "filtered" in that they never get activated (occur) during the loading cycle, while the processes having retardation times shorter or equivalent to  $t_p$  are largely recovered after each recovery cycle and therefore do not accumulate as they would if the load were maintained as in a single creep test (without periodic recovery). In effect, the pulsed periodic creep test will always produce less anelastic strain (for a given

accumulated time under load, that is  $t_1$  times the number of cycles) than a single creep test of the same time under load. It follows that the resultant "creep curve," that is peak strain vs. accumulated time under load will always be a better representation of the inelastic strain process (if any) than a single creep test. These predictions are fully justified by the experimental results to date, as described below.

## RESULTS AND DISCUSSION

Figure 3 shows a comparison between the creep strain developed during a conventional creep test and the peak strain achieved in a pulsed periodic creep test, the latter plotted vs. accumulated time under load. The pulsed data were obtained for a duty cycle consisting of  $t_1 = 10$  sec. and  $t_p = 30$  sec. Also shown is a single strain point obtained after 9600 seconds of recovery for the single creep test sample. The amount of recovery is large and shows that most of the creep strain which occurred after 4600 seconds was in fact anelastic, not inelastic.

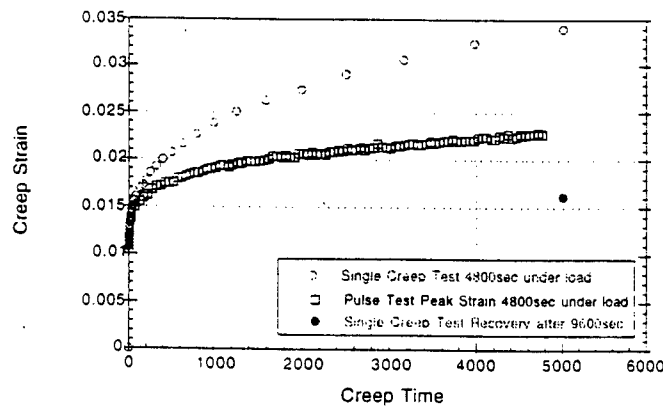


**Figure 3:** Comparison of Pulse Testing with Single Creep and Recovery test. Testing conducted at 200 MPa, 1600°C, 480 cycles (10 sec. load on, 20 sec. load off) versus 4800 sec. creep, 9600 sec. recovery.

As expected, the pulsed periodic results lie between the single creep results and the recovered strain value. Additional experiments on the effects of various duty cycles ( $t_1$  and  $t_p$  values, both as a ratio and absolute values) are currently being performed. While the recovery time to load time for the pulsed periodic test was only 2 to 1 there is still clearly a major reduction in accumulating anelastic strain. While it would be tempting to claim that the slope of the pulsed periodic creep results vs. accumulated loading time is in fact the inelastic (plastic) strain rate, this would be premature, since other duty cycles with longer

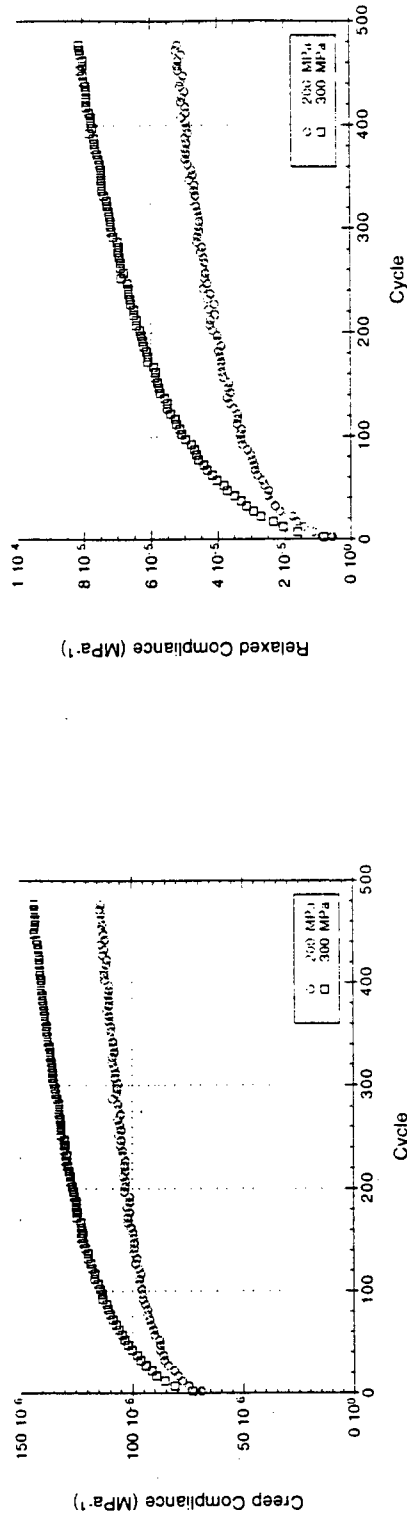


Figure 4: Comparison of Pulse Testing at 200 MPa and 300 MPa stress showing non-linearity of creep behavior. Tests conducted at 1600°C for 480 cycles (10 sec. load on, 20 sec. load off).

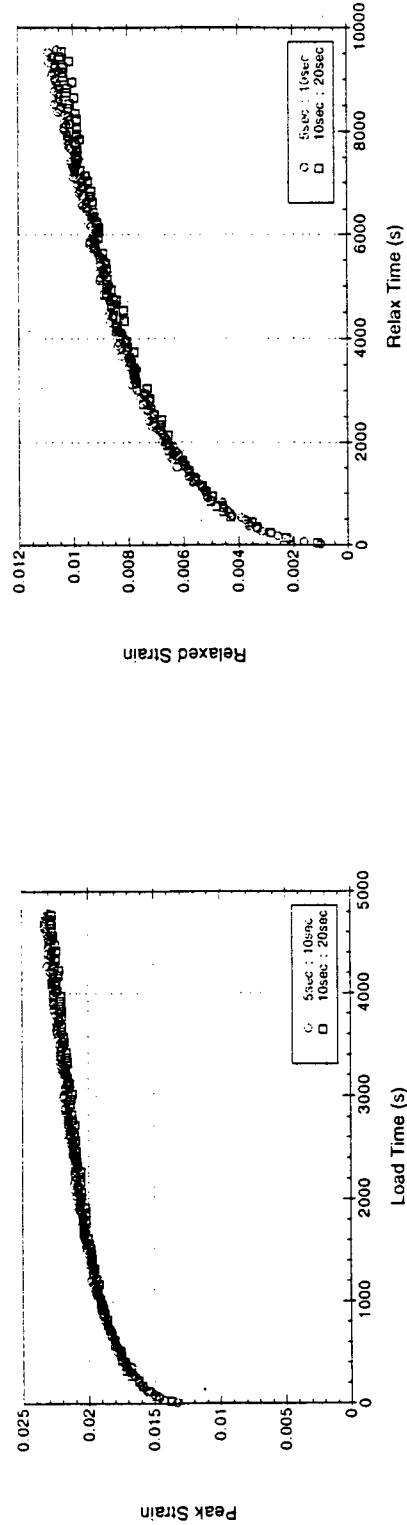


Figure 5: Comparison of various cycle times (5sec. load on, 10 sec. load on, 20 sec. load off) with 1:2 load-on:load-off time ratios. Testing at 1600°C, 200 MPa stress, 960 cycles vs. 480 cycles.



recovery to load ratios than 2/1 are required for better suppression of the anelastic strain. Nonetheless, we claim that the slope of the pulsed periodic results is closer to the true inelastic creep rate than the single creep test slope, which is clearly much larger.

The effect of stress magnitude on the pulsed periodic creep test is shown in Figure 4 for SCS-6 fibers at 1600°C, and it is seen that the creep process is nonlinear, as is also concluded from single cycle creep test data. Finally, the effect of cycle time at constant duty cycle ratio (2/1) is shown in Figure 5, where it is seen that the results for 15 and 30 second periods are virtually indistinguishable. In conclusion, it appears that the pulsed periodic creep test provides a method whereby the inelastic strain rate may be measured with higher accuracy and more quickly than with single cycle creep tests. Anelastic creep in ceramic fibers at elevated temperatures is surprisingly large in magnitude and covers wide time scales, and therefore significantly affects the slope of a single cycle creep curve, rendering the measurement of inelastic strain rates difficult if not impossible from such a test. The technique used in this study may provide an accelerated and more time efficient method for determining inelastic creep rates.

## ACKNOWLEDGMENTS

This work was supported by DARPA/ONR Contract No. N-00014-86-K-0770. Previous students C. D. Weaver and J. Beale participated in the ongoing development of the fiber tester which was modified for the present study.

## REFERENCES

- [1] Y. H. Park, J. W. Holmes, *J. Mat. Sci.*, 27 (1992) 6341
- [2] J. A. DiCarlo, *J. Mat. Sci.*, 21 (1986) 217.
- [3] E. Lara-Curzio, Thermomechanical Characterization of Silicon Carbide Fibers at Elevated Temperatures, PhD. Thesis, Rensselaer Polytechnic Institute, 1992
- [4] S. S. Sternstein, C. D. Weaver and J. Beale, *Materials Science and Engineering* A215 (1996) 9-17.
- [5] L. A. Feldman, T. B. Bahder, *J. Mat. Sci.*, 8 (1989) 307

## **IMPROVED PROPERTIES OF SILICIDE MATRIX COMPOSITES**

S. Augustin, M. Broglio, P. Lipetzky, N.S. Stoloff  
Rensselaer Polytechnic Institute, Troy, NY 12180-3590

M. Nazmy  
ABB Power Generation Ltd..  
CH 5401, Baden, Switzerland

### **ABSTRACT**

Powder processing techniques have been used to prepare monolithic and composite samples in two silicide systems:  $\text{Cr}_3\text{Si}$  and  $\text{MoSi}_2$ . Two Mo-modified  $\text{Cr}_3\text{Si}$  compounds were consolidated from prealloyed powders, as were composites reinforced either with Pt alloy fibers or Saphikon (alumina) whiskers. Composites of  $\text{MoSi}_2$ , reinforced with SiC particles or particles plus whiskers, were consolidated by reactive sintering. Physical and mechanical properties of both systems, together with oxidation data for  $\text{Cr}_3\text{Si}$  and its composites also are reported.

### **INTRODUCTION**

Intermetallic compounds, including several aluminides and silicides, offer an attractive combination of properties for high temperature structural applications. These include high melting points, low densities and excellent oxidation resistance compared to nickel-base superalloys. However, poor fracture resistance remains as the principal obstacle to commercialization of these compounds. A common approach to improving toughness has been to reinforce these compounds with ductile metal fibers, but the resulting composites usually display much lower creep and oxidation resistance, even when toughening is achieved. [1-3]. An alternative approach has been to utilize ceramic reinforcements, but these often are incompatible with the matrix due to low thermal expansion coefficients of the former. [4] In the present work, it was decided to experiment with ductile fibers with good oxidation resistance, namely platinum alloy fibers, to reinforce two modified  $\text{Cr}_3\text{Si}$  alloys that have been shown to have excellent oxidation resistance themselves. Of course, this is considered to be a model system because of the high cost of the fibers. In the case of  $\text{MoSi}_2$ , the

focus of the research has been on lowering the cost and improving the purity of composites by utilizing reactive sintering of elemental powders. For both alloy systems, uniaxial hot pressing was employed as a lower cost alternative to hot isostatic pressing.

## **EXPERIMENTAL MATERIALS AND PROCEDURES**

Cr<sub>3</sub>Si: Two Cr<sub>3</sub>Si alloys, IM939, which contains Mo and W, and IM945, which contains only Mo, were studied; compositions appear in Table I. The alloys were induction melted under argon, then crushed and milled to about 3 micron diameter powder. Hot pressing was carried out in graphite dies using a step-wise increase in temperature and pressure to 1400°C and 38MPa, respectively. The coin shaped samples were then furnace cooled at a rate of 4°C per min.

Two types of reinforcements were used: 100 micron dia. Saphikon fibers, 5mm long, and continuous Pt-6Rh alloy fibers with 0.5mm dia. Typical volume fractions were 15%, except when the two reinforcements were present simultaneously; the volume fractions of each were then 10%.

Toughness was measured at room temperature by the hardness indentation method and at room temperature and elevated temperatures by notch bending. For the latter, flat specimens 24x6x3mm were used. Flexural strength and elastic moduli were calculated from the load-displacement curves for three-point unnotched bend samples. Limited oxidation testing was done in air at 1250 and 1400°C on specimens from monolithic and Pt-6Rh-reinforced IM945.

TABLE I: CHEMICAL COMPOSITION OF THE Cr<sub>3</sub>Si ALLOYS (a%)

Alloy	Cr	Mo	W	Si
IM939	48.28	15.62	5.18	30.92
IM945	50.54	13.40	-	36.05

MoSi<sub>2</sub>: MoSi<sub>2</sub>, MoSi<sub>2</sub> + 30v/o SiC particles, and MoSi<sub>2</sub> + 30v/o SiC particles + 10v/o SiC whiskers were produced using elemental powders, except for the whiskers. The diameters of starting particles were 3-7 microns for Mo, 4-6 microns for Si and 48 microns for C. Two mixtures were made, one of Mo + Si and one of Si + C, and combined in the desired stoichiometric proportions. SiC whiskers were added in the desired amount. The mixtures were placed in an Impandix Turbula mixer for 60 minutes and placed in a desiccator for 24 hours to remove as much absorbed moisture as possible. The powders were loosely set in a graphite mold with a BN mold release and the mold was then placed in the furnace with no initial pressure applied. The furnace was evacuated for 15 minutes and then put under positive pressure with argon. The furnace was then heated at a rate of 15°C/min with loads applied in steps. A pressure drop at 1395°C indicated when the reaction between the silicon and molybdenum occurred. The pressure was applied in steps. Once the furnace reached a temperature of 1400°C the pressure was left at 59 MPa for three hours to densify the material. After three hours the sample was furnace cooled at a rate of 4°C/min.

## RESULTS AND DISCUSSION

Cr<sub>3</sub>Si: The microstructure of consolidated IM945 is shown in Fig. 1a, while that of a composite reinforced with Pt-6Rh is shown in Fig. 1b. Note that the alloy fiber is broken up by the pressure exerted during hot pressing, but that no cracks from thermal mismatch are observed. However, when Saphikon is used, Fig. 1c, cracks often are seen around the fibers.

Elastic moduli data for the alloys and composites are shown in Fig. 2. General trends reveal that stiffness is not strongly affected by the presence of reinforcements; rather, temperature plays a dominant role. These moduli are much higher than what has been reported by Shah and Anton on Al<sub>2</sub>O<sub>3</sub> fiber reinforced Cr<sub>3</sub>Si composite [5]

Results of toughness tests are shown in Table II. The results show a significantly higher toughness for the reinforced samples at elevated temperatures, while room temperature values are not significantly affected. The increase at high temperature is attributed to the combined increase in matrix ductility as well as retained strength of the Saphikon fibers.

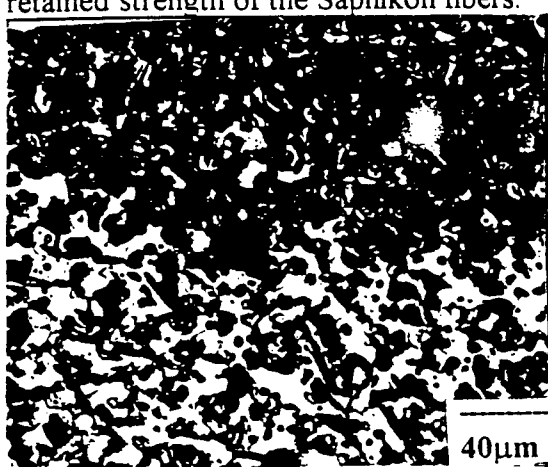


Fig. 1a). Etched microstructure of IM945

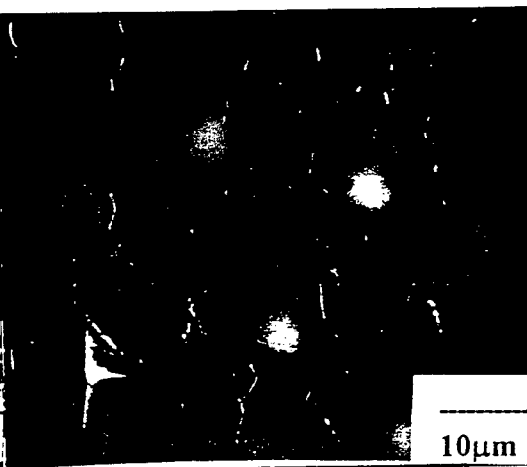


Fig. 1b). Etched microstructure of IM945 with Pt-6%Rh fiber

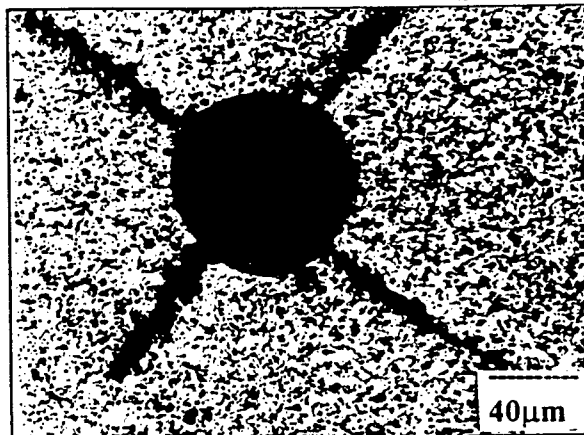


Fig. 1c). Cracking around Saphikon fibers in IM945

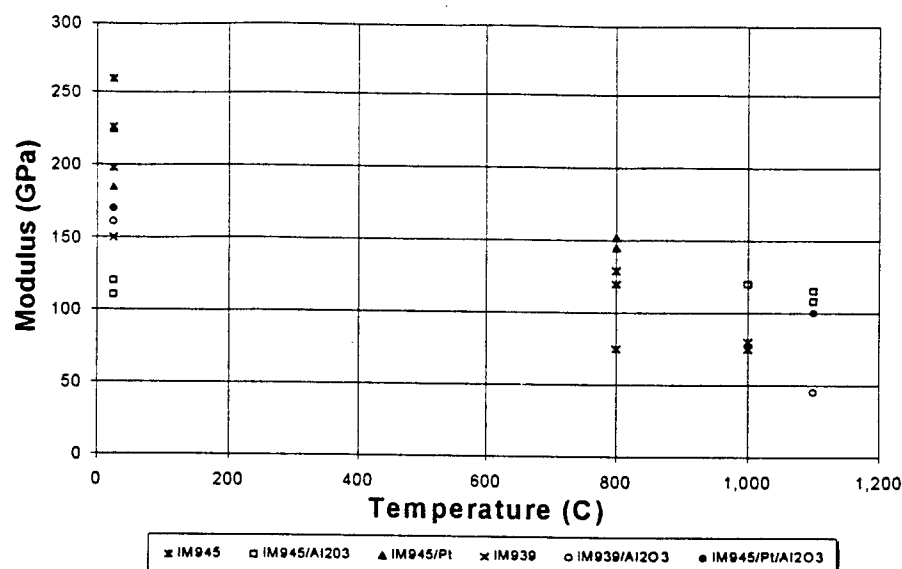


Fig. 2 The elastic modulus vs. temp for the unreinforced and composite materials

Two notched samples of IM945+Al<sub>2</sub>O<sub>3</sub> were tested at 1100°C resulting in K<sub>Q</sub>'s of 14.5 and 22 MPa<sup>1/2</sup>. One sample of IM945+Al<sub>2</sub>O<sub>3</sub>+Pt6Rh was also tested at 1100°C giving a toughness of 12 MPa<sup>1/2</sup>. For other high temperature intermetallic systems, K<sub>Q</sub> values, at room temperature, of 1.5 and 3.3 MPa<sup>1/2</sup> have been recently reported for monolithic Cr<sub>2</sub>Nb and 25% vol.% Nb/Cr<sub>2</sub>Nb composite, respectively [6]. In the same work, K<sub>Q</sub> values of 2.5 to 5 MPa<sup>1/2</sup> have been reported for monolithic Nb<sub>5</sub>Si<sub>3</sub> and 20 vol.% Nb/Nb<sub>5</sub>Si<sub>3</sub> composite, respectively [6]. For the same system, i.e., niobium silicide-base in situ composites K<sub>Q</sub> values of 12.8 to 16.4 MPa<sup>1/2</sup> were reported for Nb-16.5Si and Nb-40Ti-15Si-Al, respectively [7].

TABLE II: SUMMARY OF HARDNESS AND TOUGHNESS OF IM939 AND IM945 COMPOSITES AT ROOM TEMPERATURE AND AT 1100°C

	25°C		1100°C
	Hardness	Toughness	Bending Toughness
IM939 unreinf	1160 kg/mm <sup>2</sup>		
	5.5 MPa m <sup>1/2</sup>		
IM945 unreinf	1055 kg/mm <sup>2</sup>		
	5 MPa m <sup>1/2</sup>	2.9 MPa m <sup>1/2</sup>	
IM945 Pt6Rh		3.6 MPa m <sup>1/2</sup>	
IM945 Al <sub>2</sub> O <sub>3</sub>		2.7 MPa m <sup>1/2</sup>	18.3 MPa m <sup>1/2</sup> *
IM945 Pt6Rh/Al <sub>2</sub> O <sub>3</sub>		2.2 MPa m <sup>1/2</sup>	12 MPa m <sup>1/2</sup>
Al <sub>2</sub> O <sub>3</sub> fiber	2000 kg/mm <sup>2</sup>		
	9.3 MPa m <sup>1/2</sup>		(*average)

Figure 3 shows the fracture strength of the various composites over a range of temperatures. Remarkably, the failure strength at 1000°C and 1100°C can significantly increase from the room temperature value due to the inclusion of fibers.

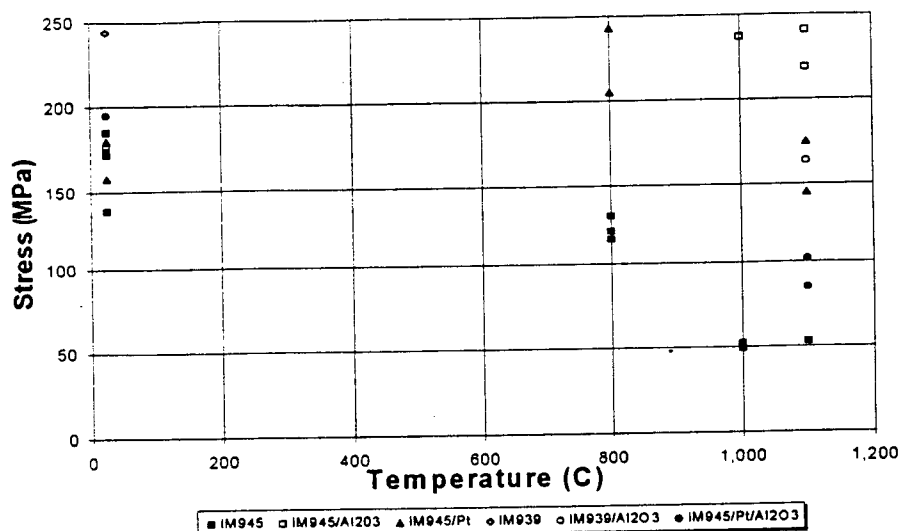


Fig. 3. Fracture strength vs. temperature for IM945 and IM939 silicides.

The load-displacement curves for three point unnotched bending specimens at room temperature for IM939 and IM945 were essentially linear prior to failure. Similar behavior was observed in Saphikon reinforced IM939 and IM945 at room temperature. The Saphikon reinforced IM945 shows some non-linearity at 1000°C and 1100°C, respectively. The load-displacement tests for IM939 reinforced with Saphikon at 1100°C exhibited limited ductility. The Pt6Rh reinforced IM945 showed limited ductility at temperatures below 800°C and did not fail at 1100°C. At this temperature deformation continues until the fixture prevents further deflection. The further inclusion of Pt6Rh with Saphikon also shows significant non-linearity in IM945 at 1100°C. All strength results are based on assumed linear elastic behavior; where this assumption is obviously violated, no value is reported. The fracture surfaces of IM945 specimens tested at room temperature exhibited a predominantly transgranular brittle failure.

The results of the limited oxidation studies of IM945 reinforced with Pt6Rh at 1400°C, as weight change vs. time are given in Fig.4. One observes weight gain followed by a continuous weight loss. This behavior is explained by the formation of  $\text{Cr}_2\text{O}_3$  and its subsequent change to  $\text{CrO}_3$  as a result of vaporization.

As was reported earlier for a similar intermetallic, one may expect the saturation of the weight change curve, after longer times, due to the formation of protective  $\text{SiO}_2$  [10]. However, such an assumption should be experimentally verified with long time oxidation tests. At 1250°C and under cyclic oxidation conditions, both alloys showed nearly no weight change in 250 hours at 1250°C. An oxidation test at 500°C for 500h on IM945 showed that this material does not suffer from the well known "pest" phenomenon.

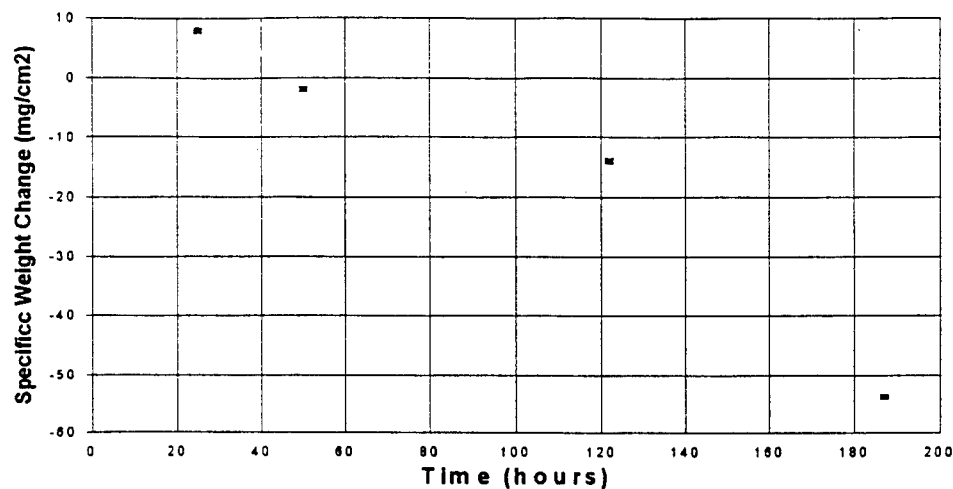


Fig. 4. Static oxidation behavior at 1400°C for Pt6Rh reinforced IM945.

MoSi<sub>2</sub>: Samples were extracted from the mold with a very high yield, and used as is, with minor polishing. The MoSi<sub>2</sub>, MoSi<sub>2</sub> + 30v/o SiC particles, and MoSi<sub>2</sub> + 30v/o SiC particles + 10v/o SiC whiskers samples had densities of 97.10%, 99.59%, and 98.35% respectively. Micrographs in Figs. 5a)-c) demonstrate the density and grain size of the MoSi<sub>2</sub> and its composites.

Hardnesses of the intermetallic and composites are shown in Table III. As can be seen from Fig. 5 monolithic MoSi<sub>2</sub> and the composites showed grain boundary pinning from the SiC particles and whiskers and no SiO<sub>2</sub> at the grain boundaries, a problem that has plagued prior studies of MoSi<sub>2</sub> fabrication. Very little porosity is evident in the MoSi<sub>2</sub> sample while MoSi<sub>2</sub> + 30v/o SiC particles and MoSi<sub>2</sub> + 30v/o SiC particles + 10v/o SiC whiskers samples showed even less porosity.

TABLE III: GRAIN SIZE AND HARDNESS OF MONOLITHIC MOSI<sub>2</sub> AND MOSI<sub>2</sub> MATRIX

	Hardness (VHN)	Grain Size (μm)
MoSi <sub>2</sub>	1060	5.0
MoSi <sub>2</sub> and 30v/o SiC Particles	1125	5.6 (in islands)
		2.5 (between SiC particles)
MoSi <sub>2</sub> and 30v/o SiC Particles and 10v/o SiC Whiskers	1100	2.0-5.0 (between SiC particles and whiskers)
		<1 in island

The high temperature strength of reinforced MoSi<sub>2</sub> increased until 1200°C, Fig. 6, indicating some effect from the smaller grains and cleaner product. With the inclusion of both SiC particles and whiskers in the MoSi<sub>2</sub> + 30v/o SiC particles + 10v/o SiC whiskers sample it is thought that the total volume of reinforcement accounts for the improved high temperature properties. Both matrices reinforced with SiC showed improved fracture stress at elevated temperatures, with MoSi<sub>2</sub> + 30v/o SiC particles + 10v/o SiC whiskers showing less improvement. This could be due to a critical reinforcement volume. Whiskers that were added to the MoSi<sub>2</sub>

matrix showed no signs of being broken during processing because of the low processing pressures, less than 60 MPa. Samples with 30v/o SiC particles and 10v/o SiC whiskers showed the best high temperature modulus possibly due to the SiC absorbing the bulk of the load and the inclusion of the directionally strengthening SiC whiskers. These whiskers could not be added to the MoSi<sub>2</sub> matrix independent from the SiC particles due to the coefficient of thermal expansion mismatch. This resulted in matrix cracking during processing.

### **SUMMARY AND CONCLUSIONS**

Fully dense Cr<sub>3</sub>Si alloys and their composites can be made by hot pressing of prealloyed powders. Dense MoSi<sub>2</sub> and composites can be produced by reactive hot pressing of elemental powders. Preliminary mechanical property and oxidation data for Cr<sub>3</sub>Si show that this is a suitable alloy system for further development. The MoSi<sub>2</sub> composites show some improved properties relative to unreinforced MoSi<sub>2</sub> at elevated temperatures. Further work is needed to optimize properties of both Cr<sub>3</sub>Si and MoSi<sub>2</sub>-base composites.

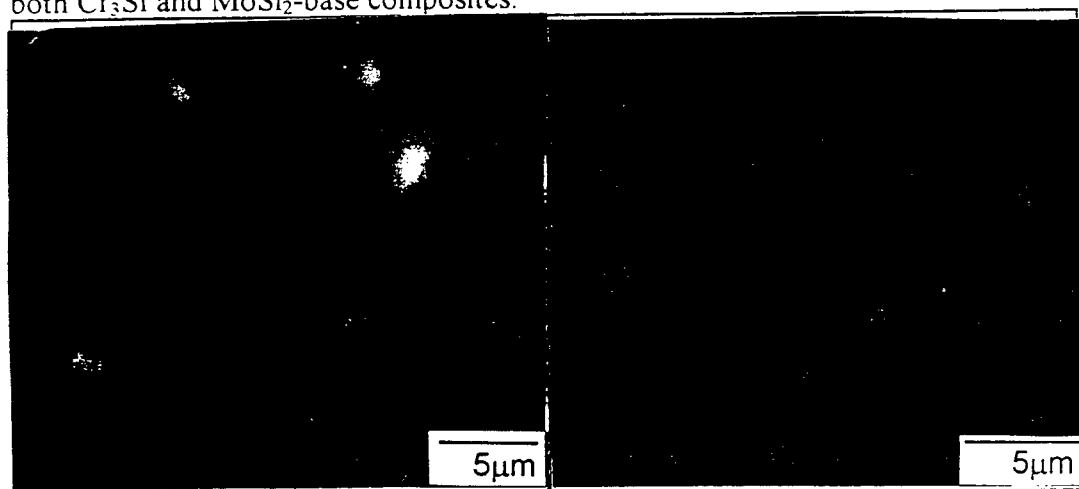


Fig. 5a). Microstructure of MoSi<sub>2</sub> Fig. 5b). Microstructure of MoSi<sub>2</sub> + 30v%SiC<sub>p</sub>

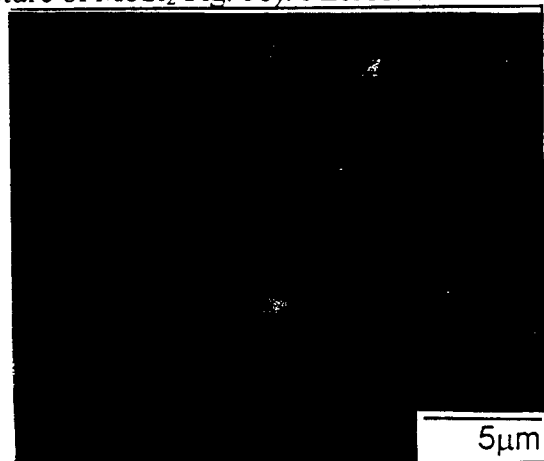


Fig. 5c). Microstructure of MoSi<sub>2</sub> + 30v%SiC<sub>p</sub> + 10v%SiC<sub>w</sub>



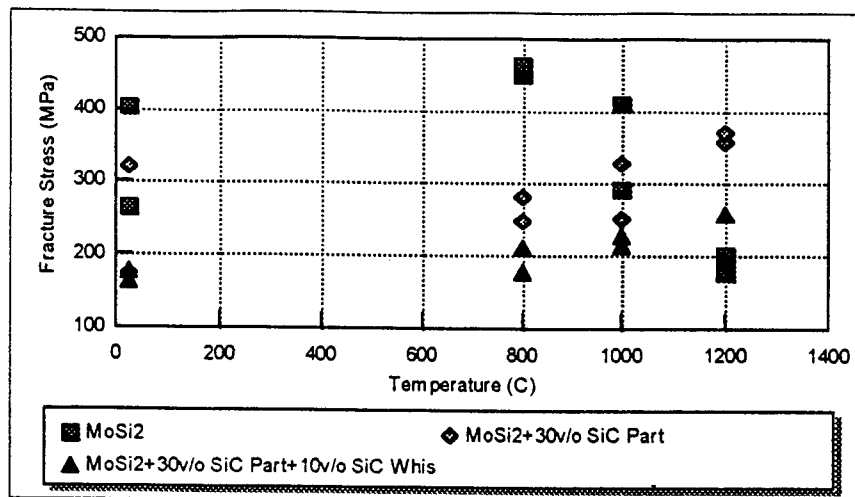


Fig. 6 Fracture stress of MoSi<sub>2</sub> and composites compared to earlier work

#### ACKNOWLEDGMENTS

The authors are grateful for the Office of Naval Research for their financial support under ARPA/ONR Contract N00014-92J-1779 and ARPA AASERT Grant Number N00014-94-1-0723, Dr. Steve Fishman, Program Monitor.

#### REFERENCES

1. J. J. Petrovic and A. K. Vasudevan in Intermetallic Composites II, eds. D. B. Miracle, D. L. Anton and J. A. Graves, Mat. Res. Soc. Proc. v. 273, p.229, 1992.
2. D. E. Alman and N. S. Stoloff, Metall. Trans. v.26A, p.289, 1995
3. D. E. Alman and N. S. Stoloff, Scripta Metall.,v. 30, p. 203, 1994
4. J. J. Petrovic, MRS Bulletin, v. 18(7), p. 35, 1993
5. D. Shah and D. L. Anton in Structural Intermetallics, eds. R. Darolia, J.J. Lewandowski, C. T. Liu, P. L. Martin, D.B. Miracle and M. Nathal, TMS, Warrendale, PA. p. 755, 1993
6. D. L. Davidson, K. S.Chan and D. L. Anton, Metall. Trans. v. 27A, p.3007, 1996
7. P. R. Subramanian, M. G. Mendiratta and D. M. Dimiduk in High Temperature Silicides and Refractory Alloys, eds. C. L. Briant, J. J. Petrovic, B. P. Bewlay, A. K. Vasudevan and H.A. Lipsitt, Mat. Res. Soc. Proc. V. 322, p. 491, 1993
8. S.V. Raj, Mat. Sci. and Eng., v.A201, p. 229, 1995

## MULTI-AXIAL RESPONSE OF A WOVEN CONTINUOUS-FIBER COMPOSITE

P. Lipetzky, G.J. Dvorak and N.S. Stoloff,  
RPI, Troy, NY 12180, Tel: 518-276-8374

### ABSTRACT

Thin-walled cylinders of a woven [0/90] continuous fiber-reinforced ceramic composite are tested in combinations of tension, torsion and internal pressure in order to characterize the stress-strain response. Damage envelopes, defined as the loci of combined load states that bound the region of elastic behavior, have also been measured. Loading beyond any given elastic limit can cause both an expansion and a translation of the original damage surface according to the maximum effective stress. Within the damage envelope Young's and shear moduli are dependent on both load angle and position in stress-space. For several different load paths an ultimate effective strain of 0.6% has been observed. An empirical model is also investigated and results are in reasonable agreement with proportional loading cases; for non-proportional loading only trends are predicted.

### INTRODUCTION

Studies exist in the literature which have examined biaxial or triaxial deformation behavior of fiber-reinforced or woven composites. The objective in such work is the understanding of deformation and fracture of materials which are subjected to arbitrary combinations of stress [1-7]. In the course of this project, extensive flat plate testing has been reported, but additional data is necessary to expand the understanding of the weave deformation tendencies [8]. The work here describes the multi-axial behavior of continuous fiber, woven SiC/SiC composite tubes in terms of damage tolerance and evolution prior to failure. By testing tubes, edge effects are minimized and the load angle can be varied arbitrarily. Using internal pressurization, tension and torsion, the three independent stress components are axial stress, circumferential stress and shear stress. Finally, models which combine specific empirical data and numerical analysis are discussed in terms

of observed constitutive relations. Given a clearer understanding of the general stress-strain behavior, design criteria can be established for this composite.

## **MATERIAL**

The composite of interest consists of continuous SiC (Nicalon) fiber-reinforced SiC manufactured by DuPont Lanxide Composites. Fiber tows are woven into a mat with a plain [0/90] weave, which is subsequently rolled into tube form and chemical-vapor infiltrated with crystalline SiC as well as additional oxidation inhibitors. In this geometry no seam exists; approximately 10 layers, all in the [0/90] orientation, exist along any radial line in the tube. Following consolidation, a final seal-coat of SiC approximately 100  $\mu\text{m}$  thick is applied. Typical tube dimensions are 8.0 in X 1.7 in (OD) X 1.5 in (ID). Residual porosity is near 15%, and the fiber volume fraction is near 30%. Specimen density is approximately 2.3 g/cc. Additional details are given elsewhere [8].

## **EXPERIMENTAL PROCEDURE**

Experimental investigation involves static tension and torsion testing at room-temperature in air. End-cap grips are bonded to the tube with a structural epoxy leaving approximately 6 inches of the tube exposed. Strain is measured using multiple resistance-type strain gauge rosettes in the center of the gauge section. Strain gauges are also applied closer to the end caps to determine the extent of end effects. Load angle is controlled by independently adjusting the tension, torsion or internal pressure.

## **NUMERICAL ANALYSIS**

Part of the multiaxial deformation analysis of this material is based on an interpolation scheme proposed by Genin and Hutchinson [1]. The model assumes that for plane stress conditions in an arbitrary [0/90] composite, the *proportional* loading behavior at any angle can be interpolated from the uniaxial loading results in the 0° direction and the 45° direction. The required input curves include the following stress-strain relationships: Axial and transverse strain as a function of tensile stress,  $\sigma$ , in the 0° configuration,  $\epsilon_I = f_0(\sigma)$  and  $\epsilon_{II} = f_{0T}(\sigma)$ , respectively; axial and transverse strain response under tensile load in the 45° orientation,  $\epsilon_I = f_{45}(\sigma)$  and  $\epsilon_{II} = f_{45T}(\sigma)$ . Given the assumption that there is no coupling between damage modes, equi-biaxial loading ( $\sigma_I = \sigma_{II} = \sigma$ ) conditions result in the following relation between axial and transverse strains:  $f_0(\sigma) + f_{0T}(\sigma) = f_{45}(\sigma) + f_{45T}(\sigma)$ . Above the elastic limit, the differences between the actual stress and elastically calculated stress,  $\Delta\sigma$ , are defined as:  $\Delta\sigma_I^0 = E^\Psi (\epsilon_I + \nu\epsilon_{II}) - \Gamma_0(\epsilon_I, \epsilon_{II})$ , where  $E^\Psi = E_0/(1-\nu^2)$ ,  $\sigma_I = \Gamma_0(\epsilon_I, \epsilon_{II})$  is the observed first principal stress-principal

strain relation for  $0^\circ$  loading and  $\nu$  is the Poisson ratio. Similarly,  $\Delta\sigma^0_{II}$ ,  $\Delta\sigma^{45}_I$  and  $\Delta\sigma^{45}_{II}$  define the stress differences for the first and second principal stresses at  $0^\circ$  and  $45^\circ$ . Following interpolation from these functions ( $\Delta\sigma^0$  and  $\Delta\sigma^{45}$ ) to the actual principal stress direction, results are rotated back into the original  $[0/90]$  configuration to give overall constitutive relations for proportional loading including material damage:

$$\begin{aligned}\sigma_{xx} &= E^p(\epsilon_{xx} + \nu\epsilon_{yy}) - \Delta\sigma_I \cos^2\theta - \Delta\sigma_{II} \sin^2\theta \\ \sigma_{yy} &= E^p(\epsilon_{yy} + \nu\epsilon_{xx}) - \Delta\sigma_{II} \cos^2\theta - \Delta\sigma_I \sin^2\theta \\ \sigma_{xy} &= G\epsilon_{xy} + (\Delta\sigma_I - \Delta\sigma_{II}) \sin\theta \cos\theta\end{aligned}$$

where  $G$  is the shear modulus and  $\theta$  is the actual principal stress or strain angle. Results based on this empirical model will be compared to experimental observations for various load paths. Other analysis methods based on effective stress and strain will also be presented and discussed below.

## RESULTS AND DISCUSSION

As the background for a general analysis, the results from simple load angles are presented first. Figure 1 shows the stress-strain behavior under tensile and torsional load; torsional strain,  $\gamma = 2\epsilon$ , is plotted. Young's modulus and shear modulus are approximately 125 GPa and 48 GPa, respectively; proportional limits are 75 MPa and 65 MPa in tension and torsion, respectively. Tension data follow an apparently bilinear constitutive relation prior to failure.

The analysis now turns to the specific load state involving tension, torsion and internal pressure which approximates uniaxial tension at  $45^\circ$  angles to the fibers. Results in Figure 2 show stress and strain at angles of  $45^\circ$  ( $\epsilon_I = f_{45}(\sigma)$ ) and  $135^\circ$  ( $\epsilon_{II} = f_{45T}(\sigma)$ ) with the linear elastic regime ending near 40 MPa. The data are roughly linear between 40 and 110 MPa; above 110 MPa the sample becomes increasingly compliant until failure.

Sufficient data now exist to implement the predictions of the empirical model described above. The constitutive relations required for input are axial and transverse behavior under uniaxial load,  $\epsilon_I = f_0(\sigma)$  and  $\epsilon_{II} = f_{0T}(\sigma)$ , and *axial* and *transverse* behavior under  $45^\circ$  load,  $\epsilon_I = f_{45}(\sigma)$  and  $\epsilon_{II} = f_{45T}(\sigma)$ . Figure 1 shows the agreement between predicted and observed shear behavior. Under conditions of equibiaxial loading it is possible to calculate  $\epsilon_{II} = f_{45T}(\sigma) = f_0(\sigma) + f_{0T}(\sigma) - f_{45}(\sigma)$ , as plotted in Figure 2. In both Figures 1 and 2 the proper trends are predicted, and good agreement exists for limited excursions into the damage regimes.

Realistic design conditions involve operation within the elastic region. Therefore, it is necessary to determine the elastic bounds as well as the

influence of a stress overload on those bounds. Define the damage envelope as the locus of points in stress-space which bounds the linear elastic region, as plotted in Figure 3. Limits are obtained by loading under various load paths until linearity is lost in either the axial or torsional stress-strain response. Altering the load path near the boundary does not affect the point where damage begins. The elastic response within the damage envelope is a function of position and stress path. For example, beginning from a combined state of 40 MPa tension and torsion (40,40), changing both stress components  $\pm 10$  MPa (4 permutations as shown on Figure 3, *i.e.* 30,50) gives axial moduli in the range of 64 - 118 GPa. Shear moduli are less sensitive, ranging from 31 - 38 GPa. The same load excursions from a state of pure tension, 40 MPa, gives axial moduli in the range of 72 - 83 GPa, and shear moduli from 30-31 GPa. These differences are attributed to the deformation coupling between axial and shear strain. Proportional loading will be defined as any load path which is perpendicular to the damage envelope.

The damage envelope can be altered as a result of tension and torsional loads beyond the original or current elastic boundary. Figure 4 shows how a pure tension overload translates the surface to a higher axial stress position without changing its shape. Similarly, both axial and torsional expansion are registered following a torsional overload. A single torsional overload in the "positive" direction causes the damage surface to expand in both the positive and negative senses.

A method of representing the damage surface must be found in order to predict the new elastic limits following an arbitrary load into the damage regime. The effective stress, or von Mises stress, plotted as a function of axial stress shows consistent, nearly parallel lines for both the original and expanded damage surfaces as plotted in Figure 5. Therefore, it is only necessary to locate a single point on the expanded damage surface from the final stress state in order to define the new damage envelope. Figure 4 also shows the agreement between points for the *predicted* and actual damage surface using this concept.

Constitutive results from Figures 1 and 2 are re-plotted on an effective stress-effective strain format in Figure 6. Tension and torsion data are now virtually coincident while samples loaded in tension at 45° display a higher compliance. Failure strain for all load cases is nearly 6000  $\mu\epsilon$ . Also plotted are deformation results for Case IV, the combined stress state of 125 MPa tension (fixed) with increasing torsion. The starting point (125 MPa tension) is in good agreement with flat-plate tensile data and the application of torsion causes a linear increase in effective strain up to failure at near 6000  $\mu\epsilon$  along a path which is consistent with other data. Apparently, non-proportional loading has little influence on the observed behavior when plotted in this way.

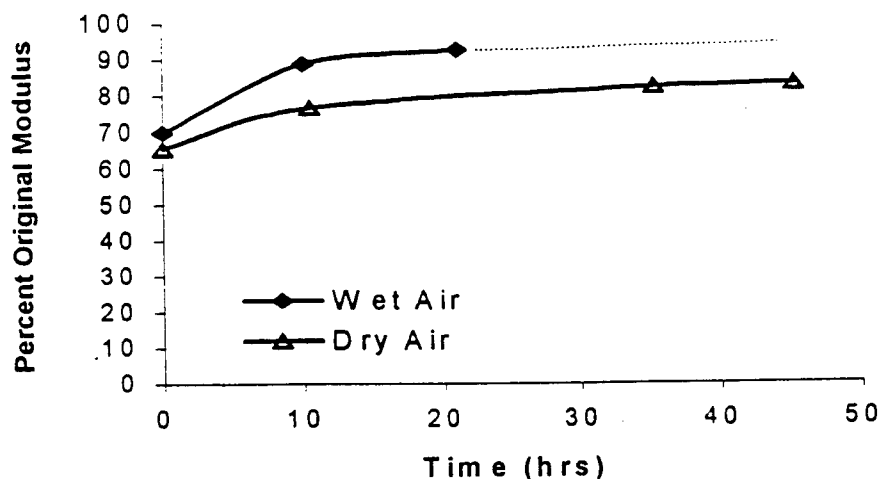


Figure 4b. SiC/Al<sub>2</sub>O<sub>3</sub> modulus recovery data (1000°C, stress-free).

## REFERENCES

1. D. Carruthers and L. Lindberg, "Critical Issues for ceramics for gas turbines," *Proc. 3rd Int. Symp. on Cer. Mat. and Comp for Engines*, Nov 1988, Amer Ceram Soc., pp1258-72.
2. J. Wessel, "Breaking Tradition with Ceramic Composites", *Chem. Engr.*, October 1996, pp80-82.
3. M. Brooks and M. Martin, "Ceramics Stand up to Acid Service", *Chem. Engr.*, October 1996, pp76-79.
4. P. Lipetzky and W. Hillig, "Benefits and limitations to the use of silicides in high-temperature applications," *Eng Fnd Conf Proc.*, to appear 1997, TMS.
5. P. Lipetzky, G.J. Dvorak and N.S. Stoloff, "Tensile properties of a SiC/SiC composite", *Mat. Sci. and Engr.*, Vol A216 (1996) pp 11-19.
6. Lanxide Technology Company, Patent Nos. 5187130, 5215566, 5262203, 5306677, 5334562, 5389450, USA, 1994.
7. R. Steinbrech, R. Khehans and W. Schaarwaechter, "Increase of crack resistance during slow crack growth in Al<sub>2</sub>O<sub>3</sub>" *J. Mat. Sci.*, Vol 18, 1983, pp 265-70.
8. S. Wiederhorn in Fracture Mechanics of Ceramics, Vol 2, Ed by R. Bradt, D. Hasselman and F. Lange (Plenum Press, NY, 1974) pg 613.
9. P. Lipetzky, M. Lieblich, W. Hillig and D. Duquette, "Effect of salt corrosion on mechanical properties of SiC/SiC in dry and moist environments" *this proceedings*.
10. P. Lipetzky, M. Lieblich, W. Hillig and D. Duquette, "Reactions and behavior of SiC/Al<sub>2</sub>O<sub>3</sub> with Na-based salts in dry and moist environments" *this proceedings*.
11. Davidson, "Ceramic-Matrix Composite Fatigue and Fracture," *Jour. of Metals*, October 1995, pg 46.

## EFFECT OF SALT CORROSION ON MECHANICAL PROPERTIES OF A SIC-SIC COMPOSITE IN DRY AND MOIST HIGH-TEMPERATURE ENVIRONMENT

P. Lipetzky, M. Lieblich, W. Hillig and D. Duquette,  
Rensselaer Polytechnic Institute Troy, NY 12180; 518-276-8374

### ABSTRACT

Oxidation and hot-corrosion effects on the mechanical and physical properties of SiC fiber-reinforced SiC have been studied under both short- and long-term exposure to dry air, argon, oxygen and water vapor up to temperatures of 1200°C. Results in all ambients show a rapid initial weight loss followed by various degrees of weight gain for times up to 20 hours. Hot corrosion studies utilize thin surface coatings of Na<sub>2</sub>SO<sub>4</sub> and NaCl. Samples exhibit a steady weight loss under these conditions which surpasses the weight loss observed during similar oxidation tests. Salt-coated samples were also exposed to moist ambients; water vapor was seen to rapidly accelerate weight loss. Mechanical properties are also reported from static fatigue tests in oxidizing and corrosive environments. It is seen that the conditions which promote weight loss are not necessarily detrimental to specimen life due to the protective coating. Finally, it is seen that minor loss or cracking of the protective surface layer can significantly shorten the life.

### INTRODUCTION

Components in high-temperature engine and heat-recovery applications are typically exposed to aggressive atmospheres which can contain sodium-, magnesium-, sulfur- and carbon-based gases as well as water vapor and numerous entrained particulates. Under these conditions, Na-based salts such as Na<sub>2</sub>SO<sub>4</sub> can deposit and degrade or remove material from the substrate. This hot-corrosion process takes place between the melting point and dew points of the respective salts and can drastically reduce the useable service time of many

high-temperature components [1]. The temperature range for such attack is typically between 800°C and 1400°C, depending on pressure and composition of the ambient gas. In silicide-based ceramics the degradation is related to the solubility of tramp elements, such as sodium, in the passivating silica layer which promotes devitrification of silica and thus lowers its effectiveness as an oxygen barrier [2]. In this work the effect of two Na-containing salts (NaCl and Na<sub>2</sub>SO<sub>4</sub>) on the oxidation behavior and mechanical properties of SiC/SiC were examined in oxidizing and inert atmospheres.

### **MATERIAL**

The material used in this investigation is a continuous SiC (Nicalon) fiber-reinforced SiC composite manufactured by DuPont Lanxide Inc. Tows of roughly 500 carbon-coated (0.2-0.4 μm) fibers are woven into a plain weave [0/90] fabric, which is subsequently chemical-vapor coated with various oxidation inhibitors and crystalline SiC. Approximately 8 such plies, all in the [0/90] orientation, are consolidated into the final plate. Tensile specimens are cut in the 0° orientation with a 20% reduction in the gauge section width. The final step is the application of a 100 micron SiC seal-coat. Figure 1 shows a cross section of the material. The fibers (~30 %) bundles and residual porosity (~15%) are visible. Further details can be found elsewhere [3,4].

### **EXPERIMENTAL PROCEDURE**

The test conditions involve atmospheric and corrosive attack while under various loads. The corrosion pre-treatment is to soak samples in a saturated salt solution followed by drying at 150°C for roughly 20 minutes. Typical salt coatings are near 10 μm, which simulates 500 hours at 900°C in a combustion application [5]. Oxidation and corrosion experiments involve weight evolution studies during stress-free thermal exposure. Temperatures between 500°C and 1200°C are investigated here because oxidative attack begins near 500°C and Nicalon fibers degrade rapidly above 1200°C. Results will be reported on the basis of weight change per exposed surface area averaged over 6 specimens. Rectangular samples for this purpose are cut from the tensile coupons such that 4 of the 6 sides are protected by the seal coat and the other 2 are left as-cut. Sample size is typically 2.5 X 2.5 X 10.2 mm, with the as-cut surface dimension being 2.5 X 10.2 mm. Effects of other ambients on oxidation are also investigated. A water vapor environment is produced by injecting pre-heated moist air (0.1 liter/min STP, dew point 90°C) into the furnace. Dry air, oxygen and argon are also supplied at this rate. Experiments investigating the effects of corrosion on mechanical properties involve the same salt pre-treatment on a complete tensile coupon followed by time to failure and



Comparing predicted and observed behavior for Case IV loading shows that the model is in poor agreement with observations for non-proportional load paths. Predicted stiffness is overestimated and the predicted non-linearity is not observed. Furthermore, the failure condition cannot be determined using this model.

### **SUMMARY AND CONCLUSIONS**

The deformation behavior of a woven [0/90] ceramic composite has been analyzed under multi-axial loading conditions. Tension and torsion results show approximately bilinear constitutive relations, while more complicated load paths do not. Boundaries for the linear elastic region are plotted as damage envelopes in stress-space. Within the elastic envelope axial and torsional modulus are highly directional. Increasing both tension and torsion produces the most compliant response, while decreasing tension and increasing torsion gives the stiffest response. Differences in modulus are as high as a factor of 2. Consistent trends are seen for damage envelope expansion and translation based on the effective stress maximum during loading. A coupled numerical-empirical model has been developed which can be used to predict behavior under proportional loading. Shear deformation is accurately predicted using this model but good agreement is not seen for non-proportional load angles. Finally, consistent results were observed for various load paths when stress-strain data were plotted in the effective stress-effective strain format. To a good approximation, effective stress and effective strain at failure are 170 MPa and 0.6%, respectively, for any general load angle.

### **FIGURES**

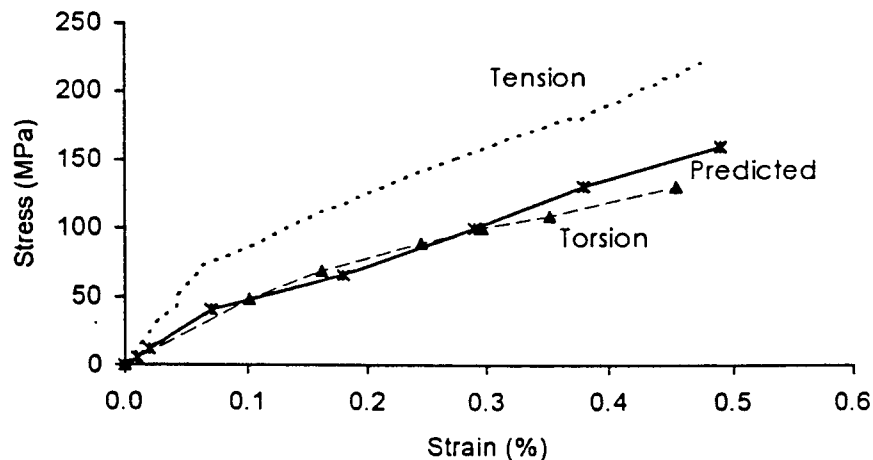


Figure 1. Stress-strain response in tension and torsion.

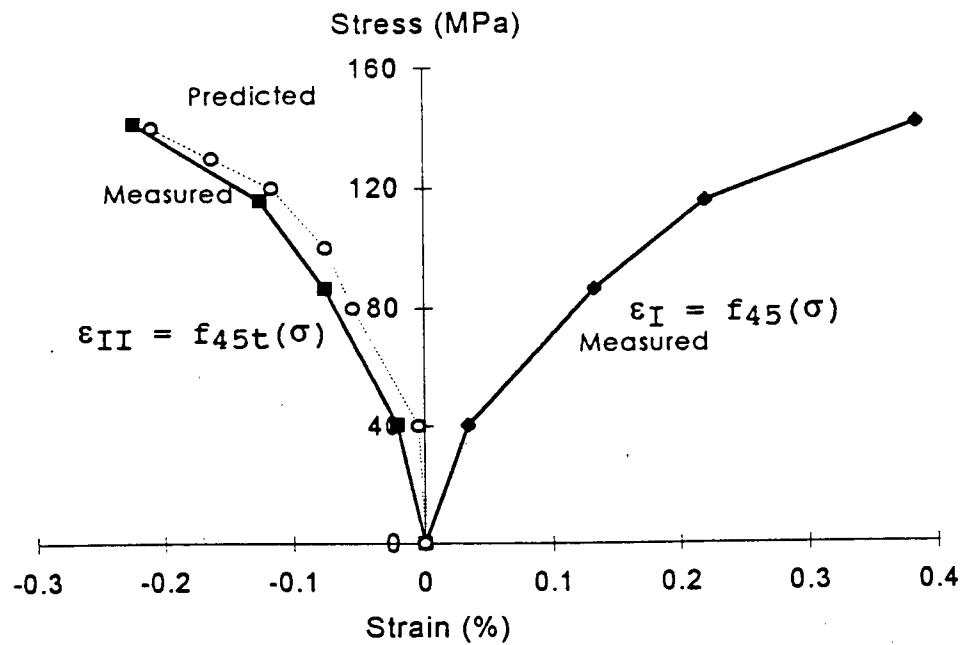


Figure 2. Axial and transverse stress-strain behavior at 45° and 135°.

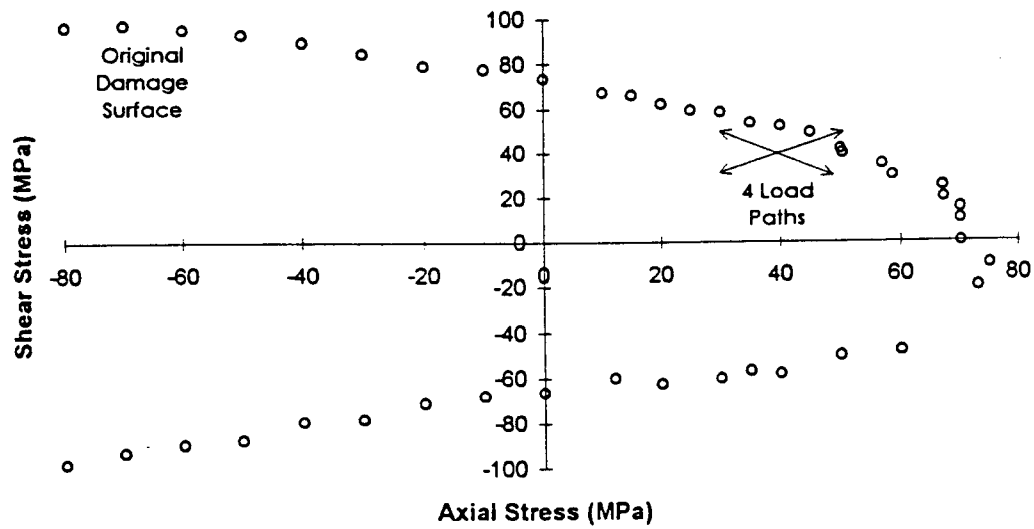


Figure 3. As-received damage envelope with elastic anisotropy.

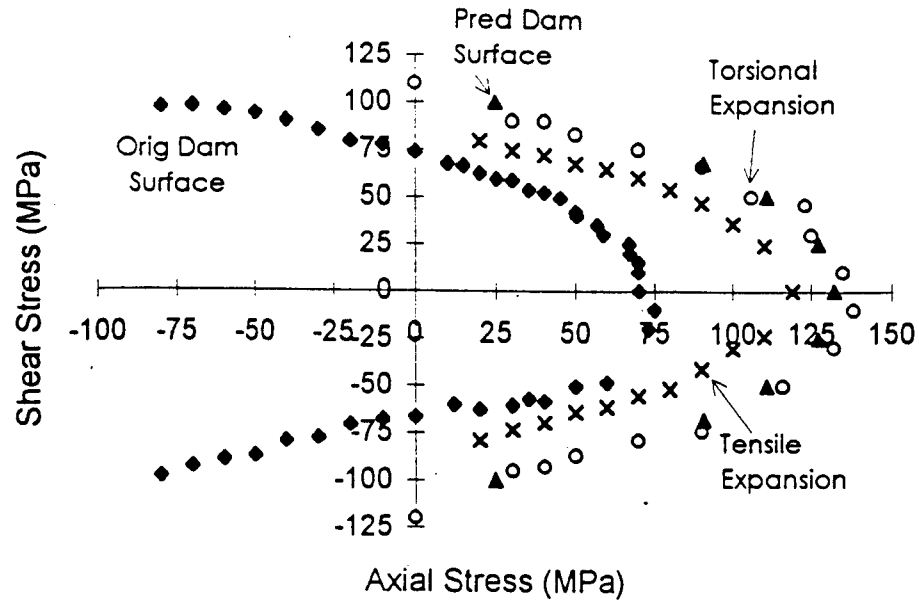


Figure 4. Original, expanded and predicted damage envelopes.

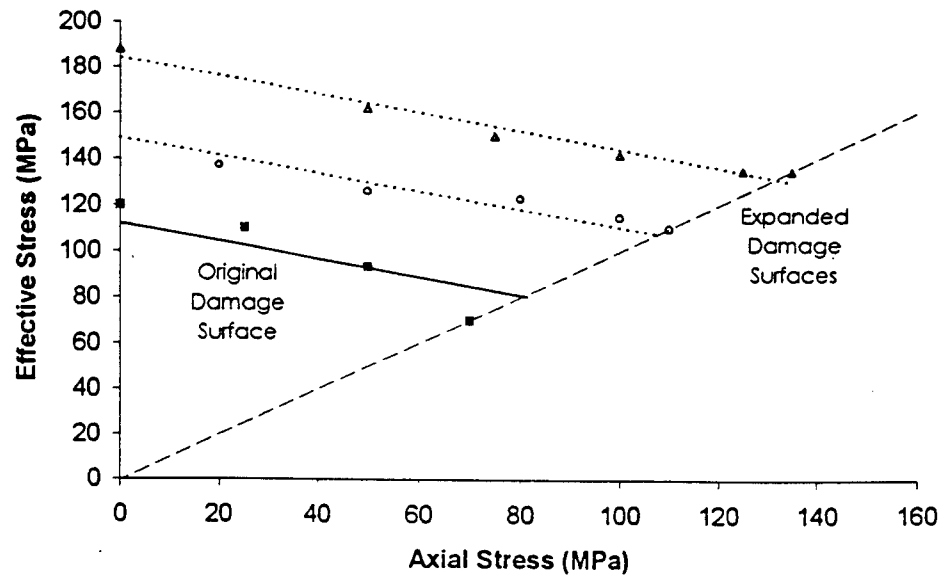


Figure 5. Approximately linear relation between effective and axial stress.

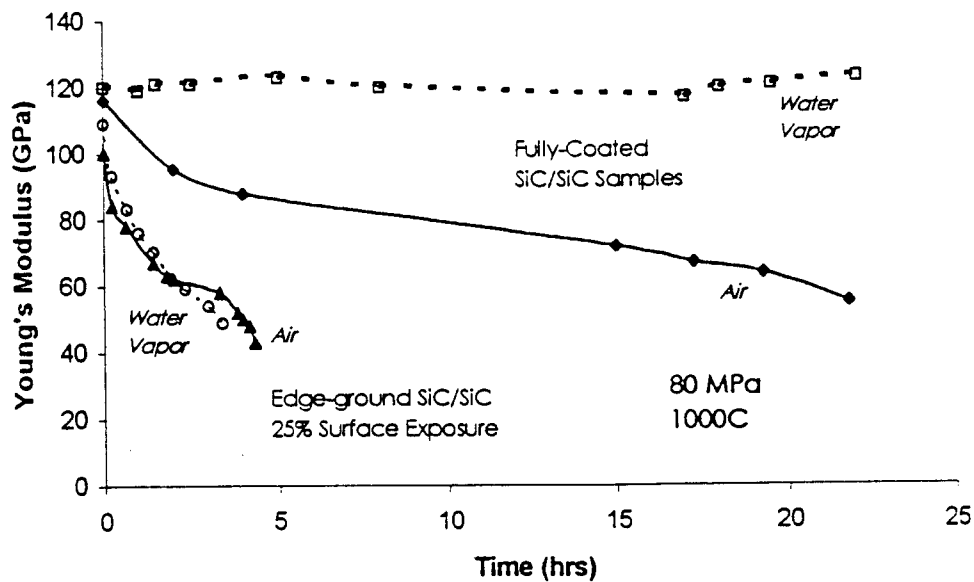


Figure 3. Modulus retention data for SiC/SiC. Coating and ambient as marked (1000°C).

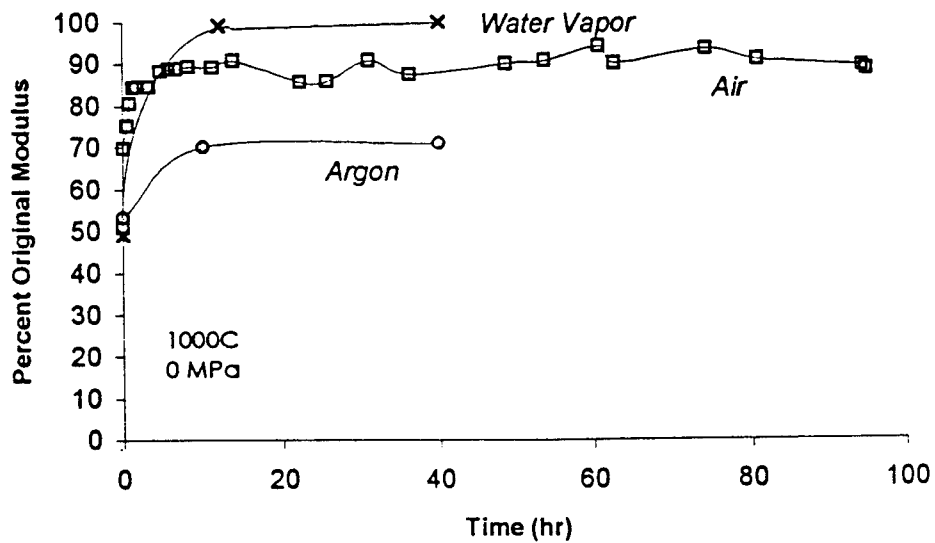


Figure 4a. Modulus recovery data for exposure at 1000°C (SiC/SiC).

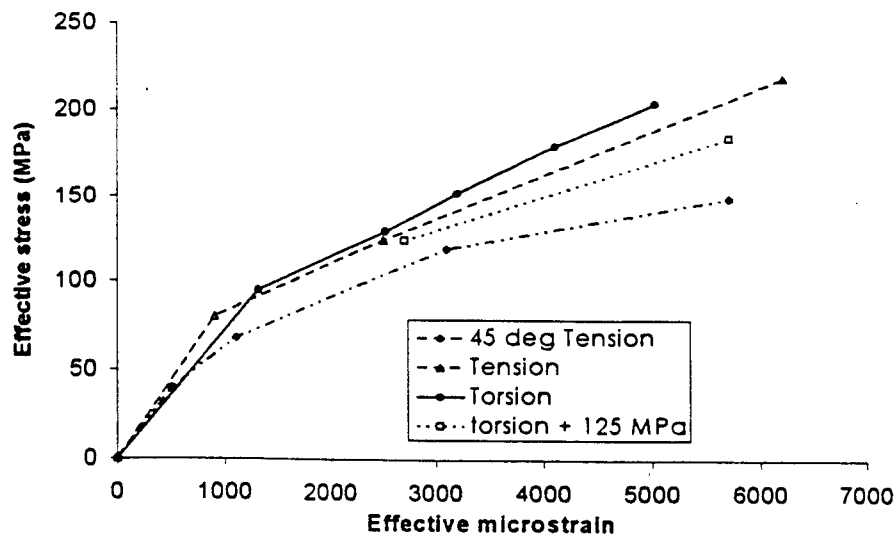


Figure 6. Effective stress-strain plot for several load paths show good consistency. Failure strain is  $\sim 0.6\%$  in all cases.

### ACKNOWLEDGMENTS

This work is supported under ARPA/ONR sponsorship through contract number 1492J007-1776. We further thank Drs. S. Fishman and W. Coblenz for oversight of this program.

### REFERENCES

1. G. Genin and J. Hutchinson, "Composite Laminates in plane stress: constitutive modeling and stress redistribution due to matrix cracking," *submitted for publication*, 1996.
2. P. Petit and M. Waddoups, "A method of predicting the nonlinear behavior of laminated composites," *J. Compos. Mater.*, [7], 1973, pg102.
3. N. Laws, G. Dvorak and M. Hejazi, "Stiffness changes in unidirectional composites caused by crack systems," *Mech. Mater.*, [2], 1983, pg123.
4. C. Tsai and I. Daniel, *Exptl Mechs*, 1990, pg 295.
5. A. Makinde, L. Thibodeau and K. Neale, *Exptl Mechs*, 1992, pg 138.
6. T. Guess and C. Haizlip, *Exptl Mechs*, 1980, pg 31
7. B. Cox, W. Carter and N. Fleck, *Acta Met.*, Vol 42, [10], 1994, pg 3463.
8. P. Lipetzky, G.J. Dvorak and N.S. Stoloff, "Tensile behavior of a SiC/SiC composite," *Mat. Sci. Engr.*, A216, 1996, pp11-19.

## ATMOSPHERIC EFFECTS ON HIGH-TEMPERATURE LIFETIME OF CERAMIC COMPOSITES

P. Lipetzky, N.S. Stoloff, G.J. Dvorak,  
RPI, Troy, NY 12180; (518) 276-8374

### ABSTRACT

This work describes the influence of atmosphere, stress and temperature on long-term life of SiC fiber-reinforced ceramic composites. Results show that at 1000°C a linear relation describes log of rupture life versus stress data for the SiC/SiC composite between stresses of 30 and 150 MPa. Conversely, the SiC/Al<sub>2</sub>O<sub>3</sub> material exhibits a run-out at a stress of ~ 80 MPa and 1000°C. Relative humidity has no direct effect on the lifetimes of either composite, although modulus retention during testing is promoted by the presence of moisture. Modulus recovery has been observed in damaged samples following stress-free high-temperature exposure; mechanisms include silica formation on internal SiC crack faces. Combined stress-temperature data show that increasing stress above the proportional limit sharply reduces the 6-hr survival temperature in both composites. The importance of surface coating is also addressed.

### INTRODUCTION

Developmental ceramics in heat management and structural applications involve both oxide and silicide matrix and fiber combinations, such as SiC<sub>f</sub>/SiC and SiC<sub>f</sub>/Al<sub>2</sub>O<sub>3</sub> which will be examined here [1-3]. Components will be required to sustain a variety of loads in oxidizing or reducing environments which may contain hydrocarbons, water vapor, carbon- and nitrogen-based oxides. A previous study has shown that water vapor can be a stronger SiC oxidant than pure oxygen [4]. The morphology of the silica is also atmosphere-dependent, and the mechanical properties reflect this difference. The present study focuses on the effect of dry and moist air on the high-temperature lifetime of these oxide- and silicide-based composites. Susceptibility to environmental attack is

also related to surface coating. Finally, aspects of damage evolution and recovery will be discussed in terms of environment.

## **MATERIAL**

The two materials used in this investigation are woven Nicalon (SiC) fiber-reinforced SiC- and  $\text{Al}_2\text{O}_3$ -matrix composites, manufactured by DuPont Lanxide Inc. The structures are shown in Figures 1a and 1b. The SiC/SiC material consists of a plain weave [0/90] fabric, which is subsequently chemical-vapor infiltrated with proprietary oxidation inhibitors and crystalline SiC. Approximately 8 such plies, all in the [0/90] orientation, are consolidated into the final plate. Tensile coupons are machined in the  $0^\circ$  direction and completely seal-coated with additional SiC. Certain of the samples have a portion of the seal-coating removed. Further details of the processing and microstructure can be found elsewhere [5]. The  $\text{Al}_2\text{O}_3$ -matrix material is similarly reinforced with a [0/90] woven mat (12 HSW) of Nicalon fibers. Processing involves applying a  $0.3\text{ }\mu\text{m}$  coating of BN to the fibers prior to a limited CVD SiC coating. This porous, rigid pre-form is subsequently encased in alumina using a directional metal oxidation ( $\text{DiMOx}$ ) process [6]. The residual aluminum alloy is chemically etched from the sample prior to the application of a final surface coating. Residual porosity is approximately 10 volume percent.

## **EXPERIMENTAL PROCEDURE**

Experimental investigation involves static tensile testing performed in dry and moist air over a range of temperatures. Details of the testing facilities have been given previously [4,5]. Static tests for lifetime stress-dependence involve holding samples at a fixed stress in a given environment at  $1000^\circ\text{C}$  until either rupture or *run-out* is reached at 240 hrs. Temperature dependence of life is investigated using a 6-hr run-out limit. Tests are performed by holding a fixed stress at a given temperature for 6 hrs or until rupture. If the sample survives these conditions, temperature is increased  $50^\circ\text{C}$  and testing continues until subsequent run-out or rupture. Young's modulus is measured periodically by slightly altering stress and observing the change in strain in order to monitor damage evolution. Damage recovery is investigated by thermally soaking samples under stress-free conditions following an initial load cycle to 120 MPa or 150 MPa for SiC/SiC and SiC/ $\text{Al}_2\text{O}_3$  respectively. Moist air is produced by bubbling air (0.1 liter/min at RTP) through a reservoir of water held at  $90^\circ\text{C}$  into an atmosphere containment jacket around the sample.

## RESULTS AND DISCUSSION

Long-term, constant stress testing of SiC/SiC reveals the stress-rupture behavior as plotted in Figure 2a. Data show no apparent *run-out* stress in dry air between 30 MPa and 150 MPa; rather, there is a consistent linear relation between the logarithm of rupture time and the applied stress. The stress dependence is stronger for the SiC/Al<sub>2</sub>O<sub>3</sub> and an apparent static fatigue limit is observed at ~80 MPa, Figure 2b. For stress levels above ~100 MPa the composite lifetimes are roughly equivalent. Similar experiments have been performed in moist air. Survival times for SiC/SiC samples tested in water vapor are comparable to dry air. However, limited data indicate that moisture may improve life at lower stresses (<70 MPa). Although Al<sub>2</sub>O<sub>3</sub> is highly susceptible to slow crack growth in the presence of water vapor, SiC/Al<sub>2</sub>O<sub>3</sub> lifetimes were not significantly affected [7,8]. Samples consistently failed in the reduced section.

Specimen compliance is often used as a gauge of composite damage. The SiC/SiC modulus evolution curves for a stress level of 80 MPa at 1000°C are plotted in Figure 3. The modulus steadily decreases prior to failure when tested in dry air, although the presence of water vapor results in a high retained stiffness. At stresses above 90 MPa no atmospheric dependence is seen and modulus decrease is steady. Conversely, for stresses below 60 MPa the SiC/SiC composite displays an "incubation period" prior to the onset of modulus loss. This phenomenon has been related to the relative rates of silica formation as well as silica density and adherence [4,9,10]. The SiC/Al<sub>2</sub>O<sub>3</sub> samples retain a high modulus in both ambients. At higher temperatures the inherent degradation of Nicalon fibers results in a significant loss of both stiffness and strength.

Temperature dependence of the stress-rupture life is addressed by performing fixed stress-rupture tests with increasing temperature. Table I lists the 6-hr survival temperature at 100, 130 and 160 MPa for both ambients.

TABLE I: STRESS TEMPERATURE CREEP RUPTURE BEHAVIOR

6-hr survival stress	SiC/Al <sub>2</sub> O <sub>3</sub>		SiC/SiC		
	dry air	wet air	dry air	wet air	uncoated
100 MPa	1000°C	1000°C	1000°C	1000°C	900°C
130 MPa	800°C	800°C	750°C	700°C	700°C
160 MPa	650°C	600°C	700°C	650°C	650°C

As in Figures 2a and 2b the materials have similar behavior at high stresses which are not strongly influenced by ambient. Temperature capability decreases steadily with increasing stress for SiC/Al<sub>2</sub>O<sub>3</sub>, but 130 and 160 MPa are equivalent in SiC/SiC.



The effects of seal-coating degradation and removal are also of interest for many engineering applications. Table I shows that SiC/SiC survival temperatures are reduced roughly 50°C when 25% of the surface seal-coat is removed. Data are also shown on Figure 3 for SiC/SiC lifetime at 1000°C for partially uncoated samples; a significant reduction in life is seen which is independent of ambient.

Damage recovery capability is also examined. Figures 4a and 4b show modulus data following pre-damage and stress-free exposure to the various ambients. The SiC/SiC material exhibits extensive modulus recovery in air and water vapor following only 10 hrs exposure with water vapor causing recovery to nearly 100% of the original stiffness. Longer exposure time does not induce any further changes. The same phenomenon is seen in SiC/Al<sub>2</sub>O<sub>3</sub> samples. The recovery mechanism is based on SiO<sub>2</sub> formation on SiC crack faces. Energy-dispersive X-ray oxygen peaks are observed on post-recovery matrix crack faces, but not after short-term failure. Following damage and 40 hrs recovery under these conditions the SiC/SiC does not lose ultimate tensile strength, although the SiC/Al<sub>2</sub>O<sub>3</sub> loses over 60%. Recovery is sufficiently robust that recovered SiC/SiC samples subjected to static fatigue conditions showed lifetimes which were consistent with undamaged samples; recovered SiC/Al<sub>2</sub>O<sub>3</sub> samples were much weaker.

Other exposure effects are also investigated. Thermally soaking as-received samples at 1200°C for 1 week in either air or argon significantly reduces both the ultimate strength (~50%) and stiffness (~10%) for both composites. Thermal cycling has also been performed between 20°C and 1000°C (20 min cycles). Following 50 cycles no strength or stiffness was lost.

## **SUMMARY AND CONCLUSIONS**

Experiments have been performed to determine the effects of temperature and environment on the mechanical behavior of continuous SiC/SiC and SiC/Al<sub>2</sub>O<sub>3</sub> composites. Results show that ambient composition does not affect short-term behavior at any temperature up to 1000°C, although long-term tests show distinct atmospheric dependence. Static fatigue life for the SiC/SiC composite at 1000°C follows a linear relation between stress and log of rupture time up to 240 hrs over a stress range of 30 - 150 MPa. Under the same conditions the SiC/Al<sub>2</sub>O<sub>3</sub> composite displays a stronger stress-dependence and reaches static fatigue *run-out* at ~80 MPa. Data at low stress indicate that moist air may promote long-term life by forming a coherent passivating silica layer which can support load and retard oxygen ingress. Silica formation in dry air is less rapid and the resulting glass appears less dense. The importance of surface coating has also been investigated. Removal of 25% of the seal-coating can

reduce specimen life up to 80%. The 6-hr survival temperatures of SiC/Al<sub>2</sub>O<sub>3</sub> are observed to decrease on the order of 6°C per 1 MPa in dry air for stresses greater than 100 MPa; moist air causes a slightly larger drop. Rate of survival temperature decrease for the SiC/SiC composite is not linear with stress; loss of surface coating and exposure to water vapor also accelerate the reduction. In general, the SiC/Al<sub>2</sub>O<sub>3</sub> composite survives a given stress at higher temperatures for longer times; it is not clear whether the difference in composition or the different weave geometry is responsible [11]. Modulus retention and recovery have been observed for various time-temperature-stress histories. Water vapor causes SiC/SiC to retain a high modulus under load, and causes recovery to nearly 100% of the original stiffness if stress is near zero. Exposure to dry air results in less modulus retention and less modulus recovery. The mechanism is based on SiC crack face adhesion due to the formation of silica. The SiC/Al<sub>2</sub>O<sub>3</sub> samples exhibit similar modulus recovery, but are not prone to modulus loss during static fatigue.

#### ACKNOWLEDGMENTS

This work is supported under ARPA/ONR sponsorship through contract number N0001492-J1779. We further thank Drs. S. Fishman and W. Coblenz.

#### FIGURES

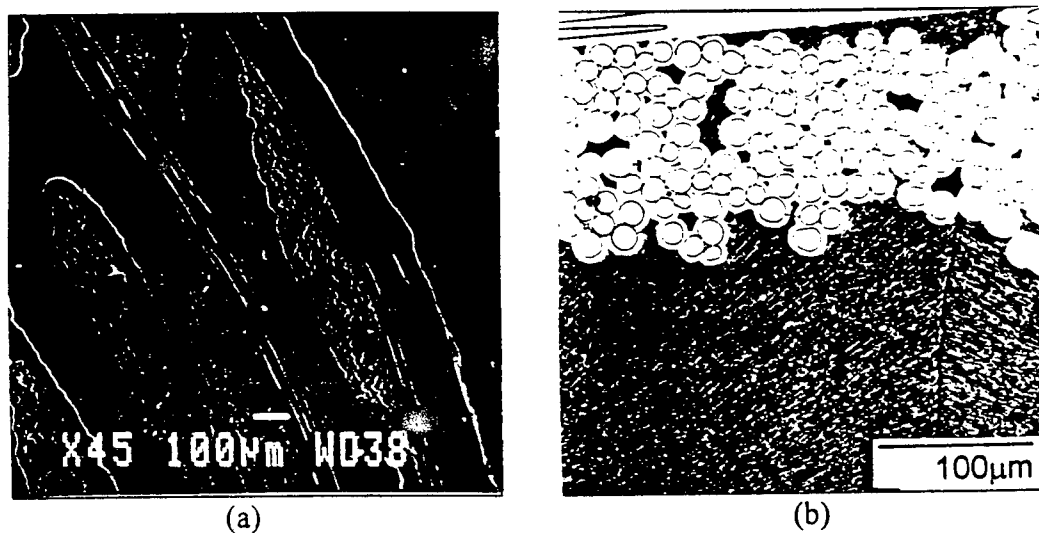
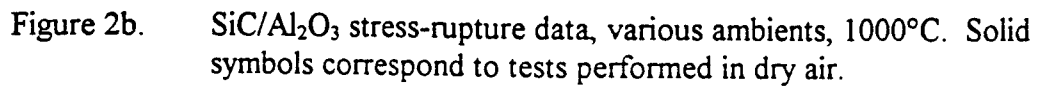
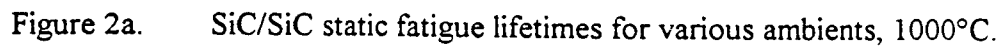


Figure 1. Micrographs of SiC/SiC (a) and SiC/Al<sub>2</sub>O<sub>3</sub> (b) structures.



modulus evolution curves for different load levels. Mechanical test temperatures are between 20°C and 1000°C. Specimens here are completely seal-coated, and are thus slightly different than oxidation samples. Mechanical testing can be performed in different ambients by continually injecting the pre-heated ambient into a high-temperature jacket around the specimen. Short-term mechanical tests are not affected by the various salt coatings or atmospheres.

## **RESULTS AND DISCUSSION**

Experimental data showing the area-normalized weight histories of as-received samples exposed to the various atmospheres are shown in Figures 2-4 for times up to 20 hours. Temperatures shown are 500°C, 850°C, 1000°C and 1200°C. Weight evolution trends for temperatures below 850°C are distinctly different than data for 1000°C and higher. However, data for all temperatures show an initial weight loss followed by a slow increase. This is in qualitative agreement with results on a similar composite reported by Fox et al. who observed rapid weight loss followed by weight gain with a parabolic rate constant of  $K_p = 0.0017 \text{ mg}^2/\text{cm}^4\text{hr}$  at 1200°C in dry oxygen [6].

The data at 1200°C from Figure 2 show that weight evolution in oxygen and dry air ambients follow the same trend as dry air at 1000°C, although oxygen causes a larger initial weight loss. The steady weight gain with parabolic kinetics can be explained by the formation of a passivating silica layer. The initial weight loss is attributed to reactions of the oxidation inhibitors and organics prior to complete passivation. The water vapor ambient results in a larger initial weight loss followed by a steeper weight gain. For tests up to 200 hours it was observed that the samples exposed to water vapor reach a peak weight at about 50 hours, followed by slow weight loss [3]. The presence of water vapor reverses the weight gain trend due to volatilization of  $\text{SiO}_2$  as  $\text{SiOH}$  [3]. Conversely, samples tested in oxygen continue to gain weight at 1200°C according to a parabolic rate constant  $K_p \sim 0.238 \text{ mg}^2/\text{cm}^4\text{hr}$ . The extreme difference in these rate constants,  $K_p$ , is due to the difference in un-coated area.

At temperatures below 850°C passivating silica forms slowly, thereby allowing extensive specimen degradation. Figure 3 shows that both dry and moist air cause extensive weight loss prior to stabilization at times over 20 hours. Recall at 1000°C stabilization in the same ambient occurs at ~5 hours. Water vapor is clearly the most aggressive environment in terms of weight loss. For example, after 5 hours at 850°C the weight loss in water vapor is nearly 4 times larger than in the other environments at any temperature. An argon ambient results in negligible weight loss at any temperature. The small weight loss observed at 500°C in air is attributed to oxidation of interfacial carbon.

Results of similar weight evolution experiments are plotted in Figure 4 for salt-coated specimens. The curves in all cases are self-similar; thermal exposure causes a net loss with no apparent minimum. Both increasing temperature and adding water vapor increase the rate of loss. At a temperature of 1200°C the atmosphere and salt play decisive roles [6-8]. Samples coated with NaCl exhibit a slightly larger weight loss than when coated with Na<sub>2</sub>SO<sub>4</sub>. The difference could be due to the volatility of NaCl and decomposition of Na<sub>2</sub>SO<sub>4</sub> at this temperature [9,10]. The most aggressive environment is clearly Na<sub>2</sub>SO<sub>4</sub> in moist air; weight loss after 20 hours is roughly 5 times the weight loss measured in dry air. Physical examination of the most degraded samples reveals extensive formation of surface glass which contains numerous bubbles and cracks, Figure 5. The poor coherence and continuity of surface glass is due to the sodium-induced devitrification of silica. Crystalline silica, tridymite and cristobalite, is weaker and has a lower resistance to oxygen diffusion than vitreous silica. Furthermore, the CTE is roughly 5X the CTE of silicon carbide [2,8]. Conversely, purely oxidative exposure results in a dense passivating vitreous layer at low temperatures and a layered structure at higher temperatures as seen in Figure 6.

The relative weight loss should be an indicator of component life. For example, after 20 hours the uncontaminated samples display stable weight, while salt-coated samples continue to lose weight rapidly. This implies that salt coatings can act to shorten composite life; water vapor may also contribute.

Mechanical testing of samples in dry air is conducted to establish a benchmark for atmosphere and surface salt comparison. Figure 7 shows time to rupture in dry air at 1000°C for stress levels from 30 to 145 MPa. The lifetime of samples follows a linear relation between stress and logarithm of survival time (hours) over the entire stress range. Below 40 MPa survival time is consistently over 240 hours. During these tests Young's modulus decreased in two distinct ways: starting immediately after load is applied; or after a long "incubation" period, during which no decrease is registered. The effect of a surface coating of Na<sub>2</sub>SO<sub>4</sub> in dry air on rupture life is also plotted on Figure 7. Survival time at low stress is not reduced by the surface salt. The life-invariance with surface contamination is in apparent contradiction to the weight loss data described above. However, the tensile samples are completely seal-coated and oxidation samples are not. Tests have also been performed in air and water vapor with 25% of the surface coating removed; results show a 5X decrease in life [3].

Finally, it is of interest to establish some indication of temperature dependence on lifetime. Specifically, the temperature that corresponds to an approximate 6 hour life at a stress of 160 MPa is 700°C for as-received samples tested in dry air. When the environment becomes more aggressive, Na<sub>2</sub>SO<sub>4</sub> in

moist air, this temperature drops to 650°C because of the chemical-induced loss of integrity of the passivating surface silica.

### SUMMARY AND CONCLUSIONS

Experiments are performed to determine the effects of sodium-based salt deposits on the oxidation, corrosion and mechanical behavior of a SiC/SiC composite. Results have shown that 1000°C defines a boundary between two reaction regimes. Above 1000°C a protective silica layer forms which slows atmospheric attack. Below 1000°C extensive weight loss is observed for all ambients. Exposure of samples to salt in moist air at 1200°C is the most detrimental in terms of relative weight change. Mechanical properties have similarly been investigated. The stress for long-term composite survivability, >240 hours, is approximately 45 MPa in the as-received condition when tested in dry air at 1000°C. At higher stresses, sample life is shortened according to a linear relation between stress and the log of rupture time. If a sample is tested in water vapor the lifetime is not affected, although the stiffness remains high until failure. The presence of both a salt coating and water vapor can affect run-out stress and modulus retention. Salt deposits can be expected to shorten life in real components by increasing the rate of environmental attack if the seal coating is damaged or removed.

### ACKNOWLEDGMENTS

This work is supported under ARPA/ONR sponsorship through contract number N0001492-J1779. We further thank Drs. S. Fishman and W. Coblenz.

### FIGURES



Figure 1. Cross section of as received SiC/SiC

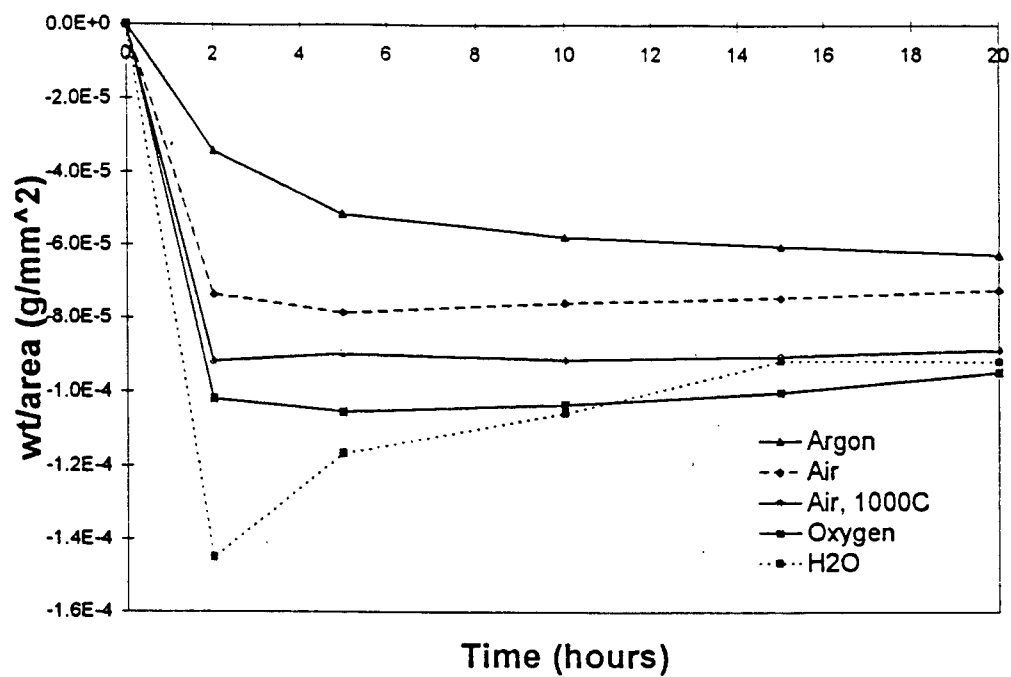


Figure 2. Weight change per area of SiC/SiC at 1200°C or 1000°C (noted)

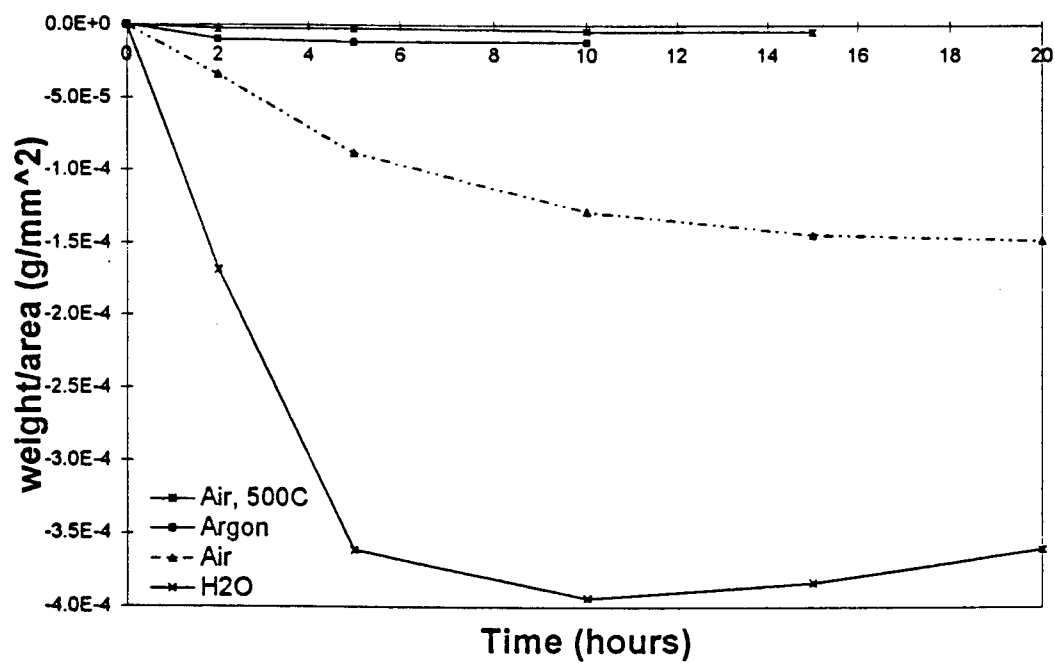


Figure 3. Weight change per area of SiC/SiC at 850°C and 500°C (noted)

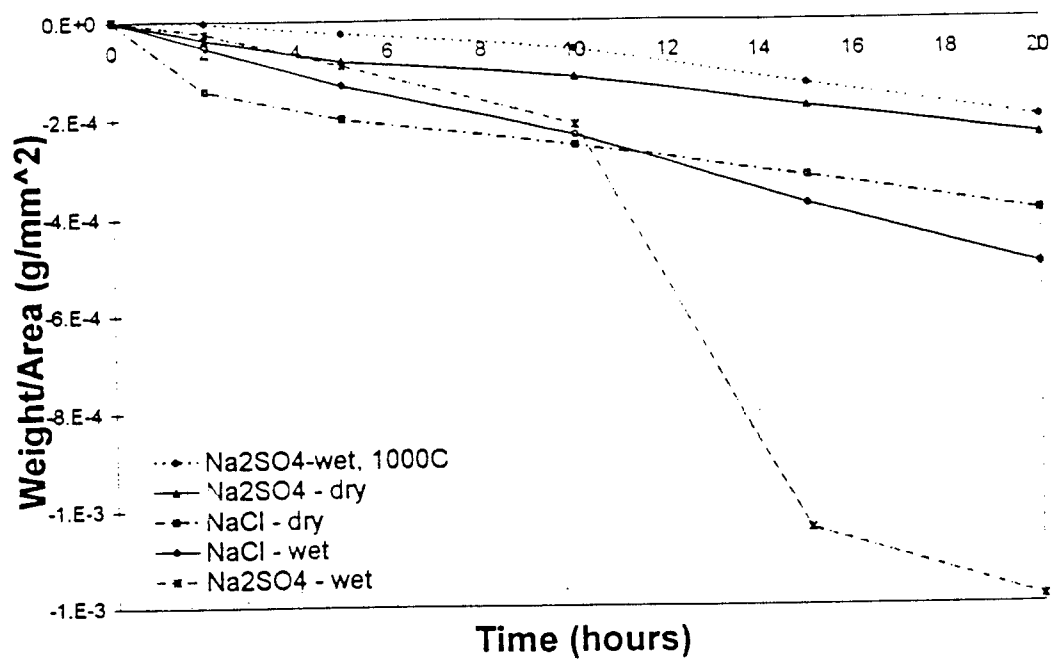
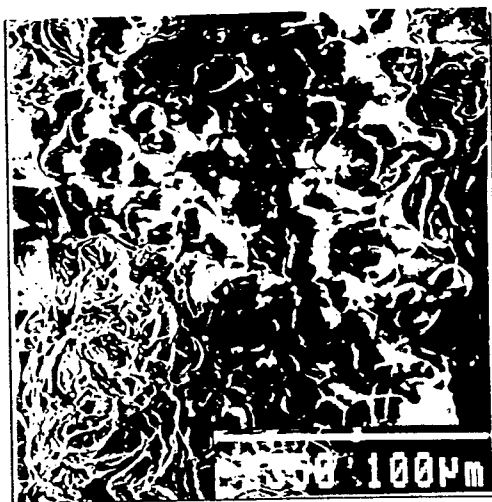
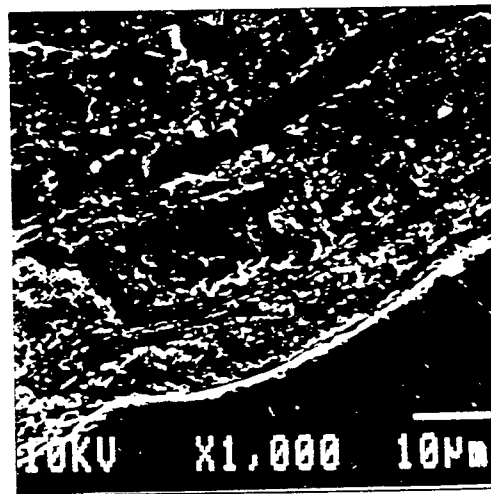


Figure 4. Change in weight per area of salt-exposed SiC/SiC at 1200°C and 1000°C (noted)



(5)

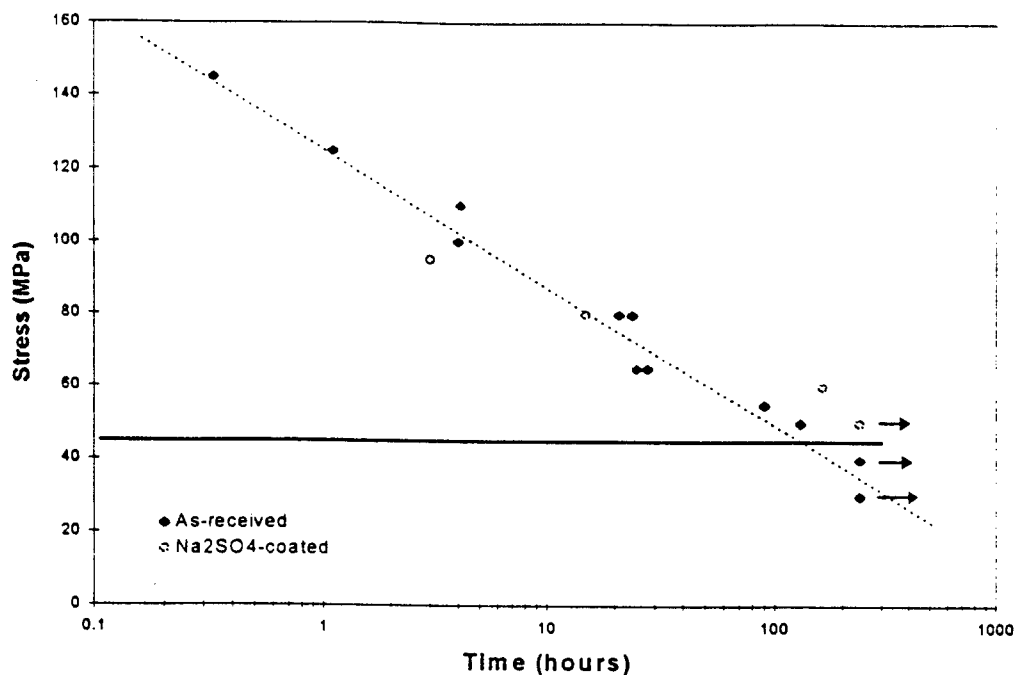


(6)

Figure 5. External view of oxidized SiC/SiC showing bubbles and cracks of glass surface.

Figure 6. Layered passivating coat of glass on oxidized SiC/SiC.





## REFERENCES

## BEHAVIOR OF SiC-FIBER/AL<sub>2</sub>O<sub>3</sub> COMPOSITE WITH Na-BASED SALTS IN DRY AND MOIST OXIDIZING ENVIRONMENTS

P. Lipetzky, M. Lieblich, W. Hillig and D. Duquette,  
Rensselaer Polytechnic Institute, Troy, NY 12180

### ABSTRACT

The current analysis focuses on thermogravimetric and mechanical properties of a SiC fiber-reinforced Al<sub>2</sub>O<sub>3</sub> matrix composite during exposure to oxidative and corrosive environments. Results show a significant weight gain at temperatures above 1000°C in oxygen as well as dry and moist air for times up to 200 hours under stress-free conditions. Below 1000°C an initial weight loss is seen in dry and moist air with no return to the original weight; this behavior is also seen for 1200°C argon exposure. Experiments have also been performed on salt-coated samples (Na<sub>2</sub>SO<sub>4</sub>) exposed to similar temperatures and atmospheres. Under these conditions continuous weight loss is observed for times up to 200 hours. Mechanisms of degradation include SiC oxidation and surface spalling. Mechanical properties have been measured following exposure to the same conditions at temperatures below 1000°C. Short-term test results are independent of ambient composition or salt coating. Long-term tests show that static fatigue life is dependent on salt coating, temperature and relative humidity.

### INTRODUCTION

Based on the high specific stiffness and inherent resistance to oxidative attack, oxide-based composites are candidate materials for applications ranging from chemical processing to combustion components. Such environments are likely to contain corrosive sodium and sulfur species as well as water vapor and reducing oxy-nitride compounds. This study focuses on the long-term effects of oxidative and corrosive environments on weight and mechanical properties of this composite at high temperatures. Atmospheres include dry and moist air as well as oxygen and argon at temperatures up to 1200°C. The corrosive salt is

$\text{Na}_2\text{SO}_4$ , which is known to deposit in typical combustion conditions and result in removal of material as well as degradation of mechanical properties [1].

## **MATERIAL**

The material used in this investigation is a continuous SiC (Nicalon) fiber-reinforced alumina composite manufactured by DuPont Lanxide using a directional metal oxidation (DiMOx) process [2]. Tows of BN-coated fibers are woven into a 12-harness satin [0/90] fabric, which is subsequently chemical-vapor coated with crystalline SiC. Approximately 10 such plies, all in the [0/90] orientation are consolidated into a plate. The porous plate is then brought into contact with a molten aluminum alloy under an oxidizing ambient for the DiMOx infiltration. Unreacted metal is subsequently etched from the alumina matrix leaving approximately 10 % void space. Reduced-section tensile coupons are machined from these plates in the  $0^\circ$  direction prior to application of a final seal-coat. Figure 1 shows a cross section of the material transverse to the loading axis. The fibers and fiber coatings as well as the matrix are visible. Numerous matrix cracks which result from thermal expansion mismatch and directional matrix growth columns are visible in the as-received state.

## **EXPERIMENTAL PROCEDURE**

Oxidation and corrosion studies are performed in wet and dry, oxidizing and inert ambients at temperatures of  $500^\circ\text{C}$ ,  $850^\circ\text{C}$ ,  $1000^\circ\text{C}$  and  $1200^\circ\text{C}$ . Specimens are cut from tensile coupons perpendicular to the loading axis so that the exterior seal-coat covers only 4 of the 6 sides. Samples are typically 0.1 X 0.1 X 0.4 inches, with the as-cut surface dimension being 0.1 X 0.4 inches. Sample preparation for stress-free corrosion exposure involves soaking cut sections in a saturated salt water solution ( $\text{Na}_2\text{SO}_4$ ) followed by air drying at  $150^\circ\text{C}$ . This results in roughly a  $10\text{ }\mu\text{m}$  surface layer which is comparable to the expected salt coating on a turbine engine component after 500 hours at  $900^\circ\text{C}$  with a sulfur fuel impurity level of 0.05% [3]. Water vapor is supplied to the furnace by passing a continuous stream of compressed air through a  $90^\circ\text{C}$  water reservoir at a rate of 0.1 liter/min. Oxidizing and inert gases are also continually supplied at this rate. All weight changes are normalized to total specimen surface area, due to the minimal effect of the seal coating.

Environmental effects on mechanical properties are also investigated using time to rupture and modulus evolution curves in the presence of the above-mentioned ambients. Details of the mechanical testing apparatus and testing procedure can be found elsewhere [4]. Environmental influence on short-term mechanical properties are not reported because no effect is observed for either atmosphere or salt coating. Mechanical property test data is limited to

temperatures below 1000°C because of the sharp drop in strength and stiffness following exposure above this limit. The time-temperature dependence of stress rupture is determined by holding a constant stress for 6 hours or until rupture. Following 6-hour survival at 500°C, temperature is increased step-wise 50°C and testing continues at that stress.

## **RESULTS AND DISCUSSION**

Experimental data from the thermogravimetric analysis for samples exposed to dry air are shown in Figure 2. Specific weight change for the as-received samples exposed to dry air at 500°C, 850°C, 1000°C and 1200°C are plotted up to 200 hours. At 500°C there is a significant weight loss during the first 5 hours followed by stable behavior. Some initial loss is seen at all temperatures followed by slow weight gain at 850°C and 1200°C. Given the hydrophilic nature of alumina, the weight loss is attributed to a process of driving off adsorbed water from internal micro-pores. This is supported by the observation that exposure to inert gas (argon) at temperatures up to 1200°C follows the same weight evolution curve as 500°C air. The decreasing levels of weight loss with increasing temperature is a result of the competition between drying rate weight loss, and oxidation rate weight gain. The subsequent weight gain which occurs at temperatures greater than 850°C is largely associated with the oxidation of SiC or residual aluminum metal (2 vol%). Behavior in 1000°C dry air is parallel to 1200°C dry air, but positioned at a lower specific weight. This exemplifies the opposing effects of the drying and the oxidation. The parabolic rate constants for weight gain in 1000°C and 1200°C air are;  $K_p = 0.053 \text{ mg}^2/\text{cm}^4 \text{ hr}$ ,  $K_p = 0.051 \text{ mg}^2/\text{cm}^4 \text{ hr}$ , respectively. Higher temperature leads to more rapid weight gain due to increased reaction rates as well as increased diffusion rates.

Exposure studies have also been conducted in other ambients as plotted in Figure 3. At a temperature of 850°C water vapor plays no decisive role in weight evolution. Apparently, the water vapor in the ambient air does not affect either the rate of internal evaporation or the rate of SiC oxidation. Conversely, at 1200°C water vapor eliminates any net weight loss over the first 2 hours by significantly increasing the rate of SiC oxidation;  $K_p = 0.080 \text{ mg}^2/\text{cm}^4 \text{ hr}$ . Pure oxygen exposure at 1200°C results in a minor initial weight loss and an even greater weight gain than air;  $K_p = 0.076 \text{ mg}^2/\text{cm}^4 \text{ hr}$ .

Results from salt-coated sample exposure are plotted in Figure 4. The  $\text{Na}_2\text{SO}_4$  coating causes a rapid and severe weight loss in all ambients 850°C and above. After 20 hours the samples have lost roughly  $8 \text{ mg}/\text{cm}^2$  compared to a weight gain on the order of  $0.5\text{-}1 \text{ mg}/\text{cm}^2$  in Figures 2 and 3. Furthermore, salt-coated samples continue to lose weight at a rate which is ~25X greater than the

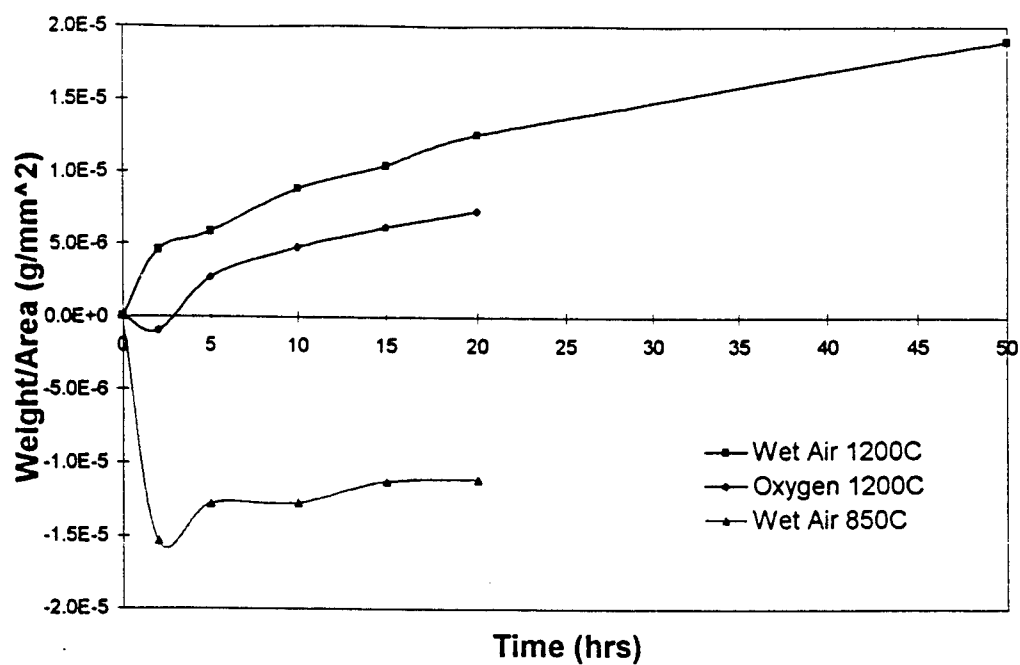


Figure 3. Change in weight per exposed area of SiC/Al<sub>2</sub>O<sub>3</sub>

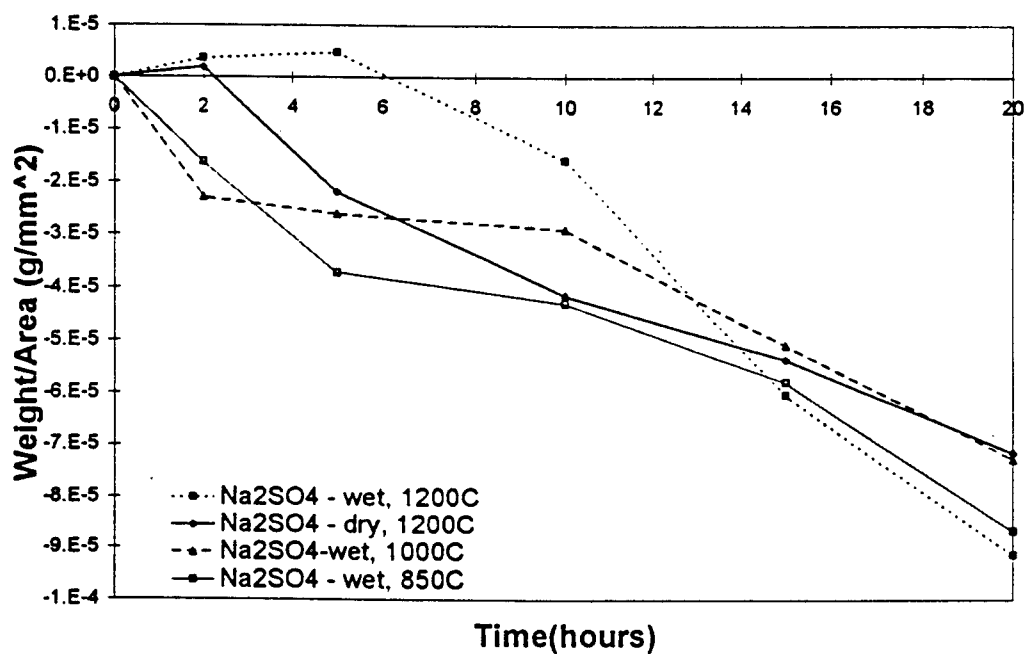


Figure 4. Change in weight per area of Na<sub>2</sub>SO<sub>4</sub>-Exposed SiC/Al<sub>2</sub>O<sub>3</sub>

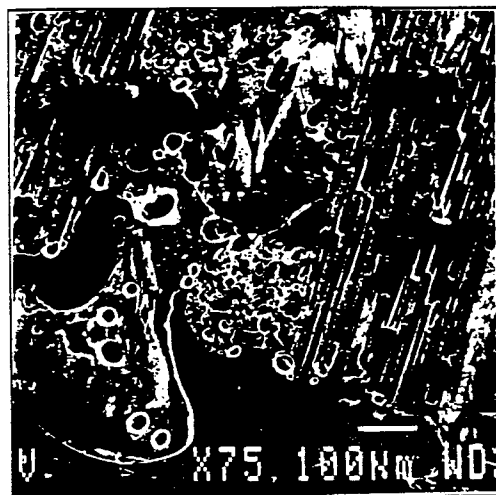


Figure 5. Structure following exposure to 1200°C and salt surface coating.

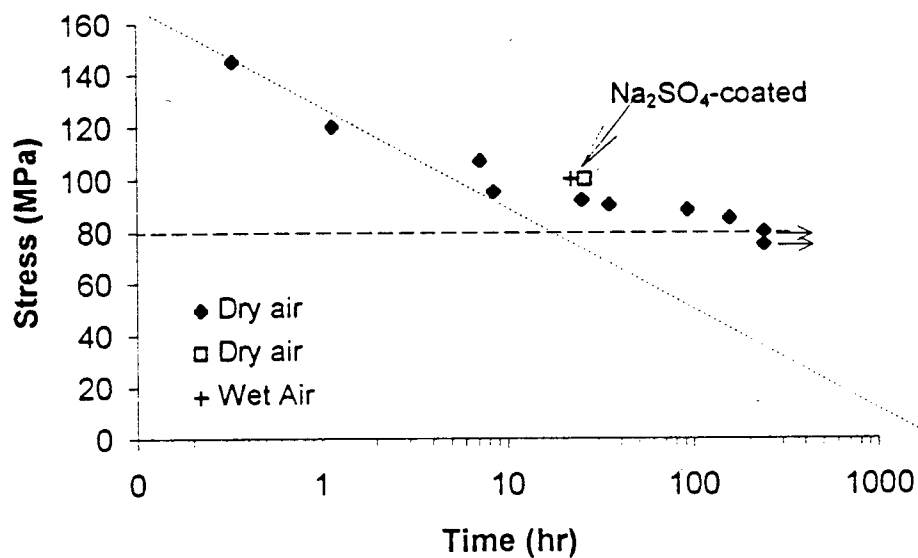


Figure 6. SiC/Al<sub>2</sub>O<sub>3</sub> lifetime under constant stress, in air 1000°C

#### ACKNOWLEDGMENTS

Support is from ONR/ARPA contract number N0001492J1779. We also thank Drs. W. Coblenz and S. Fishman for oversight of this program.

samples show a small degree of weight gain and parabolic kinetics; rate constants are reported. Mechanical properties have similarly revealed the influence of surface contaminants and atmosphere on material integrity. In the as-received condition in air, the run-out stress is approximately 80 MPa. At higher stresses, sample life is shortened according to a non-linear relation between stress and the logarithm of rupture time. Water vapor and salt coatings are more aggressive chemically, but cause only a slight reductions in life.

## FIGURES

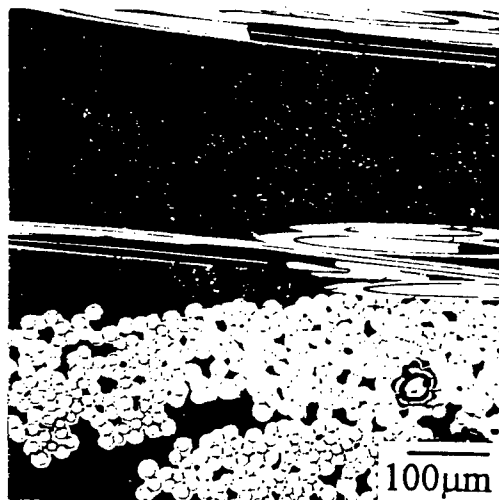


Figure 1. Cross section of as received SiC/Al<sub>2</sub>O<sub>3</sub>

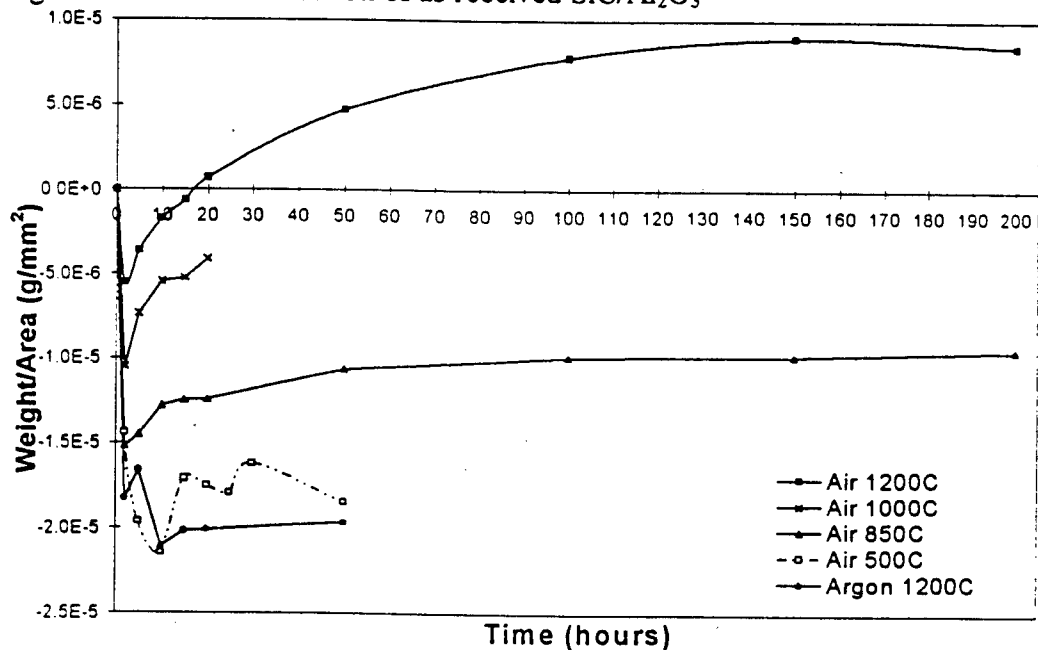


Figure 2. Change in weight per exposed area of SiC/Al<sub>2</sub>O<sub>3</sub> in air, argon

rate of weight gain with no salt. Data show that dry and moist air are equally aggressive at 850°C and above. Samples exposed to these conditions, Figure 5, show that salt causes degradation via the formation of a sodium silicate glass. However, proper interpretation of weight evolution must consider that  $\text{Na}_2\text{SO}_4$  is capable of vaporizing at these temperatures. Therefore, total weight change is a result of corrosion combined with salt decomposition and evaporation [5,6,7].

Mechanical testing of as-received composites under constant load and temperature is conducted to establish a reference baseline for material behavior. Figure 6 shows time to rupture in dry air at 1000°C for stress levels between 70 and 145 MPa. Although tests have only been conducted for a maximum of 240 hours, an apparent run-out stress is observed at 80 MPa. At higher stresses rupture time roughly follows a bilinear relation between log of rupture time and applied stress. The effect of a thin surface coating of  $\text{Na}_2\text{SO}_4$  on rupture life is also plotted on Figure 6. The  $\text{Na}_2\text{SO}_4$ -coated samples ruptured at times which were consistent with the as-received samples. This highlights the importance of surface coating integrity.

Water vapor effects are also of interest with respect to the as-received and the salt-coated material. For comparison water vapor alone results in a rupture time of ~13 hrs at 100 MPa and 1000°C. No significant decrease is seen here in spite of the stress corrosion cracking susceptibility of aluminum oxide [8,9]. Additionally, water transport through amorphous silica is roughly an order of magnitude faster than oxygen transport [10]. Therefore, both the matrix and fibers are degrading faster in the moist environment. Combining  $\text{Na}_2\text{SO}_4$  with water vapor also results in a higher level of chemical reactivity, but no significant reduction in life is seen; 100 MPa, 1000°C, rupture time is 20 hrs.

Finally, it is desired to establish the temperature at which a high level of stress can be supported for 6 hours. This indicates the design conditions which may be approached for a short-term combustion application. In dry air failure under 160 MPa load occurs within this time at a temperature of 650°C, while moist air causes failure at 600°C in the same window.

## SUMMARY AND CONCLUSIONS

This work has investigated the high-temperature oxidation and corrosion behavior of an  $\text{SiC}/\text{Al}_2\text{O}_3$  composite under dry and moist ambients. Results have shown that an initial weight loss occurs in all ambients followed by some degree of steady weight gain at temperatures above 850°C. Increasing temperature, oxygen activity and relative humidity all increase rate and extent of weight gain. Combining a salt coating in moist air is the most detrimental in terms of relative weight change. The presence of the Na-containing salt causes a rapid weight loss with apparently linear kinetics. In the absence of salt,



## REFERENCES

1. R. Kowalik, W. Wang and R. Sands, "Hot corrosion of Nicalon fiber reinforced glass - ceramic matrix composites: Microstructural effects," NAWCADWAR Final Report No. 93033-60, November 1992.
2. Lanxide Technology Company, Patent Nos. 5187130, 5215566, 5262203, 5306677, 5334562, 5389450.
3. S. Saunders and T. Gibbons, "Developments in test procedures for hot-salt corrosion of superalloys" High temperature surface interactions, 68th Meeting of structures and materials panel of AGARD in Ottawa Canada, 23-28 April 1989.
4. P. Lipetzky, G.J. Dvorak and N.S. Stoloff, "Tensile properties of a SiC/SiC composite" *Mat. Sci. Eng.* A216 (1996), pg 11-19.
5. J. Tschinkel, "Formation of Sodium Sulfate in gas turbine combustors," *Corrosion-NACE*, Vol. 28, No. 5, 1972, pp161-69.
6. R. Fryxell, C. Trythall and R. Perkins, "Physical properties of  $\text{Na}_2\text{SO}_4$ ," *Corrosion-NACE*, Vol 29, No. 11, 1973, p423.
7. M. Lawson, H. Kim, F. Petit and J. Blachere, "Hot Corrosion of Silica", *J. Am. Ceram. Soc.*, Vol 73, [4] 1990, pp989-95.
8. S. Wiederhorn in Fracture Mechanics of Ceramics, Vol 2, Ed by R. Bradt, D. Hasselman and F. Lange (Plenum Press, NY, 1974) pg 613.
9. R. Steinbrech, R. Khehans and W. Schaarwaechter, "Increase of crack resistance during slow crack growth in  $\text{Al}_2\text{O}_3$  bend specimens," *J. Mat. Sci.*, Vol 18, 1983, pp 265-70.
10. B.E. Deal and A.S. Grove, "General relationships for the thermal oxidation of silicon," *J. Appl. Phys.*, Vol. 36, 1965, pg 593.

# IMACS '94

Proceedings of the 14th IMACS World Congress on Computation and Applied Mathematics

July 11-15, 1994, Georgia Institute of Technology, Atlanta, Georgia, USA

in three volumes

## VOLUME 2

Applications of Computing  
Fluid Mechanics  
Acoustics  
Solid Mechanics  
Neural Networks

EDITED BY: W.F. AMES  
GEORGIA INSTITUTE OF TECHNOLOGY  
ATLANTA, GEORGIA, USA

Copyright © 1994 IMACS - International Association for Mathematics and Computers in Simulation

All rights reserved. No part of this publication may be reproduced, stored in a retrieval system or transmitted in any form or by any means, electronic, electrostatic, magnetic, mechanical, photocopying, recording or otherwise, without prior permission in writing from IMACS.

# ADAPTIVE METHOD OF LINES TECHNIQUES FOR VAPOR INFILTRATION PROBLEMS

S. Adjerid, J. E. Flaherty, W. Hillig, J. Hudson, and M. S. Shephard

Scientific Computation Research Center

and

Center for Composite Materials and Structures

Rensselaer Polytechnic Institute, Troy, New York 12180, USA

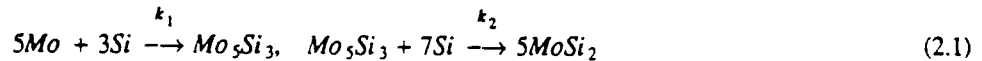
Tel: 518-276-6348 / Fax: 518-276-4033 / e-mail: flaherje@cs.rpi.edu

## 1. Introduction

Patibandla et al. [4,5] describe a reactive vapor infiltration (RVI) process for manufacturing fiber-reinforced ceramic composites where silicon carbide ( $SiC$ ) or alumina ( $Al_2O_3$ ) fibers are mixed with molybdenum ( $Mo$ ) powder and pressed at room temperature to form a porous preform. The preform is exposed to a silicon tetra-chloride ( $SiCl_4$ ) and hydrogen ( $H_2$ ) flow where molecular-surface reactions liberate  $Si$  which, when absorbed into the preform, reacts with  $Mo$  to form a molybdenum di-silicide ( $MoSi_2$ ) matrix. As a first step in modeling the RVI process, we present a mathematical model of the diffusion of  $Si$  into a compressed-powder  $Mo$  pellet to form the  $MoSi_2$  matrix. The production of an intermediate ( $Mo_5Si_3$ ) silicide layer, the growth of the  $MoSi_2$  layer, and the volume expansion of the pellet are predicted. The resulting partial differential system is solved using an adaptive software system [2] that includes capabilities for automatic quadtree-structured mesh generation, mesh refinement/coarsening (h-refinement), method order variation (p-refinement), and mesh motion (r-refinement). Computational solutions of one- and two-dimensional problems indicate that the adaptive software is a robust and effective tool for addressing composite-processing problems. The mathematical model predicts the observed parabolic growth rate of the silicide layer and the volume expansion of the pellet to a high degree of accuracy.

## 2. RVI Model

The loosely compacted pellet is subjected in a furnace to a flow of  $SiCl_4$  and  $H_2$  that reacts on the surface of grains of the pellet to liberate  $Si$  [4,5]. The  $Si$  is absorbed into the  $Mo$  pellet and reacts as



to form  $Mo_5Si_3$  and the desired  $MoSi_2$  silicide. These reactions occur in narrow fronts with free  $Si$  diffusing (principally by solid-state diffusion) through an  $MoSi_2$  layer to reach the reaction zones. The reactions (2.1) are accompanied by a 158% volume increase which fills the pores between grains of  $Mo$  powder, but may cause cracking [4,5].

Suppose the pellet contains a mixture of reactants and products and let the mass  $m_i$  (g) of species  $i$  at time  $t$  in a control volume  $V$  be

$$m_i = \int_V \rho Y_i dV, \quad i = 1, 2, 3, 4, \quad (2.2)$$

where  $\rho$  ( $g/cm^3$ ) is the mixture density and  $Y_i$ ,  $i = 1, 2, 3, 4$ , are, respectively, the mass fractions of  $Si$ ,  $MoSi_2$ ,  $Mo_5Si_3$ , and  $Mo$ . As the pellet deforms due to the volume change, we specify the position of each material point  $\mathbf{x}$  as a function of  $t$  and its initial spatial position  $\mathbf{X}$ . With this reference, considerations of mass conservation for species  $i$  imply that

$$\frac{dm_i}{dt} = - \int_{\partial V} \mathbf{J}_i \cdot \mathbf{n} d\sigma - \int_V \rho Y_i \mathbf{v} \cdot \mathbf{n} d\sigma + \int_V \dot{r}_i dV, \quad i = 1, 2, 3, 4, \quad (2.3)$$

where  $\partial V$ , with unit outer normal  $\mathbf{n}$ , is the boundary of  $V$ ;  $\mathbf{v}(\mathbf{X}, t) = \partial_t \mathbf{x}(\mathbf{X}, t)$  ( $cm/sec$ ) is the mixture velocity; and  $\dot{r}_i$  ( $g/cm^3/sec$ ) is the mass production rate and  $\mathbf{J}_i$  ( $g/cm^2/sec$ ) is the diffusive flux of species  $i$ . Assuming Fickian diffusion  $\mathbf{J}_i = -D_i \nabla(\rho Y_i)$ , with  $D_i$  ( $cm^2/sec$ ) being the diffusivity of species  $i$  in the mixture.

Applying the divergence theorem to (2.3) and using (2.2) yields the partial differential system

$$\frac{D(\rho Y_i)}{Dt} = \partial_t(\rho Y_i) + \mathbf{v} \cdot \nabla(\rho Y_i) = \nabla \cdot D_i \nabla(\rho Y_i) - \rho Y_i \nabla \cdot \mathbf{v} + \dot{r}_i, \quad \mathbf{x} \in \Omega, \quad t > 0, \quad i = 1, 2, 3, 4, \quad (2.4)$$

where  $\Omega$  is the spatial region occupied by the pellet at time  $t$ .

Mass production rates are much faster than diffusion rates and, thus, cannot be observed. We assume that all reactions are irreversible, isothermal, cease when one or more reactants are depleted, and are linear in each concentration.

$$\begin{aligned} \dot{r}_1 &= -M_1(3w_1 + 7w_2), \quad \dot{r}_2 = 5M_2w_2, \quad \dot{r}_3 = M_3(w_1 - w_2), \\ \dot{r}_4 &= -5M_4w_1, \quad w_1 = k_1 \left( \frac{\rho Y_1}{M_1} \right) \left( \frac{\rho Y_4}{M_4} \right), \quad w_2 = k_2 \left( \frac{\rho Y_1}{M_1} \right) \left( \frac{\rho Y_3}{M_3} \right). \end{aligned} \quad (2.1)$$

The variables  $k_1$  and  $k_2$  ( $\text{cm}^3/\text{sec}$ ) identify the rates of the reactions (2.1) and  $M_i$  (g) denotes the molecular weight of species  $i = 1, 2, 3, 4$  [3].

To include expansion, consider a volume  $V$  at time  $t$  where each chemical occupies the portion  $V_i$ ,  $i = 1, 2, 3, 4$ . Letting  $V_0$  denote the volume of the voids between chemical compounds,  $v(x, t) = V_0/V$  denote the porosity,  $\rho_i = (\text{g}/\text{cm}^3)$ ,  $i = 1, 2, 3, 4$ , denote species densities [3], using (2.2), and letting  $V$  tend to zero gives

$$1 - v = \sum_{i=1}^4 \frac{V_i}{V} = \sum_{i=1}^4 \frac{m_i}{\rho_i V} = \sum_{i=1}^4 \frac{1}{\rho_i V} \int_V \rho Y_i dV = \sum_{i=1}^4 \frac{\rho Y_i}{\rho_i}.$$

Multiplying (2.4) by  $1/\rho_i$ , summing over  $i$ , and using (2.6), we obtain

$$-\frac{Dv}{Dt} + (\nabla \cdot v)(1 - v) = \sum_{i=1}^4 \frac{1}{\rho_i} [\dot{r}_i + \nabla \cdot D_i \nabla \rho Y_i], \quad x \in \Omega, \quad t > 0.$$

We simplify (2.7) by including the effects of  $v$  in the densities of the mixture components. With little loss of generality, it is reasonable to neglect  $V_1/V$ . Furthermore, the diffusivities  $D_i$ ,  $i = 2, 3, 4$ , are negligible relative to  $D$ . Thus, all diffusive terms are neglected, and we approximate (2.7) as

$$\nabla \cdot v = \sum_{i=2}^4 \frac{\dot{r}_i}{\rho_i}.$$

The system is closed by the mixture momentum equation for a viscous medium

$$\rho \frac{Dv}{Dt} + v[\partial_t \rho + \nabla \cdot (\rho v)] = \nabla \cdot T$$

where the traction matrix  $T$  (Pa) has components

$$T_{ij} = (-p + \lambda \nabla \cdot v) \delta_{ij} + \mu (\partial_{x_j} v_i + \partial_{x_i} v_j)$$

with  $\lambda$  and  $\mu$  being Lamé parameters,  $p$  (Pa) being the pressure, and  $\delta_{ij}$  being the Kronecker delta.

Specification of initial and boundary conditions complete the model (2.4,5,8,9). When only Mo powder is present in the initial state, we prescribe

$$\rho(X, 0) = \bar{\rho}, \quad Y_i(X, 0) = 0, \quad i = 1, 2, 3, \quad Y_4(X, 0) = 1, \quad v(X, 0) = 0, \quad X \in \Omega \cup \partial\Omega,$$

where  $\bar{\rho}$  is the initial mixture density. Boundary conditions are developed by assuming that the reaction at the surface ceases when a full monolayer of Si atoms is present on the surface. Therefore, the flux of Si atoms absorbed into the pellet must equal the rate at which they are produced by this reaction. Moreover, we assume that the rate of absorption of Si atoms is proportional to the deviation of  $Y_1$  from twice the maximum solubility  $S$  of Si. Boundary fluxes of other species are neglected; thus,

$$D_1 \nabla (\rho Y_1) \cdot n = -\alpha(Y_1 - S), \quad D_i \nabla (\rho Y_i) \cdot n = 0, \quad i = 2, 3, 4, \quad x \in \partial\Omega, \quad t > 0.$$

### 3. Computational Results

We use an adaptive finite element software system with capabilities for automatic h-, p-, and/or r-refinement to solve dimensionless versions of (2.4,5,8,9,11,12) in one and two spatial dimensions. With mesh motion, for example, one can both follow evolving fronts and track the volume expansion as the reaction progresses. The particular combination of h- and p-refinement is remarkably effective when high accuracy is necessary. Mesh refinement and order variation are controlled by a posteriori estimates of local discretization errors [2] or error indicators. Herein, error indicators are used to control jumps in the computed flux across element boundaries [2,3].

With the origin of a Cartesian coordinate system at the center of a  $2a \times 2b \times 2c$  pellet, we introduce dimensionless variables with  $(x_1, x_2, x_3)$  scaled by  $(a, b, c)$ ,  $t$  scaled by  $M_4/k_1\bar{\rho}$ , and  $\rho$  scaled by  $\bar{\rho}$ . Employing symmetry, the initial Mo pellet is solved on  $0 < x_1 < a$  with  $x_2$  and  $x_3$  derivatives set to zero. The initial Mo pellet porosity is with  $a = 1$  (mm),  $\alpha = 10^6$  ( $\text{g}/\text{cm}^3/\text{sec}$ ),  $S = 0.00037$ ,  $k_1 = 1.5 \times 10^{-3}$  and  $k_2 = 1.5 \times 10^{-3}$ .

$D_1 = 0.37 \times 10^{-5}$ ,  $1.5 \times 10^{-5}$ , and  $4.2 \times 10^{-5}$  ( $\text{cm}^2/\text{sec}$ ), and  $D_i = 10^{-20}$  ( $\text{cm}^2/\text{sec}$ ),  $i = 2, 3, 4$ . The three values of  $D_1$  correspond to observed diffusivities of Si at, respectively, temperatures of 1100, 1200, and 1300 ( $^{\circ}\text{C}$ ) [3-5].

We compare computed and observed [4,5] results for the square of the thickness of the  $\text{MoSi}_2$  layer as a function of time for three temperatures in the left portion of Figure 1. Computed and experimental results are in excellent agreement with deviations being less than 10%. Mass concentrations of  $\text{MoSi}_2$ ,  $\text{Mo}_5\text{Si}_3$ , and  $\text{Mo}$  at a temperature of 1200  $^{\circ}\text{C}$  and  $t = 9.2$  hr are shown as a function of position in the right portion of Figure 1. The  $\text{MoSi}_2$  layer is progressing from right to left in Figure 2; thus, the right-most curve is the mass fraction of  $\text{MoSi}_2$ , the steeply-peaked center curve is the mass fraction of  $\text{Mo}_5\text{Si}_3$ , and the left-most curve is the unreacted  $\text{Mo}$ .

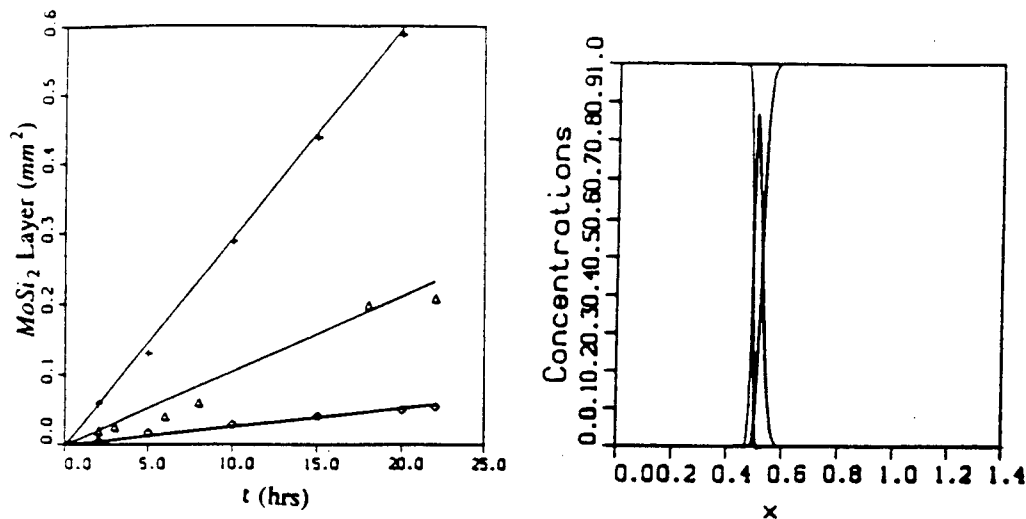


Figure 1. On the left, comparison of computed and observed values of the square of the thickness of the  $\text{MoSi}_2$  layer as a function of time for temperatures of 1100  $^{\circ}\text{C}$  (diamonds), 1200  $^{\circ}\text{C}$  (triangles), and 1300  $^{\circ}\text{C}$  (plusses). On the right, mass fractions of  $\text{MoSi}_2$ ,  $\text{Mo}_5\text{Si}_3$ , and  $\text{Mo}$  at 1200  $^{\circ}\text{C}$  and  $t = 9.2$  hr as a function of position.

Solutions shown in Figure 1 were obtained by hpr-refinement and in the left portion of Figure 2 we show the spatial mesh and method order used at 1200  $^{\circ}\text{C}$  and  $t = 9.2$  hr. A coarse mesh and first-order method are used away from the reaction zone while finer meshes and high-order methods are used near the reaction. The mesh used to solve this problem is shown as a function of time in the right portion of Figure 3. The mesh is concentrated near the front and moving to account for the expansion as the reaction occurs.

We also solved a two-dimensional problem involving a  $a = 1 \times 10$  ( $\text{mm}^2$ ) pellet with the parameters as specified for the one-dimensional problem at 1200  $^{\circ}\text{C}$ . In Figure 3, we show a quadrant of the mesh at 2, 10, and 30 hrs. obtained using piecewise-bilinear finite element approximations with Lobatto quadrature used to eliminate spurious oscillations [1]. Expansion occurs in regions having high  $\text{MoSi}_2$  concentrations.

#### 4. Discussion

We have developed a reaction-diffusion system to analyze the RVI and other chemical vapor infiltration processes of fabricating ceramic composites. When used with an adaptive finite element software system [2], the model predicted the growth of an  $\text{MoSi}_2$  layer in a siliciding application [4,5]. Production rates, volume expansion, residual stresses and other effects may be studied as functions of, e.g., initial composition, temperature, and porosity.

Future experiments will be performed with fibers embedded in a powder preform and our models will be modified to reflect this. Our investigation will seek to reveal optimal fiber placements, packing densities, and process strategies. By combining a computational and experimental program we are able to identify and verify prototypical optimal combinations much more rapidly than would be possible by using either paradigm alone.

#### 5. Acknowledgment

This research was supported by ARPA/ONR under grant N00014-92J-1779 and by AFOSR under grant F49620-93-1-0218.

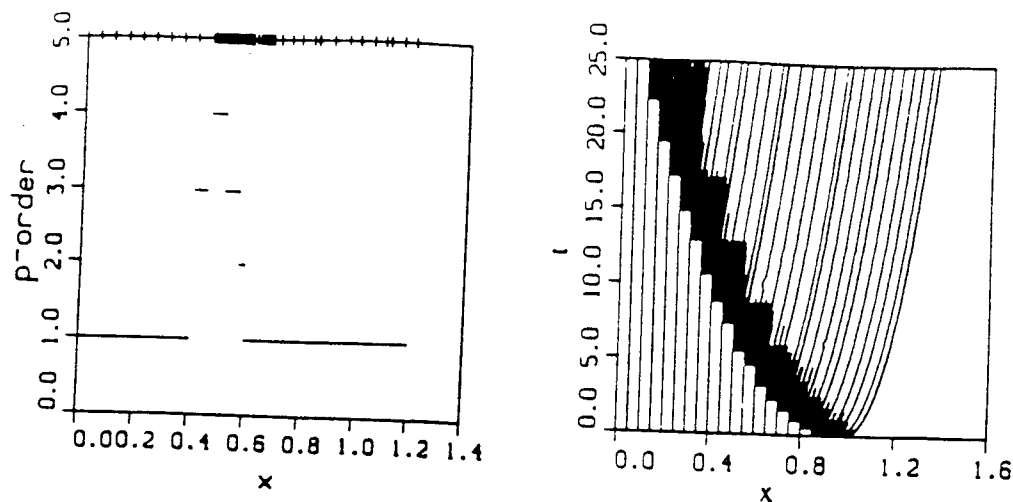


Figure 2. Method order and spatial mesh (left) and mesh position as a function of time (right).

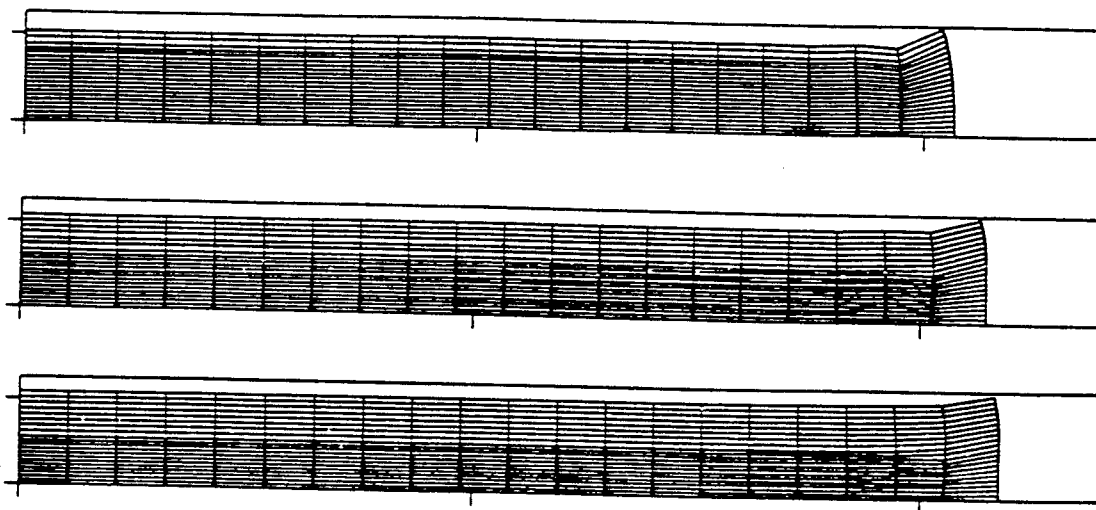


Figure 3. Meshes at 2 (top), 10 (center), and 30 (bottom) hrs. for a two-dimensional pellet.

## 6. References

1. S. Adjerid, M. Aiffa, and J.E. Flaherty, High-Order Finite Element Methods for Singularly-Perturbed Elliptic and Parabolic Problems, *SIAM J. Appl. Math.*, to appear, 1994.
2. S. Adjerid, J.E. Flaherty, P.K. Moore, and Y.J. Wang, High-Order Methods for Parabolic systems, *Physica D*, Vol. 60, pp. 94-111, 1992.
3. S. Adjerid, J.E. Flaherty, M.S. Shephard, Y.J. Wang, W. Hillig, J. Hudson, and N. Patibandla, SCREC Rep. #2-1994, Sci. Comp. Res. Ctr., Rensselaer Polytech. Inst., 1994.
4. N. Patibandla and W.B. Hillig, Processing of Molybdenum Di-silicide Using a New Reactive Vapor Infiltration Technique, *J. Am. Ceram. Soc.*, Vol. 76, pp. 1630-1634, 1993.
5. N. Patibandla, W.B. Hillig, and M.R. Ramakrishnan, *SiC Fiber Reinforced  $MoSi_2$  Matrix Composites Produced Via Reactive Vapor Infiltration*, preprint, Cent. Compos. Mat'ls. and Struct., Rensselaer Polytech. Inst., 1993.

## ADAPTIVE NUMERICAL TECHNIQUES FOR REACTIVE VAPOR INFILTRATION

S. Adjerid, J. E. Flaherty, M. S. Shephard, Y. J. Wang  
Scientific Computation Research Center  
W. Hillig, J. Hudson, N. Patibandla  
Center for Composite Materials and Structures  
Rensselaer Polytechnic Institute, Troy, New York 12180, USA

### 1. INTRODUCTION

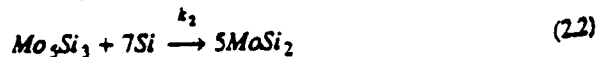
Patibandla et al. [1,2] describe a reactive vapor infiltration (RVI) process for manufacturing fiber-reinforced ceramic composites where silicon carbide ( $SiC$ ) or alumina ( $Al_2O_3$ ) fibers are mixed with molybdenum ( $Mo$ ) powder and pressed at room temperature to form a porous preform. The preform is exposed to a silicon tetrachloride ( $SiCl_4$ ) and hydrogen ( $H_2$ ) flow where molecular-surface reactions liberate  $Si$  which, when absorbed into the preform, reacts with  $Mo$  to form a molybdenum di-silicide ( $MoSi_2$ ) matrix. As a first step in modeling the RVI process, we present a mathematical model of the diffusion of  $Si$  into a compressed-powder  $Mo$  pellet to form the  $MoSi_2$  matrix. The production of an intermediate ( $Mo_3Si_3$ ) silicide layer, the growth of the  $MoSi_2$  layer, and the volume expansion of the pellet are predicted. The model, consisting of a nonlinear ordinary and partial differential system, is solved using a state-of-the-art adaptive software system [3] that includes capabilities for automatic quadtree-structured mesh generation, mesh refinement/coarsening (h-refinement), method order variation (p-refinement), and mesh motion (r-refinement). Computational solutions of one- and two-dimensional problems indicate that the adaptive software is a robust and effective tool for addressing composite-processing problems. When compared with experimental observations, the mathematical model predicts a parabolic growth rate of the silicide layer and the volume expansion of the pellet to a high degree of accuracy. Anticipated applications of the adaptive software and enhancements to the mathematical model are described in a final section.

### 2. RVI MODEL

Patibandla et al. [1,2] describe experiments where a pellet of a loosely compacted (45% porosity)  $Mo$  powder is subjected in a furnace to a flow of  $SiCl_4$  and  $H_2$  that reacts on the surface of grains of the pellet to liberate  $Si$  and hydrochloric acid ( $HCl$ ). The  $Si$  is absorbed into the  $Mo$  pellet and reacts as



to form the silicide  $Mo_3Si_3$ , which quickly reacts as



to form  $MoSi_2$ . These reactions occur in narrow fronts with free  $Si$  diffusing (principally by solid-state diffusion) through an  $MoSi_2$  layer to reach the reaction zones.



The silicide-forming reactions (2.1.2) are accompanied by a 158% volume increase which fills the pores between grains of *Mo* powder, but may cause cracking [1.2].

Suppose the pellet contains a mixture of reactants and products and let the mass  $m_i$  (g) of species  $i$  at time  $t$  in a control volume  $V$  be

$$m_i = \int_V \rho Y_i dV, \quad i = 1, 2, 3, 4, \quad (2.3)$$

where  $\rho$  (g/cm<sup>3</sup>) is the mixture density and  $Y_i$ ,  $i = 1, 2, 3, 4$ , are, respectively, the mass fractions of *Si*, *MoSi<sub>2</sub>*, *Mo<sub>5</sub>Si<sub>3</sub>*, and *Mo*. As the pellet deforms due to the volume change, we specify the position of each material point  $x$  as a function of  $t$  and its initial spatial position  $X$ . With this reference, considerations of mass conservation for species  $i$  imply that

$$\frac{dm_i}{dt} = \int_{\partial V} J_i \cdot n d\sigma + \int_V \rho Y_i v \cdot n d\sigma + \int_V \dot{r}_i dV, \quad i = 1, 2, 3, 4, \quad (2.4)$$

where  $\dot{r}_i$  (g/cm<sup>3</sup>/sec) is the mass production rate and  $J_i$  (g/cm<sup>2</sup>/sec) is the diffusive flux of species  $i$ .  $\partial V$  is the boundary of  $V$ ,  $n$  is the unit outer normal to  $\partial V$ , and

$$v(X, t) = \partial_t x(X, t) \quad (2.5)$$

is the mixture velocity.

Assuming Fickian diffusion

$$J_i = -D_i \nabla(\rho Y_i), \quad (2.6)$$

with  $D_i$  (cm<sup>2</sup>/sec) the diffusivity of species  $i$  in the mixture, applying the divergence theorem to (2.4), and using (2.3) yields the partial differential system

$$\frac{D(\rho Y_i)}{Dt} - \nabla \cdot D_i \nabla(\rho Y_i) + \rho Y_i \nabla \cdot v = \dot{r}_i, \quad x \in \Omega, \quad t > 0, \quad i = 1, 2, 3, 4, \quad (2.7a)$$

where

$$\frac{D}{Dt} = \partial_t + v \cdot \nabla \quad (2.7b)$$

is the material derivative and  $\Omega$  is the spatial region occupied by the pellet at time  $t$ .

Mass production rates are much faster than diffusion rates and, thus, cannot be observed. We assume that all reactions are irreversible and that they cease when one or more reactants are depleted. The form of the production rates should not significantly affect the results, so, for simplicity, we assume that they are linear in each concentration to obtain

$$\dot{r}_1 = -M_1(3w_1 + 7w_2), \quad \dot{r}_2 = 5M_2w_2, \quad \dot{r}_3 = M_3(w_1 - w_2), \quad (2.8a,b,c)$$

$$\dot{r}_4 = -5M_4w_1, \quad w_1 = k_1 \left( \frac{\rho Y_1}{M_1} \right) \left( \frac{\rho Y_4}{M_4} \right), \quad w_2 = k_2 \left( \frac{\rho Y_1}{M_1} \right) \left( \frac{\rho Y_3}{M_3} \right). \quad (2.8c,d,e)$$

The variables  $k_1$  and  $k_2$  (cm<sup>3</sup>/sec) identify the rates of the reactions (2.1.2) and  $M_i$  (g) denotes the molecular weight of species  $i = 1, 2, 3, 4$  (cf. Table I).

The process has been assumed to be isothermal, which should be acceptable since thermal variations produced by the reactions (2.1.2) have a negligible influence

at the temperature level of the furnace.

To include expansion, consider a volume  $V$  at time  $t$  where each chemical occupies the portion  $V_i$ ,  $i = 1, 2, 3, 4$ . Letting  $V_0$  denote the volume of the voids between chemical compounds,  $\mu(\mathbf{x}, t) = V_0/V$  denote the porosity,  $\rho_i = m_i/V_i$  ( $\text{g/cm}^3$ ),  $i = 1, 2, 3, 4$ , denote species densities (cf. Table I), using (2.3), and letting  $V$  tend to zero gives

$$1 - \mu = \sum_{i=1}^4 \frac{V_i}{V} = \sum_{i=1}^4 \frac{m_i}{\rho_i V} = \sum_{i=1}^4 \frac{1}{\rho_i V} \int \rho Y_i dV = \sum_{i=1}^4 \frac{\rho Y_i}{\rho_i} \quad (2.9)$$

Table I. Molecular Weight  $M_i$  and Density  $\rho_i$  of Each Species.

$i$	1	2	3	4
Species	Si	MoSi <sub>2</sub>	Mo <sub>5</sub> Si <sub>3</sub>	Mo
$M_i$	28	152	564	96
$\rho_i$	2.34	6.24	7.38	10.2

Multiplying (2.7) by  $1/\rho_i$ , summing over  $i$ , and using (2.9), we obtain

$$-\frac{D\mu}{Dt} + (\nabla \cdot \mathbf{v})(1 - \mu) = \sum_{i=1}^4 \frac{1}{\rho_i} [\dot{\rho}_i + \nabla \cdot D_i \nabla \rho Y_i], \quad \mathbf{x} \in \Omega, \quad t > 0. \quad (2.10)$$

The system is closed by assuming that the flow is irrotational ( $\nabla \times \mathbf{v} = 0$ ) and by specifying a porosity function of the form  $\mu(\mathbf{x}, t) = h(\rho, Y_1, \dots, Y_4)$ . Herein, we simplify (2.10) by neglecting  $\mu$ ,  $V_0/V$ , and the diffusive terms. As noted,  $\mu$  is negligible in the silicide layer. Its effect in the unreacted mixture may be included in the densities of the initial components. With very little free Si in the pellet, it is reasonable to neglect its contribution to the total volume. The diffusivities  $D_2$ ,  $D_3$ , and  $D_4$  are negligible relative to  $D_1$ . With small Si concentrations, its diffusion may also be neglected when calculating the volume expansion. With these assumptions, (2.10) becomes

$$\nabla \cdot \mathbf{v} = \sum_{i=2}^4 \frac{\dot{\rho}_i}{\rho_i} \quad (2.11)$$

Knowing the velocity divergence, we obtain the local volume change as

$$\frac{D(\det \mathbf{F})}{Dt} = (\det \mathbf{F})(\nabla \cdot \mathbf{v}) \quad (2.12)$$

where  $\mathbf{F}$  is a matrix of the deformation gradients  $\partial x_j / \partial X_k$ ,  $j, k = 1, 2, 3$ , and  $\det \mathbf{F}$  is its determinant.

Specification of initial and boundary conditions complete the model (2.7, 11, 12). When, e.g., only Mo powder is present in the initial state, we prescribe

$$\rho(\mathbf{X}, 0) = \bar{\rho}, \quad Y_i(\mathbf{X}, 0) = 0, \quad i = 1, 2, 3, \quad Y_4(\mathbf{X}, 0) = 1, \quad \mathbf{v}(\mathbf{X}, 0) = 0, \quad \mathbf{X} \in \Omega \cup \partial\Omega \quad (2.13)$$

where  $\bar{\rho}$  is the initial mixture density.

Boundary conditions are developed by assuming that the reaction (2.1) ceases when a full monolayer of Si atoms is present on the surface. Therefore, the flux of Si atoms being absorbed into the pellet must equal the rate at which they are produced by the reaction (2.1). Moreover, we assume that the rate of absorption of Si atoms is proportional the deviation of  $Y_1$  from the twice the maximum solubility  $S$  of Si in  $MoSi_2$ . Fluxes of other species through the boundaries are neglected; thus,

$$D_1 \nabla(\rho Y_1) \cdot n = -\alpha(Y_1 - S), \quad D_i \nabla(\rho Y_i) \cdot n = 0, \quad i = 2, 3, 4, \quad x \in \partial\Omega, \quad t > 0, \quad (2.14)$$

with  $\alpha > 0$  and  $S = 0.00037$ .

### 3. COMPUTATIONAL RESULTS

We use an adaptive finite element software system with capabilities for automatic h-, p-, and/or r-refinement [3] to solve dimensionless versions of (2.7,8,11-14) in one and two spatial dimensions. With mesh motion, for example, we can both follow evolving fronts and track the volume expansion as the reaction progresses. The particular combination of h- and p-refinement is remarkably effective when high accuracy is necessary. Mesh refinement and order variation are controlled by a posteriori estimates of local discretization errors that have been either proven or observed to converge at the asymptotically correct rate for a wide range of problems [4]. Problems in this section were obtained by using an error indicator involving jumps in the first derivatives of the finite element solution across element boundaries [3,4]. Convergence of this indicator to the correct error is not known.

With the origin of a Cartesian coordinate system at the center of a  $2a \times 2b \times 2c$  pellet, we introduce dimensionless variables with  $(x_1, x_2, x_3)$  scaled by  $(a, b, c)$ ,  $t$  scaled by  $M/k_1\bar{\rho}$ , and  $\rho$  scaled by  $\bar{\rho}$ . Employing symmetry, one-dimensional problems are solved on  $0 < x_1 < a$  with  $x_2$  and  $x_3$  derivatives in (2.7,11-14) set to zero. Initially, we consider a problem involving a 45% porous Mo pellet. Selecting  $a = 1 \text{ mm}$ ,  $\alpha = 10^6 \text{ (g/cm}^2\text{/sec)}$ , and  $k_1 = 1.5 \times 10^3$  and  $k_2 = 1.5 \times 10^2 \text{ (g/cm}^3\text{)}$ , we solve problems with  $D_1 = 0.37 \times 10^{-5}$ ,  $1.5 \times 10^{-5}$ , and  $4.2 \times 10^{-5} \text{ (cm}^2\text{/sec)}$  and  $D_i = 10^{-20} \text{ (cm}^2\text{/sec)}$ ,  $i = 2, 3, 4$ . The three values of  $D_1$  correspond to observed diffusivities of Si at, respectively, temperatures of 1100, 1200, and 1300 ( $^{\circ}\text{C}$ ) [1,2].

We compare computed and observed [1,2] values for the square of the thickness of the  $MoSi_2$  layer as a function of time for the three temperatures in the left portion of Figure 1. Computed and experimental results are in excellent agreement with deviations being less than 10%. Mass concentrations of  $MoSi_2$ ,  $Mo_5Si_3$ , and Mo at a temperature of 1200  $^{\circ}\text{C}$  and  $t = 9.2 \text{ hr}$  are shown as a function of position in the right portion of Figure 1. The  $MoSi_2$  layer is progressing from right to left in Figure 2; thus, the right-most curve is the mass fraction of  $MoSi_2$ , the steeply-peaked center curve is the mass fraction of  $Mo_5Si_3$ , and the left-most curve is the unreacted Mo. The thin  $Mo_5Si_3$  layer moves with constant thickness as the reaction progresses, which agrees with observation [1].

Solutions shown in Figure 1 were obtained by hpr-refinement and in the left portion of Figure 2 we show the spatial mesh and method order used at 1200  $^{\circ}\text{C}$  and  $t = 9.2 \text{ hr}$ . A coarse mesh and first-order method are used away from the reaction zone while finer meshes and high-order methods are used near the reaction. The mesh used to solve this problem is shown as a function of time in the right portion of

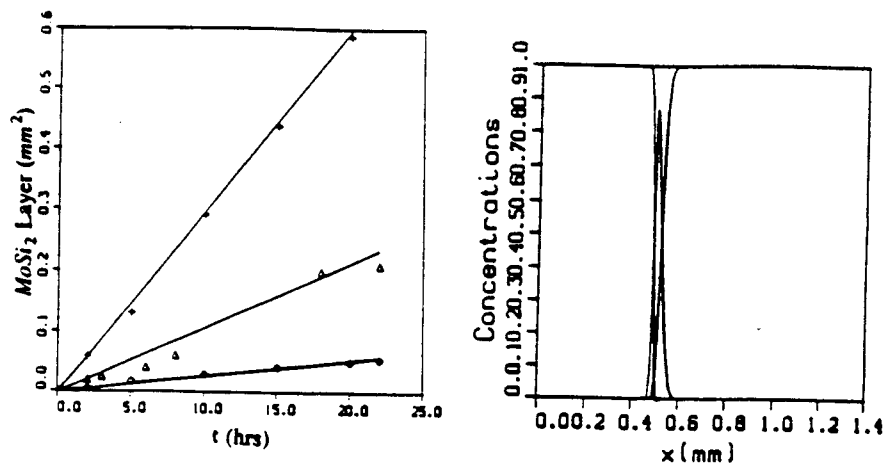


Figure 1. On the left, comparison of computed and observed values of the square of the thickness of the  $\text{MoSi}_2$  layer as a function of time for temperatures of 1100 °C (triangles), 1200 °C (plusses), and 1300 °C (diamonds). On the right, mass fractions of  $\text{MoSi}_2$ ,  $\text{Mo}_3\text{Si}_3$ , and  $\text{Mo}$  at 1200 °C and  $t = 9.2$  hr as a function of position.

Figure 3. The mesh is concentrated near the front and moving to account for the expansion as the reaction occurs.

Production times can be reduced by starting with a mixture of  $\text{Mo}$  and  $\text{MoSi}_2$  [2]. We compare computed and observed [2] values for the square of the thickness of the  $\text{MoSi}_2$  layer as a function of time in the left portion of Figure 3. Initial concentrations consisted of all  $\text{Mo}$ ; 50%  $\text{Mo}$  and 50%  $\text{MoSi}_2$ ; and 30%  $\text{Mo}$  and 70%  $\text{MoSi}_2$ . Corresponding diffusivities of  $\text{Si}$  in the mixture were  $D_1 = 1.5 \times 10^{-5}$ ,  $3.08 \times 10^{-5}$ , and  $3.08 \times 10^{-5}$  ( $\text{cm}^2/\text{sec}$ ). The reaction temperature was 1200 °C and all other parameters were as specified in the previous computation. Computationally, we assume that the initial  $\text{Mo}$ - $\text{MoSi}_2$  mixture quickly reacts to form  $\text{Mo}_3\text{Si}_3$  with an excess of either  $\text{Mo}$  or  $\text{MoSi}_2$  according to the phase equilibrium diagram. In particular, the 50%  $\text{Mo}$ - $\text{MoSi}_2$  mixture reacts to form all  $\text{Mo}_3\text{Si}_3$  at a 61% porosity and we use this as an initial state with the software. With 30%  $\text{Mo}$  and 70%  $\text{MoSi}_2$ , we begin with an initial state of 52%  $\text{Mo}_3\text{Si}_3$  and 48%  $\text{MoSi}_2$ .

On the right of Figure 3, we present the relative change in volume as a function of time with initial concentrations of all  $\text{Mo}$  at 45% porosity and 50%  $\text{Mo}$  and 50%  $\text{MoSi}_2$  at 45% porosity. In order to give some indication of the effects of porosity, we also present the volume expansion corresponding to an initial dense state of all  $\text{Mo}$ . Production times are fastest with an initial mixture of 30%  $\text{Mo}$  and 70%  $\text{MoSi}_2$  because of the need to diffuse less  $\text{Si}$  and the doubling of the diffusivity with the  $\text{Mo}$ - $\text{MoSi}_2$  mixture. This latter effect is not understood at this time. Volume expansion with the dense  $\text{Mo}$  initial state is excessive and can result in cracking. Starting

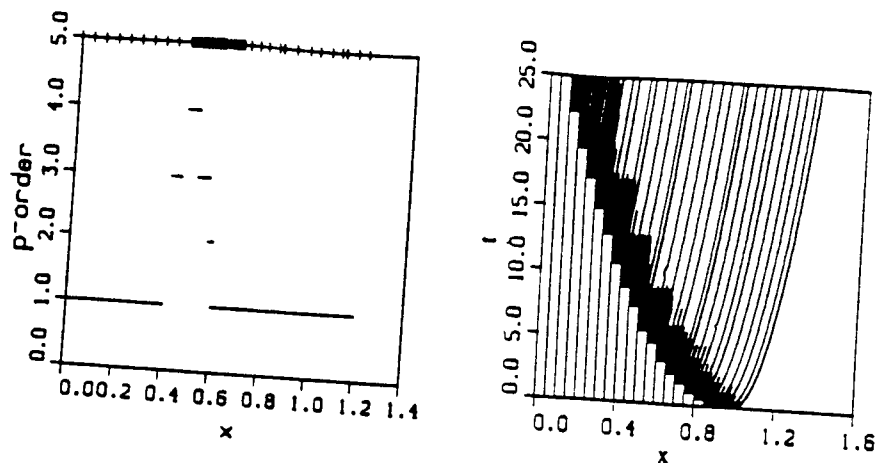


Figure 2. Method order and spatial mesh (left) and mesh position as a function of time (right).

with an initial  $Mo-MoSi_2$  mixture effectively eliminates expansion and will, hence, result in a more predictable matrix geometry.

To further illustrate the capabilities of our software, we solved (2.7,8,11-14) in two spatial dimensions for a pellet with  $a = 0.5 \text{ mm}$  and  $b = 0.125 \text{ mm}$  having an initial  $Mo$  concentration at 45% porosity. The remaining parameters were the same as in the one-dimensional examples with a temperature of  $1200^\circ\text{C}$ . For simplicity, the boundary condition (2.14a) was replaced by the Dirichlet condition  $pY_1 = 1.585\bar{p}$ . In Figure 4, we present the mass concentration of  $MoSi_2$  at 14.3 hours obtained using piecewise linear finite element approximations with adaptive h-refinement on a mesh of triangular elements. With symmetry, we have displayed the solution in a portion of a quadrant of the pellet's cross section. Shading in Figure 4 is proportional to the concentrations of  $MoSi_2$  with darker shading indicating higher concentrations. At the instant of time shown, the software has anticipated the inward propagation of the reaction zone and has concentrated the mesh towards the leading edge of the front.

#### 4. DISCUSSION

We have developed a reaction-diffusion system to analyze the RVI process of fabricating ceramic composites. When used with an adaptive finite element software system [3], the model predicted the growth of an  $MoSi_2$  layer in a siliciding application [1,2]. Production rates, volume expansion, and other effects may be studied as functions of, e.g., initial composition and porosity. The one- and two-dimensional adaptive software systems [3,4] have a symbolic interface that makes it easy to change models either to include more complex and realistic effects or to study other similar processes.

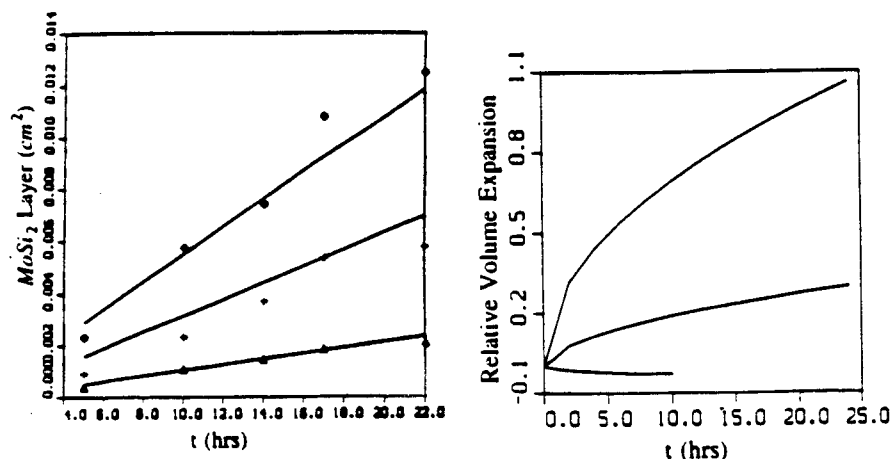


Figure 3. On the left, comparison of computed and observed values of the square of the thickness of the  $\text{MoSi}_2$  layer as a function of time for initial concentrations of all Mo (triangles); 50% Mo and 50%  $\text{MoSi}_2$  (plusses); and 30% Mo and 70%  $\text{MoSi}_2$  (diamonds) at 45% porosity. On the right, relative change in volume as a function of time for initial concentrations of all Mo with no porosity, all Mo at 45% porosity, and 50% Mo and 50%  $\text{MoSi}_2$  at 45% porosity (top to bottom).

As Mo grains react to form  $\text{MoSi}_2$ , they swell to close pores and voids between them and, eventually, exert forces on neighboring grains. The initial effect reduces or eliminates fluid infiltration into the pellet and establishes solid-state diffusion as the dominant transfer mechanism. The latter effect creates a stress field that may induce cracking [2] or residual stresses. Pores close quickly to choke fluid access with the present initial porosities; however, we intend to model this process at the granular level to better understand the effects of initial packing densities. Our software is capable of solving these fluid-solid interaction problems with varying geometries and, if not useful in our RVI application, it may be used to address other chemical vapor infiltration applications [5]. More realistic surface reaction models between solid and fluid phases will be introduced at this stage.

Even without gaseous infiltration, it is important to understand the closing of pores in the interior of the pellet to ensure that the matrix material has a homogeneous structure and chemistry. This can be studied at the macroscopic level using the model (2.7,8,11-14); however, a preliminary study at the granular level is necessary to, at least, identify an appropriate porosity function  $\mu(x,t)$  and other effective properties for granular materials. Combined mechanical and chemical processing models will be subsequently developed with a goal of predicting cracking and residual stresses.

Future experiments will be performed with fibers embedded in a powder preform and our models will be modified to reflect this. Our investigation will seek to reveal

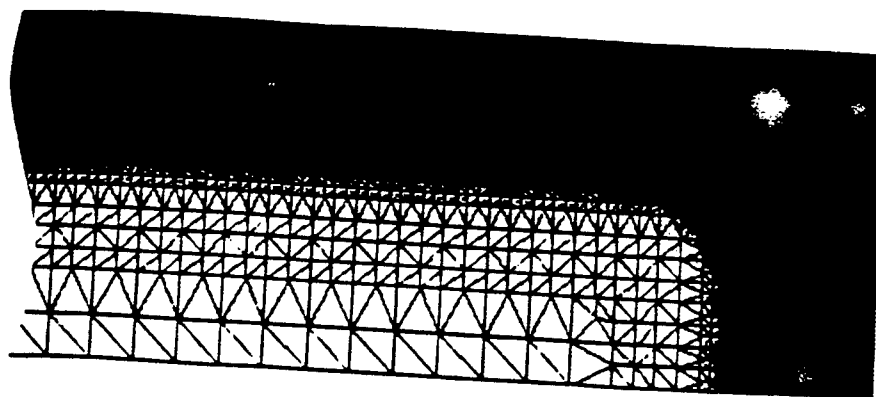


Figure 4. Mass fraction of  $MoSi_2$  in a portion of a quadrant of a two-dimensional cross section of the pellet. Darker colors indicate higher concentrations of  $MoSi_2$ .

optimal fiber placements, packing densities, and process strategies. By combining a computational and experimental program we are able to identify and verify prototypical optimal combinations much more rapidly than would be possible by using either paradigm alone.

#### ACKNOWLEDGMENT

The authors gratefully acknowledge support of this project from ARPA/ONR under grant N00014-92J-1779 "Mechanism-Based Design of Composite Structures," Steven Fishman and William Coblenz, Project Monitors.

#### References

1. N. Patibandla and W.B. Hillig, Processing of Molybdenum Di-silicide Using a New Reactive Vapor Infiltration Technique, *J. Am. Ceram. Soc.*, 76, pp. 1630-1634, 1993.
2. N. Patibandla, W.B. Hillig, and M.R. Ramakrishnan,  $SiC$  Fiber Reinforced  $MoSi_2$  Matrix Composites Produced Via Reactive Vapor Infiltration, preprint, Center for Composite Materials and Structures, Rensselaer Polytech. Inst., 1993.
3. S. Adjerid, J.E. Flaherty, P.K. Moore, and Y.J. Wang, High-Order Methods for Parabolic systems, *Physica D*, 60, pp. 94-111, 1992.
4. S. Adjerid and J.E. Flaherty, and Y. J. Wang, A Posteriori Error Estimation with Finite Element Methods of Lines For One-Dimensional Parabolic Systems, *Numer. Math.*, 65, pp. 1-21, 1993.
5. N.H. Thai and T.W. Chou, Modelling of an Improved Chemical Vapor Infiltration Process for Ceramic Composites Fabrication, *J. Am. Ceram. Soc.*, 73, pp. 1489-1498, 1990.

## MECHANISM-BASED DESIGN OF COMPOSITE STRUCTURES

Slimane Adjerid, Mark W. Beall, George J. Dvorak, Jacob

Fish, Joseph E. Flaherty, John Hudson, Kam L. Shek,

Mark S. Shephard, Rolf Wentorf

Rensselaer Polytechnic Institute  
Troy, N. Y. 12180-3590

### ABSTRACT

The paper introduces high temperature composite software developed for mechanism-based design of composite structures. Mechanism-based design is characterized by an understanding of the critical composite behaviors at several physical scales: the fibrous (micro) scale, the ply/weave (meso) scale and the laminated part (macro) scale, and by the specification of the available design parameters to achieve functionality by those behaviors. A software framework is described which integrates material modeling and analysis codes, provides automated assistance, and links to material databases. Elastic and inelastic material modeling codes suitable for high temperature composites with complex reinforcement and weave/lay-up configurations are presented and references to their underlying theories are given. Advanced analysis techniques are outlined for numerically efficient computational plasticity based on mathematical homogenization, idealization error indicators for material scale, three dimensional crack propagation in a fibrous composite, and modeling of reactive vapor infiltration and chemical vapor deposition processes.

### INTRODUCTION

Current research has been directed towards developing models of high temperature composite thermomechanical behaviors and the processes associated with their fabrication and degradation. The composite systems of interest include both metal matrix composites (MMC's) and ceramic matrix composites (CMC's), with  $\text{Al}_2\text{O}_3$ , SiC and W based reinforcements, and  $\text{Al}_2\text{O}_3$ ,  $\text{MoSi}_2$ , NiAl, SiC, and Ti based matrices. The approach used has been motivated by current fabrication technology, which allows the material's structure to be configured for an application, and by the complexity of phenomena governing the material's behavior during fabrication and during subsequent loading cycles.

The mechanism-based approach involves modeling composite behaviors at several physical scales: e.g. the fibrous (micro), the ply/weave (meso) and the laminated part (macro) scales, and by linking the behaviors at each scale. The techniques developed can be applied to design analysis by the formulation of the appropriate idealized models at the relevant scales and the integration of those models while controlling idealization errors through multi-scale, adaptive or heuristic means. An important result of the project has been the implementation of mechanism based modeling techniques as computer codes.



The new capability can support the understanding of the relationships between a material system's meso/micro structural design parameters and its large scale functionality. For example, design changes in the reinforcement's shape and orientation can be related to the overall composite properties and hence to a part's deflection under load. In the reverse change-of-scale, a macro scale cooling hole configuration under a particular thermal-mechanical loading can be linked to the type and proximity to fiber-coating-matrix debonding. Mechanism-based models allow both alternative material and component designs to be evaluated more quickly without the expense of testing all macro scale configuration/environment permutations, and can even aid the design and sizing of test fixtures for those tests which are still needed.

The rest of the paper outlines the supporting software system, the material modeling and some of the analysis techniques required to support the design of high temperature composites structures. The system overview describes the capabilities developed, the assistance provided application of the codes by non-experts, and the material property management issues. The material modeling section briefly describes the capabilities and models developed. The analysis section describes results for computational plasticity, error control for laminates, advanced multi-scale analysis techniques needed for the coupled behaviors exhibited by HTC structures, and process modeling.

## **SYSTEM OVERVIEW**

A set of software framework tools has been developed (Beall et al., 1994) to integrate and facilitate application of the material modeling and analysis codes to design problems. The framework accommodates a spectrum of solution cost and reliability alternatives, in order to support the different design process stages, and provides application expertise and visualization tools. The system applies existing commercial packages where possible. The framework tools integrate the material modeling and analysis techniques. Both of these codes groups can still be operated separately or combined and linked with other user codes.

The software interacts with a database housed in the Mvision™\* format and conforms to, or can be translated into ASTM and applicable PDES/STEP standards (PDA, 1993). The high temperature database contains more than 320 material systems or constituents, 18,000 values, and 180 material characteristics. Geometric modeling tools, built on the kernel of commercial geometric modelers, create micro-structures, weaves, plies and component scale models and source their data from a spreadsheet. The spreadsheet format allows users to arrange and annotate data to suit their needs, tie together design parameters for automatic updates, and to implement "back of the envelop" computations.

An analysis attribute code links material, boundary condition and other attributes with the corresponding geometric entities, for instance, associating a debond strength with a fiber/coating interface and a chemical concentration distribution with a matrix region of a model. In addition, finite element results on a mesh are mappable to the mesh of another analysis by means of their common geometric entity. Representative volumes containing the most important geometric entities are readily constructed from a library of constituents, typical flaws, etc., and these entities can be related to behavioral properties via associated attributes. Automatic meshing tools, generic mesh operations and data structures, and the interfaces to multiple finite element analysis codes complete the integration of automated modeling tools for FEA (Beall et al., 1993).

### **User application and assistance**

Expertise in several areas, including material and process modeling, analysis techniques and detailed software operation need to be applied simultaneously for reliable HTC analysis. High temperature composite material technology is evolving rapidly, requiring flexible application of mechanism based design tools rather than execution of prescriptive or handbook design procedures. This means that the software must support a process of i) definition of the required functionality, e.g. control heat flow in a given direction, resist a set of loading conditions within prescribed deflections, self-heal when damaged, etc. ii) development of the material behaviors and geometric features to support those functions, and iii) specification of the type of analysis results, cost (time) and reliability needed to confirm the governing behaviors or define unknown design parameters. The resulting description of the design and the analysis characteristics constitutes an "analysis goal", and is the starting point for automatically selecting and assembling material modeling and analysis codes to achieve it. The goal description is converted into

---

\* M/VISION is a registered trademark of MSC/PDA Engineering.

a plan, represented in part by a data flow model, and the plan is refined into a sequence of code executions. The result is a "strategy", the execution of which provides the desired results to the user.

The approach requires translation of concepts and nomenclature for the user and the management of information on code capabilities and operation. Code capabilities may be controlled by the underlying theory or the current implementation of the theory and are modeled in terms of their required/optional inputs and outputs, restrictions on values, cost, reliability, and a classification of the behavioral assumptions used. These code attributes determine its "applicability" for strategy creation and require hierarchical and relational data structures. The information can be used to translate between the concepts and nomenclature of the mechanism based designer and the appropriate composite theory, and to automatically assemble strategies based on compatible data flow and underlying modeling assumptions. The implementation of the approach requires the framework tools described earlier to facilitate material modeling and analysis, and a standardized exchange of data between codes developed from multiple sources.

A data flow schematic of a basic composite property strategy is diagramed in Figure 1. The arcs indicate the type of information shared by the boxed computational functions. The goal is to estimate linear elastic laminate properties in seconds from given constituent properties, micro-structural and ply lay-up. The method used can depend on the shape of the reinforcement, and this aspect of the applicability would need to be refined based on the user input before any code would be executed.

From the user's perspective, the execution of the analysis goal is no more involved than using any other spreadsheet function, requiring no expertise or involvement in software development. The current design parameters are recovered from the spreadsheet, and transferred to the goal processor. If data is missing or out of the applicability range of available strategies, then the user is informed of the specific problem, otherwise the results are automatically computed and returned to the spreadsheet, used as input for other analysis (as shown), or displayed by visualization code, e.g. such as the plots of Figure 2 and 3.

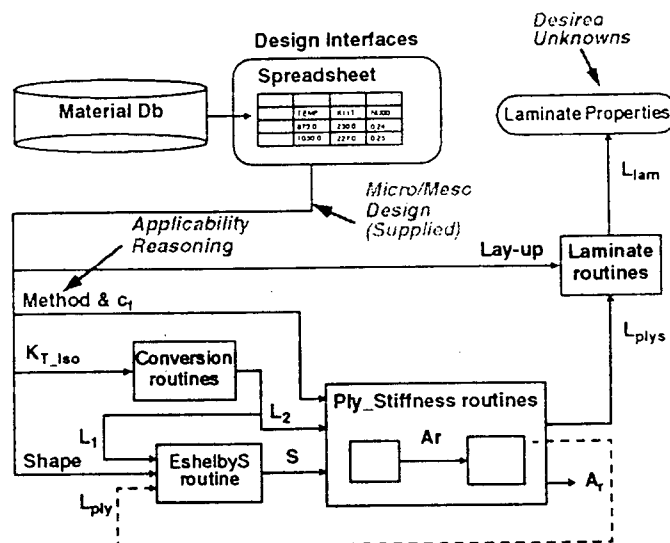


Figure 1: Data Flow for Laminate Properties

### Material Property Management

Several database related features are available which either directly support the conceptual design process in material selection, or support analysis strategies. Material data requires the structuring of data so as to define not only the value to be used in an analysis, but also the scale, specimen characteristics, source of data and the environmental parameters of the test - the "pedigree". Reliable analysis requires that the pedigree be consistent with the underlying analysis models, so the extraction of relevant data is related to the creation of strategies from modeling codes. For example, the modulus of a SiC/SiC CMC will not only vary with temperature, but also with time depending on the degree of micro mechanical damage before the measurement and the presence of water and oxygen. The material database is not only a source of material parameters, but also a source of known behaviors caused by the environment. Translation between the standard procedures and nomenclature of the testing community and the material parameter needs of analysis and design functions is also required in order to obtain meaningful data.

Sources include published papers, industry data sheets, handbooks, and test data generated at Rensselaer. Constituent properties (matrix and reinforcements), data for dog-bone and tubular test specimens, and durability of tested parts in oxidizing and corrosive environments are stored. Manufacturing size, porosity or volume fraction limitation data are available where supplied by vendors, and background documentation and SEM images of material systems are also accessible. The database facilities can be configured for automated search and merit indicity plotting (Ashby, 1992).

## MATERIAL MODELING

Software tools described here include linear elastic property estimation codes, initial failure maps of the constituents and their interfaces, and mathematical homogenization of unit cells with complex geometries. Their capabilities are presented and some example results are shown.

### Linear Elastic Properties and Limits

Routines are available to predict overall material properties for linear elastic analysis in terms of constituent thermo-elastic properties, volume fractions, and micro-structural geometry. Those related to ply properties are the Hashin-Strikman Bounds (Hashin and Rosen, 1964) for the overall elastic moduli of two-phase composites, the Mori-Tanaka (Mori and Tanaka, 1973) and the self-consistent methods (Teply and Dvorak, 1988), providing estimates for several reinforcement shapes in either aligned or random configurations. Figure 2 compares the methods for the overall transverse modulus of a fibrous ply as a function of volume fraction and Figure 3 visualizes trends in overall elastic axial shear properties as a function of volume fraction and temperature. Additional codes evaluate linear coefficients of thermal expansion (CTE) of two-phase or multi-phase composite materials in terms of overall and phase elastic moduli, phase CTE's and volume fractions.

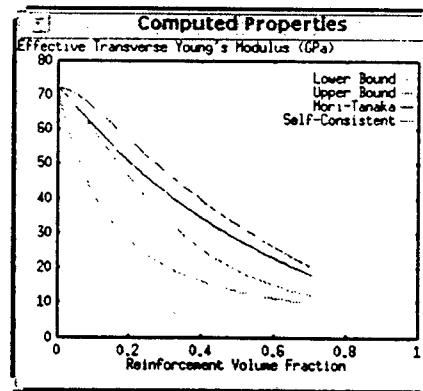


Figure 2: Method Comparison

Other codes evaluate mechanical, thermal, and transformation concentration factors, which are useful for estimating phase stress and/or strain averages in two-phase and multi-phase composites subjected to uniform overall stress or strain, a uniform change in temperature, and uniform eigenstrains in the phases (Dvorak and Benveniste, 1992). If properties for a constituent are not available from tests, they can be computed "in-situ" by the Mori-Tanaka or self-consistent methods from known overall moduli, phase volume fraction, and the known properties of the other constituent. Figure 4 shows the results of a strategy to study the effects of variations in reinforcement aspect ratio and volume fraction on the effective axial shear modulus of a single ply. The designer can easily see the effects of changes in both application temperature and volume fraction.

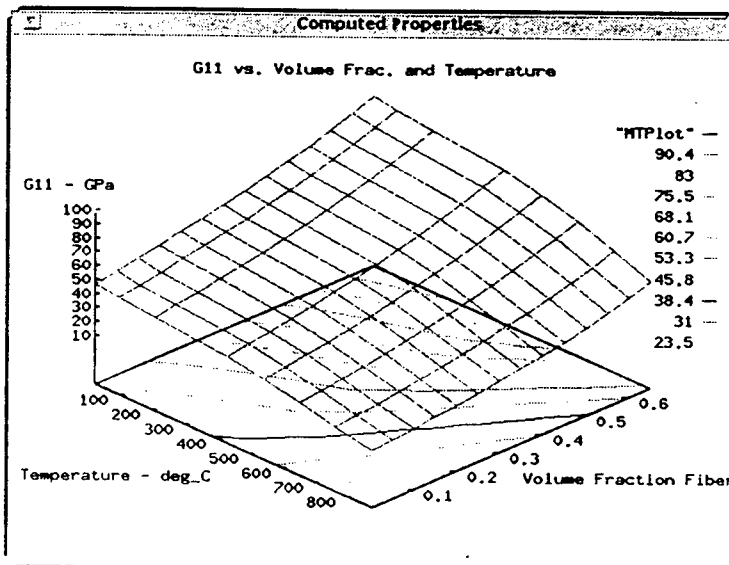


Figure 3: Ply Property Trends

At the next larger scale, the plane stress stiffness, the compliance of asymmetric laminated plates under uniform in-plane loads, and the transversely isotropic coefficients of thermal expansion of a symmetric laminated plate under a uniform temperature can be estimated. Codes evaluate the mechanical, thermal, and transformation distribution factors, leading to average stresses in plies of a symmetric laminated plate under uniform in-plane loads, temperature change, and ply eigenstrains. Other supporting routines evaluate the Eshelby tensor for transformed homogeneous inclusions of an ellipsoidal shape in an anisotropic solid, compute the P-tensor for an ellipsoidal inclusion in an anisotropic solid, perform numerical operations with tensors or mathematical expressions, and convert between elastic constants, stiffness and compliance matrix forms.

Initial brittle and plastic material failure of fibrous composites due to thermal-mechanical loading can also be predicted by the software. Debonding at the interfaces between the fiber, coating and matrix, and fracture of the fiber, coating or matrix materials are predicted for symmetric laminated plate configurations. The software implements the theory found in (Dvorak, 1992), (Dvorak and Benveniste, 1992), (Dvorak et al., 1992), by mapping

macro scale FEA temperatures and stress distributions onto the micro-mechanical failure map model. The model accounts for residual stress effects due to a difference between a stress free state, e.g. the processing temperature, and operating temperature. The model uses the linear elastic constituent properties, composite configuration and known allowable stresses in or between phases: fibers, coatings, or matrix.

Figure 5 (left) shows the application of the failure surface codes to the inside "hot" layer of a thermally loaded ceramic combustor geometry with cooling and other hardware holes. Elements are shaded based on their proximity to the given debond strength limit, indicating potential problem areas on the part. Similar distributions are available for other material failure modes. An animated stepping "through the thickness" helps visualize interior-exterior trends. Figure 5 (right) applies the model in an alternative format, plotting the required matrix cracking strength for each element in the combustor above as a function of temperature. Other codes are available to predict the onset of material plasticity (Dvorak and Bahei-El-Din, 1987).

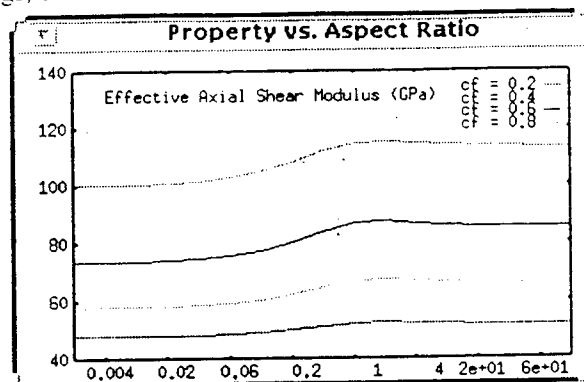
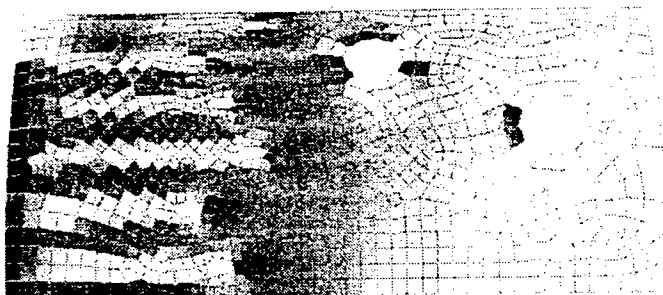


Figure 4: Aspect Ratio Variations

100 Proximity to Onset of Micro Structural Damage  
60 (% allowable stress)  
0



Fiber-matrix debonding - Level 1

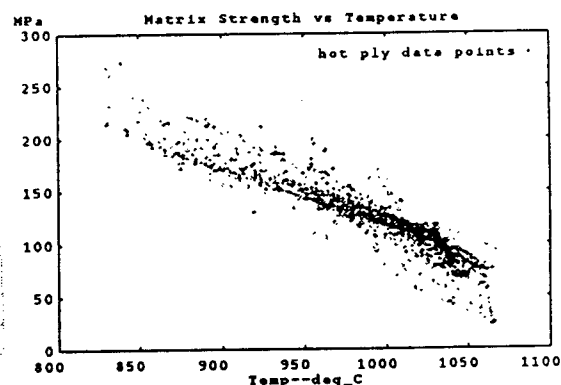


Figure 5: Failure Map Applications

### Unit Cells

The classical mathematical homogenization theory for heterogeneous medium has been generalized (Fish et al., 1996a) to account for eigenstrains. The resulting method first defines a three dimensional geometric model of a unit cell, assigns constituent material properties, automatically meshes the geometry, and then analyzes the model for homogenized properties. The software framework provides facilities to automatically create the unit cell geometric models from size parameters of the constituent features. Though it is computationally more expensive than other methods, it is useful for geometrically complex microstructures where a representative geometry can be defined. Unit cell modeling has been used in the multi-scale computational technique and for non-linear analysis with a plasticity model (Shephard et al., 1995). Given an appropriate representative geometry, it can also predict linear elastic properties for woven composites for use directly with conventional macro-scale analysis tools and can be readily adapted for thermal conductivity and chemical diffusion problems. Unit cells for oriented fibers, periodic "random" fibers, periodic "random" particles, and plain weave fabrics are available, see Figure 6 below. Unit cells for other woven fabrics, defects and more complex three dimensional fiber architectures are under development.

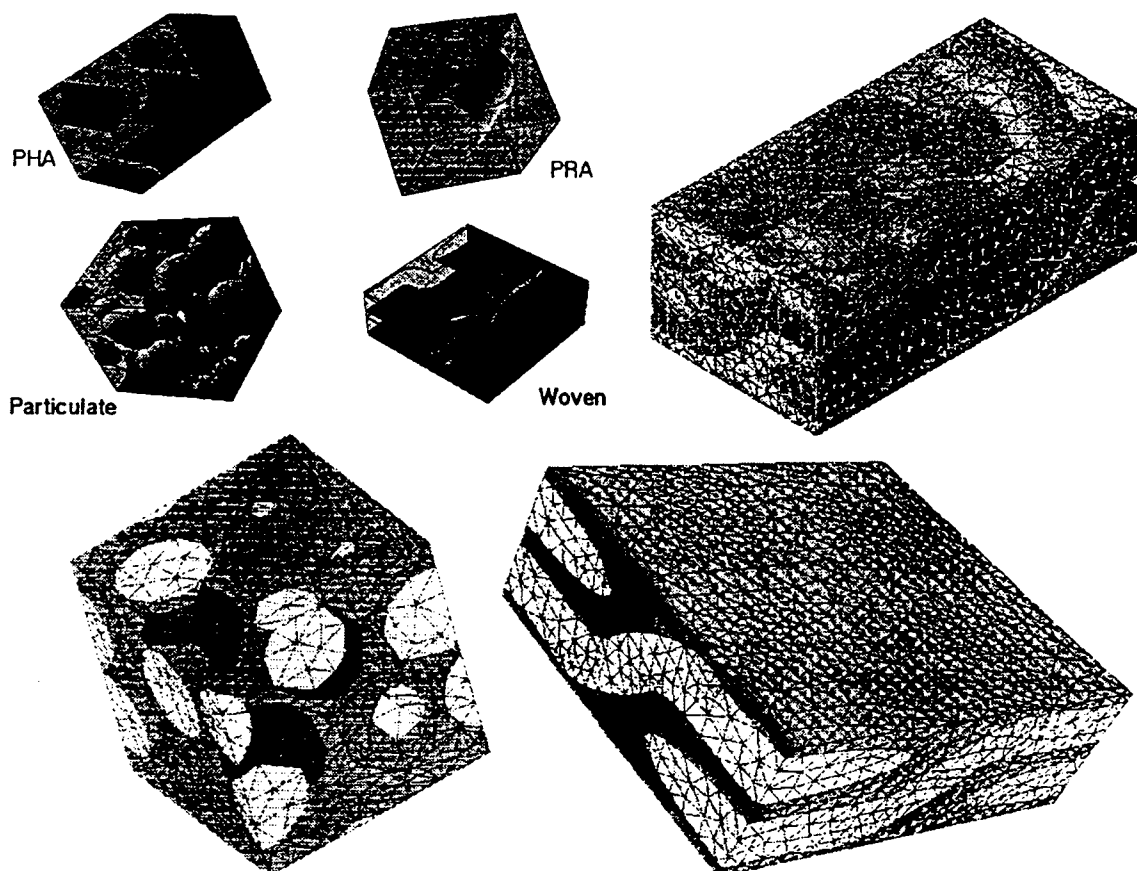


Figure 6: Unit Cell Geometry and Mesh Examples

## ANALYSIS OF COMPOSITE STRUCTURES

### Computational Plasticity for Composite Structures Based on Mathematical Homogenization

The computational challenge of solving nonlinear heterogeneous systems is enormous. While for linear problems a unit cell or a representative volume problem has to be solved only once, for nonlinear history dependent systems it has to be solved at every increment and for each integration point. Moreover, history data has to be updated at a number of integration points equal to the product of integration points at all modeling scales considered. To illustrate the computational complexity involved we

consider elasto-plastic analysis of the two-scale composite flap problem shown in Figure 7. The macrostructure is discretized with 788 tetrahedral elements (993 unknowns), whereas the microstructure is discretized with 98 elements for the fibers and 253 elements for the matrix. The CPU time on a SPARC 10/51™ for this problem was 8 hours, as opposed to 10 seconds if metal plasticity was used instead, which means that 99.7% of CPU time is spent on constitutive evaluation in the unit cells.

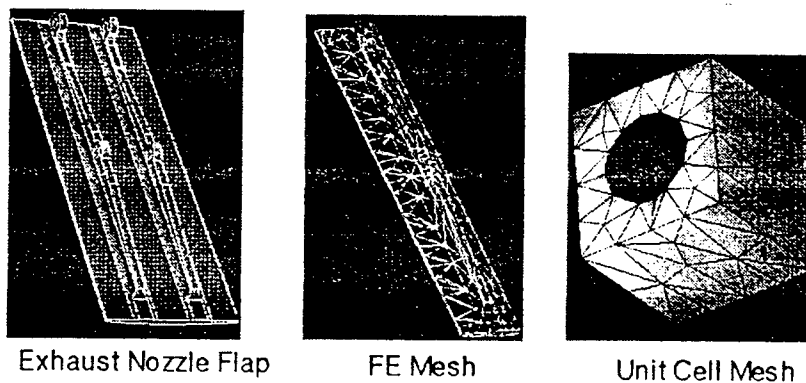


Figure 7: Engine Flap Example

The application of a novel modeling scheme based on mathematical homogenization theory with eigenstrains (Fish et al., 1996a) and transformation field analysis (Dvorak, 1992) enables the solution of these large scale structural systems in heterogeneous media at a cost comparable to problems in homogeneous media without significantly compromising on solution accuracy. The approach represents a breakthrough compared to existing modeling schemes which are either too inaccurate to provide reliable solutions for difficult problems, or too expensive due to the computational complexity involved.

The heart of this new technique is the generalization of the classical mathematical homogenization theory for heterogeneous medium to account for eigenstrains (Fish et al., 1996a). Starting from the double scale asymptotic expansion for displacements and eigenstrains we derive a close form expression relating arbitrary eigenstrains to the mechanical fields in the phases. Subsequently, the overall structural response is computed using an averaging scheme by which phase concentration factors are computed in the average sense for each phase, i.e. history data is updated only at two/three points (fiber and matrix/ interphase) in the microstructure, one for each phase. Macroscopic history data is stored in the data base and then subjected in the post-processing stage onto the unit cell in the critical location identified by microscale reduction error indicators.

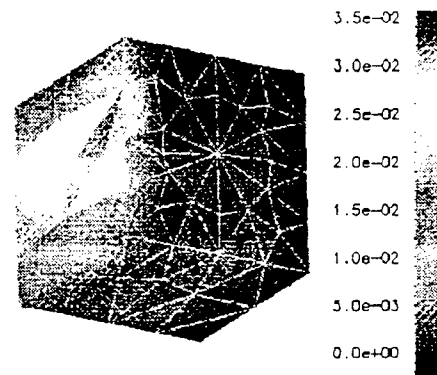


Figure 8: Unit Cell Relative Error

For the flap problem considered in Figure 7 the CPU time for the averaging scheme with variational micro-history recovery is only 30 seconds on SPARC 10/51™ as opposed to 8 hours using classical mathematical homogenization theory. Figure 8 shows that the maximum error in the micro-stress in the unit cell located in the critical region is only 3% in comparison to the classic homogenization theory.

### **Idealization Error Estimators**

Idealization error estimators for laminated composite shell structures developed in Fish et al. (1994a), Fish et al., (1994b) are aimed to quantify three sources of errors and to address the following issues:

i. What are the regions within the problem domain where the macromechanical description (shell model), which is the most inexpensive modeling capability, is insufficient, i.e., where the shell model introduces unacceptable errors with respect to a more comprehensive ply-by-ply (mesomechanical) model. Idealization error estimators should be able to identify not only the precise location within the plane of the shell, but also the layers within the laminate where the use of mesomechanical description may result in unacceptable errors of interlaminar stresses.

The Dimensional Reduction Error estimator (DRE) developed in Fish et al. (1994a) builds on a combination of mechanistic insight and a rigorous mathematical approach. By this technique the dimensional reduction error is approximated by a linear combination of some basis functions in the auxiliary mesomechanical finite element mesh that accurately represent the kinematics of individual plies (Fish et al., 1994a).

ii. Enriching the fundamental kinematics of the equivalent single-layer (macro) model with a discrete-layer (meso) model in the vicinity of the most critical layers enables to model various failure modes on the lamina level such as delamination. Unfortunately, in many cases the mechanism that causes failure is at a smaller scale - the scale of microconstituents. A common computational rationale today is to investigate various microprocesses that may lead to a progressive failure by considering a unit cell or a representative volume problem. The mechanisms that allow us to do so are the classical assumptions of periodicity and uniformity of macroscopic fields. However, in the areas of high stress concentration, which are of critical interest to the analyst, periodicity assumptions are not valid, and thus the application of conventional homogenization techniques in the "hot spots" may lead to poor predictions of local fields.

The adequacy (or lack of it) of the homogenization theory has been studied in Fish et al. (1994b) on the basis of assessing the uniform validity of the double scale asymptotic expansion, which serves as a basis of mathematical homogenization theory. The quality of the homogenization has been assessed on the basis of the relative magnitude of the first term neglected by the classic homogenization theory to those taken into account.

A closed form expression for an idealization error estimator associated with the microscale reduction has been derived in Fish et al. (1994b). The Microscale Reduction Error (MRE) estimator relates the homogenization (or scale reduction) error to macroscopic fields (strain and strain gradients) and to the details of microstructure (compliances of phases, volume fraction and the size of the unit cell). It has been found that there are four factors affecting the homogenization error: (i) the size of the unit cell in the physical domain  $Y$ , (ii) the mismatch parameter, (iii) the volume fraction, (iv) the strain gradients on the macro-scale.

Besides the discretization error indicators there are other sources of idealization errors, such as microstructure randomness, material and geometric nonlinearities, which so far have not been considered.

### **Fast adaptive Iterative Solvers for a Heterogeneous Medium**

The multigrid technology with special inter-scale connection operators has been developed in Fish and Belsky (1995a), Fish and Belsky (1995b), Fish et al. (1996a). The multigrid procedure starts by performing several smoothing iterations on the micro-scale in the regions identified by MRE indicators. Consequently, the higher frequency modes of error are damped out immediately. The remaining part of the solution error is smooth, and hence, can be effectively eliminated on the auxiliary coarse mesh. It has been shown (Fish and Belsky, 1995a), (Fish and Belsky, 1995b), (Fish et al., 1996a) that the finite element mesh on the meso-scale (ply level) serves as a perfect mechanism for capturing the lower frequency response on the micro-scale. Therefore, the residual in the finite element mesh on the micro-scale is restricted to the meso-scale, while the smooth part of the solution is captured in the finite element mesh on the meso-scale. The oscillatory part of the solution on the meso-scale is again damped out by a smoothing procedure. The lower frequency response on the meso-scale is resolved on the macro-mesh (shell level). The resulting solution on the meso-scale is obtained by prolongating displacements from the macro-mesh back to the finite element mesh on the meso-scale and by adding the oscillatory part of the solution previously captured on the meso-scale. Likewise, the solution on the micro-scale is obtained by prolongating the smooth part of the solution from the meso-scale and by adding the oscillatory part that has been obtained by smoothing. This process is repeated until satisfactory accuracy is obtained.

The adaptive strategy, illustrated by example in Figure 9, starts by employing Discretization Error indicators and adaptively refining the finite element mesh on the macromechanical (shell) level to ensure accurate Macro-solutions. Subsequently, Dimensional Reduction Error (Fish et al., 1994a) indicators identify the areas where the most critical interlaminar behavior takes place, and consequently, a more sophisticated discrete layer model is placed there. Fast iterative solvers based on the multigrid technology with special inter-scale connection operators (Fish and Belsky, 1995a), (Fish and Belsky, 1995b), (Fish et al., 1996a) are used to solve a coupled two-scale Macro-Meso model.

Once the phenomena of interest on the Macro-Meso levels have been accurately resolved, Microscale Reduction Error (Fish et al., 1994b) indicators are used to identify the location of critical microprocesses and consequently, a

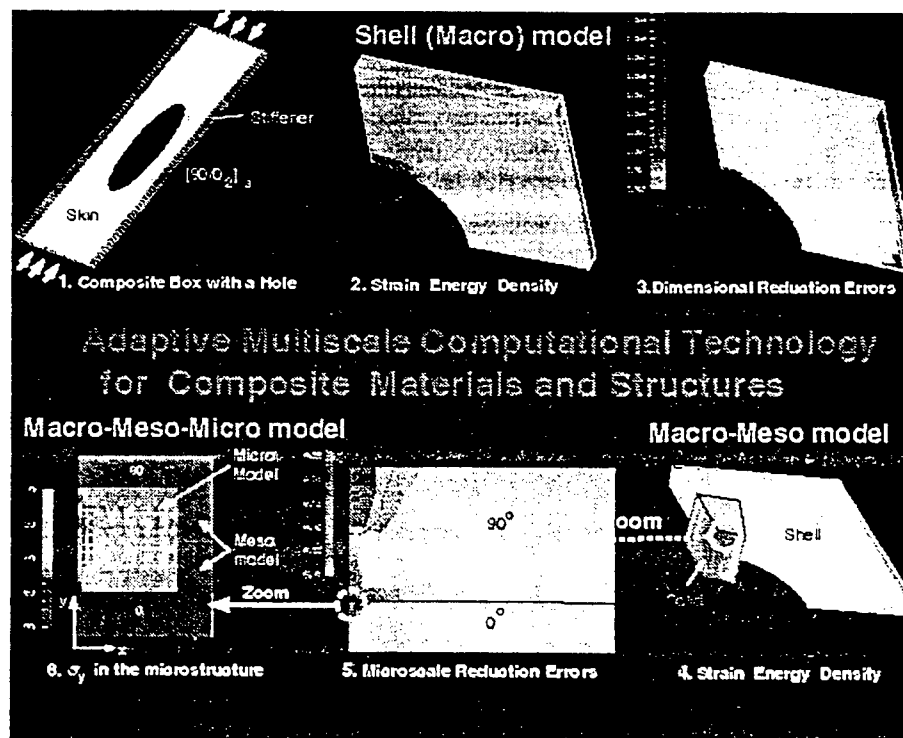


Figure 9: Multi-scale Example

micro-mesh is placed there. The three-scale coupled Macro-Meso-Micro model is again solved using a three-scale multigrid process (Fish and Belsky, 1995a), (Fish and Belsky, 1995b), (Fish et al., 1996a). Finally, Discretization Error indicators and adaptive refinement strategy are employed simultaneously at three different scales to ensure reliable multiscale simulations.

The three-scale model described in Figure 9 contains over 1,000,000 degrees-of-freedom. The estimated CPU time for solving it with conventional solvers based on skyline storage is over 700 hours on a single processor SPARCstation 10/51™, which essentially makes the model unusable from the practical point of view. Using a special purpose multigrid technology for heterogeneous media developed in (Fish and Belsky, 1995a), (Fish and Belsky, 1995b), (Fish et al., 1996a) the same problem has been solved in less than 16 hours on a single processor SPARCstation 10/51™, turning it into an overnight job

The derivation of the inter-scale transfer operators is based on the asymptotic solution expansion. The asymptotic forms of the prolongation and restriction operators were obtained by discretizing the corresponding asymptotic expansions. For unit cells of finite size the regularization functions were introduced (Fish and Belsky, 1995b) in order to obtain well-posed inter-scale transfer operators, termed homogenization based operators.

The rate of convergence of the multigrid process has been studied in Fish and Belsky (1995a). It has been proved that if the stiffness of a fiber is significantly higher than that of a matrix, then the multigrid method converges in a single iteration. This behavior of the multigrid method for heterogeneous media together with its linear dependence on the number of degrees-of-freedom, makes it possible to solve large scale coupled global-local problems with the same amount of computational effort, or faster, than would be required to solve the corresponding uncoupled problem using direct solvers.

### **Crack Growth Simulation**

In Beall et al. (1996) the crack growth analysis methodology that accounts for the dominant influence factors affecting crack growth on the micromechanical level has been investigated. An automated system has been developed that explicitly represents the microstructure of the composite at the crack front while using homogenized material properties elsewhere. Procedures for automatic construction and update of the models and meshes used in the analysis have been developed in order to avoid any time consuming human intervention. Figure 10 shows the

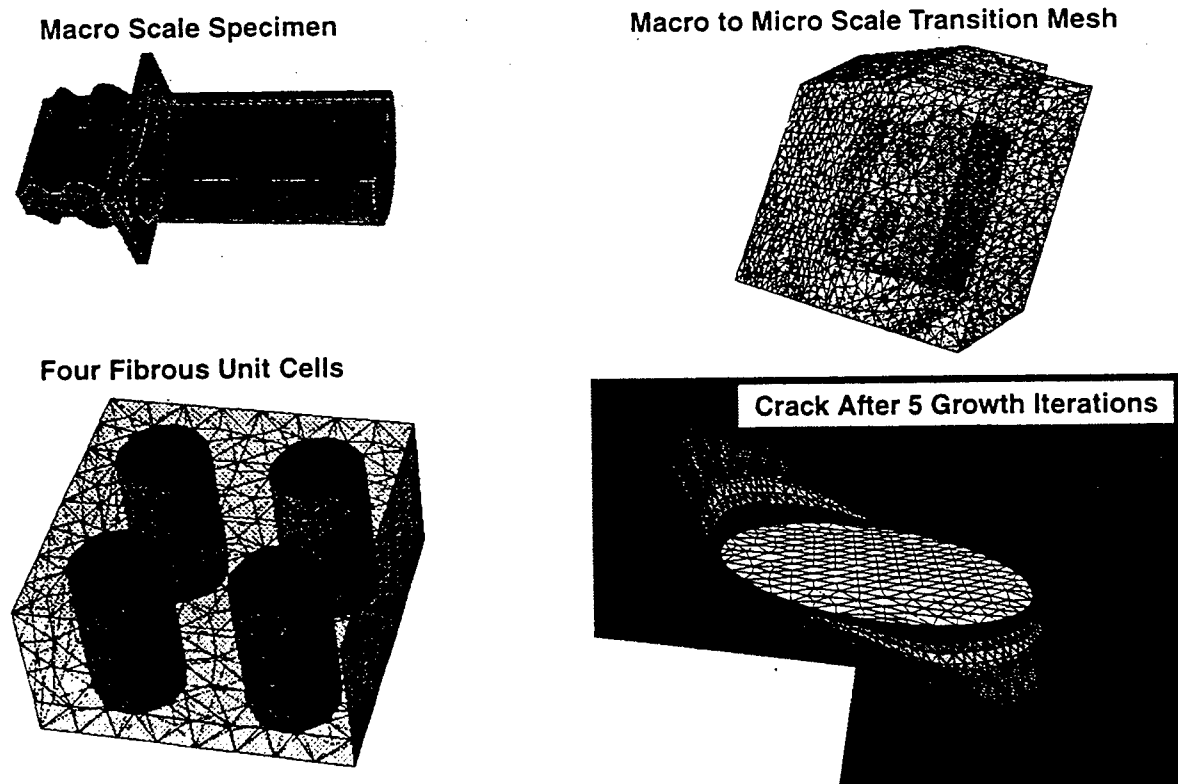


**Figure 10: Crack Propagation Models**



evolution of the micro-crack growth in the turbine blade. It has been found (Beall et al. 1996) that there is a significant difference in the crack growth pattern when accounting for the microstructure. Crack propagation criteria in the microstructure is based on the energy release rates, fracture toughnesses of the microconstituents and their interface (He and Hutchinson, 1989)

### Process Modeling

The process modeling codes simulate the time varying production, or degradation, of composite materials. The models include the reaction and transport of chemical species and material flows. Altering process parameters can improve production rates and/or minimize defects. Product designers can estimate processing residual stresses or simulate oxidation/hot corrosion for life prediction. Codes have been applied to the reactive vapor infiltration process for forming  $\text{MoSi}_2$  from Mo powder, CVD fiber coating with  $\beta\text{Al}_2\text{O}_3$ , and for oxidation simulations of SiC composites (Adjerid et al., 1995), (Adjerid et al. 1996). Inputs for the general code are the initial geometry and mesh, process attributes per phase, and boundary condition distributions as a function of time. Models input to the code are categorized as chemical reaction models, expansion, mechanical models for solid phases, diffusion models of gaseous phases, and surface models for phase interfaces. Error control parameters are given for the adaptive refinement techniques. Outputs are the time varying volume change, shape, velocity, temperature, concentration and pressure fields.

Figure 11 shows one frame of a result for the  $\beta\text{Al}_2\text{O}_3$  coating simulation. The image is a cross section of a tubular reaction chamber, through the center of which moves the fiber to be coated (left). Reactants, concentrations of which can be shown in color, are injected at the bottom of this design, and the flow field of the gaseous phase is indicated by the vectors. The code is currently used to both optimize and control the actual production hardware. Results can be animated to show the dynamic behaviors resulting from the initial design geometry and boundary conditions.

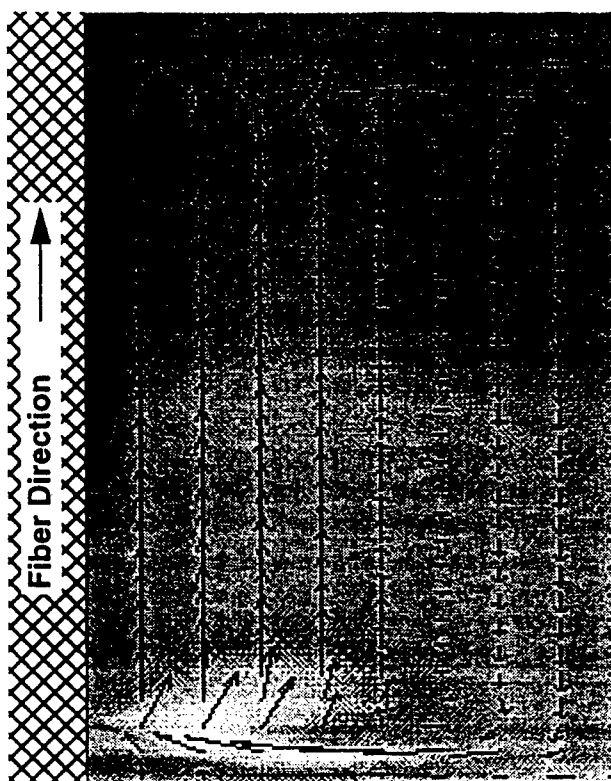


Figure 11: Fiber Coating Simulation

### CONCLUSION

Success with high temperature composites has required progressively more complex micro-structures and behavioral understanding. Design requires support by mechanism based analytical tools to take full advantage of HTC properties and to avoid material failures. The models and tools developed, integrated with their supporting framework, are capable of simulating key composite behaviors and processes at multiple scales

### ACKNOWLEDGMENT

The support of ARPA/ONR under grant number N00014-92J-1779 and NSF award ECS-9257203 are gratefully acknowledged.

### REFERENCES

Adjerid, S., Flaherty, J. E., Hillig, W., Hudson, J., and Shephard, M. S., 1995, "Modeling and the Adaptive Solution of Reactive Vapor Infiltration Problems", Modeling and Simulation in Materials Science Engineering, Vol. 3, pp. 737-752.

- Adjerid, S., Flaherty, J. E., Hudson, J. B., and Shephard, M. S., 1996, "Adaptive Solution For Fiber Coating Process", to be published in *Modeling and Simulation in Materials Science Engineering*.
- Ashby, M. F., 1992, "Materials Selection in Mechanical Design", Pergamon Press, Oxford, New York.
- Beall, M. W., Fish, J., Shephard, M. S., Dvorak, G. J., Shek, K.-L., Wentorf, R., 1994, "Computer-Aided Modeling Tools for Composite Materials", Ceramic Engineering and Science Proceedings of the American Ceramic Society's 18th Annual Meeting and Exposition, Cocoa Beach, FL, January 9-12.
- Beall, M. W., and Shephard, M. S., 1996, "Mesh Data Structures for Advanced Finite Element Applications", submitted to the *International Journal of Numerical Methods in Engineering*.
- Beall, M. W., Belsky, V., Fish, J. and Shephard, M. S., 1996, "Automated Multiple Scale Fracture Analysis", SCOREC Report, 4-1996, Rensselaer Polytechnic Institute, Troy, NY.
- Dvorak, G. J., and Bahei-El-Din, Y. A., 1987, "A Bimodal Plasticity Theory of Fibrous Composite Materials", *ACTA Mechanica*, 69, pp. 219-241.
- Dvorak, G. J., 1992, "Transformation Field Analysis of Inelastic Composite Materials", *Proc. R. Soc. Lond. A*, 437, pp 311-327.
- Dvorak, G. J., and Benveniste, Y., 1992, "On Transformation Strains and Uniform Fields in Multiphase Elastic Media", G. J. Dvorak and Y. Benveniste, *Proc. R. Soc. Lond., A* 437, pp. 291.
- Dvorak, G. J., Chen, T. and Teply, J., 1992, "Thermomechanical Stress Fields in High-temperature Fibrous Composites. I: Unidirectional Laminates", *Composites Science and Technology*, Vol. 43, pp. 347-358.
- Fish, J., Markolefas, S., Guttal, R. and Nayak, P., 1994a, "On Adaptive Multilevel Superposition of Finite Element Meshes," *Applied Numerical Mathematics*, Vol 14.
- Fish, J., Nayak, P., and Holmes, M. H., 1994b, "Microscale Reduction Error Indicators and Estimators for a Periodic Heterogeneous Medium," *Computational Mechanics: The International Journal*, Vol. 14, pp. 323-338.
- Fish, J., and Belsky, V., 1995a, "Multigrid Method for a Periodic Heterogeneous Medium. Part I: Convergence Studies for One-dimensional Case", *Comp. Meth. Appl. Mech. Engng.*, Vol. 126, pp. 1-16.
- Fish, J. and Belsky, V., 1995b, "Multigrid method for a Periodic Heterogeneous Medium. Part 2: Multiscale Modeling and Quality Control in Multidimensional Case", *Comp. Meth. Appl. Mech. Engng.*, Vol. 126, 17-38.
- Fish, J., Suvorov, A., and Belsky, V., 1996a, "Composite Grid and Adaptive Multigrid Methods for Global\_local Analysis of Laminated Composite Shells," to appear in *Applied Numerical Mathematics*.
- Fish, J., Pandheeradi, M., Shek, K., Shephard, M. S., 1996b, "Computational Plasticity for Composite Materials and Structures Based on Mathematical Homogenization: Theory and Practice", to appear in *Comp. Meth. Appl. Mech. Engng.*
- Hashin, E., and Walter Rosen, B., 1964, "The Elastic Moduli of Fiber-Reinforced Materials", *Journal of Applied Mechanics*, Transactions of the ASME, pp. 223-232, June.
- He, M., and Hutchinson, J. W., 1989, "Kinking of a Crackout of the Interface", *Appl. Mech.*, Vol. 56, pp. 270-278.
- Mori, T. and Tanaka, K., 1973, "Average Stress in Matrix and Average Elastic Energy of Materials with Misfitting Inclusions", *Acta Metallurgica*, Vol. 21, pp. 571-574, May.
- PDA Engineering, 1993, "M/VISION Material System Builder User's Guide and Reference", Release 1.2, Publication No. 2190011, 2975 Redhill Avenue, Costa Mesa, California, 92626.
- Shephard, M. S., Beall, M. W., Garimella, R., and Wentorf, R., 1995, "Automatic Construction of 3-D Models in Multiple Scale Analysis", *Computational Mechanics*, 17, pp. 196-207
- Teply, L., and Dvorak, G. J., 1988, "Bounds on Overall Instantaneous Properties of Elastic-Plastic Composites", *Jan J. Mech. Phys. Solids*, Vol. 36, No. 1, pp. 29-58.

A Posteriori Error Estimation for the Finite Element  
Method-of-Lines Solution of Parabolic Problems

Slimane Adjerid, Ivo Babuska and  
Joseph E. Flaherty

SCOREC Report #8-1997  
Scientific Computation Research Center

Scientific Computation Research Center  
Rensselaer Polytechnic Institute  
Troy, NY 12180-3590  
voice 5182766795  
fax 5182764886

# A POSTERIORI ERROR ESTIMATION FOR THE FINITE ELEMENT METHOD-OF-LINES SOLUTION OF PARABOLIC PROBLEMS

SLIMANE ADJERID<sup>†</sup>, IVO BABUŠKA<sup>‡</sup>, AND JOSEPH E. FLAHERTY<sup>†</sup>

**Abstract.** Babuška and Yu constructed a posteriori estimates for finite element discretization errors of linear elliptic problems utilizing a dichotomy principle stating that the errors of odd-order approximations arise near element edges as mesh spacing decreases while those of even-order approximations arise in element interiors. We construct similar a posteriori estimates for the spatial errors of finite element method-of-lines solutions of linear parabolic partial differential equations on square-element meshes. Error estimates computed in this manner are proven to be asymptotically correct; thus, they converge in strain energy under mesh refinement at the same rate as the actual errors.

**Key Words.** Finite element methods, method of lines, a posteriori error estimation, parabolic partial differential equations

**AMS (MOS) subject classifications.** 65M60, 65M20, 65M15, 65M50

**1. Introduction.** A posteriori estimates of discretization errors have been an integral part of adaptive finite element methods since their inception nearly twenty years ago [5, 6]. Local contributions to global error estimates furnish *error indicators* that are typically used to control adaptive enrichment through mesh refinement/coarsening (h-refinement) and/or method order variation (p-refinement). Thus, meshes are refined and/or method orders increased where error indicators are large and an opposite course is taken where

---

<sup>†</sup> Department of Computer Science and Scientific Computation Research Center, Rensselaer Polytechnic Institute, Troy, NY 12180, USA (adjerids@cs.rpi.edu, flaherje@cs.rpi.edu). This research was partially supported by the U.S. Army Research Office through Contract Number DAAH 04-95-1-0091 and by ARPA/ONR under Grant Number N00014-1779.

<sup>‡</sup> Texas Institute for Computational and Applied Mathematics, University of Texas at Austin, Austin, TX 78712.

error indicators are small. An ideal a posteriori error estimation techniques would

- i. be *asymptotically correct* in the sense that the error estimate in a particular norm approach zero under enrichment at the same rate as the actual error;
- ii. be *computationally simple* by requiring a small fraction of the solution cost;
- iii. be *robust* by furnishing accurate estimates for a wide range of meshes and method orders;
- iv. provide relatively tight *upper and lower bounds* of the true error in a particular norm; and
- v. supply local error indicators that provide global error estimates in *several norms*.

Recent surveys [8, 9, 16] indicate that no error estimates satisfy all of these criteria for all combinations of meshes, method orders, geometries, etc.

Babuška and Yu [10, 18, 19] constructed a posteriori error estimates in strain energy for the finite element solution of linear elliptic problems on square domains by using a dichotomy principal stating that the errors of odd-order approximations arise at element edges as the spacing of a square-element mesh decreases to zero while those of even-order approximations arise in element interiors in the same limit. Yu [18, 19] established the asymptotic correctness of these error estimates for finite element spaces consisting of piecewise bi-polynomials of arbitrary degree. Adjerid et al. [3] showed that similar estimates could be obtained for the spatial discretization errors of method-of-lines solutions of one-dimensional parabolic partial differential equations. We extend this earlier work by constructing a posteriori estimates for the spatial errors of finite element method-of-lines solutions of two-dimensional linear parabolic equations. We establish asymptotic correctness of these error estimates on square elements and show that temporal variations of spatial errors may be neglected for both odd- (§3) and even-order (§4.2) finite element solutions. Error estimates of even-order finite element solutions may also be obtained by

solving local parabolic problems (§4.1), which include the temporal variation of the error estimate. This procedure might be useful when error estimates are used to control mesh motion (r-refinement) [2].

Both odd- and even-order error estimation procedures are computationally simple. The odd-order estimates only require jumps in solution gradients at the four element vertices and neither element nor edge residuals are needed. Only nearest-neighbor interaction is necessary; thus, simplifying implementation on a parallel computer. Gradient jumps may be shared between elements sharing a vertex to halve the cost relative to element-by-element computation. The even-order elliptic and parabolic estimates are local to the element. No off-element communication is necessary; hence, there is no search for neighbor information and parallelization is perfect. Computations (§5) imply that the even-order estimates improve with increasing polynomial degree.

Numerical examples presented in §5 and elsewhere [1] indicate that the error estimates are applicable more widely than the present theory would suggest. Thus, for example, they appear to work in the presence of some nonlinearity, when some singularities are present, and on graded quadrilateral-element meshes. Experiments of Baehmann et al. [4] and Ilin et al. [11] would suggest that the even-order estimates are applicable to triangular elements.

**2. Formulation.** Consider the linear, scalar, two-dimensional parabolic differential equation

$$\partial_t u + Lu = f(x), \quad x = [x_1, x_2]^T \in \Omega, \quad t > 0, \quad (2.1a)$$

with

$$Lu = - \sum_{j=1}^2 \sum_{k=1}^2 \partial_{x_j} (a_{j,k}(x) \partial_{x_k} u) + b(x)u, \quad (2.1b)$$

on a bounded rectangle  $\Omega$  subject to the initial and Dirichlet boundary conditions

$$u(x, 0) = u^0(x), \quad x \in \Omega \cup \partial\Omega, \quad (2.1c)$$

$$u(\mathbf{x}, t) = 0, \quad \mathbf{x} \in \partial\Omega, \quad t \geq 0. \quad (2.1d)$$

The functions  $a_{j,k}(\mathbf{x})$ ,  $j, k = 1, 2$ , and  $b(\mathbf{x})$  are smooth with  $L$  being a positive-definite operator.

The Galerkin form of (2.1) consists of determining  $u \in H_0^1$  satisfying

$$(v, \partial_t u) + A(v, u) = (v, f), \quad t > 0, \quad (2.2a)$$

$$A(v, u) = A(v, u^0), \quad t = 0, \quad \text{for all } v \in H_0^1, \quad (2.2b)$$

where the strain energy and  $L^2$  inner products, respectively, are

$$A(v, u) = \iint_{\Omega} \left[ \sum_{j=1}^2 \sum_{k=1}^2 a_{j,k}(\mathbf{x}) \partial_{x_j} v \partial_{x_k} u + b(\mathbf{x})vu \right] dx_1 dx_2 \quad (2.2c)$$

and

$$(v, u) = (v, u)_0 = \iint_{\Omega} uv \, dx_1 dx_2. \quad (2.2d)$$

As usual, functions in the Sobolev space  $H^s$ ,  $s \geq 0$ , have the inner product and norm

$$(v, u)_s = \sum_{|\alpha| \leq s} (\partial_{x_1}^{\alpha_1} \partial_{x_2}^{\alpha_2} v, \partial_{x_1}^{\alpha_1} \partial_{x_2}^{\alpha_2} u), \quad \|u\|_1^2 = (u, u)_s, \quad (2.2e, f)$$

where  $|\alpha| = \alpha_1 + \alpha_2$ . The subscript 0 on  $H^1$  additionally restricts functions to satisfy (2.1d).

Finite element solutions of (2.2a,b) are obtained by approximating  $H^1$  by a finite-dimensional subspace  $S^{N,p}$  and determining  $U \in S_0^{N,p}$  such that

$$(V, \partial_t U) + A(V, U) = (V, f), \quad t > 0, \quad (2.3a)$$

$$A(V, U) = A(V, u^0), \quad t = 0, \quad \text{for all } V \in S_0^{N,p}. \quad (2.3b)$$

Partitioning  $\Omega$  into a uniform mesh of square elements  $\Delta_i$ ,  $i = 1, 2, \dots, N$ , define  $S^{N,p}$  as

$$S^{N,p} = \{ w \in H^1 \mid w(\mathbf{x}) \in Q_p(\Delta_i), \mathbf{x} \in \Delta_i, i = 1, 2, \dots, N \} \quad (2.4)$$

where  $Q_p(\Delta_i)$  is the space of bi-polynomial functions that are products of univariate polynomials of degree  $p$  in  $x_1$  and  $x_2$  on  $\Delta_i$ .

The following two lemmas describe standard interpolation and a priori discretization error estimates for finite element solutions of (2.2) that will be useful during the subsequent analysis.

LEMMA 2.1. Let  $W \in S_0^{N,p}$  be an interpolant of  $w \in H_0^1 \cap H^{p+1}$  that is exact when  $w \in Q_p(\Omega)$ . Then, there exists a constant  $C > 0$  such that

$$\|W - w\|_s \leq Ch^{p+1-s} \|w\|_{p+1}, \quad s = 0, 1, \quad (2.5a)$$

where

$$h = 1/\sqrt{N}. \quad (2.5b)$$

*Proof.* Cf., e.g., Oden and Carey [12].  $\square$

LEMMA 2.2. Let  $u$  and  $U$  be solutions of (2.2a,b) and (2.3), respectively. Further let

$$A(V, \hat{U}) = A(V, u), \quad \text{for all } V \in S_0^{N,p}, \quad t \geq 0, \quad (2.6)$$

be the strain energy projection of  $u$  onto  $S_0^{N,p}$ . If  $u^0 \in H_0^1 \cap H^2$  and  $u$  is smooth enough for all terms in (2.7) to be bounded, then there exist  $C > 0$  and  $t_0 > 0$  such that

$$\|\hat{U} - U\|_1^2 \leq Ch^{2(p+1)} \int_0^t \|\partial_t u(\cdot, \tau)\|_{p+1}^2 d\tau, \quad t \geq 0, \quad (2.7a)$$

$$\begin{aligned} \|\partial_t^n e(\cdot, t)\|_0 &\leq Ch^{p+1} [\|u^0\|_2 + \sum_{l=0}^n \|\partial_t^l u(\cdot, t)\|_{p+1} + \int_{t-t_0}^t \|\partial_t^{n+1} u(\cdot, \tau)\|_{p+1} d\tau \\ &\quad + \int_0^t \|\partial_t u(\cdot, \tau)\|_2 d\tau], \quad t > t_0 > 0, \quad n \geq 0, \end{aligned} \quad (2.7b)$$

$$\begin{aligned} \|\partial_t^n e(\cdot, t)\|_1 &\leq Ch^p [\|u^0\|_2 + \sum_{l=0}^n \max_{t-t_0 < \tau < t} \|\partial_t^l u(\cdot, \tau)\|_{p+1} + \left( \int_{t-t_0}^t \|\partial_t^{n+1} u(\cdot, \tau)\|_p^2 d\tau \right)^{1/2} \\ &\quad + h \|u^0\|_0 + h \int_0^t \|f\|_0 d\tau], \quad t > t_0 > 0, \quad n \geq 0, \end{aligned} \quad (2.7c)$$

where



$$e(\mathbf{x}, t) = u(\mathbf{x}, t) - U(\mathbf{x}, t). \quad (2.7d)$$

*Proof.* Cf. Wait and Mitchell [17], e.g., for the proof of (2.7a) and Thomée [15] for the proofs of (2.7b) and (2.7c).  $\square$

**2.1. Preliminary considerations.** Let  $\tilde{\pi}[\bar{z}]$  be the univariate operator that interpolates functions in  $H_0^1(\bar{z}-h/2, \bar{z}+h/2)$  at the Lobatto points of degree  $p+1$ ,  $p \geq 1$ , on  $[\bar{z}-h/2, \bar{z}+h/2]$ . Also let

$$\psi_{p+1}(\bar{z}, z) = z^{p+1} - \tilde{\pi}[\bar{z}]z^{p+1} \quad (2.8)$$

vanish at these  $p+1$  Lobatto points. Hence,  $\psi_{p+1}(\bar{z}, z)$  and  $\psi'_{p+1}(\bar{z}, z)$  are, respectively, proportional to Lobatto and Legendre polynomials on  $[\bar{z}-h/2, \bar{z}+h/2]$ , with  $(\ )'$  denoting ordinary differentiation.

We use  $\tilde{\pi}$  to define a two-dimensional interpolation operator  $\pi_i$  on element  $i$  satisfying  $\pi_i u(\mathbf{x}) = \tilde{\pi}[\bar{x}_{1,i}] \tilde{\pi}[\bar{x}_{2,i}] u(\mathbf{x}) \in \mathcal{Q}_p(\Delta_i)$ ,  $\mathbf{x} \in \Delta_i$ . Since the mesh is uniform, we will omit the elemental index  $i$  and the dependence of  $\tilde{\pi}[\bar{x}_{j,i}]$  and  $\psi(\bar{x}_{j,i}, x_j)$  on the coordinates of the cell center  $(\bar{x}_{1,i}, \bar{x}_{2,i})$ ,  $i = 1, 2, \dots, N$ , whenever confusion is unlikely.

The functions  $\psi_{p+1}(x_j)$ ,  $j = 1, 2$ , provide the dominant contributions to the spatial discretization error on element  $\Delta$  for both odd- and even-order finite element approximations. Indeed, we shall show that estimates  $E(\mathbf{x}, t)$  of  $e(\mathbf{x}, t)$  have the form

$$E(\mathbf{x}, t) = b_1(t)\psi_{p+1}(x_1) + b_2(t)\psi_{p+1}(x_2), \quad \mathbf{x} \in \Delta. \quad (2.9)$$

The following sequence of lemmas take steps in this direction.

**LEMMA 2.3.** *Let  $u \in H^{p+2}$ ,  $t \geq 0$ , then*

$$u(\mathbf{x}, t) - \pi u(\mathbf{x}, t) = \phi(\mathbf{x}, t) + \gamma(\mathbf{x}, t), \quad \mathbf{x} \in \Delta, \quad (2.10a)$$

where

$$\phi(\mathbf{x}, t) = \beta_1(t)\psi_{p+1}(x_1) + \beta_2(t)\psi_{p+1}(x_2), \quad (2.10b)$$

$$\|\partial_t^n \phi\|_{s, \Delta} \leq Ch^{p+1-s} \|\partial_t^n u\|_{p+1, \Delta}, \quad t \geq 0, \quad n \geq 0, \quad s = 0, 1, \dots, p, \quad (2.10c)$$

$$\|\partial_{x_j} \phi\|_{0,\Delta} \leq Ch^p \|u\|_{p+1,\Delta}, \quad j = 1, 2, \quad t \geq 0, \quad (2.10d)$$

$$\|\gamma\|_{s,\Delta} \leq Ch^{p+2-s} \|u\|_{p+2,\Delta}, \quad s = 0, 1, \dots, p+1, \quad (2.10e)$$

and

$$\|\partial_{x_j} \gamma\|_{s,\Delta} \leq Ch^{p+1-s} \|u\|_{p+2,\Delta}, \quad s = 0, 1, \quad j = 1, 2, \quad t \geq 0. \quad (2.10f)$$

*Remark.* Local Sobolev norms are defined like their global counterparts (2.2d,e) with  $\Omega$  replaced by  $\Delta$ .

*Proof.* Yu's [18] results for elliptic partial differential equations extend directly to the transient case.  $\square$

LEMMA 2.4. Let  $\Pi u \in S_0^{N,p}$  be an interpolant of  $u \in H^{p+2}$  for  $\mathbf{x} \in \Omega$  that agrees with  $\pi u$  when  $\mathbf{x} \in \Delta$ , then

$$|A(W, u - \Pi u)| \leq Ch^{p+1} \|u\|_{p+2} \|W\|_1, \quad \text{for all } W(\mathbf{x}) \in S_0^{N,p}. \quad (2.11)$$

*Proof.* cf. Yu [18].  $\square$

LEMMA 2.5. Let  $u \in H_0^1 \cap H^{p+2}$ ,  $U \in S_0^{N,p}$ , and  $\hat{U} \in S_0^{N,p}$ , be solutions of (2.2a,b), (2.3), and (2.6), respectively. Further let  $\Pi u \in S_0^{N,p}$  interpolate  $u$  as described in Lemma 2.4, then

$$\|\hat{U} - \Pi u\|_1 \leq Ch^{p+1} \|u\|_{p+2}, \quad \|U - \Pi u\|_1 \leq C(u) h^{p+1}, \quad (2.12a,b)$$

and

$$e(\mathbf{x}, t) = \Phi(\mathbf{x}, t) + \Theta(\mathbf{x}, t) \quad (2.13a)$$

where the restrictions of  $\Phi(\mathbf{x}, t)$  and  $\Theta(\mathbf{x}, t)$  to  $\Delta$  are  $\phi(\mathbf{x}, t)$  of (2.10b) and

$$\theta(\mathbf{x}, t) = \gamma(\mathbf{x}, t) + \pi u(\mathbf{x}, t) - U(\mathbf{x}, t). \quad (2.13b)$$

Furthermore,

$$\|\nabla \Phi\|_0^2 \leq Ch^{2p} \|u\|_{p+1}^2, \quad \|\nabla \Theta\|_0^2 \leq C(u) h^{2(p+1)}, \quad (2.13c,d)$$

and

$$\|\partial_t^n \Theta\|_s \leq C(u) h^{p+1-s}, \quad n \geq 0, \quad s = 0, 1, \quad t > t_0. \quad (2.13e)$$

*Proof.* Subtract  $A(V, \Pi u)$  from (2.6) and use (2.11) to obtain

$$|A(V, \hat{U} - \Pi u)| = |A(V, u - \Pi u)| \leq Ch^{p+1} \|u\|_{p+2} \|V\|_1, \quad \text{for all } V \in S_0^{N,p}. \quad (2.14)$$

Replacing  $V$  in (2.14) by  $\hat{U} - \Pi u$  yields (2.12a). Addition and subtraction of  $\hat{U}$  to  $U - \Pi u$  and subsequent use of the triangular inequality with (2.7a) and (2.12a) establishes (2.12b).

In order to prove (2.13c-e), use (2.10a) and (2.13b) to obtain

$$e = u - \pi u + \pi u - U = \phi + \gamma + \pi u - U = \phi + \theta, \quad x \in \Delta, \quad (2.15)$$

and, consequently, (2.13a). Squaring and summing (2.10d) over the elements of the mesh leads to (2.13c). Taking the gradient and  $L^2$  norm of (2.13b) and using the triangular inequality yields

$$\|\nabla \theta\|_{0,\Delta}^2 \leq C(\|\nabla \gamma\|_{0,\Delta}^2 + \|\nabla(\pi u - U)\|_{0,\Delta}^2) \quad (2.16)$$

The use of (2.10f) and (2.12b) with a summation over all elements yields (2.13d). In a similar manner, a combination of (2.13a), (2.7b,c), and (2.10c) yields (2.13e).  $\square$

LEMMA 2.6. *Under the conditions of Lemma 2.5, there exists a function  $\varepsilon_1$  such that*

$$\|e\|_1^2 = \|u - \Pi u\|_1^2 + \varepsilon_1 \quad (2.17a)$$

with

$$|\varepsilon_1| \leq C(u)h^{2p+1}. \quad (2.17b)$$

*Proof.* Adding and subtracting  $\Pi u$  to  $e$  yields (2.17a) with

$$\varepsilon_1 = 2(u - \Pi u, \Pi u - U)_1 + \|\Pi u - U\|_1^2. \quad (2.18)$$

Applying the Schwarz inequality and using (2.5) and (2.12b) yields (2.17b).  $\square$

**3. A posteriori error estimation of odd-degree approximations.** If  $u$  is smooth on  $\Delta$  then error estimates  $E(x,t)$  of odd-degree approximations may be constructed in terms of jumps in derivatives of  $U$  at the vertices of  $\Delta$ . Informally, use (2.7d) to and its approximation (2.9) to compute jumps in the derivatives of  $e(x,t)$  at the vertices  $p_k = (p_{1k}, p_{2k})$ ,

$k = 1, 2, 3, 4$ , of  $\Delta$  as

$$[\partial_{x_j} e(\mathbf{p}_k, t)]_j = -[\partial_{x_j} U(\mathbf{p}_k, t)]_j \approx b_1(t)[\partial_{x_j} \psi_{p+1}(p_{1k})]_j + b_2(t)[\partial_{x_j} \psi_{p+1}(p_{2k})]_j, \\ j = 1, 2, \quad k = 1, 2, 3, 4, \quad \mathbf{x} \in \Delta, \quad (3.1)$$

where  $[q(\mathbf{p})]_j$  denotes the jump in  $q$  at point  $\mathbf{p}$  in the  $x_j$  direction. Since jumps in the solution  $U$  and  $\psi_{p+1}$  are known, this overdetermined system may be solved in some sense for the coefficients  $b_j$ ,  $j = 1, 2$ . The procedure used in the following lemma and theorem is to solve (3.1) for  $b_j$ ,  $j = 1, 2$ , at each element vertex  $\mathbf{p}_k$ ,  $k = 1, 2, 3, 4$ , and average the values of  $\|E(\cdot, t)\|_{1,\Delta}$  based on the pairs of  $b_j$ ,  $j = 1, 2$ , obtained.

LEMMA 3.1. Let  $u \in H_0^1 \cap H^{p+2}$ ,  $\Pi u$  be as defined in Lemma 2.4, and  $p$  be a positive odd integer, then

$$\|u - \Pi u\|_1^2 = \frac{h^2}{16(2p+1)} \sum_{i=1}^N \sum_{j=1}^2 \sum_{k=1}^4 [\partial_{x_j} \Pi u(\mathbf{p}_k, t)]_j^2 + \varepsilon_2 \quad (3.2a)$$

where

$$|\varepsilon_2| \leq Ch^{2p+1}, \quad (3.2b)$$

*Proof.* cf. Yu [19].  $\square$

THEOREM 3.1. Let  $u \in H_0^1 \cap H^{p+2}$  and  $U \in S_0^{N,p}$  be solutions of (2.2) and (2.3), respectively. If  $p$  is an odd positive integer, then

$$\|e(\cdot, t)\|_1^2 = \|E(\cdot, t)\|_1^2 + \varepsilon \quad (3.3a)$$

where

$$\|E(\cdot, t)\|_1^2 = \frac{h^2}{16(2p+1)} \sum_{i=1}^N \sum_{j=1}^2 \sum_{k=1}^4 [\partial_{x_j} U(\mathbf{p}_k, t)]_j^2, \quad |\varepsilon| \leq Ch^{2p+1}. \quad (3.3b,c)$$

*Proof.* Adding and subtracting  $\Pi u$  on each element yields

$$\frac{h^2}{16(2p+1)} \sum_{i=1}^N \sum_{j=1}^2 \sum_{k=1}^4 [\partial_{x_j} U(\mathbf{p}_k, t)]_j^2 = \frac{h^2}{16(2p+1)} \sum_{i=1}^N \sum_{j=1}^2 \sum_{k=1}^4 [\partial_{x_j} \Pi u(\mathbf{p}_k, t)]_j^2 + \varepsilon_3 \quad (3.4a)$$

where

$$\begin{aligned} \varepsilon_3 = & \frac{h^2}{16(2p+1)} \sum_{i=1}^N \sum_{j=1}^2 \sum_{k=1}^4 \{ [\partial_{x_j}(U(\mathbf{p}_k, t) - \Pi u(\mathbf{p}_k, t))]_j^2 + \\ & 2[\partial_{x_j}(U(\mathbf{p}_k, t) - \Pi u(\mathbf{p}_k, t))]_j [\partial_{x_j} \Pi u(\mathbf{p}_k, t)]_j \}. \end{aligned} \quad (3.4b)$$

Using (3.2a) and (2.17a) in (3.4a) we obtain

$$\frac{h^2}{16(2p+1)} \sum_{i=1}^N \sum_{j=1}^2 \sum_{k=1}^4 [\partial_{x_j} U(\mathbf{p}_k, t)]_j^2 = \|e\|_1^2 - \varepsilon_1 - \varepsilon_2 + \varepsilon_3; \quad (3.4c)$$

thus, establishing (3.3a,b) with  $\varepsilon = \varepsilon_1 + \varepsilon_2 - \varepsilon_3$ . Since  $\varepsilon_1$  and  $\varepsilon_2$  are  $O(h^{2p+1})$ , it remains to find a similar bound for  $\varepsilon_3$ . To this end, an application of the Schwarz inequality to (3.4b) yields

$$\begin{aligned} |\varepsilon_3| \leq & \frac{h^2}{16(2p+1)} \sum_{i=1}^N \sum_{j=1}^2 \sum_{k=1}^4 [\partial_{x_j}(U(\mathbf{p}_k, t) - \Pi u(\mathbf{p}_k, t))]_j^2 + \\ & 2 \left\{ \frac{h^2}{16(2p+1)} \sum_{i=1}^N \sum_{j=1}^2 \sum_{k=1}^4 [\partial_{x_j}(U(\mathbf{p}_k, t) - \Pi u(\mathbf{p}_k, t))]_j^2 \right\}^{1/2} \times \\ & \left\{ \frac{h^2}{16(2p+1)} \sum_{i=1}^N \sum_{j=1}^2 \sum_{k=1}^4 [\partial_{x_j} \Pi u(\mathbf{p}_k, t)]_j^2 \right\}^{1/2}. \end{aligned} \quad (3.5)$$

Let  $\Delta_0$  be the canonical element  $-1 \leq \xi_1, \xi_2 \leq 1$  and use norm equivalence on the finite-dimensional space  $Q_p(\Delta_0)$  to show that

$$\max_{(\xi_1, \xi_2) \in \Delta_0} (|\partial_{\xi_1} v| + |\partial_{\xi_2} v|) \leq C \|\nabla v\|_{0, \Delta_0}, \quad \text{for all } v \in Q_p(\Delta_0). \quad (3.6a)$$

A subsequent linear mapping of  $\Delta_0$  to an element  $\Delta_i$ ,  $i = 1, 2, \dots, N$ , yields

$$\max_{(x_1, x_2) \in \Delta_i} (|\partial_{x_1} w| + |\partial_{x_2} w|) \leq \frac{C}{h} \|w\|_{1, \Delta_i}, \quad \text{for all } w \in Q_p(\Delta_i). \quad (3.6b)$$

Let  $\Delta_{i,n}$ ,  $n = 1, 2, 3, 4$ , denote the four elements having common edges with  $\Delta_{i,0} = \Delta_i$  and

$$\Delta_i^* = \bigcup_{n=0}^4 \Delta_{i,n}. \quad (3.7)$$

Then, using (3.6b),

$$[\partial_{x_j}(U(\mathbf{p}_k, t) - \Pi u(\mathbf{p}_k, t))]_j \leq C \max_{(x_1, x_2) \in \Delta_i} \{|\partial_{x_1}(U - \Pi u)| + |\partial_{x_2}(U - \Pi u)|\} \leq$$

$$\frac{C}{h} \|U - \Pi u\|_{1, \Delta_i}, \quad j = 1, 2, \quad k = 1, 2, 3, 4. \quad (3.8)$$

With (3.8), we have

$$\begin{aligned} \frac{h^2}{16(2p+1)} \sum_{i=1}^N \sum_{j=1}^2 \sum_{k=1}^4 [\partial_{x_j}(U(\mathbf{p}_k, t) - \Pi u(\mathbf{p}_k, t))]_j^2 \leq \\ \frac{C}{16(2p+1)} \sum_{i=1}^N \|U - \Pi u\|_{1, \Delta_i}^2 \leq C \|U - \Pi u\|_1^2. \end{aligned} \quad (3.9a)$$

Similarly, using (2.5) and (3.2), we have

$$\frac{h^2}{16(2p+1)} \sum_{i=1}^N \sum_{j=1}^2 \sum_{k=1}^4 [\partial_{x_j} \Pi u(\mathbf{p}_k, t)]_j^2 \leq C \|u - \Pi u\|_1^2. \quad (3.9b)$$

Using (3.9) in (3.5) yields

$$|\varepsilon_3| \leq C \{ \|U - \Pi u\|_1^2 + \|u - \Pi u\|_1 \|U - \Pi u\|_1 \}. \quad (3.10)$$

The estimates (2.5) and (2.12b) imply that  $\varepsilon_3 = O(h^{2p+1})$ , which completes the proof.  $\square$

**4. A posteriori error estimation of even-degree approximations.** Error estimates in terms of jumps in solution derivatives fail for even-order approximations since  $\psi_{p+1}(x_j)$ ,  $j = 1, 2$ , is continuous on  $\partial\Delta$ . Thus, with  $p$  even, we construct a Galerkin problem for  $e$  by replacing  $u$  in (2.2) by  $U + e$  to obtain

$$(v, \partial_t e) + A(v, e) = g(t, v), \quad t > 0, \quad (4.1a)$$

$$A(v, e) = A(v, u^0 - U), \quad t = 0, \quad \text{for all } v \in H_0^1, \quad (4.1b)$$

with

$$g(t, v) = (v, f) - (v, \partial_t U) - A(v, U). \quad (4.1c)$$

The error is once again approximated by  $E$  according to (2.9) and the test function  $v$  is

selected as

$$v_j(\mathbf{x}) = (x_j - \bar{x}_{j,i})\delta(x_1)\delta(x_2), \quad j = 1, 2, \quad (4.2a)$$

where

$$\delta(z) = \frac{\psi_{p+1}(z)}{z - \bar{z}}, \quad \sigma(z) = \psi'_{p+1}(z), \quad z \in [\bar{z}-h/2, \bar{z}+h/2]. \quad (4.2b,c)$$

(Although not yet needed, we define  $\sigma$  for future reference.) Since  $\psi_{p+1}(x_j)$  and  $v_j(\mathbf{x})$ ,  $j = 1, 2$ , vanish on  $\partial\Delta_i$ , the error estimate satisfies the local Dirichlet problems

$$(v_j, \partial_t E)_\Delta + A_\Delta(v_j, E) = g_\Delta(t, v_j), \quad t > 0 \quad (4.3a)$$

$$A_\Delta(v_j, E) = A_\Delta(v_j, u^0 - U), \quad t = 0, \quad j = 1, 2. \quad (4.3b)$$

where  $\Delta$  subscripts denote that inner products are restricted to  $\Delta_i$ . The time derivative of  $E$  in (4.3a) may be neglected to obtain the local elliptic problem

$$A_\Delta(v_j, E) = g_\Delta(t, v_j), \quad t > 0, \quad j = 1, 2. \quad (4.4)$$

The parabolic (4.3) and elliptic (4.4) error estimates are shown to be asymptotically correct in §4.1 and §4.2, respectively; however, prior to this, we establish some properties of  $\psi_{p+1}$ ,  $\delta$ ,  $\sigma$ , and  $v_j$ ,  $j = 1, 2$ .

LEMMA 4.1. *Let  $p \geq 2$  be an even integer, then there exist  $C > 0$  such that*

$$\iint_{\Delta} \delta(x_j) dx_1 dx_2 = Ch^{p+2}, \quad \iint_{\Delta} \psi_{p+1}(x_j)^2 \delta(x_k) dx_1 dx_2 = Ch^{3p+4}, \quad (4.5a,b)$$

$$\iint_{\Delta} \sigma(x_j)^2 \delta(x_k) dx_1 dx_2 = Ch^{3p+2}, \quad \|\sigma(x_j)\|_{0,\Delta}^2 = Ch^{2(p+1)}, \quad (4.5c,d)$$

$$ch^{2(p-s)+4} \leq \|\psi_{p+1}(x_j)\|_{s,\Delta}^2 \leq Ch^{2(p-s)+4}, \quad s = 0, 1, \quad (4.5e)$$

$$ch^{2p+1} \leq \|v_j(\cdot)\|_{1,\Delta} \leq Ch^{2p+1}, \quad j, k = 1, 2. \quad (4.5f)$$

*Proof.* A direct computation reveals the results.  $\square$

**4.1. The parabolic error estimate.** The parabolic finite element problem (4.3) may

be further simplified by neglecting the higher-order off-diagonal diffusion coefficients and the reaction term in the strain energy (2.2c), freezing the diagonal diffusion coefficients, and using symmetry properties of  $\psi_{p+1}(z)$  and  $v_j(x)$ ,  $j = 1, 2$ , to obtain the uncoupled constant-coefficient initial value problem on element  $i$

$$b'_j(t) + r_j b_j(t) = G_j(t), \quad t > 0, \quad (4.6a)$$

$$b_j(0) = \frac{A_{\Delta}(v_j, u^0(\cdot)) - U(\cdot, 0)}{\bar{a}_{j,j} \iint_{\Delta} \sigma^2(x_j) \delta(x_{(j \bmod 2)+1}) dx_1 dx_2}, \quad j = 1, 2, \quad (4.6b)$$

where

$$r_j = \bar{a}_{j,j} \frac{\iint_{\Delta} \sigma^2(x_j) \delta(x_{(j \bmod 2)+1}) dx_1 dx_2}{\iint_{\Delta} \psi_{p+1}^2(x_j) \delta(x_{(j \bmod 2)+1}) dx_1 dx_2}, \quad (4.6c)$$

$$G_j(t) = \frac{g_{\Delta}(t, v_j)}{\iint_{\Delta} \psi_{p+1}^2(x_j) \delta(x_{(j \bmod 2)+1}) dx_1 dx_2}, \quad (4.6d)$$

and

$$\bar{a}_{jk} = a_{jk}(\bar{x}), \quad j, k = 1, 2. \quad (4.6e)$$

Of course, the exact solution of (4.6) is

$$b_j(t) = b_j(0)e^{-r_j t} + \int_0^t e^{-r_j(t-\tau)} G_j(\tau) d\tau, \quad t \geq 0, \quad j = 1, 2. \quad (4.7)$$

In order to estimate the difference between the exact solution of (4.1) and its approximation by (2.9, 4.7), we substitute (2.13) into (4.1) while using (2.10b) to obtain

$$\beta'_j(t) + r_j \beta_j(t) = G_j(t) - F_j(t) - H_j(t), \quad t > 0, \quad (4.8a)$$

$$\beta_j(0) = \frac{A_{\Delta}(v_j, u^0(\cdot)) - U(\cdot, 0)}{\bar{a}_{j,j} \iint_{\Delta} \sigma^2(x_j) \delta(x_{(j \bmod 2)+1}) dx_1 dx_2} - \frac{F_j(0)}{r_j}, \quad (4.8b)$$

where



$$F_j(t) = \frac{\iint_{\Delta} \left[ \sum_{k=1}^2 \sum_{l=1}^2 a_{k,l} \partial_{x_k} v_j \partial_{x_l} \theta + \sum_{k=1}^2 \sum_{l=1}^2 (a_{k,l} - \bar{a}_{k,l}) \partial_{x_k} v_j \partial_{x_l} \phi + b v_j e \right] dx_1 dx_2}{\iint_{\Delta} \psi_{p+1}^2(x_j) \delta(x_{(j \bmod 2)+1}) dx_1 dx_2}, \quad j = 1, 2, \quad (4.8c)$$

$$H_j(t) = \frac{(v_j, \partial_t \theta)}{\iint_{\Delta} \psi_{p+1}^2(x_j) \delta(x_{(j \bmod 2)+1}) dx_1 dx_2}, \quad j = 1, 2. \quad (4.8d)$$

We may formally solve (4.8a) for  $\beta_j$  to obtain

$$\beta_j(t) = \beta_j(0) e^{-r_j t} + \int_0^t e^{-r_j(t-\tau)} [G_j(\tau) - F_j(\tau) - H_j(\tau)] d\tau, \quad t \geq 0, \quad j = 1, 2. \quad (4.9)$$

The following Lemma quantifies the differences between  $\beta_j$  and its approximation  $b_j$ ,  $j = 1, 2$ .

LEMMA 4.2. Let  $p \geq 2$  be an even integer,  $u \in H_0^1 \cap H^{p+2}$ ,  $t \geq 0$ , and  $a_{k,k}(x) > \alpha_0 > 0$ ,  $x \in \Omega$ ,  $k = 1, 2$ , and assume that

$$\|\partial_t^n e\|_1 \leq C(u), \quad n = 0, 1, \quad 0 \leq t \leq t_0, \quad (4.10)$$

Then,

$$\sum_{i=1}^N (\beta_{ji} - b_{ji})^2 \leq C(u), \quad \sum_{i=1}^N (\beta_{ji}^2 - b_{ji}^2) \leq \frac{C(u)}{h}, \quad j = 1, 2, \quad t > t_0. \quad (4.11a,b)$$

*Proof.* Letting

$$\alpha_j(t) = \beta_j(t) - b_j(t), \quad j = 1, 2, \quad (4.12)$$

and subtracting (4.7) from (4.9) and (4.6b) from (4.8b) we obtain

$$\alpha_j(t) = \alpha_j(0) e^{-r_j t} - \int_0^t e^{-r_j(t-\tau)} [F_j(\tau) + H_j(\tau)] d\tau, \quad t \geq 0, \quad (4.13a)$$

with

$$\alpha_j(0) = -\frac{F_j(0)}{r_j}, \quad j = 1, 2. \quad (4.13b)$$

Integrating (4.13a) by parts and applying the Schwarz and triangular inequalities yields

$$\alpha_j^2(t) \leq C[e^{-2r_j t} \alpha_j^2(0) + \frac{|F_j(t) + H_j(t)|^2}{r_j^2} + e^{-2r_j t} \frac{|F_j(0) + H_j(0)|^2}{r_j^2} + e^{-2r_j(t-t_0)} \int_0^{t_0} \frac{|F_j'(\tau) + H_j'(\tau)|^2}{r_j^3} d\tau + \int_{t_0}^t \frac{|F_j'(\tau) + H_j'(\tau)|^2}{r_j^3} d\tau], \quad t \geq 0. \quad (4.14)$$

It remains to bound the various terms in (4.14). To begin, apply the Schwarz and triangular inequalities to (4.8c) while using the assumed smoothness of the coefficients  $a_{k,l}$ ,  $k, l = 1, 2$ , and the dominance of the  $H^1$  norm relative to the  $L^2$  norm to obtain

$$|F_j(t) + H_j(t)|^2 \leq C \frac{\|v_j\|_{1,\Delta}^2 [\|\Theta\|_{1,\Delta}^2 + h^2 \|\Phi\|_{1,\Delta}^2 + \|e\|_{0,\Delta}^2 + \|\Theta_t\|_{0,\Delta}^2]}{[\iint_{\Delta} \psi_{p+1}^2(x_j) \delta(x_{(j \bmod 2)+1}) dx_1 dx_2]^2}, \quad j = 1, 2. \quad (4.15)$$

A summation over the elements and use of (4.6c) and (4.5) reveals that

$$\sum_{i=1}^N \frac{|F_{ji}(t) + H_{ji}(t)|^2}{r_{ji}^s} \leq C h^{2(s-p-3)} [\|\Theta\|_1^2 + h^2 \|\Phi\|_1^2 + \|e\|_0^2 + \|\partial_t \Theta\|_0^2], \quad j = 1, 2, \quad s \geq 0, \quad t \geq 0. \quad (4.16)$$

The terms on the right may be bounded for  $t > t_0$  using (2.7b) and (2.13). Additionally, since  $\|e\|_0$  is bounded on  $0 \leq t < t_0$ , (4.16) may be written as

$$\sum_{i=1}^N \frac{|F_{ji}(t) + H_{ji}(t)|^2}{r_{ji}^s} \leq \begin{cases} C(u) h^{2(s-p-3)}, & \text{if } 0 \leq t < t_0 \\ C(u) h^{2(s-2)}, & \text{if } t_0 < t \end{cases}, \quad j = 1, 2, \quad s \geq 0. \quad (4.17)$$

In a similar manner,

$$\sum_{i=1}^N \frac{|F_j'(t) + H_j'(t)|^2}{r_j^3} \leq \begin{cases} C(u) h^{-2p}, & \text{if } 0 \leq t \leq t_0 \\ C(u), & \text{if } t_0 < t \end{cases}, \quad j = 1, 2. \quad (4.18)$$

The initial data  $\alpha_j(0)$ ,  $j = 1, 2$ , may be bounded by applying the Schwarz inequality to (4.13b) and using (4.5) to obtain

$$\alpha_j(0)^2 \leq Ch^{-2(p+1)} [\|\theta(\cdot, 0)\|_{1,\Delta}^2 + h^2 \phi(\cdot, 0)\|_{1,\Delta}^2 + \|e(\cdot, 0)\|_{0,\Delta}^2], \quad j = 1, 2. \quad (4.19)$$

A summation over the elements and use of (2.13) yields

$$\sum_{i=1}^N |\alpha_{ji}(0)|^2 \leq C(u)h^{-2(p+1)}, \quad j = 1, 2. \quad (4.20)$$

A summation of (4.14) and use of (4.17), (4.18), (4.20), and the dominance of the exponential relative to any algebraic power of  $h$  yields (4.11a).

Following the reasoning used to obtain (4.14), we find

$$\begin{aligned} b_j^2(t) \leq C [e^{-2r_j t} b_j^2(0) + \frac{|G_j(t)|^2}{r_j^2} + e^{-2r_j t} \frac{|G_j(0)|^2}{r_j^2} + e^{-2r_j(t-t_0)} \int_0^{t_0} \frac{|G_j'(\tau)|^2}{r_j^3} d\tau \\ + \int_{t_0}^t \frac{|G_j'(\tau)|^2}{r_j^3} d\tau], \quad t \geq 0. \end{aligned} \quad (4.21)$$

Once again, we must bound the various terms in (4.21). Thus, applying the Schwarz inequality to (4.3a) while using (4.6d) and (4.5), we obtain

$$\begin{aligned} \sum_{i=1}^N \frac{|G_{ji}(t)|^2}{r_{ji}^s} \leq \sum_{i=1}^N \frac{C}{r_{ji}^s} \left[ \frac{\|v_j\|_{1,\Delta_i}}{\iint_{\Delta_i} \Psi_{p+1,i}^2(x_j) \delta(x_{(j \bmod 2)+1}) dx_1 dx_2} \right]^2 (\|\partial_t e\|_{0,\Delta_i}^2 + \|e\|_{1,\Delta_i}^2) \\ \leq Ch^{2(s-p-3)} (\|\partial_t e\|_0^2 + \|e\|_1^2), \quad j = 1, 2, \quad s \geq 0, 2, \quad t \geq 0. \end{aligned} \quad (4.22)$$

The estimates (2.7b,c) and assumed bounds on  $e$  yield

$$\sum_{i=1}^N \frac{|G_{ji}(t)|^2}{r_{ji}^s} \leq \begin{cases} C(u)h^{2(s-p-3)}, & \text{if } 0 \leq t \leq t_0 \\ C(u)h^{2(s-3)}, & \text{if } t_0 < t \end{cases}, \quad j = 1, 2, \quad s \geq 0. \quad (4.23)$$

Similarly,

$$\sum_{i=1}^N \frac{|G_{ji}'(t)|^2}{r_{ji}^3} \leq \begin{cases} C(u)h^{-2p}, & \text{if } 0 \leq t \leq t_0 \\ C(u), & \text{if } t_0 < t \end{cases}, \quad j = 1, 2. \quad (4.24)$$

Likewise, using (4.6b) and (4.5), we obtain

$$\sum_{i=1}^N b_{ji}(0)^2 \leq C \sum_{i=1}^N \left[ \frac{\|v_j\|_{1,\Delta_i}}{\iint_{\Delta_i} \sigma(x_j)^2 \delta(x_{(j \bmod 2)+1}) dx_1 dx_2} \right]^2 \|u^0(\cdot, 0) - U(\cdot, 0)\|_{1,\Delta_i}^2 \leq C(u) h^{-2(p+1)},$$

$$j = 1, 2. \quad (4.25)$$

A summation of (4.22) over the elements and subsequent use of (4.23-25) yields

$$\sum_{i=1}^N b_{ji}^2(t) \leq C(u) h^{-2}, \quad t > t_0. \quad (4.26)$$

Differentiating (2.10b), and using (2.10d), (4.2c), and (4.5d) we readily obtain

$$\beta_j^2(t) = \frac{\|\partial_{x_j} \phi(\cdot, t)\|_{0,\Delta}^2}{\|\sigma(x_j)\|_{0,\Delta}^2} \leq \frac{C}{h^2} \|u\|_{p+1,\Delta}^2, \quad j = 1, 2, \quad t \geq 0. \quad (4.27)$$

Combining (4.26) and (4.27)

$$\sum_{i=1}^N [b_{ji}^2(t) + \beta_{ji}^2(t)] \leq \frac{C(u)}{h^2}, \quad t > t_0. \quad (4.28)$$

Applying the Schwarz inequality

$$\sum_{i=1}^N [\beta_{ji}^2(t) - b_{ji}^2(t)] \leq C \left[ \sum_{i=1}^N (\beta_{ji}(t) - b_{ji}(t))^2 \right]^{1/2} \left[ \sum_{i=1}^N (\beta_{ji}^2(t) + b_{ji}^2(t)) \right]^{1/2} \quad (4.29)$$

while using (4.11a) and (4.28) leads to (4.11b).  $\square$

We are now in position to state and prove the main result of this section.

**THEOREM 4.1.** *Let  $u \in H_0^1 \cap H^{p+2}$  and  $U \in S_0^{N,p}$  be solutions of (2.2) and (2.3), respectively. If  $p \geq 2$  is an even integer and there is a constant  $C > 0$  such that  $\|\partial_t^n e\|_1 \leq C(u)$ ,  $n = 0, 1$ , then there exist constants  $C > 0$  and  $t_0 > 0$  such that*

$$\|e(\cdot, t)\|_1^2 = \|E(\cdot, t)\|_1^2 + \varepsilon, \quad t > t_0, \quad (4.30a)$$

where

$$\|E(\cdot, t)\|_1^2 = \sum_{i=1}^N \sum_{j=1}^2 b_{ji}^2(t) \|\sigma(x_j)\|_{0,\Delta_i}^2, \quad |\varepsilon| \leq C h^{2p+1}. \quad (4.30b,c)$$

*Proof.* Consider the identity

$$\|e(\cdot, t)\|_1^2 = \sum_{i=1}^N \iint_{\Delta_i} (|\partial_{x_1} e|^2 + |\partial_{x_2} e|^2) dx_1 dx_2 + \|e\|_0^2 \quad (4.31)$$

and use (2.10b) and (2.15) to obtain

$$\|e\|_1^2 = \sum_{i=1}^N \iint_{\Delta_i} \sum_{j=1}^2 [\beta_{ji}^2 \sigma^2(x_j) + |\partial_{x_j} \theta|^2 + 2\partial_{x_j} \phi \partial_{x_j} \theta] dx_1 dx_2 + \|e\|_0^2. \quad (4.32)$$

Adding and subtracting  $b_{ji}^2 \sigma^2(x_j)$ ,  $j = 1, 2$ , to the above integrand yields (4.30a,b) with

$$\varepsilon = \sum_{i=1}^N \sum_{j=1}^2 \iint_{\Delta_i} [(\beta_{ji}^2 - b_{ji}^2) \sigma^2(x_j) + |\partial_{x_j} \theta|^2 + 2\partial_{x_j} \phi \partial_{x_j} \theta] dx_1 dx_2 + \|e\|_0^2. \quad (4.33)$$

Applying the Schwarz and triangular inequalities and using the estimates (2.13c,d), (4.11b) and (4.5d) yields (4.30c).  $\square$

**4.2 The Elliptic error Estimate.** As in §4.1, we further simplify the elliptic error estimation problem by neglecting the off-diagonal diffusion coefficients and the reaction term in the strain energy and by freezing the diagonal coefficients. With these approximations,  $b_j(t)$ ,  $j = 1, 2$ , is determined from (4.4) as

$$b_j = \frac{g_{\Delta}(t, v_j)}{\bar{a}_{j,j} \iint_{\Delta} \sigma^2(x_j) \delta(x_{(j \bmod 2)+1}) dx_1 dx_2}, \quad t > 0, \quad j = 1, 2. \quad (4.34)$$

Substituting (2.15) into (4.1a) while using (2.10b) yields

$$\bar{a}_{j,j} \beta_j(t) \iint_{\Delta} \sigma^2(x_j) \delta(x_{(j \bmod 2)+1}) dx_1 dx_2 = g(t, v_j) - \hat{F}_j(t) \quad (4.35a)$$

where

$$\hat{F}_j(t) = \iint_{\Delta} \left[ \sum_{k=1}^2 \sum_{l=1}^2 a_{k,l} \partial_{x_k} v_j \partial_{x_l} \theta + \sum_{k=1}^2 \sum_{l=1}^2 (a_{k,l} - \bar{a}_{k,l}) \partial_{x_k} v_j \partial_{x_l} \phi + b v_j e + v_j \partial_t e \right] dx_1 dx_2, \quad j = 1, 2. \quad (4.35b)$$

Write (4.35a) in the form

$$\beta_j = \frac{g_{\Delta}(t, v_j) - \hat{F}_j}{\bar{a}_{j,j} \iint_{\Delta} \sigma^2(x_j) \delta(x_{(j \bmod 2)+1}) dx_1 dx_2}, \quad j = 1, 2. \quad (4.36)$$

The analysis parallels that of §4.1 with a preliminary Lemma establishing differences between  $\beta_j(t)$  and  $b_j(t)$ ,  $j = 1, 2$ , and a subsequent Theorem containing the convergence result.

LEMMA 4.3. *Let  $p \geq 2$  be an even integer,  $u \in H_0^1 \cap H^{p+2}$ , and  $a_{k,k}(\mathbf{x}) > \alpha^0 > 0$ ,  $\mathbf{x} \in \Omega$ ,  $k = 1, 2$ . Then, there are constants  $C > 0$  such that*

$$\sum_{i=1}^N (\beta_{ji} - b_{ji})^2 \leq C(u), \quad \sum_{i=1}^N (\beta_{ji}^2 - b_{ji}^2) \leq \frac{C(u)}{h}, \quad j = 1, 2, \quad t > t_0. \quad (4.37a,b)$$

*Proof.* Subtracting (4.34) from (4.36) we obtain

$$\alpha_j(t) = -\frac{\hat{F}_j(t)}{\iint_{\Delta} \sigma^2(x_j) \delta(x_{(j \bmod 2)+1}) dx_1 dx_2}, \quad t \geq 0, \quad j = 1, 2, \quad (4.38)$$

with  $\alpha_j(t)$ ,  $j = 1, 2$ , given by (4.12). Applying the Schwarz and triangular inequalities to (4.38) while using (4.35b), the assumed smoothness of the diffusion coefficients, and the dominance of the  $H^1$  norm relative to the  $L^2$  norm yields

$$\alpha_j(t)^2 \leq C \|v_j\|_{1,\Delta}^2 \frac{[\|\theta\|_{1,\Delta}^2 + h^2 \|\phi\|_{1,\Delta}^2 + \|e\|_{0,\Delta}^2 + \|\partial_t e\|_{0,\Delta}^2]^2}{[\iint_{\Delta} \sigma^2(x_j) \delta(x_{(j \bmod 2)+1}) dx_1 dx_2]^2}, \quad j = 1, 2. \quad (4.39)$$

Summing over the elements and using (4.5)

$$\sum_{i=1}^N \alpha_{j,i}(t)^2 \leq Ch^{-2(p+1)} [\|\theta\|_1^2 + h^2 \|\phi\|_1^2 + \|e\|_0^2 + \|\partial_t e\|_0^2], \quad t \geq 0. \quad (4.40)$$

Using (2.7b) and (2.13c,d), we establish (4.37a).

Applying the same reasoning that was used to obtain (4.22-26), we obtain

$$b_j(t)^2 \leq Ch^{-2(p+1)} [\|\partial_t e\|_{0,\Delta}^2 + \|e\|_{1,\Delta}^2], \quad j = 1, 2, \quad t \geq 0. \quad (4.41)$$

Summing over the elements while using (2.7b,c)

$$\sum_{i=1}^N b_{ji}(t)^2 \leq \frac{C(u)}{h^2}, \quad t > t_0, \quad j = 1, 2. \quad (4.42)$$

Combining (4.27) and (4.42)

$$\sum_{i=1}^N [b_{ji}^2(t) + \beta_{ji}^2(t)] \leq \frac{C(u)}{h^2}, \quad t > t_0. \quad (4.43)$$

Using (4.29) with (4.37a) and (4.43) establishes (4.37b).  $\square$

**THEOREM 4.2.** *Let  $u \in H_0^1 \cap H^{p+2}$  and  $U \in S_0^{N,p}$  be solutions of (2.2) and (2.3), respectively. If  $p \geq 2$  is an even integer, then there exist constants  $C > 0$  and  $t_0 > 0$  such that*

$$\|e(\cdot, t)\|_1^2 = \|E(\cdot, t)\|_1^2 + \varepsilon, \quad t > t_0, \quad (4.44a)$$

where

$$\|E(\cdot, t)\|_1^2 = \sum_{i=1}^N \sum_{j=1}^2 b_{ji}^2(t) \|\sigma(x_j)\|_{0,\Delta_i}^2, \quad |\varepsilon| \leq Ch^{2p+1}. \quad (4.44b,c)$$

*Proof.* The proof is the same as that of Theorem 4.1.  $\square$

**5. Examples.** We present four examples to illustrate the performance of the error estimation procedures of §3 and §4 in situations where the theory applies and does not apply. Accuracy of the error estimate is measured by the global and local *effectivity indices*

$$\eta = \frac{\|E(\cdot, t)\|_1}{\|e(\cdot, t)\|_1}, \quad \eta_i = \frac{\|E(\cdot, t)\|_{1,\Delta_i}}{\|e(\cdot, t)\|_{1,\Delta_i}}, \quad i = 1, 2, \dots, N, \quad (5.1)$$

respectively, which should converge to unity under mesh refinement. In all cases, even-order results are presented for the elliptic error estimation procedure. Results with the parabolic error estimation procedure are virtually identical.

*Example 1.* The theory applies to the linear heat conduction equation

$$\partial_t u - \Delta u = f(x, t), \quad x \in (0, 1) \times (0, 1), \quad t > 0, \quad (5.2a)$$

with  $f(x, t)$  and the initial and the Dirichlet boundary conditions specified so that the exact solution is

$$u(\mathbf{x}, t) = \cos(t) e^{-10[(x-\frac{1}{2})^2 - (y-\frac{1}{2})^2]}. \quad (5.2b)$$

We solved this problem on  $0 < t \leq 0.5$  using uniform meshes having  $N = 100, 400, 900$ , and  $1600$  square elements and uniform orders  $p = 1, 2, 3, 4$ . Temporal integration was performed using the backward difference software system DASSL [13] with error tolerances of  $10^{-6}$  for  $p = 1, 2$  and  $10^{-10}$  for  $p = 3, 4$ , which should minimize temporal discretization errors and enable us to concentrate on spatial errors. Finite element errors and effectivity indices at  $t = 0.5$  appear in Table 1. Numbers in parenthesis indicate a power of ten.

Effectivity indices are in excess of 95% of ideal for all combinations of  $p$  and  $N$ . Convergence in  $h$  of the effectivity index to unity is apparent. Based on the limited data available in Table 1, convergence in  $p$  seems plausible for even orders but not so for odd orders.

*Example 2.* Convection is not supported by the theory, but the error estimates should work as long as convection does not dominate diffusion. Thus, consider a linear convection-diffusion equation

$$\partial_t u - \Delta u + \nabla \cdot u = f(\mathbf{x}, t), \quad \mathbf{x} \in (0, 1) \times (0, 1), \quad t > 0, \quad (5.3a)$$

with the data specified so that the exact solution is

$$u(\mathbf{x}, t) = \frac{1}{2}[1 - \tanh(10x_1 + 2x_2 - 10t - 2)]. \quad (5.3b)$$

We solved (5.3) using the parameters of Example 1. Finite element errors and effectivity indices at  $t = 0.5$  appear in Table 2. As conjectured, the effectivity index appears to be approaching unity as  $N$  increases. Effectivity indices are above 80% of ideal for almost all computations. Performance of the even-order error estimates is better than that of the odd-order estimates. Again, the even-order indices suggest possible convergence in  $p$ .

*Example 3.* Although the present theory does not apply to nonlinear problems, we



TABLE 1  
Errors and effectivity indices for Example 1 on  $N$ -element uniform meshes with piecewise bi- $p$  polynomial approximations.

$p$	1		2		3		4	
$N$	$\ e\ _1/\ u\ _1$	$\eta$	$\ e\ _1/\ u\ _1$	$\eta$	$\ e\ _1/\ u\ _1$	$\eta$	$\ e\ _1/\ u\ _1$	$\eta$
100	0.151(0)	0.988	0.137(-1)	0.9961	0.987(-3)	0.948	0.587(-4)	0.9991
400	0.757(-1)	0.998	0.345(-2)	0.9990	0.124(-3)	0.983	0.369(-5)	0.9998
900	0.505(-1)	0.999	0.154(-2)	0.9996	0.369(-4)	0.992	0.731(-6)	0.9999
1600	0.379(-1)	0.999	0.864(-3)	0.9998	0.156(-4)	0.995	0.231(-6)	0.9999

TABLE 2  
Errors and effectivity indices for Example 2 on  $N$ -element uniform meshes with piecewise bi- $p$  polynomial approximations.

$p$	1		2		3		4	
$N$	$\ e\ _1/\ u\ _1$	$\eta$	$\ e\ _1/\ u\ _1$	$\eta$	$\ e\ _1/\ u\ _1$	$\eta$	$\ e\ _1/\ u\ _1$	$\eta$
100	0.239(0)	0.739	0.504(-1)	0.885	0.958(-2)	0.426	0.177(-2)	0.920
400	0.118(0)	0.928	0.127(-1)	0.970	0.125(-2)	0.754	0.118(-3)	0.979
900	0.785(-1)	0.968	0.569(-2)	0.987	0.377(-3)	0.880	0.238(-4)	0.991
1600	0.589(-1)	0.981	0.320(-2)	0.992	0.160(-3)	0.930	0.331(-4)	0.995

TABLE 3  
Errors and effectivity indices for Example 3 on  $N$ -element uniform meshes with piecewise bi- $p$  polynomial approximations.

$p$	1		2		3		4	
$N$	$\ e\ _1/\ u\ _1$	$\eta$	$\ e\ _1/\ u\ _1$	$\eta$	$\ e\ _1/\ u\ _1$	$\eta$	$\ e\ _1/\ u\ _1$	$\eta$
100	0.262(-1)	0.949	0.872(-3)	0.995	0.278(-4)	0.920	0.848(-6)	0.999
400	0.129(-1)	0.977	0.218(-3)	0.999	0.348(-5)	0.966	0.530(-7)	1.000
900	0.858(-2)	0.985	0.963(-4)	0.999	0.103(-5)	0.979	0.105(-7)	1.000
1600	0.643(-2)	0.989	0.544(-4)	1.000	0.436(-6)	0.979	0.331(-8)	1.000

expect good results when the nonlinearity is not strong and when the solution is smooth.

Thus, consider the reaction-diffusion equation

$$\partial_t u - \frac{1}{2} \Delta u = qu^2(1-u), \quad x \in (0,1) \times (0,1), \quad t > 0, \quad (5.4a)$$

with  $q \geq 0$  and the data specified so that the exact solution is

$$u(x,t) = \frac{1}{1 + e^{\sqrt{q/2}(x_1 + x_2 - t\sqrt{q/2})}}. \quad (5.4b)$$

We selected  $q = 20$  and solved (5.4) on  $0 < t \leq 0.5$  using the parameters of Example 1. Temporal tolerances were selected as  $10^{-10}$  for  $p = 1, 2, 3$ ,  $10^{-12}$  for  $p = 4$  and the three coarser meshes, and  $10^{-14}$  for  $p = 4$  and the finest mesh.

Finite element errors and effectivity indices at  $t = 0.5$  are presented in Table 3. The performance of the error estimation procedures is excellent, with effectivity indices in excess of 90% of ideal for all choices of  $N$  and  $p$ . As with the previous examples, convergence in  $h$  is apparent

*Example 4.* as a final example, consider a linear heat conduction equation of the form (5.2a) with the data specified so that the exact solution (expressed in polar coordinates) is

$$u(x, t) = u(r, \phi, t) = r^{\omega(t)} \sin \omega(t) \phi, \quad \omega(t) = (2/3) + (1/4) \sin t. \quad (5.5)$$

This solution behaves as  $O(r^{\omega(t)})$  near the origin and this singular behavior will limit the rate of convergence in  $h$ . Unless the singularity is resolved by, e.g., grading the mesh, it will "pollute" the solution and error estimate globally. Our local error estimates fail to recognize such pollution errors and may be expected to give poor performance in their presence. Were the singularity resolved to the point where the pollution errors are small relative to the local errors, we would expect reasonable accuracy.

Let us begin by solving (5.2a, 5) on  $0 < t \leq 0.3$  using the uniform meshes and polynomial degrees specified with Example 1. Temporal tolerances are  $10^{-4}$ ,  $10^{-6}$ ,  $10^{-7}$ , and  $10^{-10}$  for  $p = 1, 2, 3, 4$ , respectively. Errors and effectivity indices at  $t = 0.3$  are shown in Table 4 for all combinations of  $N$  and  $p$ . Similar data at  $t = 0.0, 0.1, 0.2$ , and  $0.3$  for a 400-element uniform mesh with  $p = 1, 2, 3, 4$  are shown in Table 5. Errors in the local  $H^1$  norm and the difference between the local effectivity indices and unity at  $t = 0.3$  for a 100-element mesh with  $p = 4$  are shown in Figure 1.

Results in Tables 4 and 5 indicate that error estimates have little to do with exact errors. An examination of the upper portion of Figure 1 reveals that large errors near the

TABLE 4  
Errors and effectivity indices for Example 4 on  $N$ -element uniform meshes with piecewise bi- $p$  polynomial approximations.

$p$	1		2		3		4	
$N$	$\ e\ _1/\ u\ _1$	$\eta$	$\ e\ _1/\ u\ _1$	$\eta$	$\ e\ _1/\ u\ _1$	$\eta$	$\ e\ _1/\ u\ _1$	$\eta$
100	0.376(-1)	0.563	0.151(-1)	0.319	0.938(-2)	0.075	0.681(-2)	0.078
400	0.229(-1)	0.581	0.112(-1)	0.319	0.561(-2)	0.075	0.407(-2)	0.078
900	0.171(-1)	0.589	0.906(-2)	0.319	0.416(-2)	0.075	0.302(-2)	0.078
1600	0.138(-1)	0.593	0.768(-2)	0.319	0.336(-2)	0.075	0.244(-2)	0.078

TABLE 5  
Errors and effectivity indices for Example 4 at  $t = 0.0, 0.1, 0.2, 0.3$  on a 400-element uniform mesh with  $p = 1, 2, 3, 4$ .

$p$	1		2		3		4	
$N$	$\ e\ _1/\ u\ _1$	$\eta$	$\ e\ _1/\ u\ _1$	$\eta$	$\ e\ _1/\ u\ _1$	$\eta$	$\ e\ _1/\ u\ _1$	$\eta$
0.0	0.372(-1)	0.519	0.204(-1)	0.268	0.111(-1)	0.054	0.841(-2)	0.064
0.1	0.317(-1)	0.541	0.168(-1)	0.288	0.889(-2)	0.069	0.663(-2)	0.071
0.2	0.270(-1)	0.561	0.137(-1)	0.303	0.708(-2)	0.072	0.520(-2)	0.074
0.3	0.229(-1)	0.581	0.112(-1)	0.319	0.561(-2)	0.075	0.407(-2)	0.078

singularity pollute the entire domain and result in large deviations from unity of local effectivity indices everywhere [7]. As anticipated, the solution is converging as  $O(h^{\omega(t)})$ .

In order to improve the performance of the error estimations, we solve (5.2a, 5) on graded meshes obtained by refining the element of a uniform mesh that is closest to the origin. We do this by dividing the two element edges along the coordinate axis into the  $n$  segments

$$\xi_j = h(j/n)^\zeta, \quad j = 0, 1, \dots, n, \quad \zeta > 0; \quad (5.6)$$

introducing a diagonal from from  $(\xi_1, \xi_1)$  to  $(h, h)$ ; and connecting line segments at the points (5.6) along the axes to similarly spaced points on the diagonal. This mesh, referred to as  $N:n$ , has  $N$  square and  $2(n-1)$  trapezoidal elements. The mesh shown in the lower portion of Figure 1 is one uniform refinement of the 25:5 mesh. Error estimates can be constructed for these quadrilateral elements by introducing minor modifications to the

formulas developed here [1].

We solve (5.2a, 5) on  $0 < t \leq 0.3$  using the meshes 25:5, 100:10, 225:15, and 400:20 with  $p$  ranging from 1 to 4. The grading parameter  $\zeta$  was selected as  $3/2$  for  $p = 1$  and  $9p/4$  otherwise. Temporal tolerances are the same as the uniform-mesh case. Errors and effectivity indices at  $t = 0.3$  are presented for all mesh and order combinations in Table 6. Similar data at  $t = 0.0, 0.1, 0.2$ , and  $0.3$  on the 132-element mesh appear in Table 7. Local errors and the difference between local effectivity indices and unity are shown in the lower portion of Figure 1.

The severe mesh grading has reduced errors on the element adjacent to the singularity. This has substantially reduced global pollution errors and improved the performance of the error estimation procedures. Global effectivity indices are within 12% of unity.

TABLE 6  
*Errors and effectivity indices for Example 4 on  $N$ -element graded meshes with piecewise bi- $p$  polynomial approximations.*

$p$	1		2		3		4	
$N$	$\ e\ _1/\ u\ _1$	$\eta$	$\ e\ _1/\ u\ _1$	$\eta$	$\ e\ _1/\ u\ _1$	$\eta$	$\ e\ _1/\ u\ _1$	$\eta$
132	0.181(-1)	0.999	0.118(-2)	0.941	0.369(-3)	3.431	0.234(-3)	0.879
472	0.112(-1)	1.004	0.468(-3)	1.016	0.453(-4)	1.279	0.682(-5)	1.039
1012	0.862(-2)	0.991	0.336(-3)	1.017	0.300(-4)	1.066	0.230(-5)	1.121
1752	0.704(-2)	0.993	0.271(-3)	1.017	0.241(-4)	0.989	0.177(-5)	1.080

TABLE 7  
*Errors and effectivity indices for Example 4 on a 472-element graded mesh with  $p = 1, 2, 3, 4$ .*

$p$	1		2		3		4	
$N$	$\ e\ _1/\ u\ _1$	$\eta$	$\ e\ _1/\ u\ _1$	$\eta$	$\ e\ _1/\ u\ _1$	$\eta$	$\ e\ _1/\ u\ _1$	$\eta$
0.0	0.156(-1)	1.024	0.713(-3)	1.017	0.760(-4)	1.304	0.121(-4)	1.024
0.1	0.139(-1)	1.025	0.624(-3)	1.017	0.642(-4)	1.297	0.100(-4)	1.035
0.2	0.125(-1)	1.019	0.541(-3)	1.016	0.540(-4)	1.288	0.827(-5)	1.029
0.3	0.112(-1)	1.004	0.468(-3)	1.016	0.453(-4)	1.279	0.682(-5)	1.039

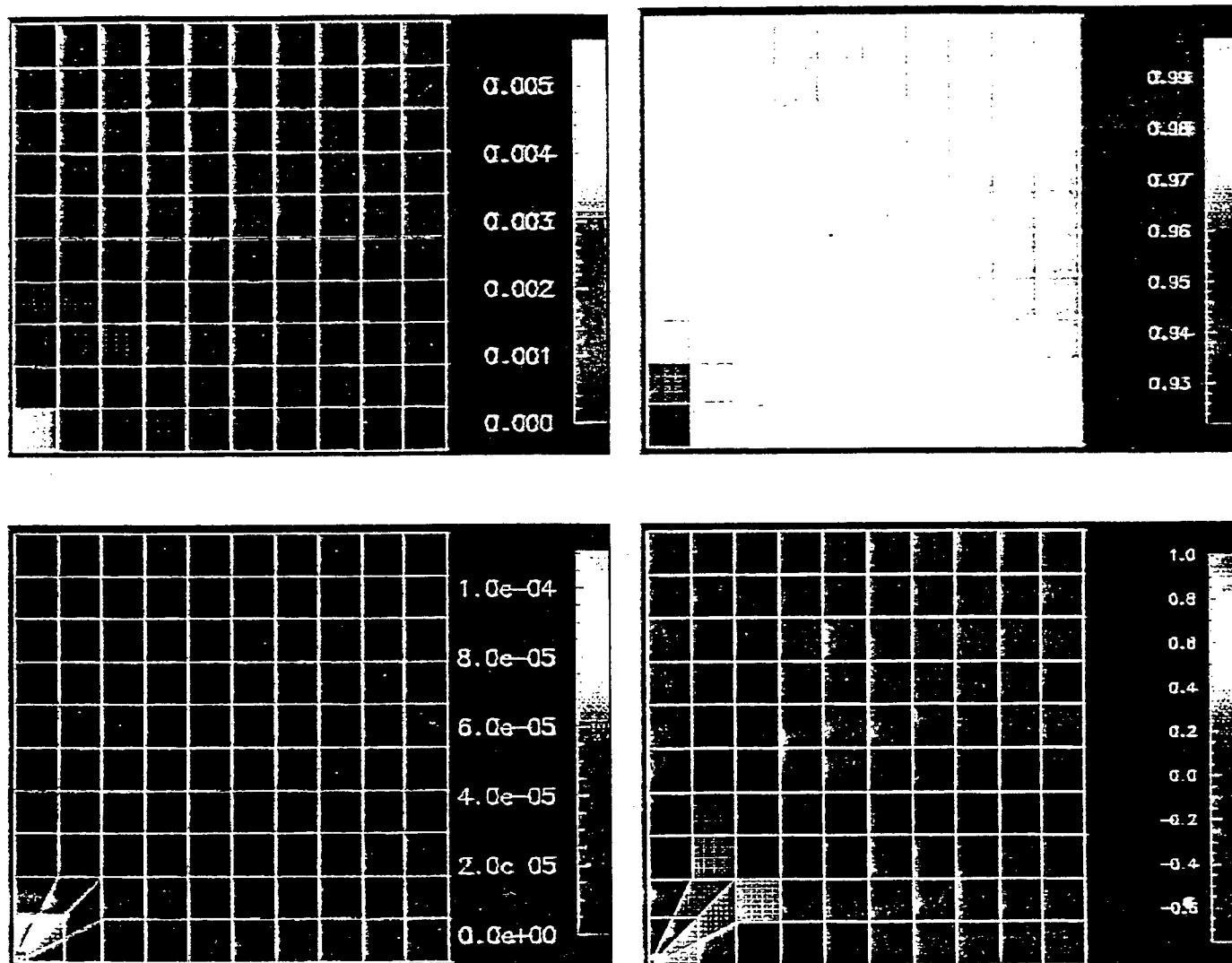


FIG. 1. Local errors (upper-left) and the difference between the local effectivity indices and unity (upper-right) for Example 4 at  $t = 0.3$  on a uniform 100-element mesh using piecewise bi-quartic polynomial approximations. Similar data for computations performed on a graded 5.5 mesh that has been uniformly refined are shown at the bottom.

**6. Discussion.** We have developed simple a posteriori procedures for estimating spatial discretization errors of piecewise bi- $p$  polynomial finite element solutions of linear parabolic partial differential equations. The theory developed for square-element meshes easily extends to rectangles. As earlier work [10, 18, 19] would suggest, the error estimation procedures divide into distinct classes for odd- and even-order approximations. Error estimates for each are asymptotically exact and involve only element level computations with, at most, nearest-neighbor communications.

The error estimates for even values of  $p$  perform better than that for odd  $p$ . Results indicate that asymptotic correctness under  $p$ -refinement is possible for even  $p$ . This is not the case for odd  $p$  where results deteriorate with increasing polynomial degree. Computational evidence further suggests that the error estimates are asymptotically correct under more general conditions than indicated by the present theory. Indeed, results of Example 4 indicate that the error estimates are asymptotically correct on graded quadrilateral-element meshes in the presence of singularities. Adjerid et al. [1] show that the error estimation procedures apply to finite element spaces other than piecewise bi- $p$  polynomials. In particular, they apply to a class of piecewise hierarchical functions that have been modified by adding "bubble functions" to a standard hierarchical basis [14].

Extending the present theory to three-dimensional linear problems on hexahedral element-meshes would be straight forward. It would be more interesting and difficult to establish correctness of the error estimates on arbitrarily graded triangular- and tetrahedral-element meshes. Nonlinearity, strong reactions, convective influences, and singularities would be other important considerations.

## REFERENCES

- [1] S. Adjerid, B. Belguendouz, and J.E. Flaherty, *A posteriori finite element error estimation for diffusion problems*, SCOREC Rep. No. 9-1996, Sci. Comput. Res. Ctr., Rensselaer Polytechnic Institute, Troy, 1996.

- [2] S. Adjerid and J.E. Flaherty, *A moving mesh finite element method with local refinement for parabolic partial differential equations*, Comp. Meths. Appl. Mech. and Engrg., 55 (1986), pp. 3-26.
- [3] S. Adjerid, J.E. Flaherty, and Y.J. Wang, *A posteriori error estimation with finite element methods of lines for one-dimensional parabolic systems*, Numer. Math. 65 (1993), pp. 1-21.
- [4] P.L. Baehmann, M.S. Shephard, and J.E. Flaherty, *Adaptive analysis for automated finite element modeling*, The Mathematics of Finite Elements and Applications VI, J.R. Whiteman, Ed., Academic Press, London, pp. 521-532, 1988.
- [5] I. Babuška, J. Chandra, and J.E. Flaherty, Eds., *Adaptive Computational Methods for Partial Differential Equations*, SIAM, Philadelphia, 1983.
- [6] I. Babuška and W.C. Reinboldt, *Reliable error estimation and mesh adaptation for the finite element method*, in Computational Methods in Nonlinear Mechanics, J.T. Oden, Ed., North-Holland, Amsterdam, 1980, pp. 67-108.
- [7] I. Babuška, T. Strouboulis, A. Mathur, and C.S. Upadhyay, *Pollution-error in the h-version of the finite-element method and the local quality of a-posteriori error estimators*, Finite Elem. Anal. Des., 17 (1994), 273-321.
- [8] I. Babuška, T. Strouboulis, and C.S. Upadhyay, *A model study of the quality of a-posteriori estimators for linear elliptic problems. Part Ia: Error estimation in the interior of patchwise uniform grids of triangles*, Tech. Note BN-1147, Inst. Physical Sci. and Tech., University of Maryland, College Park, 1993.
- [9] I. Babuška, T. Strouboulis, C.S. Upadhyay, S.K. Gangaraj, and K. Copps, *Validation of a-posteriori error estimators by numerical approach*, Tech. Note BN-1151, Inst. Physical Sci. and Tech., University of Maryland, College Park, 1993.

- [10] I. Babuška and D. Yu, *Asymptotically exact a-posteriori error estimator for biquadratic elements*, Finite Elem. Anal. Des., 3 (1987), 341-354.
- [11] A.V. Ilin, B. Bagheri, R.W. Metcalfe, and L.R. Scott, *Error control and mesh optimization for high-order finite element approximation of incompressible viscous flow*, Comp. Meths. Appl. Mech. and Engrg., 1997, to appear.
- [12] J.T. Oden and G.F. Carey, *Finite Elements: Mathematical Aspects. Vol. IV*, Prentice-Hall, Englewoods Cliffs, 1983.
- [13] L.R. Petzold, *A description of DASSL: a differential/algebraic system solver*, Rep. Sand. 82-8637, Sandia National Laboratory, Livermore, 1982.
- [14] B.A. Szabo and I. Babuška. *Introduction to Finite Element Analysis*, (J. Wiley and Sons, New York, 1991).
- [15] V. Thomée, *Negative norm estimates and superconvergence in Galerkin Methods for parabolic problems*, Maths. Comp., 34 (1980), pp. 93-113.
- [16] R. Verfürth, *A review of a posteriori error estimation and adaptive mesh-refinement techniques*, preprint, Institut für Angewandte mathematik, Universität Zürich, Zürich, 1992.
- [17] R. Wait and A.R. Mitchell, *Finite Element Analysis and Applications*, John Wiley and Sons, Chichester, 1985.
- [18] D. Yu, *Asymptotically exact a-posteriori error estimator for elements of bi-even degree*, Mathematica Numerica Sinica, 13 (1991), pp. 89-101.
- [19] D. Yu, *Asymptotically exact a-posteriori error estimator for elements of bi-odd degree*, Mathematica Numerica Sinica, 13 (1991), pp. 307-314.



# Mechanics of hot isostatic pressing in intermetallic matrix composites

Y. A. BAHEI-EL-DIN

*Structural Engineering Department, Cairo University, Giza, Egypt*

G. J. DVORAK, J. F. WU\*

*Department of Civil and Environmental Engineering, Rensselaer Polytechnic Institute, Troy, NY 12180, USA*

Thermal residual and mechanical stresses generated by hot isostatic pressing, cooling and subsequent mechanical loading of SCS6/Ni<sub>3</sub>Al and SCS6/Ti<sub>3</sub>Al composites with uncoated and carbon-coated fibres have been simulated by micromechanical modelling. The solutions were found in a periodic hexagonal array model of the microstructure with the finite element method. The intermetallic matrices were assumed to be elastic-plastic, with temperature-dependent properties. The fibre and coating were assumed to be elastic. Local stress fields and overall response were found for several processing sequences. The results suggest that plastic deformation of the matrix during cooling from fabrication temperatures reduces residual stresses. The Ni<sub>3</sub>Al matrix system yields more easily than the Ti<sub>3</sub>Al system. HIP programmes that promote such yielding are proposed and analysed in both systems. Compliant and expansive fibre coatings tend to reduce the thermal stresses, but may also enhance the interface stresses in the matrix under overall mechanical loads.

## 1. Introduction

One of the factors affecting the overall response and damage and failure resistance of composite materials is the residual stress field caused by pressure and temperature histories applied in fabrication, processing and subsequent cooling. The distribution and magnitude of such stresses is affected by the thermo-mechanical compatibility of the phases, and by the inelastic deformation that may take place under certain loading conditions in some systems. Understanding of the various factors involved is possible only with reasonably detailed modelling of the fabrication, processing and loading sequences.

The present work examines local stresses in SCS6/Ni<sub>3</sub>Al and SCS6/Ti<sub>3</sub>Al intermetallic matrix composites reinforced by coated and uncoated fibres, under thermal changes, mechanical loads, and thermomechanical loading conditions which simulate fabrication by hot isostatic pressing (HIP). The effect of fibre coating, matrix plasticity, and standard and modified HIP parameters is considered. The results focus primarily on understanding the mechanics of the HIP process and the role of the various parameters involved.

Section 2 describes the micromechanical model used in this study and the constitutive equations of the phases; Section 3 presents the material properties of the phases. The local stress concentrations found in unidirectional composites reinforced by coated and

uncoated fibres under mechanical or thermal loads are presented in Section 4. The main results of interest appear in Section 5, where we evaluate the stresses created in the two systems during standard and modified hot isostatic pressing procedures, and in subsequent mechanical loading or reheating to processing temperatures. Significantly different outcomes are found for different HIP parameters. Interpretation of the results by several models shows that higher pressures and axisymmetric rather than isotropic overall stress states promote plastic straining of the matrix and thus help to reduce the magnitudes of the residual fields.

## 2. Evaluation of local fields in fibrous media

### 2.1. Micromechanical models

The overall response and local fields in fibrous composites can be predicted by several material models which offer various approximations of the microgeometry, phase constitutive behaviour, and loading conditions. In elastic composites, the local moduli do not change during deformation, hence acceptable estimates can be found using approaches that rely on averages of local fields in the phases, such as the self-consistent [1] or Mori-Tanaka [2-4] models. Analogous techniques are available for inelastic composites. However, because the instantaneous moduli

\*Present address: ABS Americas, The American Bureau of Shipping, 263 North Belt East, Houston, TX 77060, USA.

of the inelastic phases depend on the local deformation history, the overall response may not be well represented by averages of the local fields. Indeed, a recent comparison [5] of several micromechanical models with experiments indicated substantial deviations of certain predictions from observed behaviour. This was true in particular for the self-consistent and Mori-Tanaka models. Our bimodal plasticity theory [6] provided good predictions of the observed yield surfaces, but not of overall plastic strains. This is readily understood if the overall surface is regarded as a locus of vertices of yield cones formed by clusters of yield surfaces of matrix subelements in the overall stress space, so that the plastic strain increment vectors are contained within cones of normals at each loading point [7]. Most reliable predictions are offered by models that can approximate the actual local stress and strain fields. Those are typically discretized unit cell models, such as the periodic hexagonal array model [8, 9], or its rectangular array analogous [10, 11]. Under remotely applied uniform stress or strain, one can identify a representative unit cell, derive periodic boundary conditions for the cell, discretize the volume and evaluate the local fields in terms of piecewise uniform estimates by the finite element method or by the transformation field analysis [12]. A survey of the above models can be found in the reviews by Bahei-El-Din and Dvorak [13] and Dvorak [14].

The present work employs the periodic hexagonal array (PHA) model developed by Dvorak and Teply [8, 9]. In a series of recent publications, advanced constitutive equations for elastic-plastic and viscoplastic phases have been implemented in this model [15, 16] and predictions were verified by comparisons with experimental results [5, 16-19]. The microstructural geometry in the transverse plane of a unidirectionally reinforced fibrous composite is represented by a periodic distribution of the fibres in a hexagonal array. The fibre cross-sections are approximated by

$(n \times 6)$ -sided polygons. Examples of the PHA microgeometry with hexagonal and dodecagonal fibre cross-sections are shown in Fig. 1. The hexagonal array is divided into two kinds of unit cell, as indicated by the shaded and unshaded triangles. Under overall uniform stresses or strains, the internal fields of the two sets of unit cells are related by a simple transformation. Accordingly, for uniform overall stresses or strains applied to the aggregate, only one unit cell selected from either set needs to be analysed under certain displacement boundary conditions which reflect periodicity of the local fields [9]. A three-dimensional view of the unit cell showing dimensions and support conditions is given in Fig. 2 for a fibre with hexagonal cross-section.

The actual analysis was performed by the finite element method. The unit cell was subdivided into a selected number of subelements in the matrix, fibre, and coating subdomains. The degree of mesh refinement may vary from a few elements in each subdomain to several hundred elements. In general, evaluation of the internal fields in the phases and at their interfaces requires a large number of elements [20], whereas the overall response can be adequately predicted with few elements [15, 20]. Examples of various degrees of mesh refinements are shown in Fig. 3. In the present study we implemented the PHA microgeometry in the ABAQUS finite element program [21] for the mesh shown in Fig. 3b.

## 2.2. Phase constitutive equations

The fibre and coating, if any, are assumed to be elastic and transversely isotropic. The matrix is assumed to be isotropic in the elastic deformation range confined within a current yield surface. The thermoelastic properties of the phases are, in general, functions of temperature. Using contracted notation, let  $d\sigma_r = [d\sigma_1 d\sigma_2 d\sigma_3 d\sigma_4 d\sigma_5 d\sigma_6]^T$ ,  $d\epsilon_r = [d\epsilon_1 d\epsilon_2 d\epsilon_3 d\epsilon_4 d\epsilon_5 d\epsilon_6]^T$ , denote the stress and strain

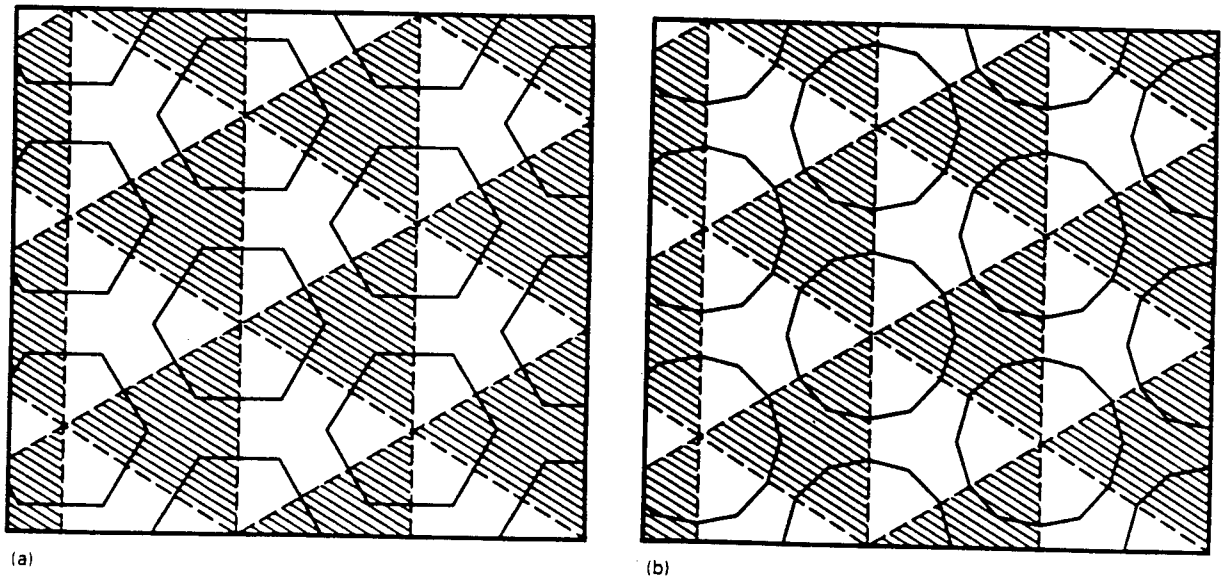


Figure 1 Transverse cross sections of the PHA microgeometry with (a) hexagonal and (b) dodecagonal cylindrical fibres.

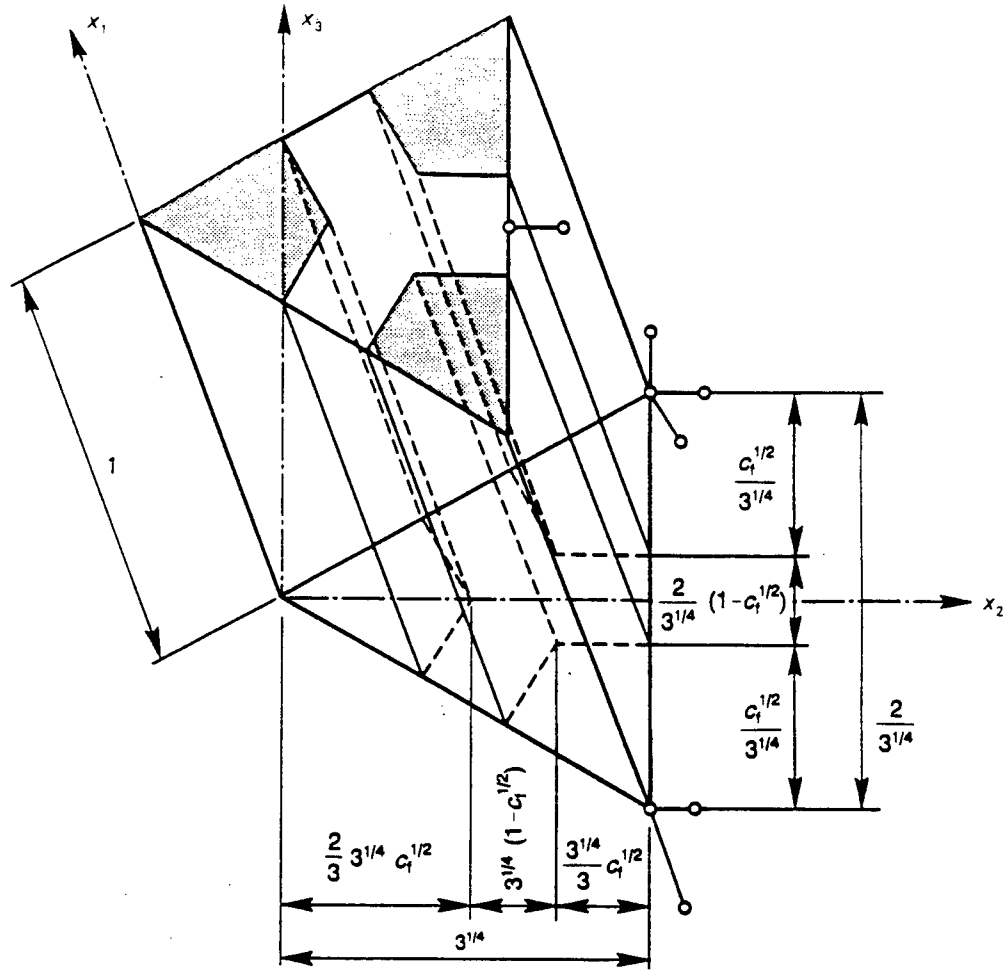


Figure 2 Geometry, dimensions and support conditions of the unit cell.

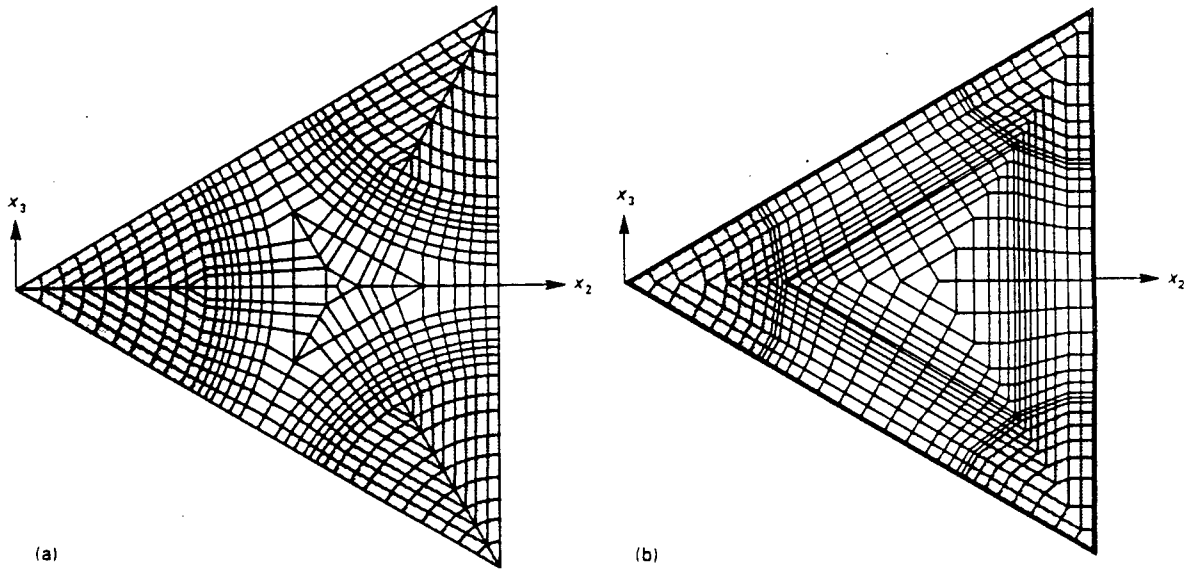


Figure 3 Examples of finite element meshes in the PHA unit cell.

increments in the fibre  $r = f$ , matrix  $r = m$ , or the coating  $r = c$ , in a Cartesian coordinate system  $x_j$ ,  $j = 1, 2, 3$ . In the presence of a temperature change,  $dT$ , the stress-strain relation for the elastic phases are

written in the incremental form [22,23]

$$d\epsilon_r = M_r^e(T) d\sigma_r + \bar{m}_r^e(T, \sigma_r) dT \quad (1)$$

$$d\sigma_r = L_r^e(T) d\epsilon_r + \bar{l}_r^e(T, \epsilon_r) dT \quad (2)$$

where

$$\tilde{m}_r^e(T, \sigma_r) = (\partial M_r^e / \partial T) \sigma_r + m_r^e(T) \quad (3)$$

$$\begin{aligned} \tilde{L}_r^e(T, \epsilon_r) &= (\partial L_r^e / \partial T) \left[ \epsilon_r - \int_{T_0}^T m_r(T) dT \right] - L_r^e(T) m_r(T) \\ &= -L_r^e(T) \tilde{m}_r^e(T) \end{aligned} \quad (4)$$

where  $L_r^e(T)$  is the phase elastic stiffness matrix,  $M_r^e(T) = [L_r^e(T)]^{-1}$  is the elastic compliance matrix,  $m_r(T) = [\alpha_A \alpha_T \alpha_T 0 0 0]^T$  is the thermal strain vector of linear thermal expansion coefficients for the axial and transverse directions, and  $T_0$  is the initial temperature. The dependence of the thermal strain on the current stress in Equation 3 satisfies the path independence requirement of the elastic solution. When integrated along the thermal loading path, Equations 1-4 provide uncoupled mechanical and thermal fields.

For a transversely isotropic phase with the axis of rotational symmetry  $x_1$ , the non-zero coefficients of the upper half of the symmetric stiffness matrix,  $L_r^e$ , at a given temperature are evaluated as

$$\begin{aligned} L_{11} &= n, \quad L_{22} = L_{33} = k + m, \quad L_{12} = L_{13} = l \\ L_{23} &= k - m, \quad L_{44} = m, \quad L_{55} = L_{66} = p \end{aligned} \quad (5)$$

The Hill's moduli [24]  $k$ ,  $l$ ,  $n$ ,  $m$ , and  $p$  of the phase are related to the engineering moduli by the relations

$$\begin{aligned} k &= -1 [(4/E_T) - (1/G_T) - (4\nu_L^2/E_T)] \quad l = 2k\nu_L \\ n &= E_L + l^2/k, \quad m = G_T, \quad p = G_L \end{aligned} \quad (6)$$

where the Young's modulus,  $E_L$ , shear modulus,  $G_L$ , the Poisson's ratio,  $\nu_L$ , refer to straining in the longitudinal direction, and  $E_T$ ,  $G_T$ ,  $\nu_T = (E_T/2G_T - 1)$  to the transverse plane.

The region of the elastic response of the matrix to thermomechanical loads is determined by certain conditions related to the existence of a yield surface  $f(\sigma_m, T) = 0$ . Assuming kinematic and isotropic hardening, the Mises yield surface is given by

$$\begin{aligned} f(\sigma_m, T) &\equiv \frac{1}{2} (s_m - \alpha_m) : (s_m - \alpha_m) \\ &\quad - (Y(T) + Q)^2 = 0 \end{aligned} \quad (7)$$

where  $s_m$  is the matrix deviatoric stress,  $\alpha_m$  is the centre of the yield surface,  $Y$  is the matrix yield stress in simple tension, and  $Q$  is isotropic stress function. In Equation 7, we used the notation  $(a:b)$  to denote the inner product of second order tensors  $a_{ij}$  and  $b_{ij}$ .

In particular, elastic response of the matrix obtains if  $f < 0$ , or if  $f = 0$  and  $[(\partial f / \partial \sigma_m) : d\sigma_m + (\partial f / \partial T) dT] \leq 0$  [25]. In this case, Equations 1-6 apply and the Hill's moduli in Equation 6 are given in terms of the bulk modulus,  $K_m$ , and shear modulus,  $G_m$ , of the isotropic matrix as  $k = G/(1 - 2\nu)$ ,  $l = K - 2G/3$ ,  $n = K + 4G/3$ ,  $m = p = G$ .

Elastic-plastic deformation takes place in the matrix if  $f = 0$  and  $[(\partial f / \partial \sigma_m) : d\sigma_m + (\partial f / \partial T) dT] > 0$ . The assumption is that the total strain increment can be additively decomposed into elastic and plastic components. The instantaneous response is then evaluated from Equations 1 and 2, providing that the elastic compliance matrix  $M_r^e$ , the stiffness matrix  $L_r^e$ , the thermal strain vector,  $\tilde{m}_r^e$ , and the thermal stress vector,  $\tilde{L}_r^e$ , are replaced by their instantaneous counter-

parts. The latter are written as [22, 26]

$$M_m = M_m^e + (3/2H)(n:n^T) \quad (8)$$

$$L_m = L_m^e - [2G_m/(1 + H/3G_m)](n:n^T) \quad (9)$$

$$\tilde{m}_m = \tilde{m}_m^e - ([3^{1/2} Y'(T)]/(2^{1/2} H))n \quad (10)$$

$$\begin{aligned} \tilde{L}_m &= [2G_m/(1 + H/3G_m)](n^T \tilde{m}_m^e \\ &\quad + [Y'(T)/6^{1/2} G_m]n - \tilde{L}_m^e \end{aligned} \quad (11)$$

$$H = [d\bar{\sigma} - Y'(T)dT]d\bar{\epsilon}^p \quad (12a)$$

$$d\bar{\sigma} = \left( \frac{3}{2} ds : ds \right)^{1/2} \quad (12b)$$

$$d\bar{\epsilon}^p = \left( \frac{2}{3} d\epsilon^p : d\epsilon^p \right)^{1/2} \quad (12c)$$

$$n = [1/(2/3)^{1/2} Y] [\bar{s}_{11} \bar{s}_{22} \bar{s}_{33} 2\bar{s}_{23} 2\bar{s}_{31} 2\bar{s}_{12}]^T$$

$$\bar{s} = \sigma_m - \alpha_m \quad (13)$$

where  $Y'(T) = dY/dT$ ,  $\epsilon^p$  is the plastic strain vector, and  $H$  is plastic tangent modulus of the stress-plastic strain curve. In Equation 9,  $n:n^T$  denotes the tensor product  $n_{ij}n_{kl}$ .

Evolution of the position of the centre of the matrix yield surface  $\alpha_m$ , the isotropic function  $Q$ , and the plastic tangent modulus  $H$  may take several different forms which are usually guided by experimental observations. In the present work we used the constitutive equations available in the ABAQUS finite element program. Specifically, we assumed linear hardening in which  $H$  is constant under isothermal loading, and specified translation of the yield surface by the Prager-Ziegler hardening rule. Except for variations of the yield stress  $Y$  caused by the temperature change, we neglected isotropic hardening of the yield surface. Other constitutive rules, such as the two-surface plasticity theory [27], could be applied as well; these would provide somewhat different magnitudes of the local fields.

### 3. The intermetallic matrix composite systems

Two intermetallic matrix composite materials reinforced by aligned continuous fibres are considered in the present study. One system has nickel aluminide (Ni<sub>3</sub>Al) matrix, the other a titanium aluminide (Ti<sub>3</sub>Al) matrix. Both systems are reinforced by silicon carbide fibre (SCS6) at 25% volume concentration. A 10  $\mu$ m thick carbon coating has been added to the fibres in some cases. The thermoelastic properties of the silicon carbide fibre and the carbon coating are taken as independent of temperature, and their specific magnitudes are given in Table I [28]. The thermoelastic properties of the two aluminide matrices vary with temperature as shown in Tables II and III [29, 30]. Variation of the Young's moduli and of the thermal expansion coefficients of the phases with temperature is shown in Figs 4 and 5, respectively, together with the Mori-Tanaka estimates of the overall moduli and expansion coefficients derived from these estimates. It is seen that the thermal coefficient mismatch between the phases in the nickel-based composite system is larger than that in the titanium-based system.

TABLE I Material properties of SCS6 fibre and carbon coating [28]

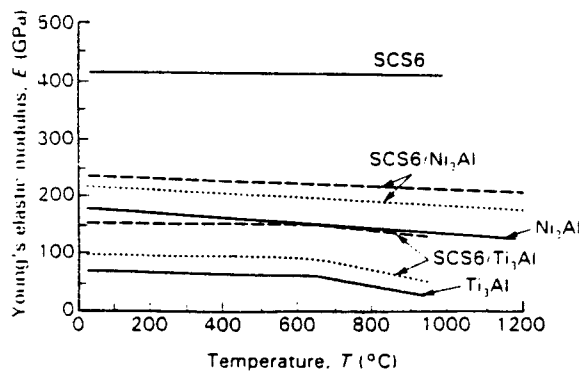
	$E_L$ (GPa)	$E_T$ (GPa)	$G_L$ (GPa)	$G_T$ (GPa)	$\nu_L$	$\alpha_L$ ( $10^{-6} \text{ } ^\circ\text{C}^{-1}$ )	$\alpha_T$ ( $10^{-6} \text{ } ^\circ\text{C}^{-1}$ )
SCS6 fibre	413.6	413.6	159.1	159.1	0.3	4.6	4.6
Carbon coating	172.4	6.9	14.5	3.8	0.3	1.8	28

TABLE II Material properties of  $\text{Ni}_3\text{Al}$  matrix [29]

$\theta$ ( $^\circ\text{C}$ )	$E$ (GPa)	$\nu$	$\alpha$ ( $10^{-6} \text{ } ^\circ\text{C}^{-1}$ )	$Y$ (MPa)	$H$ (GPa)
1200	134	0.32	20.6	137	6.70
994	142	0.32	19.0	279	7.10
776	150	0.32	17.2	459	7.50
673	154	0.32	16.4	557	7.70
642	155	0.32	16.1	564	7.75
578	158	0.32	15.6	535	7.90
376	165	0.32	14.3	356	8.25
327	167	0.32	14.0	279	8.35
206	172	0.32	13.4	156	8.60
127	175	0.32	13.0	110	8.75
21	179	0.32	12.5	79	8.95

TABLE III Material properties of  $\text{Ti}_3\text{Al}$  matrix [30]

$\theta$ ( $^\circ\text{C}$ )	$E$ (GPa)	$\nu$	$\alpha$ ( $10^{-6} \text{ } ^\circ\text{C}^{-1}$ )	$Y$ (MPa)	$H$ (GPa)
950	32.4	0.3	10.4	210	2.71
760	51.2	0.3	10.4	240	2.63
649	62.0	0.3	10.4	260	5.44
427	66.3	0.3	10.4	320	5.88
260	66.3	0.3	10.4	390	5.06
21	69.0	0.3	10.4	500	3.91

Figure 4 Elastic Young's moduli of the phases and composites (M-T estimates). (---)  $E_A$ , (---)  $E_T$ .

The yield stress,  $Y$ , and the plastic tangent modulus,  $H$ , of the  $\text{Ni}_3\text{Al}$  [29] and the  $\text{Ti}_3\text{Al}$  [30] matrices are shown in Tables II and III as function of temperature. The yield stress changes are shown in Fig. 6. The variation of the yield stress of the  $\text{Ni}_3\text{Al}$  matrix with temperature, which is not typical of intermetallic compounds, will be seen to cause early yielding of the

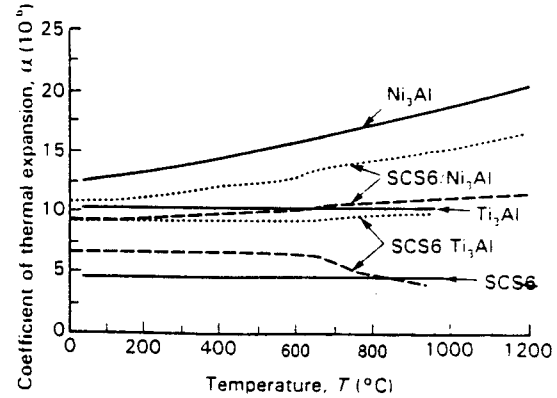
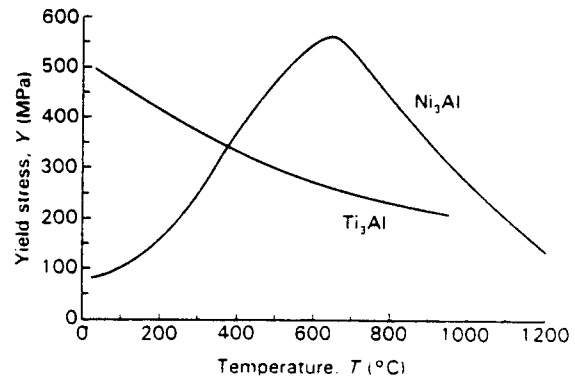
Figure 5 Coefficients of thermal expansion of the phases and composites. (M-T estimates) (---)  $\alpha_A$ , (---)  $\alpha_T$ .

Figure 6 Tensile yield stresses of the matrix materials.

nickel-based composite system during fabrication and thus reduce the local stresses in the matrix.

In a typical fabrication process of intermetallic matrix composites, particles of the matrix are sprayed on aligned fibres to create a monolayer composite [31, 32]. The required number of layers is then assembled and encapsulated in a hermetically sealed package consisting of stainless steel plates or tubes depending on the shape of the final product. The assembly is then consolidated by hot isostatic pressing (HIP) at a specified high temperature and hydrostatic pressure. After a predetermined time period, the HIP package is cooled down to room temperature and the pressure is simultaneously reduced to atmospheric pressure. Owing to the thermal mismatch present between the fibre and matrix phases, cooldown from the processing temperature cause internal stresses. Such local stresses may lead to localized effects such as yielding or damage, and thus alter the overall

performance of the composite. The following sections examine the local stress field in the two intermetallic matrix composites described above, after certain simple loading programs, and after several typical and modified HIP cycles applied during fabrication and processing. Modification of the HIP parameters and thermo-mechanical loading/unloading paths is explored to identify conditions that may lead to reduced residual stress fields.

#### 4. Stress concentrations in uncoated and coated fibre systems

##### 4.1. Elastic response

The local fields and the overall thermomechanical response of elastic composites reinforced by coated or uncoated fibres was evaluated by Benveniste *et al.* [4], Dvorak *et al.* [23], and Bahei-El-Din and Dvorak [33]. The latter, as well as our present study, also consider the effect of matrix plastic flow on the local stresses and on overall response. This section presents new data for the stresses in the above intermetallic composite systems subjected to thermal and mechanical loading. In contrast to elastic composites with constant moduli, the systems considered here have temperature-dependent properties. Therefore, all results are presented in terms of ratios of increments of local stresses to the increments of overall stress or temperature, at specified temperature. These ratios may be somewhat different at other temperatures, but they illustrate the magnitudes of changes of local fields under overall applied loads.

First, we examine the thermal and mechanical stresses generated in elastic systems at high temperature, and the overall elastic response over a range of temperatures. An initially stress-free state was assumed, and the magnitudes of thermoelastic phase moduli were taken at 1200 and 950 °C for the SCS6 Ni<sub>3</sub>Al and SCS6 Ti<sub>3</sub>Al composites, respectively. Small changes in temperature and transverse tensile stress were applied

in separate solutions for the unit cell shown in Fig. 3b, and the local fields were found using the ABAQUS finite element program. Among the six components of the local stress fields, of interest here are the contours of the ratios of the local transverse normal stress  $\Delta\sigma_{22}/\Delta T$  in the unit cell, shown in Figs 7 and 8 for systems with Ni<sub>3</sub>Al and Ti<sub>3</sub>Al matrices, respectively, and with uncoated and coated SCS6 fibres. Also of interest are the local to overall transverse normal stress ratios at room temperature, plotted in Figs 9 and 10. The dashed triangular boundary shown in Figs 7–10 indicates the unit cell used in the solution. The contours outside the unit cell were found from periodicity of the local stress field. The significant stress ratios found in these plots are listed in the top part of Table IV. Note that the transverse normal stress,  $\sigma_{22}$ , at the interface coincides with the radial normal stress in the  $x_2$ -direction, and with the hoop stress perpendicular to the  $x_3$ -direction. The magnitudes of these stresses play a significant role in initiation of fibre matrix debonding and radial cracking in the matrix at the fibre interface, respectively.

The results in Figs 7 and 8 indicate that a decrease in temperature, and the consequent differential dilatation of the phases, cause compressive radial stresses and tensile hoop stresses in the matrix, and compressive radial and hoop stresses in the fibre. Note that as long as the phases remain elastic, the magnitudes of the thermal stresses found in the titanium-based system are much smaller than those found in the nickel-based system. This is consistent with the smaller difference between the coefficients of thermal expansion of the fibre and matrix in the two systems. Fig. 5. Thermomechanical compatibility can be enhanced by applying a compliant coating to the fibre, such as the CVD-deposited carbon coating with properties described in Table I. This causes a significant reduction in the local thermal stresses, particularly at the fibre/matrix interface, Figs 7b and 8b. Compared to the matrix and fibre phases, the carbon coating has

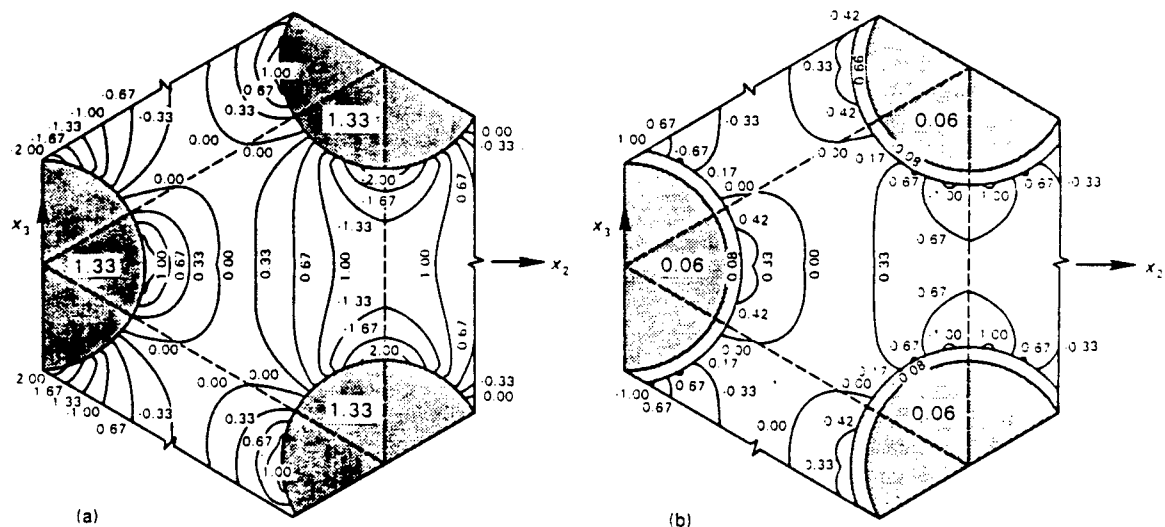


Figure 7. Transverse thermal stress concentrations,  $\Delta\sigma_{22}/\Delta T$  (MPa °C<sup>-1</sup>), in the SCS6/Ni<sub>3</sub>Al composite in the elastic range at 1200 °C: (a) uncoated fibre, (b) carbon-coated fibre.

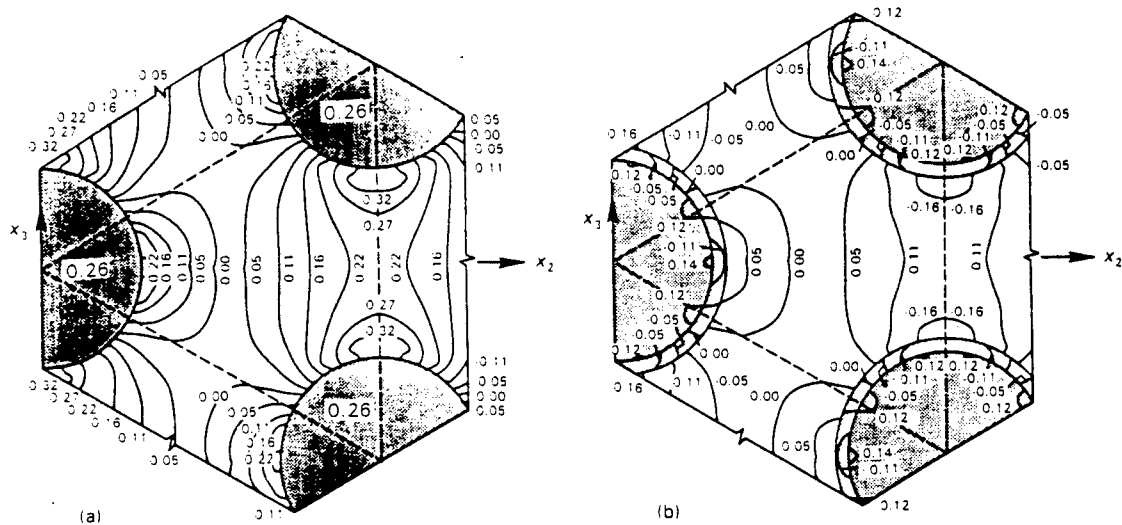


Figure 8 Transverse thermal stress concentrations,  $\Delta\sigma_{22} \Delta T$  ( $\text{MPa} \cdot ^\circ\text{C}^{-1}$ ), in the SCS6  $\text{Ti}_3\text{Al}$  composite in the elastic range at 950  $^\circ\text{C}$ : (a) uncoated fibre, (b) carbon-coated fibre.

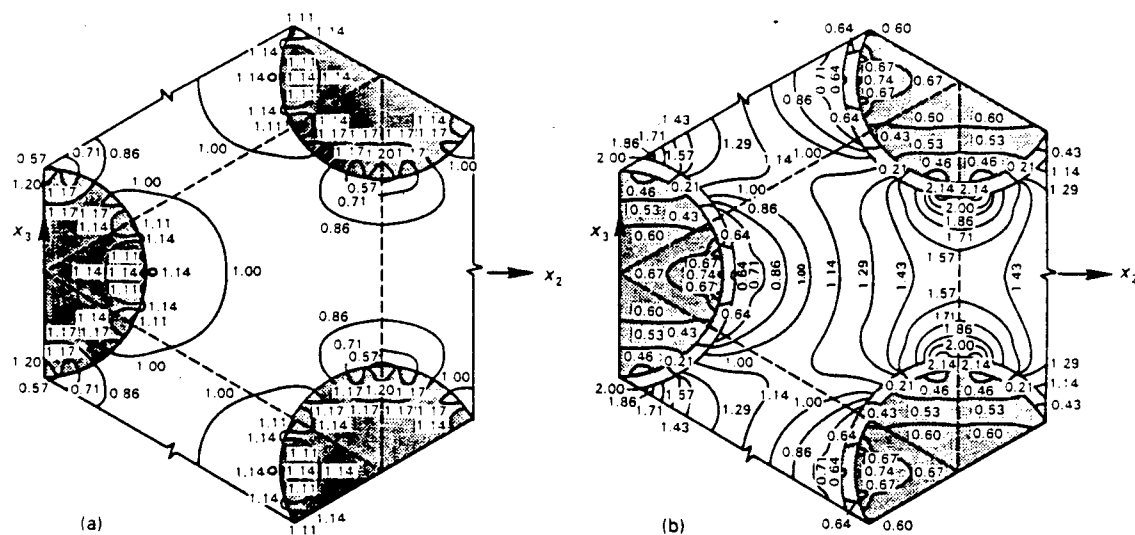


Figure 9 Transverse mechanical stress concentrations,  $\Delta\sigma_{22} \Delta\sigma_{22}$ , in the SCS6  $\text{Ni}_3\text{Al}$  composite in the elastic range at 1200  $^\circ\text{C}$ : (a) uncoated fibre, (b) carbon-coated fibre.

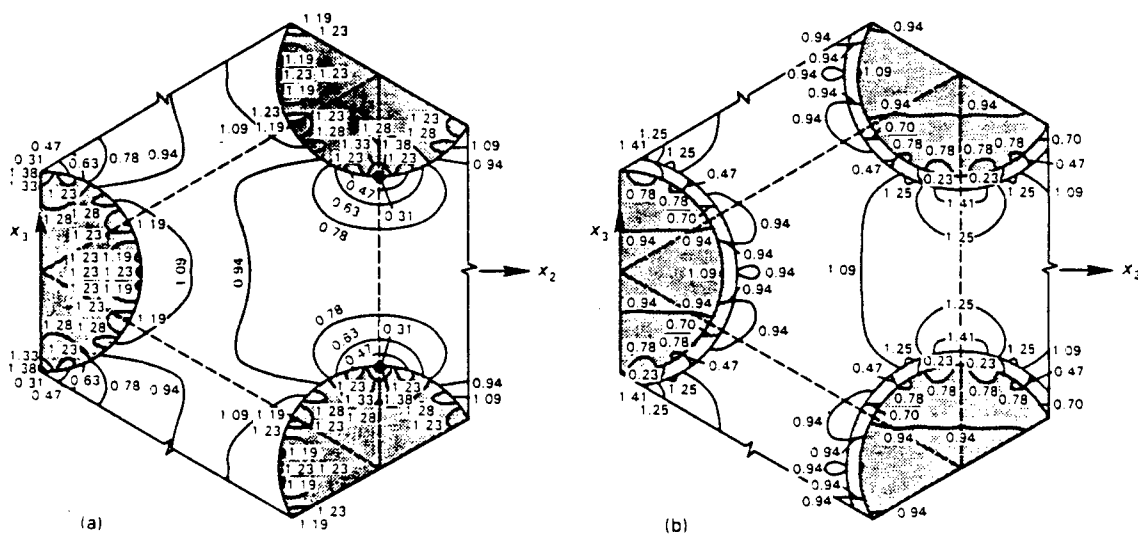
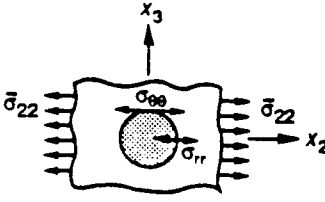


Figure 10 Transverse mechanical stress concentrations,  $\Delta\sigma_{22} \Delta\sigma_{22}$ , in the SCS6  $\text{Ti}_3\text{Al}$  composite in the elastic range at 950  $^\circ\text{C}$ : (a) uncoated fibre, (b) carbon-coated fibre.

TABLE IV Summary of stress concentrations in the matrix at fibre matrix interface



	SCS6 Ni <sub>3</sub> Al		SCS6 Ti <sub>3</sub> Al	
	Uncoated fibre	Coated fibre	Uncoated fibre	Coated fibre
<b>Elastic</b>				
$\Delta\sigma_{rr} \Delta T^a$ (MPa $^{\circ}\text{C}^{-1}$ )	1.56	0.45	0.28	0.08
$\Delta\sigma_{\theta\theta} \Delta T^a$ (MPa $^{\circ}\text{C}^{-1}$ )	-2.13	-0.90	-0.36	-0.18
$\Delta\sigma_{rr} \Delta\bar{\sigma}_{22}$	1.15	0.61	1.25	0.91
$\Delta\sigma_{\theta\theta} \Delta\bar{\sigma}_{22}$	0.57	2.01	0.28	1.37
<b>Elastic-plastic</b>				
$\Delta\sigma_{rr} \Delta T^a$ (MPa $^{\circ}\text{C}^{-1}$ )	0.13	0.08	NY <sup>c</sup>	NY <sup>c</sup>
$\Delta\sigma_{\theta\theta} \Delta T^a$ (MPa $^{\circ}\text{C}^{-1}$ )	-0.16	-0.13	NY <sup>c</sup>	NY <sup>c</sup>
$\Delta\sigma_{rr} \Delta\bar{\sigma}_{22}^b$	1.23	1.11	1.28	1.04
$\Delta\sigma_{\theta\theta} \Delta\bar{\sigma}_{22}^b$	0.11	0.56	0.34	0.93

<sup>a</sup>  $T = 1200^{\circ}\text{C}$  in SCS6 Ni<sub>3</sub>Al,  $950^{\circ}\text{C}$  in SCS6 Ti<sub>3</sub>Al.

$\Delta T(\text{elastic}) = -30^{\circ}\text{C}$ ,  $\Delta T(\text{elastic-plastic}) = T - 21^{\circ}\text{C}$ .

<sup>b</sup>  $\bar{\sigma}_{22} = 225 \text{ MPa}$  in SCS6 Ni<sub>3</sub>Al,  $605 \text{ MPa}$  in SCS6 Ti<sub>3</sub>Al.

<sup>c</sup> No yielding.

a much smaller elastic moduli in the transverse plane, Table I, hence it offers little resistance to lateral thermal deformation of either phase. Also, the coating has a large coefficient of thermal expansion in the transverse plane, and is thus able to fill or vacate the void between the fibre and matrix that expands or contracts with positive or negative changes in temperature.

Contours of the elastic stress concentration factors found in uncoated SCS6/Ni<sub>3</sub>Al and SCS6/Ti<sub>3</sub>Al composites under uniform transverse tension are shown in Figs 9 and 10, respectively, for uncoated and coated fibres. The stress concentrations found in both composite systems under overall transverse tension are of similar magnitude. In contrast to its effect under thermal changes, the fibre coating, in general, tends to elevate significantly the mechanical transverse stresses Figs 9b and 10b. In particular, as shown in Table IV, the matrix hoop transverse overall stress ratio  $\Delta\sigma_{\theta\theta} \Delta\bar{\sigma}_{22}$  increased from 0.57 to 2.01, or by a factor of 3.5 in the SCS6/Ni<sub>3</sub>Al composite and from 0.28 to 1.37, or by 4.9 in the SCS6/Ti<sub>3</sub>Al composite when the  $10 \mu\text{m}$  carbon coating was added to the fibre. Of course, the coating reduced both radial stress ratios by similar but not identical magnitudes.

#### 4.2. Elastic-plastic response

The inelastic response of solids to thermomechanical loading depends, in general, on the applied loading path. Therefore, in contrast to the elastic response, it is not possible to find overall moduli, coefficients of thermal expansion, or thermomechanical stress concentrations that are independent of loading history. In what follows we present illustrative examples of inelastic deformation of the two composite systems under monotonically increasing, overall thermal or mechanical loading. In the linearly hardening matrix

assumed herein (cf. Section 2.2), the local instantaneous moduli remain constant during sustained plastic loading along a proportional path, provided, of course, that the yield stress does not change. Therefore, under proportional mechanical loading at constant temperature which causes plastic yielding in all elements of the subdivided unit cell, the local fields change proportionally. This property may be useful in interpretation of the numerical results.

For uniform changes in temperature throughout the volume of the composite, the effect of matrix plastic flow on the local stresses was evaluated for cooldown to room temperature from a stress-free state at  $1200^{\circ}\text{C}$  for the SCS6 Ni<sub>3</sub>Al composite and from  $950^{\circ}\text{C}$  for the SCS6/Ti<sub>3</sub>Al composite. Along these thermal paths, the nickel-based matrix exhibited extensive plastic deformation, but the titanium-based matrix remained mostly elastic. This is consistent with the variation of the matrix yield stress with temperature shown in Fig. 6.

First, we consider the local stresses in a SCS6 Ni<sub>3</sub>Al composite. Figs 11-13 show stress contours of the transverse normal stress,  $\sigma_{22}$ , and the transverse shear stress,  $\sigma_{23}$ , found at room temperature in uncoated and carbon-coated fibre systems. Fig. 11 represents the actual field,  $\sigma_{22}$ , and Fig. 12 the same field normalized by the  $\Delta T = 1179^{\circ}\text{C}$  temperature difference along the cooling path. This was done to facilitate comparisons with the normalized elastic field in Fig. 7. It is seen that the local stress-temperature ratios were reduced substantially by the plastic deformation of the matrix. This can be understood by comparing the Young's moduli,  $E$ , with the plastic tangent moduli,  $H$ , in Table II. During plastic straining, the matrix becomes very compliant compared to the fibre and can therefore deform at much lower ratios of stress-temperature increments. In fact, the stiffness of the matrix in the plastic range is approximately comparable to



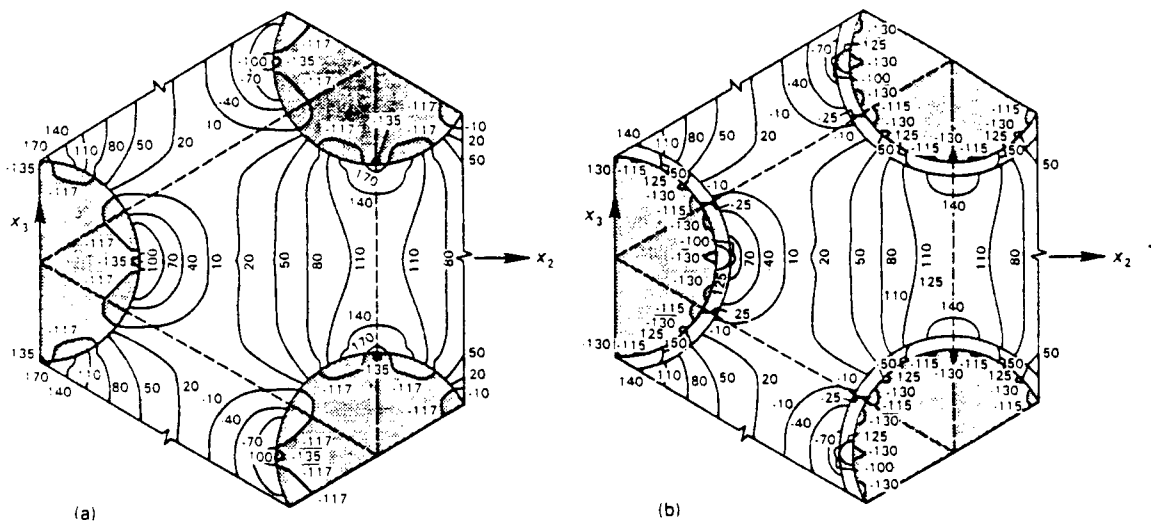


Figure 11 Transverse normal stresses,  $\sigma_{22}$ , in the SCS6 Ni<sub>3</sub>Al composite after cooling from 1200 °C to room temperature: (a) uncoated fibre, (b) carbon-coated fibre.

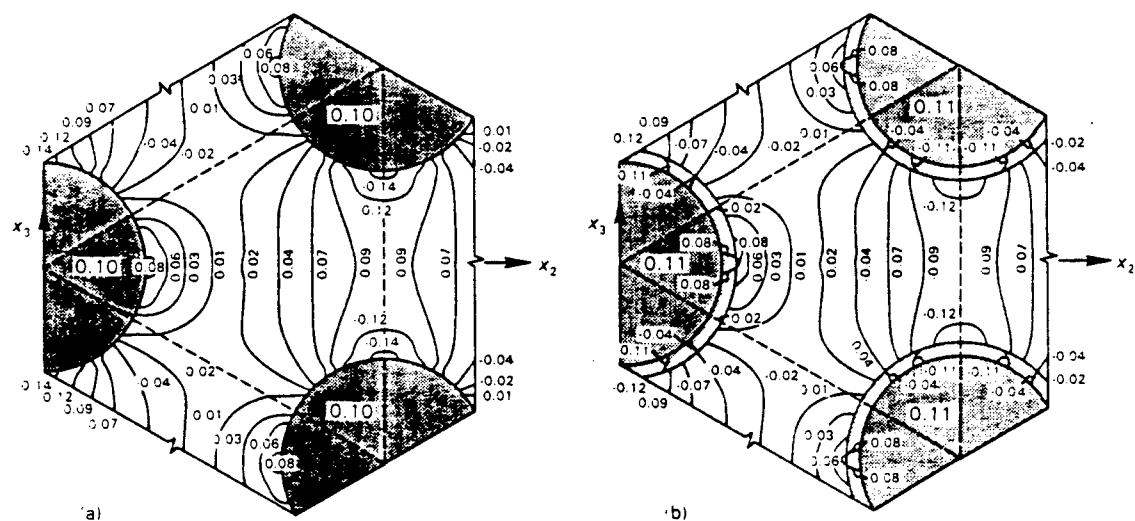


Figure 12 Transverse normal stresses in the SCS6 Ni<sub>3</sub>Al composite from Fig. 11, normalized by  $\Delta T = 1179$  °C: (a) uncoated fibre, (b) carbon-coated fibre.

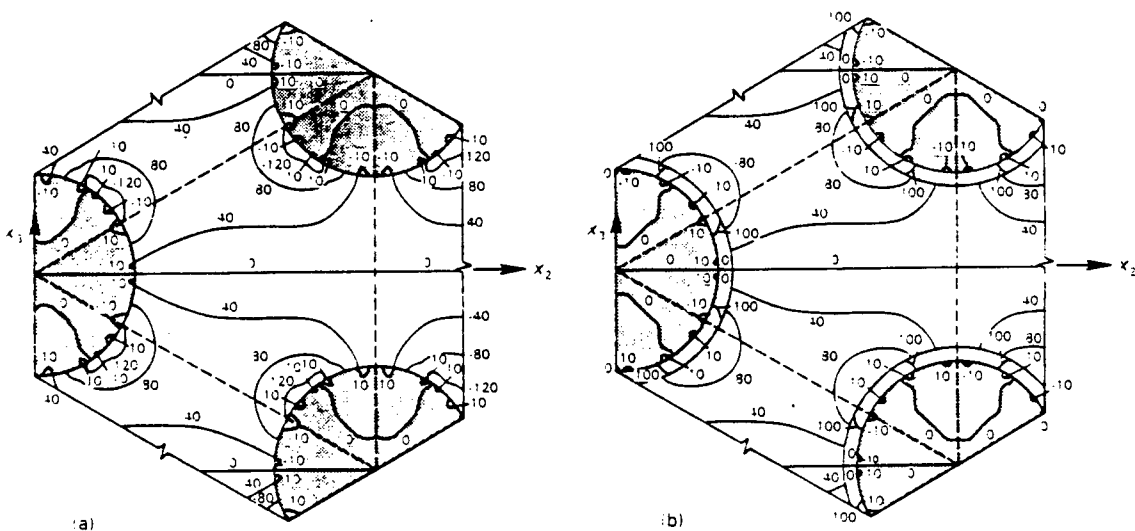


Figure 13 Shear stress,  $\sigma_{23}$ , in the transverse plane of the SCS6 Ni<sub>3</sub>Al composite after cooling from 1200 °C to room temperature: (a) uncoated fibre, (b) carbon-coated fibre.

the stiffness of the carbon coating so that the differences in the stress ratios found in the coated and the uncoated fibre systems are not significant. The deformation itself was quite extensive. For cooling from the assumed state free of internal stresses at 1200 °C, the onset of matrix yielding was found at 1140 °C, or after a -60 °C change in the uncoated fibre composite, and at 1020 °C, after a -180 °C change in the carbon-coated fibre system. Plastic yielding then proceeded along the entire cooling path to 21 °C.

Contours of the isotropic part of the local stress field are shown in Fig. 14, and of the normalized second invariant of the deviatoric stress field in Fig. 15. Large stress gradients are observed in the local fields. As expected, plastic flow of the matrix started at the fibre-matrix or coating-matrix interface where the stress concentrations were high. The stress contours indicate that the internal stresses can be approximated

by an axisymmetric field; this may not be possible at larger fibre concentrations. A comparison of Figs 14 and 15 indicates that the cooldown causes both large hydrostatic stresses and plastic flow in the entire matrix volume. Examples of evolution of plastic zones in the matrix during cooldown to room temperature are shown in Fig. 16.

Next, we turn our attention to the SCS6/Ti<sub>3</sub>Al composite. Figs 17-20 illustrate the stresses found after cooling from 950 °C to room temperature. As indicated by the variation of the yield stress of the Ti<sub>3</sub>Al matrix with temperature, Table III, the matrix remains mostly elastic in this case, Fig. 20. Consequently, relatively large stresses exist in the system after cooldown to room temperature. In the coated system, however, the stresses in the matrix are reduced by the compliant carbon coating and are similar to the stresses found in the nickel-based system.

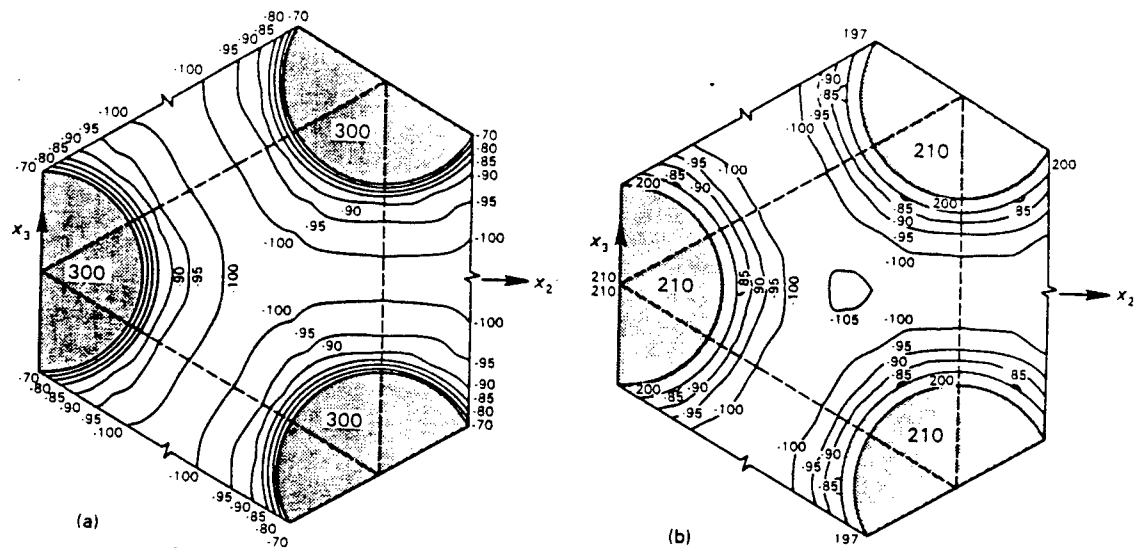


Figure 14 Isotropic stress,  $\sigma_0$ , in the SCS6 Ni<sub>3</sub>Al composite after cooling from 1200 °C to room temperature: (a) uncoated fibre, (b) carbon-coated fibre.

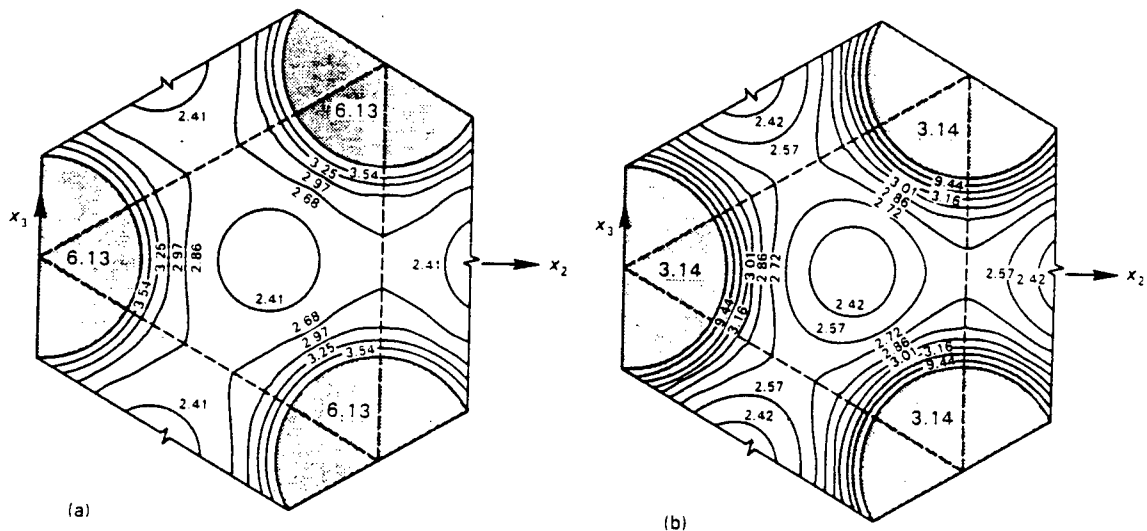


Figure 15 Effective stress  $(3J_2)^{1/2}$  in the SCS6 Ni<sub>3</sub>Al composite after cooling from 1200 °C to room temperature, normalized by  $\tau_m$  (21 °C) = 79 MPa. (a) uncoated fibre, (b) carbon-coated fibre.

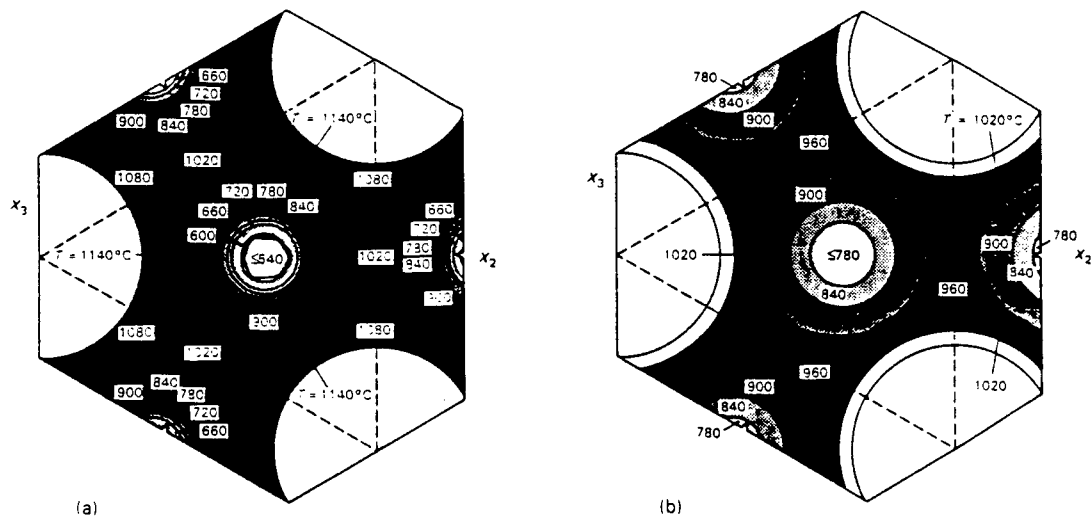


Figure 16 Evolution of plastic zones in the matrix SCS6  $\text{Ni}_3\text{Al}$  composite during cooling from 1200 C to room temperature: (a) uncoated fibre, (b) carbon-coated fibre.

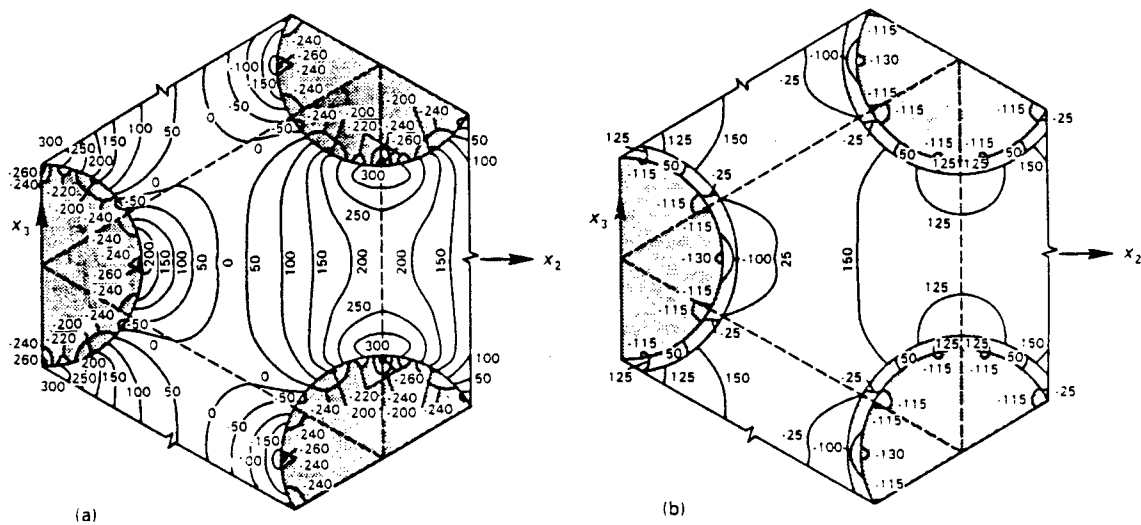


Figure 17 Transverse normal stresses,  $\sigma_{22}$ , in the SCS6  $\text{Ti}_3\text{Al}$  composite after cooling from 950 C to room temperature: (a) uncoated fibre, (b) carbon-coated fibre.

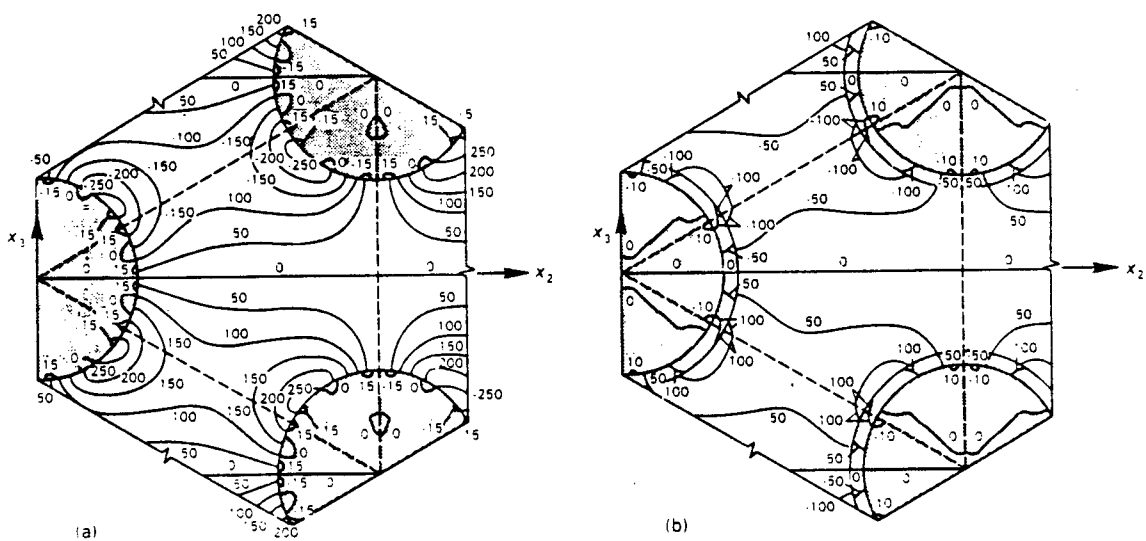


Figure 18 Shear stress,  $\sigma_{23}$ , in the transverse plane of the SCS6  $\text{Ti}_3\text{Al}$  composite after cooling from 950 C to room temperature: (a) uncoated fibre, (b) carbon-coated fibre.

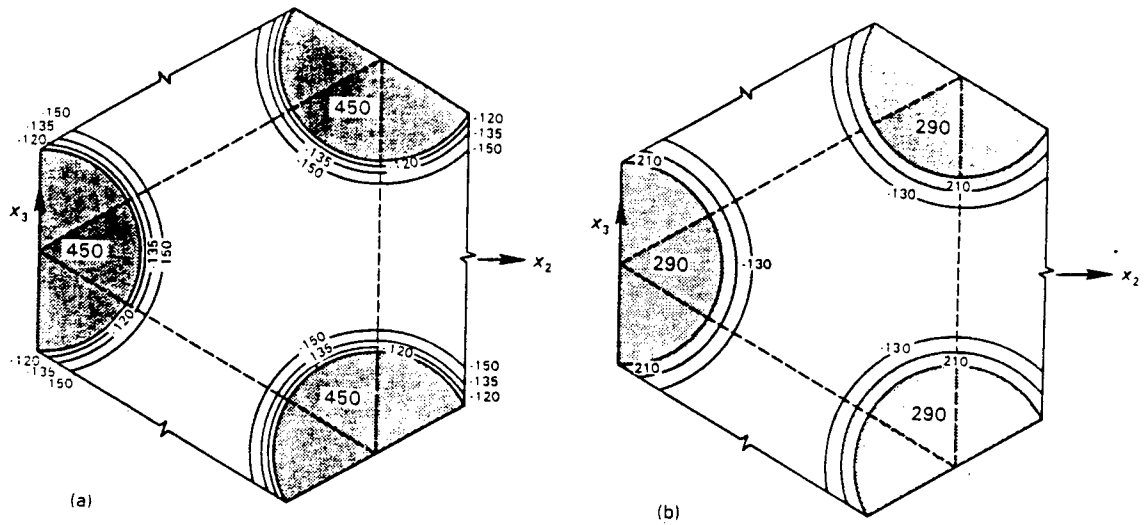


Figure 19 Isotropic stress,  $\sigma_0$ , in the SCS6  $\text{Ti}_3\text{Al}$  composite after cooling from 950 °C to room temperature: (a) uncoated fibre. (b) carbon-coated fibre.

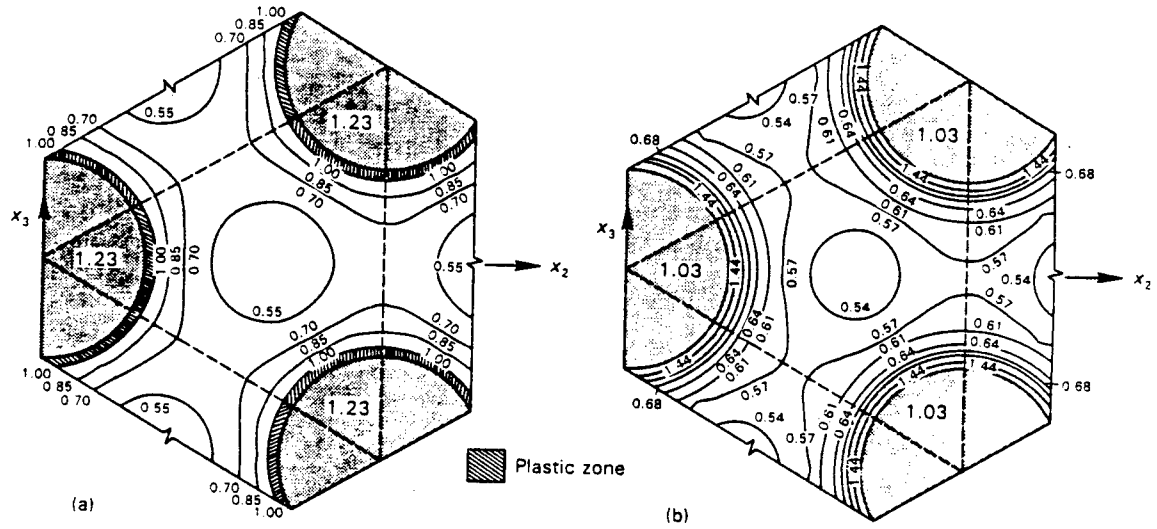


Figure 20 Effective stress,  $(3J_2)^{1/2}$ , in the SCS6  $\text{Ti}_3\text{Al}$  composite after cooling from 950 °C to room temperature, normalized by  $\sigma_m$  (21 °C) = 500 MPa (a) uncoated fibre. (b) carbon-coated fibre.

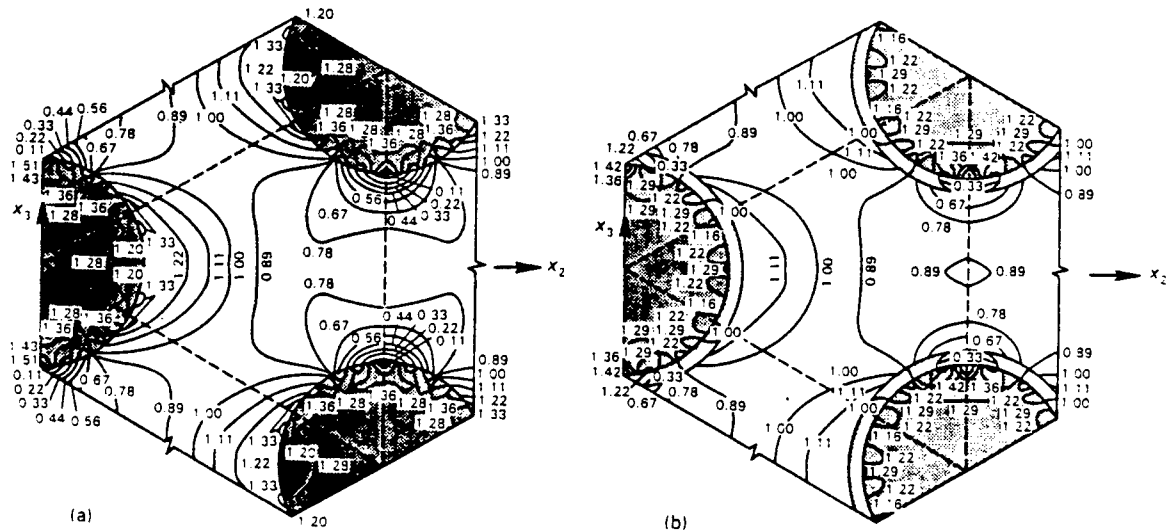


Figure 21 Normalized transverse normal stresses,  $\Delta\sigma_{22}$ ,  $\Delta\sigma_{33}$ , in the SCS6  $\text{Ni}_3\text{Al}$  composite after loading by overall transverse normal stress to  $\bar{\sigma}_{22} = 225$  MPa

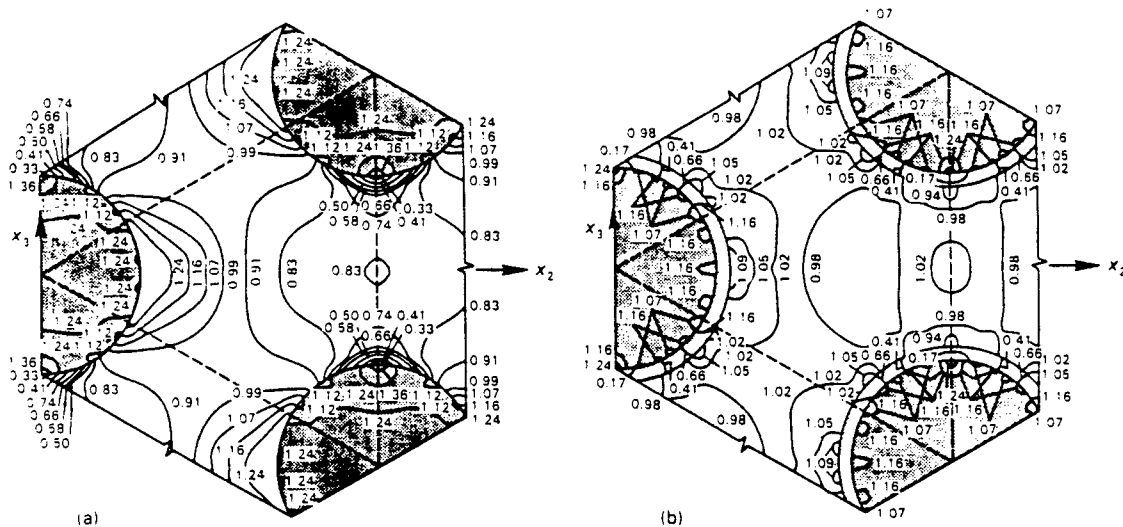


Figure 22 Normalized transverse normal stresses,  $\Delta\sigma_{22}/\Delta\bar{\sigma}_{22}$ , in the SCS6/Ti<sub>3</sub>Al composite after loading by overall transverse normal stress to  $\bar{\sigma}_{22} = 605$  MPa.

To illustrate the magnitudes of local stresses caused during inelastic deformation under mechanical loading, we present results for loading from a stress-free state by an overall transverse tension stress to such levels that produced sustained plastic straining in all subelements in the matrix volume. These were found as  $\bar{\sigma}_{22} = 225$  MPa in the SCS6/Ni<sub>3</sub>Al and  $\bar{\sigma}_{22} = 605$  MPa in the SCS6/Ti<sub>3</sub>Al matrix systems. The local stresses computed in the two composite systems at these stress levels were normalized by the applied load and contours were plotted in the unit cell, Figs 21 and 22. Selected local stress ratios appear in Table IV.

The results indicate that material selection for monotonic loading should favour uncoated fibrous systems with ductile, compliant matrices over coated fibres systems with matrices which remain elastic or rather stiff during plastic flow. However, plastic straining should be avoided under cyclic loads as it may lead to low-cycle fatigue damage of the matrix.

## 5. Simulation of hot isostatic pressing

### 5.1. Analysis of the standard process

We now proceed to examine the stress states created in the two intermetallic composite systems by hot isostatic pressing (HIP). In addition to the standard pressure-temperature cycle, we explored pressure and temperature combinations that could lead to more favourable distribution of residual stresses after cooling to room temperature and reheating to the operating temperature. The results were obtained for the PHA domain shown in Fig. 3b using the ABAQUS finite element program. The composite was assumed to be free of external loads and internal stresses at the beginning of the path at fabrication temperature. Then, the selected pressure was applied in a single step if the composite remained elastic, or incrementally when plastic straining was involved. This was followed by combined pressure and temperature changes dur-

ing cooling. As in Section 2.2, a rate-independent thermoplasticity theory was used. The analysis neglects the role of possible rate effects, and thus implies that cooldown to room temperature and reduction of the hydrostatic stress to the atmospheric value take place at a very slow rate. Evaluation of the rate effects during fabrication, which may be significant in some composite systems, requires application of a viscoplasticity theory for the ductile phases. This has been considered in our yet unpublished work using the viscoplastic constitutive equations reported by Bahei-El-Din *et al.* [16] and Shah [26].

The temperature-overall hydrostatic pressure combinations applied to the SCS6/Ni<sub>3</sub>Al composite are shown schematically in Fig. 23. Conditions similar to those shown in Fig. 23a and c were applied to the SCS6/Ti<sub>3</sub>Al system; however, the fabrication temperature was taken as  $T_0 = 950^\circ\text{C}$ , and the initial pressure as 200 or 400 MPa. In addition, we applied modified pressure conditions, with the ratio of the axial to transverse hydrostatic pressure ranging from 0–1.5, to promote plastic yielding of the matrix.

In typical HIP cycles, the cooling/unloading path to room temperature and atmospheric pressure is usually linear, as in Fig. 23a. Under the hydrostatic load, the local stress field is not necessarily isotropic, hence plastic flow may take place in the matrix during application of the pressure,  $\sigma_0$ . In the systems considered, the local stresses in the matrix are dominated by an isotropic stress field so that the matrix, which is assumed to be plastically incompressible, remains elastic at the fabrication temperature and 200 MPa hydrostatic pressure. However, the two intermetallic composites exhibited different deformation behaviour under the linear cooldown, depressurization cycle. In agreement with the variation of the yield stress with temperature of the nickel aluminide and the titanium aluminide matrix, Fig. 6, the SCS6/Ni<sub>3</sub>Al composite exhibited substantial plastic deformations while the SCS6/Ti<sub>3</sub>Al composite remained mainly elastic.

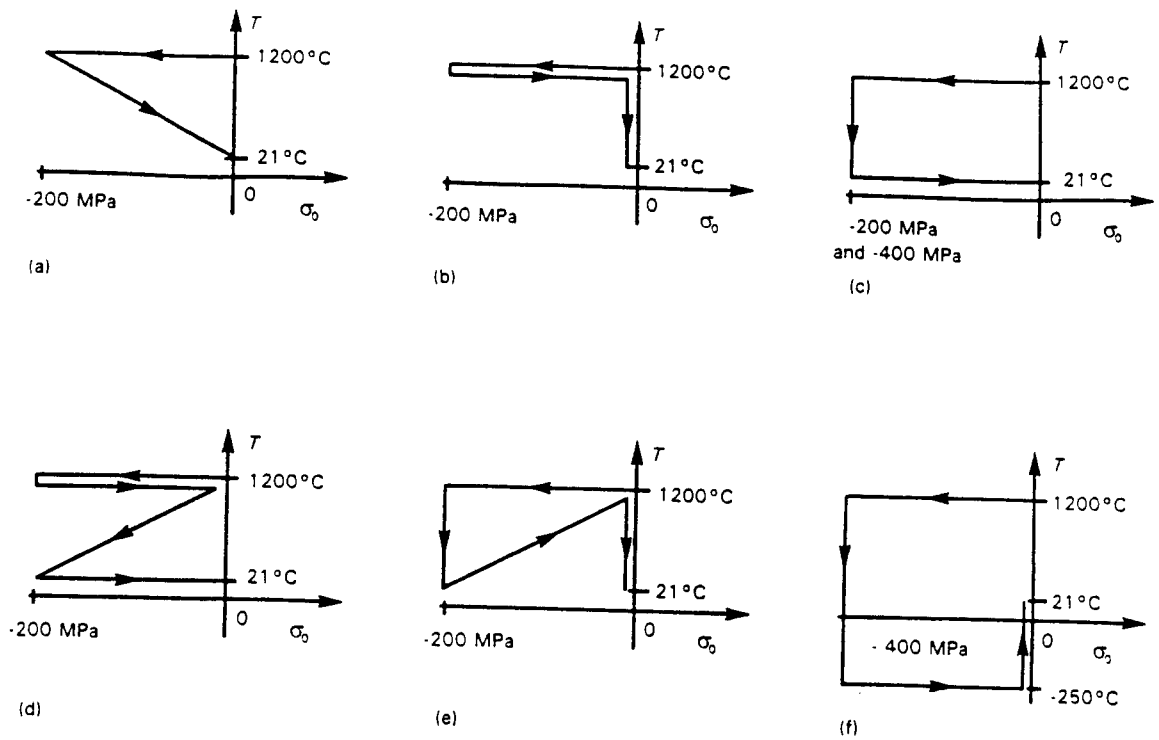


Figure 23 Thermomechanical unloading programmes applied to simulate modified hot isostatic pressing.

Fig. 24 shows the distribution of the axial, radial, and hoop stresses,  $\sigma_{11} \equiv \sigma_{11}$ ,  $\sigma_{rr}$ ,  $\sigma_{\theta\theta}$ , along the  $x_2$ -axis in the unit cell for uncoated and coated SCS6/Ni<sub>3</sub>Al composite after the HIP cycle, at room temperature and in complete unloading. The inset in the figures indicates the loading/unloading path assumed in this simulation. The axial stress in the fibre

is uniform and compressive. The magnitude of the fibre axial stress is reduced substantially if the fibre is coated by a thin carbon layer. However, the coating itself sustains large axial tensile stress after cooldown to room temperature. The matrix axial stress is also uniform, but the radial and hoop stresses are not uniform. Large tensile stresses develop in the matrix at

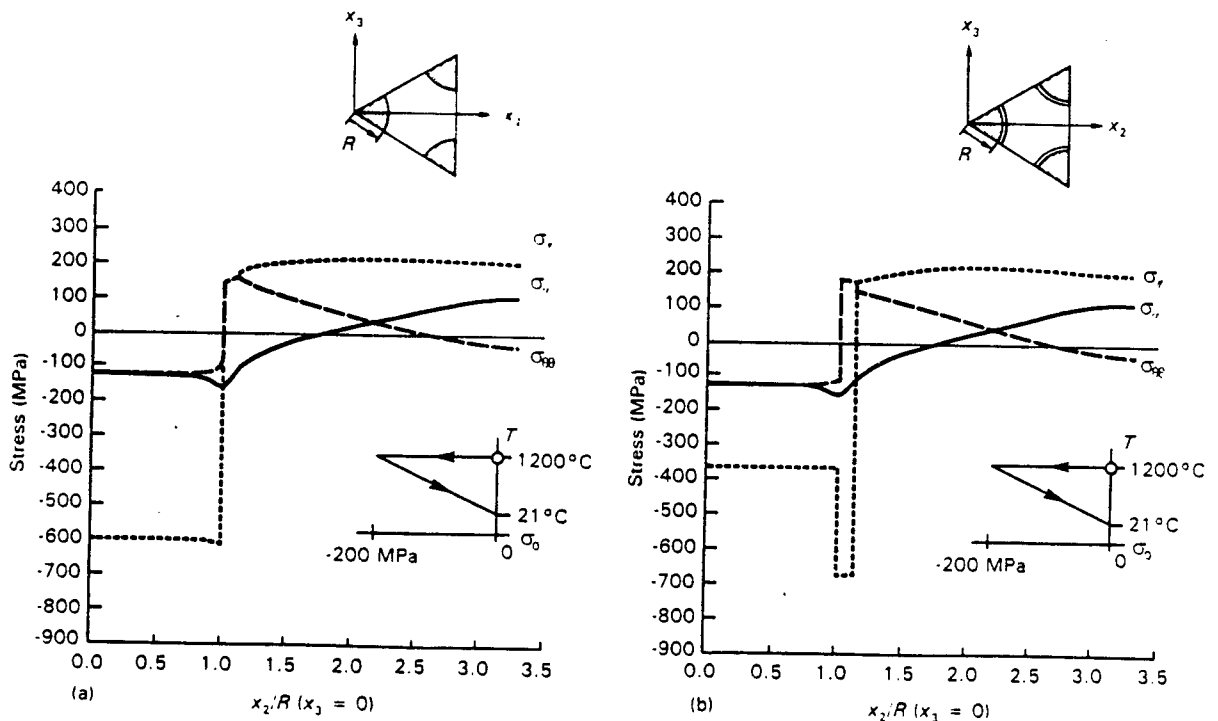


Figure 24 Distribution of axial, radial and hoop stresses in the SCS6-Ni<sub>3</sub>Al composite at room temperature after hot isostatic pressing: (a) uncoated fibre, (b) carbon-coated fibre.

the fibre matrix interface in the axial and hoop directions. Comparing the plots in Fig. 24a and b, we see that the matrix stress in the SCS6/Ni<sub>3</sub>Al composite does not benefit from the presence of the fibre coating.

Fig. 25 shows the internal stresses after reheating to 1200 °C. Because the composite deformed plastically

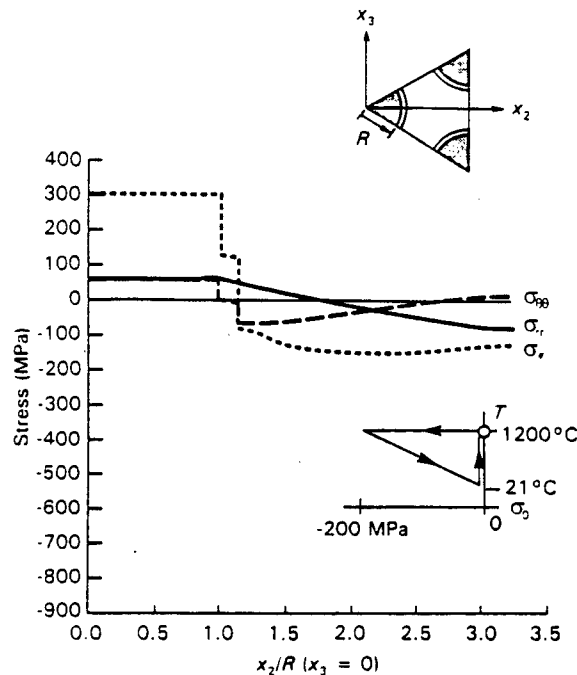


Figure 25 Distribution of axial, radial and hoop stresses in the SCS6/Ni<sub>3</sub>Al composite after hot isostatic pressing and reheating to 1200 °C: (a) uncoated fibre, (b) carbon-coated fibre.

in the cooling cycle, the residual stresses did not vanish after reheating.

Depending on the direction of the subsequent load, the residual stresses may improve or impair the overall strength. For example, if overall transverse tension is applied to the composite at 1200 °C (see the contours in Figs 9 and 12) the matrix tensile stress in the radial direction is elevated by the residual stress, whereas the tensile stress in the hoop direction is reduced by the compressive residual stress. This reduces the likelihood of developing radial cracks in the matrix and increases the possibility of debonding at the interface.

The residual stresses found at room temperature in uncoated and coated SCS6/Ti<sub>3</sub>Al composite are shown in Fig. 26. Compared to the nickel-based system, much larger thermal stresses were found in the matrix of the uncoated titanium-based system. Of course, this is the consequence of plastic straining in the Ni<sub>3</sub>Al matrix, and elastic deformation in the Ti<sub>3</sub>Al matrix. However, for the same reason, the magnitude of the radial and hoop stresses in the Ti<sub>3</sub>Al matrix were reduced by more than a factor of two by the fibre coating, Fig. 26, while remained unchanged in the Ni<sub>3</sub>Al matrix, Fig. 24. Also, the residual stresses were completely removed by reheating the Ti<sub>3</sub>Al matrix composite to 950 °C.

## 5.2. Effect of HIP parameters on residual stresses

The results presented in the preceding sections indicate that plastic flow of the matrix causes redistribution of the local stresses and reduction of the

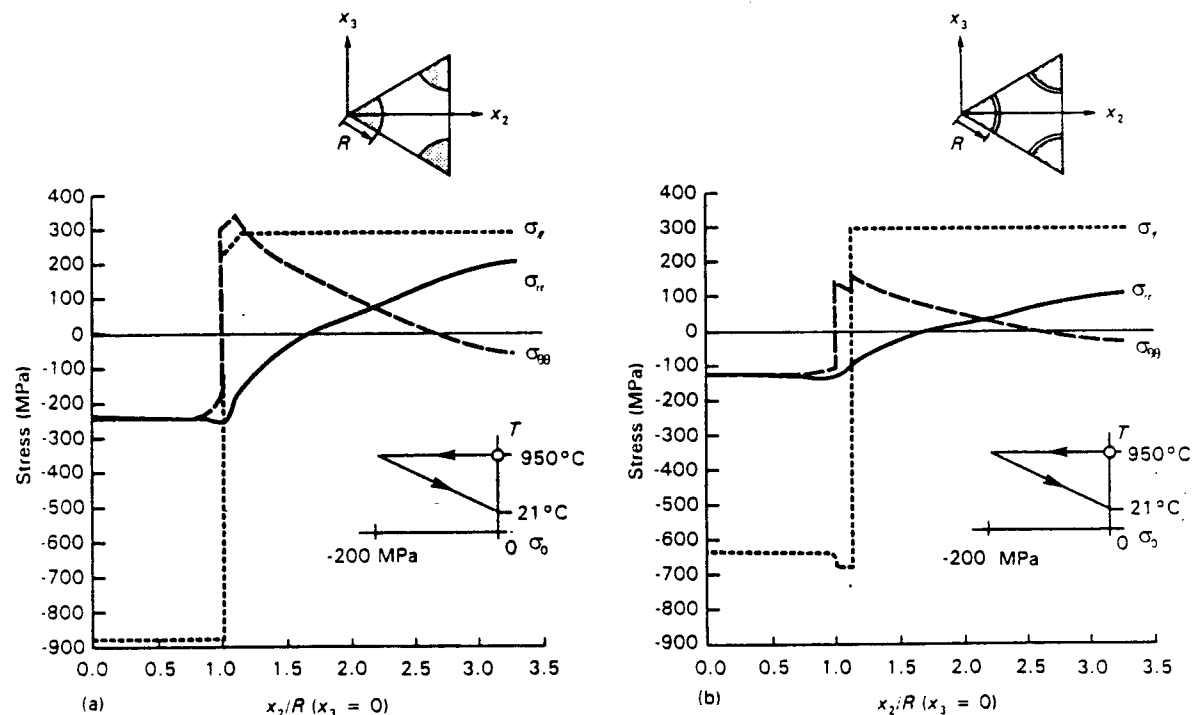


Figure 26 Distribution of axial, radial and hoop stresses in the SCS6/Ti<sub>3</sub>Al composite at room temperature after hot isostatic pressing: (a) uncoated fibre, (b) carbon-coated fibre.

interfacial stresses in the matrix. This feature can be utilized in optimizing the temperature-pressure path in order to reduce the adverse local stresses. In this section, we examine various HIP regimes and evaluate the corresponding local stresses in the two intermetallic composites considered above.

First, we computed the local residual stresses retained in the SCS6/Ni<sub>3</sub>Al system at room temperature after exposure to an HIP temperature of 1200 °C and hydrostatic pressure of 200 or 400 MPa, when unloading was reached through the various options shown in Fig. 23b-f, including an excursion below room temperature, Fig. 23f. For the loading cases shown in Fig. 23a, b, d and e, the stresses at the end of the HIP cycle were very similar. On the other hand, the tensile stresses were substantially reduced when the hydrostatic pressure,  $\sigma_0$ , was sustained during cooldown of the composite, Fig. 23c. Moreover, the tensile stresses in the phases were lower when the higher hydrostatic pressure of 400 MPa was maintained during the HIP process.

The interfacial and internal matrix stresses computed in uncoated and carbon-coated SCS6/Ni<sub>3</sub>Al composites for the various conditions are shown in Tables V and VI. Table V lists the radial stress  $\sigma_{rr}$ , hoop stress  $\sigma_{\theta\theta}$ , and axial stress  $\sigma_{11}$ , found at the interface at either point "a" or point "b" indicated on

the unit cell shown in the inset. The average isotropic stress in the matrix  $\sigma_0^m$  is also indicated. Table VI shows the local stresses found in the matrix internal point "c" (see inset of unit cell), the axial stress  $\sigma_{11}^m \equiv \sigma_{11}$ , the transverse stress  $\sigma_{22}^m$  and the isotropic stress  $\sigma_0^m$ .

Note the substantial reduction of the radial and hoop stresses at the interface between the first and last regimes in Tables V and VI. As discussed below, this reduction is mostly due to more extensive plastic straining caused by the higher and sustained hydrostatic stress. It appears that the tensile stresses would be reduced further by increasing the hydrostatic pressure, provided that fibre splitting could be avoided. The matrix interfacial tensile stresses in the coated system have been also reduced, but to a lesser extent, by following the loading path indicated in Fig. 23c, Table V. The hoop stress in the coating, however, is not affected by the thermomechanical path. The pressure applied during the HIP process did not much affect the stresses, in the coated system.

Of course, reheating to 1200 °C did not eliminate the residual stresses, Tables VII and VIII. However, the stresses in the reheated systems were not much affected by the processing path, or by the magnitude of the hydrostatic pressure,  $\sigma_0$ , applied.

Table IX summarizes the results found for the

TABLE V Maximum interface stresses found in a SCS6/Ni<sub>3</sub>Al composite at room temperature after HIP

Interface stress (MPa)	Uncoated fibre	Coated fibre	Uncoated fibre	Coated fibre	Uncoated fibre	Coated fibre	Uncoated fibre	Coated fibre
$\sigma_{rr}^m$	-98 at b	-84 at b	-79 at b	-94 at b	-60 at b	-91 at b	-34 at b	-80 at b
$\sigma_{\theta\theta}^m$	190 at b	158 at b	155 at b	152 at b	120 at b	152 at b	127 at b	139 at b
$\sigma_{11}^m$	198 at b	186 at b	179 at b	143 at b	161 at b	141 at b	153 at b	123 at b
$\sigma_{rr}^c$	-	185 at a	-	188 at a	-	188 at a	-	198 at a
$\sigma_{\theta\theta}^c$	-	-668 at b	-	-633 at b	-	-624 at b	-	-623 at b
$\sigma_{11}^c$	-98 at b	-110 at b	-79 at b	-122 at b	-60 at b	-121 at b	-34 at b	-108 at b
$\sigma_{rr}^c$	-94 at a	-108 at a	-76 at a	-117 at a	-59 at a	-116 at a	-39 at a	-104 at a
$\sigma_{\theta\theta}^c$	-605 at b	-364 at b	-552 at b	-280 at b	-500 at b	-261 at b	-397 at b	-186 at b
$\sigma_0^m$	97 at b	87 at b	85 at b	67 at b	74 at b	67 at b	82 at b	61 at b

TABLE VI Matrix internal stresses found in a SCS6/Ni<sub>3</sub>Al composite at room temperature after HIP

Stress at point c (MPa)	Uncoated fibre	Coated fibre	Uncoated fibre	Coated fibre	Uncoated fibre	Coated fibre	Uncoated fibre	Coated fibre
$\sigma_{11}^m = \sigma_{11}^c$	213	213	195	179	177	177	138	149
$\sigma_{22}^m$	115	128	96	162	76	164	42	141
$\sigma_0^m$	101	105	90	106	79	106	57	49



TABLE VII Maximum interface stresses found in a SCS6/Ni<sub>3</sub>Al composite at room temperature after HIP and reheating to fabrication temperature

Interface stress (MPa)	Uncoated fibre	Coated fibre	Uncoated fibre	Coated fibre	Uncoated fibre	Coated fibre	Uncoated fibre	Coated fibre
$\sigma_{rr}^m$	76 at a	52 at a	76 at a	50 at a	76 at a	49 at a	77 at a	51 at a
$\sigma_{\theta\theta}^m$	-55 at a	-67 at a or b	-55 at a	-66 at b	-55 at a	-66 at b	-55 at a	-67 at a or b
$\sigma_{11}^m$	-62 at a	-80 at a	-62 at a	-80 at a	-62 at a	-81 at a	-62 at a	-80 at a
$\sigma_{\theta\theta}^c$	-	7 at b	-	6 at b	-	6 at b	-	8 at b
$\sigma_{11}^c$	-	126 at a or b	-	126 at a or b	-	126 at a or b	-	126 at a or b
$\sigma_{rr}^f$	76 at a	65 at a	76 at a	64 at a	76 at a	63 at a	77 at a	64 at a
$\sigma_{\theta\theta}^f$	72 at b	60 at b	72 at b	57 at b	72 at b	57 at b	71 at b	58 at b
$\sigma_{11}^f$	372 at a	298 at a	372 at a	299 at a	373 at a	299 at a	373 at a	298 at a
$\sigma_0^m$	-14 at a	-32 at a	-14 at a	-33 at a	-14 at a	-34 at a	-13 at a	-32 at a

TABLE VIII Matrix internal stresses found in a SCS6/Ni<sub>3</sub>Al composite at room temperature after HIP and reheating to fabrication temperature

Stress at point c (MPa)	Uncoated fibre	Coated fibre	Uncoated fibre	Coated fibre	Uncoated fibre	Coated fibre	Uncoated fibre	Coated fibre
$\sigma_{11}^m = \sigma_{11}^c$	-132	-127	-132	-124	-132	-123	-132	-124
$\sigma_{22}^m$	13	13	13	14	13	15	13	14
$\sigma_0^m$	-62	-64	-62	-63	-62	-62	-62	-63

TABLE IX Maximum interface stresses found in a SCS6/Ti<sub>3</sub>Al composite at room temperature after HIP

Interface stress (MPa)	Uncoated fibre	Coated fibre	Uncoated fibre	Coated fibre
$\sigma_{rr}^m$	-210 at b	-79 at a	-178 at b	-79 at a
$\sigma_{\theta\theta}^m$	323 at b	171 at a	165 at b	171 at a
$\sigma_{11}^m$	253 at b	308 at a	133 at b	308 at a
$\sigma_{\theta\theta}^c$	-	146 at b	-	146 at b
$\sigma_{11}^c$	-	-669 at b	-	-669 at b
$\sigma_{rr}^f$	-210 at b	-105 at b	-178 at b	-105 at b
$\sigma_{\theta\theta}^f$	-182 at a	-106 at a	-149 at a	-105 at a
$\sigma_{11}^f$	-883 at b	-632 at b	-827 at b	-632 at b

uncoated and carbon-coated SCS6/Ti<sub>3</sub>Al composites. Apart from very localized matrix yielding at the fibre/matrix interface in the uncoated fibre system, this composite remained elastic when subjected to the

loading path indicated in Fig. 23a at 950 °C. The matrix also remained elastic and the local stresses were unaltered when the hydrostatic pressure,  $\sigma_0$ , was increased from 200 MPa to 400 MPa and then

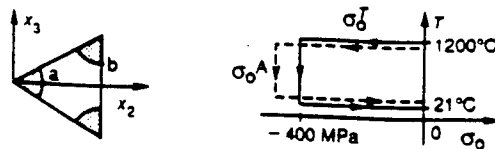
reduced proportionally during cooling. On the other hand, plastic flow of the matrix was induced early in the HIP process of the uncoated fibre system, and the matrix experienced substantial plastic deformation when the HIP path shown in Fig. 23c was followed from 950 °C at sustained hydrostatic pressure of 400 MPa. The hoop stress and the axial stress in the matrix of the uncoated system were reduced by approximately 49%. These reductions in the local stresses are larger than those found in the nickel-based system, Table V. This may be attributed to more extensive plastic straining at the low plastic tangent modulus of the titanium aluminide matrix, Table III.

### 5.3. Modified pressure ratios

To explore other possible alternatives that could magnify the favourable effect of plastic straining on the distribution of residual stresses, we applied modified HIP cycles in which the axial pressure  $\sigma_0^A$ , and the transverse hydrostatic pressure  $\sigma_0^T$ , assumed different magnitudes. The results are shown in Tables X–XIII for  $\sigma_0^T = 400$  MPa, and  $\sigma_0^A/\sigma_0^T$  ratios of 0.0, 0.5, 1.0, 1.5. In these calculations, the axial pressure and the transverse hydrostatic pressure were held constant during cooldown to room temperature.

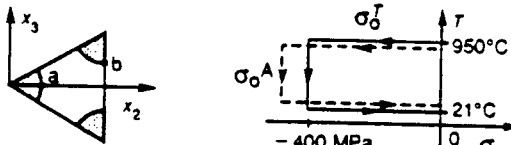
The axial tensile stress in the matrix benefited most from reducing the axial pressure during hot isostatic pressing of the composite, particularly in uncoated fibre systems. Compared to the standard HIP methods in which a three-dimensional hydrostatic pressure was applied,  $\sigma_0^A = \sigma_0^T$ , the matrix axial stress was reduced by 50%–60% in the SCS6/Ni<sub>3</sub>Al composite when  $\sigma_0^A/\sigma_0^T = 0.5$ , and by 73%–115% in the SCS6/Ti<sub>3</sub>Al composite when  $\sigma_0^A/\sigma_0^T = 0.0$ . As expected, the axial compressive stress in the fibre and

TABLE XI Interface stresses found in carbon-coated SCS6 Ni<sub>3</sub>Al composite at room temperature after HIP with modified pressure conditions



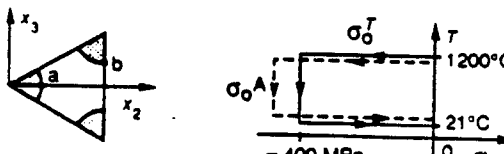
Interface stress (MPa)	$\sigma_0^A/\sigma_0^T$	0.0	0.5	1.0	1.5
$\sigma_{rr}^m$ at a		-98	-108	-113	-107
at b		-86	-90	-91	-92
$\sigma_{\theta\theta}^m$ at a		149	149	150	150
at b		156	156	152	154
$\sigma_{11}^m$ at a		112	121	134	149
at b		109	125	141	163
$\sigma_{\theta\theta}^f$ at a		160	163	166	163
at b		162	159	155	159
$\sigma_{11}^f$ at a		-571	-592	-630	-654
at b		-565	-586	-625	-649
$\sigma_{rr}^f$ at a		-154	-165	-170	-165
at b		-112	-118	-121	-120
$\sigma_{\theta\theta}^f$ at a		-107	-114	-116	-115
at b		-144	-154	-161	-155
$\sigma_{11}^f$ at a		-126	-176	-270	-327
at b		-121	-170	-265	-322

TABLE XII Interface stresses found in uncoated SCS6 Ti<sub>3</sub>Al composite at room temperature after HIP with modified pressure conditions



Interface stress (MPa)	$\sigma_0^A/\sigma_0^T$	0.0	0.5	1.0	1.5
$\sigma_{rr}^m$ at a		-174	-190	-204	-210
at b		144	-161	-178	-190
$\sigma_{\theta\theta}^m$ at a		141	139	135	141
at b		168	167	165	168
$\sigma_{11}^m$ at a		-13	37	90	148
at b		35	85	133	182
$\sigma_{\theta\theta}^f$ at a		-119	-132	-149	-156
at b		-184	-205	-219	-229
$\sigma_{11}^f$ at a		-530	-736	-815	-841
at b		-538	-748	-827	-855

TABLE X Interface stresses found in uncoated SCS6/Ni<sub>3</sub>Al composite at room temperature after HIP with modified pressure conditions

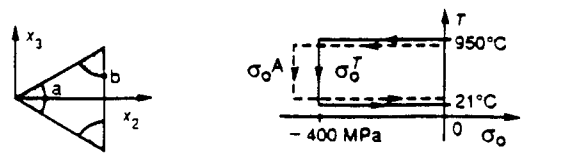


Interface stress (MPa)	$\sigma_0^A/\sigma_0^T$	0.0	0.5	1.0	1.5
$\sigma_{rr}^m$ at a		-100	-106	-107	-109
at b		-61	-62	-59	-66
$\sigma_{\theta\theta}^m$ at a		110	102	88	117
at b		131	129	120	142
$\sigma_{11}^m$ at a		55	49	125	191
at b		79	78	162	221
$\sigma_{\theta\theta}^f$ at a		-57	-59	-58	-62
at b		-86	-89	-88	-93
$\sigma_{11}^f$ at a		-194	-196	-508	-612
at b		-188	-190	-501	-606

coating was lower when the overall axial pressure was reduced.

In contrast, the tensile matrix hoop stress found in all cases considered in Tables X–XIII changed only slightly when the overall axial pressure and the transverse hydrostatic pressure had different magnitudes  $\sigma_0^A \neq \sigma_0^T$ .

TABLE XIII Interface stresses found in carbon-coated SCS6 Ti<sub>3</sub>Al composite at room temperature after HIP with modified pressure conditions



Interface stress (MPa)	$\sigma_0^A$	$\sigma_0^T$	0.0	0.5	1.0	1.5
$\sigma_{rr}^m$ at a	-93	-83	-79	-79		
at b	-101	-89	-84	-84		
$\sigma_{\theta\theta}^m$ at a	208	189	171	171		
at b	194	177	165	165		
$\sigma_{\theta\theta}^m$ at a	211	271	308	308		
at b	221	289	304	304		
$\sigma_{\theta\theta}^c$ at a	127	128	130	130		
at b	126	126	125	125		
$\sigma_{\theta\theta}^i$ at a	-584	-653	-669	-669		
at b	-586	-655	-671	-671		
$\sigma_{rr}^f$ at a	-159	-145	-139	-139		
at b	-123	-110	-105	-105		
$\sigma_{\theta\theta}^f$ at a	-123	-110	-105	-105		
at b	-148	-134	-128	-128		
$\sigma_{\theta\theta}^f$ at a	-434	-601	-640	-640		
at b	-427	-593	-632	-632		

#### 5.4. Mechanical loading of processed composites

To complete the numerical simulations of the inelastic response of the two composite systems, we applied transverse tension stresses to systems processed with

the standard and modified HIP cycles. The mechanical stress levels chosen were equal to those employed earlier to stress-free systems in Figs 21 and 22. The processing sequences and local stress magnitudes at the maximum stress are shown in Tables XIV and XV. Then, Table XVI compares the local stresses attained after fabrication alone, following the regime indicated in the table, with those found after mechanical loading applied alone from a stress-free state at room temperature (Section 4.2) and finally with those found after transverse loading of the fabricated composites with the initial residual stresses.

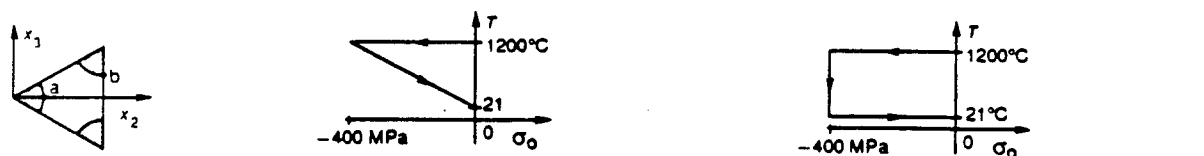
Note that during plastic straining of the fabricated systems, the differences in the residual stresses after fabrication, Tables V and VI, have no discernible effect on the final stress state. However, there are large differences between the local stresses reached after loading from the stress-free state, and from the fabricated state.

#### 5.5. Interpretation of the results

To gain a better insight into the numerical results, we present here a simplified analysis of unidirectional fibrous systems exposed to pressure/temperature loads, using the thermomechanical equivalence [34, 35]. The local fields and overall response under thermal changes applied to elastic or inelastic, unidirectionally reinforced fibrous composites can be found by superposition of a certain uniform stress field in the phases with a field corresponding to an overall mechanical load that removes the surface tractions of the uniform stress field.

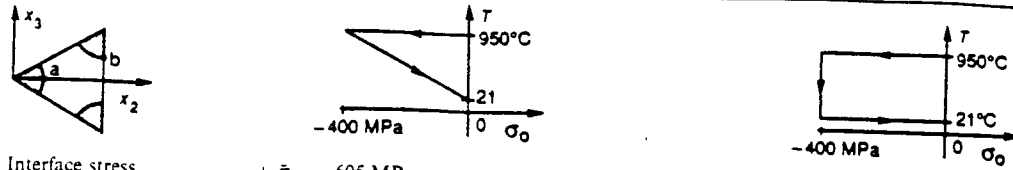
For composites with two isotropic phases of any microgeometry, which are subjected to a uniform

TABLE XIV Interface stress found in SCS6/Ni<sub>3</sub>Al composite at room temperature after HIP and transverse tension of 255 MPa




Interface stress (MPa)	$+\bar{\sigma}_{22} = 225 \text{ MPa}$		$+\bar{\sigma}_{22} = 225 \text{ MPa}$	
	Uncoated fibre	Coated fibre	Uncoated fibre	Coated fibre
$\sigma_{rr}^m$ at a	170	192	171	191
at b	-143	-135	-143	-135
$\sigma_{\theta\theta}^m$ at a	311	249	310	251
at b	170	245	169	245
$\sigma_{\theta\theta}^m$ at a	322	310	320	311
at b	104	157	99	157
$\sigma_{\theta\theta}^c$ at a	-	128	-	126
at b	-	226	-	227
$\sigma_{\theta\theta}^i$ at a	-	-674	-	-674
at b	-	-738	-	-737
$\sigma_{rr}^f$ at a	170	184	171	183
at b	-143	-125	-143	-125
$\sigma_{\theta\theta}^f$ at a	-51	-52	-49	-52
at b	257	230	259	230
$\sigma_{\theta\theta}^f$ at a	-686	-432	-684	-432
at b	-680	-439	-678	-438

TABLE XV Interface stresses found in SCS6 Ti<sub>3</sub>Al composite at room temperature after HIP with transverse tension of 605 MPa



Interface stress (MPa)	+ $\bar{\sigma}_{22} = 605$ MPa		+ $\bar{\sigma}_{22} = 605$ MPa	
	Uncoated fibre	Coated fibre	Uncoated fibre	Coated fibre
$\sigma_{rr}^m$ at a	578	593	626	593
at b	75	-53	68	-53
$\sigma_{\theta\theta}^m$ at a	500	53	348	53
at b	511	604	418	604
$\sigma_{11}^m$ at a	454	408	323	408
at b	253	287	160	287
$\sigma_{\theta\theta}^f$ at a	-	24	-	24
at b	-	244	-	244
$\sigma_{11}^f$ at a	-	-662	-	-662
at b	-	-787	-	-787
$\sigma_{rr}^f$ at a	578	664	626	664
at b	75	7	68	7
$\sigma_{\theta\theta}^f$ at a	-165	41	-74	42
at b	702	762	735	762
$\sigma_{11}^f$ at a	-1076	-733	-1009	-733
at b	-1005	-721	-972	-721

TABLE XVI Comparison of matrix interface stresses found in intermetallic matrix composites after fabrication and transverse tension



Interface stress (MPa)	SCS6: Ni <sub>3</sub> Al		SCS6: Ti <sub>3</sub> Al	
	Uncoated fibre	Coated fibre	Uncoated fibre	Coated fibre
Fabrication	$T_0 = 1200^\circ\text{C}$		$T_0 = 950^\circ\text{C}$	
$\sigma_{rr}$ at a	-107	-113	-204	-79
$\sigma_{\theta\theta}$ at b	120	152	165	165
Overall $\bar{\sigma}_{22}$	225 MPa		605 MPa	
$\sigma_{rr}$ at a	277	250	774	629
$\sigma_{\theta\theta}$ at b	25	126	206	563
	Fab. + 225 MPa		Fab. + 605 MPa	
$\sigma_{rr}$ at a	171	191	626	593
$\sigma_{\theta\theta}$ at b	169	245	418	604

temperature change  $(T - T_0)$ , one can find the uniform stress field in phases as

$$S = -[3(\alpha_f - \alpha_m)/(1/K_f - 1/K_m)](T - T_0) \quad (14)$$

where the elastic bulk modulus and coefficient of thermal expansion of the matrix and fibre are denoted, respectively, by  $K_m$ ,  $\alpha_m$ ,  $K_f$ ,  $\alpha_f$ .

If thermoelastic properties of the phases are functions of temperature, then  $K_m$  and  $K_f$  denote the magnitudes of the phase bulk moduli at the current temperature  $T$ , whereas  $\alpha_m$  and  $\alpha_f$  are replaced by the averages  $\langle \int_{T_0}^T \alpha_r(T) dT \rangle$ ,  $(T - T_0)$ ,  $r = f, m$  [36]. In typical composite systems with isotropic phases in which

$K_f > K_m$  and  $\alpha_f < \alpha_m$ , the cooldown from  $T_0$  to  $T$  causes uniform hydrostatic tension. Equation 14, in the entire composite. Because  $S$  is an isotropic stress in all phases, it does not cause inelastic deformation in a plastically incompressible material.

Of course, the internal field  $S$  is supported by corresponding surface tractions which are not actually applied at the surface of the representative volume, and must, therefore, be removed. If an overall uniform stress,  $\bar{\sigma}$ , is applied to the composite simultaneously with the temperature change, then the corresponding tractions can be added to those created by an overall stress equal to  $-S$ . The local stress  $\sigma(x)$  referred to a Cartesian coordinate system,  $x_j$ ,  $j = 1, 2, 3$ , is then given by [34, 37]

$$\sigma(x) = S1 + B(x)(\bar{\sigma} - S1) \quad (15)$$

where  $1 = [111000]^T$ , and  $B(x)$  is a  $(6 \times 6)$  stress concentration factor matrix. Note that this stress is not uniform and may cause yielding. For fibrous media with transversely isotropic phases, where  $x_1$  is the fibre axial direction, the matrix  $B$  has the form [35]

$$B = \begin{bmatrix} B_{11} & B_{12} & B_{12} & 0 & 0 & 0 \\ B_{21} & B_{22} & B_{23} & 0 & 0 & 0 \\ B_{21} & B_{23} & B_{22} & 0 & 0 & 0 \\ 0 & 0 & 0 & B_{44} & 0 & 0 \\ 0 & 0 & 0 & 0 & B_{55} & 0 \\ 0 & 0 & 0 & 0 & 0 & B_{55} \end{bmatrix} \quad (16)$$

The respective columns of  $B$  represent the local stresses corresponding to a sequence of unit overall stresses  $\sigma = i_k$ ,  $k = 1, 2, \dots, 6$ , where  $i_k$  is the  $k$ th column of a  $(6 \times 6)$  unit matrix. Actual magnitudes of the coefficients must be found from analysis of a selected micromechanical model. Such models typically

approximate the actual fields with piecewise uniform distributions in a representative volume of the composite. The periodic hexagonal array (PHA) model [8, 9] employed here is an example of this approach. Other examples are the self-consistent method [1], Mori-Tanaka model [2, 3], and the vanishing fibre diameter model [38], in which only the phase average stresses are determined. Hence, if  $N$  denotes the number of subelements, one finds  $N = 2$  for the averaging models of two-phase composites, and  $N$  equal to the number of subelements or integration points in the unit cell of the PHA model. In any case, Equation 15 is replaced by

$$\sigma_r = S1 + B_r(\bar{\sigma} - S1), \quad r = 1, 2, \dots, N \quad (17)$$

Under hot isostatic pressing of unidirectional composites, the applied overall stress is usually the three-dimensional hydrostatic stress,  $\sigma_0$ . Substituting  $\bar{\sigma} = \sigma_0 1$  in Equation 17, the local stresses caused by the thermomechanical loading are given by

$$\sigma_r = S1 + B_r S^* 1, \quad S^* = (\sigma_0 - S), \quad r = 1, 2, \dots, N \quad (18)$$

In this way, the thermomechanical HIP problem is reduced to a mechanical problem in which the composite is subjected to hydrostatic pressure  $(\sigma_0 - S)$ . Note that  $S^*$  is often negative.

In modelling of the hot isostatic pressing of SCS6/Ni<sub>3</sub>Al and SCS6/Ti<sub>3</sub>Al composites reinforced by uncoated fibres, the cooldown part of the thermomechanical loading regimes shown in Fig. 23 was converted into the stress  $S$ , using Equation 14 and the thermoelastic properties listed in Tables I-III. This stress was combined with the hydrostatic pressure,  $\sigma_0$ , applied in the HIP process, and plotted against the

current temperature. The individual points were connected by straight line segments. The hydrostatic pressure path found in this manner for selected HIP loading regimes is shown in Figs 27 and 28 for SCS6/Ni<sub>3</sub>Al and SCS6/Ti<sub>3</sub>Al composites, respectively. The non-linear variation of this normalized pressure with temperature is caused, in part, by the temperature dependence of the yield stress and thermoelastic properties of the phases.

This replacement of the actual thermomechanical loads by the pressure  $S^* = (\sigma_0 - S)$  simplifies evaluation of the onset of initial yielding of the composite under standard and modified HIP regimes. The magnitude of the overall hydrostatic stress,  $S_Y^*$ , at initial yielding in the matrix is found by substituting the local stresses given by Equation 18 into a specified yield function. Of course,  $N$  such solutions can be found, but only the lowest  $S_Y^*$  corresponds to the onset of yielding. In a  $J_2$  material, the local hydrostatic stress given by the first term in Equation 18 causes no plastic deformation. Using the local stresses given by the second term in Equation 18, and adopting the Mises yield function (Equation 7) for the matrix material, one finds the overall hydrostatic stress at initial yielding as

$$S_Y^* = Y/(B'_{11} + 2B'_{12} - B'_{21} - B'_{22} - B'_{23}), \quad r = 1, N \quad (19)$$

In the self-consistent method, Equation 19 provides a single solution. This is indicated by the upper dashed curve in Figs 27 and 28. Under the HIP loads shown, the onset of yielding is given by intersection of the applied hydrostatic pressure and the hydrostatic yield stress curves. Consistent with our finite element calculations, matrix yielding in the SCS6/Ni<sub>3</sub>Al composite

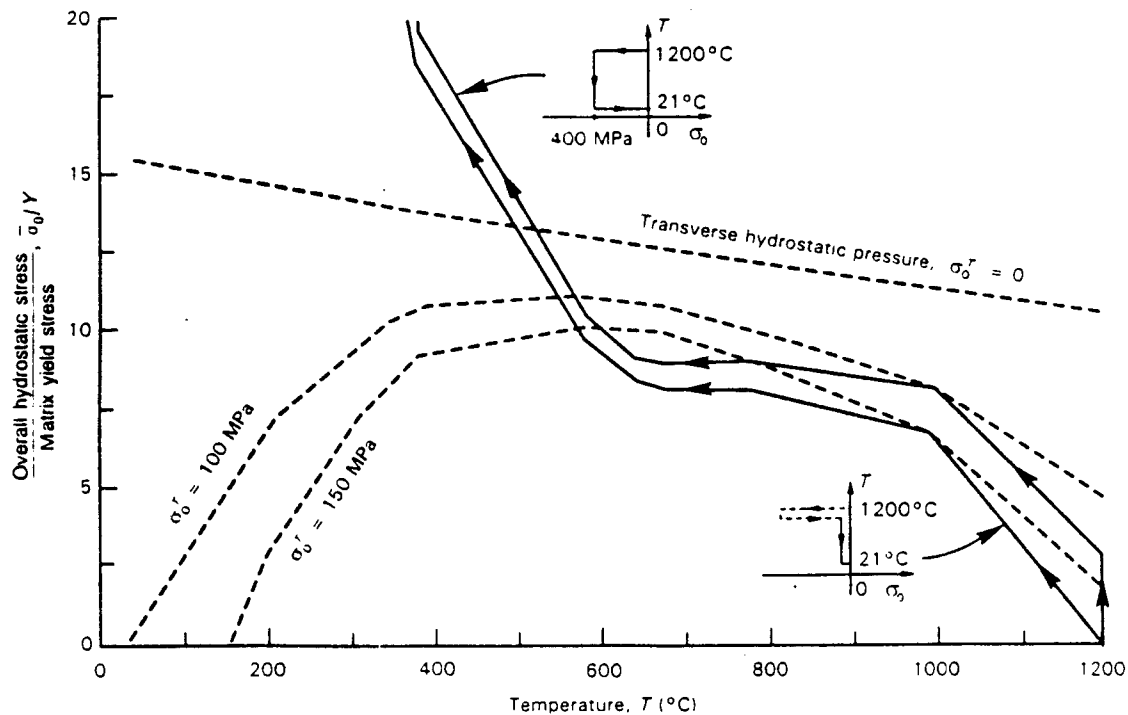


Figure 27 Variation of the (---) hydrostatic yield stress and (—) HIP equivalent hydrostatic pressure with temperature for the uncoated SCS6/Ni<sub>3</sub>Al composite.

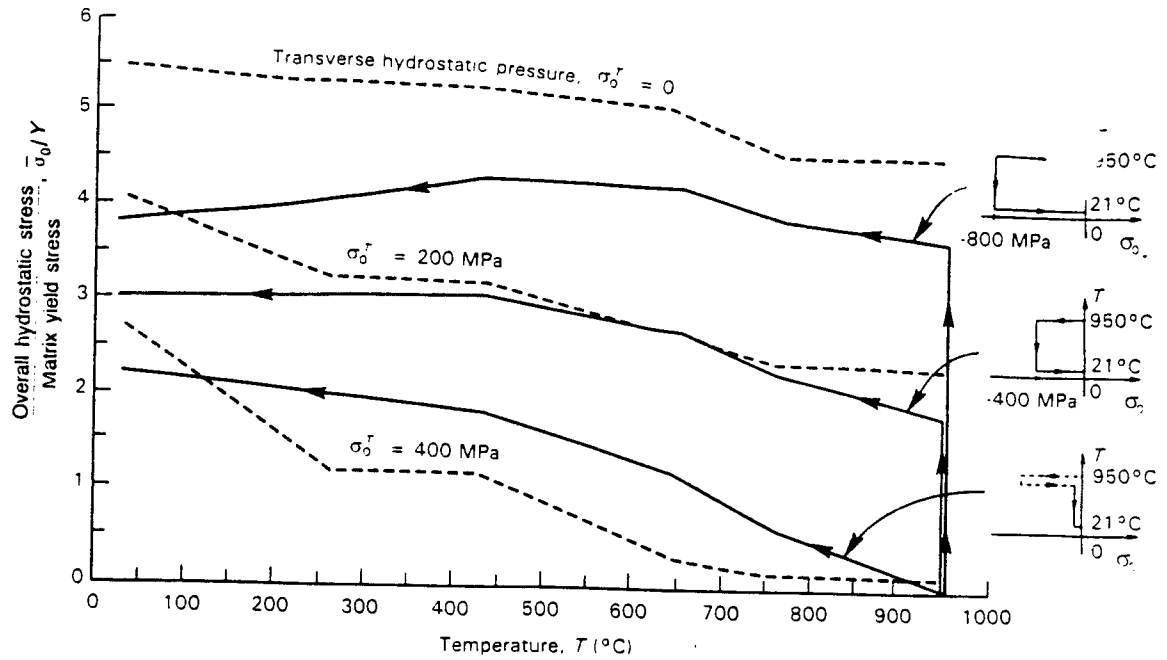


Figure 28 Variation of the (---) hydrostatic yield stress and (—) HIP equivalent hydrostatic pressure with temperature for the uncoated SCS6  $\text{Ti}_3\text{Al}$  composite.

can be induced earlier in the HIP process by maintaining the hydrostatic pressure,  $\sigma_0$ , during cooldown to room temperature. As we found earlier, this causes redistribution of the local stresses and leads to reduction of the magnitude of the matrix stress. It is also clear that increasing  $\sigma_0$  translates the applied load curve in Fig. 27 upwards in the direction of the hydrostatic yield stress curve. In this case, initial yielding of the composite takes place at a higher temperature during the cooldown path, which may further reduce the magnitude of the local stresses. The actual onset of yielding will be different from that indicated in Fig. 27 if a more refined stress field is employed. The self-consistent estimate of the initial yield stress for the SCS6  $\text{Ti}_3\text{Al}$  composite reveals no yielding during the HIP regimes shown in Fig. 28. On the other hand, our calculations with the PHA model and the finite element method indicated plastic yielding in this system for some of the HIP paths. The conclusion drawn from Fig. 28 is that initial yielding can be induced earlier in the process by modifying the HIP path such that cooldown to room temperature takes place at a constant, high pressure.

Another modification of the HIP path which may improve the local stresses, is the superposition of an isotropic stress,  $\sigma_0^T$ , in the transverse plane of the composite, as in Section 5.3. In this case, the loads applied consist of the hydrostatic stress,  $S$ , caused by the temperature change, the hydrostatic pressure,  $\sigma_0$ , and the overall transverse hydrostatic stress,  $\bar{\sigma} = [0 \ \sigma_0^T \ \sigma_0^T \ 0 \ 0 \ 0]^T$ . Substituting into Equation 17, and using the Mises yield function (Equation 7), the hydrostatic initial yield stress is found as

$$S_Y^* = [Y - \sigma_0^T(B'_{22} + B'_{33} - 2B'_{12})] / (B'_{11} + 2B'_{12} - B'_{21} - B'_{22} - B'_{23}) \quad r = 1, N \quad (20)$$

It is seen from Equation 20 that the magnitude of the initial yield hydrostatic stress is reduced by superimposing the transverse isotropic pressure,  $\sigma_0^T$ . Equation 20 is plotted in Figs 27 and 28 for selected magnitudes of  $\sigma_0^T$ , where the stress concentration factors were found with the self-consistent method. The onset of yielding was found at the intersection of the applied load curve and the  $S_Y^*$  curve. The actual yield temperature depends on the magnitude of the isotropic pressure,  $\sigma_0^T$ , maintained during the process, and it can be elevated substantially by increasing  $\sigma_0^T$ . These observations indicate how the processing parameters contribute to earlier, more extensive plastic straining, and thus to reduction of residual stresses.

## 6. Conclusion

Adverse thermal residual stresses generated during fabrication of fibrous composites can be reduced by a CVD carbon coating. The fibre coating provides a buffer that reduces the fibre/matrix constraint and the stresses caused by thermal mismatch of the phases. However, the coating may cause higher concentrations of certain stress components under mechanical loading. This is true, in particular, for the matrix hoop stress at the interface with the coated fibre, under overall transverse normal stress. The magnitude of these effects also depends on the relative stiffness of the matrix, fibre and coating.

Plastic flow of the matrix under overall transverse tension may cause substantial reductions in the tensile interfacial stresses. The implication is that mechanical compatibility in fibrous composites depends not only on the thermomechanical phase properties, but also on the inelastic response of the phases. A reasonably accurate evaluation of thermal residual stresses requires a refined micromechanical model, such as the

PHA model used here. A qualitative assessment of initial yielding during fabrication helps to identify effective HIP regimes, and can be performed with simple micromechanical models, e.g. the self-consistent or Mori-Tanaka schemes.

Numerical evaluations of the local stresses in the two intermetallic composites indicate that significant reductions in thermal residual stresses after hot isostatic pressing can be achieved by modifying the processing path. Most of the reductions in the adverse stresses in the matrix were obtained when cooldown to room temperature took place at a constant pressure. Increased pressure helped reduce the local stresses.

Another modification found effective in relieving the matrix residual tensile stresses is the application of axial compression which is smaller than the transverse hydrostatic pressure. The matrix axial tensile stress was found to be smallest when the overall axial stress was absent. In this case, the magnitudes of the fibre axial stress and the radial stress at the interface were also reduced, but remained compressive at the end of the HIP cycle. While decreasing the overall axial pressure relative to the transverse hydrostatic pressure caused significant reductions in the axial stresses and radial stresses in the phases, it also enhanced the matrix tensile hoop stress slightly. The smallest matrix hoop stress was found under three-dimensional hydrostatic pressure.

Thermal residual stresses generated in composite materials have a profound effect on their performance in service. In particular, the residual stresses may reduce or enhance the local stresses developed in the phases under service loads. The differences in the residual stresses after fabrication by variable HIP parameters, however, have a minor effect on the final stress states.

## Acknowledgements

This work was supported, in part, by the Air Force Office of Scientific Research, the Office of Naval Research, and the ONR ARPA programme at Rensselaer. The work of G. J. Dvorak was supported, in part, by the New York State NYSERDA Program. Drs Walter Jones, Yapa Rajapakse, William Coblenz and Steve Fishman served as programme monitors. Mr Amr Wafa made some finite element calculations used herein.

## References

1. R. HILL, *J. Mech. Phys. Solids* **13** (1965) 189.
2. T. MORI and K. TANAKA, *Acta Metall.* **21** (1973) 571.
3. Y. BENVENISTE, *Mech. Mater.* **6** (1987) 147.
4. Y. BENVENISTE, G. J. DVORAK and T. CHEN, *ibid.* **7** (1989) 305.
5. G. J. DVORAK, Y. A. BAHEI-EL-DIN, R. S. SHAH and H. NIGAM, in "Inelastic Deformation of Composite Materials", edited by G. J. Dvorak (Springer, New York, 1990) p. 270.
6. G. J. DVORAK and Y. A. BAHEI-EL-DIN, *Acta Mech.* **69** (1987) 219.
7. R. HILL, *J. Mech. Phys. Solids* **15** (1967) 79.
8. G. J. DVORAK and J. L. TEPLY, in "Plasticity Today: Modeling, Methods and Applications", W. Olszak Memorial Volume, edited by A. Sawczuk and V. Bianchi (Elsevier Science, Amsterdam, 1985) p. 624.
9. J. L. TEPLY and G. J. DVORAK, *J. Mech. Phys. Solids* **36** (1988) 29.
10. S. NEMAT-NASSER, T. IWAKUMA and M. HEJAZI, *Mech. Mater.* **1** (1982) 239.
11. J. ABOUDI, *Solid Mech. Arch.* **11** (1986) 141.
12. G. J. DVORAK, *Proc. R. Soc. Lond. A* **437** (1992) 311.
13. Y. A. BAHEI-EL-DIN and G. J. DVORAK, in "Metal Matrix Composites: Testing, Analysis, and Failure Modes", ASTM STP 1032, edited by W. S. Johnson (American Society for Testing and Materials, Philadelphia, PA, 1989) p. 103.
14. G. J. DVORAK, in "Metal Matrix Composites", Vol. 2, "Mechanisms and Properties", edited by R. K. Everett and R. J. Arsenault (Academic Press, Boston, 1990) p. 1.
15. Y. A. BAHEI-EL-DIN, G. J. DVORAK and R. S. SHAH, in "Computational Experiments", ASME PVP, Vol. 176, edited by W. K. Liu, P. Smolinski, R. Ohayon, J. Navickas and J. Gvildys (American Society for Mechanical Engineers, New York, 1989) p. 125.
16. Y. A. BAHEI-EL-DIN, R. S. SHAH and G. J. DVORAK, in "Mechanics of Composites at Elevated and Cryogenic Temperatures", ASME AMD, Vol. 118, edited by S. N. Singhal, W. F. Jones and C. T. Herakovich (American Society for Mechanical Engineers, New York, 1991) p. 67.
17. G. J. DVORAK, Y. A. BAHEI-EL-DIN, Y. MACHERET and C. H. LIU, *J. Mech. Phys. Solids* **36** (1988) 655.
18. H. NIGAM, G. J. DVORAK and Y. A. BAHEI-EL-DIN, *Int. J. Plasticity*, **10** (1994) 23.
19. *Idem. ibid.* **10** (1994) 49.
20. Y. A. BAHEI-EL-DIN, G. J. DVORAK, J. LIN, R. S. SHAH and J. F. WU, "Local Fields and Overall Response of Fibrous and Particulate Metal Matrix Composites" Final Technical Report, Alcoa Laboratory, Contract 379 (52R053)22L, November 1987.
21. "ABAQUS User's Manual" (Hibbit, Karlsson and Sorensen, Providence, RI, 1989).
22. Y. A. BAHEI-EL-DIN, in "Thermal and Mechanical Behavior of Ceramic and Metal Matrix Composites", ASTM STP 1080, edited by J. M. Kennedy, H. H. Moeller and W. S. Johnson (American Society for Testing and Materials, Philadelphia, PA, 1990) p. 20.
23. G. J. DVORAK, T. CHEN and J. L. TEPLY, *Compos. Sci. Technol.* **43** (1992) 347.
24. R. HILL, *J. Mech. Phys. Solids* **12** (1964) 199.
25. P. M. NAGHDI, in "Plasticity, Proceedings of the Second Symposium on Naval Structural Mechanics" (Pergamon Press, 1960) p. 121.
26. R. S. SHAH, PhD thesis, Rensselaer Polytechnic Institute, Troy, NY (1991).
27. Y. F. DAFALIAS and E. P. POPOV, *J. Appl. Mech.* **43** (1976) 645.
28. R. J. DIEFENDORF, private communication (1990).
29. N. S. STOLOFF, *Int. Mater. Rev.* **34** (1989) 153.
30. F. H. FROES, C. SURYANARAYANA and D. ELIEZER, *J. Mater. Sci.* **27** (1992) 5113.
31. M. MITTNICK, *SAMPE J.* **26** (1990) 49.
32. N. S. STOLOFF and D. E. ALMAN, *Mater. Sci. Eng. A144* (1991) 51.
33. Y. A. BAHEI-EL-DIN and G. J. DVORAK, in "Damage and Oxidation Protection in High Temperature Composites", Vol. 2, ASME AD, Vol. 25-2, edited by G. K. Haritos and O. Ochoa (American Society for Mechanical Engineers, New York, 1991) p. 21.
34. G. J. DVORAK, *J. Appl. Mech.* **53** (1986) 737.
35. *Idem*, *Proc. R. Soc. Lond. A* **431** (1990) 89.
36. Y. A. BAHEI-EL-DIN, *Int. J. Plasticity* **8** (1992) 867.
37. G. J. DVORAK, *J. Thermal Stresses* **15** (1992) 211.
38. G. J. DVORAK and Y. A. BAHEI-EL-DIN, *J. Appl. Mech.* **49** (1982) 327.

Received 28 September 1993  
and accepted 15 June 1994

Computer-Aided Modeling Tools  
for Composite Materials

Mark W. Beall, Jacob Fish,  
Mark S. Shephard, George J. Dvorak,  
Kam-Lun Shek and Rolf Wentorf

SCOREC Report #30-1993  
Scientific Computation Research Center

To appear: *Ceramic Engineering and Science Proceedings of the American Ceramic Society's 18th Annual Meeting & Exposition, Cocoa Beach, FL, January 9-12, 1994.*

Scientific Computation Research Center  
Rensselaer Polytechnic Institute  
Troy, NY 12180-3590  
voice 5182766795  
fax 5182764886



## COMPUTER-AIDED MODELING TOOLS FOR COMPOSITE MATERIALS

M.W. Beall, J. Fish, M.S. Shephard, G.J. Dvorak, K.L. Shek and R. Wentorf  
Rensselaer Polytechnic Institute, Troy, NY 12180-3590

### ABSTRACT

As part of Rensselaer's ONR/ARPA URI on *Mechanism-Based Modeling of Composite Structures* a set of computational and visualization tools are being developed and integrated together to provide scientists and engineers with the means to better design composite materials and structures. This paper briefly overviews the modular software framework which underlies the system. Some of the underlying computational techniques critical to the numerical analysis procedures are introduced, such as adaptive multiscale modeling based on hierarchic superposition techniques and effective unit cell and other micromechanical models. This paper shows examples of the application of these techniques to understanding the behavior of composite materials and structures.

### INTRODUCTION

The design of composite structures is a difficult task due to the fact that there are many different failure modes that must be taken into account. Often these failure modes occur at scales which are much smaller than the scale of a component in a structure, down to the scale of the microstructural constituents of the composite or smaller. Modeling an entire structural component at a scale that will resolve all of the important features is not a practical approach to the analysis of the problem.

To make the problem of modeling a composite structure practical, assumptions must be made about the behavior of the structure to reduce the size of the problem; these assumptions are generally referred to as idealizations. However, these idealizations are often not valid over the entire domain and generally not validated as a part of the solution process. A main focus of the current research is the development of adaptive tools that can be used to estimate the error associated with specific idealizations and automatically adapt the idealizations being used to reduce the error to the desired level.

Even after the behavior of a component is understood, the problem is not solved. Often there are great gains that can be made by adjusting some of the other parameters available in the system. One of these parameters is the processing technique used to manufacture the part being designed. Depending on the process used to create the part there may be many parameters available to adjust the final properties of the material. The ability to use these

processing parameters in design depends on being able to properly model their effects on the resulting material. To this end modeling capabilities are being developed for material processing and being integrated into an overall system for composite design.

This paper describes a system that is being developed to assist in designing with composite materials. The purpose of the system is to give the user a set of adaptive tools for the analysis of structures made from composites as well as tools to investigate processes used to create the materials and to determine their properties.

## **ANALYSIS FRAMEWORK**

### **System Overview**

The system can be broken down in four functional parts which work together to solve the overall problem of designing with composites. Each of these parts is comprised of programs which perform specific tasks. The system is designed so that any functionally equivalent part can be substituted for another without affecting other parts of the system.

**Design:** The first part of the system is the user interface to the system; it is the only part that the user directly interacts with in a design process. Two things can currently be done at this level: 1) problem specification, specifying the problem to be analyzed in terms of a geometric model, analysis attributes and the goals of the analysis, and 2) material design and selection, investigating properties of various material systems as a part of problem specification or as a stand-alone task.

**Material Property/Response Calculations:** The second part of the system is a set of tools to provide material response characteristics and homogenized material properties for various types of microstructures. Specific current capabilities include material models such as Bimodal Plasticity [1], PHA [2], and a general unit cell evaluation program. These tools are also available to other parts of the system for the same purpose.

**Thermomechanical Analysis:** The system also has tools for performing adaptive thermomechanical analysis, that is to provide accurate and efficient solutions for displacements, stresses, strains, temperatures and heat fluxes for the purpose of determining structural response and predicting failure. The specific codes that are available in this part of the system include commercial FE packages, such as ABAQUS [3], and in-house codes, such as the Mesh Superposition Research Code which implements the s-version FEM.

**Process Modeling:** The fourth functional part of the system are tools to simulate material processing. This part of the system allows the designer to investigate alternate processing procedures to increase the efficiency of the material processing and to obtain more detailed initial material properties for a thermomechanical analysis of a structure. One piece of software that is being developed models a reactive vapor infiltration process.

### **Goal Driven Methodology**

One method by which the system allows its users to get the full benefit of the various component tools is through the use of a goal driven methodology to assist in the solution of the problems to be analyzed. A main objective of the goal driven methodology is to provide

analysis expertise for use in design, in a manner which is as simple as possible to use. This is done by separating the objectives of the analysis: the goal, from the details of how it can be accomplished: the strategy.

Creation of analysis goals is primarily the responsibility of the composites designer, consisting of the definition of what is "known" or fixed, what is desired, and the allowable cost and required reliability of the analysis. Strategies are developed by analysis experts and software developers. Once an analysis goal has been specified in the system, a strategy can be automatically selected and executed to achieve it. A strategy consists of modules of software which can accomplish specific parts of an analysis goal, and a plan which provides expert guidance for implementing the analysis. During execution, inferencing details the plan by matching particular conditions of the problem with known capabilities of the methods and software modules available to the strategy.

As an example, a composite material application may have known reinforcement shape and composition and unknown instantaneous effective properties such as compliance, stiffness, thermal strain and stress vectors, mechanical and thermal concentration factors or bounds on the effective moduli. The analysis goal specifies the knowns, the desired data, plus the desired reliability of the results and the time (cost) available. A strategy plan for reaching the unknowns states that a model, e.g. PHA, random fibers in a unit cell, simple bounds, modified SCM/TFA etc., an analysis method, e.g. finite element or transformation field analysis, and a constitutive model must be determined. The details of which method and modules of software are used, and the order in which they must be executed are determined from the particular attributes of the goal and the known capabilities of the methods and software.

Strategies can readily accommodate expanded analytical capabilities. For instance, as material processing models and analytic techniques become more advanced, some of the material knowns given above could be replaced with the initial materials and processing technique parameters. The new analytical capability may then derive reinforcement shape and composition properties, helping to integrate manufacturing of the composite with the design process. The goal driven approach reduces the assumption as to how designers will want to use the new analytical capability and requires no procedures to be written or rewritten in order to accommodate those assumptions. Further details of the approach as used for idealization control can be found in [4] and [5]. A related application focusing on information dependency and planning for composite design can be found in [6].

## MULTISCALE MODELING

One of the greatest challenges in computational mechanics is to construct optimal mathematical and numerical models for large scale laminated shell structures. The challenge is to accurately determine the global behavior of the shell structure, including maximum displacements, vibration and buckling modes, as well as predicting various failure modes on the lamina level, such as delamination or ply buckling, and on the level of microconstituents, such as microcracking, debonding, microbuckling, etc. To accomplish this, research efforts have been directed in the following two areas:

- Development of idealization error estimators for laminated composite shell structures to control the quality of both mathematical and numerical models

- Development of efficient multiscale adaptive solution refinement strategies aimed at improving the quality of numerical and mathematical models

### Idealization error estimators for composite shells

Dimensional Reduction Error estimator (DRE) developed in [7] is designed to indicate areas where the equivalent single-layer model, the most inexpensive modeling tool, is insufficient. The kinematics of the model can then be enriched in these areas with a discrete-layer model to allow modeling of such failure modes as delamination. The error estimator builds on the earlier works on residual based error estimators. By this technique the dimensional reduction error  $e = u^{EX} - u^{FE} \equiv \Phi \beta$ , is approximated by a linear combination of some basis in the auxiliary FE mesh. The unknown coefficients are found by solving the auxiliary problem:

$$\frac{\partial}{\partial \beta} \left\{ \frac{1}{2} a(u^{FE} + E, u^{FE} + E)_{\Omega} - (u^{FE} + E, b)_{\Omega} - (u^{FE} + E, t)_{\Gamma} \right\} = 0 \quad (1)$$

where  $\Phi$  is defined to maintain  $C^0$  continuity of the augmented field,  $u^{FE} + E$ , and to satisfy essential boundary conditions. The auxiliary mesh is constructed by uniformly subdividing each layer into  $2^{NSD}$  self-similar subregions.

In many cases the mechanism that causes failure is at a much smaller scale - the scale of microconstituents. A common computational rationale today is to investigate various microprocesses that may lead to a progressive failure on the unit cell problem, based on a periodicity assumption. This assumption is not valid in areas of high stress concentration. Thus the application of conventional homogenization techniques to the "hot spots" leads to poor predictions of local fields. A closed form expression for a Microscale Reduction error estimator (MRE) has been derived in [8]. The proposed MRE estimator relates the homogenization error to macroscopic fields and the details of microstructure as follows:

$$\text{Homogenization Error} = X \frac{|C_1 - C_2|}{C_{eff}} \frac{\alpha(\alpha - 1)}{2} \frac{\|\nabla \varepsilon^o\|_E}{\|\varepsilon^o\|_E} \quad (2)$$

where  $C_1$  and  $C_2$  are compliances of microconstituents,  $C_{eff}$  the effective compliance of the unit cell,  $\alpha$  the volume fraction,  $X$  the size of the unit cell,  $\|\nabla \varepsilon^o\|_E$  the energy norm of the gradient of the macroscopic strain field in the homogenized FE mesh.

It can be seen that the error estimator is asymptotically exact in the sense that the microscale reduction errors vanish if either the normalized strain gradients are negligible, the unit cell is infinitesimally small, the compliances of microconstituents are almost identical or the volume fraction is close to zero or one, which corresponds to a homogeneous material. The formulation of microscale reduction error estimator is based on assessing the magnitude of the first term neglected by a classical mathematical homogenization theory [8].

### Adaptive refinement strategy

Once the sources of errors have been quantified, it is necessary to employ the most efficient solution refinement strategy. Our experience indicates that a solution strategy that exploits previous solutions and computations, such as formation and factorization of the

stiffness matrix of the lower level idealization model is likely to provide the best accuracy with a minimal computational effort. Such a hierarchical solution procedure can be obtained by superposition of finite element meshes. This procedure, known as the s-method [7][9] has the following features:

1. Overlay a discrete layer model on the equivalent single layer model in the critical regions (in-plane and through-thickness) as identified by DRE estimators
2. Overlay finite element meshes that represent the microstructure in the regions where the homogenization procedure has been identified by MRE estimator as being invalid.
3. Refine a given mathematical model (or idealization) composed of overlapping single-layer, discrete-layer and the micro finite element meshes by overlaying refined finite element meshes of the same kind in the corresponding regions until the discretization error is smaller than a user prescribed limit.

## **EXAMPLES**

### **Multiscale Modeling using the Mesh Superposition Method**

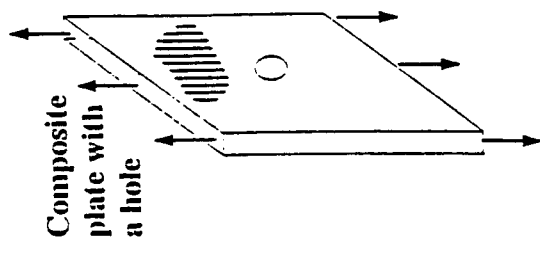
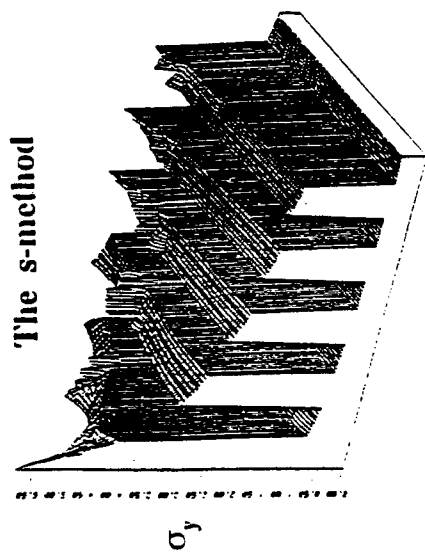
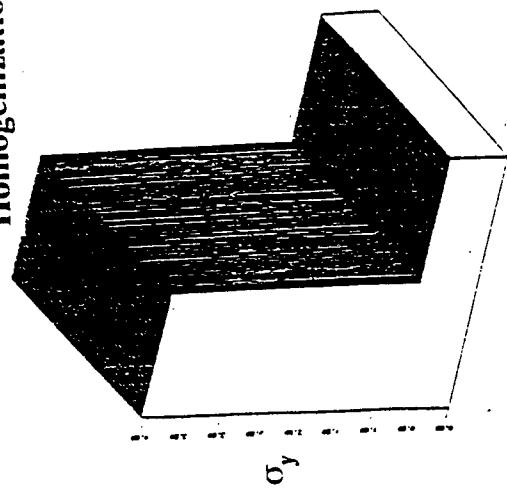
To demonstrate the performance of the method consider a single layer (2"x3") Boron-Aluminium composite plate with a centered hole (diameter 0.2") subjected to uniform loading. The MRE estimator indicated that in the radius of four unit cells from the tip of the hole the homogenization error was above 2%. In this region, as indicated in lower-middle portion of Figure 1, a micro mesh was superimposed which accurately represents the geometrical features of the microconstituents. Figure 1 shows stresses extracted from the superposition method, reference solution and the post-processing from the mathematical homogenization formulation. Note that, in the figure, the solution shown for the homogenization formulation spans only the single unit cell closest to the hole, while the other two solutions span a distance of five unit cells. The solution from homogenization does not capture the details of the stress field, while the superposition solution shows a good correspondence to the reference solution. Near the hole, the superposition method yields a maximum stress value of 5.75, while the reference solution yields 5.6 and the post-processing from homogenization, 4.0. This examples clearly demonstrates how the method of mathematical homogenization fails in areas of high solution gradients due to the fact that one of the assumptions of the method is that the gradients are small. It is, of course, these areas of high gradients that are most important to resolve.

### **Failure Surface Visualization**

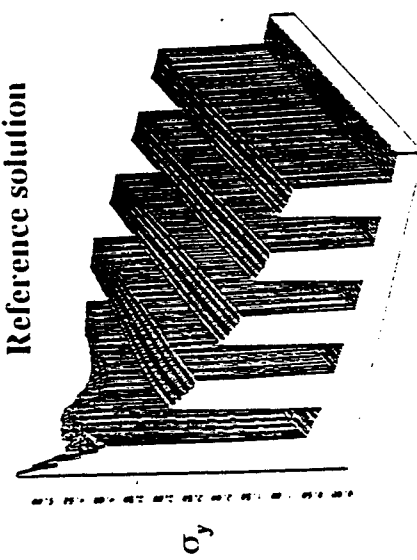
In the process of developing new materials and new processing methods, it is often desirable for the material designer to have an understanding of the behavior of a material on the microscale level. One way to look at the behavior is by using various models that predict some type of overall behavior based on the microstructure and the thermomechanical loading of the composite, such as the evolution of yield or failure surfaces.

To allow this type of information to be investigated in a natural manner a tool was developed to visualize yield and failure surfaces for composite laminates based on any theory which has a lamina-based yield or failure criteria[11]. These surfaces can be shown for

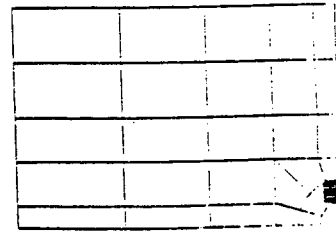
# Homogenization



# Reference solution



# Mesh Superposition



# Maximum stress sigma\_y

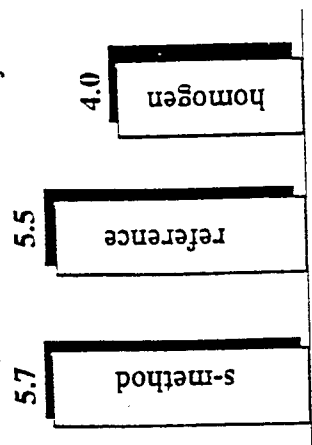
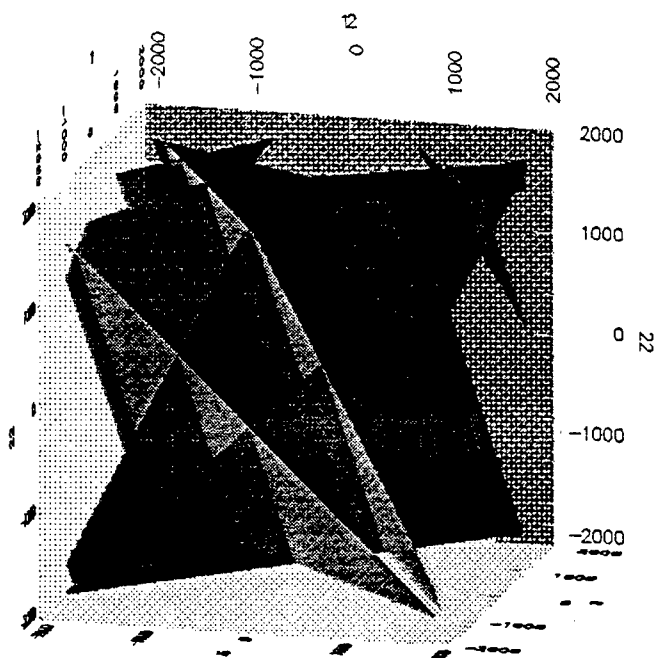


FIGURE 1. Multiscale Modeling using Mesh Superposition



Temperature = 900 C

**FIGURE 2. Failure Surfaces for a SCS6/Ti-24Al-11Nb ( $\pm 45^\circ$ )<sub>s</sub> laminate**

individual laminas in a laminate or combined to show the surface for the entire laminate. Two different failure/yield theories have been implemented: the Bimodal Plasticity theory [1] and a modified Mori-Tanaka approximation [12].

Figure 2 shows an example of the failure surfaces for each layer of an SCS6/Ti-24Al-11Nb ( $\pm 45^\circ$ )<sub>s</sub> laminate. The different surfaces indicate the stresses required to initiate various failure modes for each layer of the composite, each of the surfaces is colored to indicate the failure mode to which it corresponds. The inner envelope of these surfaces gives the initial failure envelope for the laminate. The external loading and applied temperature can be interactively changed and the failure surfaces are automatically updated. The tool was implemented using IBM Visualization Data Explorer [10] for the user interface and general visualization capabilities.

#### ACKNOWLEDGMENTS

The authors gratefully acknowledge support of this project from ARPA/ONR under grant N00014-92J-1779, "Mechanism-Based Design of Composite Structures", Steve Fishman and William Coblentz project monitors.

## REFERENCES

1. G.J. Dvorak and Y.A. Bahei-El-Din, "A Bimodal Plasticity Theory of Fibrous Composite Materials". *Acta Mechanica*, 69, 1987.
2. J.L. Teply and G.J. Dvorak, "Bounds on Overall Instantaneous Properties of Elastic-Plastic Composites," *J. Mech. Phys. Solids*, 36, pp. 29-58, 1988.
3. ABAQUS User's Manual, Hibbitt, Karlsson & Sorensen, Inc, Rhode Island, 1992.
4. M.S. Shephard and P.L. Baehmann, and M.K. Georges, and E.V. Korngold, "Framework for the Reliable Generation and Control of Analysis Idealizations", *Comp. Meth. Appl. Mech. Engng.*, vol. 82, pp. 257-280, 1990.
5. R. Wentorf, and M.S. Shephard, "Automated Analysis Idealization Control", *CONCURRENT ENGINEERING: Automation, Tools, and Techniques*, Andrew Kusiak Eds., John Wiley, New York, pp. 41-73, 1993.
6. P.M. Sargent, "Information Dependency and Cost", *Proceedings for the W4 Workshop, The 2nd International Conference on Artificial Intelligence in Design*, Carnegie Mellon University, PA, USA, pp. 47-51, June 1992.
7. J.Fish and S.Markolefas, R.Guttal and P.Nayak, "On Adaptive Multilevel Superposition Of Finite Element Meshes," *Applied Numerical Mathematics*, Vol 14., 1994.
8. J.Fish, P.Nayak, and M.H.Holmes, "Microscale Reduction Error Indicators and Estimators for a Periodic Heterogeneous Medium," accepted in *Computational Mechanics: The International Journal*, 1993.
9. J.Fish and A.Wagiman, "Multiscale Finite Element Method for Heterogeneous Medium," Vol. 12, pp. 1-17, *Computational Mechanics: The International Journal*, 1993.
10. IBM. IBM Visualization Data Explorer, User's Guide, 1992.
11. K.L. Shek, M.W. Beall, G.J. Dvorak, M.S. Shephard, "Bimodal Plasticity Evaluation Tool". SCOREC Report #23-1993. Scientific Computation Research Center, Rensselaer Polytechnic Institute, Troy NY, 12180-3590, 1993.
12. G.J. Dvorak, T. Chen and J. Teply, "Thermomechanical Stress Fields in High-Temperature Fibrous Composites. II: Laminated Plates," *Composites Science and Technology*, 43, pp. 359-368, 1992.



Automated Multiple Scale Fracture  
Analysis

Mark W. Beall, Vladimir Belsky,  
Jacob Fish and Mark S. Shephard

SCOREC Report #4-1996  
Scientific Computation Research Center

Scientific Computation Research Center  
Rensselaer Polytechnic Institute  
Troy, NY 12180-3590  
voice 5182766795  
fax 5182764886

# Automated Multiple Scale Fracture Analysis

Mark W. Beall, Vladimir Belsky, Jacob Fish, Mark S. Shephard  
Scientific Computation Research Center  
Rensselaer Polytechnic Institute  
Troy, NY 12180

**Abstract.** This paper discusses a system for automated analysis of crack propagation in heterogeneous materials. The system uses a multiscale analysis technique to account for the effect of the microstructure on the propagation of the crack. The multiscale analysis allows the microstructure of the composite to be explicitly represented in the vicinity of the crack front while using homogenized material properties elsewhere. Procedures for automatic construction and update of the models and meshes used in the analysis are described.

## 1 Introduction

The continued improvement in the price-performance of high performance workstations, and the parallel computers which build upon them, is having a dramatic impact on the ability to solve more complex physical problems. However, to take full advantage of these hardware speed improvements, advances in computational methodologies are required. One advance needed is to effectively employ the power of parallel processing. Although, this will increase the problem size possible, it does not address issues associated with (i) the need for a more detailed accounting of the physics of the problem, (ii) ensuring the reliability of the computation, or (iii) removing the labor intensive aspects of generating the numerical analysis discretizations. This paper considers the problem of discrete fracture simulation in heterogeneous three-dimensional structures and presents a set of com-

putationally efficient procedures which can automatically provide a reliable solution to these problems, while explicitly accounting for behavior at two physical scales.

To understand the failure of heterogeneous materials systems, such as reinforced concrete and structural composites, it is necessary to understand the interactions and failure of the individual constituents of the system as driven by the local stress and strain fields. The determination local fields are dictated by the behavior of the entire structure. However, it is not feasible to analyze the entire structure explicitly representing the constituents throughout the domain. This problem can be addressed by the application of multiple scale analysis methodologies which correctly combine overall models (macromechanical) for the majority of the domain with local models (micromechanical) in critical regions. The reliable application of multiple scale techniques requires mathematically sound methodologies to transfer information between the two physical scales and the ability to adaptively determine those portions of the domain where the local models are needed. Section 2 discusses the techniques used to perform and adaptively control multiple scale analyses.

Even with the ability to effectively employ multiple scale representations, the resulting discrete systems are very large and must be solved with appropriate equation solving technologies. As also indicated in Section 2, iterative equation solvers based on multigrid techniques can take direct advantage of multiple scale representations.

The failure processes considered in this paper are governed by the propagation of discrete cracks at the micromechanical level. The simulation of discrete crack growth requires criteria to indicate under what conditions a crack will propagate, in which direction it will

propagate, and how far it will propagate. Section 3 discusses the criteria used in the present work for crack propagation and discusses issues associated with the effective numerical implementation of these processes.

A final key to an effective multiple scale fracture simulation is the ability to generate and control the required models and meshes. Since any need for human intervention would introduce an expensive bottleneck, all model update and mesh generation processes must be automated. Sections 4 and 5 describe the techniques and procedures developed to support the generation of local models and meshes from a geometric model of the overall domain and a description of the microstructure. Since the geometry evolves as the crack propagates, both the models and the meshes must be updated to account for the propagation of the crack using the procedures discussed in Section 6.

It is worth noting that the entire set of procedures described in this paper employ methodologies consistent with those used in a set of parallel automated adaptive finite element procedures (Shephard et. al. 1995, de Cougny et. al. 1995) developed to take full advantage of scalable distributed memory parallel computers.

Section 7 demonstrates the application of the procedures described to crack growth in a unidirectional composite material. A comparison is made between the crack growth predicted with and without explicit consideration of the effect of the microstructure.

## **2 Adaptive Multiscale Computational Techniques for Heterogeneous Media**

In analyzing large scale structures made of heterogeneous materials it is common in practice to carry out at least three distinct levels of analysis corresponding to different length

scales: (i) macroscale (structural level), (ii) mesoscale (component level), and (iii) microscale (the level of material heterogeneity). On the structural level, structural components are treated discretely, while individual components are idealized to adequately determine their overall properties. On the component level, individual subcomponents are treated discretely, while microconstituents are treated collectively as a homogenized medium where homogenized material properties can be determined experimentally, or predicted from micromechanics. For micromechanical analysis individual phases are treated discretely, while lower scales such as material grains or atoms are treated as homogeneous.

These steps comprise a sequence of interdependent analyses in the sense that the output from one level is used as input to the next level, using constitutive laws to serve as the bridging mechanisms between the scales. It is important to note that any level of analysis is performed totally independent of the others if the required input data is available, perhaps from experiment. There is no doubt that this approach reflects a necessary compromise aimed at bridging the length scales in excess of several orders of magnitude in time and space. The obvious question arises as to the validity limits of such a step-by-step procedure. Is there a need for a coupled approach that will simultaneously consider phenomena at several different scales, and if the answer is positive, is the current status of software and hardware tools mature enough for such coupled multiscale considerations?

Let's start by addressing the first issue. Figure 1 depicts the shear stress distribution in the axial tension problem in a  $(90/0_4/90)_s$  laminate (Fish and Belsky 1994). Results are shown for one quarter of the plate cross section in the x-y plane. The lines of symmetry are at the bottom and on the right hand side of the cross section. The uniform tension load is applied normal to the x-y plane. The zoomed area of shear stress distribution in the close vicinity

to the free edge is also shown. Results of the classical step-by-step procedure based on the homogenization theory are compared to the reference solution where the size of finite elements is of the same order of magnitude as that of material heterogeneity. It can be seen that a classical step-by-step procedure predicts accurate shear stress distribution except for the close vicinity to the free edge, where it significantly underestimates maximum stress values, and along the entire interface between the two dissimilar layers. The reference solution shows oscillatory shear stresses along the entire interface, while the solution based on the classical step-by-step approach shows no such stress concentration. The magnitude of these oscillatory shear stresses is roughly  $1/3$  of the maximum shear stresses developed at the interface, but even so, these interface shear stresses may significantly affect the propagation of cracks emanating from the free edge.

Recent theoretical and numerical studies (Fish and Wagiman 1993, Fish and Markolefas 1994) have shown that in the areas of high gradients, primarily developed in the boundary layers at free edges and interfaces, the classical uncoupled step-by-step procedure may lead to poor predictions of local fields, since it assumes uniformity of macroscopic fields over the unit cell domain.

Simulation of the evolution of failure processes in heterogeneous media poses an even greater obstacle to the classical step-by-step approach. Sometimes the failure is catastrophic, and the ability to compute only the onset of failure is sufficient. Although computing the onset of failure is still a very difficult task, particularly in heterogeneous media, it is a goal that has largely been accomplished by means of a classical uncoupled step-by-step approach. However, in determining the vulnerability or survivability of a structure, a computation beyond the onset of failure is critical because there may be a considerable

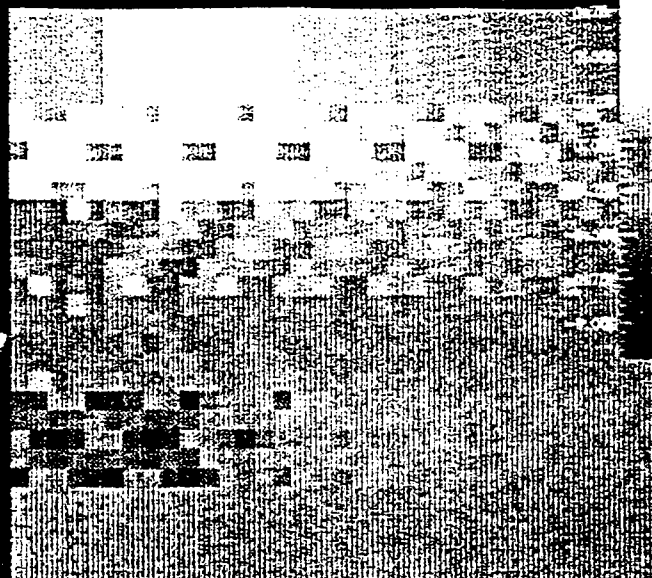
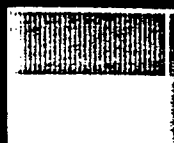
# Multigrid Solution for axial tension problem

$(90/0_4/90)_S$

1.00

$\sigma_{xy}$

'90' layer



1.00

0.75

0.50

0.25

0.00

-0.25

-0.50

-0.75

-1.00

Homogenization Theory Solution

1.00

0.75

0.50

0.25

0.00

-0.25

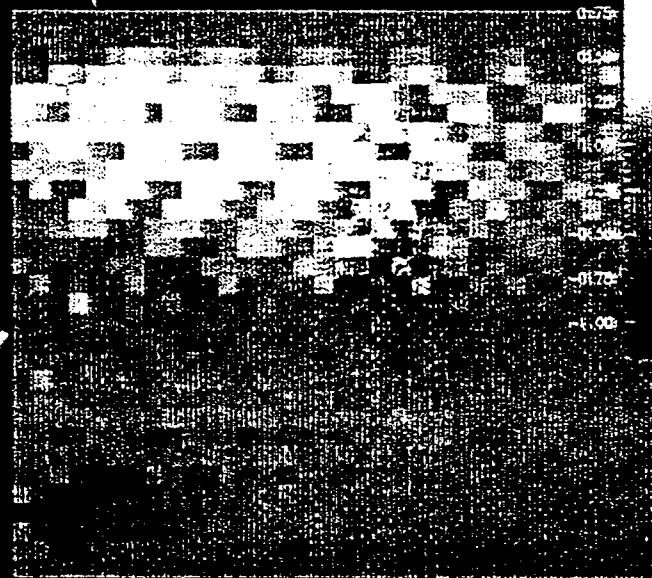
-0.50

-0.75

-1.00

$\sigma_{xy}$

'0' layer



1.00

0.75

0.50

0.25

0.00

-0.25

-0.50

-0.75

-1.00

Multigrid Micro Solution

reserve strength. Reliable simulations of failure processes in heterogeneous media emanating from the smallest scale, such as microvoid nucleation and followed by their coalescence and structural failure, require revitalization of classical bridging mechanisms between various modeling levels.

It is now feasible to use more sophisticated mathematical models and more refined discrete models, which account for close interaction between different scales. However, it is appropriate to recall the statement made by Einstein, "The model used should be the simplest one possible, but not simpler." Adaptive multiscale modeling techniques enable the analyst to start from a simpler model and then adaptively refine both the mathematical and numerical models to permit coupled multiscale considerations, whenever and wherever needed, until the simplest possible model that provides an accurate solution is obtained.

To address the question regarding the maturity of existing hardware and software tools needed for such multiscale holistic considerations, Figure 2 demonstrates the application of this approach to analyzing a typical composite structure. The adaptive multiscale strategy starts by employing classical discretization error indicators (Zienkiewicz and Zhu 1992, Oden et. al. 1989) and adaptively refining the finite element mesh on the macromechanical (shell) level to ensure accurate macro-solutions. Subsequently, dimensional reduction error indicators (Fish et. al. 1994) identify the areas where the most critical interlaminar behavior takes place, and consequently, a more sophisticated discrete layer model is placed there. Fast iterative solvers based on the multigrid technology with special inter-scale connection operators (Fish and Belsky 1995a,b) are used to solve a coupled two-scale macro-meso model. Once the phenomena of interest on the macro-meso levels have been accurately resolved, microscale reduction error indicators (Fish et. al., 1994) are



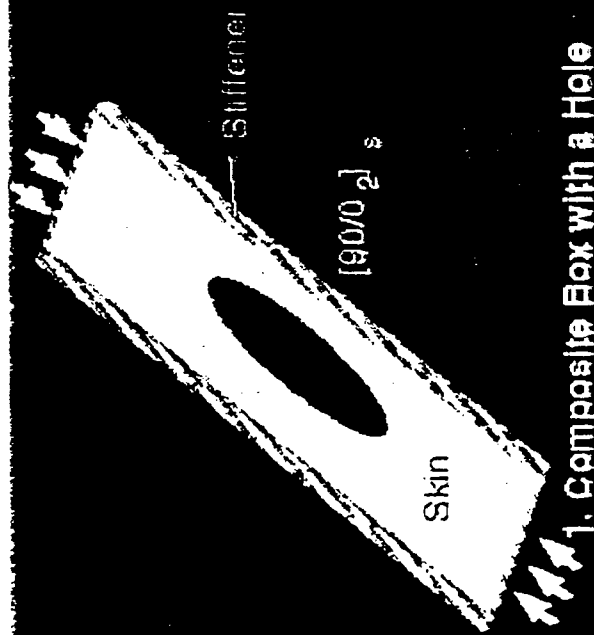
used to identify the location of critical microprocesses and consequently, a micro-mesh is placed there. The three-scale coupled macro-meso-micro model is again solved using a three-scale multigrid process (Fish and Belsky 1995a,b). In this methodology, discretization error indicators and adaptive refinement strategy are employed simultaneously at three different scales to ensure reliable multiscale simulations.

The three-scale model described in Figure 2 contains over 1,000,000 degrees-of-freedom. The estimated CPU time for solving it with a conventional direct solver based on skyline storage is over 705 hours on a single processor SPARCstation 10, which essentially makes the model intractable. With a special purpose multigrid technology for heterogeneous media, developed in (Fish and Belsky 1995a,b), the same problem has been solved in less than 16 hours on a single processor SPARCstation 10, turning it into a practical overnight job.

The derivation of the inter-scale transfer operators for the three-scale multigrid method is based on the asymptotic solution expansion, which assumes infinitesimality of the unit cell. The asymptotic forms of the prolongation and restriction operators are obtained by discretizing the corresponding asymptotic expansions. For unit cells of a finite size, the regularization function has been introduced to obtain well-behaved inter-scale transfer operators, termed as homogenization based operators. The resulting homogenization based prolongation operator is given by:

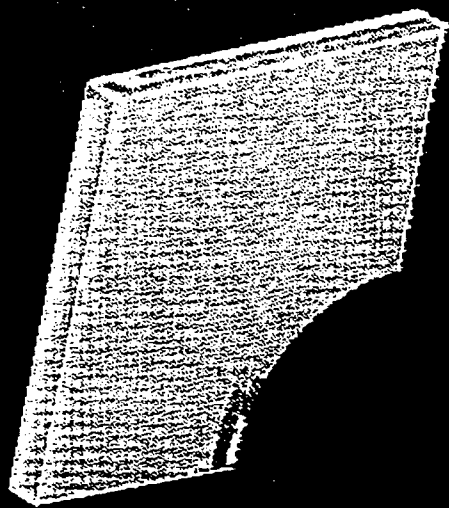
$$\tilde{Q} = Q + dQC\nabla_s N(X_g) \quad (1)$$

where  $Q$  is the standard multigrid linear prolongation operator,  $d$  is the unit cell solution,  $\nabla_s N(X_g)$  is the symmetric gradient of the shape functions in the auxiliary grid evaluated



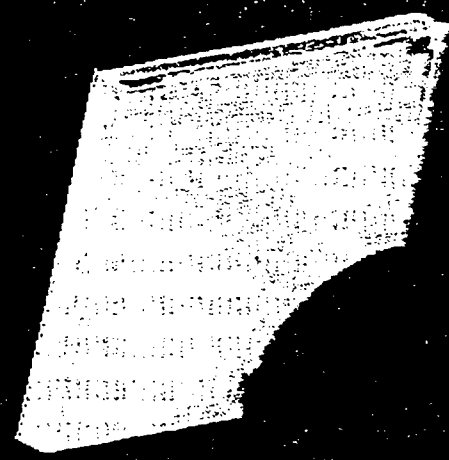
1. Composite Box with a Hole

Shell (Macro) model



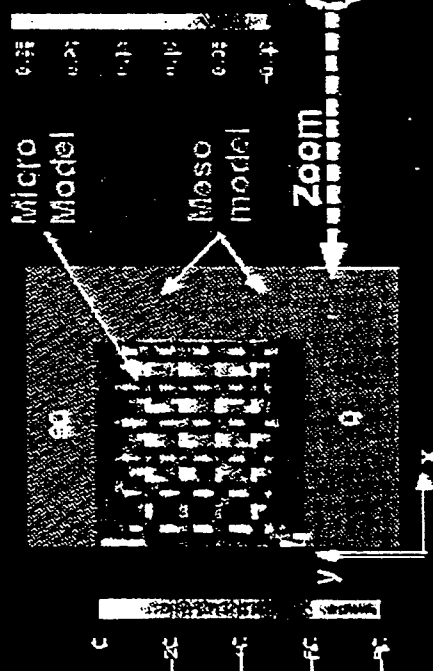
2. Strain Energy Density

3. Dimensional Reduction Errors

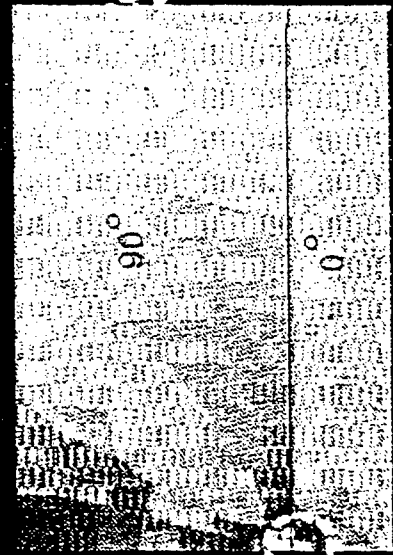


# Adaptive Multiscale Computational Technology for Composite Materials and Structures

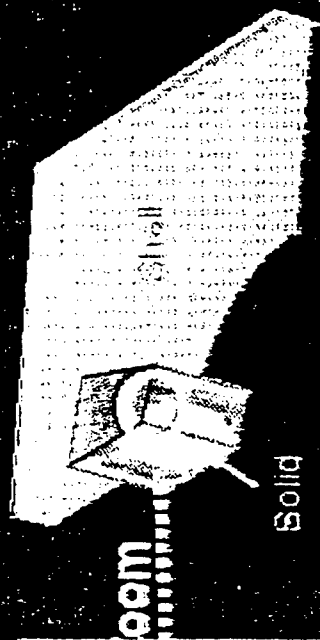
## Macro-Meso-Micro model



6.  $\sigma_y$  in the microstructure



5. Microscale Reduction Errors



4. Strain Energy Density

## Macro-Meso model

at the Gauss points in the auxiliary mesh,  $C$  is the projection operator aimed at maintaining  $C_0$  continuity of the displacement field on the micro-scale. For a technical description of these operators see (Fish and Belsky 1995b).

The rate of convergence of the multigrid process for heterogeneous media has been studied in (Fish and Belsky 1995a,b). It has been proved that for periodic 1-D heterogeneous media problems, the rate of convergence of the two-grid method with special inter-scale transfer operators is given by:

$$\|e^{i+1}\| = \frac{q}{4-q} \|e^i\| \quad q = \frac{\sqrt{d_1 d_2}}{0.5(d_1 + d_2)} \quad (2)$$

where  $d_i$  represent the stiffnesses of microconstituents. Note that if the material is homogeneous and the mesh is uniform ( $d_1 = d_2$ ) a classical two-grid estimate is recovered:

$$\|e^{i+1}\| = \frac{1}{3} \|e^i\|. \text{ Otherwise } q < 1 \text{ resulting in } \|e^{i+1}\| < \frac{1}{3} \|e^i\|. \quad (3)$$

Note that if the stiffness of a fiber is significantly higher than that of a matrix, i.e.  $d_1 \gg d_2$ , then the multigrid method converges in a single iteration. In multidimensions, convergence of the multigrid process for periodic heterogeneous media has been studied (Fish and Belsky 1995b). It has been found that convergence trend characteristics found in the 1-D cases are closely followed in multidimensions. In practice, for fiber/matrix stiffness ratios,  $d_1/d_2$ , of approximately ten, 4 to 6 multigrid cycles are sufficient to obtain converged results.

### 3 Crack propagation procedures

There are two common approaches taken in the development of crack propagation procedures. The 'global' approach assumes that crack extension takes place in an idealized anisotropic homogeneous material with gross combined properties of the constituents. The 'local' point of view, often referred to as micromechanical approach, considers material as heterogeneous. The 'local' approach takes into consideration local damage patterns. In the present study we adopt a global-local approach by which 'local' description is used in the vicinity of the crack front while elsewhere the medium is treated as homogenized.

Crack growth simulations, in general, are difficult to perform because of the need for continual geometry and computational mesh updates. This process becomes even more challenging for problems in heterogeneous media where in addition to the geometry and mesh, the mathematical model has to be updated.

The crack propagation increment  $\mathbf{x}_A - \mathbf{X}_A$  is defined in terms its shape  $\{\tilde{\mathbf{S}}_A\}_{A=1}^n$  and amplitude  $\alpha$

$$\mathbf{x}_A = \mathbf{X}_A + \alpha \tilde{\mathbf{S}}_A \quad (4)$$

where  $\mathbf{X}_A, \mathbf{x}_A$  denote position of the finite element node  $A$  located at the crack front interface before and after incremental update, respectively, and  $n$  is the number of nodes on the crack front interface. Prediction of crack trajectory requires determination of  $\{\tilde{\mathbf{S}}_A\}_{A=1}^n$  and  $\alpha$ .

No generally accepted criterion exists for predicting trajectories of cracks in three-dimensional heterogeneous media. Among the popular phenomenological theories for predicting instantaneous angle of crack propagation in two-dimensional homogeneous media are

maximum tangential stress criterion, maximum energy release criterion and minimum strain energy density criterion. Two major obstacles in applying these criteria to three dimensional applications in heterogeneous media with arbitrary crack surfaces are summarized below:

1. Crack growth depends on the geometry, boundary conditions and material characteristics of microconstituents, including strength and fracture toughness.
2. Asymptotic fields are generally not known in these cases.

To overcome these difficulties we propose the following generalization of the classical crack propagation criteria:

1. The preliminary crack propagation shape  $\{\tilde{S}_A\}_{A=1}^n$  is defined on the basis of the following normalized criteria:

$$\|S_A\| = \frac{F_A}{G_A} \quad (5)$$

where  $\| \cdot \|$  denotes Euclidean norm of a vector,  $F_A$  is either maximum energy release rate, maximum tangential stress, or minimal strain energy density.  $G_A$  is either fracture toughness, strength in tension or critical energy density, respectively.

2. The unit vector  $e_A = S_A / \|S_A\|$  defining the crack propagation direction at node A points in the direction of the maximum ratio  $F_A / G_A$  (among the elements connected to node A) projected onto the plane normal to the crack tip interface at node A.
3. Deformation and stress fields are either directly extracted from the finite element analysis or by postprocessing finite element solution (Niu and Shephard 1993, Niu and Shephard 1994).

4. Smoothing is applied to the crack propagation shape as obtained from equation (5) to avoid numerically defined oscillations.

The process of finding the smoothed crack propagation shape can be viewed as constrained optimization problem, which states:

Find the smoothed crack propagation shape increment,  $\|\tilde{S}_A\|$ , such that

$$\int_L (\|S_A\| - \|\tilde{S}_A\|)^2 dL \rightarrow \min \quad (6)$$

subjected to the smoothness constraint:

$$\int_L \left( \frac{\partial}{\partial L} \|\tilde{S}_A\| \right)^2 dL < \varepsilon^2 \quad (7)$$

where  $L$  is a coordinate along the crack tip, and  $\varepsilon$  is the smoothness parameter. Solution of the constrained optimization problem yields the following differential equation:

$$\left( I - \gamma \frac{\partial^2}{\partial L^2} \right) \|\tilde{S}_A\| = \|S_A\| \quad (8)$$

subjected to periodic boundary condition. Note that the parameter  $\gamma \ll 1$  is defined by the user. Equation (8) can be solved using finite element method using bi-linear discretization of  $\|\tilde{S}_A\|$ .

Due to the history dependence of crack growth, the problem of evaluating the amplitude  $\alpha$  can be stated in terms of an ordinary delay differential equation (Fish and Nath, 1993):

$$\frac{dx_A}{d\alpha} = \tilde{S}_A(\alpha) \quad (9)$$

The special nature of ordinary delay differential equations has the effect of making the crack path smoother with evolution in 'time' if the evolution of the right hand side vector in (9) is smooth. For problems in heterogeneous media  $G_A$ , and thus  $\tilde{S}_A$ , are  $C^{-1}$  continuous functions in  $\alpha$  and thus the optimal integrator for such a differential equation should be based on a type of integration scheme which does not rely on the smoothness of the crack path. The simplest form of such integrator is based on a predictor-corrector scheme:

$$\begin{array}{ll} \text{Predictor} & \bar{x}_A = X_A + \tilde{S}(X_A)\alpha \\ \text{Corrector} & x_A = X_A + \frac{1}{2}(\tilde{S}(X_A) + \tilde{S}(\bar{x}_A))\alpha \end{array} \quad (10)$$

The normalized local truncation error,  $\beta$ , is given as:

$$\beta = \sqrt{\sum_{A=1}^n \frac{(x_A - \bar{x}_A)^2}{(x_A - X_A)^2}} = \sqrt{\sum_{A=1}^n \frac{(\tilde{S}(\bar{x}_A) - \tilde{S}(X_A))^2}{(\tilde{S}(\bar{x}_A) + \tilde{S}(X_A))^2}} \quad (11)$$

The crack propagation amplitude may increase or decrease to keep the magnitude of the normalized truncation error,  $\beta$ , below the user prescribed tolerance.

## 4 Problem Definition to Support Automated Model Construction

The effective application of multiple scale analysis requires automation of the entire process. Without automation the analysis is effectively impossible due to the time and effort required to update the models and meshes needed as the analysis progresses. The automation of a set of engineering analyses requires all analysis models, and their discretizations, be derived from a single problem definition. The two key components of the problem definition are the domain description (the geometric model), and the analysis attributes

defined in terms of it. For sake of discussion, this single problem definition, from which all other models are derived, is referred to as the primary problem definition.

#### **4.1 Geometric Model**

The geometric models constructed from the primary problem definition in support of multiscale analyses vary from a representation of the middle surface of a composite structure, to one containing multiple volumes representing the micromechanical structure of a composite material. The representations used must be able to support the requirements of automated discretization construction procedures (Shephard and Finnigan 1989, Shephard and Georges 1991). The primary model must be structured such that the various idealized engineering analysis models can be automatically constructed, and the interactions between those models controlled. For example, at the highest level, a composite structure is idealized as a surface (a shell model), while at a portion is represented as a multi-layer volume, and in a local region the microstructural components are represented as volume elements. The relation of all of these models to each other must be understood by the analysis, this done by relating all of them back to the primary problem definition.

The model construction and discretization processes can be effectively supported by geometric modeling systems supporting non-manifold representations of general combinations of volumes, surfaces and curves (Weiler 1988). In addition to taking direct advantage of the massive development effort required to produce such geometric modelers, this approach can properly support all the geometry needs of automatic mesh generation (Shephard and Georges 1992).



The approach of defining the primary geometric model as a detailed geometric representation at the lowest physical scale is not advantageous for several reasons, including: (i) the model sizes would be unacceptably large, (ii) the automatic construction of the higher level models can be more complicated than the automatic construction of low level models, and (iii) user effort to construct detailed lower level models would be burdensome to the design process. The approach taken here is to store an overall geometric representation supplemented with the additional geometric feature data required to automatically construct needed idealized geometric models. Usually this means that a simple, engineering-type geometric model is used to describe the structure and attributes are used to describe the details required for the analysis, such as the material microstructure. This approach also corresponds well to the design process, where different portions of a structure will be understood to different levels of detail at various times.

The most geometrically demanding processes involve the construction of the idealized geometric models for specific analyses from the primary geometric model. One class of such operations are dimensional reductions where, for example, the middle surface of a complex three-dimensional solid, which is thin in some through-the-thickness, direction is needed for an analysis. Another example is constructing a multi-material solid model of a representative unit cell from basic composite specifications when micromechanical models are included in the analysis process. The approach used to address these needs is to employ the geometric construction functionality of commercial solid modelers, driven by appropriate knowledge housed in the primary model and the analysis strategy being executed. Figure 3a shows the a unit cell for a composite weave automatically constructed in the Parasolid non-manifold solid modeler (Parasolid 1994) using the basic manufacturing

parameters defining the weave and the procedures described in Section 5. The automatically generated mesh of this model is shown in Figure 3b.

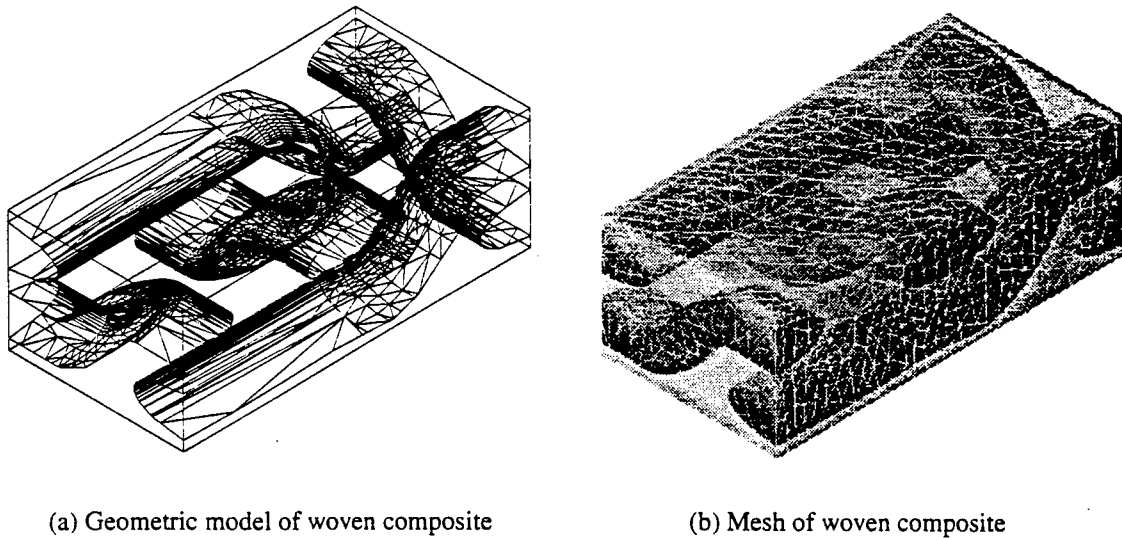


**FIGURE 3. Automatically constructed and meshed unit cell model**

#### **4.2 Analysis and Idealization Attributes**

Analysis attributes consist of the information past the geometric model needed to specify an analysis model. Analysis attributes include material property, boundary condition, load, and initial condition information. Idealization attributes define the information needed to convert a primary model to the idealized model used in an analysis process. Examples of idealization information are specification of the use of the middle surface for an overall deformation analysis, and the information defining the microstructure of a unit cell. To support an automated environment, the analysis and idealization attributes must be defined directly in terms of the physical parameters and associated directly with the geometric representation of the primary geometric model (Shephard 1988, Wong 1994). When defined in this manner they can be properly transferred to the idealized analysis models and their discretizations.

The physical description of all analysis attributes are in terms of tensorial quantities. The components of the structure used to define the attributes' physical information include (i) the order of the tensor, (ii) an indication of the coordinate system the tensor is defined in, (iii) the symmetries possessed by the tensor, and (iv) the distribution information defining each component of the tensor in the given coordinate system.

Since a number of basic attributes, such as material parameters, are likely to be used in multiple analyses, it is advantageous to allow the single specification of an attribute and to collect the attributes appropriate for an analysis into the specific analysis case desired. A hierarchical organization structure that allows the convenient collection of attributes, including the application of multipliers has been put into place.

Finally, attributes must be associated with the entities in the geometric description of the domain. Complications are introduced in the case of multiple scale analyses since it is necessary properly transfer the appropriate attribute information from the primary attribute definition to the idealized analysis models. The transfer of the attributes must correctly deal with such processes as dimensional reductions and replacement of a set of heterogeneous constituents with a homogeneous continuum.

## **5 Automatic Generation of Models and Meshes for Multiscale Analysis**

The multiscale analysis used here treats the problem being solved as a three level problem. The top level is the component (macro) level, where all the material properties are considered to be homogenized. The bottom level is the microstructural level where all the details of the microstructure, and damage that is occurring to the microstructure, are represented.

The middle level serves as a transition between these two level and incorporates any macro level damage.

For the discrete crack propagation problem discussed here primary problem definition consists of a solid geometric model of the physical structure being analyzed (the macro model) with appropriate analysis attributes and idealization attributes that describe the layup and microstructure of the composite. These attributes include the type of microstructure, the parameters needed to build a unit cell, the material properties of the constituents and the orientation of the unit cell with respect to the macro model. The models that represent the lower levels of the analysis are constructed using the information in this problem definition. The initial crack geometry is also specified in the primary problem definition.

### **5.1 Unit Cell Construction**

The primary model definition includes a definition of the unit cell that describes the microstructure. This definition is in terms of the parameters that define the unit cell (such as volume fraction and fiber diameter for a continuous fiber composite). The geometric model of the unit cell is created by the system when needed.

Currently, the microstructure geometry is assumed to be periodic which allows it to be represented by the repetition of a single unit cell. This unit cell is used for the calculation of homogenized material properties using standard homogenization procedures (Bakhvalov and Panasenko 1989, Guedes and Kikuchi 1991) and for construction of the microscale model of the composite. Both the model and the mesh of the unit cell must be periodic.

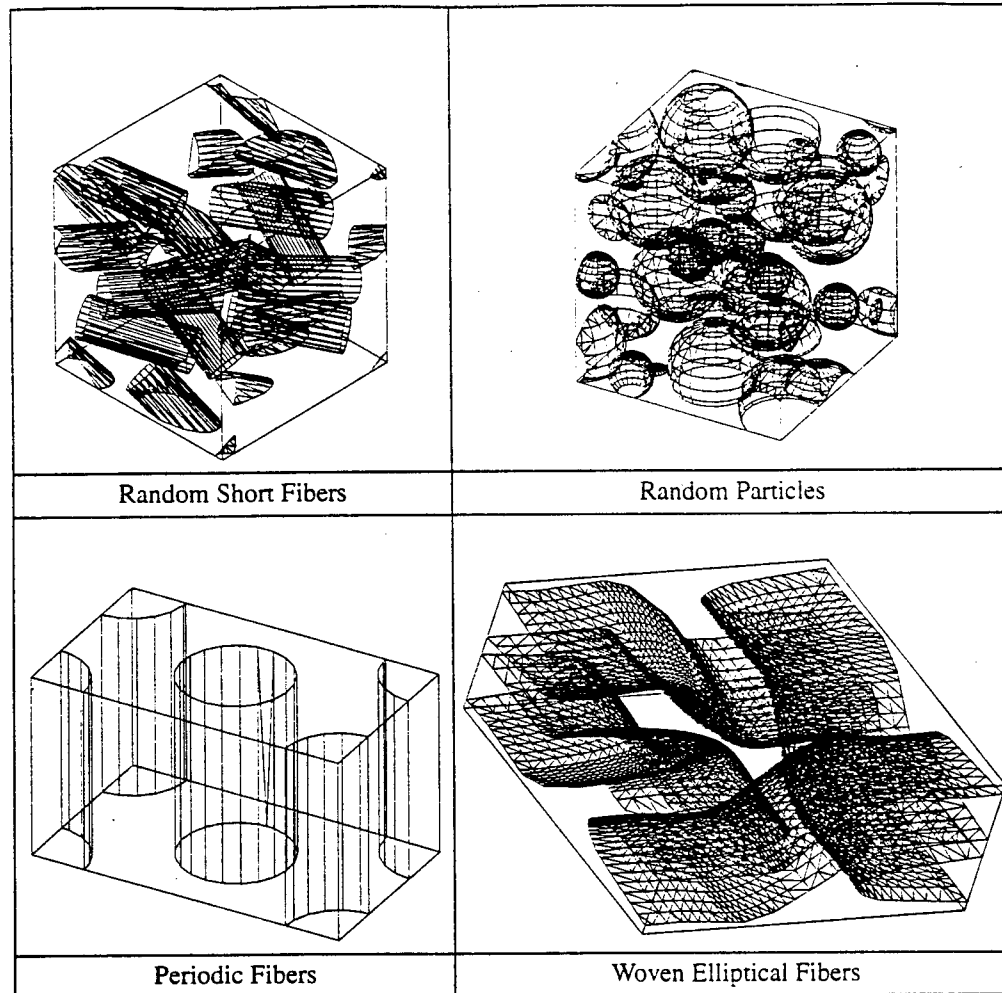
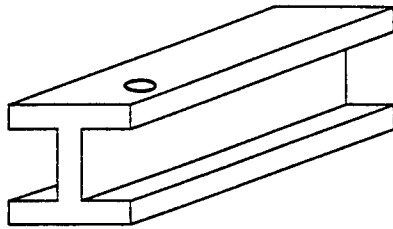


**FIGURE 4. A sample of the various types of unit cells that can be created.**

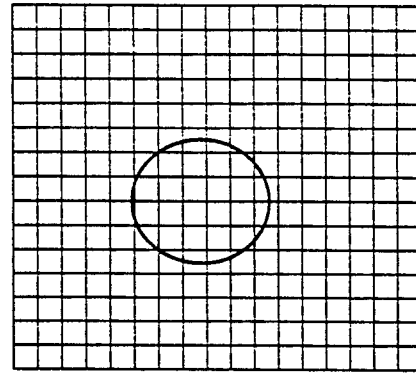
Common composite unit cells are: aligned fibers, random chopped fibers, random particles, and woven fibers (Figure 4). The unit cells fall into two categories: those with prescribed structure and those with random structure. The unit cells with prescribed structure, such as the aligned fiber and the woven fiber cells in Figure 4, are created from a parametric model of the unit cell. The parameters in the model include fiber size, volume fraction, and other geometric properties of the unit cell. The unit cells with random structure, such as chopped fibers and particles, are generated using a stochastic procedure that randomly inserts appropriate reinforcements into the unit cell while enforcing the periodicity requirement (Shephard et. al. 1995b).

## 5.2 Microscale Model

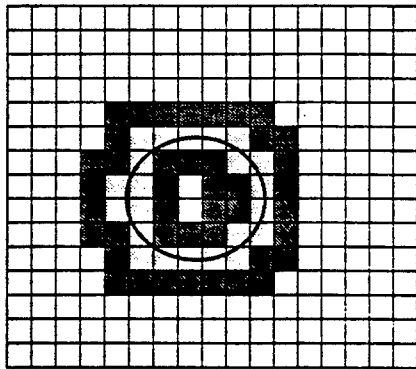
The domain of the micro model is the set of unit cells that encompass the critical areas of the model where it is necessary to resolve local fields. For the crack propagation problem this area is the unit cells that enclose the crack front. The steps to find this domain for the crack propagation problem are:



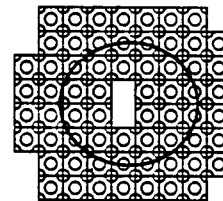
(a) Macro model with crack location indicated



(b) unit cell grid overlaid on model



(c) domain of micro model found



(d) micro model created

**FIGURE 5. Defining the domain of the micro model.**

1. Given the overall model (Figure 5a) a regular grid is defined over the portion of the macro model that encompasses the required microscale domain. Each grid cell is one unit cell in size (illustrated in Figure 5b with the third dimension removed for clarity).

This grid must be defined to be aligned with the microstructure such that when the unit cells are inserted in the grid cells, the correct microstructure is created. The grid is only "defined", it is not actually created in the geometric modeler.

2. The grid cells containing the crack front, the minimal domain for the micro model, are determined as follows: Pick a point on the curve defining the crack front and determine which cell the point is in. Add this cell to the list of cells that the crack front passes through. Find which cell face, edge or vertex the curve passes through as it exits the cell by intersecting the curve with the planes defined by each cell face of the current cell. Add the cell on the opposite side of the face to the list of cells that the crack front passes through. If the crack front passes through an edge or vertex then add all the cells touching that edge or vertex. Continue this procedure, tracking the curve as it passes from one cell to another until the entire curve has been traversed. This is illustrated by the light grey filled cells in Figure 5c.
3. This minimal domain is extended by adding  $n$  layers of cells surrounding the minimal cells to the model (Figure 5c shows one layer of these cells added, shaded dark grey) giving the domain of the micro model. The number of additional layers depends on how far the crack will be allowed to advance in a single analysis step. The crack front must always remain within the micro model.

Once the domain of the micro model has been determined, the actual model can be constructed. For each cell in the grid that has been determined to be in the domain of the micro model, the model of the unit cell is duplicated, translated and rotated so that it corresponds to the position and orientation of that grid cell. The boundaries of adjacent unit cell are then sewn together to make a single model. This model, when unioned with the portion

of the crack model that is interior to the unit cells, makes up the microscale model. Material property attributes are then associated with the entities in the micro model by copying them from the corresponding entities in the unit cell model. The result of this process for a delamination problem is shown in Figure 6.

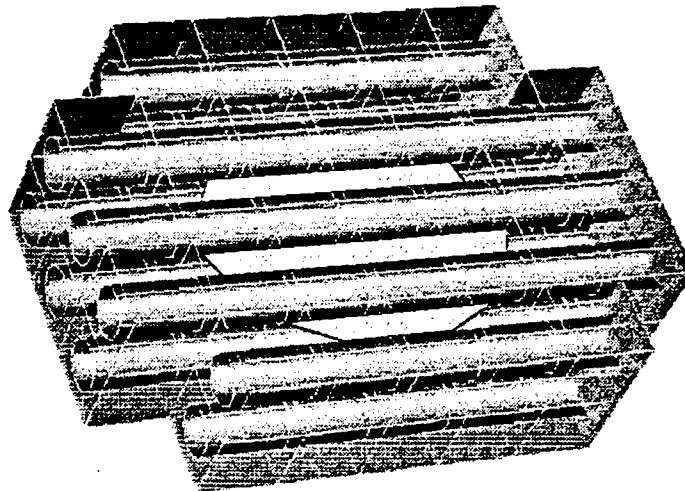


**FIGURE 6. Microscale model of delamination crack**

To support the analysis procedures, the mesh on the micro model boundary must be identical to that which is on the boundary of the unit cell that was used to calculate the homogenized material properties. The mesh on the interior of the model has no restrictions. This requirement is enforced by copying the mesh from the boundary of the unit cell to all the faces on the boundary of the model, then meshing the other (interior) faces of the model using the Finite Octree mesh generator (Shephard and Georges 1991). Finally the interior of the model is meshed using an element removal procedure that works from the given boundary mesh.



### 5.3 Transition Model

The transition model is used to connect the macro model, with its coarse mesh and homogenized material properties, and the micro model, with its fine mesh and explicit microstructure. The outer boundary of the transition model is the boundary of the union of all the elements in the macro mesh that the micro model is interior to (Figure 7). (In addition some elements that the micro model is very close to may be added). Imbedded in the interior of the transition model are a set of non-manifold faces (faces with model regions on both sides) that represent the outer boundary of the micro model and the portion of the crack face that is external to the micro model (Figure 7c). The portion of the crack internal to the micro model does not need to be represented, but it can be, and is in the examples shown here (whether or not this part of the crack is represented is irrelevant since the micro model represents the correct geometry in that portion of the domain). The transition model created for the delamination crack in Figure 6 is shown in Figure 8.

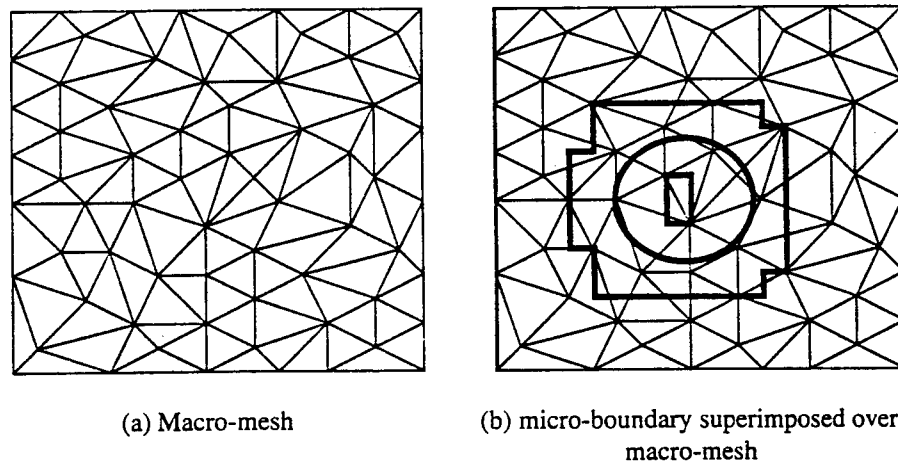


**FIGURE 7. Construction of the transition model**

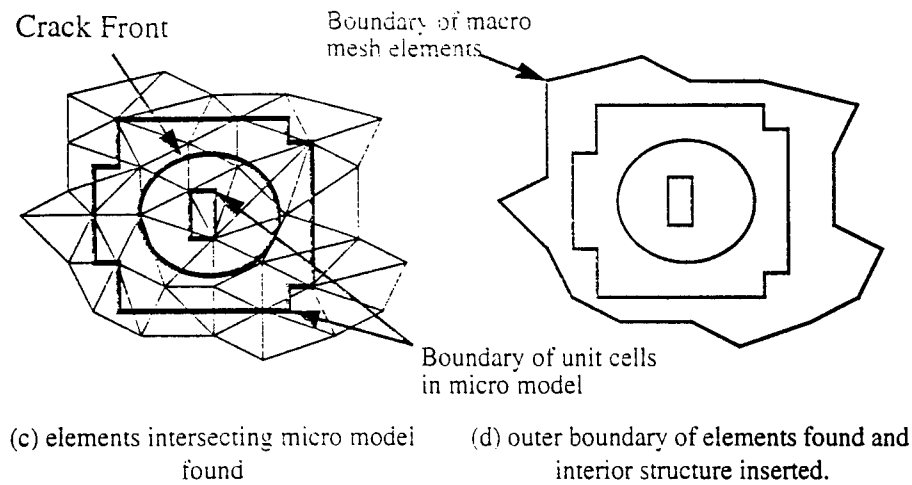


**FIGURE 7. Construction of the transition model**

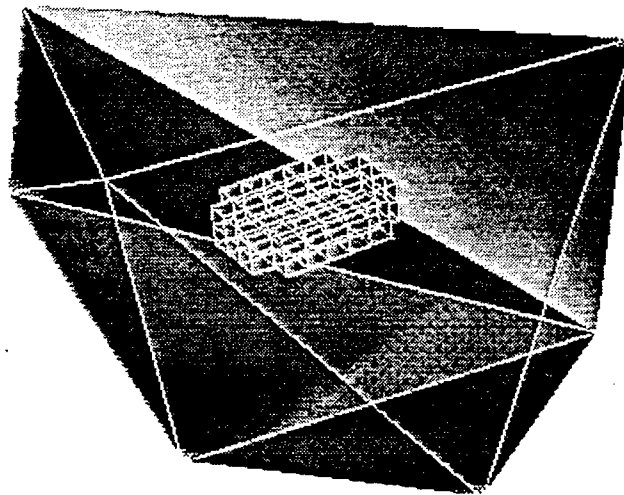


**FIGURE 8. Transition model**

The mesh for the transition model does not need to be compatible with the mesh of the macro model, however there should be no elements on the boundary of the transition mesh that are in more than one macro mesh element face. This is ensured by constructing the transition model so that the edges of the macro mesh are retained on the boundary (i.e. coplanar faces on the boundary are not unioned to make a single face so the edges that define the original faces are retained). Although compatibility of the mesh is not required, it is

desirable, from a convergence standpoint, to have the size of the elements in the transition mesh roughly (within a factor of 3 to 5) the same size as the elements in the macro mesh on its outer boundary and roughly the size of the elements in the micro mesh on that interior boundary.

## **6 Model and Mesh Updates for Crack Propagation**

To simulate the growth of the crack for a step, the analysis must update the representation of the crack to account for the growth predicted at the last step. This process can be made efficient by performing local modifications to the models and meshes to reflect the growth of the crack. This works well since the majority of the updates only change the representation at the micro level. As the crack grows, it eventually approaches the boundary of the micro model, requiring the micro model domain and, thus, the transition model and mesh to be updated. The updates of the higher level models only happen occasionally. An outline of the steps in the model update are as follows:

1. From the results of the analysis determine the updated geometry of the crack.
2. Update the crack representation in micro model and mesh to reflect the crack growth.
3. If the crack front nears the boundary of a unit cell, the micro and transition models are updated as follows:
  - a. Add unit cells ahead of crack and remove them behind, to ensure that the micro-model exists for the desired distance ahead of the crack front.
  - b. Update the transition model to reflect the new micro model domain.

## 6.1 Crack Update

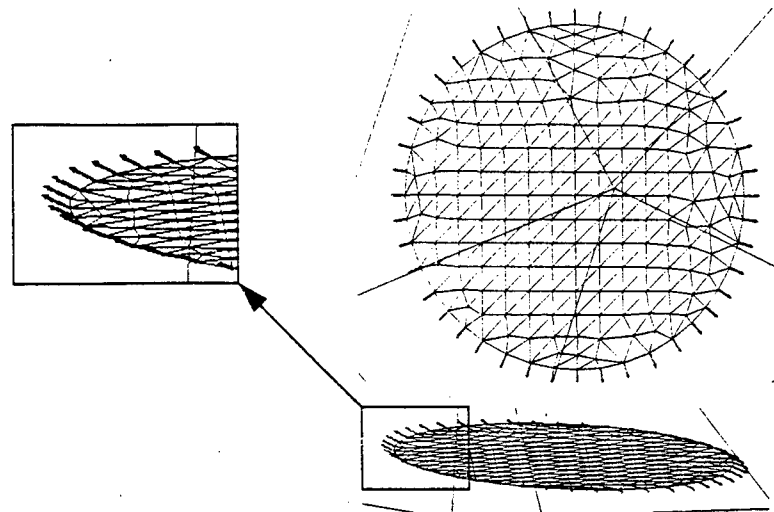


**FIGURE 9. Analysis results showing predicted crack growth.**

As shown in Figure 9, the analysis provides the direction and magnitude of the crack growth at each vertex on the crack front. This information is used to define the “crack extension” which is the geometric representation of the new crack surface. To avoid placing unnecessary constraints on the growth of the crack the crack extension is defined independently of the mesh. It is defined as a set of triangular faces extending from the current crack front to new locations for the vertices on the crack front given by the analysis (Figure 10).

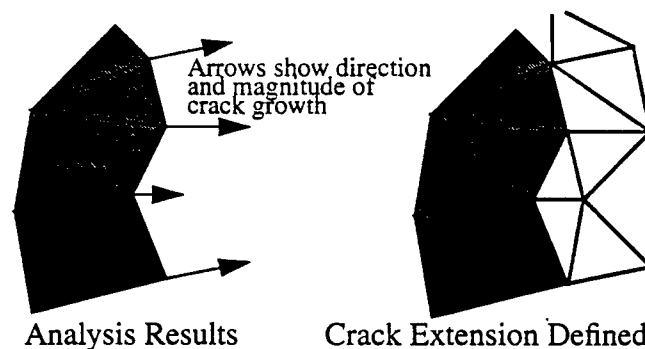


**FIGURE 10. Definition of crack extension from analysis results**

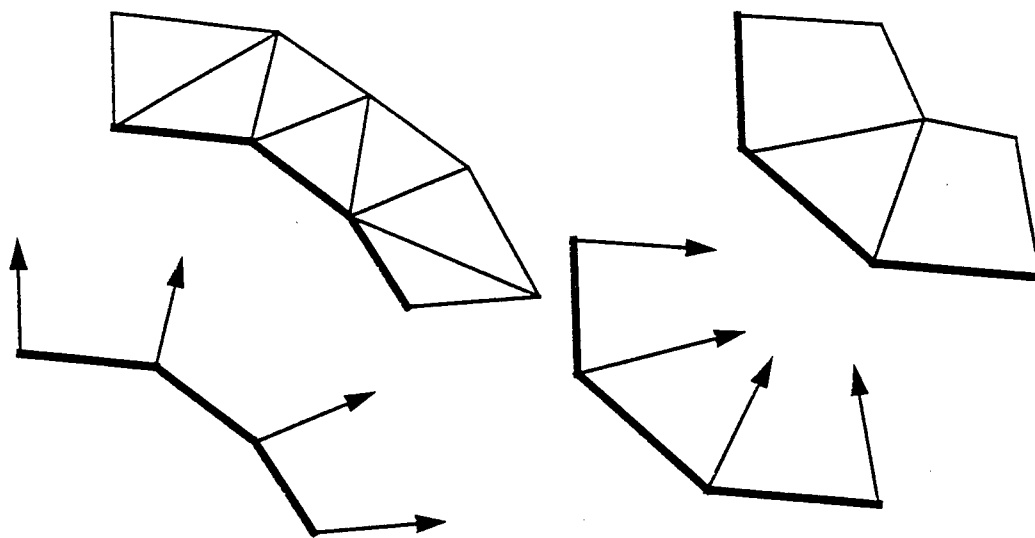
To construct the crack extension, the direction and magnitude of growth from each node on the crack front is added to the nodes current location and a new position is found. A triangular mesh is then constructed that extends from the old crack front to these new locations. The triangulation procedure must account for crack front expansion or contraction as illustrated in Figure 11, using the following procedure:

Let  $d_{ij}$  be the distance between two adjacent vertices,  $i$  and  $j$  that will form the new crack front.  $l_{max}$  is the maximum desired edge length on the crack front.  $\alpha$  ( $\alpha > 1$ ) and  $\beta$  ( $\beta < 1$ ) are two constants that define a criteria to guide the triangulation process to account for expansion and contraction.

If  $d_{ij} > \alpha l_{max}$ , then crack front is expansion must be accounted for by the introduction of new vertices on the front. A new vertex is introduced midway between those two vertices and the mesh is created accordingly as shown in Figure 11a.

If  $d_{ij} < \beta l_{max}$ , then the crack front contraction must be accounted for by coalescing the two adjacent vertices into a single vertex as shown in Figure 11b. This procedure helps prevent the crack from locally self intersecting as the crack front contracts.

For the examples shown later in this paper,  $l_{max}$  was selected to be equal to the maximum amount of propagation of the crack for a given step. This was done to ensure well shaped elements could be created around the propagating crack since the mesh currently created around the new crack will use these faces as faces in the mesh (as described in the next section). The other two parameters were selected as:  $\alpha = 1.2$  and  $\beta = 0.3$ , which can be shown to maintain control of the element shapes.



(a) Expanding crack front

(b) Contracting crack front

**FIGURE 11. Special cases for creating crack extension**

## 6.2 Micro mesh update

The crack extension is taken as the geometric representation of the growth of the crack. Since the crack extension intersects elements in the current mesh at places other than their boundaries, a method is needed to update the mesh to make it conform to the crack extension. Two approaches have been developed to allow this arbitrary crack growth: local remeshing and mesh modification. Local remeshing deletes the portions of the mesh that are intersected by the crack extension, and then creates a new mesh that reflects the presence of the new crack growth in this local area. Mesh modification uses the geometry defined by the crack extension to split mesh entities in the existing mesh to reflect the crack growth. Only the local remeshing procedure will be discussed in this paper, the mesh modification will be described in detail in a later paper.

The first step in growing the crack is to determine the interaction of the crack extension with the existing mesh. For each face in the crack extension, the mesh regions it interacts with are found as follows:

1. Get the mesh regions surrounding any mesh vertices on original crack front.
2. Intersect edges of extension face with faces of the regions, if intersection is found add the region on the other side of the intersected face to the list regions to be checked.
3. Intersect the extension face with edges of the regions found in step 2, add any new regions of the intersected edges and vertices to the list of regions to be checked.
4. Repeat 2 and 3 until no more regions are found.

This step is repeated for each face in the crack extension, resulting in a list of mesh regions in the original mesh that the crack extension touches or passes through.

The next step is to delete all of the mesh regions that were found to interact with the crack extension, creating a hole in the mesh into which the crack extension mesh is inserted. One additional layer of mesh regions surrounding this hole in the mesh is then also deleted, for two reasons. First, the mesh in front of the crack needs to be refined to allow a good solution to be obtained. By removing this additional layer of mesh regions and refining the mesh on the boundary of the hole (by splitting mesh edges which are longer than a certain length) this is easily accomplished. Second, the original hole in the mesh can be extremely close to the crack extension, which can result in a poor mesh being created when the hole is remeshed. By moving this boundary away from the crack extension a much better mesh is obtained.

After the hole has been cleared out in the existing mesh, the crack extension mesh is inserted as shown in Figure 12. The hole is then meshed using a face-removal meshing procedure.

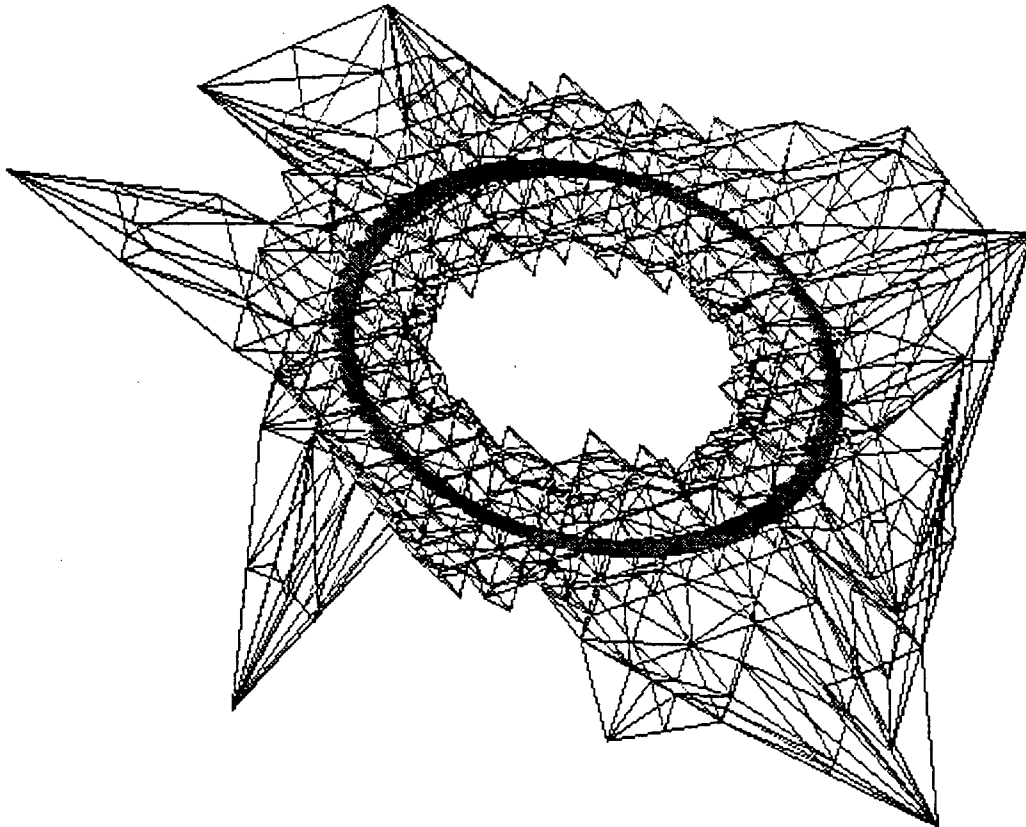


**FIGURE 12.** Boundary of hole in mesh created for local remeshing procedure. Grey surface is the crack extension

There are issues that arise in the local remeshing procedure when the growing crack intersects a material boundary in the model (such as growing from the matrix into a fiber). One consideration is whether or not such a situation can be detected. In the procedures described here the situation can be easily detected while the interaction of the crack extension with the micro mesh is found. This is done by checking the classification (relation of the mesh entities to the model entities they are discretizations of) of the mesh regions that are found to interact with the crack extension. This classification information is stored as



part of the data structure describing the mesh (Beall and Shephard 1995). Given the list of the mesh regions that a crack extension face interacts with, if the classification of any mesh region in the list differs from the others, then the crack extension face interacts with a model boundary. Once this situation has been detected there are issues involving both the analysis procedure and the mesh update procedure. Since the analysis does not take into consideration that the crack may propagate from one material to another it may not be correct to update the model to reflect this occurrence. The local remeshing mesh update procedure described here requires does not handle the situation of propagating the crack across material boundaries without modification. A more general mesh update procedure has been developed that does handle this situation without having to consider special cases. Both of these issues will be addressed further in a subsequent paper.

### **6.3 Micro and transition model update**

Eventually, as the crack front moves through the micro model, the original selection of the domain for the micro model will no longer be optimal for the analysis for one of two reasons. First, the crack front needs to be sufficiently far away from the boundary of the micro model for the analysis to be accurate. When the crack approaches the boundary the micro model will need to be extended. Second, there will be unit cells in the micro model that are no longer close to the crack front. This makes the micro model larger than it needs to be, reducing the efficiency of the analysis. These unit cells should be removed from the micro model.

Modification of the domain of the micro model requires updating the transition model. This is due to the change in the boundary of the micro model and also, possibly due to the

need to expand the transition model, by adding more elements from the macro mesh, due to the changes of the micro model. The process of updating the transition model is illustrated in Figure 13.

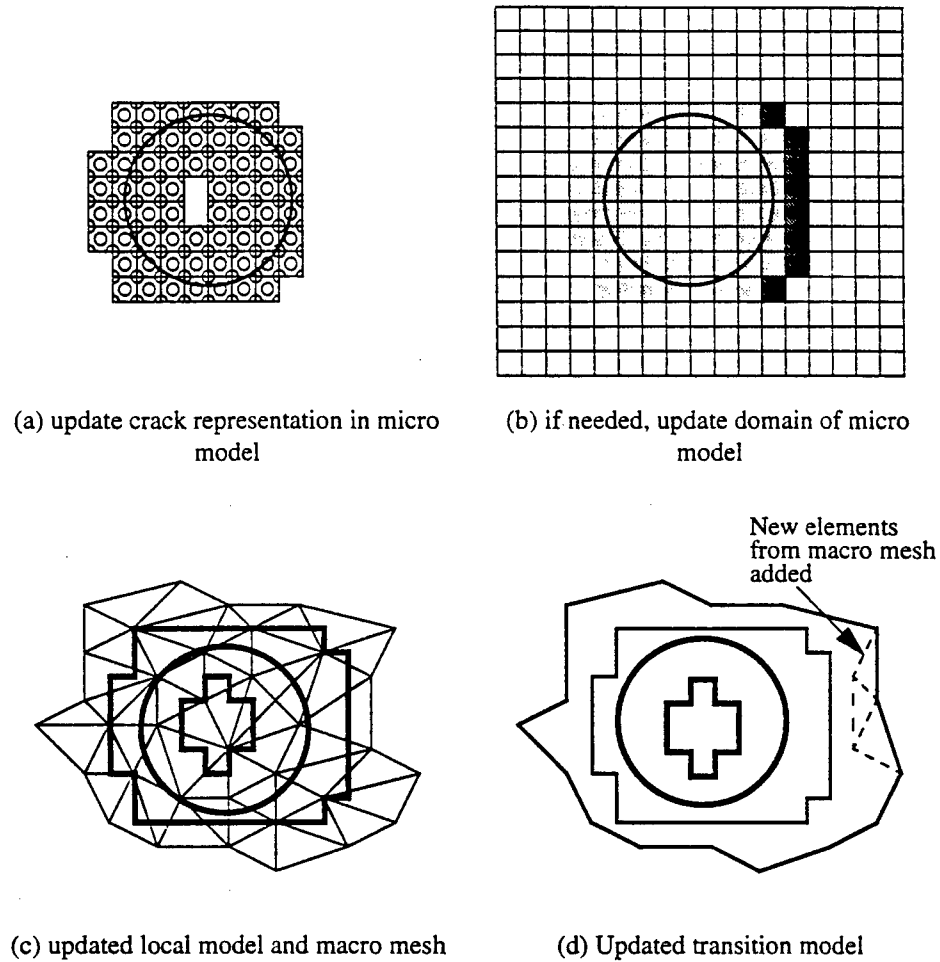


**FIGURE 13. Construction of the transition model.**

When new unit cells are added to the micro model, they can be meshed using the mesh that was created on the unit cell when the homogenization procedure was done. This is a simple procedure since the mesh on the boundary of the micro-mesh is identical to the mesh on the boundary of the unit cell.

When unit cells are removed from the micro model, the domain of the transition model cannot be reduced since all of the geometry of the crack must still be contained interior to transition model. For these analyses this is done by only adding macro-mesh elements to the domain of the transition model and never removing them as the crack grows. Thus, although the micro model domain only surrounds the area immediately around the crack tip, the transition model encompasses the entire crack.

Figure 14 shows the boundary of the micro model, before and after the crack grows. It can be seen that after the crack growth there is a portion of the model near the center of the crack where unit cells have been removed from the micro model since they are far from the current crack front.

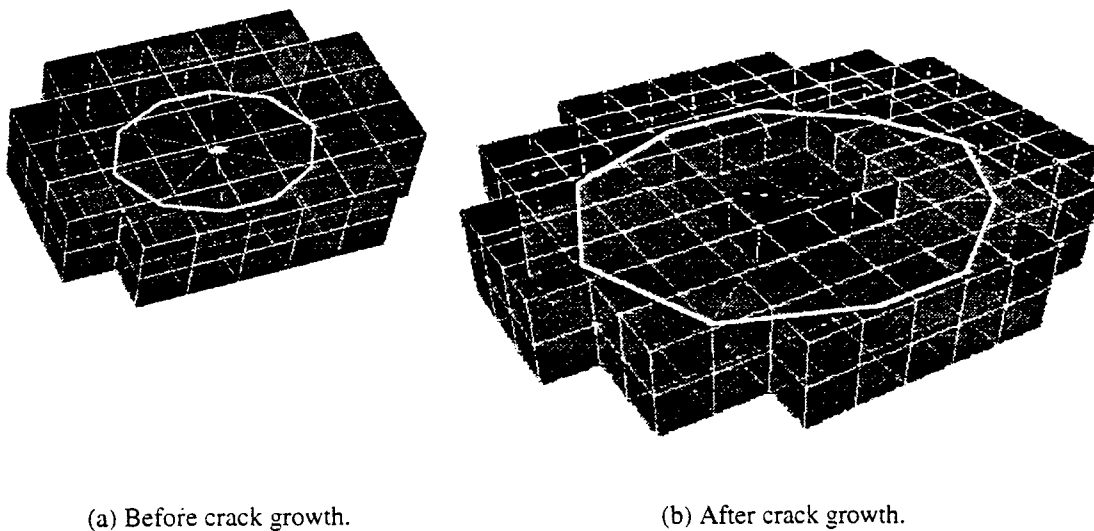


**FIGURE 14. Boundary of micro model.**

## 7 Results

The procedures described in the previous sections have been put together into a system for analyzing the propagation of discrete cracks in heterogeneous media. The following two analyses are an example of the difference in crack growth that is found comparing an anal-

ysis using homogenized material properties to one using explicitly represented microstructure.

In both cases the problem being analyzed is an initially circular crack. The macro model is a cube loaded in off axis tension at an angle of 45 degrees to the crack surface (Figure 15). The material used is a unidirectional fiber reinforced composite. Both the fiber and matrix are taken as isotropic with the fiber properties:  $E_f = 50000$ ,  $\nu_f = 0.25$  and the matrix properties:  $E_m = 10000$ ,  $\nu_m = 0.25$ .

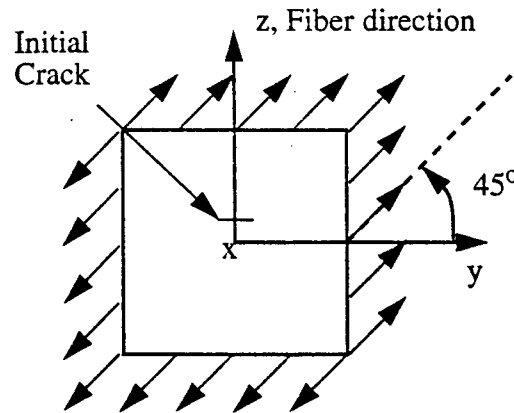
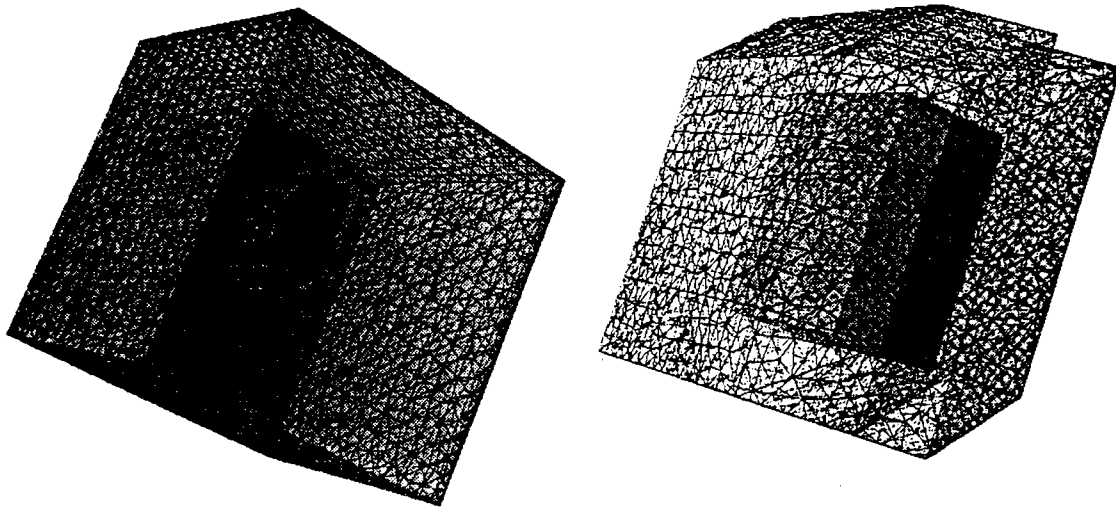


FIGURE 15. Test problem.

The first analysis was run using homogenized material properties, calculated from the unit cell of the composite, throughout the problem domain. The second analysis uses explicit microstructure in the vicinity of the crack front. The current capabilities of the system do not allow the crack to propagate through the fibers so only the initial growth of the crack can be analyzed (A new local mesh modification procedure, which is just nearing completion, will allow this. Results of that capability will be given in a future paper).

Figures 16 and 17 show the models that were automatically created by the analysis. Figure 16a shows the transition model in relation to the macro model. Figure 16b shows



(a) Macro model with embedded transition model      (b) Transition model with embedded micro model

**FIGURE 16. Models created by the analysis**

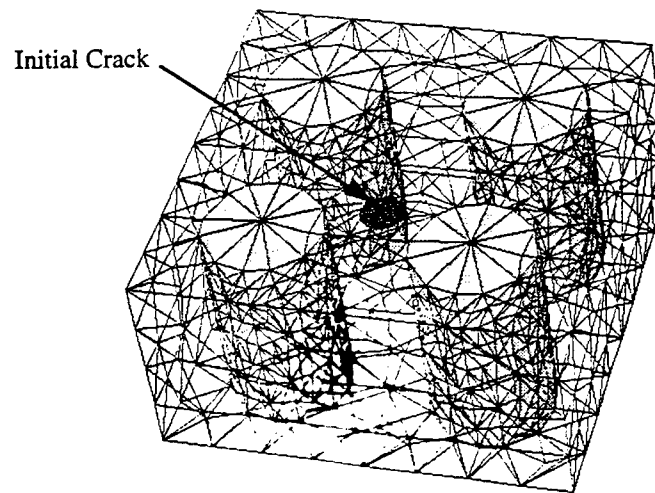


**FIGURE 17. Micro scale model with crack location indicated**

the micro model in relation to the transition model. The micro model consists of four unit cells. The initial crack is circular and located approximately a quarter of a fiber diameter away from the nearest fiber as shown in Figure 18. The same micro model was used throughout the analysis since the amount of crack growth was small.

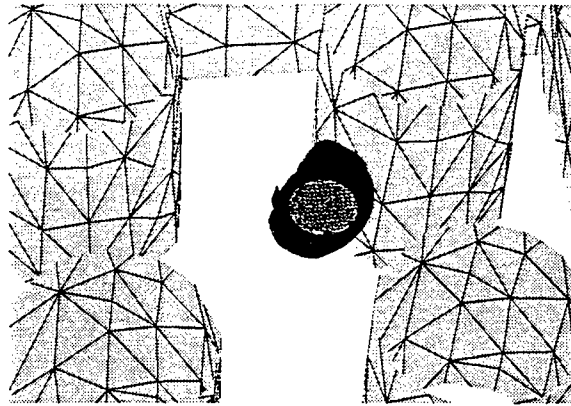


**FIGURE 18. Crack growth shown in relation to composite microstructure**

Figure 19 shows the crack growth predicted from the two analyses. The crack in the homogeneous material is shown in the lighter grey and the crack for the heterogeneous material is shown in dark grey. The closest fiber is on the right side of the view.

The analysis with the homogeneous material exhibits the expected behavior in this situation. The crack is growing so that it becomes perpendicular to the direction of the loading. The final step shown in the results is right after the crack would have come in contact with the fibers.

In the inhomogeneous case the crack exhibits more complicated behavior. It can be clearly seen that the presence of the fibers is affecting the growth of the crack. As the crack is approaching the fiber on the right side it bends away from the fiber and becomes more parallel to it.

## **8 Closing Remarks**

The analysis system described in this paper builds on several important technologies. First, a multigrid, multiscale solution technique that correctly accounts for the coupling

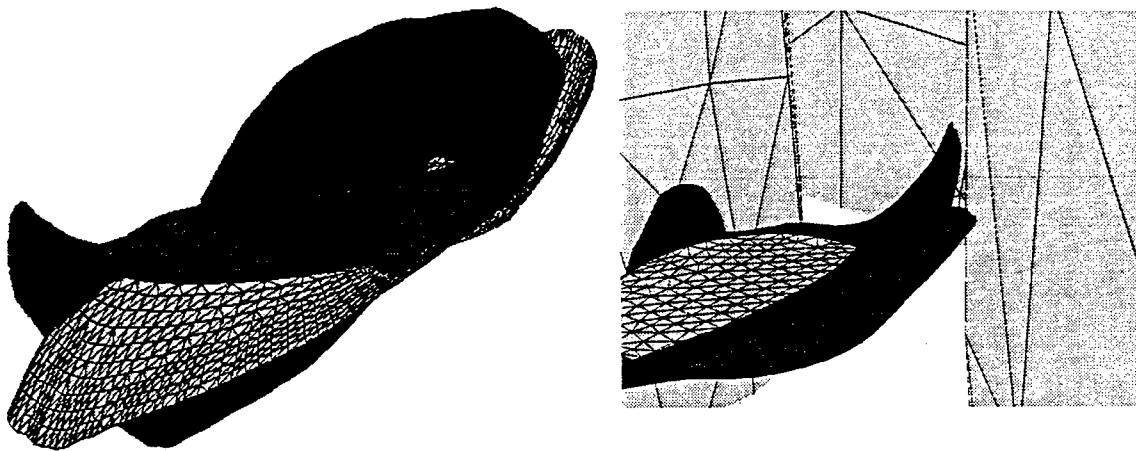


**FIGURE 19.** Analysis results showing the difference in crack growth when accounting for the microstructure. The light grey crack grew in a homogeneous material, the dark grey crack grew with the microstructure explicitly represented.

between overall models with homogenized material properties and local models with explicitly represented microstructure.

Second, automatic model and mesh generation procedures required to automate the complex analysis process involving several evolving models and meshes. These procedures operate from a common description of the analysis problem defined in terms of geometric model and attributes.

All of the procedures described in this paper have been implemented in a manner consistent with those used for parallel automated adaptive finite element analysis. Although the current simulations are being run on single processor workstations, larger problems will be able to take advantage of parallel processing.

Further development of the system is underway which will allow a microscopic flaw to be propagated until it grows to the point where macroscale failure of the component occurs. At this point analyses can be run to investigate the ultimate failure strength of components in the presence of various types of initial flaws.

## 9 Acknowledgments

This research was supported by ARPA/ONR under grant N00014-92J-1779.

## 10 References

Bakhvalov, N. S.; Panasenko, G. P. (1989). "Homogenization: averaging processes in periodic media." *Mathematical Problems in the Mechanics of Composite Materials*, Kluwer Academic Publishers.

Beall, M. W. and Shephard, M. S. (1995). "Mesh data structures for advanced finite element computations." Technical Report 19-1995, Scientific Computation Research Center, Rensselaer Polytechnic Institute, Troy, NY 12180-3590. submitted to *Int. J. Num. Meth. Engng.*

de Cougny, H. L., Devine, K. D., Flaherty, J. E., Loy, R. M., Ozturan, C., and Shephard, M. S. (1995). "Load balancing for the parallel solution of partial differential equations." *Applied Numerical Mathematics*, 16, p. 157-182.

Fish, J. and Wagiman, A (1993). "Multiscale finite element method for heterogeneous medium." *Computational Mechanics: The International Journal*, 12, 1-17.

Fish, J. and Markolefas, S., Guttal, R. and Nayak, P. (1994). "On adaptive multilevel superposition of finite element meshes," *Applied Numerical Mathematics*, Vol 14., 135-164.



Fish, J., Nayak, P. and Holmes, M.H. (1994). "Microscale reduction error indicators and estimators for a periodic heterogeneous medium." *Computational Mechanics: The International Journal*, 14, 323-338.

Fish, J. and Belsky, V. (1995a). "Multigrid method for a periodic heterogeneous medium. Part I: Convergence studies in 1-D case." *Comp. Meth. Appl. Mech. Engng.*, 126, 1-16.

Fish, J. and Belsky, V. (1995b). "Multigrid method for a periodic heterogeneous medium. Part 2: multidimensions," *Comp. Meth. Appl. Mech. Engng.*, 126, 17-38.

Fish, J. and Nath, A. (1993). "Adaptive and hierarchical modeling of fatigue crack propagation", *Int. J. Num. Meth. Eng.*, 36, 2825-2836.

Guedes, J. M.; Kikuchi, N. (1991). "Premat/postmat. A computer software for computational mechanics of composite materials." *Proceedings of the International Conference and Exhibition on Computer Applications to Materials Science and Engineering*, Elsevier Science Publishers.

Niu, Q. and Shephard, M. S. (1993). "Superconvergent extraction techniques for finite element analysis." *Int. J. Num. Meth. Eng.*, 36, 811-836.

Niu, Q. and Shephard, M. S. (1994). "Superconvergent boundary stress extraction and some experiments with adaptive pointwise error control." *Int. J. Num. Meth. Eng.* 36(5), 877-891.

Oden, J. T., Demkowicz, L., Rachowicz, W. and Westermann, T. A. (1989). "Toward a universal h-p adaptive finite element strategy, Part 2. A posteriori error estimation", *Computer Methods in Applied Mechanics and Engineering*, 77, 113-180.

Parasolid Version 6 KI Programming Reference Manual (1994). Electronic Data Systems Corporation, Parker's House, 46 Regent Street, Cambridge CB2 1DB England.

Shephard, M.S. (1988). "The specification of physical attribute information for engineering analysis." *Engineering with Computers*, 4, 145-155

Shephard, M.S.; Finnigan, P.M. (1989). "Toward automatic model generation. State-of-the-Art Surveys on Computational Mechanics, A.K. Noor and J.T. Oden, editors, NY, ASME, 355-366.

Shephard, M.S.; Baehmann, P.L.; Georges, M.K.; Korngold, E.V. (1990). "Framework for the reliable generation and control of analysis idealizations." *Comp. Meth. Appl. Mech. Engng.*, 82, 257-280.

Shephard, M.S.; Georges, M.K. (1991). "Automatic three-dimensional mesh generation by the finite octree technique." *Int. J. Numer. Meth. Engng.* 32(4), 709-749

Shephard, M.S.; Georges, M.K. (1992). "Reliability of automatic 3-D mesh generation." *Comp. Meth. Applied Mechanics and Engng.* 101, 443-462.

Shephard, M. S., Flaherty, J. E., de Cougny, H. L., Ozturan, C., Bottasso, C. L. and Beall, M. W. (1995a). "Parallel automated adaptive procedures for unstructured meshes", *Parallel Computing in CFD, AGARD, Neuilly-Sur-Seine, France, R-807*, 6.1-6.49.

Shephard, M. S., Beall, M. W., Garimella, R., Wentorf, R. (1995b). "Automatic construction of 3-D models in multiscale analysis." *Computational Mechanics*, 17(3), 196-207.

Weiler, K.J. (1988). "The radial-edge structure: A topological representation for non-manifold geometric boundary representations." Geometric Modeling for CAD Applications, M.J. Wozny, H.W. McLaughlin and J. Encarnacao, editors., North Holland, 3-36

Wentorf, R.; Shephard, M. S.; Korngold, E. V. (1989). "The use of functional models to control engineering idealizations." Proceedings of the 1989 ASME International Computers in Engineering Conference and Exposition, Anaheim, California, July, 63-70.

Wentorf, R.; Shephard, M. S. (1993). "Automated analysis idealization control." Concurrent Engineering: Automation, Tools, and Techniques, Andrew Kusiak Eds., John Wiley, New York, 41-73,

Wong, V.S. (1994). "Qualification and management of analysis attributes with application to multi-procedural analysis of multi-chip modules", TR23-1994, Scientific Computation Research Center, Troy, NY

Zienkiewicz, O. C. and Zhu, J. Z. (1992). "Superconvergent derivative recovery techniques and a posteriori error estimation in the finite element method - part 2: The Zienkiewicz-Zhu a posteriori error estimator." Int. J. Numer. Meth. Engng., 33, 1365-1382.

A Geometry-Based Analysis Framework

Mark W. Beall and Mark S. Shephard

SCOREC Report #25-1996  
Scientific Computation Research Center

Scientific Computation Research Center  
Rensselaer Polytechnic Institute  
Troy, NY 12180-3590  
voice 5182766795  
fax 5182764886

# A GEOMETRY-BASED ANALYSIS FRAMEWORK

Mark W. Beall  
Mark S. Shephard  
Scientific Computation Research Center  
Rensselaer Polytechnic Institute  
Troy, NY 12180-3590

## SUMMARY

This paper provides an overview of an analysis framework which operates directly from a general geometry-based specification. The framework is designed using object-oriented methodologies to allow for easy extension to analyze new problem classes and introduce additional adaptive control techniques.

## INTRODUCTION

The numerical analysis of a physical problem can be seen as a series of idealization steps, each of which may introduce errors into the solution. The manner in which these errors can be understood and controlled is through error estimation and solution adaptivity. Since adaptive control should be applied to each idealization step, the numerical analysis procedures must operate from the original problem definition which is best described with respect to a geometric model. This paper provides a brief overview of an analysis framework which operates directly off such geometry-based problem specifications.

To increase the usefulness of the framework, it is designed for easy extension to include new analysis capabilities and adaptive idealization control techniques. This extensibility is aided by the application of object-oriented programming techniques.

We can identify three levels of description that arise in the analysis of a physical problem (Figure 1). The highest level description is that of the physical problem. The physical problem description is posed in terms of physical objects interacting with their environment. Since we often want to estimate the response through modeling we idealize the behavior in terms of a mathematical problem description. The mathematical problem description consists of a domain definition (geometry), a description of the external forces acting on the object and the properties of the object (attributes), and, in the classes of physical problems considered here, a set of appropriate partial differential equations which describe the behavior of interest. Construction of a numerical problem from a mathematical problem involves another set of idealizations. From a single mathematical problem it is possible to construct any number of levels of numerical problems, which are idealizations of one another.

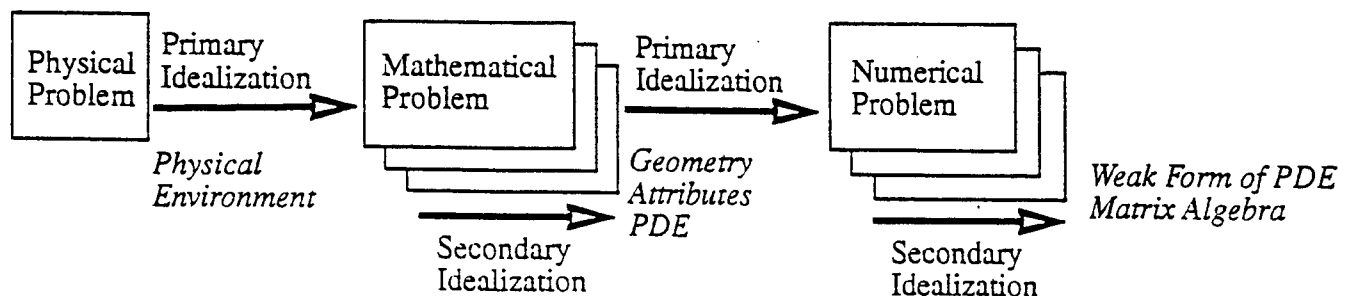


Figure 1. Idealizations of a physical problem to be solved.

The framework described in this paper starts at the level of a mathematical problem description, allowing multiple numerical problems to be formulated, solved, and the solution related back to the original problem description. The analysis framework is designed to be extended. It is possible to add new problem types that can be solved as well as adding new solution techniques. Current implementation efforts are focused on finite element discretizations. However, the framework is designed to be general to utilize other types of numerical solution procedures.

Since the analysis framework must take a problem description consisting of a geometric model and attributes and construct a solution to the problem specified, it is important to understand abstractions for the various types of data that the framework uses. As outlined in the next section, geometry-based descriptions are best suited to meet these needs. The following section briefly introduces the process of performing geometry-based analyses.

## DATA COMPONENTS OF A GEOMETRY-BASED ANALYSIS FRAMEWORK

The structures used to support the problem definition, the discretizations of the model and their interactions are central to the analysis framework. The two structures of the geometric model and attributes are used to house the problem definition. The general nature of the attribute structures allow them to also be used for defining numerical analysis attributes. The analysis discretizations are housed in the mesh structure which is linked to the geometric model. The final structure is the field structure which houses the distributions of numerical solution results over the domain of the problem.

### Geometric Model

The geometric model representation used by the analysis framework is a boundary representation based on the Radial Edge Data Structure (Weiler 1988). In this representation the model is a hierarchy of topological entities called regions, shells, faces, loops, edges and vertices (Figure 2). This representation is completely general and is capable of representing non-manifold models that are common in engineering analyses. The use of a boundary representation is very convenient for attribute association and mesh generation processes since the boundaries of the model are explicitly represented.

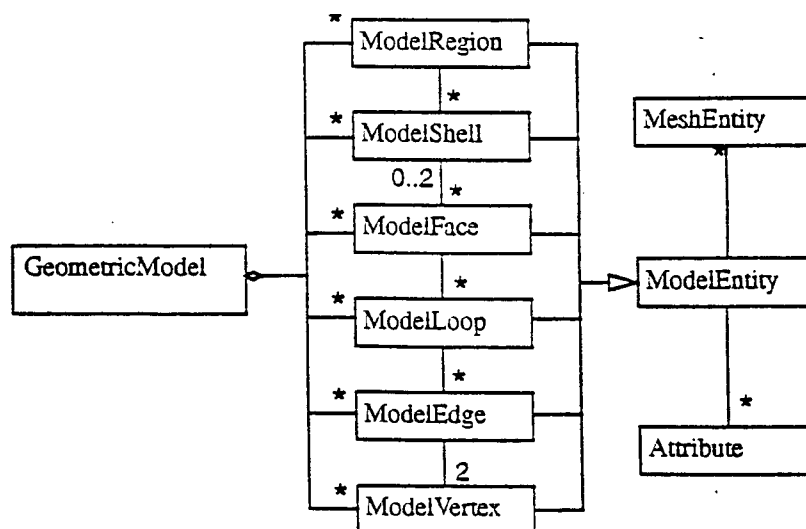


Figure 2. Boundary representation.

The geometric model classes support operations to find the various model entities that make up a model and to find which model entities are adjacent to a given entity. Other operations relating to performing geometric queries are also supported. The details of these operations are not important in the current context. Much more important is the fact that there are associations between the ModelEntity class and both the Attribute and MeshEntity classes. These associations are central to being able to support generalized adaptive analysis procedures that operate from a general problem definition.

### Attributes

In addition to geometry, information that describes such things as material properties, loads and boundary conditions (Shephard 1988) is needed. This other information is described in terms of tensor valued attributes that may vary in both space and time. Attribute information is organized into a directed acyclic graph (DAG). There are three basic types of nodes in the graph. The leaf nodes of the graph are information nodes. These nodes hold the actual attribute information (e.g. an information node might define a vector with a certain variation in space and time). Above the information nodes are two types of grouping nodes which allow for the flexible combination of attributes to form analysis cases which drive the numerical analysis process.

Tensor valued attributes only make sense when applied to and associated with a geometric model entity. During this process the graph is traversed, and when the information nodes are encountered at the leaves of the graph, attribute objects are created. These attributes are a particular instance of the information represented in the attribute graph. One reason for the distinction between the information nodes and attributes is that the interpretation of the information node can depend on the path in the graph traversed to get to that node. Thus one information node may give rise to multiple attributes with different values.

A simple example of a problem definition is shown in Figure 3. The problem being modeled here is a dam subjected to loads due to gravity and due to the water behind the dam. There are a set of attribute information nodes that are all under the attribute case for the problem definition. When this case is associated with the model, attributes (indicated by triangles with A's inside of them) are created and attached to the individual model entities on which they act.

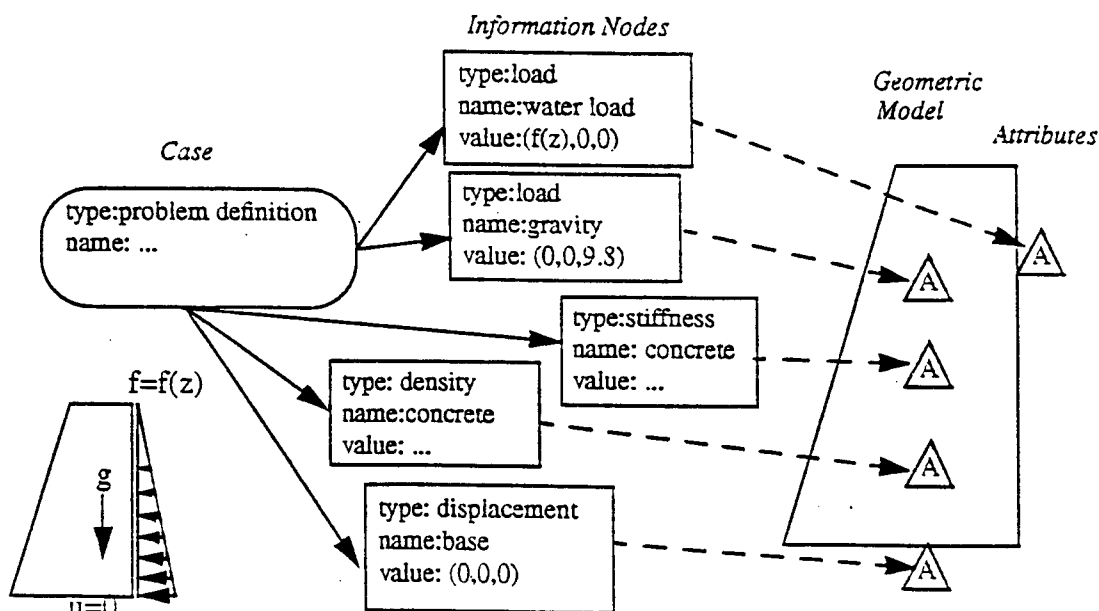


Figure 3. Attribute example.

Nodes in the attribute graph have another important property. They can represent an object that is to be created when the attribute graph is traversed. This object is called the image of the attribute and represents the run time interpretation of the information of the attribute node and its children.

### Mesh

The representation used for a mesh is similar to that used for a geometric model (Beall & Shephard 1997). A hierarchy of regions, faces, edges and vertices makes up the mesh. In addition, each mesh entity maintains a relation, called the classification of the mesh entity, to the model entity that it was created to partially represent as indicated in Figures 2 and 4. This representation of the mesh is very useful for mesh adaptivity. Also understanding how the mesh relates to the geometric model allows an understanding of how the solution relates back to the original problem description. The topological representation can be used to great advantage in performing adaptive p-version analyses as polynomial orders can be directly assigned to the various entities (Shephard, Dey & Flaherty 1996).

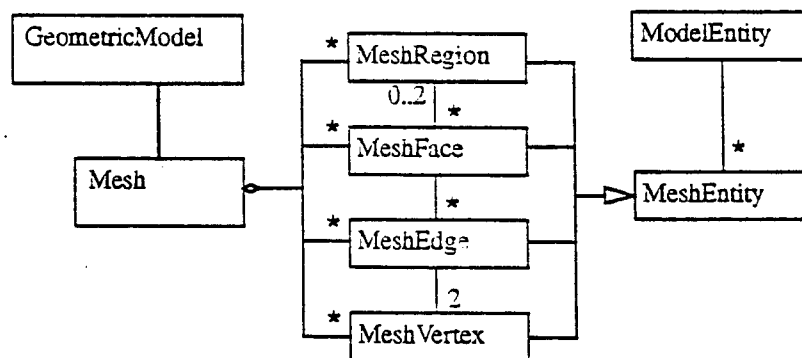


Figure 4. Mesh representation.

### Field

A problem with many "classic" finite element codes is that the solution of an analysis is given in terms of the values at a certain set of discrete points (e.g. nodal locations or integration points). However the finite element discretization actually has more information than just the values at these points, there is also information about the interpolations that were used in the analysis. Therefore, when the standard process of storing just the discrete pointwise values is maintained, information is lost after the analysis is run. Without knowing the specifics of the analysis code it is impossible to reconstruct the interpolations used and one can not define the values at general locations. This makes it much more difficult to use the solution in a subsequent step in the analysis (e.g. error estimation, or as an attribute for another analysis). The analysis framework eliminates this problem by introducing a construct known as a field.

A field describes the variation of some tensor field over one or more entities in a geometric model. The spatial variation of the field is defined in terms of interpolations defined over a discrete representation of the geometric model entities, which is currently the finite element mesh. A field is a collection of individual interpolations, all of which are interpolating the same quantity (Figure 5). Each interpolation is associated with one or more entities in the discrete representation of the model.



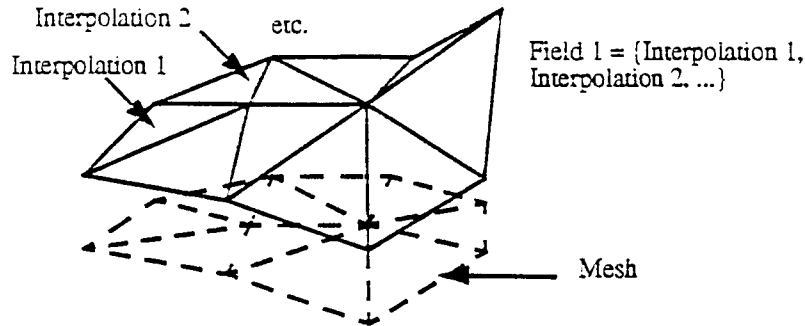


Figure 5. Example of a field.

## GEOMETRY-BASED ANALYSIS PROCESSES

The framework represents the analysis process as a series of transformations of the problem from the original mathematical problem description through to the sets of algebraic equations approximately representing the problem (Figure 6). This transformation starts at the mathematical problem description level

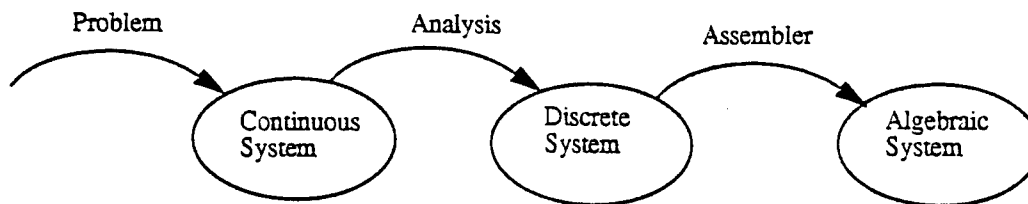


Figure 6. Analysis transformation process.

which contains the geometric model and the attributes which apply to that model. The attributes for a particular problem are specified by a particular case node in the attribute graph. All of the attributes under this case node are used for the given problem. An instance of a ContinuousSystem is then transformed to an instance of the class DiscreteSystem which represents the discretized version of the model and attributes and the weak form of the partial differential equation (PDE). This transformation is done by an object that is an instance of a class that is part of a hierarchy of analysis classes. The particular analysis class that is used depends on the selected weak form of the PDE to be solved.

For each problem definition it is possible to define any number of analyses. An analysis is defined by combining a problem definition with one or more cases that contain the rest of the information needed to perform the analysis. Here an analysis is defined by combining a problem definition case with a numeric case (which contains information relating to the specific numerical techniques used to solve the problem) and a meshing case (which contains information describing the parameters needed to generate a mesh for the model being used). The responsibilities of an Analysis class are to:

1. Create a DiscreteSystem of a type appropriate for the problem.
2. Interpret attributes associated with the geometric model and appropriately create StiffnessContributors, ForceContributors and EssentialBCs and add them to the DiscreteSystem.
3. Create an AlgebraicSystem with an appropriate solver.

4. Invoke the solve method of the AlgebraicSystem.

The DiscreteSystem class represents the problem in terms of contributions from a set of objects that live on the discrete representation of the model. These objects are called SystemContributors. There are three types of SystemContributors: StiffnessContributors contribute coupling terms between degrees of freedom of the system. ForceContributors contribute terms to the right hand side vector, Constraints set specific values to given degrees of freedom (e.g. setting the value of a certain degree of freedom to zero). The SystemContributors are created by the Analysis object and correspond to an interpretation of attributes consistent with the weak form that the Analysis implements. For example, in a heat transfer analysis, material property attributes will give rise to StiffnessContributors, applied heat fluxes will give rise to ForceContributors and prescribed temperatures will give rise to Constraints. Typically a SystemContributor corresponds to a mesh entity classified on the model entity where the attribute is applied.

The Analysis class creates all of the SystemContributors and adds them to an instance of a DiscreteSystem. There is a hierarchy of DiscreteSystem classes that represent different time orders of PDEs. This transformation of the problem from the ContinuousSystem to the DiscreteSystem allows the various solution routines to work on a representation that is independent of the type of problem being solved.

The next step in the solution process is to set up and solve the linear algebra. The setting up of the linear algebra consists of transforming a DiscreteSystem into an AlgebraicSystem. This transformation is handled by an Assembler object. Essentially an Assembler maps the contributions of each StiffnessContributor and ForceContributor in a DiscreteSystem into the correct entries in the global stiffness matrix and global force vector in an AlgebraicSystem.

Each type of operation that needs to form a global matrix or vector must use an assembler (either defining a new one or using an existing one). The base class Assembler provides the operations needed to do the perform the process of assembling the global system through it's assemble method (this method is only accessible to subclasses of Assembler). Each derived class must implement the operations that need to be carried out on the matrices returned by the ForceContributors and StiffnessContributors and then call the base classes assemble method.

## REFERENCES

- Beall, M. W.; Shephard, M. S. (1997): A general topology-based mesh data structure. *International Journal for Numerical Methods in Engineering*, to appear.
- Shephard, M. S. (1988): The specification of physical attribute information for engineering analysis. *Engineering with Computers*, Vol. 4, pp. 145-155.
- Shephard, M. S.; Dey, S.; Flaherty, J. E. (1996): A straightforward structure to construct shape functions for variable p-order meshes. *Computer Methods In Applied Mechanics and Engineering*, to appear.
- Weiler, K. J. (1988): The radial-edge structure: A topological representation for non-manifold geometric boundary representations. M.J. Wozny, H.W. McLaughlin, J.L. Encarnacao, editors. *Geometric modeling for CAD applications*, North Holland, pp. 3-36.

A Geometry-Based Framework for Reliable  
Numerical Simulations

Mark W. Beall and Mark S. Shephard

SCOREC Report #7-1997  
Scientific Computation Research Center

Scientific Computation Research Center  
Rensselaer Polytechnic Institute  
Troy, NY 12180-3590  
voice 5182766795  
fax 5182764886

# A Geometry-Based Framework for Reliable Numerical Simulations

Mark W. Beall  
Mark S. Shephard

## 1 Introduction

The computer modeling of a physical problem can be seen as a series of idealizations, each of which introduces errors into the solution as compared to the solution of the initial problem. Since these idealizations are introduced to make solving the problem tractable (due to constraints on either problem size and/or solution time), it is necessary to understand their effect on the solution obtained and to have procedures to reduce the errors to an acceptable level with respect to the reason the analysis is being performed. Understanding of the effects of idealizations requires a more complete definition of the problem than is typically used in numerical analysis procedures. In particular it is necessary to have a complete geometric description of the original domain and have the rest of the problem defined in terms of that geometry. This paper provides an overview of an object oriented analysis framework which operates directly off a geometry-based problem specification to support adaptive procedures.

We can identify three levels of description that arise in the analysis of a physical problem (Figure 1). The highest level description is that of the physical problem which is posed in terms of physical objects interacting with their environment. We often want to obtain reliable estimates of the response of these objects through modeling. Modeling physical behavior requires a mathematical problem description which introduces some level of problem idealization, which we want to control as well as possible. The mathematical problem description consists of a domain definition (geometry), a description of the external forces acting on the object and the properties of the object (attributes), and, in the classes of physical problems considered there, a set of appropriate partial differential equations which describe the behavior of interest. For any one physical problem there are any number of mathematical problems that can be constructed. Quite often one mathematical problem description is constructed as an idealization of another. If the mathematical problem as stated cannot be solved analytically, numerical techniques can be used. Construction of a numerical problem from a mathematical problem involves another set of idealizations. Again from a single mathematical problem it is possible to construct any number of levels of numerical problems, which are idealizations of one another.

The framework described in this paper starts at the level of a mathematical problem description, allowing multiple numerical problems to be formulated, solved, and the solution related back to the original problem description. The analysis framework is designed to be extended. It is possible to add new problem types that can be solved as well as adding new solution techniques. Current implementation efforts are focused on finite element procedures [6,7]. However, the framework is designed to be general to utilize other types of numerical solution procedures.

Since the analysis framework must take a problem description consisting of a geometric model and attributes and construct a solution to the problem specified, it is important to understand

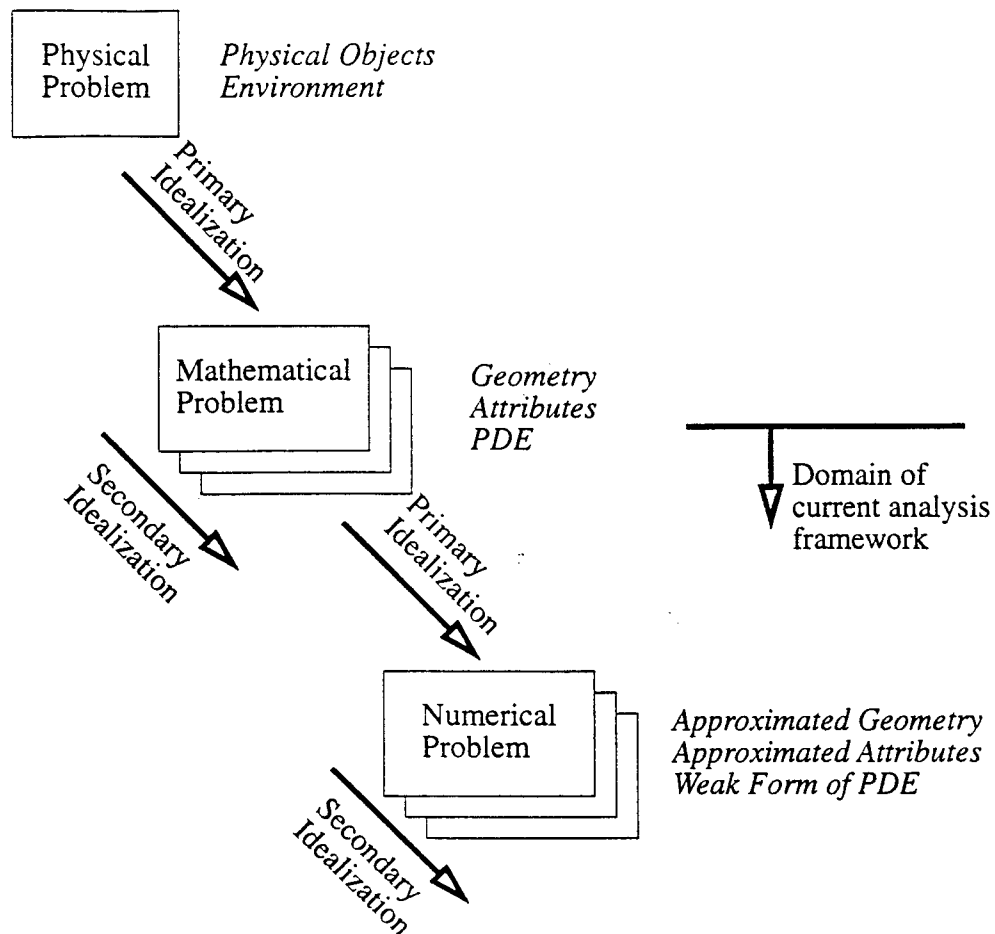


Figure 1. Idealizations of a physical problem to be solved

abstractions for the various types of data that the framework uses. As outlined in the next section, geometry-based descriptions are best suited to meet these needs. The following section briefly introduces the data needed to perform geometry-based analyses.

## 2 Data Components of a Geometry-Based Analysis Framework

The structures used to support the problem definition, the discretizations of the model and their interactions are central to the analysis framework. The two structures of the geometric model and attributes are used to house the problem definition. The general nature of the attribute structures allow them to also be used for defining numerical analysis attributes. The analysis discretizations are housed in the mesh structure which is linked to the geometric model. The final structure is the field structure which houses the distributions of numerical solution results over the domain of the problem.

## 2.1 Geometric Model

The geometric model representation used by the analysis framework is a boundary representation based on the Radial Edge Data Structure [1]. In this representation the model is a hierarchy of topological entities called regions, shells, faces, loops, edges and vertices. This representation is completely general and is capable of representing non-manifold models that are common in engineering analyses. The use of a boundary representation is very convenient for attribute association and mesh generation processes since the boundaries of the model are explicitly represented. Figure 2 shows an object diagram of related to the model package (All of the object diagrams in this paper use the UML notation [5]).

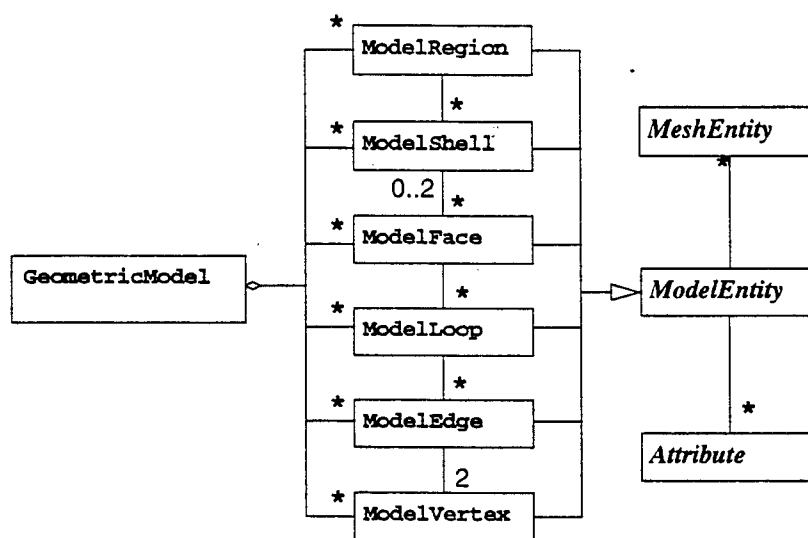


Figure 2. Class hierarchy of the geometric model representation

The classes support operations to find the various model entities that make up a model and to find which model entities are adjacent to a given entity. Other operations relating to performing geometric queries are also supported. The details of these operations are not important in the current context. Much more important is the fact that there are associations between the ModelEntity class and both the Attribute and MeshEntity classes. What these associations are and their importance is detailed below.

## 2.2 Attributes

In addition to geometry, the definition of a mathematical problem requires other information that describes the such things as material properties, loads and boundary conditions [3]. This other information is described in terms of tensor valued attributes that may vary in both space and time. In addition attributes are used to describe information that is non-tensorial in value and may represent some concept (such as a time integration algorithm and it's associated parameters).

Attributes information is organized into a directed acyclic graph (DAG). There are three basic types of nodes in the graph. The leaf nodes of the graph are information nodes. These nodes hold the actual attribute information (e.g. an information node might define a vector with a certain vari-

ation in space and time). Above the information nodes are two types of grouping nodes. The first of these is called a group which is simply used to represent the grouping of certain information nodes. The other grouping node is called a case. The case node has important semantics, it represents a point in the graph where all the information below it makes a meaningful whole with respect to some operation.

Tensor valued attributes are only meaningful when applied to a geometric model entity. This process of applying attributes to a geometric model is called association. During this process the graph is traversed, starting from a case node, and when the information nodes are encountered at the leaves of the graph, attribute objects are created. These attributes (represented by the Attribute class) are a particular instance of the information represented in the attribute graph. One reason for the distinction between the information nodes and attributes is that the interpretation of the information node can depend on the path in the graph traversed to get to that node. Thus one information node may give rise to multiple attributes with different values.

An simple example of a problem definition is shown in Figure 3. The problem being modeled here is a dam subjected to loads due to gravity and due to the water behind the dam. There are a set of attribute information nodes that are all under the attribute case for the problem definition. When this case is associated with the model, attributes (indicated by triangles with A's inside of them) are created and attached to the individual model entities on which they act.

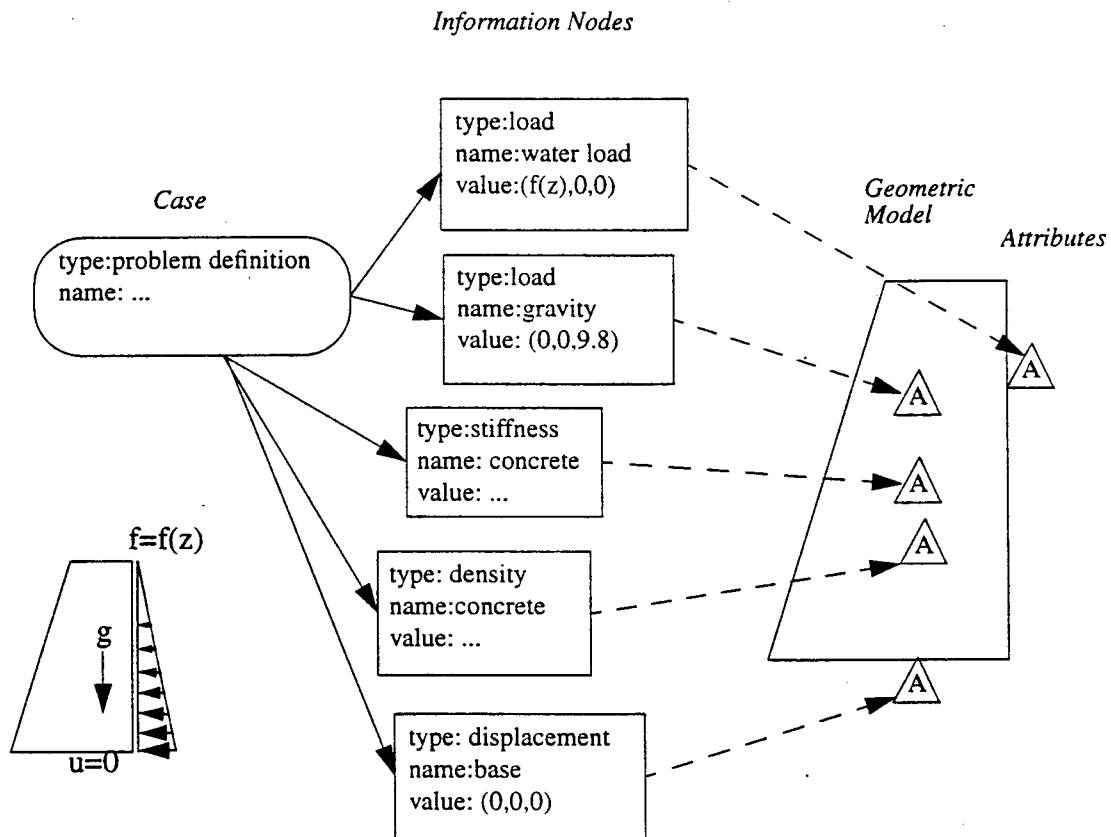


Figure 3. Example geometry-based problem definition

Nodes in the attribute graph have another important property. They can represent an object that is to be created when the attribute graph is traversed. This object is called the image of the attribute and represents the run time interpretation of the information of the attribute node and its children. Each attribute node that will give rise to an image has a string that identifies the class of the object to create as its image. The current implementation maps these strings to creator functions for the objects which take in the attribute node as an argument.

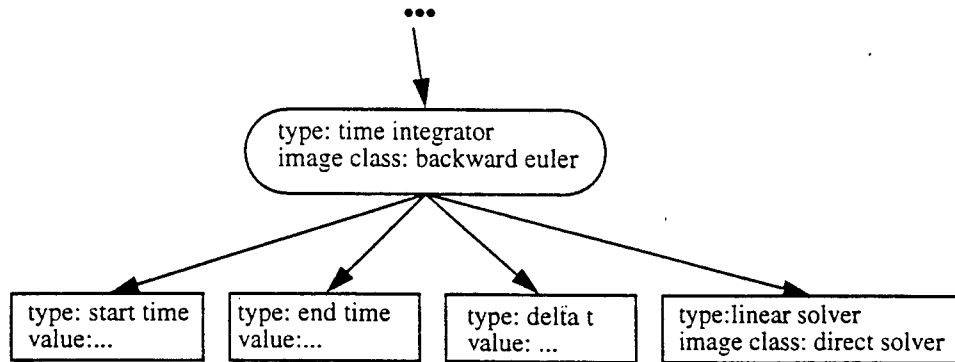


Figure 4. Portion of an attribute graph specifying a time integrator.

Figure 4 shows an example of the portion of the attribute graph that specifies a time integrator to be used in solving a particular analysis. In this case a backward Euler integrator is specified as indicated by the image class field of the group node of type “time integrator”. This means that, at run time, an object of the class mapped to the image name “backward euler” (which is the class BackwardEuler) will be created. When the object is created it is passed the node that specified its creation so that it can extract additional information that it needs. In this case the additional information is the starting time, ending time, the time step to use, and the linear solver to use to solve the systems of equations that it constructs. Note that the linear solver node also has an image class specified which means that an object will be created representing this node (which will be used by the time integrator object). In this example, to change the type of linear solver used, it is simply a matter of changing the image class of the “linear solver” information node. For example its image class could be changed to “conjugate gradient” and then the time integrator would use this solver to solve its equations. This technique is used throughout the framework to allow the users to specify the run time behavior of the program.

## 2.3 Mesh

The representation used for a mesh is similar to that used for a geometric model [2]. A hierarchy of regions, faces, edges and vertices makes up the mesh. In addition, each mesh entity maintains a relation, called the classification of the mesh entity, to the model entity that it was created to partially represent as indicated in Figures 2 and 5. This representation of the mesh is very useful for mesh adaptivity, the support of which is important for the framework. Also understanding how the mesh relates to the geometric model allows an understanding of how the solution relates back to the original problem description. The topological representation can also be used to great advantage in performing adaptive p-version analyses as polynomial orders can be directly assigned to the various entities [4].



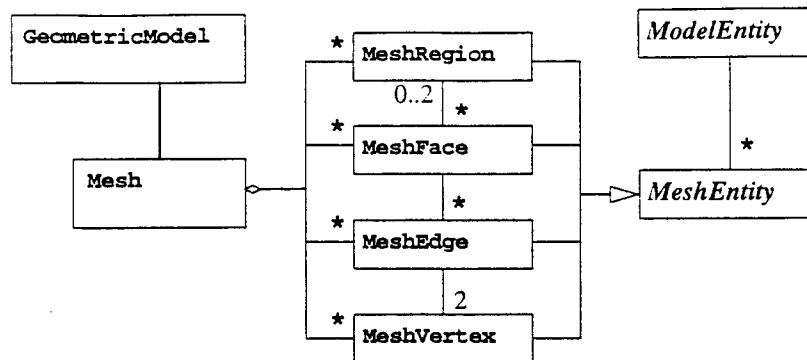


Figure 5. Class hierarchy for representing a mesh

## 2.4 Field

A problem with many "classic" numerical analysis codes is that the solution of an analysis is given in terms of the values at a certain set of discrete points (e.g. nodal locations or integration points). However the finite element discretization actually has more information than just the values at these points, there is also information about the interpolations that were used in the analysis. Therefore, when the standard process of storing just the discrete pointwise values is maintained, information is lost after the analysis is run. Without knowing the specifics of the analysis code it is impossible to reconstruct the interpolations used and one can not define the values at general locations. This makes it much more difficult to use the solution in a subsequent step in the analysis (e.g. error estimation, or as an attribute for another analysis). The analysis framework eliminates this problem by introducing a construct known as a field.

A field describes the variation of some tensor over one or more entities in a geometric model. The spatial variation of the field is defined in terms of interpolations defined over a discrete representation of the geometric model entities, which is currently the finite element mesh. A field is a collection of individual interpolations, all of which are interpolating the same quantity (Figure 6). Each interpolation is associated with one or more entities in the discrete representation of the model.

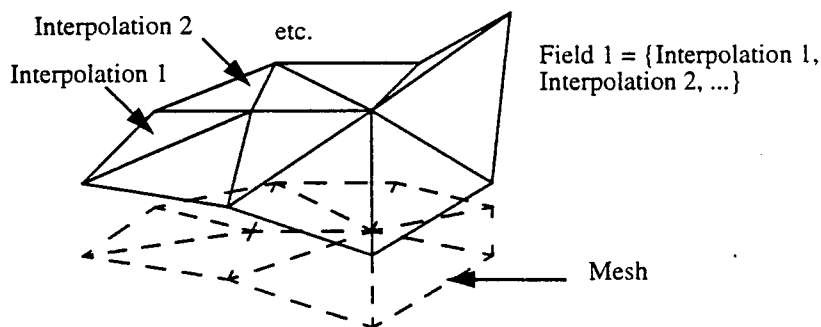


Figure 6. Representation of a field defined over a mesh

One general form of a tensor field is a polynomial interpolation with an order associated with each mesh entity. Since in some cases it is desirable to have multiple tensor fields with matching interpolations, the polynomial order for a mesh entity is specified by another object called a PolynomialField which can be shared by multiple Field objects.

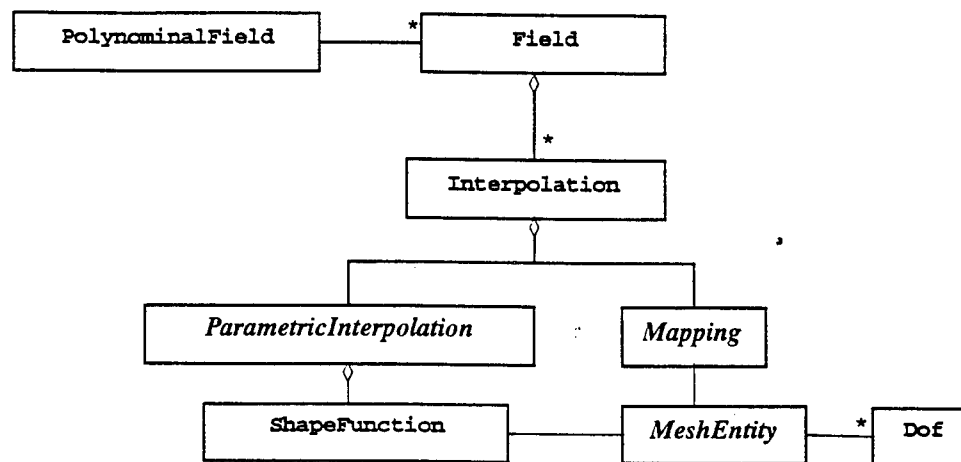


Figure 7. Classes used to represent a field

### 3 The Analysis Process

The framework presents the analysis process as a series of transformations of the problem from the original mathematical problem description through to sets of algebraic equations approximately representing the problem. This transformation starts at the mathematical problem descrip-

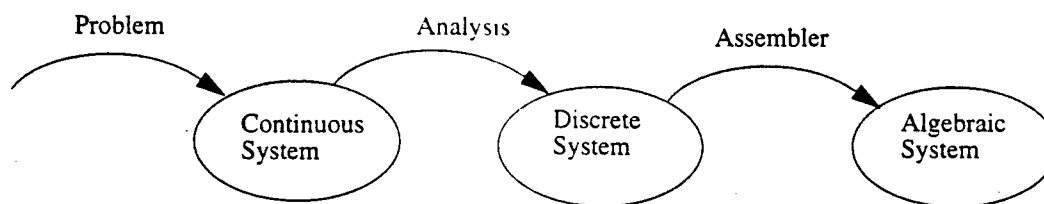


Figure 8. Solution of a mathematical problem description as a series of transformations

tion level which is described by a class named ContinuousSystem, which contains the geometric model and the attributes which apply to that model. The attributes for a particular problem are specified by a particular case node in the attribute graph. All of the attributes under this case node

are used for the given problem. An instance of a ContinuousSystem is then transformed to an instance of the class DiscreteSystem which represents the discretized version of the model and attributes and the weak form of the partial differential equation (PDE). This transformation is done by an object that is an instance of a class that is part of a hierarchy of analysis classes. The particular analysis class that is used depends on the selected weak form of the PDE to be solved.

### 3.1 The Analysis Classes

For each problem definition it is possible to define any number of analyses. An analysis is defined by combining a problem definition with one or more cases that contain the rest of the information needed to perform the analysis, as shown in Figure 9. Here an analysis is defined by combining a problem definition case with a numeric case (which contains information relating to the specific numerical techniques used to solve the problem) and a meshing case (which contains information describing the parameters needed to generate a mesh for the model being used).

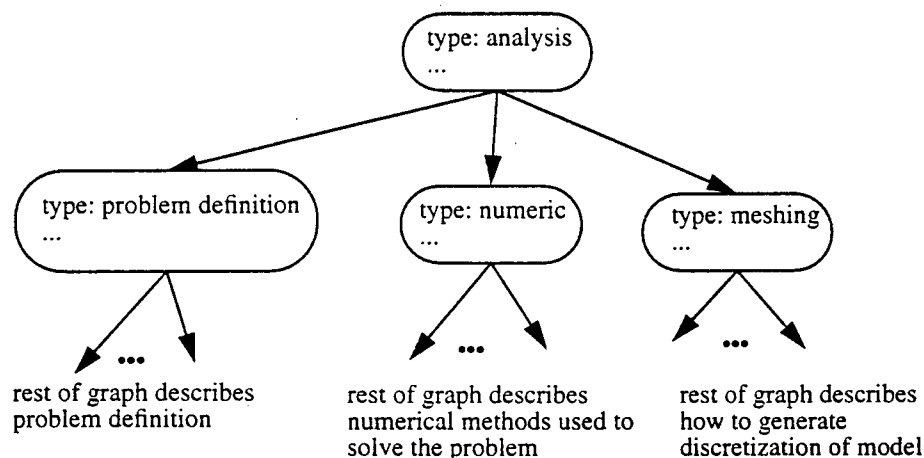


Figure 9. Structure of an analysis definition

The information contained in each of these cases is responsible for controlling a particular aspect of performing the analysis. The system is data driven using the information contained in the attribute graph.

Analysis classes (those derived from the base class Analysis) implement behavior that is specific to a particular type of analysis. In this context a “type of analysis” corresponds to a particular weak form of the PDE being solved. For each type of problem there can be more than one analysis (representing different ways to solve the same problem).

The responsibilities of an Analysis class are to:

1. Create a DiscreteSystem of a type appropriate for the problem
2. Interpret attributes associated with the geometric model and appropriately create StiffnessContributors, ForceContributors and EssentialBCs and add them to the DiscreteSystem.
3. Create a solver of the appropriate type, passing it the DiscreteSystem

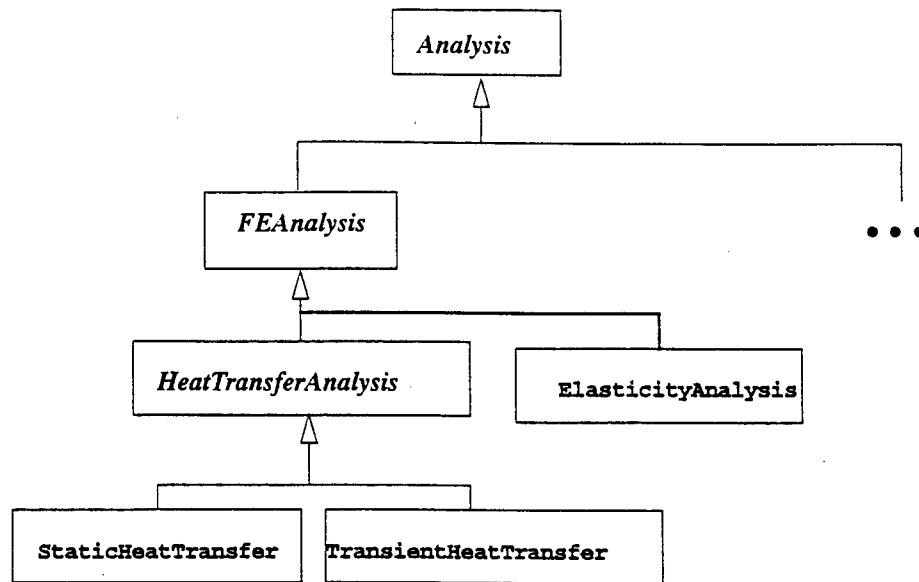


Figure 10. Class Hierarchy of the analysis classes

### 3.2 Discrete System

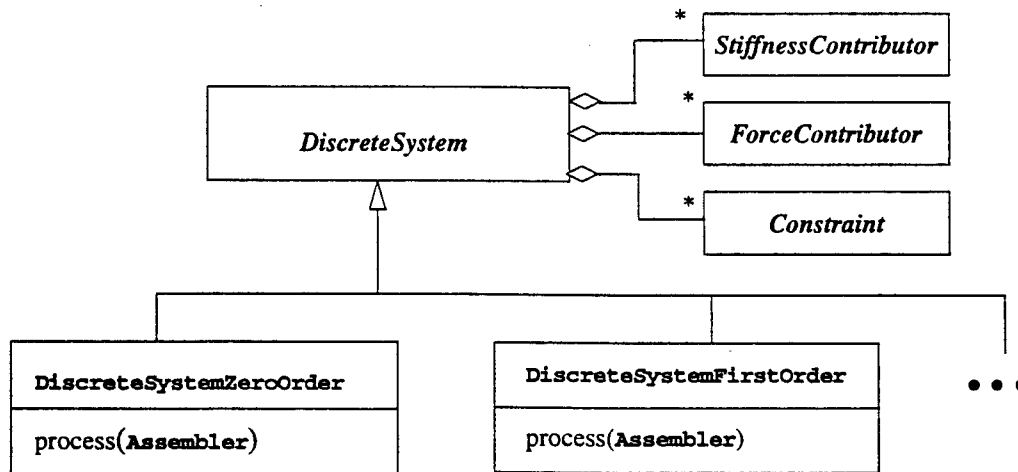


Figure 11. The DiscreteSystem and derived classes

The *DiscreteSystem* class represents the problem in terms of contributions from a set of objects that live on the discrete representation of the model. These objects are called *SystemContributors*. There are three types of *SystemContributors*: *StiffnessContributors* contribute coupling terms between degrees of freedom of the system, *ForceContributors* contribute terms to the right hand side vector, *Constraints* set specific values to given degrees of freedom (e.g. setting the value of a certain degree of freedom to zero). The *SystemContributors* are created by the *Analysis* object and correspond to an interpretation of attributes consistent with the weak form that the *Analysis*

implements. For example, in a heat transfer analysis, material property attributes will give rise to StiffnessContributors, applied heat fluxes will give rise to ForceContributors and prescribed temperatures will give rise to constraints. Typically a SystemContributor corresponds to a mesh entity classified on the model entity where the attribute is applied.

The Analysis class creates all of the SystemContributors and adds them to an instance of a DiscreteSystem. There is a hierarchy of DiscreteSystem classes that represent different time orders of PDEs. DiscreteSystemZeroOrder represents an equation of the form  $F(x, t) = 0$ , DiscreteSystemFirstOrder represents an equation of the form  $F(x, x', t) = 0$  and so on. This transformation of the problem from the ContinuousSystem to the DiscreteSystem allow the various solution routines to work on a representation that is independent of the type of problem being solved.

### 3.3 Algebraic System

The next step in the solution process is to set up and solve the linear algebra. The setting up of the linear algebra consists of transforming a DiscreteSystem into an AlgebraicSystem. This transformation is handled by an Assembler object. Each solution algorithm (e.g. a backward Euler time integrator or a SIRK) must create an Assembler that knows how to create the specific algebraic equations that the solution algorithm needs. This Assembler is used by the algebraic system to construct or update it's internal representation of the equations to be solved.

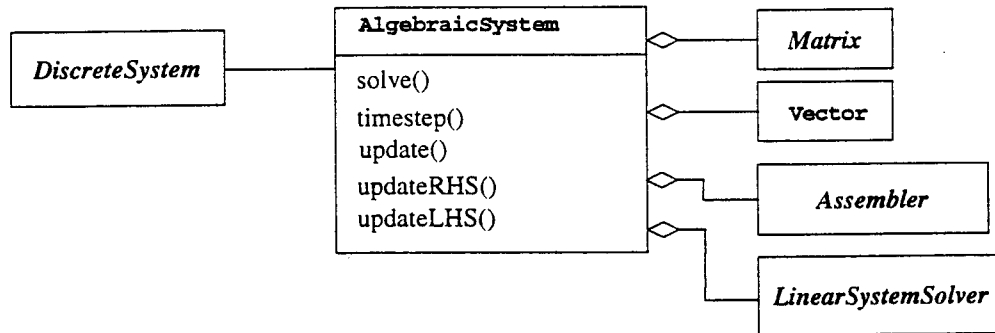


Figure 12. Structure of the AlgebraicSystem class

Essentially an Assembler maps the contributions of each StiffnessContributor and ForceContributor in a DiscreteSystem into the correct entries in the matrix  $A$  and vector  $b$  in an AlgebraicSystem. The easiest way to understand this is to consider a simple example of using Backward Euler to solve a first order PDE. In this case the equation we are solving is:

$$M\dot{u} + Ku = f$$

where each of the global matrices and vectors is the sum of the contributions of the individual system contributors ( $M_{sc}$ ,  $K_{sc}$ ,  $f_{sc}$ ):

$$M = \sum M_{sc}, K = \sum K_{sc} \text{ and } f = \sum f_{sc}$$

when the Backward Euler algorithm is applied to Eq. the resulting equation is of the form:

$$(M + K\Delta t)u_{n+1} = f + Mu_n$$

If this equation is then mapped into  $Ax = b$  we find that:

$$A = M + K\Delta t$$

$$b = f + Mu_n$$

and, of course, basically the same thing happens at the level of the individual system contributors.

In the solution process what needs to be done is to form Equation from the contributions of the individual system contributors. It would be inefficient to first form a global  $M$ ,  $K$  and  $f$  and then perform the algebra needed to form the final equation. A more efficient way to do this would be to separately transform the individual contributions according to Equation and directly assemble them into the desired form. This is the task of the assembler.

Each type of operation that needs to form a global matrix or vector must use an assembler (either defining a new one or using an existing one). The base class `Assembler` provides the operations needed to do the actually assembly into a global system through its `assemble()` method (this method is only accessible to subclasses of `Assembler`). Each derived class must implement the operations that need to be carried out on the matrices return by the `ForceContributors` and `Stiffness contributors` and then call the base classes `assemble()` method.

Two examples of `Assembler` subclasses are shown in Figure 13. One, the `BackwardEulerAssembler`, was discussed above. The other, the `MatrixAssembler`, just directly assembles the matrix contributions with no additional manipulations.

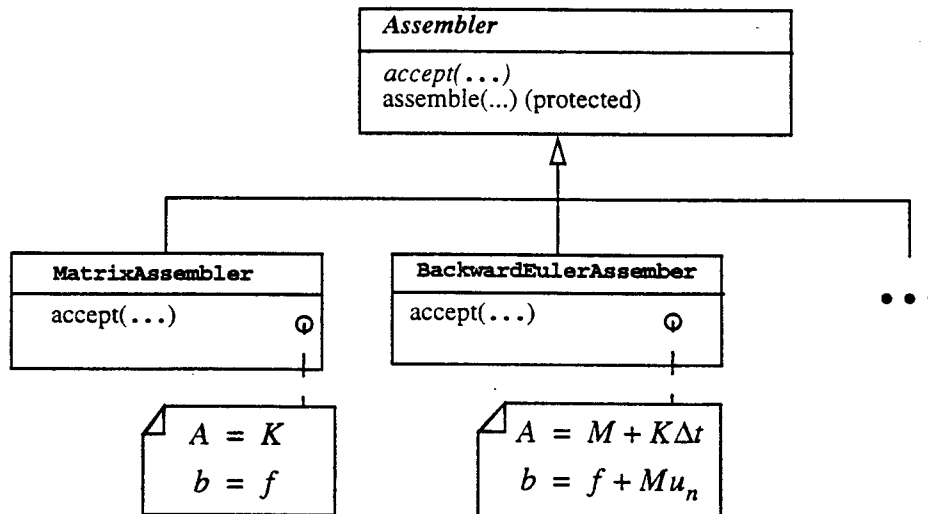


Figure 13. Part of the `Assembler` class hierarchy

An assembler gets the contributions from the individual system contributors by being passed to a `DiscreteSystem` `process()` method. For all the appropriate system contributors contained in the `DiscreteSystem`, this method passes the assembler to the contributors `accept()` method. The contributor then calculates what is it contributing to the system and passes the result (which is either an `ElementMatrix` or a `ForceVector`) to the assembler's `accept()` method.

## 4 Extending the Framework

One of the most important goals of designing the analysis framework is to make it easily extendable to meet unforeseen needs. There are two major categories of extension that the framework allows: adding new types of analyses and providing replacements for functional components that can be used by any analysis (e.g. linear solvers, time integrators, etc.).

### 4.1 Adding a New Analysis

To add a new analysis type to the framework a class derived from Analysis (e.g. the HeatTransferAnalysis class in Figure 10) must be defined for the new analysis and system contributors appropriate for the analysis must be written. The class derived from Analysis embodies the knowledge of how to interpret attributes that are applied to the geometric model in a manner consistent with the weak form of the PDEs being solved and create the appropriate system contributors.

Also the various system contributor for the analysis must be written. In the case of the heat transfer example, there are three classes that need to be written (Figure 14): the HeatTransferSC (stiffness contributor) that calculates coupling between degrees of freedom of the temperature field on the interior of the domain, HeatFlux which calculates contributions due to applied heat fluxes and TemperatureBC which is a constraint that arises due to prescribed values of temperature.

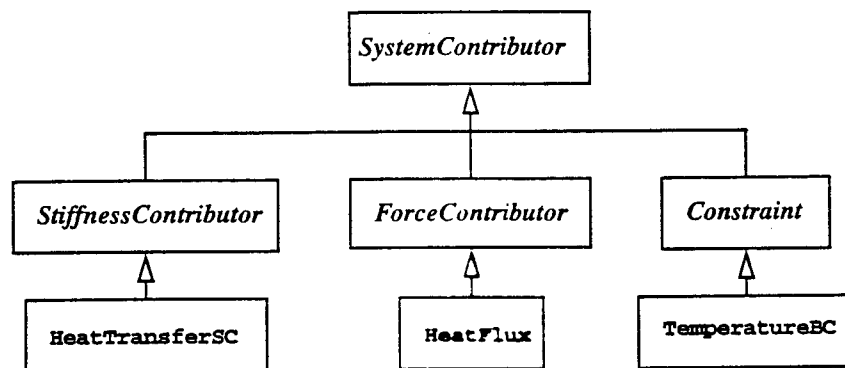


Figure 14. System contributor classes for heat transfer analysis

### 4.2 Adding a New Functional Component

Many of the functional components of the framework are designed for easy replacement. Among these are the mappings and interpolations used to define a field, solvers for linear and non linear system and spatial and temporal integration procedures.

Each of these are replaceable by deriving a new class that implements the appropriate functionality from the appropriate base class and registering the new class with the framework so that it can be created as needed.

## 5 Closing Remarks

This paper has described an object oriented framework for performing geometry-based finite element analyses. The geometry-based approach was selected to give a firm foundation for performing adaptive procedures. An object oriented design and implementation was used to allow the framework to be easily extended to new problem areas. The resulting framework has been used to implement a number of different types of analyses. Current efforts are focused on implementing adaptive strategies within the framework.

## 6 References

1. Weiler K.J. The radial-edge structure: a topological representation for non-manifold geometric boundary representations. In Wozney M.J; McLaughlin H.W.; and Encarnacao J.L., editors. *Geometric modeling for CAD applications*, North Holland; 1988. p 3-36.
2. Beall M.W and Shephard M.S. A general topology-based mesh data structure. *International Journal for Numerical Methods in Engineering* (1997) accepted.
3. Shephard M.S. The specification of physical attribute information for engineering analysis. *Engineering with Computers*, 4 (1988) 145-155.
4. Shephard, M. S.; Dey, S.; and Flaherty, J. E. A straightforward structure to construct shape functions for variable p-order meshes. *Computer Methods In Applied Mechanics and Engineering*, (1996) to appear.
5. Booch, G.; Jacobson, I. and Rumbaugh, J. *Unified Modeling Language for Object-Oriented Development Documentation Set Version 0.91 Addendum*, Rational Software Corporation, Santa Clara, CA, 1995.
6. Hughes, T. J. R., *The Finite Element Method: Linear Static and Dynamic Finite Element Analysis*, Prentice Hall, Englewood Cliffs, NJ, 1987.
7. Zienkiewicz, O. C. and Taylor, R. L., *The Finite Element Method - Volume 1*, 4th Edition, McGraw-Hill Book Co., New York, 1987.





## COMPUTER-AIDED MULTISCALE MODELING TOOLS FOR COMPOSITE MATERIALS AND STRUCTURES\*

V. BELSKY, M. W. BEALL, J. FISH, M. S. SHEPHARD and S. GOMAA

Rensselaer Polytechnic Institute, Troy, NY 12180, U.S.A.

**Abstract**—This paper presents recent research efforts at Rensselaer Polytechnic Institute aimed at developing computer-aided multiscale modeling tools for composite materials and structures aimed at predicting the *macromechanical* (overall) structural response, such as critical deformation, vibration and buckling modes, as well as various failure modes on the *mesomechanical* (lamina) level, such as delamination and ply buckling, and on the *micromechanical* (the scale of microconstituents) level, such as debonding, microbuckling, etc.

The building blocks of this technology are (i) idealization error estimators aimed at quantifying the quality of the numerical and mathematical models of composites, (ii) multigrid technology aimed at superconvergent solution of the multiscale computational models, (iii) mathematical homogenization theory aimed at constructing inter-scale transfer operators for rapid and reliable information flow between the scales, (iv) system identification for *in situ* characterization of the phases and their interface, and (v) multiscale model construction and visualization.

### 1. BACKGROUND

#### 1.1. Idealization error estimators

Idealization error estimators for laminated composite shell structures are aimed to quantify three sources of errors and to address the following issues:

(i) Identifying the regions within the problem domain where the macromechanical description (shell model), which is the most inexpensive modeling capability, is insufficient, i.e., introduces unacceptable errors with respect to a more comprehensive ply-by-ply (mesomechanical) model. Idealization error estimators should be able to identify not only the precise location within the plane of the shell, but also the layers within the laminate where the use of mesomechanical description may result in unacceptable errors of interlaminar stresses.

The Dimensional Reduction Error estimator (DRE) developed in Ref. 1 builds on the earlier works on residual based error estimators. By this technique dimensional reduction error  $\mathbf{e} = \mathbf{u}^{\text{EX}} - \mathbf{u}^{\text{FE}} \cong \Phi\beta$  is approximated by a linear combination of some basis in the auxiliary *mesomechanical* finite element mesh. The unknown coefficients  $\beta$  are found by solving the auxiliary problem:

$$\frac{\partial}{\partial \beta} \{0.5a(\mathbf{u}^{\text{FE}} + \Phi\beta, \mathbf{u}^{\text{FE}} + \Phi\beta)_{\Omega} - (\mathbf{u}^{\text{FE}} + \Phi\beta, \mathbf{b})_{\Omega} - (\mathbf{u}^{\text{FE}} + \Phi\beta, \mathbf{t})_r\} = 0 \quad (1)$$

where  $\Phi$  is defined to maintain  $C^0$  continuity of  $\mathbf{u}^{\text{FE}} + \mathbf{e}$ , and to satisfy essential boundary conditions;  $a(\mathbf{u}, \mathbf{v})$  and  $(\mathbf{u}, \mathbf{v})$  are bilinear symmetric forms defined by

$$a(\mathbf{u}, \mathbf{v}) = \int \nabla' \mathbf{u}^T \mathbf{D} \nabla' \mathbf{v} \, d\Omega \quad \text{and} \quad (\mathbf{u}, \mathbf{v}) = \int \mathbf{u} \mathbf{v} \, d\Omega;$$

$\nabla' \mathbf{u}$  represents the symmetric gradient of  $\mathbf{u}$  and  $\mathbf{D}$  is a constitutive tensor. To ensure that the dimensional reduction error estimation takes only a small fraction of the entire computational effort, the Hessian matrix resulting from (1) is replaced by a diagonal or block diagonal form. For details see Ref. 1.

(ii) Enriching the fundamental kinematics of the equivalent single-layer (macro) model with a discrete-layer (meso) model in the vicinity of the most critical layers enables modeling of various failure modes on the lamina level such as delamination. Unfortunately, in many cases the mechanism that causes failure is at a much smaller scale—the scale of microconstituents. A common computational rationale today is to investigate various microprocesses that may lead to a progressive failure by considering a unit cell or representative volume problem. The mechanism that allows us to do so is a periodicity assumption. However, in the areas of high stress concentration, which are of critical interest to the analyst, periodicity assumptions are not valid, and thus the application of conventional homogenization techniques in the “hot spots” may lead to poor predictions of local fields.

The adequacy (or lack of it) of the homogenization theory has been assessed in Ref. 2 on the basis of

\*Paper presented at the 3rd National Symposium on Large-Scale Structural Analysis for High-Performance Computers and Workstations, held 8-11 November 1994, Marriott Waterside, Norfolk, VA, U.S.A.

the uniform validity of the double scale asymptotic expansion, which serves as a basis of mathematical homogenization theory. The double scale asymptotic expansion of the form

$$u(z, y) = u^0(y) + \epsilon H(z) \nabla u^0(y) + \epsilon^2 P(z) \nabla^2 u^0(y) \dots \quad (2)$$

is considered to be uniformly valid if the terms in the asymptotic sequence are rapidly decreasing. In Eq. (2)  $y$  is the position vector on the meso-scale and  $z = y/\epsilon$  is the coordinate in the unit cell;  $\nabla$  is the symmetric gradient operator; functions  $u^0(y)$ ,  $H(z)$ ,  $P(z)$  are found by inserting asymptotic expansion into the strong form of equilibrium conditions and by identifying equal powers of  $\epsilon$ . The quality of homogenization is assessed on the basis of the relative magnitude of the first term neglected by the classical homogenization theory  $\epsilon^2 P(z) \nabla^2 u^0(y)$  to the first two taken into account.

A closed form expression of idealization error estimators associated with the Microscale Reduction has been derived in Ref. 2. The proposed MRE estimator relates the homogenization (or scale reduction) error to macroscopic fields (strain and strain gradients) and to the details of microstructure (compliances of phases, volume fraction and the size of the unit cell). A simplified form of such homogenization error (or MRE) has been derived in Refs 2, 3 which shows that

Homogenization error

$$= Y \frac{|C_1 - C_2|}{C_{\text{eff}}} \frac{\alpha(1 - \alpha)}{2} \frac{\|\nabla \epsilon^0\|_E}{\|\epsilon^0\|_E} \quad (3)$$

where  $C_1$  and  $C_2$  are the compliances of the micro-constituents,  $C_{\text{eff}}$  the effective compliance of the unit cell,  $\alpha$  the volume fraction,  $Y$  the size of the unit cell,  $\|\nabla \epsilon^0\|_E$  the energy norm of the gradient of the macroscopic strain field in the homogenized FE mesh.

From the above expression it is evident that there are four factors affecting the homogenization error: (i) The size of the unit cell in the physical domain  $Y$ , (ii) the normalized compliance difference  $|C_1 - C_2|/C_{\text{eff}}$ , (iii) the volume fraction  $\alpha(1 - \alpha)/2$ , (iv) the strain gradients on the macro-scale.

### 1.2. Fast iterative solvers for a heterogeneous medium

The multigrid technology with special inter-scale connection operators has been found to possess superconvergent characteristics for the periodic heterogeneous medium.<sup>3,4</sup> The multigrid procedure starts by performing several smoothing iterations on the micro-scale in the regions identified by MRE indicators, typically using Gauss-Seidel or Conjugate Gradient method with diagonal scaling. Consequently, the higher frequency modes of error are damped out immediately. The remaining part of the solution error is smooth, and hence, can be effectively

damped out on the auxiliary coarse mesh. It has been proved<sup>3,4</sup> that the finite element mesh on the meso-scale (ply level) serves as a perfect mechanism for capturing the lower frequency response on the micro-scale. Therefore, the residual in the finite element mesh on the micro-scale is restricted to the meso-scale, and the smooth part of the solution is captured in the finite element mesh on the meso-scale. The oscillatory part of the solution on the meso-scale is again damped out by one of the classical smoothing procedures. The lower frequency response on the meso-scale is perfectly captured on the macro-mesh (shell level). The resulting solution on the meso-scale is obtained by prolongating the displacement field from the macro-mesh back to the finite element mesh on the meso-scale and by adding the oscillatory part of the solution previously captured on the meso-scale. Likewise, the solution on the micro-scale is obtained by prolongating the smooth part of the solution from the meso-scale and by adding the oscillatory part that has been captured by smoothing. This process is repeated until satisfactory accuracy is obtained.

The derivation of the inter-scale transfer operators is based on the asymptotic solution expansion, which assumes infinitesimality of the unit cell size. The asymptotic forms of the prolongation and restriction operators are obtained by discretizing the corresponding asymptotic expansions. For unit cells of a finite size the regularization function is introduced to obtain a well-behaved inter-scale transfer operators. The resulting homogenization based prolongation operator is given by:

$$\tilde{Q} = Q + dQC\nabla_s N(X_g) \quad (4)$$

where  $Q$  is the standard linear prolongation operator;  $d$  is the unit cell solution;  $\nabla_s N(X_g)$  the symmetric gradient of the shape functions in the auxiliary grid evaluated at the Gauss points in the auxiliary mesh;  $C$  the projection operator aimed to maintain  $C^0$  continuity of the displacement field on the micro-scale. For more details see Ref. 3.

The rate of convergence of the multigrid process has been studied in Ref. 4. It has been proved that for problems in periodic 1-D heterogeneous media the rate of convergence of the two-grid method with special inter-scale transfer operators is given by:

$$\|e^{i+1}\| = [q/(4 - q)] \|e^i\|$$

and

$$q = \{(D_1 D_2)^{1/2} / [0.5(D_1 + D_2)]\}^2 \quad (5)$$

where  $D_i$  represent the stiffnesses of microconstituents. Note that if the material is homogeneous and the mesh is uniform, then  $D_1 = D_2$  and we recover a classical two-grid estimate:  $\|e^{i+1}\| = 1/3 \|e^i\|$ . Otherwise  $q < 1$  resulting in  $\|e^{i+1}\|/\|e^i\| < 1/3$ .

Note that if the stiffness of a fiber is significantly higher than that of a matrix, i.e.  $D_1 \gg D_2$ , then the

multigrid method converges in a single iteration. In multidimensions, convergence of the multigrid process for periodic heterogeneous media has been studied in Ref. 3. It has been found that a convergence trend characteristic of the 1-D cases is closely followed in multidimensions.

### 1.3. The inverse problem—calibration of the constitutive laws

The success of the multiscale computational technology depends on the *in situ* characterization of nonlinear behavior of phases and their interaction through the interface. Thus it is necessary to construct a systematic approach aimed at calibrating the material parameters of the matrix and the interface to the observed boundary measurements. The observable experimental data could be of a very global nature, such as average strains or lower frequency modes, as well as of a very local nature on the micromechanical level.<sup>5</sup> For example, using moiré interferometry,<sup>5</sup> it is possible to measure displacements on the surfaces with spatial resolution of up to 0.4  $\mu\text{m}$ . Experimental data of a lesser detail can be obtained by photodepositing a mesh of dark and bright lines on the specimen surface. This technique has been successfully used in Ref. 6 to measure the localized shear strains in the metal matrix emanating from the crack tip.

The inverse problem for estimating the control variables, defining the shape and the size of the failure surfaces of the matrix and the interface, is formulated on the basis of regularized least squares principle, which states:

Find: the control variables  $\mathbf{h}$

Such that:

$$\Phi(\mathbf{d}) = K_1 \int_{\Gamma_{\text{obs}}} (\mathbf{N}\mathbf{d} - \mathbf{Z}_d, \mathbf{N}\mathbf{d} - \mathbf{Z}_d) d\Gamma + K_2 (\epsilon(\mathbf{d}) - \mathbf{Z}_\epsilon, \epsilon(\mathbf{d}) - \mathbf{Z}_\epsilon) \Rightarrow \min(\mathbf{d}) \quad (6a)$$

Subjected to:

$$\begin{aligned} \mathbf{r} &\equiv \mathbf{f}_{\text{ext}} - \mathbf{f}_{\text{int}}(\mathbf{d}, \mathbf{h}) \\ &= 0 \text{ and } \mathbf{h}_{\min} \leq \mathbf{h} \leq \mathbf{h}_{\max} \end{aligned} \quad (6b, c)$$

where  $\mathbf{N}$  and  $\mathbf{d}$  represent the finite element shape functions and nodal displacement vector, respectively;  $\mathbf{Z}_d$  is the experimental data of the displacement field on  $\Gamma_{\text{obs}}$ ;  $\mathbf{Z}_\epsilon$  are the overall strain measurements obtained from the strain gauges and  $\epsilon(\mathbf{d})$  are the corresponding average finite element strains;  $K_1$  and  $K_2$  are weighting parameters, which are used to scale two different sources of information;  $\mathbf{f}_{\text{ext}}$  and  $\mathbf{f}_{\text{int}}$  are external and internal force vectors;  $\mathbf{h}_{\min}$  and  $\mathbf{h}_{\max}$  are some bounds on control variables that might be possible to obtain from the experimental data on

individual constituents. The scalar product of the two vectors  $\mathbf{u}$  and  $\mathbf{v}$  is denoted by  $(\mathbf{u}, \mathbf{v})$ . In Eq. (6) the experimental "noise" function is omitted. For details see Ref. 7.

### 1.4. Multiscale model construction

The use of multiscale analysis in an adaptive environment requires the ability to automatically construct models of different kinds. Microstructural models must be constructed as necessary as well as transition models between the different analysis scales. The construction of these microscale models is done from a microstructural description that includes information on the geometry and material properties of the constituents, and the composition of the composite in terms of these constituents. These microscale models are more complex than just a simple unit cell model as they must conform to the geometry of the macroscale model, not just the geometry of a unit cell. Currently we are producing these microscale models by the repetition of a mesh of a unit cell model which limits the microstructure models to being on planar faces in the macro model. This mesh is made periodic by special mesh matching procedures in the Finite Octree mesh generator.<sup>9</sup> The transition mesh between the two models is made by first creating a geometric model that is composed of a region that represents the boundary of the unit cells embedded in a region that is the union of elements in the macro mesh that are being modeled at the micro level. This nonmanifold model is then meshed using the Finite Octree mesh generator.<sup>8</sup>

## 2. ITERATIVE GLOBAL-LOCAL PROCEDURE FOR PERIODIC HETEROGENEOUS MEDIA WITH TRANSITION ZONE

In this section we describe an iterative global-local algorithm for solving problems in a periodic heterogeneous medium, where the local region of interest  $\Omega_1$  is modeled on the microscale, while elsewhere the medium is treated as homogeneous. The local region(s) are selected in the portion of the macro problem domain  $\Omega_0$  ( $\Omega_1 \subset \Omega_0$ ) where microscale reduction error indicators<sup>2</sup> indicate that the classical homogenization theory is invalid. We assume that there might be a lack of conformity between the boundary of rectangular array of unit cells forming the local region and the element boundaries in the unstructured macro-mesh. In order to patch between the two meshes, we introduce an intermediate mesh on  $\Omega_2$  as the smallest region so that the local region is embedded within  $\Omega_2$  ( $\Omega_1 \subset \Omega_2 \subset \Omega_0$ ) and the boundaries of intermediate mesh on  $\Omega_2$  match the element boundaries in the global grid as shown in Fig. 1. The transition mesh as well as the macro-mesh are assumed to possess homogenized material properties.

In the following we describe a three-level multigrid like process in the spirit of adaptive composite grid

## Local Models for Multiscale Analysis

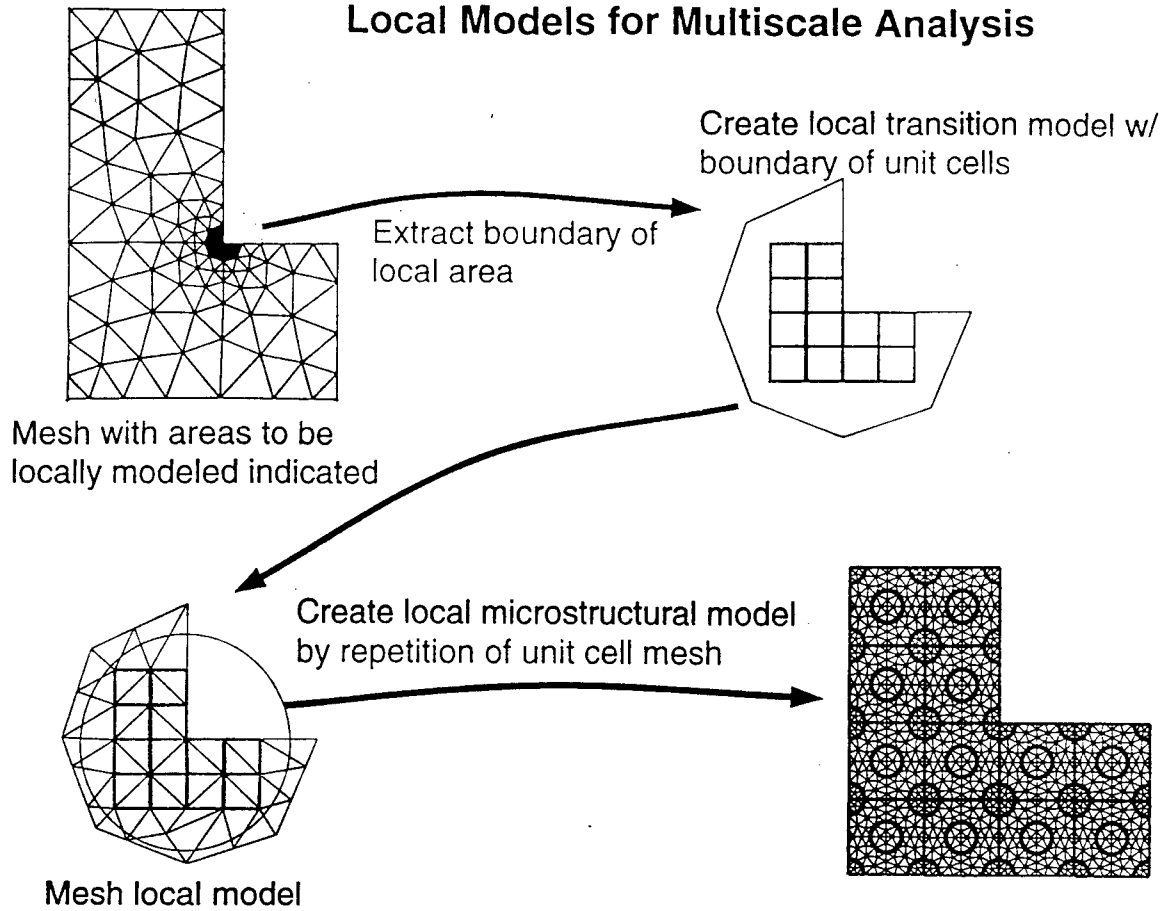


Fig. 1. Illustration of macro-mesh, transition mesh and micro-mesh.

method (FAC)<sup>9,10</sup> and multilevel adaptive technique (MLAT).<sup>11</sup>

1. Solve the global problem on the auxiliary macro-grid. Let  $\mathbf{f}_0$  and  $\mathbf{A}_0$  denote the force vector and the stiffness matrix on the auxiliary macro-mesh, then the solution  $\mathbf{u}_0$  on the auxiliary macro-mesh can be schematically expressed as

$$\mathbf{u}_0 = \mathbf{A}_0^{-1} \mathbf{f}_0. \quad (7)$$

2. Select the critical region using MRE indicators.
3. Encompass selected elements in the critical region with a rectangular array of unit cells and define the transition region, such that it entirely encompasses selected unit cells. External boundaries of the transition zone are defined as a minimal space occupied by the elements in the macro-mesh encompassing the selected rectangular array of unit cells.
4. Prolongate the macro solution onto the interface  $\Gamma_{os}$  between the macro domain and the intermediate mesh

$$\mathbf{u}_s(\Gamma_{os}) = \mathbf{Q} \mathbf{u}_0 \quad (8)$$

where subscript  $s$  denotes the quantities in the intermediate mesh.

5. Solve the problem on the intermediate mesh, subjected to the interface essential boundary conditions

$$\mathbf{u}_s = \mathbf{A}_s^{-1} \mathbf{f}_s$$

subject to

$$\mathbf{u}_s = \mathbf{u}_s(\Gamma_{os}) \text{ on } \Gamma_{os} \quad (9)$$

where the subscript  $s$  is used to denote various quantities in the intermediate mesh.

6. Prolongate solution onto the interface  $\Gamma_{sl}$  between the intermediate mesh and the rectangular array of unit cells forming the micro-grid using homogenization based prolongation operator (4). The subscript  $l$  is reserved for the micro-mesh

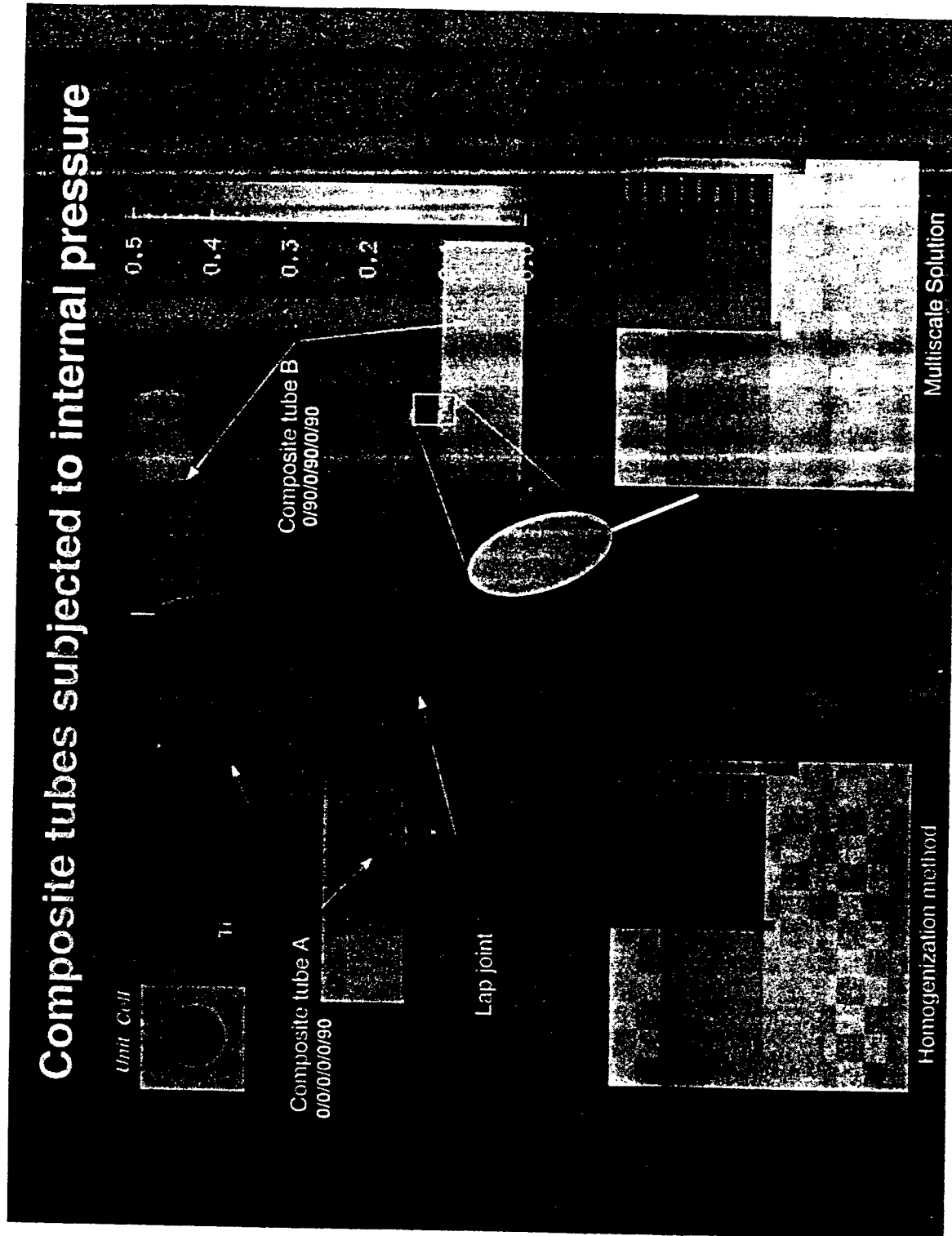
$$\mathbf{u}_l(\Gamma_{sl}) = \bar{\mathbf{Q}} \mathbf{u}_s. \quad (10)$$

7. Solve the problem on the intermediate mesh, subjected to the interface essential boundary conditions on  $\Gamma_{sl}$

$$\mathbf{u}_l = \mathbf{A}_l^{-1} \mathbf{f}_l$$

subject to

$$\mathbf{u}_l = \mathbf{u}_l(\Gamma_{sl}) \text{ on } \Gamma_{sl} \quad (11)$$



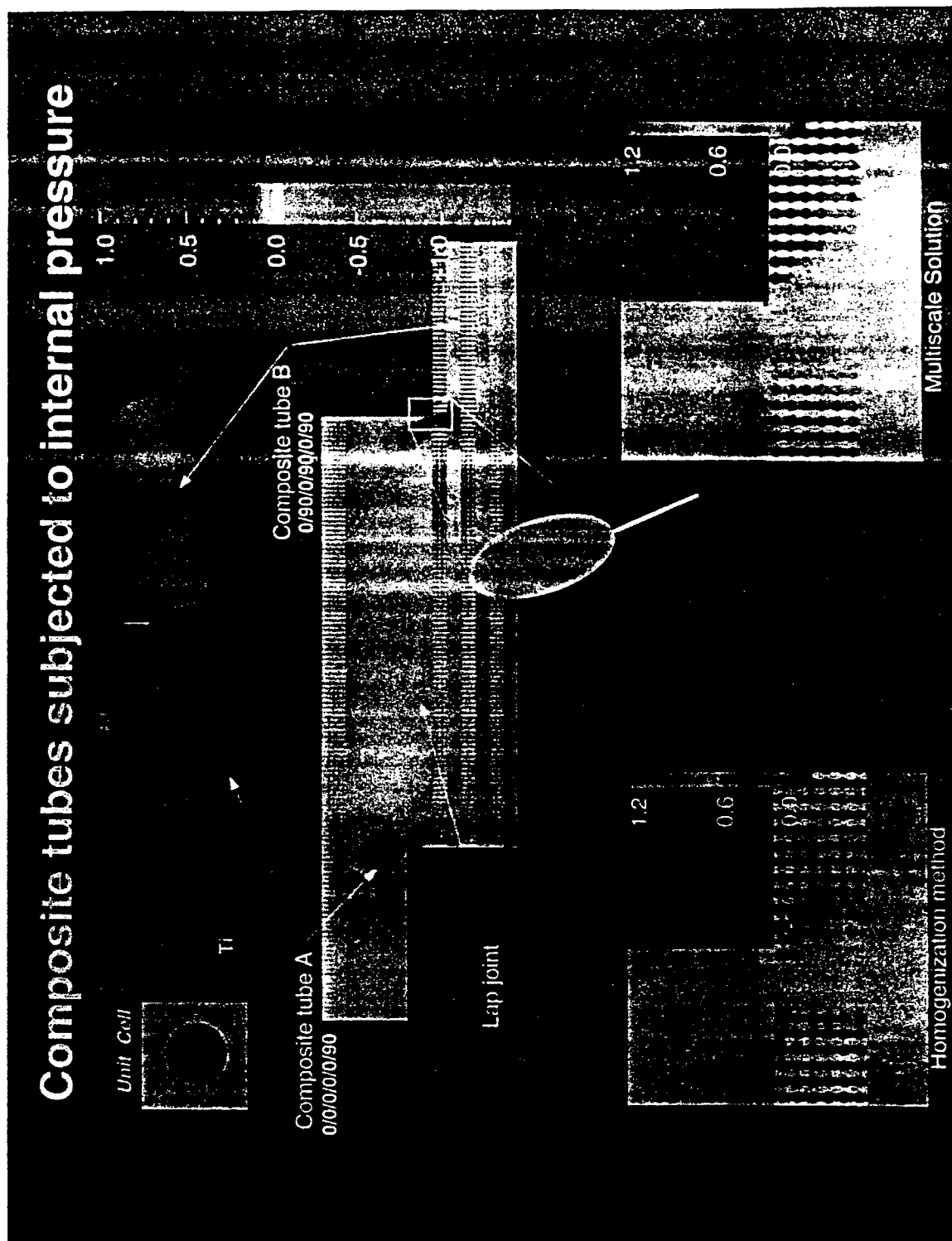


Fig. 3. Lap joint of two cylinders. Distribution of axial stresses ( $\sigma_{xx}$ ).

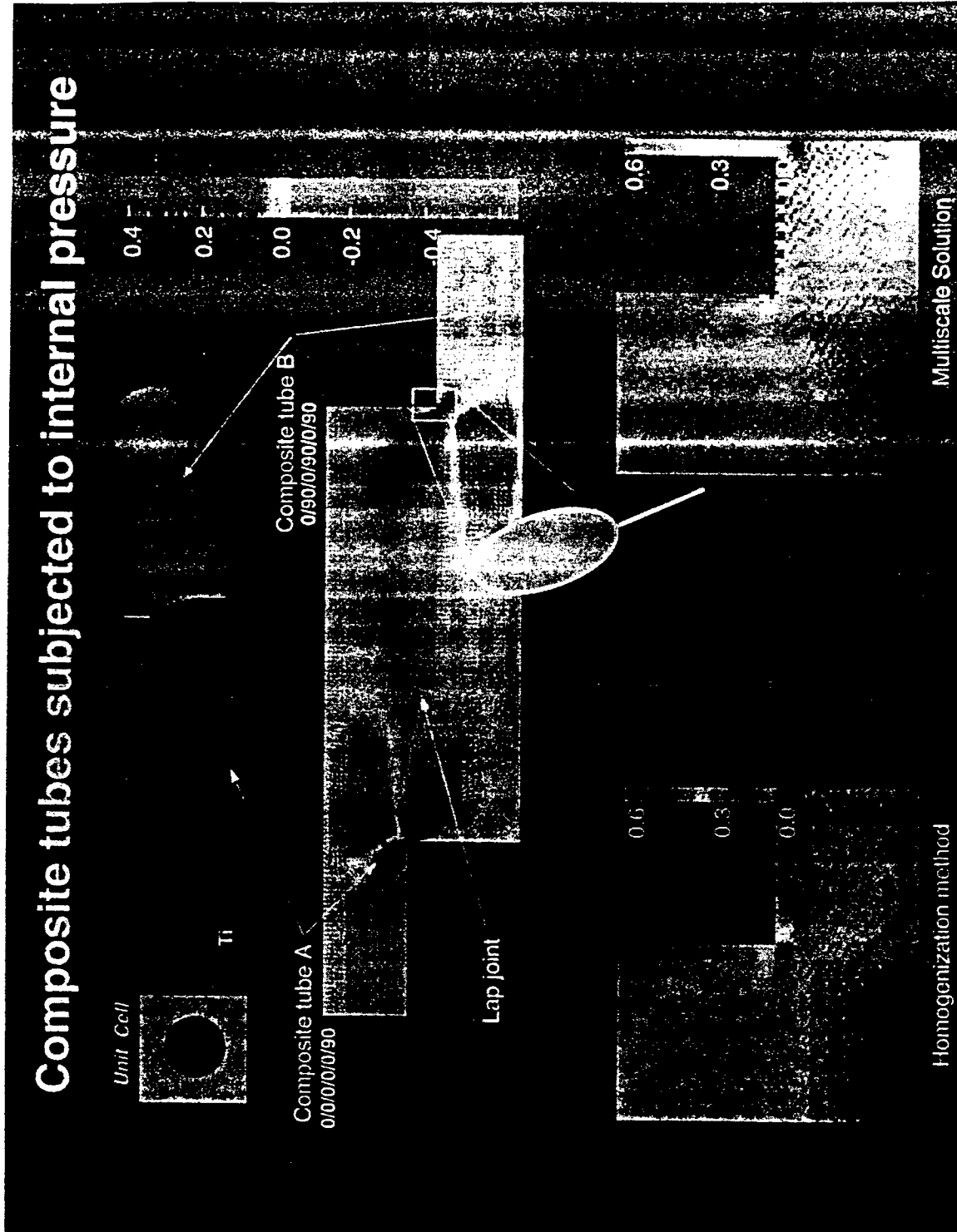


Fig. 4. Lap joint of two cylinders. Distribution of shear stresses ( $\sigma_{xy}$ ).

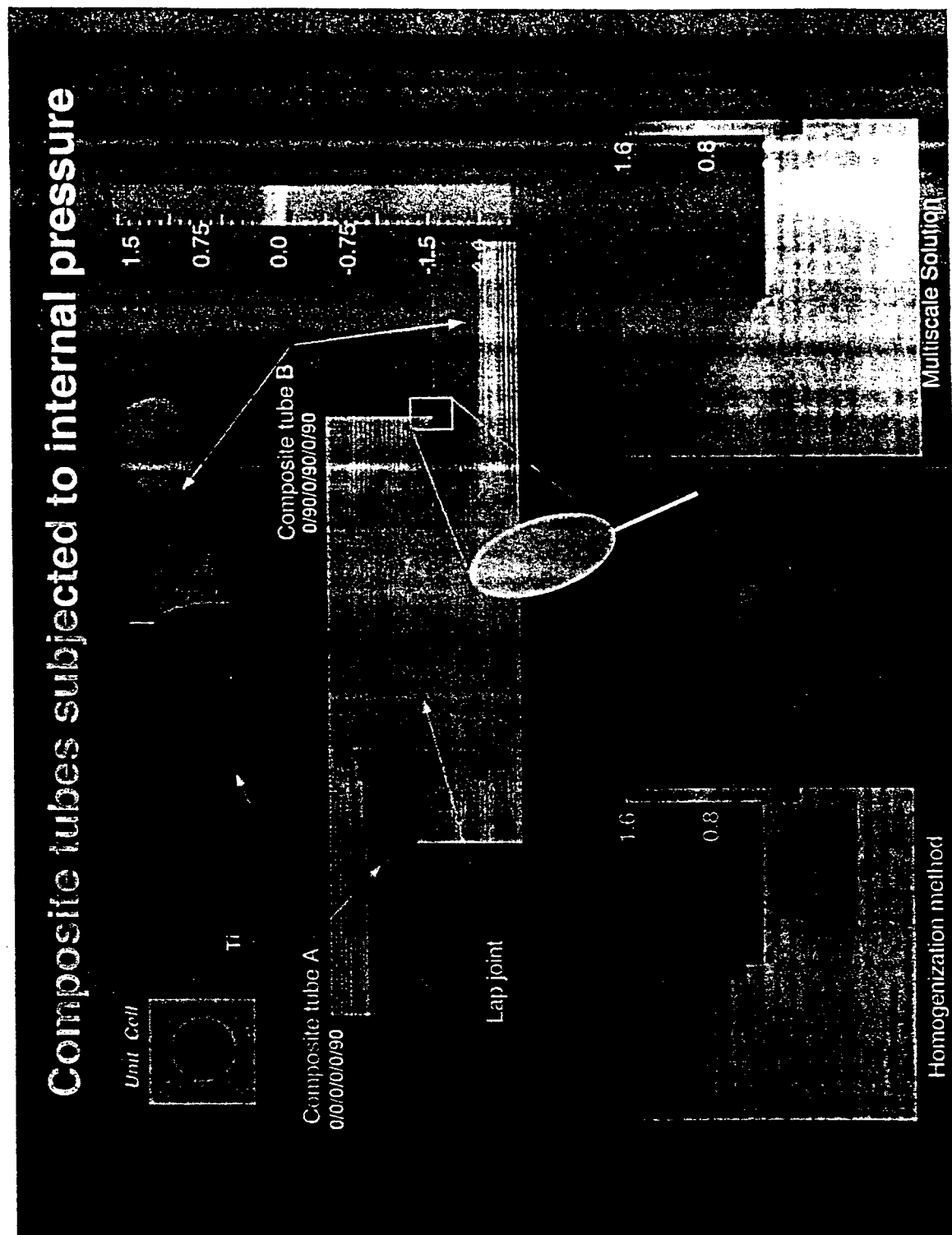


Fig. 5. Lap joint of two cylinders. Distribution of peeling stresses ( $\sigma_{ry}$ ).



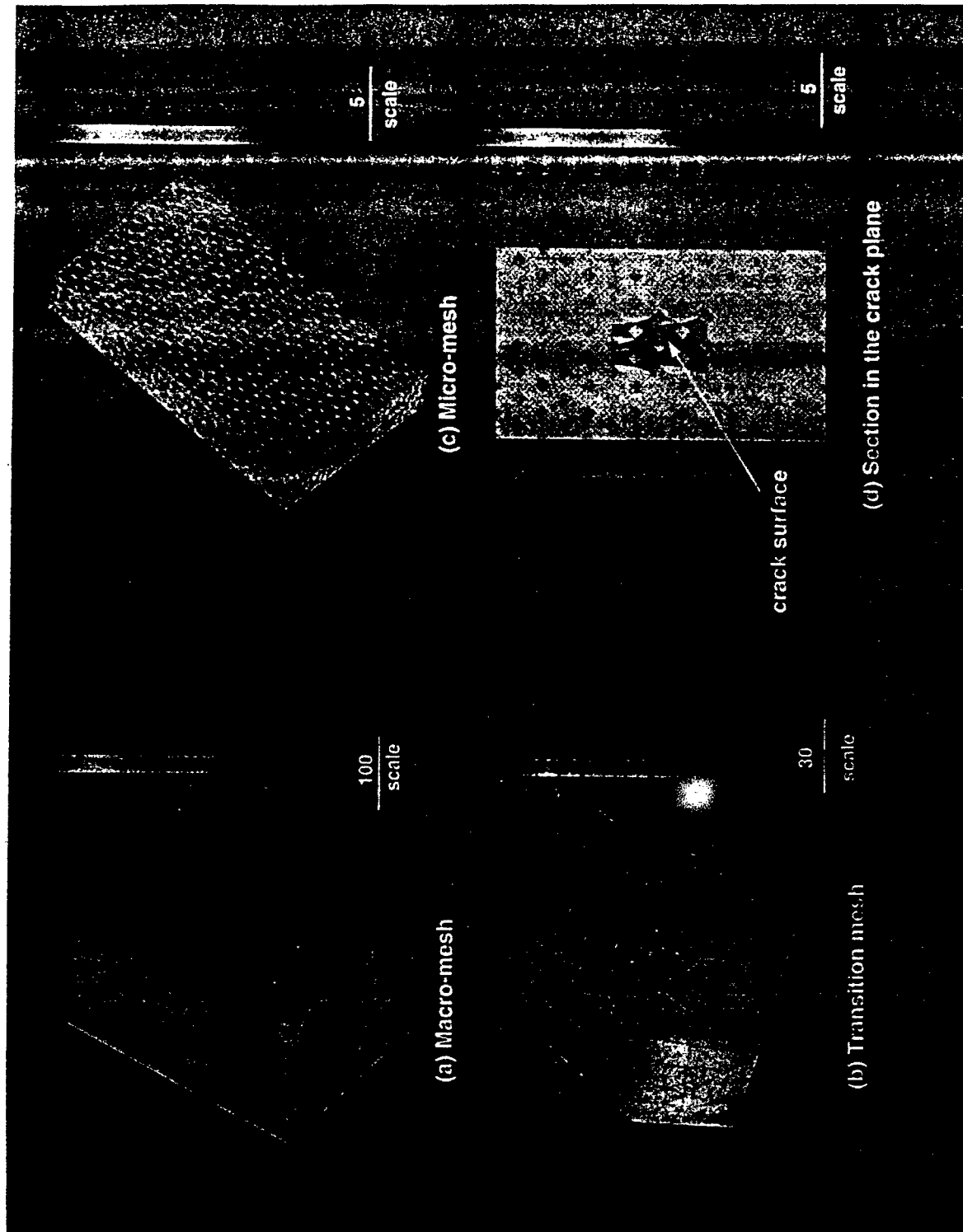


Fig. 6. Axial tension problem of cracked specimen. Axial stresses in macro-, transition and micro-meshes.

The system of equations described in (11) can be solved either directly or iteratively. The latter is a two-grid process with an auxiliary grid corresponding to the finite element mesh with homogeneous material properties. This variant has been successfully used in Ref. 3 and has been found to have a clear advantage over the direct method in the case of a large number of unit cells.

8. Restrict the residual to  $\Gamma_{sl}$  using a homogenization based restriction operator

$$\mathbf{r}_s = (\mathbf{f}_s - \mathbf{A}_s \mathbf{u}_s)_{\Omega_s/\Omega_i} + \tilde{\mathbf{Q}}^*(\mathbf{f}_i - \mathbf{A}_i \mathbf{u}_i)_{\Omega_i} \quad (12)$$

9. Correct the solution on the intermediate mesh

$$\mathbf{u}_s := \mathbf{u}_s + \mathbf{w}_s \mathbf{A}_s^{-1} \mathbf{r}_s \quad (13)$$

where  $\mathbf{w}_s$  is intermediate mesh relaxation parameter.

10. Restrict the residual to  $\Gamma_{\infty}$

$$\mathbf{r}_0 = (\mathbf{f}_0 - \mathbf{A}_0 \mathbf{u}_0)_{\Omega_0/\Omega_i} + \mathbf{Q}^*(\mathbf{f}_s - \mathbf{A}_s \mathbf{u}_s)_{\Omega_s} \quad (14)$$

11. Correct the solution on the intermediate mesh

$$\mathbf{u}_0 := \mathbf{u}_0 + \mathbf{w}_0 \mathbf{A}_0^{-1} \mathbf{r}_0 \quad (15)$$

where  $\mathbf{w}_0$  is the macro-mesh relaxation parameter.

The solution is considered as converged if the  $L_2$ -norm of residuals in the composite grid defined by  $\{\mathbf{r}_i(\Omega_i), \mathbf{r}_s(\Omega_s/\Omega_i), \mathbf{r}_0(\Omega_0/\Omega_s)\}$  is much smaller than the corresponding initial norm.

### 3. NUMERICAL EXAMPLES

Our numerical experimentation agenda includes two test cases. In the first, we consider a lap joint made of high-temperature composite tubes subjected to internal pressure. The composite is fabricated from silicon carbide fibers embedded in a titanium matrix. The layouts of tubes A and B shown in Fig. 2 are [0/0/0/0/90] and [0/90/0/90/0/90], respectively. Each layer is represented with 6 unit cells. The silicon carbide-titanium composite system has been considered with the following properties of micro-constituents: SiC:  $E_1 = 425$  GPa,  $\nu_1 = 0.25$ , Ti:  $E_2 = 106.9$  GPa,  $\nu_2 = 0.32$ . The internal pressure was selected as 0.055 GPa. The micromechanical finite element mesh included 16 elements per each unit cell.

The multi-grid process has been carried out on the 4 different mesh levels: micro-mechanical (fine) mesh and three macro-mechanical meshes. The V-cycle has been used with 1 pre- and 1 postsmoothing Gauss-Seidel iteration on the intermediate levels; 3 pre- and 3 postsmoothing Jacobi iterations on the finest level and direct solver on the coarsest level.

It was necessary to perform 34 multi-grid cycles to achieve convergence with a tolerance of 0.001. The distribution of homogenization errors is indicated in Fig. 1. In the bottom of Fig. 1 we compare the distribution of the strain energy absorption at the intersection of the two tubes as obtained with the proposed multiscale procedure and on the basis of classical homogenization theory. The distribution of the peeling, shear and normal axial stresses in the whole domain as well as in the critical regions are presented in Figs 2-4, respectively. It can be seen that the classical homogenization theory underestimates maximum stresses in the critical regions.

In the second example we consider an axial tension problem of the cracked composite specimen with the following normalized material properties:  $E_1/E_2 = 5$ ;  $\nu_1 = \nu_2 = 0.25$ . The microcrack was embedded between two unit cells in the center of the specimen as shown in Fig. 5. The problem has been analyzed using three different meshes: (i) The crack-free macro-mesh with homogenized material properties in the whole problem domain, (ii) the crack free transition mesh placed inside the middle macro element with homogenized material properties, and (iii) the micro-mesh, describing the microstructure of the composite system in the close vicinity ( $7 \times 7 \times 2$  unit cells) of the microcrack. Adaptive composite grid method (FAC) with homogenization-based restriction and prolongation operators has been employed, where the information between the different meshes flows through the interfaces only. Note that in the present example the macro- and micro-meshes represent different mathematical models. It was necessary to carry out 23 cycles to achieve the convergence with a tolerance  $10^{-6}$ . The distribution of the normal stresses on the different levels is depicted in Fig. 6, which reflects the force redistribution due to fiber breakage.

**Acknowledgements**—The support of ARPA/ONR under grant A10234, and NSF award ECS-9257203 are gratefully acknowledged.

### REFERENCES

1. J. Fish, S. Markolefas, R. Guttal and P. Nayak, "On adaptive multilevel superposition of finite element meshes," *Appl. Num. Math.* **14**, 135-164 (1994).
2. J. Fish, P. Nayak and M. H. Holmes, "Microscale reduction error indicators and estimators for a periodic heterogeneous medium," *Comput. Mech.* **14**, 323-338 (1994).
3. J. Fish and V. Belsky, "Multigrid method for periodic heterogeneous media. Part 2: Multiscale modeling and quality control in multidimensional case," *Comp. Meth. Appl. Mech. Engng* (in press, 1995).
4. J. Fish and V. Belsky, "Multigrid method for periodic heterogeneous media. Part I: Convergence studies for one-dimensional case," *Comp. Meth. Appl. Mech. Engng* (in press, 1995).
5. D. Post, R. Czarnek, D. Joh, J. Jo and Y. Guo, "Deformation of a metal-matrix tensile coupon with a central slot: an experimental study," *J. Composite Tech. Res. ASTM* **9**, 3-9 (1987).

6. G. J. Dvorak, Y. A. Behei-El-Din and L. C. Bank, "Fracture of fibrous metal matrix composites—I. Experimental results," *Engng Fracture Mech.* **34**, 87-104 (1989).
7. J. Fish and V. Belsky, "On calibration of constitutive laws," in preparation.
8. M. S. Shephard and M. K. Georges, "Automatic three-dimensional mesh generation by the finite octree technique," *Int. J. Numer. Meth. Engng* **32**, 709-749 (1991).
9. J. Fish and A. Wagiman, "Multiscale finite element method for a locally nonperiodic heterogeneous medium," *Computat. Mech.* **12**, 164-180 (1993).
10. S. F. McCormick and J. W. Thomas, "The fast adaptive composite grid (FAC) method for elliptic equations," *Math. Comput.* **46**, 439-456 (1986).
11. Achi Brandt, "Multi-level adaptive solutions to boundary-value problems," *Math. Comput.* **31**, 333-390 (1977).

Towards an Ultimate Finite Element Oriented  
Solver on Unstructured Meshes

Vladimir Belsky and Jacob Fish

SCOREC Report #4-1995  
Scientific Computation Research Center

Proceedings of *ASME/CIE*, 1995

Scientific Computation Research Center  
Rensselaer Polytechnic Institute  
Troy, NY 12180-3590  
voice 5182766795  
fax 5182764886

---

---

## TOWARDS AN ULTIMATE FINITE ELEMENT ORIENTED SOLVER ON UNSTRUCTURED MESHES

Vladimir Belsky and Jacob Fish

Department of Civil Engineering

Rensselaer Polytechnic Institute

Troy, New-York

### ABSTRACT

The paper investigates computational efficiency of various finite element solvers, including the state-of-the-art iterative methods based on multigrid-like and Modified Incomplete Cholesky preconditioners, as well as sparse direct solver recently developed at NASA Langley. These methods are compared to the newly developed Finite Element Oriented Solver (FEOS), which combines the advantages of the iterative and direct solution techniques. Numerical tests are conducted for both well-conditioned three dimensional problems as well as poor-conditioned problems, such as thin shells. The proposed FEOS solver has been found to possess a remarkable robustness and computational efficiency, by far superior to its comprising ingredients.

### INTRODUCTION

The performance of linear solvers in terms of CPU time for symmetric positive definite systems can be approximated as  $CN^\beta$ , where  $N$  is the number of degrees-of-freedom, and  $C, \beta$  are solution dependent parameters. The major advantage of direct solvers is their robustness, which is manifested by the fact that parameters  $C$  and  $\beta$  are independent of problem conditioning (except for close to singular systems). Direct solvers are ideal for solving small up to medium size problems (since the constant  $C$  for direct methods is significantly smaller than for iterative solvers), but becomes prohibitively expensive for large scale problems since the value of exponent for direct solvers is higher than for iterative methods. For large well conditioned three dimensional problems the storage and CPU time requirements for direct methods are so large that serious consideration of competing methods is a virtual reality.

Recent years saw a re-emergence of iterative solvers in finite element structural analysis due to increasing demand to analyze very large finite element systems. Nevertheless, the major obstacle that needs to be overcome before iterative solvers can be routinely used in commercial packages is circumventing their pathological sensitivity to problem conditioning, which is manifested by the

increase of constant  $C$  with degradation in problem conditioning. Moreover, for linear static analysis any type iterative method requires (except for the stiffness and preconditioner formation and factorization) for each load case a new iterative process (whereas in a direct solution, factorization is performed only once, and each load case requires only forward reduction and back substitution).

This paper presents a Finite Element Oriented Solver (FEOS), which exploits specific properties of the problem, including a finite element discretization and estimated problem conditioning in constructing a nearly optimal solution strategy. The FEOS is a hybrid solver with built in strategist that combines multigrid-like principles with efficient Incomplete Cholesky based smoothing techniques and state-of-the-art sparse direct methods for solving auxiliary preconditioned systems. Its major characteristics are summarized below:

- Computational efficiency and robustness:* FEOS is faster and requires less storage than the sparse direct solver for wide range of practical problems including those with distorted geometries, unstructured meshes, strong anisotropies - all giving rise to poor conditioned problems.

- Fully automated:* FEOS a priori selects an optimal solution strategy based on the estimated conditioning, problem size, number of load cases, etc.

Subsequent sections describe the building blocks of FEOS. Numerical experiments comparing the performance of FEOS with its basic constituents alone are given in the last section.

### SPARSE DIRECT SOLVERS

Consider a sparse symmetric positive definite linear system

$$Au = f \quad u \in R^n \quad f \in R^n \quad (1)$$

where  $A$  is the  $n \times n$  symmetric and positive definite matrix;  $u$  and  $f$  are vectors of order  $n$ . Traditionally, the linear equation solvers employed have been envelope, band or frontal type. The common idea behind all these methods is that zeros outside the envelope of  $A$  are preserved in its Cholesky factor  $L$ . In order to reduce the storage requirements for the factor, the linear

system is reordered to reduce the envelope, band or front size. Among the effective envelope-reducing algorithms include the reverse Cuthill-McKee (George, 1981), Gibbs-Poole-Stockmeyer (Crane, 1976) and Gibbs-King (Lewis, 1982) ordering algorithms. Generally, zero entries within the envelope structure are not exploited as they are in true sparse solvers, and thus for large problems envelope-type methods can be much more demanding than true sparse solvers. Yet envelope-type methods have been very popular primarily due to their simplicity and ease of reordering algorithms.

A true sparse solver attempts to reduce an overall storage and arithmetic requirements by storing and computing only the logical nonzeros of the factor matrix. By this technique the linear system of equations is reordered to reduce the number of nonzeros in the factor matrix irrespective of any envelope structure. Indeed, effective ordering algorithms for true sparse solvers, such as Minimum Degree algorithm (George, 1987) generally scatter many of the nonzeros away from the diagonal and thus are entirely inappropriate for an envelope-type methods. Nevertheless, true sparse matrix methods have not gained wide acceptance among the software developers for large-scale applications primarily because general sparse orderings were difficult and time-consuming.

Our numerical experiments comparing envelope-type solvers with recently developed sparse direct solver at NASA Langley show that major shortcomings have been overcome, and that a good implementation of the sparse direct solver outperforms envelope-type solvers by orders of magnitude in both execution time and storage requirements.

## MULTIGRID PRINCIPLES

Since the pioneering work of Fedorenko (1962), multigrid literature has grown in astonishing rate. This is not surprising since the multigrid-like methods possess the highest rate of convergence among the iterative techniques for solving symmetric positive definite linear systems. The principal idea of multigrid consists of capturing the oscillatory response of the system by means of smoothing, whereas remaining lower frequency response is resolved on the auxiliary coarse grid.

To clarify the basic principles we will denote the auxiliary grid functions with subscript 0. For example,  $u_0$  denotes the nodal values of the solution in the auxiliary grid, where  $u_0 \in R^m$ ,  $m < n$ . We also denote the prolongation operator from the coarse grid to the fine grid by  $Q$ :

$$Q: R^m \rightarrow R^n \quad (2)$$

The restriction operator  $Q^T$  from the fine-to-coarse grid is conjugated with the prolongation operator, i.e.:

$$Q^T: R^n \rightarrow R^m \quad (3)$$

The superscripts are reserved to indicate the iteration count. Let  $r^i$  be the residual vector in the  $i$ -th iteration defined by

$$r^i = f - Au^i \quad (4)$$

where  $u^i$  is the current approximation of the solution in the  $i$ -th iteration.

The problem of the coarse grid correction consists of the minimization of the energy functional on the subspace  $R^m$ , i.e.:

$$\frac{1}{2} (A(u^i + Qu_0^i), u^i + Qu_0^i) - (f, u^i + Qu_0^i) \Rightarrow \min u_0^i \in R^m \quad (5)$$

where (...) denotes the bilinear form defined by

$$(u, v) = \sum_{j=1}^n u_j v_j \quad u, v \in R^n \quad (6)$$

A direct solution of the equation (5) yields a classical two-grid procedure. Alternatively, one may introduce an additional auxiliary grid for  $u_0$  and so forth, leading to a natural multi-grid sequence. To fix ideas we will consider a two-grid process resulting from the direct minimization of (5) which yields

$$A_0 u_0^i = Q^T (f - Au^i) \quad (7)$$

where  $A_0 = Q^T A Q$  is the restriction of the matrix  $A$ . The resulting classical two-grid algorithm can be viewed as a two-step procedure:

a) *Coarse grid correction*

$$\begin{aligned} r^i &= f - Au^i \\ u_0^i &= A_0^{-1} Q^T r^i \\ \tilde{u}^i &= u^i + Qu_0^i \end{aligned} \quad (8)$$

where  $\tilde{u}^i$  is a partial solution obtained after the coarse grid correction. Even though the auxiliary system of equations is much smaller than that of the source problem, its solution for large scale systems can be most efficiently obtained by means of sparse direct solver.

b) *Smoothing*

$$u^{i+1} = \tilde{u}^i + P^{-1} (f - A\tilde{u}^i) \quad (9)$$

where  $P$  is a smoothing preconditioner. For example, if the Jacobi method is employed for smoothing, then

$$P = \omega (\text{diag}(A)) \quad (10)$$

where  $\omega$  is a weighting factor. A more efficient preconditioner of the form of Incomplete Cholesky factor is described in the next section.

To assess the rate of convergence we can associate the error vectors  $e^i, \tilde{e}^i$  defined by

$$e^i = u - u^i \quad \tilde{e}^i = u - \tilde{u}^i \quad (11)$$

where  $u$  is the exact solution of the source problem. Then the error resulting from the coarse grid correction (8) can be cast into the following form

$$\tilde{e}^i = (I - QA_0^{-1}Q^T A) e^i \quad (12)$$

where  $I$  is the identity  $n \times n$  matrix. Combining equations (9), (11), the influence of smoothing on error reduction is given by:

$$e^{i+1} = (I - P^{-1}A) \tilde{e}^i \quad (13)$$

and from the equations (12), (13) the error vector of the two-grid

process with one post-smoothing iteration can be expressed as:

$$e^{i+1} = (I - P^{-1}A)(I - QA_0^{-1}Q^T A)e^i \quad (14)$$

Denoting

$$\begin{aligned} G &= I - P^{-1}A \\ T &= I - QA_0^{-1}Q^T A \end{aligned} \quad (15)$$

equation (14) can be rewritten in the following concise form

$$e^{i+1} = GTe^i \quad (16)$$

It is essential to note that  $T$  and  $S = I - T$  are  $A$ -orthogonal projectors, namely:

$$(ATw, Sv) = 0 \quad \forall w, v \in R^n \quad (17)$$

$$\|v\|_A^2 = \|Tv\|_A^2 + \|Sv\|_A^2 \quad (18)$$

which yields that

$$\|T\|_A \leq 1 \quad (19)$$

Note that the projector  $T$  eliminates the effect of the prolongation operator, i.e.:

$$TQ = 0 \quad (20)$$

The rate of convergence of the two-grid method in heterogeneous media for one-dimensional problems has been assessed by Fish and Belsky (1994), and has been shown to be governed by a factor  $q^2/(4 - q^2)$ , where

$$q = \left( \sqrt{d_1 d_2} \right) / \frac{1}{2} (d_1 + d_2) \quad (21)$$

and  $d_i$  represent the stiffnesses of the microconstituents. Note that if the media is homogeneous and the mesh is uniform, then  $d_1 = d_2$  and one recovers the classical multigrid estimate, which states that asymptotically the error reduces by a factor of three with each new multigrid cycle. On the other hand if one phase is significantly stiffer than the other, i.e.  $d_1 \gg d_2$ , then the multigrid method converges in a single cycle or very few cycles at most.

For poor conditioned problems it is necessary to accelerate the rate of convergence of the multigrid method. Using (14) the reduction of error in a single cycle  $s^i = e^{i+1} - e^i$  can be expressed as linear function of the residual, i.e.,  $s^i = M^{-1}r^i$ , where  $M$  is termed as multigrid preconditioner. Various forms of the second-order acceleration schemes can be expressed as follows

$$u^{k+1} = \beta^k u^k + (1 - \beta^k) u^{k-1} + \beta^k \alpha^k M^{-1} r^k \quad (22)$$

where acceleration parameters  $\alpha, \beta$  are found by either (i) minimizing the energy functional or  $L_2$  norm of residuals, or by (ii) conjugate gradient method, which imposes orthogonality condition of the form

$$(M^{-1}AM^{-1}r^{k+1}, r^j) = 0 \quad \forall j \leq k \quad (23)$$

The major drawback of the multigrid method for general unstructured meshes is the fact that it requires construction of mesh hierarchy in the solution process. This linkage seems to be undesirable for general purpose FE codes, unless it is utilized in

the adaptive context, where the sequence of meshes generated by the process of adaptivity is exploited in the solution process. Algebraic multigrid (Ruge, 1987), on the hand, does not require formulation of continuous problem, which corresponds to the given algebraic system equations, and no grids are involved, but as a result of that the efficiency suffers. Instead, FEOS automatically constructs auxiliary mesh hierarchies from the source grid by recursively simplifying the kinematics of the source grid.

## INCOMPLETE CHOLESKY PRECONDITIONERS

Perhaps one of the most efficient smoothers for multigrid-like methods is based on Incomplete Cholesky Factorization. By this technique an approximate factorization of the stiffness matrix is introduced without generating too many fill-ins. Such an approach leads to the factorization of the type  $LDL^T = A - E$ , where  $E$  is an error matrix which is not explicitly formed. For this class of methods the error is introduced by either prescribing the position of elements to be rejected (Manteuffel, 1980) or by discarding those elements in the factor which are smaller than specified tolerance (Axelsson, 1983). This rejection process often leads to an unstable factorization that may result in a nonpositive definite preconditioner. Several remedies have been proposed including modification of factorization by making it more diagonally dominant (Manteuffel, 1980) or by correcting diagonal elements in the factorization process (Axelsson, 1983).

Our experience with multigrid-like methods suggests that the simplest version of Incomplete Cholesky Factorization, which preserves the sparsity pattern of the source stiffness matrix and ensures its stability by means of diagonal scaling, is the most suitable smoothing procedure. Heavier MIC-based smoothers, which allow partial fill-ins suffer from duplication of computational effort in the sense that they are acting on the same lower frequency modes of error which can be adequately captured on the auxiliary coarse mesh

## PERFORMANCE STUDIES

The performance comparisons between the FEOS, PCG with Modified Incomplete Cholesky (MIC) preconditioner and NASA Langley sparse direct solvers were carried out on the SPARC 10 workstation. The numerical results are summarized in Table 1. The convergence criterion for the FEOS and PCG solvers was selected as  $1.0e-8$  in the relative residual norm. Note that the sparse direct solver outperformed the envelope-type solver by orders of magnitude for the problems considered, and therefore the envelope-type solver's results were not included in the Table. Our numerical experimentation agenda included three 3D solid mechanics problems (intersection of two cylinders - model 1, inclusion problem - model 2, bracket problem - model 3) and two cylindrical shell problems with thickness/span ratio of 1/100 for model 4 and 1/300 for model 5. The finite element mesh for the Model 3 is presented in Figure 1.

# AUTOMATED ANALYSES OF THREE-DIMENSIONAL COMPOSITE UNIT CELLS

R. Collar, R. Wentorf, M. S. Shephard, J. Fish, Y. Qu, K.-L. Shek

Scientific Computation Research Center

Rensselaer Polytechnic Institute

Troy, NY 12180-3590, U.S.A.

## SUMMARY

This paper describes automated tools for the analysis of three-dimensional composite unit cells *via* the finite element method. These tools include an automated matched mesh generation algorithm, a constituent mesh volume fraction adjustment algorithm, and an iterative solver with efficient handling of the multiple right hand sides necessary for homogenization analyses. The described algorithms are used to examine the effect of the constituent volume fractions on the homogenized material properties. The local stresses within a representative composite weave are also examined.

**KEY WORDS:** automatic mesh generation; finite element; unit cell; volume fraction; woven composite

## 1. INTRODUCTION

Effective design with composite materials requires the ability to predict their behavior. This behavior is partially influenced by the configuration of the constituents and other small scale features such as microcracks and voids. This paper is concerned with general automated methods allowing materials researchers and composite designers to understand



the effects of constituent geometric configurations on the functions which the material must perform (*e.g.* support loads, resist deflection, transfer heat, or reflect radiation).

The large number of complex small-scale interactions in composites makes the complete characterization of the overall behavior of composites for all permutations of manufacturing and operation variables impractical. This has led to the development of multi-scale approaches where overall composite properties are derived from smaller-scale (more detailed) models of the constituents, and the effects of overall loadings are transformed into effects on the constituents. As shown in Figure 1, the small-scale modeling process begins with the definition of constituent phases and their significant features, the constitutive model(s) and associated property parameters of the solid phases, and the boundary conditions needed for the analysis. The constituent geometric features may be given either directly as idealized geometric features, *e.g.* cylindrical fibers, whose size and position are controlled by parameters <sup>1, 2</sup> or by scanned sample data with given discretization, noise processing and interpretation parameters <sup>3</sup>. The constitutive model is chosen based upon the material constituents, the environment, loading and expected lifetime and the tested property parameters obtained. The boundary conditions depend on the formulation of the subsequent analysis.

After a representative model has been developed, an analytical or numerical solution technique is employed to calculate the average material properties and constituent stress concentrations. These approaches include analytical methods based on elasticity theory for classical shapes (ellipsoids or circular fibers) included in infinite media. Such methods are the Mori-Tanaka method <sup>4</sup>, which entails a closed form solution, the Self

Consistent method <sup>5</sup>, which entails numerical root finding, differential schemes <sup>6</sup>, which entail solving ordinary differential equations, composite moduli bounding methods <sup>7</sup>, and methods based on transformation strains <sup>8</sup>. These methods are characterized by quick solution times, do not require complicated model generating procedures, and require only material design parameters such as volume fractions and linear elastic moduli as input. However, they are limited to specific inclusion geometries.

Numerical methods for solving unit cell problems are applicable to general constituent geometries, and may be utilized wherever periodicity assumptions are valid (*i.e.* in portions of the large-scale problem domain which are not near boundaries or regions of high stress gradients). In regions of the large-scale problem domain where assumptions about the periodicity of the solution are not valid, localized approaches such as multigrid techniques <sup>9</sup> can be utilized. In areas of the large-scale model where periodicity assumptions are valid the homogenization technique allows for great flexibility in the choice of the included small-scale features, but at the expense of complicated model building and meshing procedures and more computationally intensive solutions. The generation of valid finite element meshes <sup>10, 11</sup> within the problem domain is critical to the success of these analyses. The topological and geometrical complexity of three-dimensional woven composite unit cells, and the need to analyze multiple unit cell models to optimize microstructure for a given application make the ability to generate meshes without user intervention a practical necessity. The difficulties inherent in generating three dimensional finite element meshes of geometrically complex domains may be greatly simplified by employing digital image based finite element techniques, as done

by Hollister and Kikuchi <sup>3</sup>. This method has been shown to provide good results for the homogenization analyses they were performing, but the poor geometric representation of material interfaces does not directly permit reliable computation of local stresses near constituent boundaries. In reference <sup>12</sup> Dasgupta *et. al.* determine the thermal and thermo-mechanical properties of a woven composite using discretizations which provide a smoother representation of constituent boundaries. However, meshes and results are shown for only a plain weave, and their modeling and discretization algorithms do not appear to be applicable to more complicated weave patterns. The unit cell model may also be used to determine the local stresses in the woven composite, as shown by Whitcomb *et. al.* <sup>13</sup> in two dimensions.

The large number of equations resulting from the numerical modeling of three-dimensional unit cells requires an efficient solution technique. The practical value of detailed unit cell representations in the design process is very limited if the computational cycle for analyzing a single microstructure entails more than a couple of hours. Application of direct equation solution methods, including state-of-the-art multifrontal solvers, is inappropriate due to the very dense structure of the stiffness matrix. However, the use of standard iterative methods is questionable due to poor conditioning caused by strong heterogeneities and anisotropies. Moreover, the need for analyzing unit cell models for multiple forcing functions (6 in classical homogenization, 24 in higher order homogenization theory <sup>14</sup>) further complicates the efficient utilization of iterative methods. In this paper a multilevel solution technique developed in <sup>15, 16</sup> is utilized for solving the linear systems of equations arising from complex microstructures.

This paper describes a set of automated finite element modeling procedures for performing homogenization analyses of woven composite unit cells. Sections 2 through 4 detail the description of the unit cell model, the generation of matched meshes on opposing faces of the unit cell, and a procedure for controlling the unit cell constituent volume fractions. Section 5 describes the solver features aimed at efficiently handling poorly conditioned linear systems subject to multiple right hand sides. Section 6 discusses the calculation of homogenized stiffness parameters, and section 7 discusses the determination of local stress values in the unit cell models. Closing remarks are made in section 8.

## 2. UNIT CELL MODEL DESCRIPTION

The definition of the geometry of the unit cell representing the chosen composite weave geometry is needed as input to the automated unit cell analysis. The overall shape of the unit cell is a rectangular prism. Boundary conditions and other analysis attributes are associated with this basic model. For example, homogenization analysis requires that the displacement fields vary identically over opposing faces of this prism<sup>17</sup>. However, geometric model creation and mesh generation operations must be performed with respect to the geometry of the constituents of the weave structure. This weave structure is complex, and may be comprised of matrix, fiber bundle, and void geometries as shown in Figure 2, and may also contain cracks in the matrix material. Consideration of both the basic unit cell model and the geometric model of the weave geometry components is necessary in the modeling and analysis process. The weave characteristics and analysis attributes of the composite being modeled may be altered to optimize the composite as shown in Figure 3.

The schematic in Figure 3 depicts the inputs and outputs (arcs) for each function (boxes) used to implement the automated homogenization "Solution Technique" of Figure 1. The "Geometric Modeler" (top of Figure 3) provides a non-manifold boundary representation<sup>18</sup> of the composite weave geometry comprising the unit cell. This representation is comprised of both topology, which describes the relationships of the model entities, and geometry, which describes the shape of the model entities.

The "Matched Mesher" function (middle right of Figure 3) uses the geometric model information and constraints dictated by the periodic boundary conditions to automatically create a three-dimensional mesh of the composite weave. A set of "Mesh Copy Operations" is used to create matching surface mesh topology and geometry on opposing faces of the unit cell. The mesh matching requirements are specified *via* the rectangular prism "Unit Cell Template" (middle left of Figure 3), and are independent of the composite weave geometric model. The topology of the composite weave geometric model is associated with the topology of the unit cell template by the "Classify on Unit Cell" function shown in Figure 3. After the mesh has been generated, mesh queries and manipulations are performed *via* the "Generic Mesh Database Operations"<sup>19</sup> indicated on the right side of Figure 3.

The unit cell template is also used to automatically "Identify Moveable Constituent Topology", as indicated in the center of Figure 3. This function determines the topological entities of the given "Target Constituents" in the composite weave model for which the associated mesh may be altered to "Adjust Constituent Mesh Volumes" to the given "Target Volume Fractions" by the subsequent function shown in Figure 3.

The "Material Property" function (lower left of Figure 3) forms the constitutive relations for each constituent in the composite. The necessary constituent material properties are selected from a relational material property database indexed by compound, form, manufacturer, environment, or other factors. Alternatively, the properties are computed from a lower scale analysis of the average properties of micro-constituents. Complete definition of material properties also requires inter-scale transformation geometries to provide local coordinate systems orienting non-isotropic material models. Data from the geometric modeler is used to associate the material properties (and other analysis attributes <sup>20</sup>) with the geometric model topology. Associating these properties with the geometric model makes them independent of the mesh, and the mesh can therefore be altered without requiring their respecification.

The "Kinematic B.C. Attributes" function (lower right in Figure 3) specifies the appropriate boundary conditions for the homogenization analysis. These attributes and the constitutive relations are associated with the correct finite element mesh entities and formatted as necessary for the finite element solver by the "Associate and Format" function shown at the lower center of Figure 3. The resulting system of equations is provided to the finite element solver ("FE Solver" at the bottom of Figure 3), and the resulting solution data is supplied to appropriate post processing routines.

### 3. MATCHED MESH GENERATION

Since the homogenization modeling is performed *via* the finite element method, the necessary periodic boundary conditions are specified to the equation solver in terms of nodal displacement requirements (multi-point constraints). Since the displacement

solution field is not constant over a cell face, the displacement of a given node, referred to as the subordinate node, on one face of the unit cell is defined as a function of the displacements of specific nodes, referred to as control nodes, on the opposing unit cell face. That is

$$\underline{u}_i = \sum_{j=1}^{N_{con}} a_j \underline{u}_j \quad (1)$$

where  $\underline{u}_i$  denotes the displacements of the  $i^{th}$  subordinate node,  $\underline{u}_j$  denotes the displacements of the  $j^{th}$  control node,  $a_j$  are weighting values, and  $N_{con}$  is the number of control nodes associated with the current subordinate node. The displacement function for a given node is written in terms of the shape functions of the element face which contains the projection of the given node on the opposing unit cell face, as shown in Figure 4. This approach requires an expensive search process to determine within which element faces the projected node lies. The projected point must also be located in the parametric  $(\xi_1, \xi_2, \xi_3)$  space of the element face to express the displacement of the subordinate node in terms of the control nodes. The complexity of this calculation is increased if higher order polynomial element geometry interpolations are utilized.

Specification of the periodic boundary conditions is substantially simplified if the finite element nodes on opposing unit cell faces match. In this case the periodic boundary condition for a given subordinate node reduces to

$$\underline{u}_i = \underline{u}_j \quad (2)$$

where  $\underline{u}_j$  is the displacement of the sole control node. With *a priori* knowledge of the correspondence between nodes on opposing faces of the unit cell, no searching is

required and it is not necessary to locate a projected point in real space within the parametric space of an element face.

Matched meshes are generated by first discretizing the weave geometric model outer boundary entities which are defined as "control" entities, and then copying the meshes to the matching "subordinate" weave geometric model entities. In order to generate a matched mesh of the weave geometric model, it is therefore necessary to identify the control-subordinate relationships of the weave geometric model outer boundary topological entities. For convenience, the outer boundary of the weave geometric model is denoted as  $\partial M$ . The control-subordinate relationships are determined by associating the topological entities of  $\partial M$  with the predetermined control and subordinate topology of the unit cell template.

One unit cell template face of each opposing pair of faces is specified as the control face, and the other is specified as the subordinate face. One of the three such pairs of faces is indicated on the unit cell template shown in Figure 5(a). Periodicity in each direction normal to the faces of the unit cell requires that parallel edges of the box-shaped unit cell template undergo the same variations in displacement and must have identical meshes. One unit cell template edge in each group of four parallel edges is specified as the control edge, and the other three are designated as subordinate edges. One of the three such control-subordinate edge groups is shown in Figure 5(a). All eight vertices of the unit cell undergo the same displacement, and (trivially) must have identical meshes.

Each  $\partial M$  face associated with a control face of the unit cell template is identified as a control face, and the matching  $\partial M$  face is identified as a subordinate face, as shown for



a typical pair of weave geometric model faces in Figure 5(b). If a  $\partial M$  edge lies within a control face of the unit cell template, then it has one matching  $\partial M$  edge lying within the opposing subordinate face of the unit cell template. If a  $\partial M$  edge lies on a control edge of the unit cell template, it has three matching edges lying on the parallel subordinate edges of the unit cell template, as shown for one group of  $\partial M$  edges in Figure 5(b). The  $\partial M$  vertices similarly inherit control-subordinate designations.

Generating meshes in a hierarchic manner (*i.e.* meshing vertices first, then edges, faces, and volumes) allows the periodicity requirements to be easily satisfied during the meshing process, since discretizing the weave geometric model face boundaries first ensures that the necessary matching meshes can be generated in their adjacent faces.

The control  $\partial M$  edges are meshed first, as shown in Figure 6(a). As described in reference <sup>21</sup>, the edge meshing is done such that the resulting discrete edges are of approximately the same size as requested by the user. The meshes on the control edges are then copied to the subordinate weave edges. This is done by first creating a new subordinate mesh vertex as shown in Figure 6(b). A new mesh edge is then created and classified on the subordinate weave edge, as shown in Figure 6(c).

The weave faces are then meshed by a surface meshing algorithm which discretizes the model faces in their parametric spaces <sup>21</sup>. The weave face boundary mesh is first copied into the parametric space, as shown for the face with four curved edges in Figure 7(a). The surface mesh is then created using a Delaunay insertion method as illustrated in Figure 7(b). After the surface mesh has been created in the parametric space, it is copied back to the weave face in the real space by obtaining the corresponding  $xyz$  coordinates

for each of the mesh vertex parameter values as shown in Figure 7(b). The matching mesh on the subordinate weave face is created by also copying the temporary mesh to the corresponding subordinate weave face.

The region meshing process is comprised of three steps <sup>22, 23</sup>. In the first step an underlying variable level octree is created to reflect mesh size control information during the region meshing procedure. The octants residing far enough inside the model interior are then meshed using templates. Finally, a face removal procedure is used to connect the surface triangulation to the interior elements.

#### 4. CONTROL OF CONSTITUENT VOLUME FRACTIONS

The efficiency of the analysis process is increased by using the fewest number of degrees of freedom which can achieve the desired accuracy for the requested parameters. In finite element analyses the solution accuracy is affected by both discretization error and geometric approximation error. Discretization error is caused by the projection of the solution field into a finite dimensional space. If this error is dominant, then the discretization must be suitably refined to improve solution accuracy.

Geometric approximation error is caused by the piecewise approximation of curved model geometry. The presence of curved geometries in composite microstructures is illustrated by the cross-sectional view of a planar weave composite shown in Figure 8. The matrix and fiber bundle geometries are clearly visible in this image, as are the individual fibers comprising the fiber bundles. The weave geometric models presented in this paper consist of fiber bundle and matrix constituents only. The smaller-scale modeling of the fibers within the bundles is done *via* the Mori-Tanaka method. Since the

fiber bundles are convex in cross-section and are curved to form the weave, geometric approximation creates errors in the constituent volume fractions calculated from the finite element mesh. The mesh constituent volume fractions,  $C_c^{FE}$ , are defined as

$$C_c^{FE} = \frac{V_{cons}^{FE}}{V_{cell}} \quad (3)$$

where  $V_{cons}^{FE}$  is the volume of the elements classified inside the constituent regions of the geometric model, and  $V_{cell}$  is the total volume of the unit cell. The errors in the mesh volume fractions can be sizeable, as illustrated by the circular geometric model of radius  $r$  in Figure 9(a). The circle is discretized such that there are four finite element mesh edges of equal length around the circumference as shown in Figure 9(b), and each edge is of length  $\sqrt{2}r$ . The resulting mesh area is  $2r^2$ , and the “lost” area not contained within the mesh is  $\pi r^2 - 2r^2$ , as indicated by the shaded portions of Figure 9(b). The area error of the mesh is therefore  $-36\%$ .

In homogenization analyses, the results presented here indicate that the  $C_c^{FE}$  values influence the evaluation of the homogenized material parameters more strongly than does the discretization error. The  $C_c^{FE}$  errors must therefore be reduced to improve the analysis accuracy. There are several methods by which these errors may be reduced. The simplest method consists of refining the mesh to improve the approximation of the model geometry. This process dramatically increases the number of degrees of freedom in the domain, as illustrated by the meshes of a base one planar weave geometric model shown in Figure 10. Only the mesh faces classified on the interior fiber bundle surfaces are shown in these figures. The mesh in Figure 10(a) contains 21,850 elements and 4,608 nodes. The mesh fiber bundle volume fraction,  $C_b^{FE}$ , of this mesh is 0.2527, which is in

error by -19.4% when compared to the geometric model fiber bundle volume fraction of 0.3137. The mesh in Figure 10(b) was created through uniform refinement and contains 154,020 elements and 28,858 nodes. The fiber bundle volume fraction is 0.298761, which is in error by -4.8%. The approximation of the fiber bundle volume fraction by the finite element mesh improved, but still underestimates the fiber bundle volume fraction of the geometric model, and the number of degrees of freedom in the domain increased by a factor of greater than 6. The memory requirements and large increases in solution time for the highly refined meshes needed to adequately approximate the fiber bundle volume fraction make this an expensive method.

Another approach for reducing the errors in  $C_c^{FE}$  values entails making adjustments to the geometric model such that the constituent volume fractions of the geometric model are higher than the constituent volume fractions of the actual composite material. The constituent volume fractions of the finite element mesh generated within this model then more closely approximate the constituent volume fractions of the composite material. This method requires iterations of the model construction and mesh generation processes to reduce the  $C_c^{FE}$  errors to a given level. Further, since  $C_c^{FE}$  values are a function of discretization size, meshes of different degrees of refinement require the construction of different geometric models to obtain the same  $C_c^{FE}$  values.

The chosen method for reducing the  $C_c^{FE}$  errors involves the modification of an existing mesh. This method begins with an initial mesh which is valid and of acceptable element shape quality, and relocates the mesh vertices classified on the surfaces of the constituents under consideration to correct  $C_c^{FE}$  values of those constituents. The mesh

vertices are relocated in a manner such that the validity and quality of the mesh is maintained. In the current implementation, the quality of the mesh is measured by the largest dihedral angle <sup>24</sup>. Although this  $C_c^{FE}$  adjustment method is an iterative procedure, it does not require the creation of a new finite element mesh for each iterative step. Instead, the same mesh topology is used throughout the process with changes being made only to the locations of specific mesh vertices.

The values of the desired mesh bundle volume fraction,  $\overline{C}_b$ , and the bundle volume fraction of the existing mesh,  $C_b^{FE}$ , are utilized to determine how the mesh should be altered. Since the area  $A$  of an ellipse is given by <sup>25</sup>

$$A = \int r(\theta)^2 d\theta \quad (4)$$

where  $r$  is the distance from the bundle centerline to a point on the bundle surface and  $\theta$  is the angular measure around the ellipse, the volume of a given fiber bundle is proportional to the square of the radius of the elliptical bundle cross-section

$$V_b \propto r^2(\theta, s) \quad (5)$$

where  $V_b$  is the volume of the bundle, and  $s$  is a parametric measure along the bundle centerline. Using equation (5), the new bundle radius  $R$  required to achieve the desired fiber bundle volume  $\overline{V}_b$  is expressed as

$$R(\theta, s) \propto \sqrt{\overline{V}_b} \quad (6)$$

The new bundle radius  $R$  is therefore calculated as a function of the current bundle radius

$$R(\theta, s) = \sqrt{\frac{\overline{V}_b}{V_b}} r(\theta, s) \quad (7)$$

If all of the fiber bundles in the geometric model are of the same cross-sectional geometry, equation (7) may be expressed in terms of the volume fraction measures  $\overline{C}_b$  and  $C_b^{FE}$

$$R(\theta, s) = \Phi r(\theta, s) \quad (8)$$

where  $\Phi = \sqrt{\overline{C}_b / C_b^{FE}}$  is the bundle volume adjustment factor.

The new position of each mesh vertex on the bundle surfaces is calculated as a function of the bundle volume adjustment factor,  $\Phi$ , as illustrated for a typical ellipsoidal bundle cross-section in Figure 11. The current positions  $\underline{x}_i$  of the vertices in the inscribed surface discretization of the bundle cross-section are located distances  $r_i$  from the center of the bundle cross-section, as shown in Figure 11(a). If the bundle volume adjustment factor is greater than one, each of the mesh vertices is located radially outward from its current position to its new location  $\underline{X}_i$  at a distance  $R_i$  from the bundle center, as shown in Figure 11(b). The coordinates to which the vertex is relocated are therefore calculated as

$$\underline{X} = \underline{x} + (\Phi - 1)\underline{r} \quad (9)$$

where  $\underline{r}$  denotes the vector from the bundle center to the current location of the vertex. Scaling the bundle cross-section by  $\Phi$  in this manner maintains the original shape of the bundle cross-section, as can be seen by examining the aspect ratios of the meshes in Figure 11. The aspect ratio  $\alpha_I$  of the original discretization is calculated as

$$\alpha_I = \frac{r_1}{r_2 \cos \theta_2} \quad (10)$$

and the aspect ratio  $\alpha_{II}$  of the adjusted discretization is calculated as

$$\alpha_{II} = \frac{R_1}{R_2 \cos \theta_2} \quad (11)$$

Substitution of equation (8) in equation (11) results in

$$\alpha_{II} = \frac{r_1}{r_2 \cos \theta_2} \quad (12)$$

After moving a given vertex to the new position determined from equation (9), the validity and quality of the mesh is evaluated. If any of the dihedral angles affected by the vertex movement exceed the largest dihedral angle in the original mesh, a new vertex position is determined by bisecting the distance the vertex was moved and again checking the quality of the mesh. The vertex relocation procedure is repeated until a location is found for which the mesh quality does not degrade. The vertex is returned to its original location if after five distance bisections no location can be found for which the quality of the mesh does not degrade. This process permits the bundle surface mesh to be altered anisotropically if the movement of mesh vertices is constrained in some manner. Such constraints are caused by the proximity of geometric model entities, or by the topology and geometry of the mesh surrounding the fiber bundle surface.

After the mesh vertices on the bundle surfaces have been moved to their new positions, a constrained Laplacian smoothing<sup>26</sup>, utilizing a specific element shape parameter<sup>27</sup>, is employed to improve the shapes of the altered elements. The surface and edge smoothing techniques usually employed in automatic mesh generation algorithms would pull the vertices classified on the bundle surfaces back to the surfaces of the geometric model, thereby restoring the original constituent mesh volume fractions. Therefore, in the current implementation only the mesh vertices classified on the interior of the geometric model regions are subjected to smoothing operations.

The following example demonstrates the ability of the algorithm to adjust  $C_b^{FE}$  to a prescribed value. The geometric model for this example was created with the Shapes<sup>TM</sup> <sup>28</sup> geometric modeler. The example consists of a unit cell containing a single cylindrical fiber bundle. The unit cell is of height  $h = 2$ , width  $w = 2$ , and length  $l = 5$ . The fiber bundle is of radius  $r = 0.5$ . The exact bundle volume fraction,  $\overline{C}_b$ , is 0.19635. The initial mesh of the unit cell model is shown in Figure 12. The exterior of the mesh is shown in Figure 12(a), and the interior mesh faces on the surface of the fiber bundle are shown in Figure 12(b). The  $C_b^{FE}$  of this mesh is 0.13421, which represents a -31.6% error. The mesh volume fraction correction algorithm was then used to adjust the mesh to the correct bundle volume fraction. The exterior faces of the adjusted mesh are shown in Figure 12(c), and the interior mesh faces classified on the surface of the bundle are shown in Figure 12(d). In this case the topology and geometry of the volume mesh outside of the bundle region prevented some mesh vertices from moving to the full extent of the relocation prescribed by the volume fraction adjustment algorithm without degrading the mesh quality. Three iterations of the mesh volume fraction correction procedure were required to raise the bundle volume fraction to within 1% of  $\overline{C}_b$ . The value of the mesh volume fraction at the end of each of the three iterations is listed in Table 1. Section 6 contains examples of composite weave geometries where similar improvements were obtained.

## 5. ITERATIVE SOLUTION OF UNIT CELL PROBLEMS

The Generalized Aggregation Method (GAM) is utilized for solving the unit cell problems. These problems are characterized by a large system of linear equations with



Table 1. Mesh bundle volume fraction and percent error at each iteration of the volume fraction correction of the single fiber bundle example.

Mesh Move Iteration	Mesh Bundle Volume Fraction (desired = 0.19635)	Mesh Bundle Volume Fraction Error (%)
initial mesh	0.13421	-31.6
1	0.18209	-7.3
2	0.19369	-1.3
3	0.19579	-0.3

multiple right hand sides and multi-point constraints, and may be written as

$$\underline{Q}^T \hat{\underline{K}} \underline{Q} \underline{u}_m = \underline{Q}^T \underline{f} \quad (13)$$

where  $\hat{\underline{K}}$  is the unit cell stiffness matrix,  $\underline{f}$  is a forcing matrix given by

$$\underline{f} = - \int_{\theta} \underline{B}^T \underline{D} d\theta \quad (14)$$

$\underline{B}$  is a strain-displacement matrix,  $\theta$  is the unit cell domain,  $\underline{D}$  is the small-scale constitutive tensor, and  $\underline{Q}$  is the multi-point constraint matrix relating the control degrees of freedom  $\underline{u}_c$  to the set of all degrees of freedom  $\underline{u}$  as

$$\underline{u} = \underline{Q} \underline{u}_m \quad (15)$$

Further details are contained in <sup>15</sup>.

## 5.1 SOLVER DESCRIPTION

GAM is a multilevel solution scheme based on the multigrid philosophy, which captures the lower frequency response by solving an auxiliary coarse model, whereas the higher frequency response is resolved by smoothing on the source grid. As such GAM possesses an optimal rate of convergence by which the CPU time grows linearly

with the problem size. Unlike the multigrid method GAM does not require construction of auxiliary grids. Furthermore, because of the adaptive control of the structure of the preconditioner GAM is insensitive to problem conditioning in terms of number of iterations. In GAM the auxiliary coarse model is directly constructed from the source grid by decomposing the whole set of nodes into non-intersecting blocks to be referred to as aggregates, and then for each aggregate assigning a reduced number of degrees of freedom. By doing so one reduces the dimensionality of the source problem, while maintaining the compatibility of the solution. Theorems quantifying the optimal approximation properties aimed at ensuring that the coarse model will effectively capture the lower frequency response of the source system and at the same time will be sparse and rapidly computed have been described in <sup>15</sup>.

## 5.2 MULTIPLE RIGHT HAND SIDES

A combination of two mechanisms is employed to provide a rapid solution for linear systems of equations (13) with multiple right hand sides:

1. Construction of the preconditioner aimed at reducing the overall cost of the iterative process at the expense of increasing the computational cost of computing the preconditioner;
2. Acceleration of the GAM scheme with the block conjugate gradient method.

### 5.2.1 GAM PRECONDITIONER FOR PROBLEMS WITH MULTIPLE RIGHT HAND SIDES

One of the key aspects of the GAM scheme is a selection of the coarse model cut-off frequency parameter  $\gamma$ , below which all the eigenvectors of the eigenvalue problem

on the aggregate are included within the prolongation operator. In order to make this parameter dimensionless, the eigenvalue problem on each aggregate  $a$  is formulated in the following manner:

$$\underline{K}^a \underline{\phi}^a = \lambda^a \underline{D}^a \underline{\phi}^a \quad (16)$$

where  $\underline{D}^a$  is the diagonal of  $\underline{K}^a$ .

The value of the parameter  $\gamma$  determines the effectiveness of coarse grid correction. In the limit as  $\gamma \rightarrow \max_a \lambda^a$ , the auxiliary problem captures the response of the source system for all frequencies and therefore the two-level procedure converges in a single iteration even without smoothing. On the negative side, for large values of  $\gamma$ , the eigenvalue analysis on each aggregate becomes prohibitively expensive and the auxiliary matrix becomes both large and dense. At the other extreme, in the limit as  $\gamma \rightarrow 0$  the prolongation operator contains the rigid body modes of all the aggregates only, and thus the auxiliary problem becomes inefficient for ill-posed problems.

For problems with multiple right hand sides the value of  $\gamma$  should be increased to reduce the number of iterations, and consequently to reduce the overall computational cost.

### 5.2.2 BLOCK CONJUGATE GRADIENT ACCELERATOR

The system of linear equations with  $s$  load cases given in (13) can be expressed in a block structure as

$$\underline{K} \underline{U} = \underline{F} \quad (17)$$

where  $\underline{U} = [\underline{u}_1, \underline{u}_2, \dots, \underline{u}_s]$ ,  $\underline{F} = [\underline{f}_1, \underline{f}_2, \dots, \underline{f}_s]$  and  $\underline{u}_i, \underline{f}_i$  are the  $i^{th}$  load vector and the corresponding solution, respectively. The matrix  $\underline{K} \in \mathbb{R}^{n \times n}$  is the global stiffness matrix which is symmetric, positive definite and sparse.

The forcing functions are orthonormalized using the Gram-Schmidt procedure to obtain  $\overline{\underline{F}} (\underline{F} = \overline{\underline{F}} \underline{H}_m)$  and to ensure that the resulting set of forcing functions is linearly independent

$$\delta_i \overline{\underline{f}}_i^0 = \underline{f}_i^0 - \sum_{j=1}^{i-1} \gamma_j^i \overline{\underline{f}}_j^0 \quad i = 1, \dots, s \quad (18)$$

where

$$\gamma_j^i = (\overline{\underline{f}}_i^0)^T \underline{f}_j^0 \quad (19)$$

and  $\delta_i$  is the set of parameters which normalize  $\underline{f}_i$ . The original problem  $\underline{K} \underline{U} = \underline{F}$  can then be transformed into  $\underline{K} \overline{\underline{U}} = \overline{\underline{F}}$  where  $\underline{F} = \overline{\underline{F}} \underline{H}_m$  and  $\underline{H}_m$  is an upper triangular matrix of the form:

$$\underline{H}_m = \begin{bmatrix} \delta_1 & \gamma_1^2 & \dots & \dots & \gamma_1^s \\ & \delta_2 & & & \vdots \\ & & & & \vdots \\ & 0 & & \delta_{s-1} & \gamma_{s-1}^s \\ & & & & \delta_s \end{bmatrix} \quad (20)$$

The block conjugate gradient acceleration scheme described below utilizes the GAM cycle as a preconditioner. To clarify ideas consider the following energy functional

$$\underline{\Phi}(\underline{U}) = [\Phi_1(\underline{u}_1) \ \Phi_2(\underline{u}_2) \ \dots \ \Phi_s(\underline{u}_s)] \quad (21)$$

where  $\Phi_i(\underline{u}_i) = \frac{1}{2} \underline{u}_i^T \underline{K} \underline{u}_i - \underline{u}_i^T \underline{f}_i$ . The corresponding block residual matrix  $\underline{R}_i \in \mathbb{R}^{n \times s}$  at the  $i^{th}$  step is  $\underline{R}_i = \underline{F} - \underline{K} \underline{U}_i$  and the corresponding solution  $\underline{U}_{i+1} \in \mathbb{R}^{n \times s}$  is defined as

$$\underline{U}_{i+1} = \underline{U}_i + \underline{V}_{i+1} \underline{A}_i \quad (22)$$

where  $\underline{V}_i \in \mathbb{R}^{n \times s}$  spans the subspace of search directions, and  $\underline{A}_i \in \mathbb{R}^{s \times s}$  is the matrix representing the step length determined by the minimization

$$\frac{\partial \Phi(\underline{U}_i + \underline{V}_{i+1} \underline{A}_i)}{\partial \underline{A}_i} = 0 \quad (23)$$

which yields  $\underline{V}_{i+1}^T \underline{R}_{i+1} = 0$ . The subspace  $\underline{V}_{i+1}$  is subsequently constructed by

$$\underline{V}_{i+1} = \underline{Z}_i + \underline{V}_i \underline{B}_i \quad (24)$$

where the parameter matrix  $\underline{B}_i \in \mathbb{R}^{s \times s}$  is determined from the block conjugacy condition  $\underline{V}_{i+1}^T \underline{K} \underline{V}_i = 0$ , and  $\underline{Z}_i$  is the predictor from a single GAM cycle. The complete algorithm is summarized below.

*Step 1: Initiation*

$$\underline{U}_0 = \underline{0} \quad \underline{R}_0 = \underline{F}$$

$$\underline{B}_0 = \underline{0} \quad \underline{Z}_0 = \underline{0}$$

*Step 2: Do  $i=0, 1, \dots$  until all right hand sides converge*

$$\underline{Z}_i = \text{GAM}(\underline{R}_i, \underline{K})$$

$$\left( \underline{R}_{i-1}^T \underline{Z}_{i-1} \right) \underline{B}_i = \underline{R}_i^T \underline{Z}_i$$

$$\underline{V}_{i+1} = \underline{Z}_i + \underline{V}_i \underline{B}_i$$

$$\underline{X}_{i+1} = \underline{K} \underline{V}_{i+1}$$

$$(\underline{V}_{i+1}\underline{X}_{i+1})\underline{A}_i = \underline{R}_i^T \underline{Z}_i$$

$$\underline{\bar{U}}_{i+1} = \underline{\bar{U}}_i + \underline{V}_{i+1}\underline{A}_i$$

$$\underline{R}_i = \underline{R}_i - \underline{X}_{i+1}\underline{A}_i$$

Convergence is checked for each right hand side. If one of the right hand sides converges, it is removed from the iterative process. Once all the right hand sides have converged, the final solution is recovered as

$$\underline{U} = \underline{\bar{U}} \underline{H}_m \quad (25)$$

### 5.3 MULTIPLE POINT CONSTRAINTS

The GAM scheme can deal with multi-point constraints in a conventional way if all the elements containing at least one "subordinate" node form a separate aggregate. Each multi-point constraint can then be represented as follows:

$$\underline{u}_s = \underline{T} \underline{u}_c \quad (26)$$

where  $\underline{u}_s$  are the subordinate" degrees of freedom, and  $\underline{T}$  is a transformation matrix representing the multi-point constraint data:

$$\underline{u} = \begin{bmatrix} \underline{T} \\ \underline{I} \end{bmatrix} \underline{u}_s = \underline{Q} \underline{u}_s \quad (27)$$

## 6. CALCULATION OF HOMOGENIZED STIFFNESS PARAMETERS

The effect of  $C_b^{FE}$  on the homogenized stiffness parameters of a composite material is easily seen in an analysis of a single bundle unit cell. This model consists of a cylindrical fiber of radius  $r = 0.5$  embedded in a block of matrix of length  $l = 2$ , width  $w = 2$ , and height  $h = 2$ . The isotropic matrix material modulus and Poisson's ratio were chosen as 6.89 msi and 0.33, which are representative of Titanium. The isotropic bundle material modulus, shear modulus, and Poisson's ratio were chosen as 37.9 msi, 15.7 msi, and 0.21 which are representative of a silicon carbide fiber.

A series of meshes of increasing levels of uniform refinement was generated, as shown in Figure 13. The coarsest mesh, shown in Figure 13(a), contains 93 vertices and 284 elements. The mesh shown in Figure 13(b) contains 576 vertices and 2,549 elements. The mesh shown in Figure 13(c) contains 4,156 vertices and 21,951 elements. The finest mesh, shown in Figure 13(d), contains 20,615 vertices and 110,638 elements. Homogenization analyses were performed with each of the four meshes, and also with the volume fractions of the four meshes corrected to within  $\pm 0.5\%$  of the correct volume fraction for the geometric model.

The most relevant stiffness parameter for the single bundle model is the parameter corresponding to the axial stiffness of the bundle. For the model under consideration the fiber bundle axis is aligned with the  $z$  direction, making the  $G_{33}$  term of the homogenized material stiffness matrix  $\underline{G}$  of greatest relevance. The values of  $G_{33}$  computed using the various discretizations were compared to  $G_{33}$  computed with the finest mesh adjusted to 0.0% bundle volume fraction error.

Table 2. Mesh bundle volume fraction and homogenized material stiffness differences for the discretizations shown in Figure 13.

Number of Vertices	Mesh Bundle Volume Fraction	Mesh Bundle Volume Fraction Error (%)	$G_{33}$ ( $\times 10^7$ psi)	$G_{33}$ Difference (%)
93	0.14998	-23.61	1.4906	-8.79
93	0.18409	-6.24	1.5976	-2.24
93	0.19263	-1.89	1.6244	-0.6
93	0.19623	-0.06	1.6357	0.09
576	0.18440	-6.09	1.5972	-2.26
576	0.19351	-1.45	1.6257	-0.52
576	0.19630	-0.02	1.6345	0.02
4,156	0.19334	-1.53	1.6248	-0.57
4,156	0.19633	-0.01	1.6342	0.00
20,615	0.19558	-0.39	1.6318	-0.15
20,615	0.19635	0.00	1.6342	0.00

The percent differences between the  $G_{33}$  values and the  $G_{33}$  value of the finest mesh are listed in Table 2. This data may be examined in two manners. The first entails viewing the homogenized axial stiffness parameter differences as a function of the  $C_b^{FE}$  error. The  $C_b^{FE}$  of each mesh was adjusted to match the initial  $C_b^{FE}$  values of the finer discretizations and also to  $\bar{C}_b$ . The change in the value of the axial stiffness parameter for a given mesh corrected to different  $C_b^{FE}$  values shows the effect of improving the geometric approximation only. This data shows that all of the discretizations adjusted to within  $\pm 0.5\%$  of  $\bar{C}_b$  produced nearly the same axial stiffness parameter. In particular, the coarse discretization and the fine discretization produced results which differed by only 0.09%. This result indicates that it is possible to use coarse discretizations and achieve accurate results if the geometric approximation error is controlled. This



shortens the analysis cycle since it is much quicker to generate coarse discretizations and also much quicker to perform the homogenization analysis on the coarse discretization. The CPU time required for the mesh generation and homogenization solution of the coarse discretization was 444 times faster than the time required for the most refined discretization.

Examining the homogenized axial stiffness differences for meshes corrected to within  $\pm 0.5\%$  of the same  $C_b^{FE}$  shows a small change in this parameter with increasing mesh refinement. When all the discretizations were corrected to within  $\pm 0.5\%$  of  $\bar{C}_b$ , changing the number of mesh vertices by two orders of magnitude resulted in only a 0.09% change in the homogenized axial stiffness parameter estimate. In contrast, changing the volume fraction of the coarse discretization by less than 2% resulted in a 0.69% change in the homogenized axial stiffness parameter accuracy, indicating that the analysis of this model is affected more by the geometric approximation error than by the discretization error.

The second example consists of a base two satin weave composite<sup>29</sup>. The parameters used to construct the geometric model of this weave were taken from a series of micrographs of a representative sample of the composite. The design target bundle fraction was 0.55. The matrix is an amorphous glass composed of silicon, oxygen, and carbon. The matrix was modeled as a transversely isotropic material with degraded properties to represent the through-thickness matrix cracks in the as-processed composite. The axial Young's and shear moduli of the matrix are 11.5 msi and 4.0 msi. The transverse Young's and shear moduli are 8.1 msi and 3.3 msi. The Poisson's ratio is 0.26. These values will be compared with specimen test data in future work<sup>30</sup>. The fibers are a

ceramic material. The axial Young's and shear moduli of the fiber bundles are 16.6 msi and 6.55 msi. The transverse Young's and shear moduli of the fiber bundles are 16.2 msi and 6.52 msi. The Poisson's ratio of the bundles is 0.24.

Meshes of varying amounts of uniform refinement were generated within the constructed geometric model. The coarsest mesh, (Figure 14) contains 2,380 vertices and 11,050 elements, the mesh created with one level of refinement (Figure 15) contains 10,475 vertices and 52,509 elements, and the finest mesh (Figure 16) contains 62,436 vertices and 338,253 elements. Meshes of each of the three levels of uniform refinement were also generated with the mesh volume fraction corrected to within  $\pm 0.5\%$  of the target volume fraction of 0.55. The mesh faces classified on the interior fiber bundle surfaces of each of the volume fraction corrected meshes are shown in Figure 17. The number of mesh vertices and mesh volume fraction data of all of the meshes are listed in Table 3.

Homogenization analyses were performed and the in-plane stiffness parameters were examined. For the modeled composite weave the in-plane fiber bundle directions correspond to the  $x$  and  $z$  axes, with the  $y$  axis normal to the plane of the composite. The in-plane material parameters are therefore the values of  $G_{11}$ ,  $G_{33}$ ,  $G_{55}$ , and  $G_{13}$ .

The homogenized stiffness parameters were compared to the values calculated using the finest discretization corrected to  $0.17\% C_b^{FE}$  error. The in-plane normal stiffness parameter data determined from these analyses are shown in Table 3, and the in-plane shear and Poisson effect stiffness parameter data are shown in Table 4. The values for the coarsest and finest discretizations differed by at most  $1.64\%$  when adjusted to within

Table 3. Mesh sizes, mesh bundle volume fractions, and in-plane normal homogenized stiffness parameter values of the discretizations of the base two satin weave geometric model.

Number of Vertices	Mesh Bundle Volume Fraction	Mesh Bundle Volume Fraction Error (%)	$G_{11}$ ( $\times 10^7$ )	$G_{11}$ Difference (%)	$G_{33}$ ( $\times 10^7$ )	$G_{33}$ Difference (%)
2,380	0.3905	-29.00	1.3099	-11.5	1.3085	-11.6
2,380	0.4460	-18.91	1.3651	-6.54	1.3636	-6.60
2,380	0.4593	-16.50	1.3783	-5.64	1.3769	-5.69
2,380	0.5526	0.47	1.4715	0.74	1.4688	0.60
10,475	0.4441	-19.25	1.3582	-7.01	1.3570	-7.05
10,475	0.4594	-16.5	1.3734	-5.97	1.3723	-6.00
10,475	0.5515	0.28	1.4649	0.29	1.4635	0.24
62,436	0.458	-16.7	1.3690	-6.28	1.3677	-6.31
62,436	0.5509	0.17	1.4607	0.0	1.4600	0.0

Table 4. Mesh sizes, mesh bundle volume fraction errors, and in-plane shear and Poisson effect homogenized stiffness parameter values of the discretizations of the base two satin weave geometric model.

Number of Vertices	Mesh Bundle Volume Fraction Error (%)	$G_{55}$ ( $\times 10^6$ )	$G_{55}$ Difference (%)	$G_{13}$ ( $\times 10^6$ )	$G_{13}$ Difference (%)
2,380	-29.00	4.5536	-8.05	3.7119	-12.94
2,380	-18.91	4.7007	-5.07	3.9193	-8.08
2,380	-16.50	4.7387	-4.31	3.9694	-6.91
2,380	0.47	5.0334	1.64	4.3233	1.39
10,475	-19.25	4.6717	-5.66	3.8825	-8.94
10,475	-16.5	4.7115	-4.86	3.9399	-7.60
10,475	0.28	4.9753	0.47	4.2853	0.50
62,436	-16.7	4.6904	-5.28	3.9182	-8.11
62,436	0.17	4.9520	0.00	4.2639	0.00

$\pm 0.5\%$  of the correct bundle volume fraction.

There is also little change in the stiffness parameters with large changes in the number of degrees of freedom in the model, indicating that the homogenization analysis is affected more by the amount of geometric approximation error than by the amount of the discretization error.

The results of this example again show that it is possible to achieve accurate homogenization results with coarse finite element discretizations if the  $C_c^{FE}$  values are adjusted to the correct values. The total CPU mesh generation and solving time required for the coarsest discretization was 44 times faster than the time required for the finest discretization.

## 7. DETERMINATION OF LOCAL STRESSES

A thorough analysis of a given composite weave must also include the calculation of the local stresses in the weave which result from loadings on the larger-scale homogenized material. These local values aid in the design of composite microstructure by indicating areas of high stress which may lead to failure of the composite. The meshes generated by the procedures described in this paper conform to the model geometry, and are therefore capable of producing reliable local stress data.

The local unit cell stresses corresponding to the strain field  $\hat{\underline{\epsilon}}$  existing at a given point in the larger-scale model are given by

$$\underline{\sigma}_i = \underline{A}_i \hat{\underline{\epsilon}} \quad (28)$$

where  $\underline{\sigma}_i$  are the stresses at the  $i^{th}$  integration point in the unit cell model, and  $\underline{A}_i$  is the stress concentration matrix relating the strain field at a given point in the macroscopic model to the stresses at the  $i^{th}$  integration point in the unit cell model <sup>31</sup>.

The following example of local stress calculation uses the base two satin weave composite unit cell of section 6. The homogenized material stiffness parameters were used to calculate  $\underline{\hat{\epsilon}}$  corresponding to a 100 ksi uniaxial stress in the x-direction. This direction corresponds to the warp direction of the unit cell.

The results of applying equation (28) to every integration point in the coarse mesh adjusted to 0.47%  $C_b^{FE}$  error (shown in Figure 17(a)) are shown in Figure 18. This figure represents an exploded view of the unit cell, with the groups of elements comprising the matrix (at the left), warp bundles (at the top), and weft bundles (at the bottom) separated for clarity. Linear elements were used for the homogenization analysis of this example, and the elements in this figure are colored according to the values of the maximum principal stress calculated at their single integration points. The correspondence between the colors and the stress values is shown by the color bar at the top of Figure 18.

The stresses in the warp bundles show concentration “bands” near the crossovers where the warp and weft bundles are woven together. This is due to the load carrying capacity of bundles being reduced when their axes do not align with the loading direction, and the load therefore being transferred to the neighboring bundles which are aligned in the loading direction. The matrix material shows bands of stress values due to additional reinforcement by the transverse stiffness of the weft bundles. The peak stress in the warp bundles is 148.0 ksi.

The medium mesh (Figure 17(b)) adjusted to 0.28%  $C_b^{FE}$  error was also analyzed to examine the effect on the peak stress. The local stresses calculated with the medium mesh (Figure 19) exhibit the same characteristics as the coarse mesh. The peak stress in the warp bundles is 160 ksi.

## 8. CONCLUSIONS

This paper presented a system for the efficient three-dimensional homogenization analyses of complex composite materials. These capabilities include a matched meshing algorithm which simplifies the specification of periodic boundary conditions, and an iterative solver algorithm capable of efficiently handling the multiple right hand sides required for homogenization analyses. An algorithm was also developed to correct the mesh volume fraction, and the effect of the mesh volume fraction error on the values of homogenized material stiffness parameters was shown to be greater than that of the discretization error. Acceptable homogenization results may therefore be obtained with coarse discretizations if the mesh volume fraction is controlled. The reliable calculation of local stresses permitted by the mesh conforming to the model geometry was also demonstrated.

## 9. ACKNOWLEDGMENTS

The support of ARPA/ONR under grant number N00014-92J-1779, and of the Allison Advanced Development Company under the LC<sup>3</sup> project is gratefully acknowledged.

## 10. REFERENCES

1. R. Wentorf, M. S. Shephard, G. J. Dvorak, J. Fish, M. W. Beall, R. Collar, and K.-L. Shek, "Software framework for mechanism-based design of composite structures," in *Proceedings of the 21st Annual Cocoa Beach Conference on Composite Advanced Ceramics, Materials and Structures*, 1997. to appear.
2. J. Shah, "Conceptual development of form features and feature modellers," *Research in Engineering Design*, pp. 93–108, 1991.
3. S. J. Hollister and N. Kikuchi, "Homogenization theory and digital imaging: A basis for studying the mechanics and design principles of bone tissue," *Biotechnology and Bioengineering*, vol. 43, pp. 586–596, 1994.
4. T. Mori and K. Tanaka, "Average stress in matrix and average elastic energy of materials with misfitting inclusions," *Acta Metallurgica*, vol. 21, pp. 571–574, 1973.
5. R. Hill, "A self-consistent mechanics of composite materials," *Journal of the Mechanics and Physics of Solids*, vol. 13, p. 213, 1965.
6. A. N. Norris, "A differential scheme for the effective moduli of composites," *Mechanics of Materials*, vol. 4, 1985.
7. E. Hashin and W. B. Rosen, "The elastic moduli of fiber-reinforced materials," *Journal of Applied Mechanics, Transactions of the ASME*, pp. 223–232, 1964.
8. G. J. Dvorak and Y. Benveniste, "On transformation strains and uniform fields in multiphase elastic media," *Proc. R. Soc. Lond.*, vol. 437, p. 291, 1992.
9. J. Fish and V. Belsky, "Multi-grid method for periodic heterogeneous media .2.

- multiscale modeling and quality control in multidimensional case," *Computer Methods in Applied Mechanics and Engineering*, vol. 126, pp. 17–38, 1995.
10. M. S. Shephard and M. K. Georges, "Reliability of automatic 3-D mesh generation," *Comp. Meth. Appl. Mech. Engng.*, vol. 101, pp. 443–462, 1992.
  11. W. J. Schroeder, *Geometric Triangulations: with Application to Fully Automatic 3D Mesh Generation*. PhD thesis, Rensselaer Polytechnic Institute, Scientific Computation Research Center, RPI, Troy, NY 12180-3590, May 1991. SCOREC Report # 9-1991.
  12. A. Dasgupta, R. K. Agarwal, and S. M. Bhandarkar, "Three-dimensional modeling of woven-fabric composites for effective thermo-mechanical and thermal properties," *Composites Science and Technology*, vol. 56, pp. 209–223, 1996.
  13. J. Whitcomb, K. Srirengan, and C. Chapman, "Evaluation of homogenization for global/local stress analysis of textile composites," *Composite Structures*, vol. 31, pp. 137–149, 1995.
  14. J. Fish, P. Nayak, and M. H. Holmes, "Microscale reduction error indicators and estimators for a periodic heterogeneous medium," *Computational Mechanics: The International Journal*, vol. 14, pp. 1–16, 1994.
  15. J. Fish and V. Belsky, "Generalized aggregation multilevel solver," *Submitted to: Int. J. Numer. Meth. Engng.*, 1997.
  16. J. Fish and A. Suvorov, "Automated adaptive multilevel solver," *Submitted to: Comp. Meth. Appl. Mech. Engng.*, 1997.



17. B. Hassani, "A direct method to derive the boundary conditions of the homogenization equation for symmetric cells," *Communications in Numerical Methods in Engineering*, vol. 12, pp. 185–196, 1996.
18. M. Mäntylä, *Introduction to Solid Modeling*. Rockville, Maryland: Computer Science Press, 1988.
19. M. W. Beall and M. S. Shephard, "Mesh data structures for advanced finite element computations," Tech. Rep. 19-1995, Scientific Computation Research Center, Rensselaer Polytechnic Institute, Troy, NY 12180-3590, 1995. submitted to Int. J. Num. Meth. Engng.
20. M. S. Shephard, "The specification of physical attribute information for engineering analysis," *Engineering with Computers*, vol. 4, pp. 145–155, 1988.
21. H. L. de Cougny and M. S. Shephard, "Surface meshing using vertex insertion," in *Proceedings of the 5th International Meshing Roundtable*, 1996.
22. H. L. de Cougny, M. S. Shephard, and C. Ozturan, "Parallel three-dimensional mesh generation on distributed memory MIMD computers," *Engineering with Computers*, vol. 12, no. 2, pp. 94–106, 1996.
23. M. S. Shephard, J. E. Flaherty, H. L. de Cougny, C. Ozturan, C. L. Bottasso, and M. W. Beall, "Parallel automated adaptive procedures for unstructured meshes," in *Parallel Computing in CFD*, vol. R-807, pp. 6.1–6.49, AGARD, Neuilly-Sur-Seine, France, 1995.
24. M. Krizek, "On the maximal angle condition for linear tetrahedral elements," *SIAM J. Numer. Anal.*, vol. 29, pp. 513–520, 1992.

25. E. W. Swokowski, *Calculus with Analytic Geometry*. Prindle, Weber and Schmidt, 1979.
26. D. A. Field, "Laplacian smoothing and Delaunay triangulations," *Comm. Appl. Num. Meth.*, vol. 4, pp. 709-712, 1987.
27. H. L. de Cougny, M. S. Shephard, and M. K. Georges, "Explicit node point smoothing within the Finite Octree mesh generator," Tech. Rep. 10-1990, Scientific Computation Research Center, Rensselaer Polytechnic Institute, Troy, NY 12180-3590, 1990.
28. XOX Corporation, Two Appletree Square, Suite 334, Minneapolis, Minnesota 55425, *SHAPES Reference Manual, Release 2.0.8*, July 20, 1993.
29. N. Pan, "Analysis of woven fabric strengths: Prediction of fabric strength under uniaxial and biaxial extensions," *Composites Science and Technology*, vol. 56, pp. 311-327, 1996.
30. R. Wentorf, R. Collar, J. Fish, and M. S. Shephard, "Influences of some constituent features on the homogenized mechanical properties of composite materials," *In Preparation*, 1997. Scientific Computation Research Center, Rensselaer Polytechnic Institute, Troy, NY.
31. J. Fish and A. Wagiman, "Multiscale finite element method for a locally nonperiodic heterogeneous medium," *Computational Mechanics*, vol. 12, pp. 164-180, 1993.

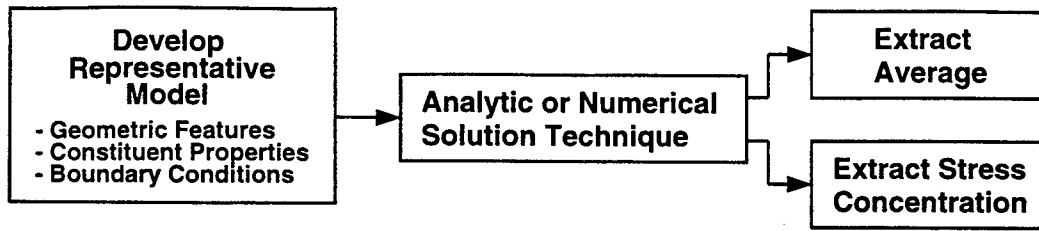


Figure 1. Schematic of small-scale composite thermo-mechanical modeling process.

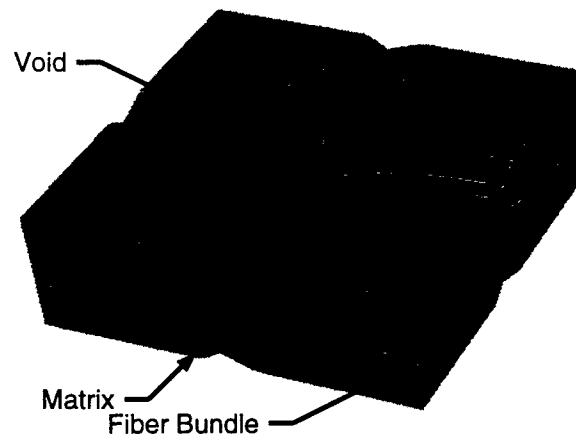


Figure 2. Typical composite weave with fiber bundles, matrix, and void geometries.

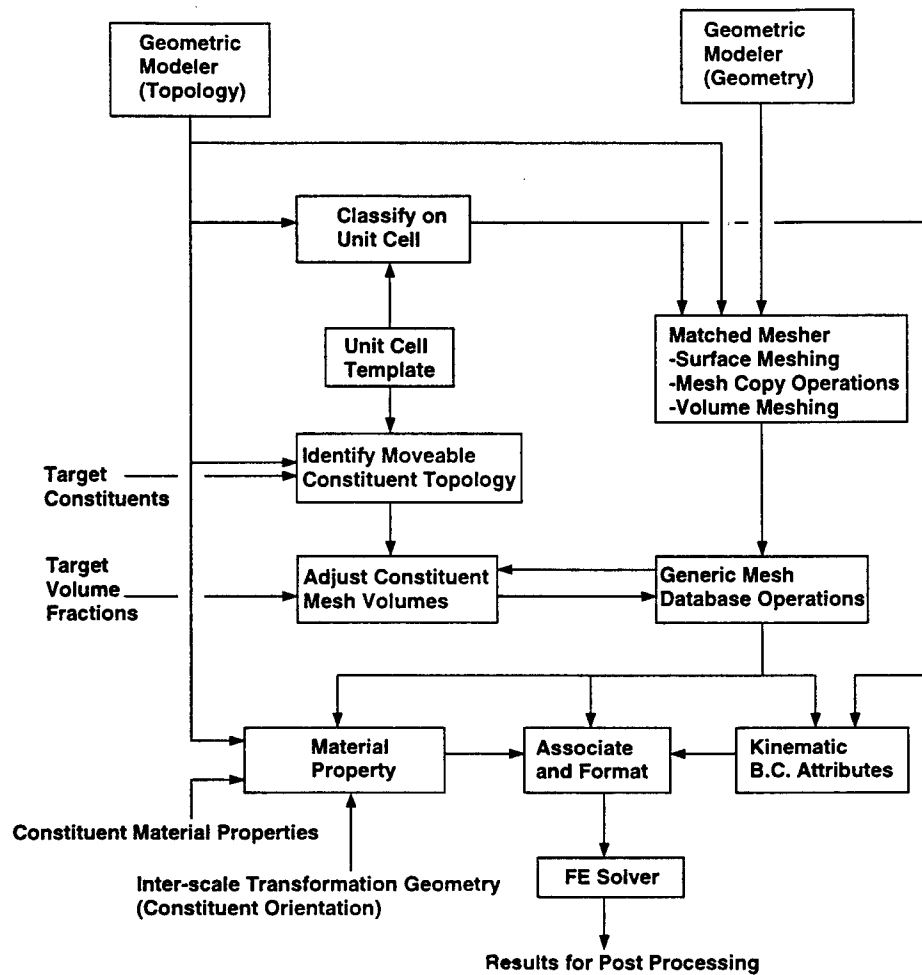


Figure 3. Details present in the automated finite element based homogenization analysis of composite unit cells.

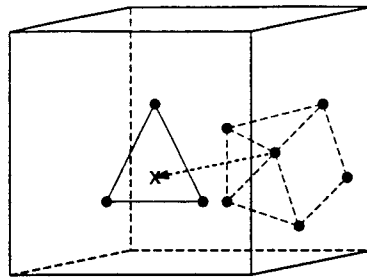


Figure 4. Projection of node from back face of unit a cell to an element face on the opposing unit cell face.

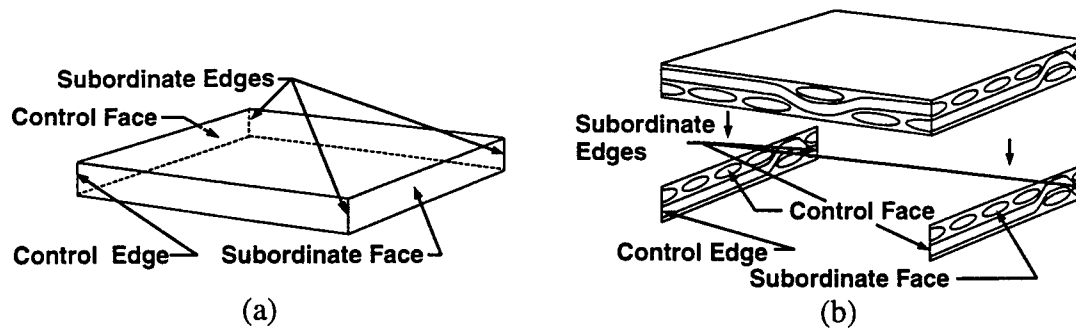


Figure 5. Determining control-subordinate relationships for the weave geometric model. (a) Typical relationships on the unit cell template. (b) Corresponding relationships on the weave geometric model.

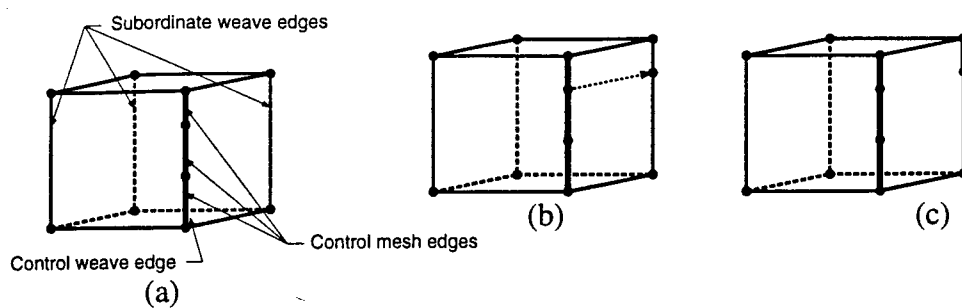


Figure 6. Edge meshing procedure. (a)Control edge is meshed. (b)Mesh vertices from control edge are copied to subordinate weave edge. (c)New mesh edge is created on subordinate weave edge.



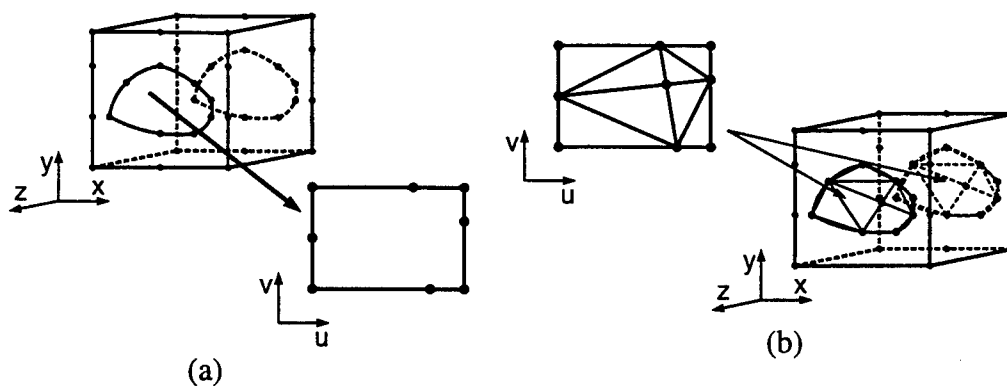


Figure 7. Weave Face meshing. (a) Boundary mesh is copied into the parametric space. (b) Delaunay insertion method is used in the parametric space, and face mesh is copied back into the real space.



Figure 8. Micrograph of a planar weave composite.

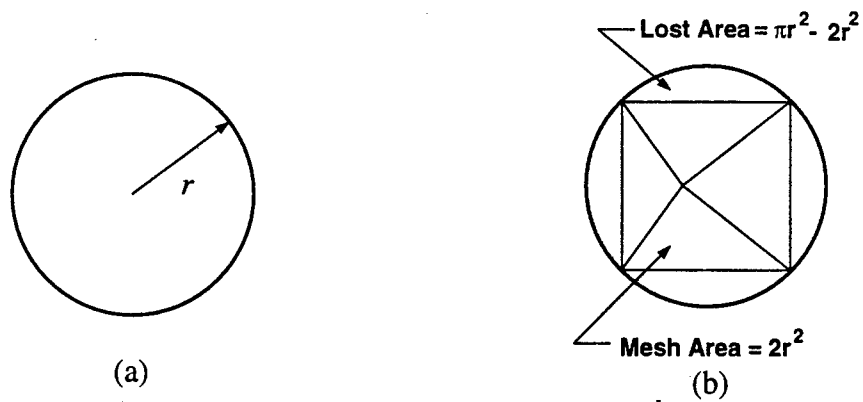


Figure 9. Mesh volume error example. (a)Circular geometric model of radius  $r$ . (b)Inscribed mesh.

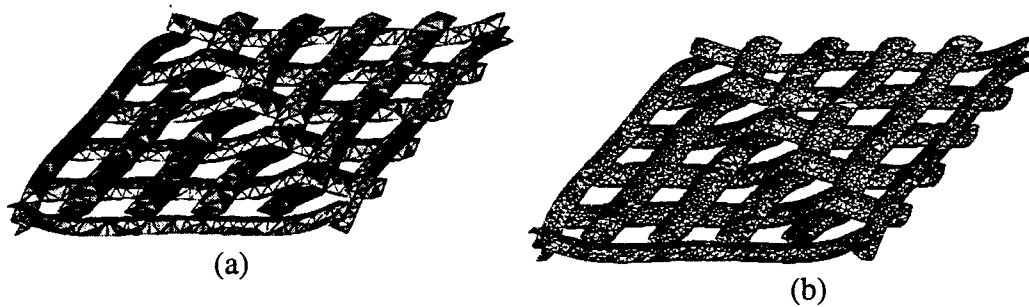


Figure 10. Solid mesh of base one planar weave model. Only mesh faces on interior bundle surfaces are shown. (a)Coarse mesh of 21,850 elements. (b)Fine mesh of 154,020 elements.

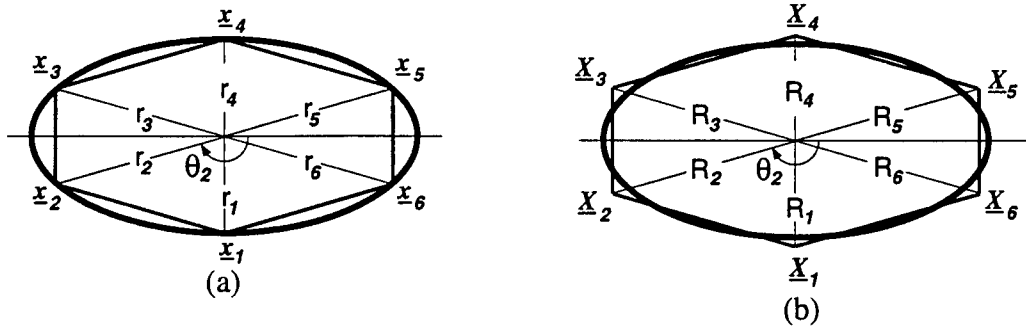
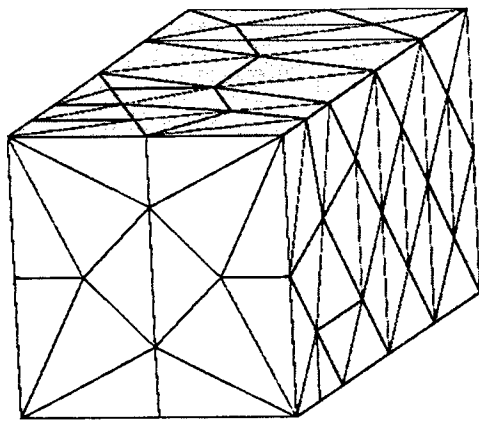
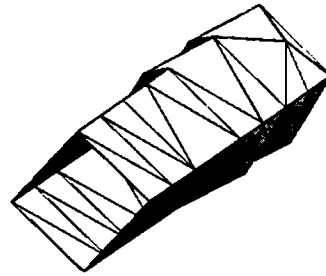


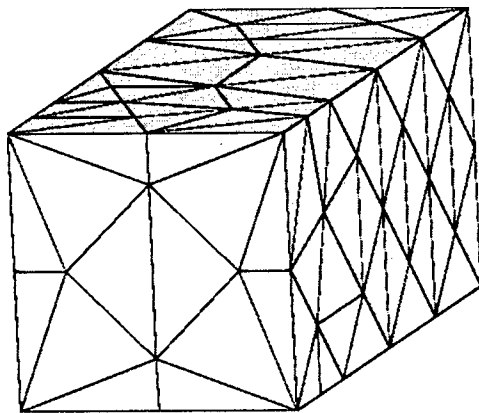
Figure 11. Cross section of an ellipsoidal fiber bundle. (a) Inscribed discretization, and distance to mesh vertex. (b) Distance to relocated vertex.



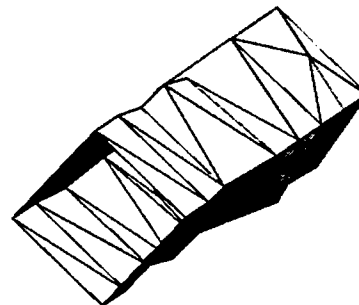
(a)



(b)

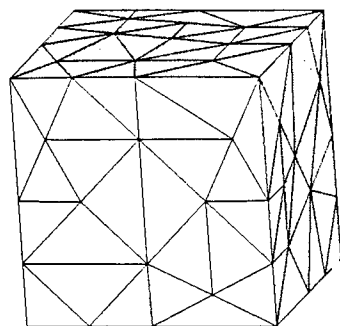


(c)

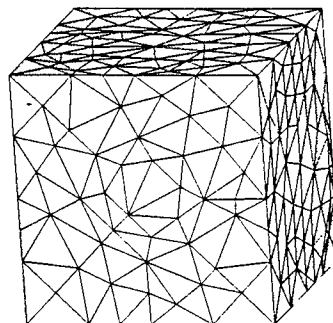


(d)

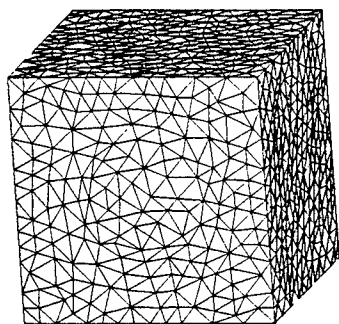
Figure 12. Single fiber bundle example meshes. (a)Exterior mesh faces of initial mesh (31.6% bundle volume fraction error). (b)Initial mesh faces classified on interior fiber bundle surface. (c)Exterior mesh faces of adjusted mesh (-0.3% bundle volume fraction error). (d)Adjusted mesh faces classified on interior fiber bundle surface.



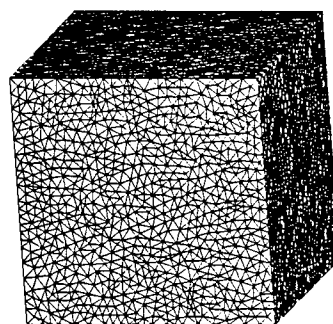
(a)



(b)

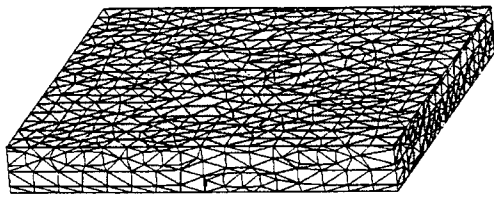


(c)

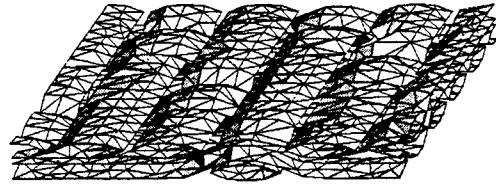


(d)

Figure 13. Finite element meshes of the single fiber bundle model. (a)93 vertices and 284 elements. (b)576 vertices and 2,549 elements. (c)4,156 vertices and 21,951 elements. (d)20,615 vertices and 110,638 elements.



(a)



(b)

Figure 14. Coarse mesh of base two satin weave model.  
(a) External mesh faces. (b) Fiber bundle surface mesh faces.



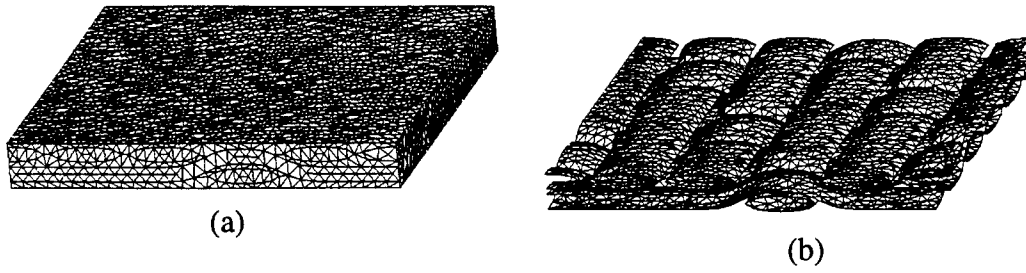


Figure 15. Medium mesh of base two satin weave model.  
(a)External mesh faces. (b)Fiber bundle surface mesh faces.

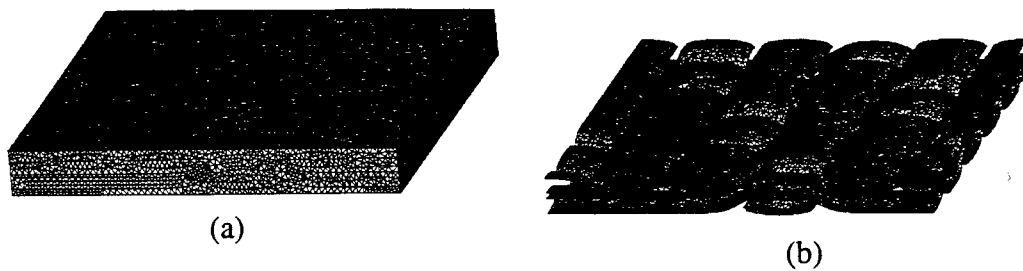
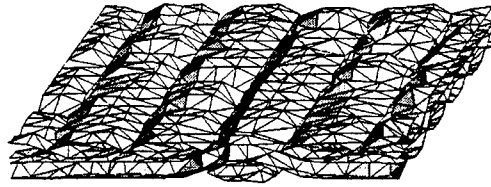
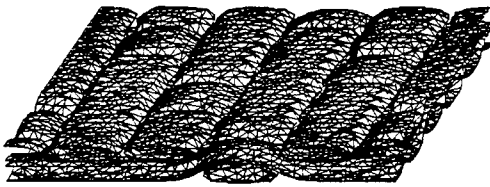


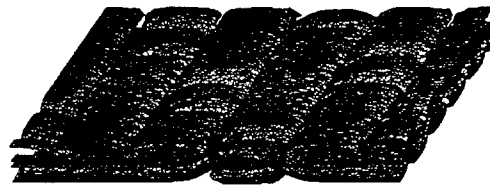
Figure 16. Fine mesh of base two satin weave model.  
(a)External mesh faces. (b)Fiber bundle surface mesh faces.



(a)



(b)



(c)

Figure 17. Fiber bundle surface mesh faces of meshes corrected to 0.55 volume fraction. (a)Coarse mesh. (b)Medium mesh. (c)Fine mesh.

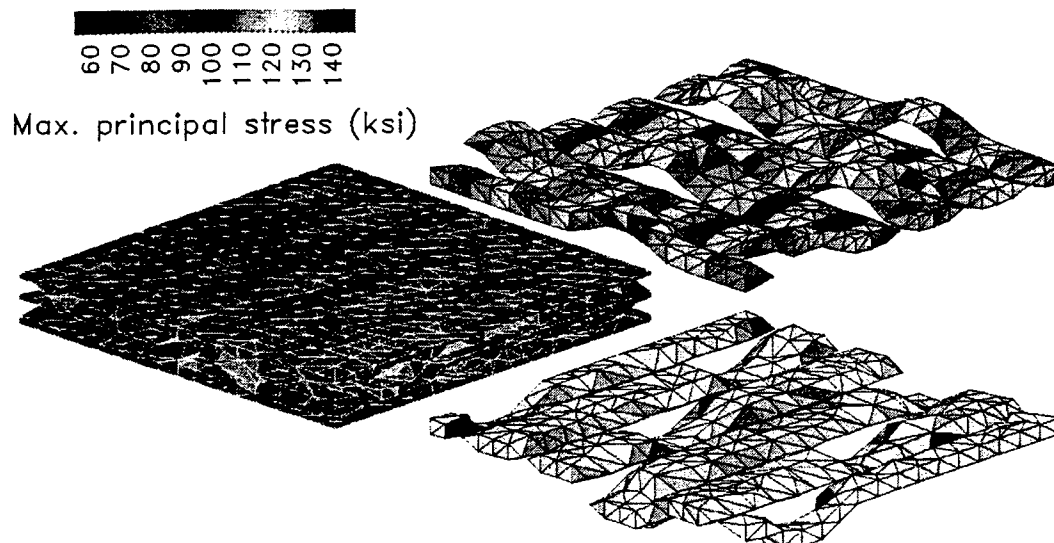


Figure 18. Maximum principal stress values in a base two satin weave composite resulting from a uniaxial x-direction stress of 100 ksi applied to the homogenized material (Coarse mesh). The peak stress in the warp bundles is 148.0 ksi

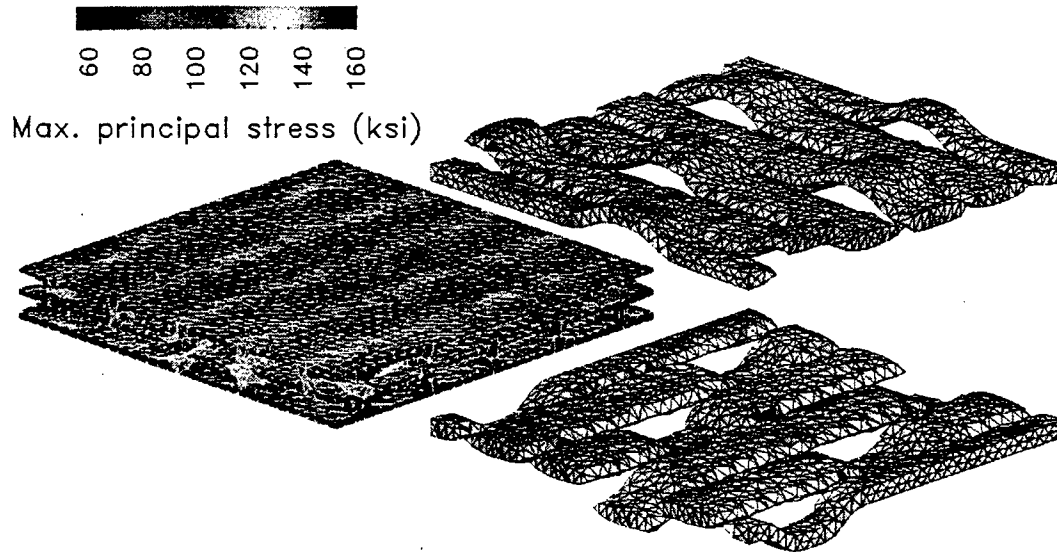


Figure 19. Maximum principal stress values in a base two satin weave composite resulting from a uniaxial x-direction stress of 100 ksi applied to the homogenized material (Medium mesh). The peak stress in the warp bundles is 160 ksi.

## REPORT DOCUMENTATION PAGE

Form Approved  
OMB No. 0704-0188

1a. REPORT SECURITY CLASSIFICATION Unclassified			1b. RESTRICTIVE MARKINGS		
2a. SECURITY CLASSIFICATION AUTHORITY			3. DISTRIBUTION / AVAILABILITY OF REPORT  Unrestricted		
2b. DECLASSIFICATION / DOWNGRADING SCHEDULE					
4. PERFORMING ORGANIZATION REPORT NUMBER(S)			5. MONITORING ORGANIZATION REPORT NUMBER(S)		
6a. NAME OF PERFORMING ORGANIZATION CENTER FOR COMPOSITE MATERIALS AND STRUCTURES - RENSSELAER POLYTECHNIC INSTITUTE		6b. OFFICE SYMBOL (If applicable)	7a. NAME OF MONITORING ORGANIZATION  OFFICE OF NAVAL RESEARCH		
6c. ADDRESS (City, State, and ZIP Code)  RENSSELAER POLYTECHNIC INSTITUTE TROY, NEW YORK 12180-3590			7b. ADDRESS (City, State, and ZIP Code)  800 NORTH QUINCY STREET ARLINGTON, VA 22217-5000		
8a. NAME OF FUNDING / SPONSORING ORGANIZATION DEFENSE ADVANCED RESEARCH PROJECTS AGENCY		8b. OFFICE SYMBOL (If applicable)	9. PROCUREMENT INSTRUMENT IDENTIFICATION NUMBER  #N00014-92J-1779		
8c. ADDRESS (City, State, and ZIP Code)  1400 WILSON BLVD. ARLINGTON, VA 22209			10. SOURCE OF FUNDING NUMBERS		
			PROGRAM ELEMENT NO.	PROJECT NO.	TASK NO.
11. TITLE (Include Security Classification)  MECHANISM-BASED DESIGN OF COMPOSITE STRUCTURES					
12. PERSONAL AUTHOR(S)  George J. Dvorak					
13a. TYPE OF REPORT FINAL		13b. TIME COVERED FROM 920501 TO 970830		14. DATE OF REPORT (Year, Month, Day) 970930	
15. PAGE COUNT 698					
16. SUPPLEMENTARY NOTATION					
17. COSATI CODES			18. SUBJECT TERMS (Continue on reverse if necessary and identify by block number)		
FIELD	GROUP	SUB-GROUP	HIGH TEMPERATURE COMPOSITES, COMPUTER-AIDED DESIGN, PROCESSING, PERFORMANCE		
19. ABSTRACT (Continue on reverse if necessary and identify by block number)  Final results obtained on the Mechanism-Based Design of Composite Structures Program at Rensselaer Polytechnic Institute, are described in three volumes. Volume one contains the Executive Summary and reprints of papers on Micromechanics and Computer-Aided Design Tools. Volume two is a continuation of reprints of papers on Micromechanics and Computer-Aided Design Tools. The third Volume contains reprints of papers on Processing and Performance.					
20. DISTRIBUTION / AVAILABILITY OF ABSTRACT <input checked="" type="checkbox"/> UNCLASSIFIED/UNLIMITED <input type="checkbox"/> SAME AS RPT. <input type="checkbox"/> DTIC USERS			21. ABSTRACT SECURITY CLASSIFICATION Unclassified		
22a. NAME OF RESPONSIBLE INDIVIDUAL			22b. TELEPHONE (Include Area Code)		22c. OFFICE SYMBOL